Failure Mechanisms in the Valve Regulated Lead/acid Battery

Ball, Richard

Award date:
2000

Awarding institution:
University of Bath

Failure Mechanisms in the Valve Regulated Lead/acid Battery

Ball, Richard

Award date:
2000

Awarding institution:
University of Bath

Failure Mechanisms in the Valve Regulated Lead/acid Battery

Richard James Ball

2000

Failure Mechanisms in the Valve Regulated Lead/acid Battery

submitted by Richard James Ball
for the degree of Doctor of Philosophy
of the University of Bath
2000

……

Acknowledgements

I would like to thank my academic supervisor Prof. Ronald Stevens for his encouragement and guidance throughout the course of this work. Thanks are also due to Hawker Energy Products for funding this project and both Dr Rodri Evans and Dr Raju Kurian, of Hawker Energy, for many useful discussions and advice over the past three years.

I am also extremely grateful to Hugh Perrott, Glynn Love and Ursula Potter from the Centre for Electron Optical Studies, University of Bath, for their help and advice during sample preparation and analysis. Acknowledgement must also be given to the Engineering and Physical Sciences Research Council who have provided funding for much of the electron optical/analytical equipment utilised. Special thanks are due to Barry Chapman, from the Department of Physics, for his assistance and advice with x-ray diffractometry.

I would particularly like to thank Mark Deven for his invaluable help and advice, concerning the metallographic preparation of samples and Buehler/Krautkramer, Coventry, for the use of their polishing equipment, without which many of the cross-sectional images would not have been possible.

Thanks are also extended to Chris Arnold for his help and assistance with mechanical testing, and Frank Hammett, and Ian Trussler for their advice on the fabrication of many essential items in the university workshop.

I would also like to thank Dr Richard England for the use of the diffusion rig in his laboratory and Fernando Acosta and Sungsoo Kim for their essential help in modifying the rig and getting it to work.

Finally I would like to thank my parents for their financial assistance and support during the last three years.

On a lighter note I would also like to thank Yeunwoo Chung and Andy Brown for showing me that the working day does not necessarily start in the morning and that there is more than one type of single malt!

Abstract

Recent advances in lead/acid battery technology have resulted in the development and widespread use of the valve regulated lead acid (VRLA) battery. The major differences between the VRLA, and traditional flooded design, is the use of an immobilised electrolyte and inclusion of a gas release valve. These features allow the oxygen recombination reaction to occur. Advantages of this battery type include low maintenance and the ability to operate in any orientation. Typical applications include, standby power supplies, SLI (starting, lighting and ignition) and electric vehicle power.

This programme of work has investigated a number of design and operational features that determine VRLA battery performance. These include grid alloy composition, positive active material composition and separator paper type. Specimen batteries were cycled using a C5 cycling regime until the failure point, at 80% of original capacity, was reached. Following cycling batteries were dismantled and the cells exhibiting the most and least reduction in voltage during a constant current discharge extracted. Removed cells were subsequently examined using a range of analytical techniques to establish the cause of failure and determine the relative operational characteristics of battery variants.

The main analytical techniques used to examine positive and negative electrodes were, light and electron microscopy, electron probe microanalysis, x-ray diffraction and metallographic techniques. This involved examination of both active materials and positive grid corrosion layers. Correlation between current density and corrosion layer thickness on the positive electrode grid was established using a numerical modelling technique. Finally, a number of different separator paper types were examined using electron microscopy. The diffusive and compressive properties of the sample separator papers were characterised at varying saturation levels using specifically designed equipment.

Table of Contents

List of Figures

List of Tables

1 General Introduction

Valve regulated lead acid (VRLA) batteries first appeared on the market several decades ago. Since their arrival improvements in design have lead to greater performance compared to the more traditional flooded design. Valve regulated cells differ from flooded cells in a number of respects, the prime ones are principally immobilised electrolyte and the presence of a Bunsen valve which seals the battery allowing only hydrogen gas to escape during operation. These features result in making the battery virtually maintenance free and giving it the ability to operate efficiently in any orientation.

Factors such as component design, materials selection and manufacturing methods influence the operational characteristics of the battery. Changes can be made to the battery design allowing tailoring of characteristics to optimise performance for specific applications. This versatility has allowed VRLA batteries to be utilised in a variety of diverse applications such as standby power supplies, starting, lighting and ignition, and electric vehicles.

The objective of the work was to gain a better understanding of the processes occurring within the battery during operation by investigating the influence of different materials on performance. Research has centred on the analysis of a number of test batteries, all of which were manufactured at Hawker Energy, Newport. The baseline product design adopted for manufacture of test batteries was the SBS40 (Sealed Battery System, 40 Amp hour) valve regulated lead acid battery.

Batteries were cycled using computer controlled Digitron charge/discharge equipment. Cells of failed batteries were subsequently monitored over a discharge/charge cycle using data loggers measuring voltage to establish the relative state of each cell. This allowed the best and worst performing cells, within the battery, to be identified for subsequent detailed examination and analysis. Information on the behaviour of individual electrodes was obtained for a number of battery samples by measuring the potential, relative to a mercury sulphate reference electrode, during a discharge/charge cycle.

Following completion of the electrical testing phase of analysis, batteries were dismantled and the active materials and components such as the grid and separator papers characterised. Important properties of active materials are structure and composition as these influence operation. Structural and morphological information was obtained using both scanning and transmission electron microscopes. BET surface areas were also obtained and pycmnometric

density and four point conductivity measurements were taken for a number of samples. The main source of compositional information was from x-ray diffraction. However, for increased accuracy, a wet chemical analysis was used for quantifying the amount of lead present.

During operation and especially during overcharging, corrosion of the positive grid occurs. This affects battery performance as the resistance of the electrode increases due to the reduced cross-sectional area of the grid wires and the formation of a non-conducting lead monoxide surface layer. The approach adopted for characterising corrosion layers was to produce a cross-section of the grid wire for analysis. This was achieved using either a metallographic grinding and polishing method or an ultra microtoming technique. Once high quality cross sections of the grid and associated corrosion layers were obtained, light and electron microscopy were used to produce images of the corrosion layer structure. Electron probe microanalysis was employed to obtain quantitative compositional information. Corrosion layer thickness was determined from digital images analysed using Optimas image analysis software.

Observations of corrosion layers indicated that in a number of cells the thickness of the layer varied depending on the location around the grid wire periphery. A finite element model was set up using ANSYS to check for correlation between corrosion layer thickness and current density. The model was then used to demonstrate the effect of changing grid and active material geometry on current density. This illustrated the potential for changes to grid wire and associated active material geometry to mitigate the effects of failure from corrosion.

Battery components such as the separator paper, which do not react chemically within the battery, were demonstrated to have a significant influence on cycling performance. Batteries containing different separator paper designs were cycled to failure and their relative performances compared. The separator papers used in the manufacture of the test batteries were characterised using a number of different techniques. These included wicking tests, pore size distribution and scanning electron microscopy. The effects of saturation on separator diffusivity and compressive characteristics were also investigated. Measurement of both of these properties involved the use of specially designed equipment.

The final part of the thesis comprises a general discussion and recommendations for further work.

2 LITERATURE REVIEW

2.1 INTRODUCTION

As an introduction to this project the following chapter presents a review of the literature which is of relevance to current work. A general overview of the main uses and applications of valve regulated lead acid batteries is given in the initial section. Following from this, descriptions of the fundamental electrochemical reactions that occur during the various stages of manufacture and battery operation are described. Each step in the battery processing method is discussed with details of variations in procedure where appropriate. The influence of each component used in the manufacture of a battery in terms of its effect on operation and performance is described. Finally, all major battery components are discussed in terms of material, chemical and structural properties, with particular reference paid to manufacturing methods and techniques utilised in their production.

2.2 ASPECTS OF THE VALVE REGULATED LEAD ACID BATTERY

2.2.1 THE DESIGN OF THE VALVE REGULATED LEAD ACID BATTERY

The design of the VRLA battery is very similar to that of the conventional lead acid battery where each cell consists of interleaved positive and negative plates. The electrochemical reactions that generate the current are also the same, comprising of the oxidation of lead and reduction of lead dioxide. However, there are a number of important differences. The most prominent of these being the recombination of oxygen at the negative electrode. The presence of this reaction is indicated from the common terms used to describe this battery type such as ‘recombinant lead acid battery’.

In addition to the differences in internal chemistry the physical construction of the battery varies as well. The most visible difference from a conventional battery being a pressure valve that allows gases produced during battery operation to escape. Consequently this valve is necessary for the oxygen recombination reaction to occur. Another difference, which is perhaps not so obvious, is the immobilisation of electrolyte. This is achieved by either the addition of additives to form a gel, or the use of a porous separator paper.

Additional names used to describe valve regulated lead acid batteries also include; maintenance-free, sealed, recombinant-electrolyte, starved electrolyte and immobilised electrolyte batteries [1].

2.2.2 ADVANTAGES OF THE VRLA BATTERY

The performance of the conventional lead acid battery was initially better than early valve regulated batteries, which had a shorter cycle life and inferior low-rate performance. Today, VRLA batteries are capable of providing superior performance when compared to conventional designs. This is partly due to advances in design but also as their use has become more widespread, increasing familiarity has reduced instances of abuse and incorrect use that limit performance [2,3,4]. Current VRLA batteries have the advantages of requiring no water maintenance and there is little chance of acid spill and negligible emission of hydrogen. No special ventilation is needed and minimal overcharge is required at normal temperatures. Transportation is easy and operation when tilted at an angle is possible. However, there is also a number of disadvantages. The batteries are not as resistant to overcharge as flooded cells and must be charged very carefully to maximise service life. The specific gravity of the electrolyte cannot be measured and there is a limited shelf life of two years. There is also an increased risk of thermal runaway. The advantages and disadvantages are summarised in Table 2.1:

Table 2.1: Advantages and Disadvantages of VRLA batteries with respect to flooded-electrolyte batteries [5].

Advantages	Disadvantages
No water addition	Careful charging required
No acid spillage	Thermal management is more critical, especially for AGM batteries
Negligible acid fumes	Significant variation in top of charge voltages
Easy transport	Increase in overcharge required at elevated temperatures
No special ventilation requirements	Deep-cycle life often inferior under optimum operating conditions
Can be operated horizontally	Cannot measure specific gravity
Smaller footprint (batteries can be multi-stacked)	Not available in dry charge state
Negligible acid stratification (gel-type only)	Shelf life of two years maximum
Less overcharge required at room temp	
Good high rate, discharge capacity (Absorptive Glass Mat type only)	

2.2.3 APPLICATIONS OF VALVE REGULATED LEAD ACID BATTERIES

Lead acid batteries can be used in a large number of applications. These include for example, remote area power supplies, aircraft starting, emergency lighting, portable equipment and telecommunications. Depending on the application, the operating conditions can vary

enormously. Factors such as discharge rates and depth of discharge can have a large impact on the mechanisms occurring in the battery. Generally these different applications can be divided into three main categories, details of which are given below.

- **Starting, Lighting and Ignition (SLI)**

  This category includes the type of batteries found under the bonnet of a car. The battery must be capable of operating in cold winter conditions initially to start the engine, but then operate at much higher temperatures once the engine has warmed up. Starting an engine involves drawing a high current for a short period, the battery must therefore resist repeated high discharge rates.

- **Motive Powers**

  This type of battery would be used to power electric vehicles such as small motorcycles, cars and agricultural machinery [6,7]. In comparison to the SLI batteries, these must be capable of resisting the damaging effects of repeated cycling to high depths of discharge, approximately 80%, at moderate temperatures. An additional important property is the capability to be recharged in as little a time as possible. Suzuki, [8] among other researcher's [9] has highlighted the importance of these batteries with respect to growing environmental concerns. Government programmes aimed at reducing pollution from vehicles are increasing motivation to improve battery designs [10]. The need for reliable portable power supplies in the future is of great importance and these batteries will play an important role in supplying the increasing demand [11].

- **Uninterruptible power supplies (UPS)**

  These are used in standby applications for powering computer or telecommunication systems and hospitals, etc. when the normal supply is interrupted. The duration of power supply may be a few minutes while backup generators are started or in the case of a computer system, for instance, 10-15 minutes while computer files are saved and the system is shut down. Due to the nature of this application, the battery may only be used a relatively few times during its service life compared to other types of battery. In order to combat the degenerative effects of the self-discharge reactions the battery will be subject to continual float charging or periodic top-up charges. Discharge rates and depths may also vary depending on the exact nature of the application. Fluctuation in operating temperature would be expected to be low.

2.3 ELECTROCHEMISTRY OF THE LEAD ACID BATTERY

In order to understand the operation of the lead acid battery it is necessary to have knowledge of the electrochemical processes at work. In this section a brief outline of the various reactions during charge and discharge in relation to thermodynamic and kinetic parameters will be given. Battery properties such as capacity and cycle life will also be described in terms of the electrochemical processes.

2.3.1 FUNDAMENTALS OF THE BATTERY

During discharge a battery converts chemical energy stored in the active materials into electrical energy. A rechargeable battery then has the ability to use electrical energy from an external power source to reverse the discharge chemical reactions allowing the battery to be reused. In the case of the lead acid battery, the chemistry can be described in terms of a galvanic cell. This comprises of two dissimilar electrodes submerged in a conducting medium such as a fused salt, or as in the case of the lead acid battery a liquid electrolyte.

The electric current produced during battery operation can be explained in terms of the Fermi levels of the materials in the electrodes. The Fermi level corresponds to the maximum energy of a valence electron in the conduction band. When two materials with different Fermi levels are bridged, electrons flow from the material with the highest Fermi level to that with the lowest. A potential difference results due to the electron transfer and separation of charge. The consequence of this is that the materials used in the construction of the battery define the voltage that the cell will produce. For the lead acid battery this is approximately 2.1V.

2.3.2 CHARGE / DISCHARGE REACTIONS

The electrochemical reactions that occur in the lead acid battery involve oxidation of lead at the negative electrode and the reduction of lead at the positive electrode. These reactions can be represented by the equations shown below [12].

Oxidation $Pb \Leftrightarrow Pb^{2+} + 2e^-$ (2.1)

Reduction $Pb^{4+} + 2e^- \Leftrightarrow Pb^{2+}$ (2.2)

Equations 2.1 and 2.2 can be combined to give the following half reactions.

Neg. electrode $Pb + H_2SO_4 \Leftrightarrow PbSO_4 + 2H^+ + 2e^-$ (2.3)

Pos. electrode $PbO_2 + H_2SO_4 + 2H^+ + 2e^- \Leftrightarrow PbSO_4 + 2H_2O$ (2.4)

Because Pb2+ ions have a very low solubility in sulphuric acid and Pb4+ ions only occur in compound form, a more realistic representation of the electrode reactions shown above is their combination to the overall cell reaction:

$$Pb + PbO_2 + 2H_2SO_4 \Leftrightarrow 2PbSO_4 + 2H_2O \qquad (2.5)$$

Further modification of the equation to take into account the dissociation of sulphuric acid in water leads to the following equation.

$$Pb + PbO_2 + 2H^+ + 2HSO_4^- \Leftrightarrow 2PbSO_4 + 2H_2O \qquad (2.6)$$

Discharging a lead acid battery results in the accumulation of lead sulphate on the negative and positive plates. During charging the reactions are reversed and the sulphate and basic sulphates are converted back into lead and lead dioxide. Equation 2.7 shows the conversion of lead sulphate into lead and sulphuric acid. This reaction occurs at the negative electrode.

$$PbSO_4 + 2H^+ + 2e- \rightarrow H_2SO_4 + Pb \qquad (2.7)$$

At the positive electrode lead dioxide is reformed from lead sulphate and water. This is shown in equation 2.8, below.

$$PbSO_4 + 2H_2O \rightarrow PbO_2 + H_2SO_4 + 2e^- + 2H^+ \qquad (2.8)$$

When equations 2.7 and 2.8 are combined, an equation for the overall reaction is produced showing the conversion of leads sulphate and water to lead at the negative electrode, lead dioxide at the positive electrode and sulphuric acid in the electrolyte.

$$2PbSO_4 + 2H_2O \rightarrow Pb + PbO_2 + 2H_2SO_4 \qquad (2.9)$$

Figure 2.1 summarises how the proportions of the various compounds change during the different stages of cycling.

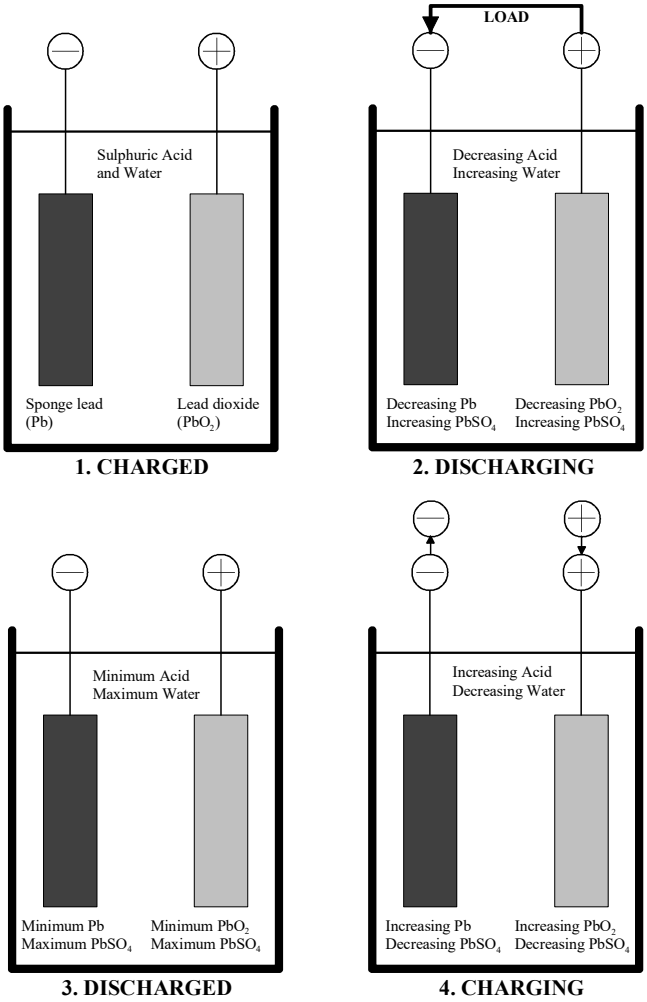

Figure 2.1: Chemical reactions in a lead-acid battery during charge and discharge

During discharge of the battery, sulphuric acid is converted into water. This produces a variation in acid concentration thereby allowing the battery's state of charge to be determined from the specific gravity or density of the electrolyte.

2.3.3 OXYGEN RECOMBINATION

The valve regulated lead acid battery works on the principle of the internal oxygen cycle [13]. During charging of the battery and especially during over charging when the plates are almost totally charged, oxygen will be evolved at the positive electrode. This is produced by the electrolysis of water and the reaction can be written as follows:

$$H_2O \rightarrow \frac{1}{2} O_2 + 2H^+ + 2e^- \qquad (2.10)$$

Some of the oxygen evolved will diffuse to the positive grid and react to form the lead oxide corrosion layer according to the reactions such as those below:

$$\frac{1}{2} O_2 + Pb \rightarrow PbO \qquad (2.11)$$

$$2OH^- + PbO \rightarrow PbO_2 + H_2O + 2e^- \quad (2.12)$$

The remaining oxygen will either escape from the battery through the valve in the lid or diffuse into the negative electrode and recombine to form water. Pavlov [14] suggests that this can be either a purely electrochemical reaction or a combined chemical and electrochemical reaction, see equations below:

- $\frac{1}{2} O_2 + 2H^+ + 2e^- \rightarrow H_2O$ (electrochemical reaction)

(2.13)

- $\frac{1}{2} O_2 + Pb \rightarrow PbO$ (chemical reaction)

  $PbO + H_2SO_4 \rightarrow PbSO_4 + H_2O$ (chemical reaction)

  $PbSO_4 + 2e- + 2H^+ \rightarrow H_2SO_4 + Pb$ (electrochemical reactions)

(2.14)

The extent to which grid corrosion occurs will be determined by the amount of oxygen that reaches the positive grid. This is consequently related to the amount that recombines at the negative electrode or escapes.

The ease by which oxygen can reach the negative electrode has been described by Matthes [15] in terms of the battery parameters summarised below. Since the proportion of oxygen that reaches the negative electrode is inversely proportional to the amount that reaches the positive grid, these also have a direct influence on grid corrosion in addition to recombination efficiency.

- Ease of oxygen transport out of positive active material
- Positive to negative electrode spacing or separator thickness
- Separator saturation
- Separator tortuosity
- Surface area of negative electrode
- Presence of electrolyte film on negative electrode

When the rate of oxygen recombination at the negative electrode is comparable to oxygen evolution at the positive, the majority of oxygen generated will recombine to form water. If oxygen evolution rates are greater than recombination rates the resulting increase in oxygen gas within the cell will promote grid corrosion and oxygen escape through the valve.

An additional consequence of high recombination efficiency is an increase in the potential of the positive electrode. This can result in a higher charging efficiency, however an additional effect is a shift of the negative electrodes potential to a value where charging is less efficient. In practice partially charged negative electrodes are sometimes observed in batteries that have been float charged for long periods.

2.3.4 SELF DISCHARGE REACTIONS

In order for a battery to operate efficiently the active materials should only react during discharge, while generating external current, or during the charging reaction. In practice additional reactions, called self-discharge reactions, occur. These are due to the fact that both lead and lead dioxide are thermodynamically unstable in the battery at open circuit potential. When a battery is left these reactions will convert the current generating active materials into lead sulphate. The major reactions at each electrode are shown below:

Positive electrode $PbO_2 + H_2SO_4 \rightarrow PbSO_4 + H_2O + ½O_2$ (2.15)

Negative electrode $Pb + H_2SO_4 \rightarrow PbSO_4 + H_2$ (2.16)

In practice these reactions can usually be reversed by charging, however this is not possible if the sulphate particles are too big, or isolated from the current conducting active material. The lead sulphate produced coats the plates giving them a white appearance. Plates in this condition are commonly referred to as being ‘sulphated’.

The rate of self-discharge is usually slow and accounts for a capacity loss of less that 0.2% a day. Increasing the acid concentration or temperature can accelerate the self-discharge reaction rate. It is also increased by the presence of some impurities. Self-discharge is the greatest problem in batteries used in standby applications where they might be left at open circuit voltages for long periods. A common method used to reduce the effects of self-discharge is to continuously trickle charge the battery.

2.3.5 THERMODYNAMICS OF THE LEAD ACID BATTERY

The thermodynamic state of the battery influences the reactions that occur. Figure 2.2 shows a summary of the reactions at the cathode and anode in terms of thermodynamic parameters in relation to electrode potential. Equilibrium potentials are shown as framed numbers and polarisation as η_+ and η_- where is η is the over/under potential.

Equilibrium potentials of the charge/discharge reactions, $Pb/PbSO_4$ and $PbSO_4/PbO_2$, are represented in the diagram by columns thus indicating their dependence on acid concentration. The equilibrium potentials correspond to an acid density of 1.23 g/cm^3.

In addition to the charging and discharging reactions a number of secondary reactions are possible, shown in Figure 2.2. The secondary reactions occur because their equilibrium potentials are within the potential range covered by the voltage in the battery cell. These reactions are explained in greater detail below.

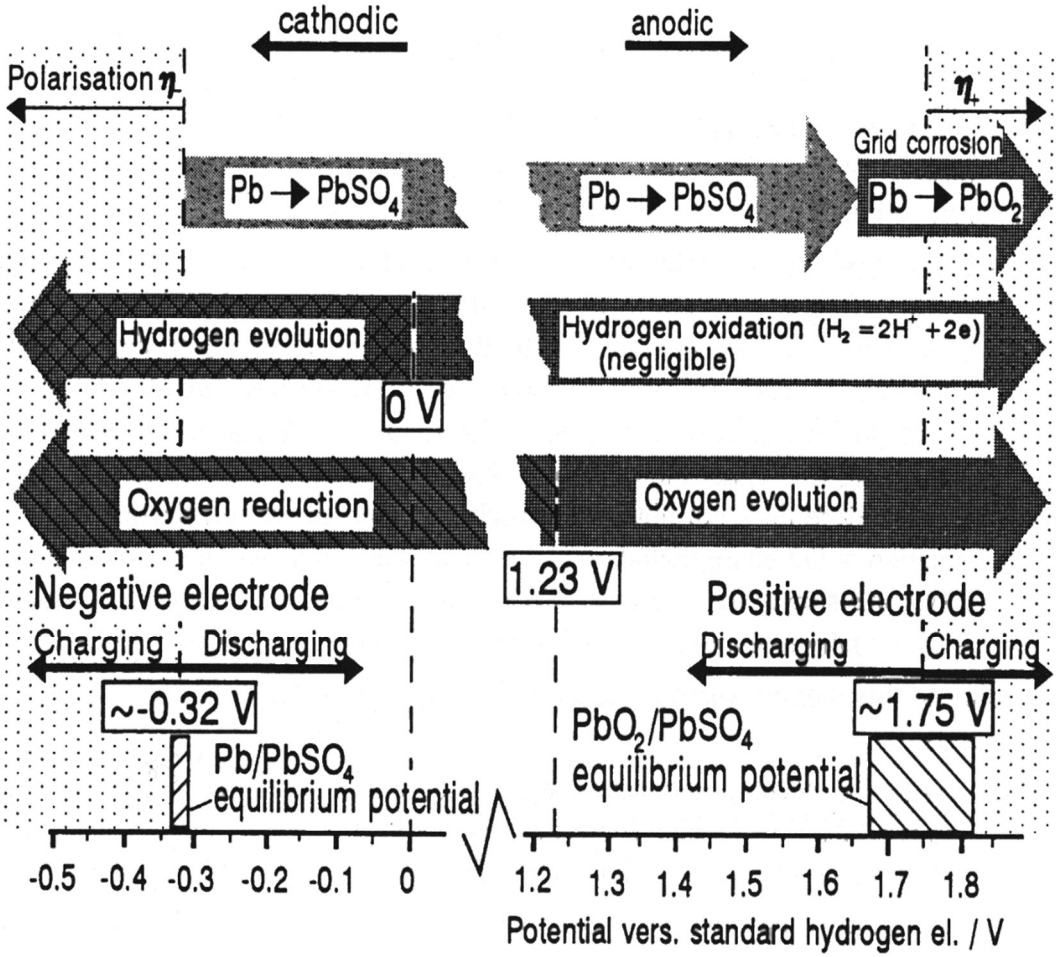

Figure 2.2: Reactions that occur in lead-acid batteries dependent on electrode potential [16]

- Hydrogen evolution occurs at electrode potentials below 0V. The open circuit potential of the negative electrode is about 0.3V below this.
- Oxygen evolution occurs when the electrode potential is greater than 1.23V. The positive electrode potential is about 0.5V above this.
- Oxygen reduction is possible below 1.23V against a standard hydrogen electrode. Oxygen produced at the positive electrode is reduced at the negative electrode. This reaction establishes the internal oxygen cycle in valve regulated batteries.

- Hydrogen oxidation is possible above 0V but is hindered due to the high hydrogen over potential on the PbO_2 surface to such an extent that it can be neglected. This means that hydrogen produced during operation of a VRLA battery will escape through the valve.
- Lead corrosion on the positive battery grid normally occurs at potentials around the $PbO_2/PbSO_4$ equilibrium potential during charging. The lead oxide corrosion layer formed is a conductor and therefore does not hinder the other electrochemical processes in the battery. The corrosion layer can act as a protective barrier to a certain extent, although the situation at the phase boundary is unstable and corrosion will penetrate slowly into the grid.

If the lead acid battery system is considered from a thermodynamic standpoint, it is unstable. This is due firstly to unavoidable water decomposition caused by the evolution of gas [17] and secondly, the corrosion of lead to PbO_2, which occurs when all conducting elements are connected to the positive electrode. In the case of water decomposition the kinetics of the reactions are slow and a small amount of water loss can be tolerated during the life of a battery. The corrosion of grid wires is potentially a very serious problem. However, the corrosion rate is reduced due to passivation and its long-term effect on battery performance is decreased.

2.3.6 KINETICS OF THE LEAD ACID BATTERY

During operation of the lead acid battery the active materials participating in the reactions do so in the dissolved state. Products of the reactions are precipitated from the electrolyte, in the form of solids, back onto the surface of the active material. The various steps in these reactions are shown in Figure 2.3.

During discharging, electrons flow from the negative to the positive electrode. This is a result of the oxidation of Pb at the negative and reduction of Pb^{4+} at the positive. Both of these reactions result in the formation of Pb^{2+} ions that are dissolved in the electrolyte, adjacent to the electrodes. The negative charge transfer is equal to the number of electrons that have moved between the electrodes.

Due to the presence of HSO_4^- or SO_4^{2-} ions, from the acid, the lead ions have a limited solubility. As a result, the sulphate ions react immediately with the lead ions forming lead sulphate, most of which is precipitated within the pore system. An additional reaction that occurs at the positive electrode during discharge is the formation of water, by the reaction of O_2^- ions, released from the lead dioxide and protons from the acid.

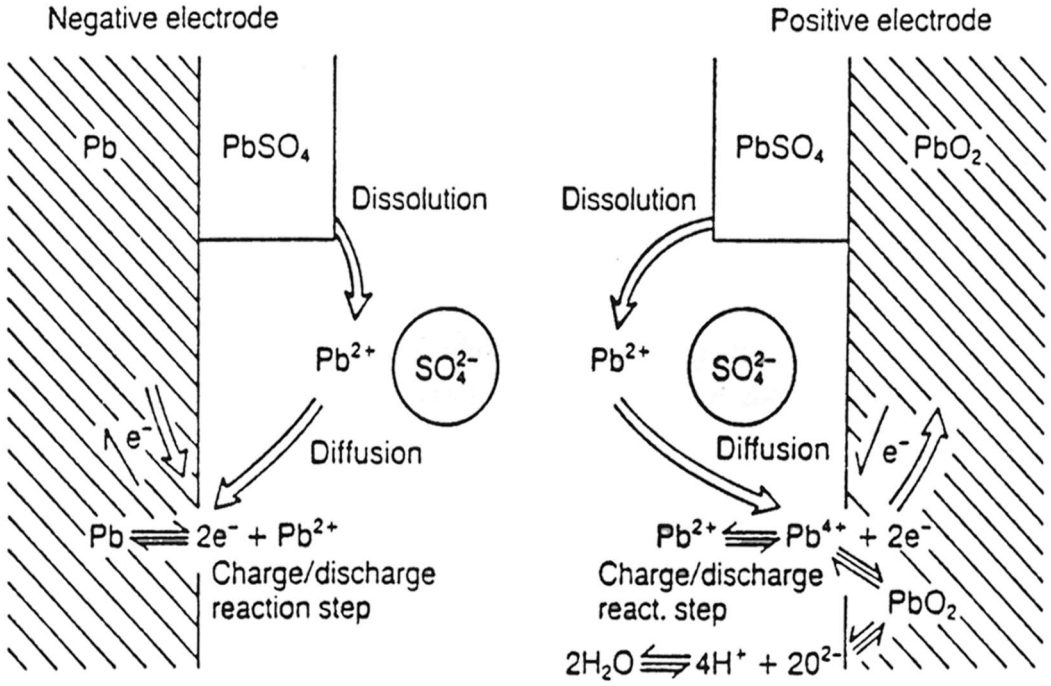

Figure 2.3: Reaction steps in the lead acid battery [18]

During charging the reactions occur in the opposite direction. Lead and lead dioxide is formed from lead sulphate. For this to take place the dissolution of the lead sulphate on each of the electrodes is necessary. The reformation of lead at the negative and lead dioxide at the positive can only occur with the flow of electrons. Since lead sulphate is a non-conductor the lead ions must diffuse to the electrode surface where electrons can be accepted, in the case of the negative, or donated in the case of the positive.

It is apparent that the operation of the lead acid battery is highly dependent on the transportation of dissolved ions through the electrolyte. The majority of the material transport occurs over the micrometre range. Limitation in battery performance caused by transportation is most noticeable as a reduction in the amount of available energy with increased load. As discharge current is increased there is not only a reduction in cell voltage, but the ampere hours delivered by the battery is reduced. This reduction in energy is a result of increased internal resistance and decreased active material utilisation which can be accounted for by the limiting diffusion rates, or the covering of active material by a layer of sulphate. At high rates of discharge, this is a particular problem because the high concentrations of lead ions leads to the formation of a compact sulphate layer that grows quickly.

2.3.7 CYCLE LIFE

Cycle life is defined as the number of discharge/charge cycles the battery can sustain before failure is encountered. This is normally taken as the point where the capacity drops below a predefined limit. The main causes of failure, which can be associated with cycles, are positive active material shedding and grid corrosion. An important factor that determines the severity of these mechanisms is the depth of discharge (DOD). DOD is the percentage of the available electrical energy taken from a battery for a given discharge rate. For example, 50% DOD at *x*Ah would mean that half the available energy, at a discharge rate of *x*Ah, had been used. Generally the deeper a battery is discharged the fewer the cycles to failure. This is because more of the active material is converted into lead sulphate and the changes in active material structure at the end of each cycle are increased. This is illustrated in Figure 2.4, which shows the cycle life versus depth of discharge for a sealed lead acid battery [19].

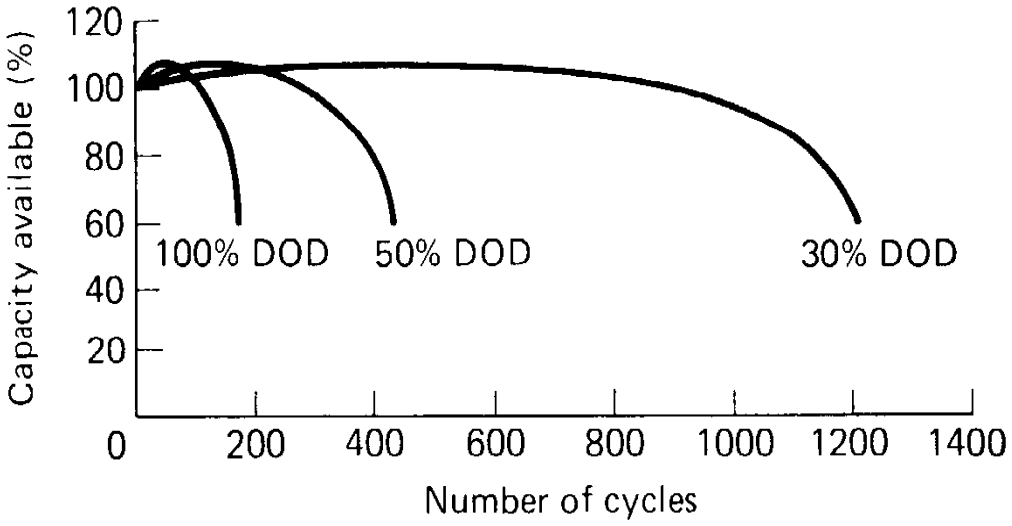

Figure 2.4: Capacity versus cycle life for various depths of discharge

The relationship of positive active mass structure and cycle life has been studied by Caulder and Simon [20]. They concluded that this was an important factor in the reduction of cycle life and loss of capacity. A mechanism in which electrochemically active lead dioxide is transformed into an inactive form has been suggested. This is believed to be due to structural reordering resulting in the loss of hydrogen species. A more detailed explanation is given in section 2.6 of this review.

2.4 A DESCRIPTION OF THE PROCESSES INVOLVED IN BATTERY MANUFACTURE

A lead acid battery comprises of one or more cells, each of which comprises positive and negative plates stacked alternately. Each plate consists of a lead grid, which supports the active material and provides a means of current collection. Ionic conduction between the plates is achieved via an electrolyte held in a separator paper. The components of each cell are housed in a corrosion resistant box with a separate compartment for each cell.

The voltage produced by each cell is approximately 2.1V. This is determined by the electrode materials used rather than the configuration. Negative electrodes consist of a very porous form of lead, commonly referred to as sponge lead and the positives of lead dioxide. Both of these materials are formed from lead monoxide during the 'formation' stage of battery manufacture as this method of production allows the high surface areas required to be attained. Electrodes are then immersed in a sulphuric acid electrolyte. The production processes used to manufacture the components are described in the following section. Figure 2.5 shows a flow chart representing the process used by Hawker Energy, Newport.

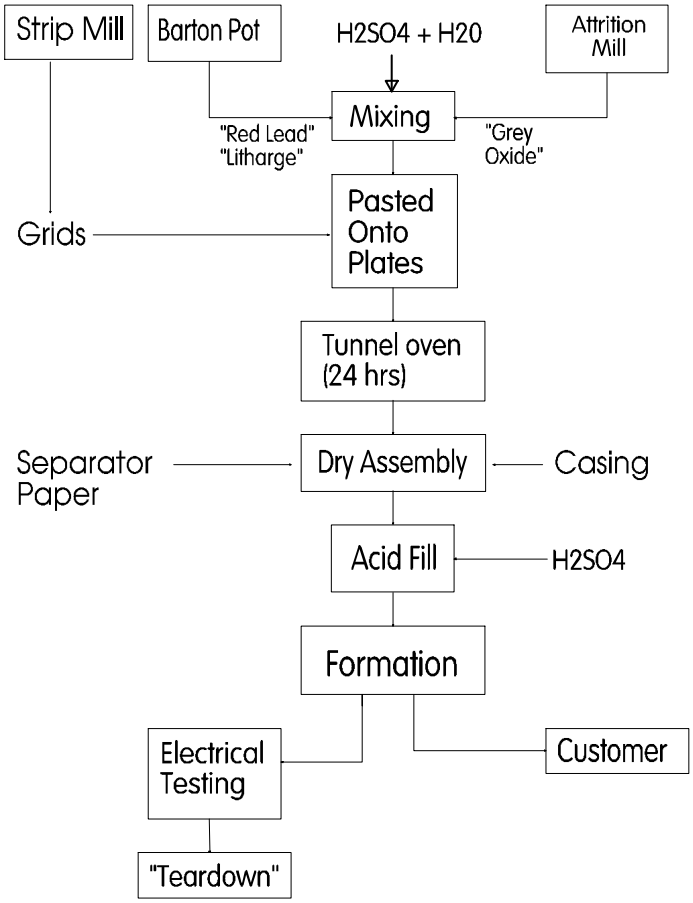

Figure 2.5: Flow Chart of Hawker Energy's Production Process [21]

2.4.1 LEAD OXIDES FOR PASTE PRODUCTION

Active materials of the lead acid battery are formed from the paste in the positive and negative grids during the "formation stage" of battery manufacture. The materials used to manufacture the paste will influence the properties and performance of the resulting active material. Formed negative active material consists of lead and positive of lead dioxide. Lead can exist in several oxidation states resulting in the different lead oxide compounds, summarised in Table 2.2. The presence of each of these oxides will have a different effect on the operation of the battery.

Table 2.2: Lead Oxides

Chemical Name	**Chemical Formula**	**Crystal Structure**	**Common Name**
Lead Monoxide - Red	α-PbO	Pseudo-tetragonal and at same time rhombic	Litharge
Lead Monoxide - Yellow	β-PbO	Orthorhombic	Massicot
Red lead	Pb_3O_4 (II,III)		Minium
Lead Dioxide - Blue/Grey	α-PbO_2	Orthorhombic	
Lead Dioxide - Red/ brown	β-PbO_2	Tetragonal	

The main constituents of unformed active materials are Litharge, Massicot and Minium. These oxides are produced using different methods [22,23] the most common being the Barton Pot process and Attrition Mill. Factors such as oxide pore volume, pore diameter, surface area and acid absorption will be influenced by the method of manufacture used. Boden [24] has shown that values of pore volume and pore diameter do not vary significantly between the two methods. There is little difference in the performance of batteries made using the two different oxides. This suggests that pore volume and diameter are more important than surface area and acid absorption, which vary between the oxides.

Research by Lam [25] suggests that battery oxides can be improved by minimising the impurities in the lead (to be oxidised) such as arsenic and cobalt. However, other elements, such as bismuth, can have a beneficial effect by reducing gas evolution rates.

2.4.2 PRODUCTION OF PASTES

There are many different formulations for both positive and negative battery pastes. Paste manufacture is one of the critical steps of battery production and requires careful control over the processing parameters. Factors such as the specific gravity of the electrolyte and the ratio of α to β lead dioxides can affect the properties of the resulting paste [26]. Paste properties can be controlled in terms of the following parameters:

- Paste density
- Paste consistency
- Porosity of pasted plate
- Texture*
- Workability*
- Adhesiveness*

* Qualitative estimate

Normally the paste is produced by mixing a blend of lead monoxide, metallic lead, water and sulphuric acid, in that order. On addition of water reactions occur with the oxide forming hydrates. These are described by the reactions below.

$$2PbO + H_2O \rightarrow 2PbO.H_2O \quad (2.17)$$

$$3PbO + H_2O \rightarrow 3PbO.H_2O \quad (2.18)$$

$$5PbO + 2H_2O \rightarrow 5PbO.2H_2O \quad (2.19)$$

Lead monoxide is unstable in sulphuric acid and on addition, reacts according to the following equation to form lead sulphate and water:

$$PbO + H_2SO_4 \rightarrow PbSO_4 + H_2O \qquad (2.20)$$

The heat generated by this reaction normally causes some water to evaporate; therefore excess water is normally added to account for this. Under the influence of excess lead monoxide and water, the lead sulphate is not stable and basic sulphates form. These consist of different numbers of lead monoxide molecules bonded to lead sulphate. In some cases, these compounds can become hydrated. The reactions are shown below.

$$PbO + PbSO_4 \rightarrow PbO.PbSO_4 \qquad \textit{(mono-basic lead sulphate)}$$

$$3PbO + PbSO_4 \rightarrow 3PbO.PbSO_4 \qquad \textit{(tri-basic lead sulphate)}$$

$$4PbO + PbSO_4 \rightarrow 4PbO.PbSO_4 \qquad \text{(tetra-basic lead sulphate)}$$

$$3PbO + PbSO_4.xH_2O \rightarrow 3PbO.PbSO_4.xH_2O \qquad \textit{(hydrated tri-basic lead sulphate)}$$

(2.21)

Pavlov and Papazov [27] have identified tribasic lead sulphate as the dominant form although the other compounds have been observed. They suggest that temperature is an important factor in determining the relative quantities of each of these compounds. The tetrabasic modification is favoured at temperatures above 70°C whereas tribasic lead sulphate is favoured below 70°C.

It is important to control the composition, as the ratio of these compounds can influence the structure of the lead dioxide produced during the formation stage. This is due to the morphology and relative surface area of the crystal modifications. Tribasic lead sulphate has the highest surface area and is the favoured paste component. For this reason paste mixers may have a built in cooling facility to promote the formation of the tri-basic variant.

Kordesch [28] has measured the pH of the paste at this stage of manufacture. He concludes that despite the addition of the acid a pH of 9-10 is normal. This is an important observation because the pH value influences the structure of the lead dioxide obtained during battery formation.

2.4.3 GRID PRODUCTION

When designing a battery grid the manufacturing method and alloy composition must be considered. Both of these can influence the grid microstructure and subsequent battery performance. Some of the methods that are used to manufacture battery grids are listed below:

- Gravity casting
- Expanded grid
- Punched continuous cast strip
- Punched and then rolled continuously cast strip
- Pressure die-casting

Each method has advantages and disadvantages in terms of cost, material utilisation, manufacturing time and complexity of grid geometry achievable. This section will focus on the characteristics of grids that are manufactured by casting, rolling and punching as these are the methods used to produce the grids in the batteries examined.

Rolling a grid to reduce its thickness before punching can result in a modification of the grain structure [29]. A coarse microstructure can cause brittleness, low compressive strength and a low hardness, whereas a fine-grained microstructure results in a higher yield stress.

A large number of alloying elements can be added to lead grids to improve properties. However, these can improve one aspect of the performance while detracting from another. The effect of various alloying elements in conjunction with the manufacturing method has been investigated by a number of researchers.

Prengaman [30] investigated the influence of tin content on a number of grids. He concluded that grids with a high tin content that are continuously cast rather than rolled can exhibit large directional grain structures. This can be a disadvantage during processing into grids as non-uniform deformation can occur at grain boundaries.

N.Y. Tang [31] demonstrated that the mechanical and electrochemical properties of continuously cast, low-antimony lead strip is strongly dependent on the arsenic content in the alloy. He showed the importance of the Sn:Ca ratio in Pb-Ca-Sn alloys and its effect on the development of the mechanical properties and microstructure.

S Zong et. al. [32], investigated the effect of adding tin, aluminium, bismuth, silver and sodium to lead-calcium grids. Results showed that the creep strength and corrosion resistance of grid alloys could be improved by the addition of silver. However, a disadvantage of this is an increase in gases produced during battery operation. The addition of sodium can improve mechanical properties by refining the grain structure although grids of inferior corrosion resistance are then produced.

Investigations conducted by L. Albert *et. al.* [33] have identified a number of transformations that occur during manufacture of lead battery grids containing calcium and tin. During manufacture if the grids are cooled rapidly the lead matrix becomes over saturated which allows the precipitation of calcium compounds. Of the transformations identified they were often found to be incomplete immediately after cooling. More transformations were identified in alloys with tin/calcium ratios of around 7, compared to ratios around 15.

2.4.4 PASTING OF PLATES

Battery plates are produced, by applying the paste to the grid under pressure. This is normally done automatically on a continuous basis. The whole pasted grid is sandwiched between two sheets of 'paper', made from glass similar to that of the separator paper, to improve ease of handling. The plates are then cut from the pasted grid by a continuous process using a cylindrical cutter prior to curing.

2.4.5 CURING

Curing is the term given to the stage where the battery plates are dried out. Not all battery manufacturers cure their plates. This is mainly because the curing stage is time consuming and costly and the advantages in terms of battery performance may not justify the additional expense. One of the advantages of curing, however, is to counteract the effects of inconsistencies in batches due to atmospheric changes such as temperature and humidity [34].

Plate curing is one of the most critical stages in the manufacture of the battery. Rand *et. al*., [35] showed that the conditions under which a plate is cured could have a direct influence on the chemical composition and morphological structure of the paste. These factors have important implications for the battery during its service life in terms of capacity and mechanical stability. Capacity can be measured electrically and mechanical stability has been quantified by measuring the force needed to push the tablet from the grid or the shear force needed to punch a small hole through the paste [36]. The first method gives information on the adhesive properties of the grid paste interface and the second on the cohesive properties of the paste.

During curing as the plate dries large proportions of α-PbO and β-PbO are converted into the basic lead sulphates shown below:

- monobasic $PbO.PbSO_4$
- tribasic $3PbO.PbSO_4.H2O$
- tetrabasic $4PbO.PbSO_4$

Varma [37] reported the occurrence of a fourth compound, dibasic lead sulphate, $2PbO.PbSO_4$ under some curing conditions where tetrabasic sulphates are formed. However, this was rarely observed in practice.

During curing, an interlocking crystalline network of the basic sulphate compounds develops effectively consolidating the paste. The paste thixotropic properties influence this process and have to be carefully controlled by the addition of the correct quantity of acid during the paste mixing and pasting stages. If an excess of acid is added the paste becomes sticky and if not enough is added the paste is soft. In both cases the result is a fragile paste which will exhibit high levels of shedding during battery operation.

When the correct quantity of acid is added a small amount of PbO remains unconverted and the rest forms basic sulphates. An additional transformation of α-PbO to β-PbO may also occur. The presence of monobasic sulphate is known to promote active material shedding during battery cycling and it is therefore advisable to restrict the level of this sulphate.

Vilhunen and Tummavuori [38] have studied the processes that occur during the preparation of plates from tetrabasic lead sulphate pastes. They concluded that tetra basic pastes have a much faster growth rate compared to tri basic pastes. A disadvantage of this is the higher temperature requirements needed although performance is better in heavy-duty batteries for automotive applications.

The four reactions, shown below, that occur during the curing of battery pastes, have been identified by Lam and Rand [39].

- Progressive growth of basic lead sulphate crystals.
- Development of basic lead carbonates, i.e. hydrocerussite, $2PbCO_3.Pb(OH)_2$, especially on the surface of the plate material.
- Conversion of metallic lead particles to α-PbO with liberation of heat.
- Corrosive attack of metallic grid.

They occur either on their own or simultaneously. Overall, these reactions result in a hardening of the active material and an increase in the paste–grid bond strength. Material consolidation is promoted by the growth of the basic lead sulphates while the paste–grid bond is improved by corrosion.

The effect of adding surfactants to modify the dimensions of the tetra basic lead sulphate crystals formed during curing has been investigated by S. Laruelle et. al [40].

Polyvinylpyrrolidone was found to influence the size of the tetrabasic lead sulphate crystals formed. The basic sulphate precursors used were shown to also have an influence on the crystal morphology.

2.4.6 ASSEMBLY OF BATTERY COMPONENTS

During the assembly stage all the components of the battery are put together. The positive and negative plates are stacked alternately with separator papers to make each cell. The cells are then compressed prior to the application of the cast-on-straps at the top of each set of positive and negative plates, Figure 2.6. Each cell is then placed in the container and the cast-on-straps are welded connecting the cells. Finally the top of the battery case is plastic-welded into position before the battery is filled with acid.

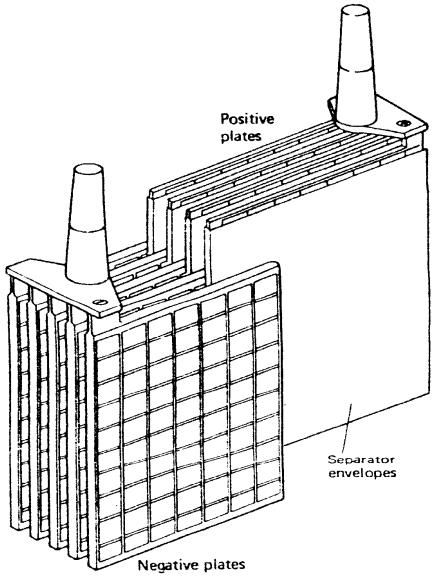

Figure 2.6: Configuration of positive and negative plates, separator paper and cast on straps before insertion into battery case [41].

2.4.7 ADDITION OF ACID

This is a fairly simple stage in the battery production route. However there are a number of points that should be noted. Firstly, it is important that each cell is filled with the correct quantity of acid. This is normally done by metering the amount of acid entering each cell or by over filling and then removing excess acid by suction. An excess or deficiency of acid can lead to premature failure of a cell and ultimately the battery.

2.4.8 SOAKING

Before formation can be initiated time must be allowed for the sulphuric acid to infiltrate the pores of the active materials. This occurs due to capillary forces and takes only a few minutes.

In order to enhance the electrical conductivity of the active materials it is advisable to allow time for the slightly acidic reaction between the acid and active materials to occur. In this reaction sulphuric acid reacts with basic sulphates according to the equation below.

$$3PbO.PbSO_4 + 3H_2SO_4 \rightarrow 4PbSO_4 + 3H_2O \qquad (2.22)$$

The result is a reduction in the pH of the electrolyte to around 5, and a sufficiently wetted oxide/sulphate layer to provide a high conductivity.

2.4.9 FORMATION OF ACTIVE MATERIALS

After the battery has been assembled, acid filled and sufficient time allowed for soaking, the non-conducting lead monoxide in the positive and negative plates must be converted into the positive and negative active materials. This stage in the battery manufacturing process is called 'formation'.

During formation, sponge-lead is created at the negative electrode and lead dioxide at the positive. This process is equivalent to the battery's first charge and on completion leaves the battery in the fully charged state. Formation is an electrolytic process and therefore requires carefully controlled charge conditions. Kiessling [42] identified the following factors as important in ensuring that the desired electrode mass and porosity are obtained.

- Temperature
- Electrolyte composition
- Current density

Microscopic investigations carried out by Bagshaw [43] show that the formation process initiates from the grid-active material interface and progresses in an outwards direction through the active material and away from the grid. This is not surprising however, since a flow of electrons is needed in order for the formation reactions to occur and both forms of lead monoxide are electrical insulators.

2.4.9.1 FORMATION OF THE POSITIVE ACTIVE MATERIAL

During formation of the positive plate different phases of lead dioxide are formed in which the crystal structure can be orthorhombic, (α-PbO_2), or tetragonal, (β-PbO_2). The alpha modification is formed in alkali environments and preferably at elevated temperature when in the presence of low concentration sulphuric acid. The crystals formed tend to be compact agglomerates with low specific surface area. In comparison the beta form is produced in acidic environments and consists of small crystals with poor adhesive properties and a high specific

surface area. For this reason better discharge properties are obtained from beta lead dioxide compared to alpha. However, the poor cohesive properties of the beta modification make it more prone to shedding and less desirable in standby battery applications. Generally it is best to have an active material consisting of both forms where the large alpha lead dioxide crystals can form a stable structure to support the beta lead dioxide crystals which are the major contributor to performance.

The ratio of the α to β phases formed is influenced by a number of factors. These include the pH of the surrounding region [44], formation current density, paste density [45] and temperature. It has been shown that variations in pH are due to the diffusion processes that occur within the plate and which are in turn influenced by the types of basic sulphate used to manufacture the paste.

Research has been conducted by Butler and colleagues [46] on the initial formation steps of the positive paste using electron microscopy, X-ray diffraction and chemical analysis. The initial step identified is the formation of lead sulphate from $3PbO.PbSO_4.H_2O$ and beta lead monoxide. Tetragonal lead monoxide was found to be less readily converted compared to the beta form. The oxide and sulphate are subsequently converted to lead dioxide by an electrochemical process. Reactions occurring at the active material surface and interior were essentially the same with the exception of the orthorhombic, alpha form of lead dioxide. This nucleated preferentially in the interior of the electrode near the grid interface and was not observed on the surface of the electrode. [28]

Bullock and colleagues [47] investigated the effect of adding ozone to unformed positive plates. From their results, they concluded, that such an addition enhances formation, creating a conductive layer on the plate surface and oxidising free lead in the paste to lead monoxide.

2.4.9.2 FORMATION OF THE NEGATIVE PASTE

The cured negative plate consists of large amounts of tetragonal lead monoxide and tribasic lead sulphate in addition to smaller amounts of lead. These compounds are unstable in the presence of sulphuric acid and decompose in chemical sulphation reactions simultaneously with electrochemical reactions during the formation process.

The reaction of lead monoxide, tribasic lead sulphate and sulphuric acid result in lead sulphate formation in the paste adjacent to the surfaces. It has been found that sulphation of lead

monoxide and tribasic lead sulphate initiate at the paste surface and progress towards the middle.

Pavlov [48] has shown that the formation of the negative active material occurs in two distinct stages. In the first stage a lead network is produced upon reduction of hydrated tribasic lead sulphate and lead monoxide. Subsequently, in the second stage, lead is produced from lead sulphate and deposited on the existing network.

During formation, lead sulphate dissociates according to the following reaction.

$$PbSO_4 \rightarrow Pb^{2+} + SO_4^{2-} \qquad (2.23)$$

Free lead ions are present in the electrolyte adjacent to the lead grid and network, this allows them to pick up electrons and precipitate as metallic lead. When lead is precipitated it grows as a dendrite with primary, secondary and sometimes tertiary branches. This gives the structure a high surface area, which is beneficial in high performance batteries as the electrolyte/active material contact area is maximised.

Due to the participation of sulphuric acid in the above reactions a change in acid concentration is observed as formation progresses. This process can be characterised by two distinct stages. The first involves penetration of sulphuric acid into the paste and its subsequent reaction resulting in a decrease in bulk electrolyte concentration. The second stage involves the formation of reaction products from the first stage, which leads to sulphuric acid formation. Thus through diffusion of acid out of the plates an increase in acid concentration occurs. Sulphation of the paste ceases when the lead zone occupies the entire paste volume.

2.5 CONSIDERATION OF MATERIAL AND DESIGN

In the previous section the influence of manufacturing method and formulation of active materials was discussed. In this section the influence of the materials and design of the battery will be considered. Components such as battery case, grid design and separator paper which are not involved directly with the ‘current producing’ electrical reactions can also have an influence on performance.

2.5.1 GRID DESIGN

The purpose of the grid in a valve regulated lead acid battery is to support the positive active material and provide a means of current transfer out of the cell. The primary role is to transfer current, as additional support for the paste is obtained from the separator papers positioned each side of the grid.

The grids are invariably made of lead or an alloy of lead, as this is the only material that can survive the high potentials of the positive electrode. Even very stable metals such as gold will oxidise if used. The formation of a dense passivating layer of lead monoxide on the surface of the grid allows it to resist oxidation. This layer does not prevent corrosion but has the effect of significantly reducing the rate. Non-conducting materials can survive and plastic grids with pure lead strip current collectors are used where weight saving advantages are important [41].

Research by Maia, [49] suggests that the grid geometry has a significant effect on the ohmic losses at high discharge rates. His results demonstrated that the best geometry for a lead acid battery electrode consists of a square grid with the lug positioned at the upper centre of the electrode, as this produces symmetrical resistance contours. On many battery grids the lug is positioned to one side for ease of connection, which results in asymmetric contours. However, any disadvantage arising from this asymmetry is usually so small that it is acceptable. Some grid designs use diagonal elements to improve discharge efficiency [50], however this gives a relatively small improvement and is not economically viable when additional manufacturing costs are considered. Previous work [51] has shown that a reduction in mesh size increases the utilisation of the PAM by increasing the grid surface area.

2.5.2 SEPARATORS

The two electrodes in a battery must be physically separated so that the electrolyte forms the only conducting path between them. In order to ensure separation of the electrodes VRLA batteries use a separator material. Separators must be porous to allow the penetration of electrolyte and movement of gases produced during battery operation [52].

Separators for use in early battery designs were manufactured from a wide range of materials. These included microporous Ultra-high molecular weight polyethlene [18,6,53], microporous PVC, sintered PVC, microporous rubber, resin-bonded paper, Latex/Kieselguhr, Polyethylene/cellulose and even wood [54]. Development has since lead to the wide acceptance of an absorptive borosilicate glass microfibre separator for use with valve regulated lead acid batteries [55].

Glass separators contain fibres with diameters in the range of 0.25-4μm and lengths of around 1mm. This results in a material with a very high porosity, of approximately 95%. Borosilicate glass is inert and has a contact angle of zero with sulphuric acid [56]. Additional functions of the separators are to absorb excess electrolyte and reduce the risk of dendrite formation, which can form short circuits between plates resulting in a damaged cell. May [57] suggests dendrites form

most readily under conditions of over discharge where pH levels can reach high levels. The absorptive Glass micro-fibre separators (AGM) [58] were initially used by the Gates Rubber Company in 1972 with flat plates [5]. An additional advantage of glass micro-fibre separators is excellent high rate discharge properties in the battery [5].

Although battery separator papers do not themselves react chemically during battery operation they have a significant influence over the charge and discharge reactions and are not inactive barriers as is the case for flooded cells. In recent years research has been conducted on separators in order to investigate how they influence battery operation. Previous work has concentrated on the characterisation of separator properties in an attempt to identify those most crucial to battery performance.

In addition to the obvious role as a material to absorb and immobilise electrolyte, subtle changes in porosity and compression characteristics can have significant effects on battery performance. Also, the relative importance of various separator properties are dependent on the depth of discharge and number of cycles the battery will be subjected to.

A number of properties that are required in a good separator have been identified by Zguris [59]. In addition to immobilising the electrolyte, so that the battery will operate at an angle, a separator that applies a consistent and uniform compression on the plates during the life of the battery is required. A number of key points which must be considered when designing a separator are summarised below:

- Retention of separator thickness during saturation is important as this maintains plate compression when the separator is wetted.
- As variations in temperature have been observed to result in changes in compression force of up to 10%, it is important that the separator is insensitive to the effects of draughts impinging on the outside of the battery.
- Resiliency of the separator, when subject to a crushing force, is important as failure to recover can lead to changes in the active material pore structure with resulting decline in battery performance.
- Studies have shown that as a stack of plates is compressed into a cell, not all separators deform equally. Uniform stack compression is important to ensure active mass consistency between plates.

The way a separator behaves when subjected to compression will have a significant influence on the operation of the battery. Research by Zguris [60] suggests that increasing cell compression can delay the failure mechanism in float applications and increase the cycle life. The most likely explanation for this is that during cycling particles may become detached from the main electrode. Under a high level of compression, although there may be no significant mechanical bond between the particle and electrode, electrical contact is maintained. This allows the detached particle to be converted back into the active material on charging thus reducing the rate of capacity loss.

Another important property of a separator paper is porosity. Its influence is greatest during over charging of the battery when the oxygen recombination reaction occurs. Changes in oxygen diffusion rate can increase or decrease the charging efficiency. However, the effective porosity of the separator is influenced by a number of factors. The fibre lengths, diameters and orientation will all influence the pore distribution within the paper. Oxygen diffuses through the voids within the paper so saturation will have an effect.

Currently used methods for the evaluation of separators can be divided into two distinct groups.

The first is concerned with the flow of liquid through the paper. These include wicking and drainage tests. Both of these characteristics have been investigated by Culpin [56] in some detail. He investigated the drainage characteristics of separators in both the free and compressed state. Testing in the compressed state simulates the forces exerted whilst in the cell. Paper saturation was calculated from the dimensions and weight difference of the papers between the saturated and dry state.

The second type of test evaluate the behaviour of the separator whilst under a compressive load [61,62]. This is normally combined with measurement of the change in force or strain associated with variations in paper saturation. More detailed information on these are given later in the section.

There is no universally agreed standard method for the determination of a simple parameter such as separator thickness. Both ‘The Battery Council International’ and ‘The Japanese Industrial Standards (JIS)’ propose different methods. The BCI utilise a 29mm anvil and 10.34kPa load, whereas the JIS use ten 10x10cm samples with a 20kPa load [60]. These different test methods can give variations in measured parameters of up to 20% for the same material. It is therefore important to design batteries using one test protocol only. The compressive force

exerted on the battery plates by the separator will be influenced by a number of factors, which must be taken into account. The most significant of these are listed below [63].

- How thickness is measured
- Variation in separator
- Variation of the plates
- Draught on battery case
- Separator compression used (Restrained thickness / Unrestrained thickness)
- Acid saturation level
- Density of separator
- Surface area of separator
- Case material used
- Uniformity of compression between plates

When considering the problem of characterising a more complex property such as its behaviour under compressive loading, whilst saturated with electrolyte, there is even more opportunity to vary procedures. For example, the viscoelastic properties of the paper will influence results depending on what load rate is used. Sample dimensions are also significant.

Nakamura et. al. [61] have studied the compressive properties of separators using a jig, where a stack of 5 separator papers are mounted horizontally between two plates. The distance between the plates is variable and measurements of load taken via a load cell. Samples were compressed to a specified load and then the acid added after a period of one hour had elapsed.

An alternative approach adopted by McGregor et. al.[62] utilised a specially designed piston cell. This consisted of a normal battery cell with one of the walls connected to a piston thus allowing variations in cell compression to be made. Separator papers were held in the vertical position and dividing plates inserted between the papers. Compressive loads were applied and measured using a pressure gauge attached to a regulated gas supply and the cell piston.

Results from both researchers showed the general trend of a reduction in thickness or force applied by the paper as saturation was increased from 0%. However, results from Nakamura, suggest a reversal of this trend and an increase in force after a saturation of approximately 50% is reached.

In addition to the compression properties, Crouch [64] has investigated separator resistance and purity. Resistance measurements were obtained using a 1kHz impedance bridge connected

between two graphite plates, between which the separator was placed. He concludes that the separator resistance is constant above a saturation of approximately 80%, below which there is an increase in resistance as the separator dries out. However, the effect of internal surface area and applied pressure on this 'break-point' was not determined. Separator purity was determined by analysing sulphuric acid that had been in contact with the separators. Of the separators analysed none were contaminated with significant proportions of any impurities.

2.5.3 ELECTROLYTE

The electrolyte used in the valve regulated lead acid battery is a mixture of sulphuric acid, H_2SO_4, and water. It acts as an ionic conductor between the two electrodes of the cell. During cycling of the battery, the specific gravity and viscosity will change due to the oxidation and reduction of lead sulphate. This means that the properties of the electrolyte can be used to monitor the state of the battery [65].

It is important to fill each cell with the correct quantity of acid, since the amount required is dependent on the weight and porosity of the active materials. A cell with an incorrect quantity of acid is prone to fail prematurely leading the total failure of the battery [66].

Various claims have been made regarding improvements that can be gained by the addition of additives to the electrolyte. Sulfonic acid surfactants are sometimes used to lower surface tension therefore, improving wetting properties and the addition of cobalt salts has been found to reduce grid corrosion [67]. Improvements in battery performance achieved by the addition of boric acid have been investigated by Badawy [68]. His results showed a marked improvement in the kinetics of the $PbO_2/PbSO_4$ couple and disappearance of problems such as capacity loss and decrease in charging efficiency which are often encountered when phosphoric acid is used.

Some batteries do not contain a separator paper but use a gelled electrolyte [69], which has the advantage of being more resistant to acid stratification. This is made by mixing fine particles of silicon dioxide with sulphuric acid to produce a gel. Gelled electrolytes have been available since the early 1960's.

2.5.4 CASING

The casing of a valve regulated lead acid battery fulfils a number of important functions; it must contain the acid within each cell, provide mechanical support for the plates and connectors and also withstand the internal pressures generated by gas evolution and compressed separators. It must also be inert and not react with any of the compounds contained within the battery, such

as the electrolyte, and be able to withstand the high temperatures generated during the welding of the lead contacts.

Polypropylene has become the predominant container material. This is mainly due to its high impact resistance, moderate price, weld ability, rigidity over a wide temperature range and ease of manufacture by injection moulding [70,71,72]. A diagram of a typical battery case is shown in Figure 2.7, below.

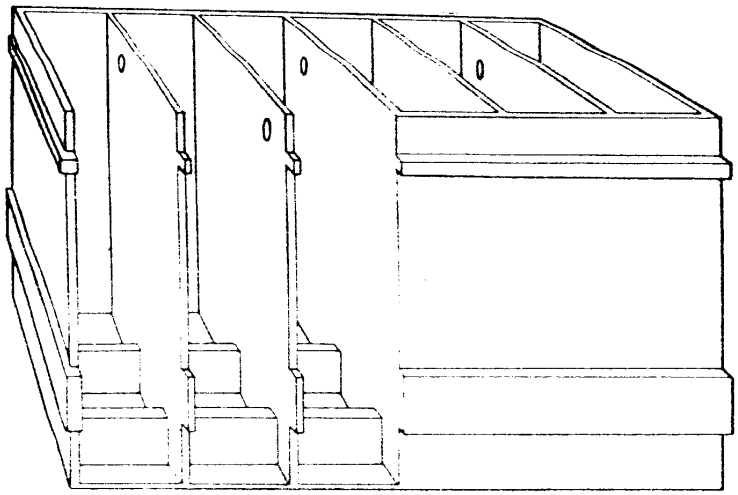

Figure 2.7: Injection Moulded Case.

2.6 THE POSITIVE ELECTRODE OF THE LEAD ACID BATTERY

The positive electrode of the lead acid battery has always been of great scientific interest. This is mainly because the majority of battery failures can be attributed to failure of the positive, rather than the negative electrode although this is not always the case. Lead acid batteries are normally positive limited, meaning that for a given cycle when the positive plate is fully exhausted, the negative plate is not. Due to the formation of lead sulphate during discharge positive plates are normally only used to around 50% of their theoretical capacity. Deterioration of the electrode during cycling is often observed due to the instability of the positive active material. A number of models exist which describe this process [73].

Three structural elements form the positive lead-acid battery plate. These are the grid, active material and corrosion layer. Each of these has the potential to limit the service life of the battery. The design and technology used in the manufacture of the positive plate determines capacity and cycle life. The main features of the positive electrode are described in the following section.

2.6.1 DESIGN AND OPERATIONAL CONDITIONS OF THE POSITIVE ELECTRODE

In addition to the formulation and structure of the positive active material, the grid design and operational conditions can also influence cycle life. The factors that are most influential on cycle life are summarised below.

- Coefficient of PAM (positive active mass) utilisation
- Current profile during charge and discharge
- Duration and distribution of overcharge
- Open circuit periods

If the optimum manufacturing technology and plate design are utilised the influence exerted by the operational parameters is reduced. The use of a less developed design will result in a lowered plate capacity resource and therefore the conditions of operation will affect the plate to a greater extent.

Mechanically confining the active mass produces dimensional stability of the paste and reduces these detrimental effects, which increases the life of the plate [74,75]. An example of this is tubular electrodes, where the life can be double that of pasted plates.

In addition to the active material composition and formation processes there are other parameters that can be changed when designing a battery plate. An important parameter in plate design is the ratio between the grid surface area and positive active material weight. Variations will result in a change of current density along the grid surface. A basic objective of grid design is to achieve as uniform a current density distribution as possible. One way of achieving this is to have as constant an active mass distribution over the grid bars as possible.

2.6.2 THE POSITIVE ACTIVE MATERIAL

The positive active material is a key component of the electrode as it is this that reacts to produce current. The efficiency at which this is achieved is determined by a number of factors such as structure, composition and surface area. In turn, depending on these parameters, the way in which the structure and therefore performance changes during cycling, will also be determined.

The surface appearance of the charged positive electrode consists of porous agglomerates ranging in size between ≈ 4 - 10μm. The composition is approximately half pores and half lead dioxide, by volume. This allows a high electrolyte/active mass surface contact area which is important as all current producing reactions occur on the surface of the active material.

Initially the plate contains both polymorphs of lead dioxide, α-PbO_2 being stable in alkaline environments and β-PbO_2 in acidic environments. The α polymorph is produced in areas of limited acid access within the paste during the formation stage of manufacture whereas the β polymorph is formed in acidic regions.

A unique characteristic of the lead acid positive electrode is the change in the α to β lead dioxide ratio during cycling. This can be explained by considering the following reactions. During discharge lead sulphate is formed by the reduction of lead dioxide. On charging the sulphate is oxidised and converted back into lead dioxide. However, the presence of sulphuric acid during charging lowers the pH, thus making only β-PbO_2 formation possible. In time this results in a concurrent decrease of the α- content, and increase of the β content during cycling, thereby changing the plate's properties.

Discharged positive active material consists of coarse crystals of lead sulphate which are radically different to those of the oxide. This difference means that the reformed structure of the oxide after each re-charge will be different from that of the previous one. The existence of this restructuring process is detrimental to the battery performance and also proportional to the depth of discharge. Battery life can therefore be greatly reduced by repeated deep discharging.

The reduction in battery performance and capacity observed during cycling is mainly due to the loss of mechanical strength caused by the conversion of the coarsely agglomerated initial structure into a weakly bonded accumulation of fine crystals. Changes in inter-particle contact and crystal structure can also act as charge capacity limiting factors. The relative proportion of α and β PbO_2 within the paste affects the degree of structural disorder. Ruetschi [76] showed that electrodes containing a large amount of α-PbO_2 generally have higher discharge efficiency. This can be accounted for by vacancies in the cation sub-lattice. The opposite, low discharge efficiency is observed in electrodes containing mostly β-PbO_2 which have high degrees of structural order.

Perkins and Coyle [73] have conducted a study of the sub-structural network observed in positive lead-acid battery plates. Test cells were constructed using two negative plates sandwiching a positive with a large excess of electrolyte. After charging the cell was trickle-discharged. The morphology of the active materials was observed using light microscopy. They identified the formation of fine scale whisker shaped lead dioxide crystals in the plates. These were found to give the active material good electrochemical characteristics and structural integrity.

Afifi [77] and colleagues have studied the effect of adding zeolite, graphite and lead hydroxide to the positive active material. Zeolite acts as an ion exchanger increasing the capacity of the electrode. Additions of more than 3 wt. % were shown not to provide any additional benefits. An addition of 1wt.% graphite was found to increase the capacity of the plate. However, greater additions increased the amount of gassing and resulted in mechanical disintegration of the electrode. Lead hydroxide increased plate capacity at 10wt.% but deviations resulted in a decrease of capacity. The exact reason for this is not yet understood.

2.6.3 LEAD OXIDE STOICHIOMETRY

The ratio of lead to oxygen within the oxides found in the positive plate is normally non-stoichiometric. This non stoichiemetry can be described in terms of lead dioxide disorder models. Models have been proposed considering the following factors [78]:

- Oxygen vacancies
- Interstitial protons
- Quasi-free electrons

Different formulas have been proposed by a number of researchers for expressing the stoichiometric ratio. In early models lead dioxide has been represented by the formula [78]:

$$PbO_{2-\delta}\ (xH_2O) \qquad (2.24)$$

Where the partial pressure of oxygen within the oxide is used to determine the parameter δ. However, improvements have been made on the earlier cruder models and currently Ruetschi and Giovanoli [79] describe the deviations in stoichiometry found in terms of O, OH^- Pb^{4+} and Pb^{2+} ions and cation vacancies within the structure. They proposed the formula below, equation (2.6.2), where x denotes the cation vacancy and y denotes the fraction of Pb^{2+} ions with respect to the total number of cationic sites.

$$Pb^{4+}_{1-x-y}Pb^{2+}_{y}O^{2-}_{2-4x-2y}OH^{-}_{4x+2y} \qquad (2.25)$$

It is suggested that cation vacancies may form layers and consequently behave like internal surfaces between well ordered crystallographic layers. Pb^{2+} ions, are believed to be located, adjacent to cation vacancy layers or external surfaces.

2.6.4 STRUCTURAL ASPECTS OF THE PAM

In general the capacity of the plate increases with the BET surface area of the paste. However, it has been shown that the active material structure of some plates which show a comparatively

low surface area have a high capacity. This suggests that BET surface area is not the capacity limiting factor. Results reported by Pavlov [80] have shown that the plate structure is a capacity limiting factor. The main structural properties causing this are, the volume of transport pores, which determines how easily the ions taking part in the reactions can move through the canals in the paste and, the surface area built up by agglomerates, which provide the surfaces on which reactions can occur. Also, newly formed $PbSO_4$ crystallites have the effect of reducing the pore cross sectional area. As the battery is cycled there is a change in measured surface area and in the actual size of the plate. Initially, at low numbers of cycles, the paste is rigid and able to withstand the mechanical stresses caused by dimensional changes of the paste with increasing number of cycles. Experimental and calculated variations in the pore volumes are found to be in good agreement with this. As the number of cycles increases, both the strength of the paste decreases and volume variations increase, which leads to swelling. This reduces the contact between agglomerates, thus resulting in a reduction of capacity and eventually failure of the plate.

A reduction in the surface area of the active material during discharge is generally observed in lead acid battery plates. This continues during the period when the battery is at open circuit voltage. It is thought that re-crystallisation of lead sulphate during this rest period is the most likely cause for the reduction in surface area.

Further research by Pavlov and Bashtavelova [80] concerning crystal morphology and structure of the positive active material produced the following results. They observed that after discharge, lead sulphate crystallites are identifiable on certain sites. These were not clearly defined, but intimately linked to the surrounding active material. Regions of super-saturation were thought to be the most probable cause for the formation of these sites.

It followed that this process was the main cause of plate swelling since sulphate has a much larger molecular volume, compared to lead dioxide. This produced tensile stresses in the skeleton structure as its volume increased. In the rest period, when the battery is at open circuit voltage, the sulphuric acid concentration throughout the plate reaches an equilibrium, which results in a reduction in the regions of super saturation. Dissolution of the non-equilibrium lead sulphate crystals then occurs with the precipitation of well-formed crystallites having equilibrium surface facets and edges.

During discharge of the plate, reduction of lead dioxide to lead sulphate occurs. This is followed by a re-crystallisation process, during which Pb^{2+} ions are transported through pore channels to

form the equilibrium lead sulphate crystals. The reverse process, oxidation of sulphate, will depend on whether the sulphate had crystallised or not.

Charging of the discharged active material following a rest period was observed to occur at a higher polarisation. This effect was most obvious in the first 15 to 30 minutes of charging. Pavlov concluded that the hindered dissolution of lead sulphate crystals, or transport hindrance, is the most probable cause for this phenomenon.

Further work by Pavlov [81] suggests two types of PAM skeleton can be formed; thin and thick branched. These have a direct influence on the properties of the positive active material. The thin-branched structure is normally obtained from tribasic lead sulphate and the thick branched from tetrabasic lead sulphate. During discharge, the cross-section of the branches is reduced. When the cross-sectional area of a branch reaches a critical size the resistance is such that only a limited current can flow and the battery is unable to operate efficiently. The time at which this point is reached will be determined by the thickness of the branches in the structure. It therefore follows that plate capacity is influenced by the skeleton structure. Representative diagrams of these structures are shown in Figure 2.8.

The particular structure formed is dependent on the types of basic lead sulphates present in the initial paste. Tri-basic sulphate pastes are composed of agglomerates ranging in size between 2 and 3μm compared to tetra-basic sulphates, which contain crystals between 10 and 50μm in size. Typical capacity versus cycle curves for 1, 3 and 4 basic sulphates are shown in Figure 2.9.

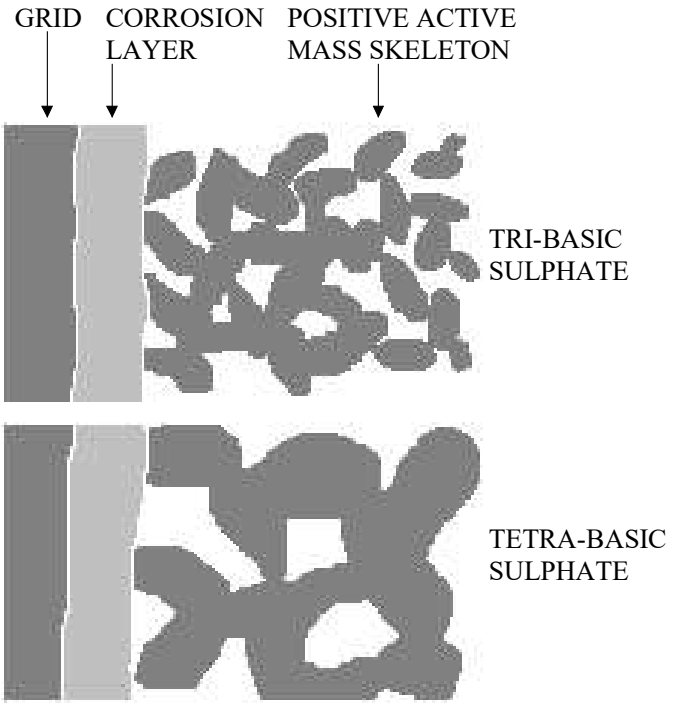

Figure 2.8: Model for the CL/PAM interface. PAM skeleton is built of two types of agglomerates [81].

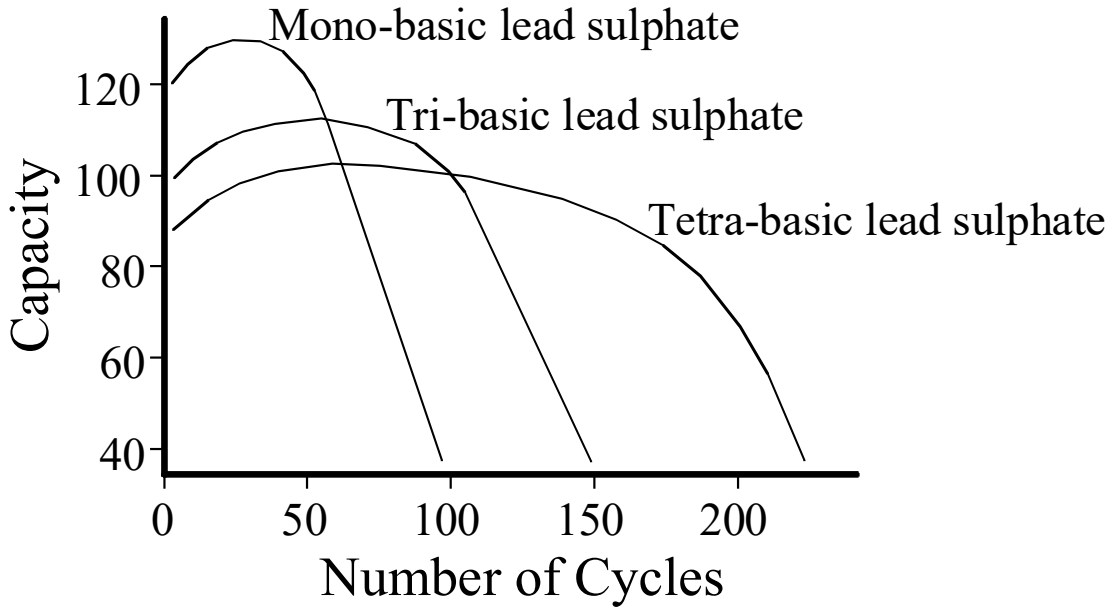

Figure 2.9: Dependence of plate capacity on the number of cycles for positive plates prepared with mono, tri and tetra basic lead sulphate pastes that yield three different types of PAM skeleton [82].

Takehara [83] has shown that the type of sulphate crystals formed at the PAM/grid interface is dependent on the porosity of the lead dioxide. Under certain conditions large plate-like crystals are formed at the interface. The effect of these is to increase the resistance to such an extent that oxidation of the sulphate is prevented.

An ‘agglomerate-of-spheres’ model has been used by researchers, Bashtavelova and Winsel [84], to explain the structural changes that occur in the positive active material during cycling. They suggest that the formation of spheres and changes in chemical composition can be described as an electrometasomatic process involving the introduction of gas or liquid into the bulk material. Their study compares the behaviour of positive pastes manufactured from tri and tetra basic lead sulphate and demonstrates that the varying pore size distributions in the two active materials influence the diffusion path of lead ions. The result of this is a variation in the location of lead sulphate during discharge. Lead sulphate was deposited within the tetrabasic lead sulphate paste where the diffusion path was longer. They also concluded that the current distribution is almost homogeneous throughout the electrode except during the beginning of recharge and end of discharge when there is a restriction of current to the material adjacent to the edge of the grid.

2.6.5 CYCLE LIFE OF THE POSITIVE ELECTRODE

The cycle life of a positive electrode will be influenced by a range of variables from the plate design and formation method, to the composition of the positive active material. Often failures can occur due to variations in the intensity of the destructive processes that occur in the PAM during operation. This is generally a function of plate design but is also influenced by the formation of cracks and degradation of the active material.

A reduction of the electrical contact and surface area of lead dioxide particles will affect cycle life. Research has suggested that the occurrence of an electrochemically inactive form of β-PbO_2, which increases in proportion as the battery is cycled, may be an important factor. Caulder and Simon [20] explained its formation by a loss in hydrogen species from the crystal structure and an increased structural order of the oxide. A mechanism proposed by Hill and Houchin [85] suggests that hydrogen is incorporated into beta lead dioxide via surface hydrolysis during particle growth. However, the hypothesis proposed by Caulder and Simon, suggesting loss of intrinsic lead dioxide activity, has been disputed by Hill and Madsen [86] who suggest that loss of hydrogen is an unlikely cause for the decline in capacity. They proposed that the gradual loss in capacity of the battery with cycle life cannot be correlated with the observed relatively sudden increase in crystallite size or structural order. Their main justification for this was that the crystallite size in batteries operated at 25 and 50°C with β-PbO_2 was around 250A and these increased in size with cycling. However, in the case of 50°C, a crystallite size of around 900A is observed after the operational life has reached 10%. The gradual loss of capacity

within the battery cannot be correlated with the observed increase in crystallite size and/or structural order during the early stages of operation.

Later research by Hill and Jessel [87] identified two different sites in which protons can be incorporated in the surface of lead dioxide. One site was associated with mobile isolated adsorbed hydroxyl groups and could be removed by out gassing. The other was not removed by out-gassing and is likely to correspond to water molecules and/or hydroxyl groups trapped on integral crystal surfaces.

2.6.6 THE CORROSION LAYER

The corrosion layer is one of the most important aspects of the positive electrode. It influences the operation of the battery since all electrons generated must flow through it and the ease with which this can occur is dependant on its geometry, composition and thickness. High currents can be generated as a result of the large difference in surface area between the PAM and grid. For a typical grid with a surface area of around $50cm^2$ the corresponding PAM area will be in the region of $500m^2$ [81].

The corrosion layer is first formed during curing of the plate; it then increases in thickness as the plate is cycled. During this stage temperature, humidity and oxygen concentration all influence the thickness. Curing at temperatures in the region of 0°C has been found to produce good adhesion between the grid and corrosion layer [81].

Corrosion layers commonly consist of a multi-layered structure comprising of lead oxides of different stoichiometry. Normally the concentration of oxygen within the corrosion layer increases with distance away from the grid. This is because it has to diffuse from the outer surface towards the grid.

The contact resistance of the grid/corrosion layer interface has been measured using a dc method by Calabek and Micka [88]. They describe the decrease of resistance in terms of the solid state diffusion of sulphate ions. It was demonstrated that the interface is insensitive against discharge up to 60% of the capacity.

The change in molar volume that occurs when Pb is oxidised to PbO_2 is greater than 38%. A consequence of this is the generation of internal stresses, which cause cracks to form, when the corrosion layer reaches a critical thickness. This process occurs within the corrosion layer and at the corrosion layer/PAM interface. Non uniform heating of the corrosion layer is another cause for the formation of cracks. Crack formation is undesirable as it reduces the strength and

conductivity of the material. However, elastic elements present within the corrosion layer and PAM offset this effect; these are commonly referred to as gel zones and allow stresses to be relieved and help in reducing the incidence of cracking [89,11]. The formation of gel zones is dependent on the state of hydration of the corrosion layer. This is influenced by the alloying elements present within the grid.

Lappe [90] investigated the relationship between electronic conductivity and stoichiometric coefficient of lead oxides. It was demonstrated that when the stoichiometric coefficient of an oxide reaches 1.35 there is a rapid increase in conductivity. He also found that when the ratio of oxide ions reaches 1.5 the conductivity is nearly equal to that of PbO_2. This is shown diagrammatically in Figure 2.10.

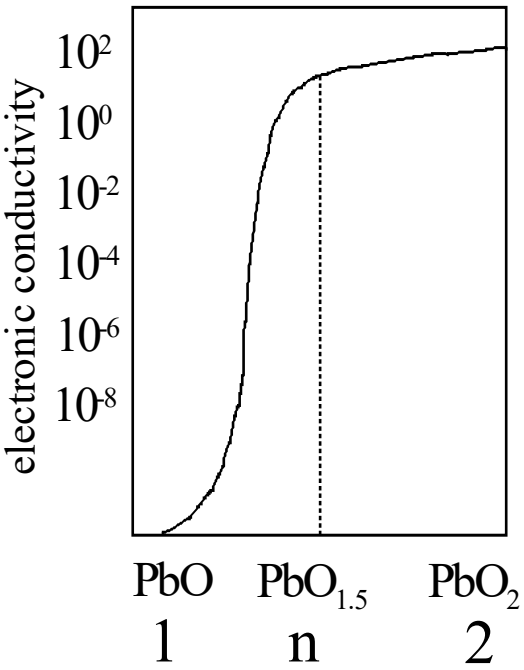

Figure 2.10: Dependence of the specific electronic conductivity of lead oxides on their stoichiometric coefficient [90]

Growth of a corrosion layer is dependent on the initial oxidation of the grid to form lead monoxide. The lead monoxide must then react with more oxygen to form oxides of higher stoichiometric coefficient. These reactions have been expressed as chemical equations by Pavlov [81]. The three basic reactions that must occur in order to convert the lead grid into lead dioxide are shown below.

$$Pb + O \xrightarrow{v_1} PbO \tag{2.26}$$

$$PbO + (1-n)O \xrightarrow{v_2} PbO_n \qquad (1 < n < 2) \tag{2.27}$$

$$PbO_n + (2-n)O \xrightarrow{\nu_3} PbO_2 \qquad (2.28)$$

The rate of each of the reactions above can be described in terms of a rate coefficient. Depending on the relative rates of the reactions corrosion layers of different stoichiometric coefficient will be formed. By considering the stoichiometric coefficient and conductivity, Pavlov [81] proposed the following general rules:

$\nu_1 > \nu_2$	low valency lead oxide	high specific resistivity corrosion layer
$\nu_1 < \nu_2, \nu_3$	high valency lead oxide	low specific resistivity corrosion layer

In addition to these reactions the self-discharge reaction between Pb and PbO_2 should also be considered. Its rate is determined by a fourth rate coefficient ν_4.

$$Pb + PbO_2 \xrightarrow{\nu_4} 2PbO \qquad (2.29)$$

The occurrence of this reaction leads to a decrease in the overall stoichiometric coefficient of the oxide and an increase in specific resistivity.

2.6.7 EFFECT OF ALLOYING ADDITIONS IN THE GRID

The alloying elements present in the grid influence the structure of the corrosion layer [91] by determining the type and rate of reactions occurring. A consequence of this is a variation in stoichiometric coefficient of the oxides and therefore conductivity.

Work conducted by Pavlov [81] and colleagues indicated that alloying additions within the grid influence the conductivity of the corrosion layer by either acting as an electrocatalyst or inhibitor to the reactions given by equations 2.26 to 2.29 [92,93]. They also found that: antimony increases the rate of reaction 2.27 and inhibits reaction 2.28, Tin catalyses reactions 2.27 and 2.28, and Lead grids that contain either one or both of these additives have corrosion layers with higher stoichiometric coefficients.

Pavlov identified a second influence of alloying additions that involved altering the semiconducting properties of the corrosion layer. As the corrosion layer is formed the ions of the alloying elements are incorporated within the structure of the oxide. The formulae of the oxides are:

$Pb_{1-x}D_xO_2$ in the case of PbO_2

and $Pb_{1-x}D_xO_n$ in the case of PbO_n (D = dopant)

Depending on the specific alloying addition, the principle effect is to increase or decrease the specific conductivity of the oxides, depending on the mobility of the charged carriers. Mixed oxides allow reduction at more negative potentials than those needed for PAM reduction. This allows the corrosion layer to remain conductive during reduction of the PAM and processes within the PAM therefore determine the plate potential.

2.6.8 PASSIVATION

Passivation of the positive plate is associated with the formation of lead monoxide. If the thickness of this layer exceeds a critical value it acts as a high resistance strata within the corrosion layer and can insulate the grid from the active material. The effect is to decrease the voltage at which discharge will occur on the plate. Passivation occurs via the reaction, $Pb + O \rightarrow PbO$, where the electrode system $Pb/PbO/PbO_2$ is formed. At open circuit the self-discharge reaction, $Pb + PbO_2 \rightarrow 2PbO$ occurs, also producing the high resistance lead monoxide layer [94]. A third situation where lead monoxide is formed is during the drying stage of formed plates at high temperature, although this is not relevant for all battery types. This reaction is commonly referred to as thermopassivation [95].

The rate at which passivation occurs on the positive plates can be affected by dopants present within the grid alloy and corrosion layer. Depassivation can occur by two processes, the first being the reduction of PbO to Pb by cathodic valancy [96] and the second by oxidation of PbO by the O_2 produced during overcharge, which produces a lower resistance oxide with higher valancy [95].

An impedance spectroscopy technique has been used by Simon et. al. [97,98] to investigate the passive layers formed on lead tin alloys in tetraborate and sulphuric acid solutions. This is of particular importance since passive layers can determine the life of the battery. Results showed that the polarisation resistance of the passivated electrodes increased with tin content in the tetraborate solution but decreased in the sulphuric acid solution. A tin content of approx 1.5wt% is required to ensure a high electronic conductivity and resistance to corrosion of the passive films. The sharpest increase was found between 1 and 1.5 weight percent. Surface films identified on alloys containing a high proportion of tin were more electronically conducting. The weight percent tin in the grid was shown to influence the semiconducting properties of the grid corrosion layer and to favour the formation of lead oxides with stoichiometric coefficients greater than 1 [99].

2.7 THE NEGATIVE LEAD ACID BATTERY PLATE

The negative battery plate is manufactured in much the same way as the positive. Lead oxides and additives are mixed into a paste with sulphuric acid and water, the paste is then mechanically pushed into the grid before curing in an oven. Negative plates are assembled with the positives before formation.

Negative active material is formed electrochemically by the reduction of lead monoxide and the basic sulphates. This leads to the formation of a very porous form of lead commonly referred to as "sponge lead". Acquiring this structure, and successfully maintaining it, during the operational life of the battery is dependent on the addition of additives, expanders, and additionally the operational conditions.

Expanders and additives are an essential component of the negative paste mix. Common expanders include, barium sulphate, carbon black and salts of lingnosulphonic or humic acid. Natural or synthetic tanning substances are also sometimes used [100]. Expanders help to prevent degradation of the active material that would otherwise be caused by structural changes and passivation of the electrode surface. This is of particular importance in maintaining high levels of porosity. During battery operation, a number of electrochemical reactions occur on the surface of the negative electrode. These involve the dissolution and precipitation of lead and lead sulphate during charging and discharging. The extent to which these changes occur is dependent on a number of factors, most commonly depth of discharge and number of cycles.

When the expanders cease to function a number of changes occur that can lead to battery failure. These include the formation of a thin film of lead sulphate that cannot be removed during charging. This effectively insulates the plate from the electrolyte and initiates a breakdown of the initial porous lead leading to a structure with lower surface area. Each expander present in the electrode has its own individual function. Boden [101] has carried out a comprehensive review of expander materials. Details of the most common expanders and their role within the negative active material are described below.

- **Barium Sulphate**

  Barium sulphate has similar structural characteristics to lead sulphate. When added to the negative paste mix, it provides sites where lead sulphate crystallites can be nucleated. Within the battery it is electrochemically inactive and has a low solubility so it does not

influence the electrochemical processes. Its main function is to prevent the formation of thin passivating sulphate films.

- **Lignosulfonates**

  Lignosulfonates are complex aromatic polyethers derived from lignin. Within the negative active material, they act as strong anti-flocculents. Their composition consists of a large hydrophobic organic part, R^+ and a small hydrophilic inorganic fraction, SO_3^-. Within the electrolyte the molecule disassociates as shown in the equation below:

  $$RSO_3Na \Leftrightarrow RSO_3^- + Na^+ \qquad (2.30)$$

  The hydrophobic part is adsorbed onto the surface of the lead particles while the hydrophilic part faces the electrolyte. The increased repulsive potential results in an increase in the force preventing the particles from coalescing. Lignosulfonates increases the performance at low temperature and high rates of discharge.

- **Carbon**

  The addition of carbon black can be advantageous since its presence increases the conductivity of the active material. This is particularly important during periods of deep discharge when large amounts of lead sulphate are present. Increased conductivity due to carbon black can improve discharge efficiency and aid the conversion of sulphate to lead during recharging.

For the full beneficial effects of expanders to be exploited, it is critical that they are added in the correct concentrations and their distribution is uniform. The proportions will vary depending on the application of the battery. For this reason, it is often recommended that battery manufacturers should premix the expanders in the correct ratio before addition to the oxide paste mix. This approach can reduce the risk of errors and aid consistent mixing.

Determination of the required proportions of expanders is important in order to use them to their full potential. A reduction from the correct quantity generally results in a decrease in the expander's influence on structural changes and consequently a decrease in effectiveness. It is equally important not to add expanders in excess amounts. For example, the organic constituent of lignosulfonates has a strong effect on the hydrogen over-potential and large excesses can reduce the active materials electrical conductivity by causing over-expansion of the plate.

Shiomi [102] *et. al.* have studied the effect of carbon on the cycle-life performance of VRLA batteries. This was done by measuring changes in crystallinity, particle size and conductivity of negative plates. Investigations have shown that the addition of carbon in increasing amounts reduces accumulation of sulphate, thereby extending the battery life performance. Batteries operating in a partial state of charge appear to benefit from the addition of carbon the most. This improvement was attributed to the conductive network of carbon particles.

Pavlov and Iliev [103] have examined the structure of the negative active mass and concluded that it is similar in structure to that of the PAM. They describe the composition as consisting of primary and secondary structures. The primary (skeleton) structure is produced during the first formation stage by the reduction of the lead oxides and basic sulphates. This provides both mechanical support and current collection between the grid bars and active material [48,104]. The secondary structure consists of many lead crystals that are attached to the surface of the primary skeleton structure. These are formed during a secondary formation stage involving the reduction of lead sulphate [103,48,104].

During charge and discharge of the battery the secondary lead crystals are oxidised and reduced. It has been deduced that these crystals determine plate capacity [103]. The presence of an expander is important since without this only a small number of long dendrites are formed.

One of the main failure mechanisms of the negative plate is the accumulation of lead sulphate crystals resulting in a decrease in battery performance. Negative plates generally have a better charging efficiency compared to positive plates due to their higher hydrogen over potential. However, if negative plates are left in the discharged condition the reduction of lead sulphate to lead on charging becomes more difficult. This is because the overcharge current is utilized for oxygen reduction on lead rather than sulphate reduction. The accumulation of lead sulphate on negative plates can be attributed to the following:

- A negative active material with a large particle size will lead to enlarged lead sulphate crystals which are very difficult to reduce due to their small specific surface area.
- Hindered charge acceptance caused by absorption of organic additives.
- Low local conductivity of localised lead sulphate (sulphation), which is usually observed on plates that have been left standing for long periods at high temperatures.

The current density on a lead negative plate will have an influence on the microstructure as the plate is cycled and therefore also on performance. Wales, Caulder and Simon [105] have

investigated this by examining plates cycled to different extents at varying current densities. Analysis techniques used were optical and electron microscopy, image analysis and BET surface area analysis. They were able to conclude that the change in capacity corresponded approximately to the change in the size of the lead sulphate crystals within the range of current densities studied. An increase in porosity was also observed in the plates as they were cycled. It is generally accepted that passivation is increased as the size of the crystals forming the passivating barrier decreases.

Research by Atlung [106] has highlighted the connection between negative plate failure and gas recombination within the battery. Plates that failed after a few hundred deep cycles in a valve-regulated battery were found to perform approximately 1400 deep cycles in flooded mode. Examination of the negative plates showed evidence of failure due to sulphation. It was concluded that at high recombination efficiencies, in the valve-regulated battery, the evolution of hydrogen prevented the reduction of sulphate crystals. This lead to a build up of sulphate resulting in a reduction of the cycle life.

2.8 CONCLUDING REMARKS

Advances in the materials and design of traditional lead acid batteries have resulted in the initial manufacture and development of the valve regulated lead acid battery. Today valve regulated batteries, working on the principle of oxygen recombination, have overtaken the more traditional designs in terms of performance and now dominate the market in the majority of applications. There are two basic designs, using either tubular or flat electrodes. Research included in this project has been focused on the study of the flat electrode design.

Performance levels obtained from a battery are dependent on a number of factors. The most obvious of these being the design, manufacturing method and materials used. Other considerations include the battery application and environmental conditions such as humidity and temperature. As a battery is cycled its capacity decreases due to degradation of the active materials. The failure of a battery is traditionally taken as the point when the capacity drops below a predefined value. If a battery fails unusually early within its service life this phenomena is commonly referred to as premature capacity loss. It can normally be accounted for by manufacturing defects or improper use.

Cycling has become the accepted method for battery testing. Specialised charging units have been developed which allow test batteries to be charged and discharged at predefined rates allowing a wide range of possible operating conditions or applications to be simulated. Data

logging units are used to measure battery or individual cell currents and voltages at different stages throughout the life of the battery giving an insight into how the materials within the battery are performing or failing.

A wealth of information can be gleaned from detailed examinations of the various battery components during both manufacturing and electrical testing stages. Battery materials have been studied using a wide range of analytical techniques available to the scientist today. These include methods such as light microscopy, which gives a macroscopic view of the coarse structure of an active material, to nuclear magnetic resonance, that allows the position of individual atoms within a crystal lattice to be determined.

Previous research has covered almost every area of battery production. However, the majority are concerned with the positive electrode. This is a particularly popular area of research as it is a common cause of failure although a large amount of information is available in other areas such as the negative electrode and separator paper.

2.9 REFERENCES

1. L. S. Holden, Valve-regulated lead/acid batteries: they are not all the same!, Journal of Power Sources, Vol. 59, (1996), pp. 115-118
2. D. A. J. Rand, L. S. Holden, G. J. May, R. H. Newman, K. Peters, Valve-regulated lead/acid batteries, Journal of Power Sources, Vol. 59, (1996), pp. 191-197
3. P. T. Moseley, Lead/Acid battery myths, Journal of Power Sources, Vol. 59, (1996), pp. 81-86
4. Rainer Wagner, Failure modes of valve-regulated lead/acid batteries in different applications, Journal of Power Sources, Vol. 53, (1995), pp. 153-162
5. R. H. Newnham, Advantages and disadvantages of valve-regulated lead/acid batteries, Journal of Power Sources, Vol. 52, (1994), pp. 149-153
6. T. Isoi, H. Furukawa, Valve-regulated lead/acid batteries for SLI use in Japan, Journal of Power Sources, Vol. 59, (1996), pp. 143-146
7. K. Takahashi, H. Yasuda, H. Hasegawa, S. Horie, K. Kanetsuki, Eight years experience with valve-regulated batteries for automotive use, Journal of Power Sources Vol. 53, (1995), pp. 137-141
8. K. Suzuki, K. Nishida, M. Tsubota, Valve-regulated lead/acid batteries for electric vehicles: present and future, Journal of Power Sources, Vol. 59, (1996), pp. 171-175

9. D.A.J. Rand, The lead/acid battery - a key technology for global energy management, Journal of Power Sources, Vol. 64, (1997), pp. 157-174
10. P. J. Brown, Overview of U.S. government programs on electric vehicles, Electric and Hybrid Propulsion Division, Office of Transportation Systems, U.S. Department of Energy
11. G. J. May, Operational experience with valve-regulated lead/acid batteries, Journal of Power sources, Vol. 53, (1995), pp. 111-117
12. D. Berndt, Maintenance Free batteries, Wiley & Sons, 2nd Ed., (1997), p. 7
13. James S. Symanski, Basanta K. Mahato, Kathryn R. Bullock, Defining a Recombination Efficiency for Sealed, Lead-Acid Batteries, Journal of the Electrochemical Society, March (1998), Vol. 135, No. 3, pp. 548-551
14. D. Pavlov, Energy balance of the closed oxygen cycle and processes causing thermal runaway in valve-regulated lead/acid batteries, Journal of Power Sources, Vol. 64, (1997), pp. 131-137
15. K. Matthes, B. Papp, R.F. Nelson, Recombination chemistry and thermal management in sealed lead-acid systems, pp. 1-31
16. D. Berndt, Maintenance Free batteries, Wiley & Sons, 2nd Ed., (1997), p. 97
17. S. Bodoardo, M. Maja, N. Penazzi, Processes involving gases in valve-regulated lead/acid batteries, Journal of Power Sources, Vol. 55, (1995), pp. 183-190
18. D. Berndt, Maintenance Free batteries, Wiley & Sons, 2nd Ed. (1997), p112
19. T. R. Crompton, Battery Reference Book, Butterworth & Co. (1990), Part. 1
20. S. M. Caulder, A. C. Simon, Thermal decomposition mechanism of formed and cycled lead dioxide electrodes and its relationship to capacity loss and battery failure, Journal of the electrochemical society, Vol 121, No. 12 pp. 1546-1551, Dec (1974)
21. E. M. Lawrence, Novel Materials In Lead-Acid Batteries, PhD Thesis, September (1997)
22. T. L. Blair, Lead oxide technology - Past, Present and future, Journal of Power Sources, Vol. 73 (1998) pp. 47-55
23. M. Brachet, PROC 3rd INT. CONF. LEAD, VENICE, SEP. (1968)
24. D. P. Boden, Improved oxides for production of lead/acid battery plates, Journal of Power Sources, Vol. 73, (1998), pp. 56-59
25. L.T. Lam, O. V. Lim, N. P. Haigh, D.A.J. Rand, J. E. Manders, D. M. Rice, Oxide for valve-regulated lead-acid batteries, Journal of Power Sources, Vol. 73, (1998), pp. 36-46
26. V. H. Dodson, Some important factors that influence the composition of the positive plate Material in the lead-acid battery, Journal of the Electrochemical Soc., May (1961), pp. 400-405

27. D. Pavlov, G. Papazov, Dependence of the properties of the lead-acid battery positive plate paste on the processes occuring during its production, Journal of Applied Electrochem., Vol. 6 (1976) pp. 339
28. K. Kordesch, Marcle Dekker, Batteries, Vol. 2, (1977), p117
29. Private communication, Hawker Energy, NEWPORT
30. R. David Prengaman, The metallurgy and performance of cast and rolled alloys for battery grids, Journal of Power Sources, Vol. 67, (1997), pp. 267-278
31. N. Y. Tang, Microstructure and properties of continuously cast, lead-alloy strip for lead/acid battery grids, Journal of Power Sources, Vol. 59, (1996), pp. 63-69
32. S. Zong, H. K. Liu, S. X. Dou, M. Skyllas-Kazacos, Evaluation of lead-calcium-tin-aluminium grid alloys for valve-regulated lead/acid batteries, Journal of Power Sources, Vol. 59, (1996), pp. 123-129
33. L. Albert, A Chabrol, L. Torcheux, Ph. Steyer, J. P. Hilger, Improved lead alloys for lead/acid positive grids in electric-vehicle applications, Journal of Power Sources, Vol. 67, (1997), pp. 257-265
34. D. Berndt, Maintenance Free batteries, Wiley & Sons, 2nd Ed. (1997), p184
35. D. A. J. Rand, RJ Hill, M McDonagh, Improving the curing of positive plates for lead/acid batteries, Journal of Power Sources, Vol. 31, (1990), p. 205
36. M. E. D. Humphreys, R. Taylor, S.C. Barnes, The curing of lead acid battery plates, International Power Sources Symposium, 6th, Brighton, (1968)
37. B. P. Varma, CW Fleischmann, Dibasic Lead Sulphate in Lead-acid Battery Plates, Technical Notes, Electrochemical Society, Vol. 124, No. 5, p. 718
38. J. K. Vilhunen, J. Tummavuori, Processes during preparation of lead/acid battery positive plates from tetrabasic lead sulphate (4BS) pastes, Journal of Power Sources, Vol. 46, (1993), pp. 269-283
39. L. T. Lam, D. A. J. Rand, The curing - or killing - of lead-acid positives, 3ELBC – Workshop 2, Batteries International, October (1992)
40. S. Laruelle, S. Grugeon-Dewaele, L. Torcheux, A. Delahye-Vidal, The curing reaction study of the active material in the lead-acid battery, Journal of Power Sources, Vol. 77, (1999), pp. 83-89
41. CA Vincent, Modern Batteries, Edward Arnold Ltd. UK, (1984), pp. 9–11
42. Reiner Kiessling, Lead Acid Battery Formation Techniques, Digatron Firing Circuits Inc, Box 2007, Norwalk, CT 06852

43. K. P. Bagshaw, Microscopic examination of active materials from lead acid cells, Electrochem. Acta, Vol. 10, (1965), p. 867
44. P. Ruetschi et. al., Oxygen overvoltage and electrode potentials of alpha and beta PbO2 Journal Electrochem. Soc., Vol. 106, (1959), No. 7, pp. 547-551
45. F. Steffens, Journal of Power Sources, Vol. 31, (1990), pp. 233-241
46. W. O. Butler, C J. Venuto, D. V. Wisler, Electron Microscope study of positive lead-acid electrodes during formation, Journal Electrochem Soc., Vol. 117, (1970), No. 11, pp. 1339-1342
47. K. R. Bullock, B. K. Mahato, W. J. Wruck, Use of Conductive Materials to enhance Lead-Acid Battery Formation, Journal of the Electrochemical Society, Vol. 138, No. 12, December (1991), p. 3545
48. D. Pavlov, V. live, G. Papazov, E. Bashtavelova, Formation Processes of the Lead-Acid Battery Negative Plates, J Electrochemical Soc. Vol 121, No. 7 (1974), pp. 854-860
49. G. Maia, E. A. Ticianelli, E. R. Gonzalez, A modeling approach to the optimization of lead-acid battery electrodes, Journal of Applied Electrochemistry, 23 (1993) 1151-1161
50. J. O. Wirtz, Batteries International, Issue 3, April (1990), p. 16
51. P. Faber, "Power Sources", Vol 4, Oriel Press (1973), pp. 525-540
52. W. Bohnstedt, Challenges for automotive battery separator development, Journal of Power Sources, Vol. 67, (1997), pp. 299-305
53. L. C. Wang, et, al, Ultra-high molecular weight polyethylene (UHMW-PE) and its application in microporous separators for lead/acid batteries, Journal of Power Sources, Vol. 73, (1998), pp. 74-77
54. R. G. Robinson, R. L. Walker, Separators and their effect on lead-acid battery performance International Symposium, Bournemouth, October (1962), pp. 15-42
55. K. Peters, Influence of separator structure on the performance of valve-regulated batteries, Journal of Power Sources, Vol. 42, (1993), pp. 155-164
56. B. Culpin, Separator design for valve-regulated lead/acid batteries, Journal of Power Sources, Vol. 53, (1995), pp. 127-135
57. G. J. May, Development of valve-regulated lead/acid batteries for distributed power requirements, Journal of Power Sources, Vol. 59, (1996), pp. 147-151
58. John Devitt, An account of the development of the first valve-regulated lead/acid cell, Journal of Power Sources, Vol. 64, (1997), pp. 153-156
59. G. C. Zguris, A review of physical properties of separators for valve-regulated lead/acid batteries, Journal of Power Sources, Vol. 59, (1996), pp. 131-135

60. G. C. Zguris, Absorptive glass-mat separators for valve-regulated lead/acid batteries - thoughts on compression, Journal of Power Sources, Vol. 67, (1997), pp. 307-313
61. K. Nakamura, M. Shiomi, K Takahashi, M. Tsubota, Failure modes of valve-regulated lead / acid batteries, Journal of Power Sources, Vol. 59, (1996), pp. 153-157
62. K. McGregor, Effects of compression on recombant battery separator mats in valve-regulated lead-acid batteries, Journal of Power Sources, Vol. 73, (1998), pp. 65-73
63. G. C. Zguris, A broad look at separator material technology for valve-regulated lead/acid batteries, Journal of Power Sources, Vol. 73, (1998), pp. 60-64
64. D. A. Crouch, J. W. Reitz, Relating recombination mat separator properties to sealed lead/acid battery performance, Journal of Power Sources, Vol. 31, (1990), pp. 125 -133
65. H. G. Brown, The lead storage battery, 3rd Ed., (1974), pp. 6-7
66. D. Berndt, Maintenance Free batteries, Wiley & Sons, 2nd Ed., (1997), p. 340
67. K. Kordesch, M. Dekker, "Batteries", Vol. 2, (1977), p. 102
68. W. A. Badawy, S. S. El-Egamy, Improvement of the performance of the positive electrode in the lead/acid battery by addition of boric acid, Journal of Power Sources, Vol. 55, (1995), pp. 11-17
69. Hans Tuphorn, Valve-regulated lead/acid batteries: systems, properties and applications, Journal of Power Sources, Vol. 46, (1993), pp. 361-373
70. S. Goodman "How Polypropylene Won Its Case", Batteries International, Vol. 17, Oct. (1993), pp. 88-89
71. D. Berndt, Maintenance Free Batteries, Wiley & Sons, 2nd Ed. (1997), p. 327
72. K. Kordesch, M. Dekker, "Batteries", Vol. 2, (1977), p. 39
73. J. Perkins, M. T. Coyle, Observation of a substructural network in the positive plates of lead-acid storage batteries, J. Electrochem. Soc., April (1977), Vol. 124, No. 4, pp. 524-52
74. K. K. Constanti, A. F. Hollenkamp, M. J. Koop, K. McGregor, Physical change in positive-plate material – an underrated contributor to premature capacity loss, Journal of Power Sources, Vol. 55, (1995), pp. 269-275
75. D. Pavlov, N Kapkov, High – Temperature Curing of the Lead – Acid Battery Positive Plates, J. Electrochem. Soc., Vol. 137, No. 1, January (1990), pp. 21-28
76. P. Ruetschi, Influence of crystal and interparticle contact on the capacity of PbO2 electrodes, Electrochem. Soc., Vol. 139, No. 5, May (1992), pp. 1347-1351
77. S.E. Afifi, A. E. Saba, A. Y. Shenouda, Performance characterisitics of lead oxides in pasted lead/acid battery electrodes, Journal of Power Sources, Vol. 46, (1993), pp. 285-296

78. S. R. Ellis, N. A. Hampson, M. C. Ball, F. Wilkinson, The lead dioxide electrode, Journal of applied electrochemistry, Vol. 16, (1986), pp. 159-167
79. P. Ruetschi, R. Giovanoli, The presence of OH- ions, Pb2+ ions and cation vacancies in PbO2, Power Sources 13, Ch. 11, pp. 81-97
80. D. Pavlov, E. Bashtavelova, Structural Properties of the PbO2 Active Mass Determining Its Capacity and the "Breathing" of the Positive Plate During Cycling, Journal Electrochemical Soc., (1986), pp. 241-248
81. D. Pavlov, A theory of the grid/positive active-mass (PAM) interface and possible methods to improve PAM utilization and cycle life of lead/acid batteries, Journal of Power Sources, Vol. 53, (1995), pp. 9-21
82. D. Pavlov, B. D. McNicol, D. A. J. Rand, Power Sources for Electric Vehicles, ELSEVIER, AMSTERDAM, (1984), p. 344
83. Zen-ichiro Takehara, The Oxidation of lead sulphate formed at the interface between the lead plate and the porous active material of a lead acid battery, J. Electrochem. Soc., Vol. 137, No. 3, March (1990), pp. 800-804
84. E. Bashtavelova, A Winsel, Paste structure and its influence on the agglomerate-of-spheres parameters of the PbO2 electrode, Journal of Power Sources, Vol. 53, (1995), pp. 175-183.
85. R. J. Hill, M. R. Houchin, Incorporation of hydrogen into lead dioxide by a surface hydrolysis mechanism, Electrochemica Acta, Vol. 30, No. 4, (1985), pp. 559-561
86. R. J. Hill, I. C. Madsen, Structural parameters of beta-PbO2 and their relationship to the hydrogen-loss concept of lead-acid battery failure, J. Electrochem. Soc., July (1984), Vol. 131, No. 7, pp. 1486-1494
87. R. J. Hill, A. M. Jessel, The Electrochemical Activity of PbO2, A nuclear magnetic resonance study of hydrogen in battery and chemically prepared material, Journal of the Electrochemical Society, Vol. 134, No. 6, June (1987), pp. 1326-1330
88. M. Calabek & K. Micka, On the resistance of the grid/active material interphase in lead-acid battery electrodes, Electrochimica Acta, Vol. 37, No. 10, (1992), pp. 1805-1809
89. D. Pavlov, The lead-acid battery lead dioxide active mass: A gel-crystal system with Proton and Electron Conductivity, J. Electrochem. Soc., Vol. 139, No. 11, (1992), pp. 3075-3080
90. F. Lappe, Some Physical Properties of Sputtered PbO2 Films, J. Phys. Chem. Solids, Vol. 23, (1962), pp. 1563-1572
91. A. F. Hollenkamp, K.K. Constanti, M.J. Koop, L. Apateanu, M. Calabek, K. Micka, Effects of grid alloy on the properties of positive-plate corrosion layers in lead/acid batteries.

Implications for premature capacity loss under repetitive deep-discharge cycling service, Journal of Power Sources, Vol. 48, (1994), pp. 195-215.

92. B. Monahov & D. Pavlov, Influence of Antimony on the structure and the degree of Hydration of the Anodic PbO2 layer formed an Pb-Sb Electrodes, J. Electrochem Soc., Vol. 141, No. 9 (1994) pp. 2316-2326
93. D. Paolov & B. Monahov, Mechanism of action of Sn on the Passivation Phenomena in the Lead-Acid Battery positive plate (Sn Free Effect), J. Electrochem Soc., Vol. 136, (1989), pp. 27-34
94. J. Garche, N. Anastasijevic and K. Wiesener, Electrochimica. Acta, Vol. 26, No. 10, (1981), pp. 1363-1373
95. D. Pavlov, S. Ruevski, Thermopassivation of the lead dioxide plate of lead acid batteries, J. Electrochem. Soc., Vol. 126, (1979), p. 1100
96. R.F. Nelson and D.M. Wilson K., Power Sources, No. 33, (1991) pp. 165-185
97. P. Simon, N. Bui, N. Pebere, F. Dabosi, L. Albert, Characterization by electrochemical impedance spectroscopy of passive layers formed on lead-tin alloys, in tetraborate and sulfuric acid solutions, Journal of Power Sources, Vol. 55, (1995), pp. 63-71
98. P. Simon, N. Bui, N. Pebere, F. Dabosi, In situ redox conductivity, XPS and impedance spectroscopy studies f passive layers formed on lead-tin alloys, Journal of Power Sources, Vol. 53, (1995), pp. 163-173
99. N. Bui, P. Mattesco, P. Simon, N. Pebere, Fundamental research on the role of alloying tin as a means to eliminate the passivation phenomena in lead/acid batteries, Journal of Power sources, Vol.73, (1998), pp. 30-35
100. K. Kordesch, Marcel Dekker, “Batteries 2”, Inc., (1977), pp. 84-87
101. D. P. Boden, Selection of pre-blended expanders for optimum lead/acid battery performance, Journal of Power sources, Vol. 73, (1998), pp. 89-92
102. Masaaki Shiomi, et. al., Effects of carbon in negative plates on cycle-life performance of valve-regulated lead/acid batteries, Journal of Power Sources, Vol. 64, (1997), pp. 147-152
103. D. Pavlov, V. Iliev, “Structure and Organisation of the active mass in the negative plates of lead acid batteries”, Journal of the Electrochem., Soc. 131, No. 8, (1984), Abstract No. 283c
104. D. Pavlov, V. Iliev, J. Power Sources, 7 (1981/82), p. 153
105. C. P. Wales, S M Caulder, A C Simon, Effect of discharge current density on structure of the lead negative plate, Journal of the Electrochem. Soc., Feb (1981), pp. 236-242

106. Sven Atlung, Failure mode of the negative plate in recombinant lead/acid batteries, Journal of Power Sources, Vol. 52, (1994), pp. 201-209

3 EXPERIMENTAL METHODS FOR BATTERY CHARACTERISATION

3.1 CHARACTERISATION OF CELLS

For this study the failure of a battery has been defined arbitrarily, as the point when the capacity after charging is 80% of the initial capacity. The reduction in capacity of all cycled batteries can be attributed to changes that have occurred in the individual cells. However, the extent to which these destructive processes have developed in each cell is often different. Any differences can be quantified by measuring the reduction in voltage of each cell with time.

A GRANT Squirrel data logger, series 1000 or 1200, was used to log the voltages with time. Connections from each cell to the data logger were made by inserting nails through the battery case lid into the underlying cast-on straps. Each cell was connected to a different channel of the data logger prior to the battery being subjected to a C1 (100% depth of discharge in 1 hour) capacity discharge to 6V. The discharge current was 27.6A and recharge voltage 14.7V. Voltages were logged at one-minute intervals. After discharge, the battery was recharged and squirrel data downloaded into a PC and displayed on an Excel spreadsheet. The circuit used is shown in Figure 3.1.

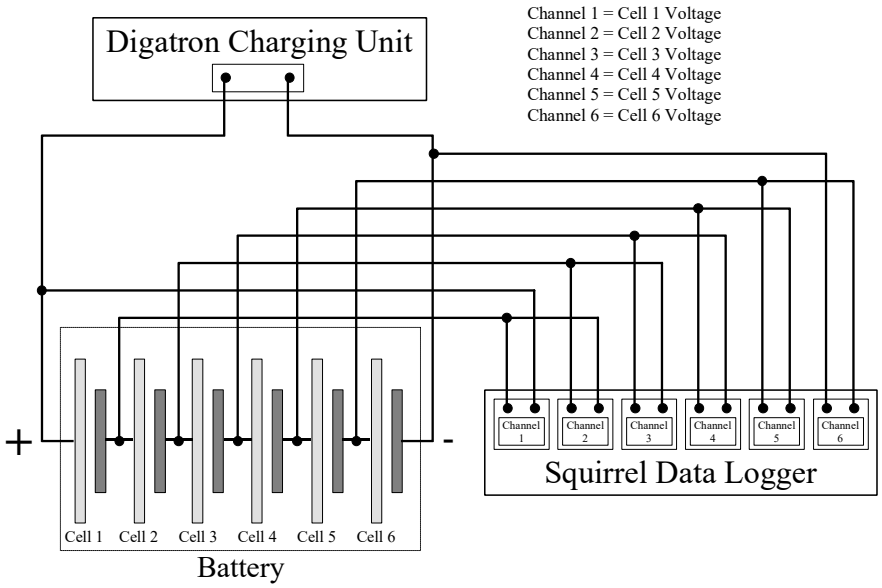

Figure 3.1: Circuit used to monitor voltages of individual cells

3.2 DETERMINATION OF INDIVIDUAL ELECTRODE POTENTIALS

On a number of the batteries investigated, the potentials of the positive and negative electrodes in the most and least healthy cells were measured. This was done using a mercury sulphate

reference electrode and a Squirrel data logger. A hole was drilled in the case above the cell under examination to allow insertion of the mercury sulphate reference electrode, which rested on the electrolyte held in the separator paper at the top of the cell. Contact to individual cells was achieved by inserting nails through the polypropylene battery lid into the underlying cast on straps. The positive and negative electrodes were then connected to the reference electrode. Three channels were used on the data logger for each cell, channel 1 to measure the negative electrode potential, channel 2 for the positive electrode potential and channel 3 for the total cell voltage. The voltages of the positive plates, negative plates and cell were logged while the battery was discharged and then recharged. A diagram of the circuit used is shown in Figure 3.2.

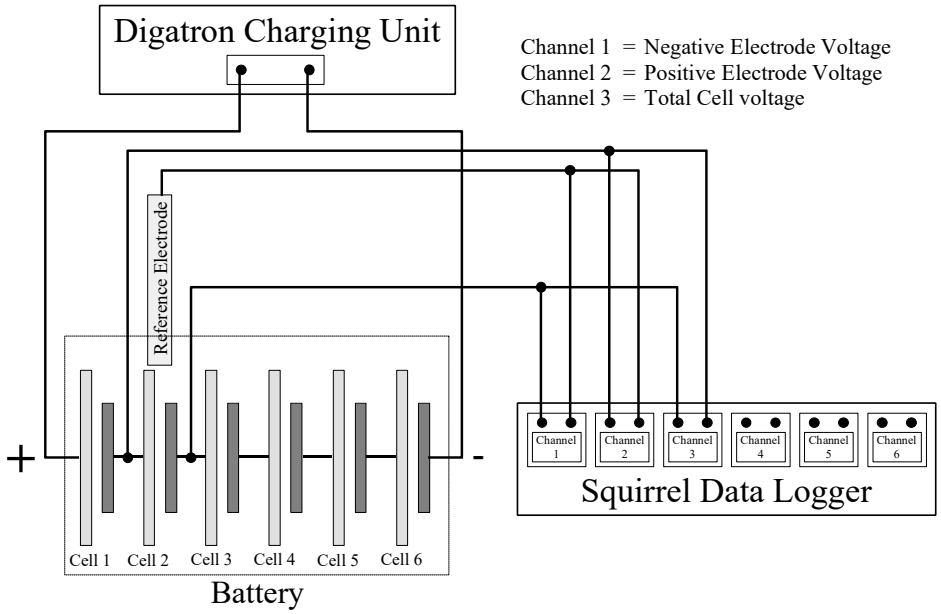

Figure 3.2: Circuit diagram used for monitoring voltages of positive and negative plates within a cell

3.3 DESCRIPTION OF BATTERY 'TEAR DOWN' PROCEDURE

All batteries were dismantled and examined using a standard "tear down" procedure which is described below.

The battery weight was firstly recorded on a digital balance. This was done to an accuracy of +/-1 gram. The voltage of the battery was then measured using a standard voltmeter. A Hewlett Packard 4338B milliohmmeter was used to obtain a value for the total impedance of the battery.

Voltage and impedance measurements were taken for the six individual cells of the battery. In order for this to be achieved, it was necessary to firstly gain access to the cast on straps of each cell. This was done by carefully removing the polypropylene battery lid. The biggest problem

encountered when attempting this was the risk of damage to the cast on straps connected to the positive and negative electrodes on the end cells, as these are directly connected to the battery lid. In order to overcome this problem, the lid was cut around the edges of the electrodes, with a saw, thereby separating the electrodes from the rest of the lid. The lid could then be removed by chiselling around the plastic weld without the risk of disrupting the underlying cast-on straps or cells. Once the lid had been removed, it was necessary to remove the oxide build up on the cast on straps to allow good electrical contact to be made with the volt and impedance meter probes. This was easily achieved by scraping with a sharp blade.

With the battery lid removed it was then possible to check the integrity of the inter-cell welds. This was done by chiselling the connecting weld at an angle of approximately forty five degrees, taking care not to push the cast-on strap down excessively, to avoid causing shorts to occur between the electrodes. Welds were examined for defects such as voids.

Finally, the most and least healthy cells were removed from the battery case for further examination. This was done by pulling the cell directly upwards, out of the battery case using a pair of pliers. It is worth noting that before this was carried out all swarf from the lid welds was removed to avoid snagging the electrodes and to avoid causing a short circuit within the cell.

Once the cells had been removed from the battery case, the individual positive and negative electrodes were separated. This was achieved by pulling off the cast-on straps with a pair of pliers, which conveniently doubled as an integrity check for the welds between the electrode and cast-on strap. The cell as a whole was then examined for defects such as damaged plates or separator paper.

Measurements of the specific gravity of the electrolyte were taken at the top and bottom of each cell, to allow the extent of acid stratification to be assessed, using a surface tension method. Electrolyte was obtained by squeezing it out from a sample of the separator paper taken from a representative position within the cell.

Representative positive and negative plates, from both good and bad cells, were placed in a beaker of distilled water for approximately 30 minutes to dilute and remove acid. Plates were rinsed with industrial methylated spirits and placed in a vacuum oven at 60°C for 24 hours until totally dried. After the plates had dried the oven heater was switched off and the plates were allowed to cool to room temperature whilst still under vacuum. This was to prevent oxidation.

Dried plates were then stored in a dessicator, containing silica gel, before further examination and analysis.

3.3.1 VARIATIONS IN 'TEAR DOWN' PROCEDURE FOR BATTERIES CONTAINING DIFFERENT SEPARATORS

A number of batteries that contained different separator types were examined. For these, a more extensive procedure was followed in order to obtain data on separator saturation and acid specific gravity at different heights within the battery cell. After the cell had been removed from the battery case, it was split exposing a sheet of separator paper. The paper was cut into five horizontal strips, each approximately one inch in width, and then each strip weighed to an accuracy of 0.0001g. Distilled water was used to remove residual acid from the strips before drying in an oven. After the strips had been washed and dried, they were re-weighed allowing the weight of acid in each strip to be calculated. This procedure was then repeated, on a new separator sheet, except that instead of weighing the strips, the specific gravity was measured. Three sets of five strips were examined using this method from each cell. Care was taken to weigh the strips as quickly as possible to reduce the errors caused by evaporation and the strips being held horizontally. Once cut, the order in which the strips were weighed was randomised to remove the possibility of introducing systematic errors into the results. Finally, the area of each strip was measured to allow the separator saturation to be calculated.

Areas were obtained by placing the separator paper strips, and a ruler, on a flat bed scanner. The image was then exported into Optimas 6 image analysis software that was able to automatically measure the surface area of each piece. Values of surface area obtained were calibrated to units of millimetres squared using the ruler image.

4 EXPERIMENTAL METHODS FOR CELL CHARACTERISATION

4.1 SCANNING ELECTRON MICROSCOPY (SEM) OF ACTIVE MATERIAL FRACTURE SURFACES

An effective method of determining the structure of the positive and negative active materials is to examine fracture surfaces in a scanning electron microscope. This can give valuable information on the composition and structural properties such as particle size, shape and porosity.

4.1.1.1 SAMPLE PREPARATION

In order to produce a high quality image of the structure it is important to have a flat fracture surface so that the highest and lowest points are within the 'depth of field' of the microscope. This allows the whole picture to be in focus at low magnifications. Additionally, a steep surface sloping upwards away from the area under examination can act as a shield, if it is between the sample and detector, resulting in a shadowing effect reducing the quality of the image.

Active material tablets were extracted from the grid by initially cutting them out with the grid wires still attached. This was done using a razor blade cutting down onto a piece of glass. The grid wire was cut away from the top and bottom using the razor blade leaving a number of tablets joined with only lengths of grid wire between them. This is shown in **Error! Reference source not found.**.

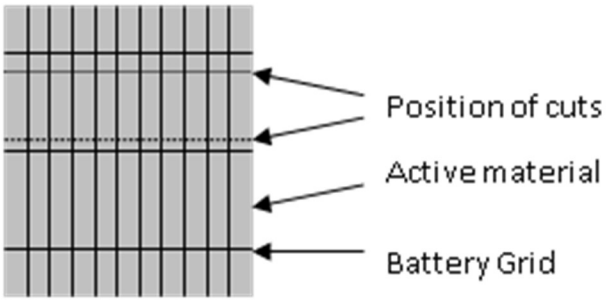

Figure 4.1: Positions of cuts for removing active material from grid

Remaining grid wire at the edges of the tablet was then peeled away leaving the tablet undamaged. The tablet was then fractured across its width using tweezers to obtain as straight a break as possible. This produced a cross section exposing the active material immediately adjacent to the grid wire and in the centre of the tablet. It was found to be progressively more

difficult to obtain neat fracture surfaces on samples from batteries that had been cycled large numbers of times. The most likely cause for this is the reduction in active material strength caused by cycling.

The fractured tablet was attached to a planchette with Araldite adhesive. This technique was adopted, rather than using the more traditional methods such as conductive pads, carbon dag or carbon 'plasticine', because the samples produced were more robust. Samples were stored in a desiccator, until required for examination in the SEM, to prevent the adsorption of water. Using an Edwards Sputter coater a thin layer of gold was applied to the sample, to improve conductivity and reduce charging. A coating time of five minutes was used.

4.1.1.2 EXAMINATION PROCEDURE

After insertion into the SEM photographs of the microstructure were taken at various magnifications of different areas of the specimen. Photographs of similar magnification were taken as often as possible to make comparisons easier, although this was not always possible. Additional photographs, some at different magnifications, were taken if the initial photographs did not give an accurate representation of the structure or there were additional features present requiring more detailed examination. When photographing negative active material, fibres were often observed protruding from the fracture surface. These were particularly prone to charging and areas containing these fibres were avoided whenever possible.

All images were secondary electron and produced using a JEOL 6310 scanning electron microscope. At high magnifications, the smallest spot size that could be used easily was selected. Working distances were reduced as much as possible to enhance image quality and a beam voltage of 15kV was found to give good quality images.

4.2 BET SURFACE AREA ANALYSIS

The surface area of both positive and negative active materials is an important property to consider when studying batteries. It will have a direct influence on the way in which the battery operates since all electrochemical reactions that occur, within a battery during operation, do so on the surface of the active materials. Surface area can be related to material properties such as rate of solubility, chemical reactivity, density and porosity in many instances.

In the case of battery materials, the BET surface area, named after the scientists Brunauer, Emmett and Teller, is an effective method. Values of surface area are obtained by measuring the volume of gas required to form a monolayer on the sample surface. If the cross sectional

area of the gas molecule adsorbed and the number of molecules are known, it follows that the surface area of the sample can be calculated. The gas used was nitrogen, which has a cross sectional area of 1.62×10^{-20} m^2.

The analysis was performed using a Micromeritics Gemini 2360 VS.OO. This equipment is used to measure the volume of gas adsorbed with change in pressure. During gas adsorption onto the surface a number of processes occur which can be shown diagrammatically by plotting relative pressure, P/P_0 versus number of molecules adsorbed, N, shown in Figure 4.2.

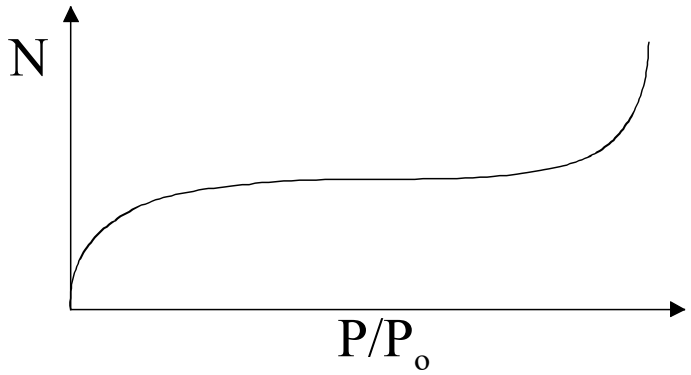

Figure 4.2: Typical plot of N versus P/P_0

The first half of the curve represents the formation of a mono-layer on the sample surface. The rapid increase in adsorption in the second half of the curve represents the formation of a multi-layer or different adsorption mechanism.

The BET surface area is obtained by plotting the linear form of the BET equation.

$$\frac{1}{V\left(P_0 / P - 1\right)} = \frac{\left(c - 1\right)}{V_m} \times \frac{P}{P_0} + \frac{1}{V_m c} \qquad (4.1)$$

where: V = Volume Adsorbed

V_m = Volume of gas required to form complete monolayer

P = Pressure

P_0 = Pressure of sample at liquid nitrogen temperature under vacuum

c = Constant

The gradient and intercept of the line is used to calculate V_m, which allows the sample surface area to be calculated from the sample weight and cross sectional area of a nitrogen molecule.

However, there are a number of physical effects, which this method does not take into account, such as chemisorption, dipole-dipole interactions and hydrogen bonding. A consequence of these is the addition of errors into the results, the magnitude of which will be determined by the

sample properties. The method assumes only physical adsorption occurs as a result of the formation of weak Van der Waals bonds. When the rate of adsorption equals that of desorption, the monolayer formed is assumed to be in dynamic equilibrium and readings are taken.

4.2.1.1 SAMPLE PREPARATION

BET surface area analysis was conducted on samples of positive and negative active material after they had been removed from the battery. The method used to remove and stabilise the electrodes is described in the previous section on battery 'teardown procedure'. Active material was removed from the battery grid and broken into pieces small enough to fit into the sample tube. Care was taken not to break the pieces more than necessary, as this artificially increases the surface area and therefore the measured value.

4.2.1.2 EXPERIMENTAL PROCEDURE

In order to carry out a successful analysis it is necessary to know the weight of the sample. The easiest way of determining this is to weigh the sample tube before and after it is filled, this was done to an accuracy of 0.0001g. Several sample tubes were available in different sizes for use with the Micromeritics Gemini. Due to the relatively low surface area of active materials the largest sample tube available was used in order to maximise the surface area for analysis; this had a volume of approximately 7cm^3. A visual inspection of the sample tube was made to ensure it was clean before use, as contaminants can cause errors in the results. After the weighed tube had been filled, it was necessary to remove any volatile species, which may have been present on the surface. This process is referred to as 'degasing' and achieved using Micromeritics Flow Prep 060. A temperature of approximately 60ºC was used, for a duration of at least 45 minutes, under a constant flow of nitrogen gas. After degassing the sample and tube were removed, weighed and the sample weight calculated. This was entered into the Micromeritics Gemini input console and the measurement procedure initialised.

4.3 X-RAY DIFFRACTION (XRD)

The German physicist Roentgen discovered X-rays in 1895. However, it was not until 1912 that their exact nature was established and the phenomenon of X-ray diffraction by crystals was discovered. XRD proved the wave nature of X-rays and provided a new method with which to investigate the fine structure of matter.

X-rays are classed as electromagnetic radiation and can therefore be produced over a range of different wavelengths. The wavelength used for diffraction is in the range of 0.5-2.5Å. This is small compared to that of visible light, which has a wavelength of approximately 6000Å [1]. X-

rays are generated by firing an electron beam at a piece of metal. Different metals will produce x-rays with varying wavelengths. For the purposes of this study, copper K_α radiation was used which has a wavelength of 1.5405Å.

4.3.1 METHODS OF ANALYSIS

XRD can be used to identify phases present in a sample thereby providing a qualitative analysis, and also obtaining information on the relative abundance, giving a quantitative analysis. Both of these methods are used in the analysis of battery materials.

4.3.1.1 QUALITATIVE ANALYSIS

X-ray diffraction patterns can be obtained for all compounds with a crystalline structure where the number of lines present in the pattern is determined by the complexity of the material. For example a simple cubic structure will not have as many lines as a more complex one such as face-centered cubic or hexagonal close packed. This is accounted for by the greater number of planes available to diffract x-rays. The positions of the lines on a x-ray diffraction pattern can be described by Bragg diffraction. Because incident and diffracted x-rays are coherent at certain angles of diffraction, constructive interference occurs and the x-rays are enforced. Bragg's law can be written as.

$$N\lambda = 2d \sin \theta \qquad (4.2)$$

where: λ = Wavelength of x-rays

θ = Angle of diffraction (theta value, *2-theta normally plotted*)

n = unit number

d = distance between the planes diffracting x-rays (d-spacing)

If a mixture is formed from more than one phase, the resulting diffraction pattern will contain all the lines from each phase present. When an unknown sample is analysed, its composition is determined by identifying the phase responsible for producing each line. This process is most difficult for compounds with similar crystal lattices as these produce similar patterns with lines that overlap. It becomes progressively more complex as the number of phases within the sample increases.

For this reason, analysis of multiphase samples containing many lines is often problematic and in order to identify the compounds present with confidence a logical approach is necessary. Initially a prediction is made of the compounds, which the sample is likely to contain, and then

validated by comparing the test pattern with previously obtained patterns. These are available from the two main sources described below.

1. Information on almost every common crystalline compound is available from the Joint Committee for Powder Diffraction Standards (JCPDS) files [2]. These contain basic crystallographic information on the compound and a list of the 2-theta values and relative intensity for each of the diffracting planes in the compound's lattice.
2. To complement this information, it is sometimes useful to refer to an actual diffraction pattern visually as this allows all the lines present in the pattern to be compared simultaneously. This is particularly useful as slight changes in sample height during analysis can shift the peaks to the left or right. The result of this is that when 2-theta values are being compared they rarely match exactly and it is usually not apparently obvious if a line under examination is part of the compound suspected or a different one.

Table 4.1 below gives the JCPDS file number and the source used to obtain a sample for each of the common compounds found in the lead acid battery.

Table 4.1: JPCDS file numbers and source of samples

PHASE	JCPDS file No.	Source of sample
Dibasic lead sulphate	02 - 1376	Produced by the reaction of PbO and PbSO4 in the ratio 2:1 at 973K for 24 hours, grinding and then at 973K for a further 24hours
Tetrabasic lead sulphate	23 - 0333	Produced by the reaction of PbO and PbSO4 in the ratio 4:1 at 1023K for 24 hours, grinding and then at 1023K for a further 0.25 hours
Tribasic lead sulphate	02 - 1376	
α-PbO2	37 - 0517	
β-PbO2	41 - 1492	BDH, Lead Dioxide 94%, (contains some α-PbO_2)
Pb3O4	41 - 1493	Hopkin & Williams Ltd. Lead Oxide (Minium, Red Lead)
Monobasic lead sulphate	37 - 0516	Produced by the reaction of PbO and PbSO4 in the ratio 1:1 at 973K for 24 hours, grinding and then at 973K for a further 24hours
β-PbO	38 - 1477	Fluka, Lead (II) Oxide, Red 99%
PbSO4	36 - 1461	Fluka, Lead (II) Sulphate 98%
Pb	04 - 0686	Negative battery electrode
α-PbO	05 - 0561	Fluka, Lead (II) Oxide, Yellow 99.0%

4.3.1.2 QUANTITATIVE ANALYSIS OF BATTERY PLATES

Quantitative analysis of a mixture can be obtained as the intensity of the peaks on a diffraction pattern, corresponding to a particular phase, are related to the proportion of that phase [3]. Several different techniques exist for relating the peak area or intensity to the proportion of the corresponding phase in the mixture. The most common of these methods include:

1. Simple correlation between peak height and the amount of phase present.
2. The external standard method, which uses a line from a pure phase as a reference.
3. The direct comparison method, which uses a line from another phase in the mixture.
4. The internal standard method, which uses a line from a foreign material.

The accuracy of the methods described above vary depending on the nature of the materials being analysed and how susceptible they are to the introduction of errors caused by factors such as preferred orientation, phase impurity, and variations in particle size and shape. For the purposes of examining battery materials, the errors introduced by these factors are significant, and benefits can be gained by using a method that takes these into account.

Researchers have developed a computer program, called PEAKS, that is specifically designed for the quantitative analysis of materials commonly found in the lead acid battery. Their program uses the direct comparison method, which has the advantages of requiring no internal standard. The use of calculated pre-determined reference intensity ratios reduces uncertainty caused by varying degrees of crystallinity, particle size and lattice distortion. A description of the program is given in the following section.

Description of PEAKS

The PEAKS program was developed by the CSIRO in the Division of Mineral Products under sponsorship from Pasminco Metals Ltd. [5]. The program is capable of determining the relative abundance of the lead phases commonly found at the different stages of lead acid battery manufacture and service. Peak intensities from the XRD patterns are entered into the "*input screen*" of the program and the relative abundance of each phase is calculated. Initial corrections are made for background radiation and peak overlap before average intensities are calculated for up to three of the peaks from each phase present. Data is then normalised for differences in scattering power using pre-determined calculated reference intensity ratios[6]. Compounds included in the program and the 2-theta value of the peaks required are shown in Table 4.2. It should be noted that the peak positions quoted by the program and shown in the

table are theoretical values only, and small deviations from these are often encountered in practice. This can be accounted for by the height of the sample within the diffractometer.

Table 4.2: 2-theta values of peaks required for analysis using PEAKS program

Phase	**2 theta value(s)**
Tribasic lead sulphate	9.03, 27.40
Tetrabasic lead sulphate	10.70, 27.58, 33.58
α-PbO_2	23.25, 50.55
β-PbO_2	25.40
$Pb3O_4$	26.35
Monobasic lead sulphate	26.65
β-PbO	29.08, 30.32, 37.81
$PbSO_4$	29.68
Pb	31.27, 36.26, 52.22
Hydrocerussite	34.16
α-PbO	48.59, 54.76

The PEAKS program includes a total of 11 compounds, which can be entered into the quantitative analysis calculation simultaneously. A consequence of this is that the peak positions required for each compound are not necessarily the 100% intensity peaks, which from a statistical point would be the first choice to minimise errors provided that no peak overlap was present. The reason for doing this is to reduce the introduction of errors due to overlapping peaks. However, it should be recognised that the analysis may not use the most appropriate selection of peaks in every instance.

Despite the factors mentioned previously, it was decided to use the PEAKS program, rather than write a new analysis program. On balance, the advantages of using an existing piece of software, which had been subject to testing and validation were considered to outweigh the relatively minor disadvantages identified.

4.3.2 SAMPLE PREPARATION

XRD samples were prepared from the dried plates by pushing a number of tablets from the centre of the grid and then grinding to a fine powder using a pestle and mortar. The ground powder was placed in an aluminium XRD holder with a glass slide back. This was then inserted into the X-ray diffractometer for analysis.

4.3.3 EQUIPMENT AND PROCEDURE

A Philips PW1730/00 diffractometer using Cu K_α radiation, was used for all analyses. Samples were scanned over a range of 5 to 90 degrees in order to obtain background values at 9 and 19

for quantitative analysis using the PEAKS program. A scan speed of 0.5 seconds per step and a step size of 0.01° was used.

4.4 DETERMINATION OF LEAD CONTENT BY WET CHEMICAL ANALYSIS

When the PEAKS program is used to analyse x-ray diffraction data, the abundance of lead oxides and sulphates is calculated to +/- 4%, whereas the error on lead is +/- 10% [5]. In order to obtain more accurate values for the lead content an alternative method must be used. A common and reliable approach commonly used within the battery industry is to use *Mannitol solution*, the method of which is described below.

Composition of Mannitol Solution

Mannitol solution consists of the following compounds dissolved in distilled water. It works on the principle that lead monoxide is soluble in sodium hydroxide solution while metallic lead is not. The hydrazine sulphate allows higher oxides of lead to be reduced.

- 200g Sodium Hydroxide
- 50g Mannitol
- 1g Hydrazine Sulphate
- 1dm^3 Distilled Water

Experimental Method

In order to determine the proportion of lead in a sample the following method was followed.

1. Weigh approximately 5g of the sample into a conical flask to an accuracy of 0.0001g (W1).
2. Add approximately 100ml of Mannitol solution and boil until all oxide is dissolved. The time required for this varies depending on how much lead oxide is in the sample. It is harder to determine this point for negative active materials as the carbon black additive is released into the solution turning it into a cloudy black colour. As a rule, the time required was rarely greater then 20 minutes.
3. Filter the solution through a pre-weighed (W2) sintered glass bottomed crucible, lined with some thin fibre glass paper, using a vacuum pump and wash until all residual solution is removed.
4. Dry crucible with sample at 105°C for 1 hour
5. Reweigh crucible after removal from oven (W3)
6. Calculate percentage free lead using the equation 4.3 below:

$$\%\,\mathrm{FreeLead} = \frac{(\mathrm{W3} - \mathrm{W2})}{\mathrm{W1}} \cdot 100\% \qquad (4.3)$$

Although this method is more accurate than x-ray diffraction, errors can be introduced into the results. In addition to those caused by the weighing, the most significant is the surface oxidation of lead during drying in the oven. This is normally identified when the calculation gives a free lead value of greater then 100%. The severity of this error varies from sample to sample and was never more than a few percent for the results contained within this study.

4.5 DENSITY MEASUREMENTS

The density of samples was measured using a Micromeritics Accupyc 1330 fully automatic pycnometer. The Accupyc obtains the density using a gas displacement method. A holder is filled with a known weight of sample that is then placed in a calibrated volume within the equipment. The volume of the sample is deduced by measuring the pressure change of helium gas in the sample chamber. Density is then calculated using equation 4.4.

$$\rho = \frac{m}{V} \qquad (4.4)$$

The pycnometer obtained 10 values for the sample density and then calculated an average.

Sample Preparation

Samples were prepared using the same method described in section 4.2 for BET surface area analysis.

Procedure

Initially the sample holder was weighed on a digital balance accurate to 0.0001g. It was then filled and re-weighed, therefore allowing the sample weight to be calculated. The sample weight was then entered into the pycnometer's memory using the 'input key pad' before the analysis was initiated.

4.6 TRANSMISSION ELECTRON MICROSCOPY

Transmission electron microscopy allows samples to be examined at much higher resolutions than with scanning electron microscopy. This is possible due to the method of operation, passing a collimated beam of electrons through the sample and onto a fluorescent screen mounted at the bottom of the microscope. Although this technique produces high resolution and high magnification images, it requires specially manufactured samples, which can be time consuming and difficult to prepare successfully.

Energy dispersive analysis of x-rays was used to identify the elements present in the sample and electron diffraction patterns to deduce the structure. The type of transmission electron microscope used was a Jeol 2000FX.

Sample Preparation

Transmission electron microscopy samples must be thin enough to allow an electron beam to pass through them, but thick enough to survive heating by the beam. There is a wide range of methods available for the production of TEM specimens, each of which has its advantages and disadvantages. Normally the type of sample being prepared dictates which methods are appropriate. For examination of negative active material, ultra micro-toming samples mounted in resin was utilised. A description of the method used is described below.

Samples of negative active material were removed from the negative grids after drying in the vacuum oven. In order to produce small particles of active material, tablets were snapped into two pieces whilst held over a piece of cigarette paper to catch the particles dislodged. This method not only produced a suitable amount of small particles but also minimised the risk of particle damage, which may have been caused by grinding. The particles were then soaked for 3-4hours in a solution of Silane and alcohol. Silane acts as a wetting agent for the resin and promotes the formation of a strong bond between the particles and resin on curing. After soaking, the particles were dried on another piece of cigarette paper with a fold down the middle. The paper was then held at an angle, and the particles moved down the fold by gentle tapping. This proved an effective method of separating the large agglomerated particles from the smallest ones, required for the analysis. These particles were then submerged in Taab resin for a number of hours whilst being agitated to encourage infiltration of the resin into particles surface porosity. The process was then repeated with fresh resin for an additional number of hours. It was possible to pour the excess resin off as the particles tended to sink to the bottom due to their higher density. Finally, the particles were placed in special holders for ultramicro-toming and cured in the oven.

Cured samples were trimmed and sectioned using a diamond knife, to a thickness of <100nm, before being placed on a plastic coated copper grid.

4.7 RESISTIVITY MEASUREMENTS OF NEGATIVE ACTIVE MATERIAL

For a battery to operate efficiently it is important that the active materials maintain a high conductivity throughout its life. Resistivity was measured for a number of negative active materials.

Sample Preparation

In order for resistivity to be measured accurately, a sample of active material of known dimensions was required. Due to the brittleness of the active material, it was necessary to first mount the electrode in resin to stabilise before cutting into blocks for measurement. To increase accuracy, it is advantageous to measure the resistivity over as large a sample as possible. The length between two grid bars restricts this distance therefore samples were prepared by cutting along the grid bars of the mounted electrode, leaving the maximum amount of active material sandwiched between two pieces of resin. In order to ensure high geometrical accuracy while cutting samples, it was found easiest to use a milling machine to remove unwanted material. A 3mm-diameter end mill was used for this purpose.

Theory

Generally to obtain a value for a materials resistivity a resistance measurement using a multimeter on a sample of known dimensions is taken. However, if the sample has a low resistance this task becomes slightly more complicated. A common method used is to measure the voltage drop across a known distance when a constant current is flowing. This can be achieved using either a two-point or four-point conductivity method. For the purposes of negative active battery material, the four-point measurement is the most appropriate as this minimises errors caused by contact and wire resistances [7].

The equation used for calculating the resistivity of the active material is obtained by substituting Ohms law into the expression for resistivity shown below.

$$\rho = \frac{R \cdot w \cdot t}{l} = \frac{V}{I} \cdot \frac{w \cdot t}{l} \qquad (4.5)$$

Where: ρ = Resistivity
R = Resistance
V = Voltage
I = Current
h,w = sample dimensions (height, width)
l = 0.008m (length between spring probes)

Equipment

The equipment used to measure the resistivity of the negative active material consisted of a Philips PM2518X ammeter, Linepower electronics constant current power supply and copper contacts (to hold the sample), connected in series. Spring probes, connected to a voltmeter, were then pressed against the side of the sample, at a distance of 8mm, as shown in Figure 4.3 below.

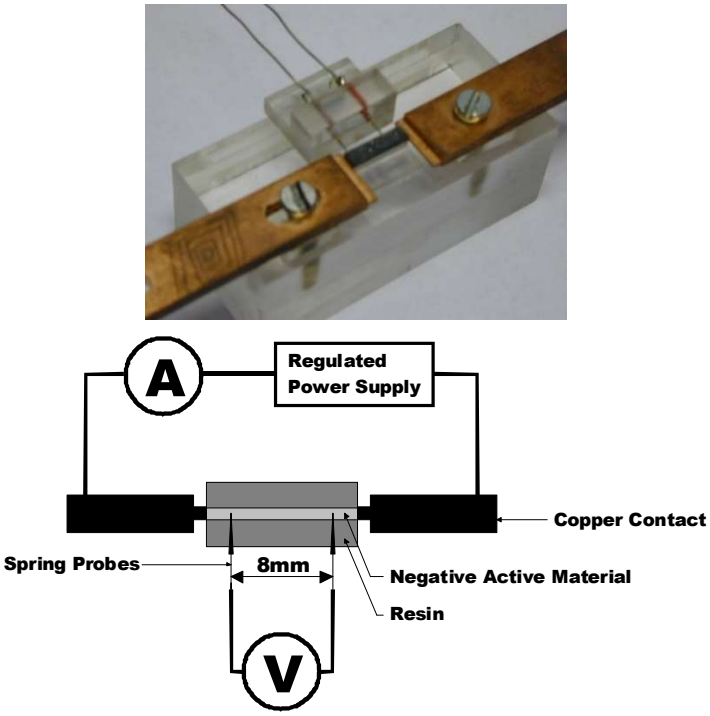

Figure 4.3: Apparatus used to measure negative active material resistivity

Procedure

Sample dimensions were measured using digital vernier callipers. The resistance was obtained by plotting a graph of current versus voltage for each sample and then calculating the slope. Measurements of voltage were taken at constant currents of +/-2, 1.5, 1 and 0.5 amps. The resistance and dimensions could then be substituted into the equation above and a value for resistivity obtained. Measurements were taken on 8 samples for each active material type.

4.8 INTERFACIAL ANALYSIS (METALLOGRAPHIC TECHNIQUE)

The macroscopic structure of both the positive and negative active materials, and the corrosion layer on the positive grid wires can provide important information as to why a battery cell has failed. An effective way to study these features is to examine a polished cross section using optical or electron microscopy.

Method of Sample Preparation

Dried battery plates consist of a soft lead grid, with very low stiffness, surrounded by crumbly, brittle active material. When handling plates great care must be taken to avoid unnecessary bending as this can lead to the formation of additional cracks in the active material. In order to minimise the risk of causing further damage to the plates after tear down, they were stabilised by encapsulation in resin. This was achieved by laying the plates horizontally, jacked up on small plastic blocks approximately 3mm high, within a specially made latex mould. Resin was

then poured into the mould to a height of approximately 7mm, thus surrounding each side of the plate in several millimetres of resin.

After encapsulation plates were cut and remounted into suitable sizes for polishing. In order to ensure consistency of results, cross-sections of the electrodes were always taken from the middle position of the plate. However, exceptions to this procedure were made if this area contained cracked active material caused by post tear down damage. Samples were normally taken by cutting a strip of electrode approximately 15mm in width from the centre of the plate. This strip was then cut into smaller sections and remounted in smaller cylindrical moulds.

Polishing Procedure

The procedure used for polishing the sections consisted of a number of different stages. Although some polishing was done automatically, it was found that the best results were achieved by hand. A common problem encountered when polishing a multi-phase material, such as a battery plate, is the risk of a particle of the hard phase such as the oxide, becoming dislodged and consequently, damaging the softer lead phase. Little can be done to prevent this. However, damage can be minimised in two ways. Firstly, by having a small sample of electrode and secondly, by holding the sample so that its length is in the same orientation as that of the grinding wheel. Due to the variation in property, no two samples behaved in the same way when being polished. For this reason, it was necessary to periodically check the sample at the end of each stage of preparation using light microscopy to ensure the next stage could be started.

- **Planar Grinding Stage**

  Samples were initially ground using silicon carbide paper however; a problem with this approach is small particles of carbide breaking off or becoming dislodged. If this occurs, particles often become embedded into the soft lead grid. This proved to be unavoidable. However, the severity and quantity of embedded carbide could be reduced in two ways. Firstly, a bar of steel was rubbed against each fresh sheet of silicon carbide paper, with a generous amount of water flowing, for a few seconds before the sample was ground. The purpose of this was to remove any loose carbide particles and to break off and remove any sharp spikes of carbide that were likely to break inside the lead. Secondly, a layer of candle wax was applied to the paper. This acted, as a soft medium in which any loose particle would become stuck, rather than embedding in the lead. A series of different grades of silicon carbide material were used ranging from 300 to 1200 grit and a platen speed of 150rpm was used. Water was used as a lubricant and only a light

pressure was applied to the sample. The papers were replaced after 30 seconds to 1 minute of grinding.

- **Sample Integrity Stage**

  The sample integrity stages of preparation were conducted using a Texmet polishing cloth loaded with alumina suspension. A platen speed of 100rpm was used and normally a good sample finish was achieved after polishing with 5 and then 0.3 micrometer alumina. Polishing was again conducted by hand and periodic checks of the surface using light microscopy was required to identify the point at which the next stage could be started.

- **Polishing Stage**

  The polishing stage was conducted using a Buehler Vibromet 2. Masterpolish was used as a polishing media on a Texmet cloth. A duration of 30 minutes was found to produce the best results.

Examination of finished samples

Samples were examined using optical and electron microscopes. For observation in the electron microscope a layer of gold was applied to the surface using an Edwards S150B sputter coating unit. This was to prevent charging of the resin. When observing the polished samples care must be taken in the interpretation of the image, especially at the interface between the lead and positive active material. Even after vibratory polishing slight differences in height between the lead and corrosion layer were noticeable. However at larger magnifications, this effect is less obvious and a shadowing effect is often observed which could easily be mistaken as an interface or feature of the sample. Another phenomenon was reaction of polishing media with the lead grid. This was most noticeable when comparing lead and lead tin grid wires as they often showed a slight variation in colour. The most misleading effect was a reaction of the polishing media with the lead grid adjacent to the corrosion layer. On certain samples this reaction layer looked convincingly like an additional phase of the grid corrosion layer. An example is shown in Figure 4.4 below.

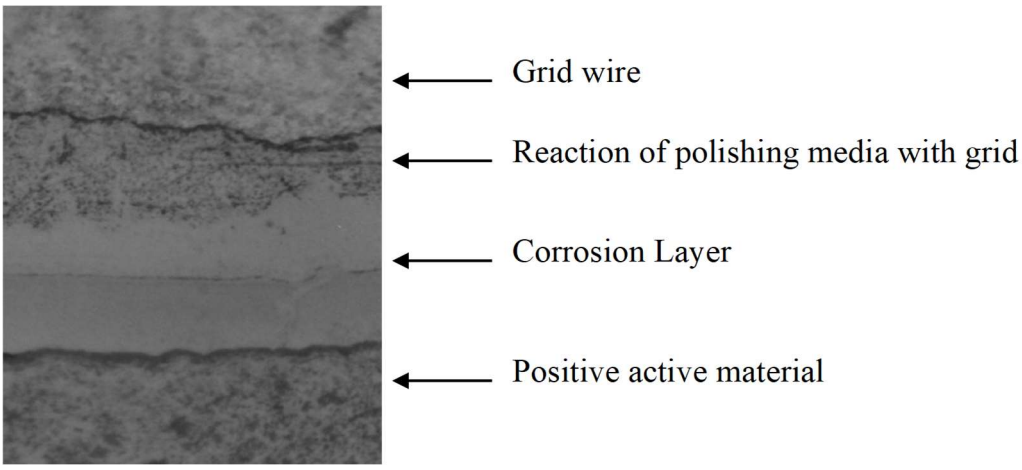

Figure 4.4: Example of the reaction of polishing media with positive grid wire

Measurement of corrosion layer thickness

Photographs were taken of typical grid wires from batteries cycled various numbers of times using either scanning electron or light microscopy. Due to variations in surface finish of the samples, there was no consistent trend of one method being superior to the other.

An optical microscope with camera attachment was used to acquire images of grid wires for image analysis. The thickness of the corrosion layer was measured at various positions on the grid wire using Optimas 6 image analysis software[8].

4.9 GRID / CORROSION-LAYER INTERFACIAL ANALYSIS (ULTRA-MICROTOME)

Although mechanical polishing of cross-sections was successful for obtaining images of corrosion layers several tens of microns thick, it proved impossible to obtain an image of any quality of the grid/corrosion-layer interface using this method. This was due to the difference in properties between the soft lead grid wire and hard lead oxide ceramic corrosion layer, which wore down at different rates under the same polishing media. Ultra-microtoming, however, was a successful method of preparation.

Ultra-microtoming, although mainly used for biological samples, can be used for preparation of metals and ceramics as long as the correct method is used. For the purpose of obtaining a good quality grid/corrosion-layer cross-sectional image, the microtome needs only to be used as a tool to obtain a flat surface that can then be examined by scanning electron microscopy, rather than to produce thin sections.

Method of Sample Preparation

In order to produce a sample, a suitable section of positive grid wire must firstly be obtained. This was done by cutting sections of grid wire out of a positive electrode and then breaking away the positive active material. Due to the relative strengths of the grid/corrosion-layer bond and corrosion-layer/active-material bond, the corrosion layer stayed intact with the grid in the majority of instances as the active material was removed. Once a suitable section of grid wire had been obtained containing a uniform layer of corrosion with a minimum amount of positive active material attached, it was mounted in resin. Latex moulds, specially designed to produce samples for the ultra-microtome, were used to cast the resin. A good contact between the resin and sample was ensured by soaking the samples in the resin for 4 hours. The samples were then removed from the resin, placed in the mould, and topped up with fresh resin. In order to cure the samples the moulds were placed in an oven at 60°C for a period of at least 24 hours.

Once cured, the sample was trimmed to a suitable size and dimensions for ultra-microtoming. This was initially done using a razor blade. A cross section was trimmed to a trapezium shape with the grid/corrosion-layer interface in the same orientation as that for sectioning, see Photograph 4-1. The trapezium had sides of length approximately 400 microns.

Sectioning was done so that the knife cut from the widest side to the opposite, narrowest side of the trapezium, along the length of the interface. Initial trimming was done using a glass knife and the final sections were cut using a diamond knife in order to obtain as clean a cut as possible.

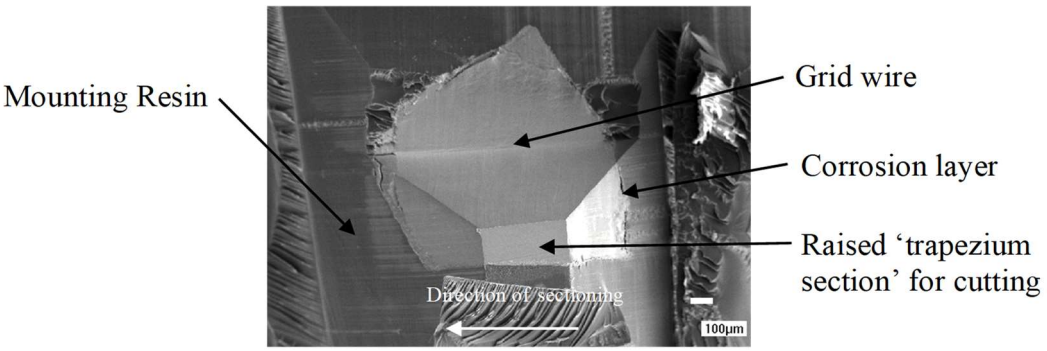

Photograph 4-1: Ultra-microtomed section

Once a high quality cross-section had been obtained, a thin layer of gold was deposited onto the surface to prevent charging of the resin in the SEM. This was done using an Edwards sputter coating unit.

4.10 ELECTRON PROBE MICROANALYSIS

When electrons of energy greater than several kilovolts strike the surface of a solid specimen a number of interactions occur. One on these is the generation of x-rays. Since the 1950's it has been realised that this phenomena could be used to examine the composition of very small areas of a much larger specimen. Today, microanalysis has become an important tool in the examination of a variety of materials.

When an electron beam interacts with a sample the resulting x-rays can be used to obtain both qualitative and quantitative information. If an electron beam is aimed at a pure sample the intensity of the x-rays generated will be greater at specific wavelengths which are characteristic to that element only. The characteristic wavelengths can be related to interactions in the electron shells. When an unknown sample is analysed, the wavelengths at which large intensities of x-rays are produced can be compared with existing data, and atoms that produce x-rays at that same wavelength identified. Where there is more than one possible match the initial consideration is to decide whether it is likely that the element in question is in fact present in the sample. If it is, then the electron interaction producing that x-ray must be considered.

Once a qualitative analysis has been carried out on the sample and all the elements present identified, a quantitative analysis can be done. As stated previously, a certain atom will produce x-rays at a specific wavelength. If the number of x-rays produced at that wavelength are counted for a known length of time, N_{spec}, and then compared with the number counted from a standard, N_{std}, of known composition, C_{std}, a measure of the concentration in the specimen, C_{spec}, can be calculated using expression 4.6 below [8]:

$$C_{spec} = \frac{N_{spec}}{N_{std}} \times C_{std} \qquad (4.6)$$

However, in practice a number of complicating factors makes the use of this equation on its own impractical. Because the counts on the standard and specimen are carried out at different times care must be taken to ensure that conditions are identical. In addition, standards are likely to vary in composition and density when compared to the sample, which will produce additional errors. In order to reduce these errors ZAF corrections were made on the results. This method takes into account the three main sources of errors, described below, and makes corrections for them.

- **The atomic number correction, Z.**

  This is principally concerned with the efficiency of x-ray production. It depends on, (i) the distance an electron can pass through a sample before its energy is below the value required to excite an x-ray, and (ii) the number of electrons which fail to excite x-rays due to backscattering. This is strongly dependent on the atomic number of the element. Generally, the Z correction is greater if two elements of different atomic mass are contained within the same sample.

- **The absorption correction, A**

  X-rays are produced beneath the sample surface and are therefore required to travel through the specimen in order to reach the detector. During this process, x-rays will be absorbed, the number depending on the mass absorption coefficient. The mass absorption coefficient is likely to be different between the standard and sample so even if the interactions are identical, variations in count rate will be observed.

- **Fluorescence, F**

  Low energy fluorescent radiation can sometimes be induced by high energy x-rays in materials where elements of similar atomic mass are present. Fluorescence is an inefficient process and is not significant in the analysis of battery materials.

The ZAF corrections are calculated using approximate solutions developed over a period of several decades. Computer software, linked to the analytical equipment, contains all the solutions and approximates each of the values. This has to be calculated using an iterative process since the ZAF correction can be improved at the end of each interation by doing a new calculation with the previously predicted composition.

Selection of standards

Table 4.3: Standards used for electron probe microanalysis

Element	Possible 'states' of element in sample	Standard Selected and Source	Notes
Lead, Pb	Pb PbO_n (1<n<2)	Lead monoxide, PbO	Lead is present in the form of lead or lead oxide, this standard gives a good match in composition and structure.
Oxygen, O	PbO_n (1<n<2)	Lead monoxide, PbO	The standard is almost identical in composition to the sample, therefor this is a very good match.
Tin, Sn	Sn SnO_n (1<n<2)	Pure Tin, Sn (C.M. Taylor Corp. 12921-5)	This is again a suitable standard to use.
Sulphur, S	R-SO_4	Iron Sulphide (Pyrite), FeS_2 (C.M. Taylor Corp. 11540-1)	The sulphate and sulphide are likely to have varying characteristics. Errors may therefore be slightly larger than with the previous elements.

Electron probe microanalysis was used to examine the positive electrodes from batteries containing lead and lead/tin grids, in particular the corrosion layer. A qualitative analysis detected Lead, Oxygen, Sulphur and Tin within the sample. The standards used to calibrate the EPMA for each of these elements is given in the Table 4.3.

Sample Preparation and Coating

Positive electrodes were examined in the form of cross-sections of the grid wires. These were prepared using techniques described in the previous sections of this chapter. In order to carry out a successful analysis it is important that the surface of the sample should be conducting to prevent charging effects. Because the samples were mounted in non-conducting resin, and the possibility of them containing lead monoxide, which is an insulator, existed, the decision to coat them was taken. Samples are often coated in a conducting layer of gold, however this is unsuitable in applications where the analysis of light elements, such as oxygen, is required. For this reason, the samples were coated with a thin layer of carbon. This was done using an Edwards coating unit.

Even a light element such as carbon will adsorb a small proportion of the x-rays generated, as they pass through the sample surface and coating. The errors produced by this can be reduced by also coating the standards. It is important that the coating is of uniform thickness on all samples and standards, and the easiest way to achieve this is to do all coating simultaneously.

Care must be taken, as the position within the coating unit will influence the carbon layer thickness depending on the distance from the 'discharge'. To minimise this effect both the standards and samples were coated at the maximum distance from the 'discharge', and care was taken to ensure they were all at the same height level.

Accelerating voltage and beam current

When an electron beam interacts with a sample a number of physical processes occur. In addition to the generation of x-rays, the surface can charge and heat up. The result of this is either physical changes in the sample structure, or deposition of contaminants present within the vacuum system onto the surface. In the majority of cases, these processes are unavoidable, but can be minimised by reducing the energy of the electron beam. However, a lower energy beam has the disadvantage of producing a lower resolution picture in SEM mode and in analysis mode only low energy x-rays within the sample are excited. In practice a compromise is reached, the beam current and voltage chosen will depend on the sample and type of analysis required. An accelerating voltage of 10kV and a beam current of $5x10^{-8}$A was found to be suitable for the analysis of battery samples.

Selection of X-ray lines and crystals

The accuracy of a quantitative analysis can be optimised by selecting the most appropriate x-ray lines and crystals for each element under investigation. This is achieved by running a qualitative analysis for a range of wavelengths on each crystal. Lines identified can then be matched to each element and those with the highest intensity selected. Figure 4.5 shows a qualitative analysis for a number of standard crystals for the range 65 and 250mm.

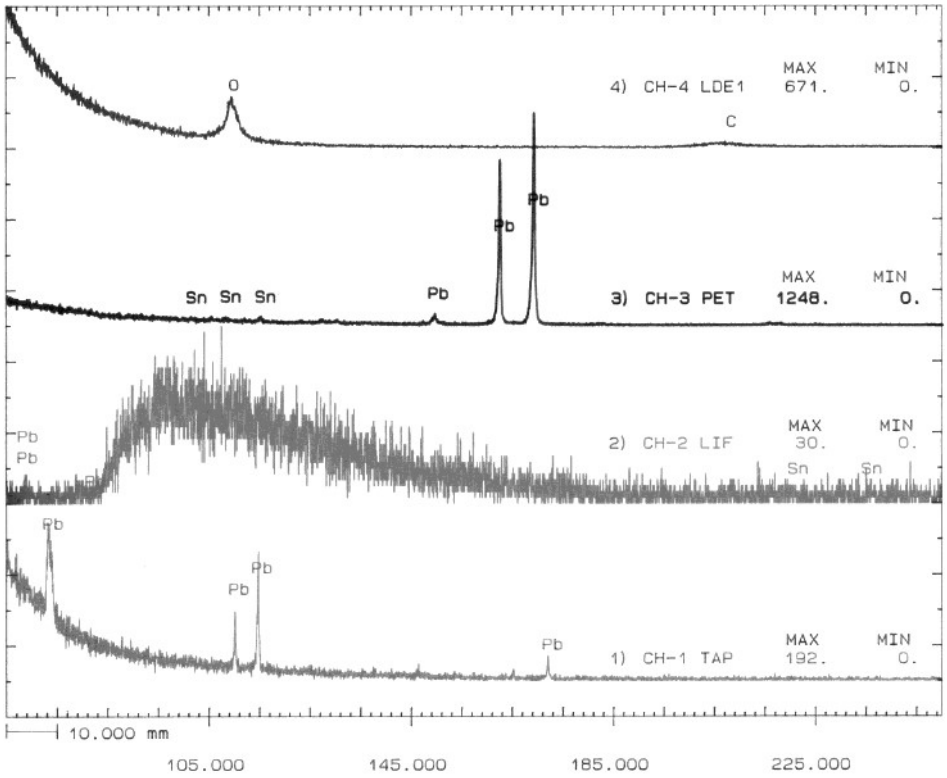

Figure 4.5: Qualitative Analysis using LDE, PET, LIF and TAP crystals at 10kV

All the peaks within the range of wavelengths obtained from the LiF (lithium flouride) crystal have too low an intensity to be identified above the background radiation. Lead peaks are present on both the TAP (thallium acid phthalate) and PET (Pentaerythritol) crystals. However, the counts from the PET are significantly higher which give a more accurate analysis statistically. The LDE (tungsten/silicon multilayer) crystal was therefor used for oxygen detection and PET for lead, tin and sulphur.

Calculation of peak height

In order to obtain an accurate peak height for the analysis, the background level of radiation must be subtracted. This changes with wavelength and must therefore be measured either side of the peak. The distance the background is measured away from the peak is given by the variables Peak Background Upper, P-B_U, and Peak Background Lower, P-B_L, as shown in Figure 4.6 below.

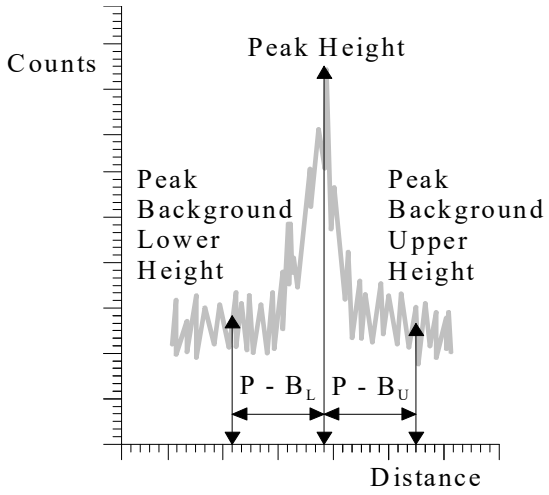

Figure 4.6: Measurements taken to calculate peak intensity

Peak heights are calculated from the number of counts measured at each of the positions in figure 4.6 using equation 4.7.

$$P_I = P_h - \left[\frac{PB_U + PB_L}{2}\right] \qquad (4.7)$$

Where: P_I = Peak Intensity

P_h = Peak height

PB_U = Peak background upper height

PB_L = Peak background lower height

An additional variable that will determine the number of counts is the 'counting time'. Separate values can be entered for the peak and both background values.

Selection of X-ray lines and variables

Figure 4.7 below shows the peaks identified when using the LDE and PET crystals. All the elements of interest have peaks covered by this range of wavelengths.

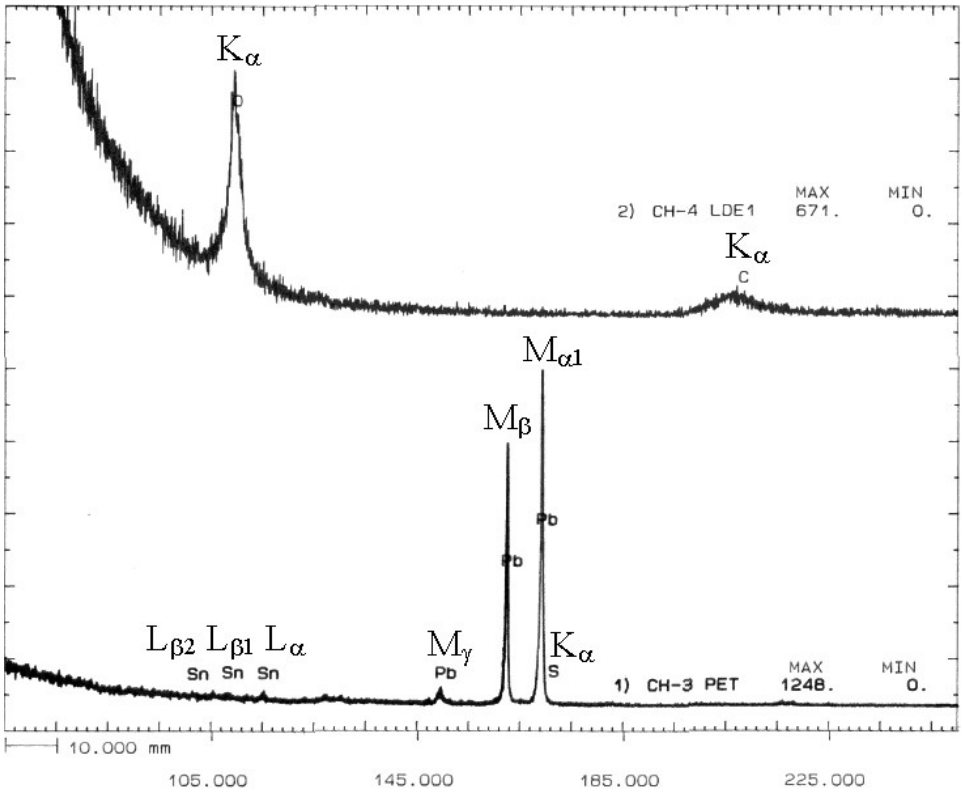

Figure 4.7: Qualitative analysis for LDE and PET crystals showing lines identified

From Figure 4.7 it can be seen that the lead $M_{\alpha 1}$ peak and Sulphur $K_{\alpha 1}$ peak have very similar positions. During analysis, the x-rays are counted between two energy values either side of the peak of interest. The computer will automatically calculate the peak position and intensity from the background counts either side. As the two peaks are very close together it is necessary to reduce the distance that wavelengths are counted either side of the peak to minimise the risk of an adjacent peak giving an inaccurate background value. An enlarged trace of the sulphur and lead peak is shown in Figure 4.8.

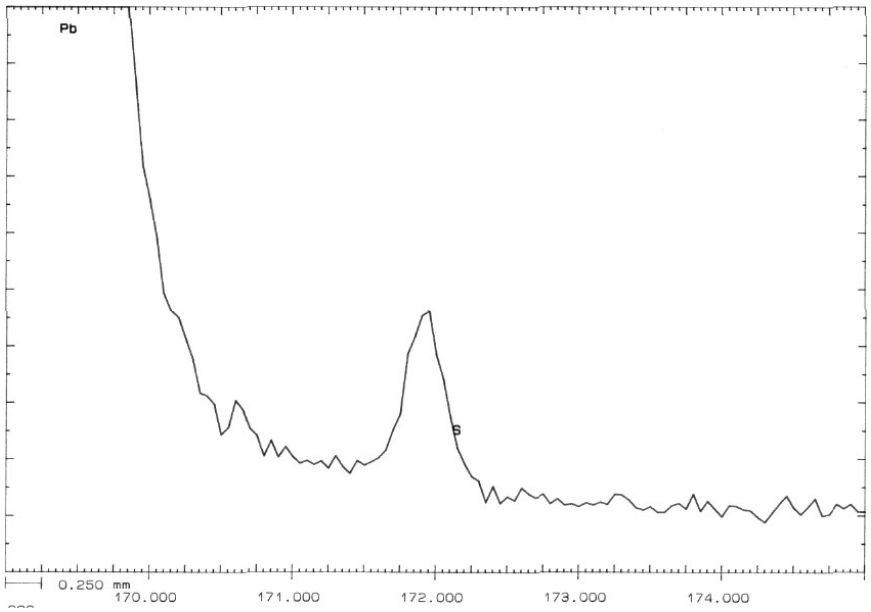

Figure 4.8: Kα line for sulphur

Summary of data

Taking into account the peak sizes, shapes and positions, the variables shown in Table 4.4 below, were entered into the diffractometer for the analysis.

Table 4.4: EPMA settings for quantitative analysis

Element	Line	X-tal	Peak Position (mm)	Peak Background (mm)		Counting Time (s)	
				Lower	Upper	Peak	Background
Lead, Pb	$M_{\alpha 1}$	PET	169.090	4.000	4.000	30.0	5.0
Oxygen, O	$K_{\alpha 1}$	LDE	109.440	8.800	8.800	30.0	5.0
Tin, Sn	$L_{\alpha 1}$	PET	115.125	4.000	4.000	10.0	5.0
Sulphur, S	$K_{\alpha 1}$	PET	172.010	0.800	0.800	10.0	5.0

4.11 REFERENCES TO CHAPTER 4

1. B. D. Cullity, Elements of X-Ray Diffraction, 2nd ed., Addison-Wesley Publishing Company, Inc., (1978)
2. Joint Committee for Powder Diffraction Standards, PDF-2 Database Sets 1-45, (1995), International Centre for Diffraction Data, 12 Campus Boulevard, Newtown Square, Pennsylvania, 19073-3273, U.S.A.
3. R. Jenkins, J.L de Vries, An Introduction to X-ray Powder Diffraction, N. V. Philips, Gloeilampenfabrieken, Eindhoven – Holland, (Manufactures handbook).
4. D. A. J. Rand, R. J. Hill, M. McDonagh, Improving the curing of positive plates for lead/acid batteries, Journal of Power Sources, Vol. 31, (1990), pp. 203–125.

5. K. Harris, R. J. Hill, D. A. J. Rand, Crystalline phase composition of positive plates in lead/acid traction batteries under simulated electric vehicle service, Journal of Power sources, Vol. 8, (1982), pp. 175-196
6. Low Level Measurements, Keithley Instruments, Inc. 28775, Aurora Road, Cleveland, Ohio 44139, (Copyright 1992), Number 1559119230kGL, pp. 2-17
7. *OPTIMAS 6.1*, Optimas UK Ltd., West Maling, Kent, UK.
8. P. J. Goodhew, F. J. Humphreys, Electron Microscopy and Analysis, 2nd Edition, Taylor & Francis, (1988), p. 188

5 EXPERIMENTAL METHODS FOR SEPARATOR PAPER CHARACTERISATION

5.1 INTRODUCTION

Separator papers play an important role in the operation of a battery in several ways. In addition to providing a means by which to immobilise the electrolyte and prevent positive and negative plates from coming into contact with each other, they can influence the reactions occurring within the battery.

Two main characteristics of separators, which influence performance, are their compressive and diffusive properties, both of which are functions of saturation. The experimental methods described below allow these properties to be characterised and the results used to predict how the paper may perform in the battery.

5.2 WICKING TESTS

The rate at which an electrolyte rises up a sample of separator paper by capillary action will be influenced by both separator structure and material. It would be extremely difficult to model the flow of electrolyte through a fibrous material such as a separator, however if the pores are assumed to be round in cross section the wicking characteristics can be described using the Washburn equation. The equation relates the velocity of the liquid at a given height to other properties of the system and can be written in the following form [1]:

$$v = \frac{dh}{dt} = \frac{2r\gamma\cos\theta}{8\eta h} - \frac{r^2\rho g}{8\eta} \qquad (5.1)$$

Integration of the above equation ignoring the gravity term yields [1]:

$$h^2 = \frac{\gamma r t\cos\theta}{K^2 2\eta} \qquad (5.2)$$

Where: γ = surface tension
r = pore radius
t = time
η = viscosity
K = tortuosity
h = height
θ = contact angle
g = gravitational constant

Equation 5.2 predicts that for values of $h<<h_m$, where h_m is the maximum height reached, at infinite time, the relationship between h^2 and t is linear [2]. Wicking characteristics of different separator papers were compared by plotting height squared, h^2, versus time, t, where the gradient is proportional to the wicking rate.

Sample Preparation

Wicking tests were conducted using strips of separator paper 20x155mm. Separator paper is manufactured as strip using a continuous process. Samples were cut in the manufacturing and at 90° to the manufacturing direction of the paper. A cocktail stick was then used to apply dots of saturated methyl red indicator solution in ethanol at 10mm intervals along the length of the strip, starting 5mm from one end. The indicator is orange and turns to a deep red on contact with acid making the electrolyte front visible.

Experimental Procedure

Each strip was suspended in electrolyte so that the meniscus was level with the first dot 5mm from the strip end. The time the electrolyte front reached each dot was then noted until the strip was totally saturated and all the dots had changed colour.

5.3 SEPARATOR COMPRESSION TESTS

The compressive properties of a separator paper can influence battery performance. Throughout the operational life of a battery the separator paper will operate under varying amounts of saturation. Compressive properties are influenced by saturation so this must be taken into account. In justifying the method used to characterise a separator paper for battery performance it is firstly necessary to consider the processing route of the batteries under examination and how this may affect the separator.

Cells are assembled by wrapping the separator paper around the positive plates and then stacking them alternately with negative plates. At this stage the cell width is greater than the allowed space in the battery case. For assembly to be possible it is necessary to compress the cell to the same width as that of the battery case, to allow easy insertion without risk of damaging the outer electrodes in the process. Hawker energy currently use a specially designed jig for this purpose which also functions as a clamp to allow the cast-on-straps to be fitted to the tabs at the top of each electrode. The attachment of the cast on straps limits the amount the separator can expand once removed from the jig. During manufacture the separator paper is therefore compressed before insertion into the case.

The apparatus used to characterise the separator papers consisted of a horizontal jig mounted in an Instron mechanical testing machine. Loads were monitored using a load cell with range 0-500N. The load cell output was recorded using a chart recorder. A diagram of the apparatus is shown in Figure 5.1.

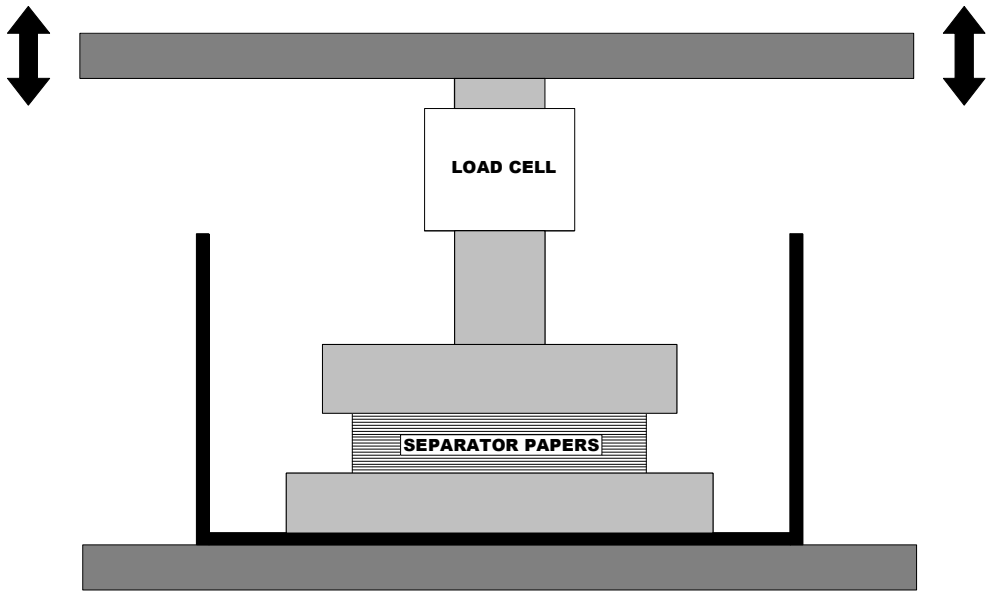

Figure 5.1: Apparatus for the measurement of separator compression properties

Experimental Method

A stack of 20 sheets, each 10 × 10cm, was used for each test. These values were chosen since there are 18 sheets each 8 × 15cm of separator paper in the actual battery cell and it is advantageous to test similar size samples. Separator paper was provided in the form of a roll and samples were taken in a line along the centre of the paper. Initial thickness measurements of single samples of the paper under a load of 10KPa gave a maximum coefficient of variation of 0.021 or less for the papers tested. This indicated that there was no significant variation in thickness along the roll. Once inserted into the testing machine the stack of papers was compressed until a force equivalent to a pressure of 25kPa was measured, the same as in the compression jig used by Hawker Energy during battery manufacture [3].

Separator papers exhibit visco-elastic behaviour, the consequence of this being a steady decrease in the force applied by the paper with time after compression had ceased. The rate of the decrease in force is directly proportional to the compression rate; therefore a slow cross-head (loading) rate of 1mm per minute was used as this minimised the rate of reduction in force due to paper relaxation.

Measurements taken indicated that the actual difference in thickness between the two stacks of papers compressed to 25kPa was 2.3%, and the difference between this thickness and that calculated for the battery was approximately 6%. This indicates that any trends or differences should be noticeable between the separator papers that may affect battery performance.

Following compression of the separator papers an amount of electrolyte equivalent to one fifth of the total pore volume was added. After the electrolyte had been adsorbed into the separator paper a reading of the force was taken. Initial measurements indicated that steady state conditions were not reached after a period of more than 6 hours. Waiting for this period of time has a number of disadvantages such as electrolyte evaporation. However approximately 90% of the total change in force measured after a period of 30 minutes from the addition of acid occurred in the first ten minutes. It was therefore decided to take measurements of force after a set time of 30 minutes, since after this length of time the majority of the change in force had been observed and changes due to evaporation would be insignificant. This step was repeated allowing the force to be monitored at saturation levels of 0, 20, 40, 60, 80, and 100%. Plots were then made of force versus saturation.

Flexure of Rig

Because of the loading platen geometry and stiffness, relative to the separator paper compression geometry and stiffness (when compressed), see figure 5.1, it is assumed that any effects arising from rig flexibility are insignificant and can be safely ignored.

Calculation of Pore volume

In order to obtain a value for the pore volume the separator thickness must be determined. This can be calculated using equation 5.3 below.

$$T = \frac{H_t - H_b}{N} \qquad (5.3)$$

Where: T = Separator Thickness (cm)
H_t = Height of top platen (cm)
H_b = Height of bottom platen (cm)
N = Number of sheets

The fibre volume is then calculated per unit area of separator paper using the equation 5.4.

$$V = \sum_n \frac{W_f \cdot P}{\rho_n} \qquad (5.4)$$

Where: V = Fibre volume per 1.0cm^2 of separator paper (cm^3)

W_f = Weight fraction of fibre type, n
P = Weight of paper per unit area (gcm^2)
ρ_n = Density of fibre type, n (gcm^{-3})
n = Fibre material

The total pore volume, V_p, is calculated using the equation 5.5.

$$Vp = (T \times 10 \times 10) - (V \times 10 \times 10) \quad (5.5)$$

This volume can be multiplied by the number of separator sheets and divided by 5 to obtain the volume of acid that must be added to fill 20% of the pore volume.

5.4 POROSITY DISTRIBUTION AND PERMEABILITY MEASUREMENTS

The pore size distribution of a material can be determined using a liquid displacement method. This method relies on the principle that there is a rise of liquid in a capillary due to surface tension. At equilibrium, the following expression can be written for liquid rising up a capillary.

$$2\pi r\gamma \cos\theta = r^2\pi h\rho g \quad (5.6)$$

Where: r = radius of capillary (or pore)
h = height of column of liquid
γ = surface tension of liquid
ρ = density of liquid
θ = contact angle between the liquid and capillary wall
g = acceleration due to gravity

By substituting pressure, (P) = $h\rho g$, into equation 5.6, equation 5.7 is obtained.

$$Pr = 2\gamma \cos\theta \quad (5.7)$$

Where: $\gamma \cos\theta$ = Wilhelmy surface tension

If the wetting liquid is assumed to have a contact angle of 0 then equation 5.7 can be re-written in terms of the pore diameter allowing the porosity distribution to be obtained:

$$\text{Pore diameter} = 2\gamma / P \quad (5.8)$$

Initially the pores of the sample are filled with a wetting liquid. Coulter *Porofil* was used for this purpose as it has a low contact angle and wets the majority of materials. The sample is then mounted in the apparatus so that the gas flow through the sample and pressure can be measured. Initially, the gas flow and pressure are measured for both a 'wet' and 'dry' run.

The pressure is gradually increased from zero. Since all the pores are filled with liquid the pressure increases but the gas flow through the sample remains at zero. At a critical pressure the liquid is expelled from the largest pore and a gas flow is detected and measured. As the pressure is increased further, liquid is expelled from smaller pores allowing the gas flow to increase. This is continued until the pores no longer contain any liquid. Plotting pressure against flow gives a curve for a 'wet' run. A series of pressure and flow reading are then repeated for the dry sample giving the curve for a 'dry' run. By plotting the 'wet' and 'dry' curves together, values for the maximum, minimum, and mean porosity are obtained as shown in Figure 5.2.

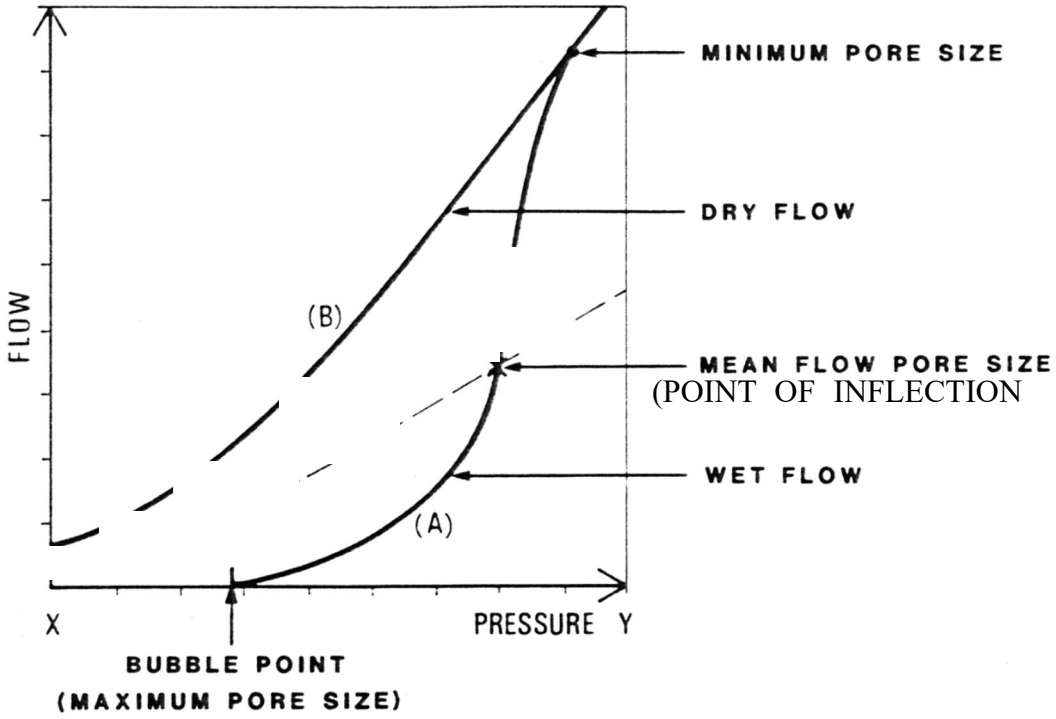

Figure 5.2: Wet, (A), and Dry, (B), flow curves for obtaining porosity distribution [8]

The permeability is determined by measuring the volume of gas that passes through the sample under a pressure of 0.100bar.

Equipment and Procedure

Porosity distribution and permeability values were obtained for each of the separator papers characterised. Values were obtained using a Coulter *Porometer II*. A disc of separator paper 25mm in diameter was cut from a larger sheet using a punch. The sample was then submerged in the wetting liquid for a minimum of 2 minutes to allow total saturation of all pores. The wetted sample was subsequently placed into the machine and measurements taken. Permeability was measured after porosity since a dry separator is required for this.

5.5 DIFFUSIVITY MEASUREMENTS

The diffusivity of battery separator papers at varying amounts of saturation was measured using a specifically designed and built diffusion rig. A description of the rig, and all relevant information regarding its use is given in the following section.

5.5.1 DESCRIPTION OF DIFFUSION RIG

The diffusion rig consists of three principal components: the diffusion cell, sampling valve and gas chromatograph. A schematic diagram of the apparatus is shown in Figure 5.3. Nitrogen and oxygen flow on each side of the sample held within the diffusion cell. The oxygen side of the cell is vented to atmosphere while the nitrogen side is connected to a sampling valve. Switching the sampling valve allows gas in the sample loop, from the nitrogen side of the cell, to be directed into the gas chromatograph. The quantity of oxygen that has passed through the separator paper in the diffusion cell can therefore be determined. Each of the components is described in greater detail below.

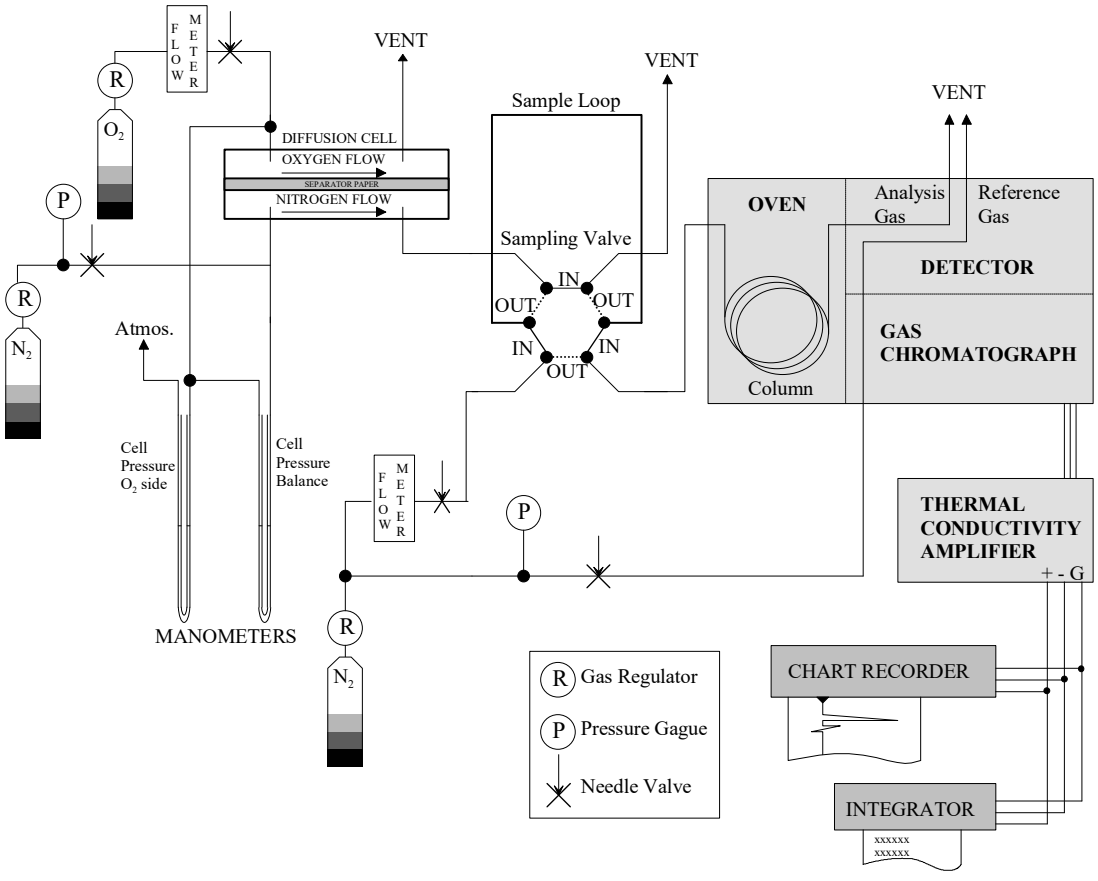

Figure 5.3: Diagram of diffusion Rig

- Gas supply and regulators

  Nitrogen and oxygen was obtained from standard 175 and 215 bar cylinders supplied by BOC. Saffire Series 3 nitrogen and oxygen regulators were used to control the supplies of gas. The desired flow rates were achieved by setting the regulators to approximately 2 bar. A slightly higher pressure was used for the nitrogen supply to the gas chromatograph.

- Tubing and connectors

  1/8" stainless steel and copper tubing was used for all pipe work with the exception of the glass manometers that were connected using rubber tubing and the connections to the column and TCD detector which required 1/16" tubing. Swagelok stainless steel connectors were used to make joints.

- Diffusion cell

  The diffusion cell was manufactured from stainless steel. A diagram with dimensions is shown in Figure 5.4a&b. The gaskets were made from 0.4mm PTFE sheet. 1/8" quick release tubing connectors were attached to the inlet and outlet pipes to allow easy sample replacement. Due to the brittle nature of the glass fibres within the separator paper, it was found that when crushed, the paper turned into a glass powder.The gaskets were manufactured with an internal hole slightly smaller than that of the diffusion cell to allow them to hold the paper in position without risk of damaging it.

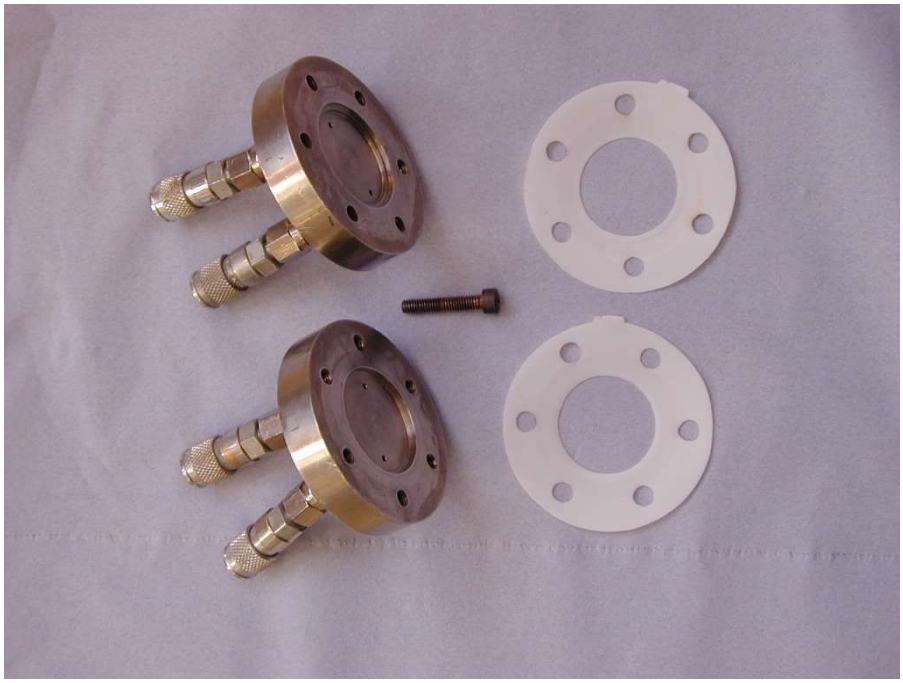

Figure 5.4a: Diffusion Cell

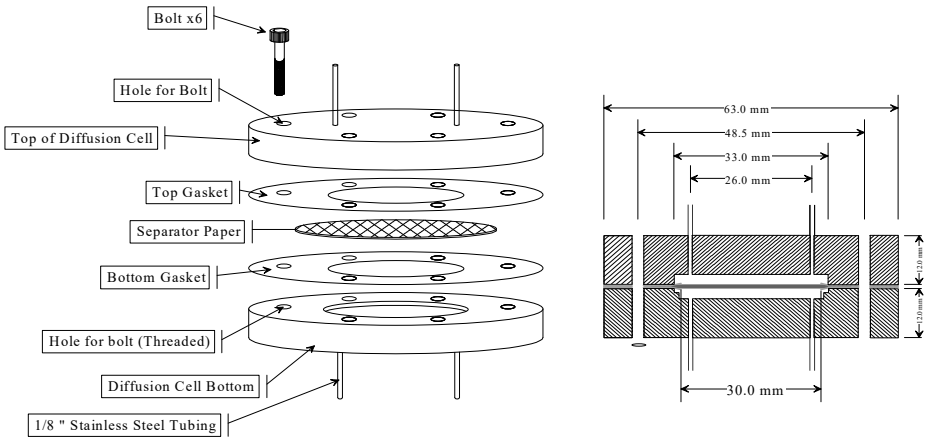

Dimension on Sample	Diameter (mm)	Area (cm^2)
Total Width	43.0	14.5
Unclamped Area	33.0	8.55
Exposed Area	30.0	7.07

Figure 5.4b: Diffusion Cell

- Flow meters and needle valves

  Brooks model 8744 Flow Control needle valves and KDG flow meters were used to control the gas flows through the gas chromatograph and diffusion cell. Flow meters were cleaned using chromic acid and calibrated relative to a bubble flow meter before the first use.

- Manometers

  Manometers were made from 2.85mm diameter glass tubing heated and bent into a U shape. Clamping was achieved by attaching to a sheet of 8mm thick clear perspex using cable ties. 1mm square graph paper was attached behind the glass tubes to allow easy measurements of pressure.

- Sampling valve and loops

  4 sampling loops were used in total, one for measurements and an additional 3 having various volumes for calibration purposes. When selecting a sample loop size it is important that the volumes of gas to be analysed lie within the linear range of the detector; Figure 5.5shows linear dynamic ranges for a number of different detectors.

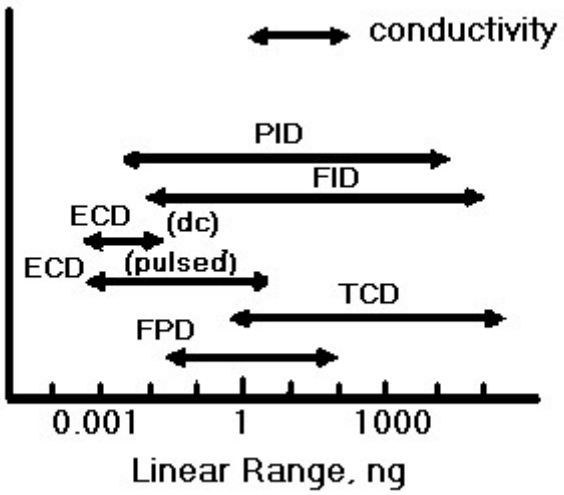

Figure 5.5: Linear Range for a number of different detectors [4]

For the 490µL loop the maximum volume of oxygen that could enter the detector for an infinitely permeable membrane is 245µL. This is equivalent to 1750ng of oxygen, which can be seen to fall well within the linear range for the TCD detector. Loop details are given in Table 5.1 below.

Table 5.1: Sample loop details

Use	Loop Volume (µL)	Loop internal diameter (inch)	Tubing material
Measurement and Calibration	490	0.085	Stainless steel
Calibration	238	0.052	Teflon
Calibration	163	0.032	Teflon
Calibration	87	0.032	Teflon

The sampling valve required a sampling loop with 1/8" steel tubing on the end. In order to allow the thinner diameter Teflon sampling tubes to be used 50mm lengths of 1/8" diameter stainless steel tubing was glued to the end of the Teflon tubing using Araldite. The Teflon tubing passed through the entire length of the stainless steel tubing to allow easy calculation of the sample loop volume. A picture of the sampling valve and loops is shown in Figure 5.6 below.

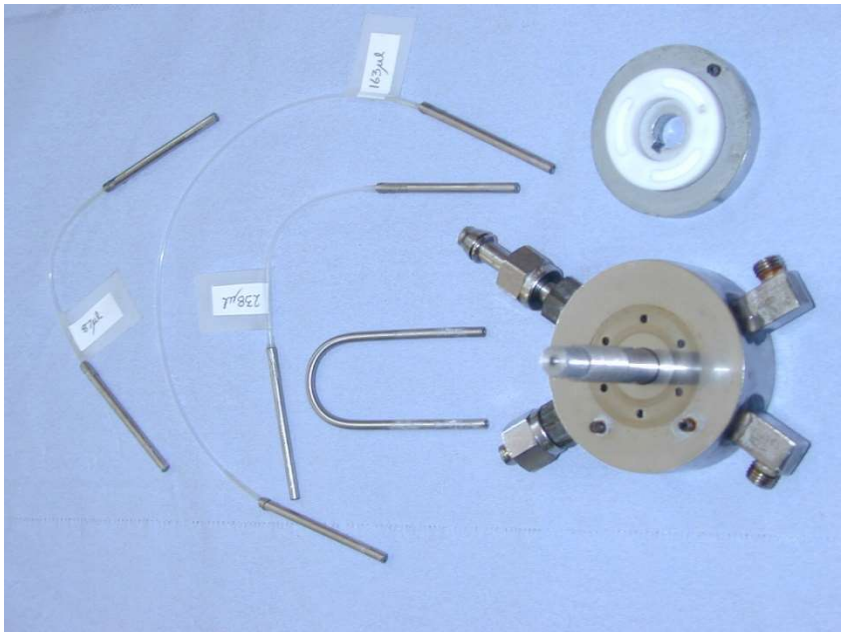

Figure 5.6: Sampling valve and loops

Sample loops were constructed to the volumes above, as these covered the range of oxygen samples expected during experimentation. The sample loop volume for measurement was 490µL, therefore 50% is approximately 283µL. The 163µL and 87µL loops are approximately 66 and 33% of 283, therefore giving evenly spaced points on the calibration curve.

- Gas Chromatograph

  A Philips PU4500 gas chromatograph was used to determine the volume of oxygen in the sample of gas.

- Column

  The water vapour and oxygen contained in the sample of nitrogen gas were separated using an Alltech Porapak®S washed molecular sieve column. This column is traditionally used for the analysis of flue gases, but proved suitable for this application. Before use, it was necessary to condition the column to remove impurities. This was achieved by heating at 250°C for 1 hour. Due to the time required for this, once conditioned the column was kept in the chromatograph oven, at the operating temperature with a flow of gas, for the entire duration of experimentation.

- Detector

  A Philips thermal conductivity detector (TCD) was used to determine the volume of oxygen in each sample of gas. In order to ensure consistency of results the detector was switched off as little as possible during the duration of experimentation.

The detector consists of four heated filaments manufactured from rhenium-tungsten alloy. Two of the filaments lie in the sample cell and two in the reference cell as shown in Figure 5.7.

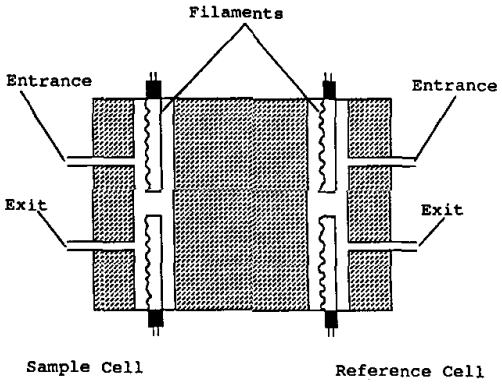

Figure 5.7: Thermal Conductivity Detector [5]

Filaments are connected together forming a Wheatstone bridge circuit, Figure 5.8.

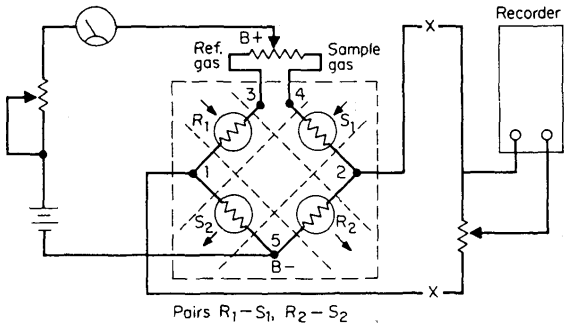

Figure 5.8: Circuitry for thermal conductivity (four-filament) cells [4]

When the sample of gas enters the sample cell, the conductivity of the gas around the filament is decreased relative to that of the carrier gas. This results in an increase in filament temperature, and therefore resistance, which unbalances the Wheatstone bridge. The change in signal is then amplified and measured as a change in voltage.

A disadvantage of using a thermal conductivity detector for the detection of oxygen is the susceptibility of the filaments to oxidation. A build up of an oxide layer on the filaments in the sample cell can unbalance the bridge by affecting the heat flow between the filament and sample gas. For this reason the detector was operated at its minimum temperature setting. Comparison of calibration curves indicated that the response of the detector did not change significantly during the course of experimentation, this indicates that any oxidation which may have occurred was negligible.

- Chart recorder and integrator

  The output from the thermal conductivity amplifier was connected in parallel to a Philips 8251 single pen chart recorder and Hewlett Packard 3390A Integrator. A chart speed of 10mm/min and range of 0 to 10mV was used on the chart recorder. The integrator was used to calculate the area under the oxygen peak. Peak areas, triangle ABC, were defined as the area enclosed by a straight line, AB, drawn between the bottom of each side of the peak, Figure 5.9.

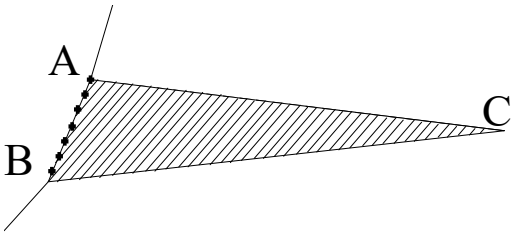

Figure 5.9: Definition of peak area

5.5.2 CALIBRATION OF DIFFUSION RIG

Due to sensitivity of the detector to flow rate and temperature it was necessary to calibrate the rig before each set of readings was taken. This was achieved by connecting the oxygen supply directly to the sampling valve thus filling the sampling loop with pure oxygen. The valve could then be turned and a known quantity of oxygen passed into the detector. In order to obtain an accurate calibration a total of 4 sampling loops of varying volume were fitted to the sampling valve in turn. The peak area obtained was then plotted against the corresponding sample loop size and a calibration curve was obtained. The relationship between volume of oxygen and peak area is linear, therefore the gradient, m and intercept, c of the curves are used in the calculation of diffusivity. An example of a calibration graph is shown in Figure 5.10 below.

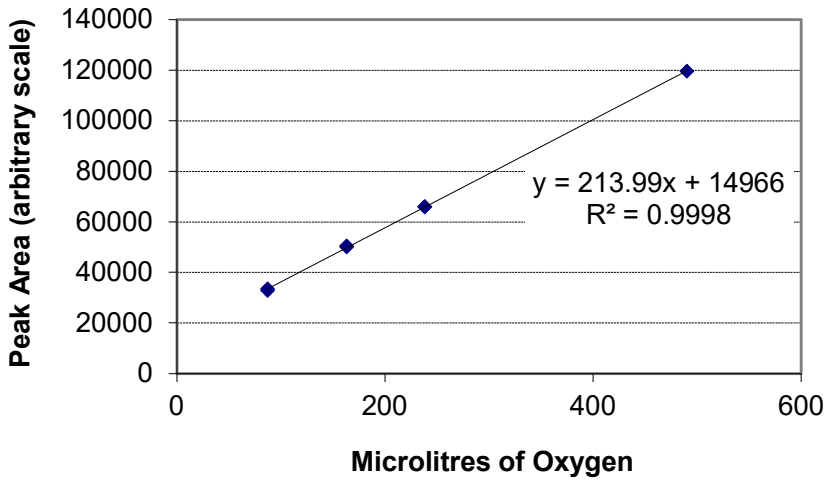

Figure 5.10: Example calibration graph

The procedure used for calibration is described below.

1. Switch on the nitrogen gas supply to the detector and oxygen supply to the sampling valve.
2. Check for gas flow through the detector at both main and reference outlets, using a bubble flow meter.
3. Switch on the gas chromatograph, thermal conductivity amplifier, chart recorder and integrator.
4. Condition column by heating to 250°C at 5°/min, holding at 250°C for 1 hour and then cooling.
5. Set initial and final column temperatures to 80°C on GC oven control.
6. Set detector temperature to 34°C – Note: The detector temperature was found to increase from this value due to the relatively higher column temperature.
7. Leave for 1-2 hrs or until detector temperature stabilised and detector output becomes constant; see chart recorder.
8. Set main and reference gas supplies to 40ml/min using bubble flow meter. Use a gas sample size of 10ml therefore requiring a time of 15seconds.
9. Leave detector to equilibrate to new flow rates, approximately 10 minutes.
10. Set zero on integrator using TCD amplifier BACKOFF adjuster
11. Set zero on chart recorder using ZERO adjuster.
12. Connect oxygen supply directly to sampling loop.
13. Switch sampling valve to IN position.
14. Press START button on integrator.

15. Observe oxygen peak on chart recorder.
16. Press STOP button on integrator.
17. Switch sampling valve to OUT position.
18. Wait for baseline to recover.
19. Repeat steps 13 to 18 as necessary.
20. Change sample loop size
21. Repeat steps 13 to 20 as necessary.

5.5.3 EXPERIMENTAL METHOD

Once calibrated, measurements of oxygen diffusion through the paper could be made. The procedure is described below.

1. Cut 43mm diameter circular sample of separator paper using specially manufactured metal punch.
2. Weigh sample of separator paper using balance accurate to 0.0001g.
3. Saturate inner area of separator paper using distilled water. Apply using a syringe and hypodermic needle. Dry separator to desired saturation using hot air.
4. Reweigh saturated separator paper.
5. Clamp separator paper into stainless steel cell between PTFE gaskets tightening opposing screws in rotation to ensure uniform pressure on gaskets.
6. Connect inlet and outlet pipes on cell, to rig.
7. Adjust oxygen gas flow rate to 40ml/min using needle valve and flow meter.
8. Adjust nitrogen gas flow rate so pressures are equal on each side of the cell using needle valve and manometer.
9. Take pressure reading
10. Switch sampling valve to IN position.
11. Press START button on integrator.
12. Observe oxygen peak on chart recorder.
13. Press STOP button on integrator.
14. Switch sampling valve to OUT position.
15. Wait for baseline to recover.
16. Recheck pressure balance in cell using manometer.
17. Repeat steps 10 to 16.
18. Disconnect inlet and outlet pipes from cell.
19. Remove separator paper from cell with gaskets.

20. Weight separator paper with gaskets attached.
21. Calculate separator weight by subtracting weight of gaskets.

5.5.4 DETERMINATION OF SEPARATOR PAPER PERCENTAGE SATURATION

Due to the design of the diffusion cell, it was not possible to constrain the surfaces of the sample. A consequence of this was that the thickness of the sample could not be determined directly. When a separator paper is wetted with a liquid the surface tension causes the fibres to be pulled together, reducing the effective paper thickness. Because of this, the thickness of the samples in the diffusion cell can only be obtained experimentally.

The rough surface texture of separator paper and variations in thickness mean that normally thicknesses are determined under a load of 10KPa, however this causes an excessive amount of compression and is an unsuitable method for this application.

A load, which applied a uniform pressure of 500Pa, was found to be high enough to flatten the samples of separator paper without causing an excessive amount of crushing. 21 discs of each separator type, of area 14.5cm^2, were saturated to different amounts and compressed under a pressure of 500Pa. The method used to obtain the data is described below.

1. Cut 21 discs of separator paper and stack.
2. Weigh samples of separator paper.
3. Apply a pressure of 500Pa and measure height.
4. Increase sample saturation by approximately 10%.
5. Repeat steps 2 to 4 until 60% saturation reached.
6. Use saturation and height data to construct curves described in section 5.5.6.

5.5.5 INTERPRETATION OF RESULTS FROM THERMAL CONDUCTIVITY DETECTOR (TCD)

The output from the detector is monitored on the chart recorder. In order to understand the detector output, the operation of the sampling valve and influence of sampling loop and column must be considered. The sampling valve is constructed of a polished stainless steel plate with 6 equally spaced holes in a circular arrangement. Each hole is connected to an output pipe from the valve. Connections are made between holes by a circular Teflon disc with milled slots that can be rotated about the centre of the stainless steel plate. A two dimensional diagrammatic representation of a cross section of the valve is shown in Figure 5.11.

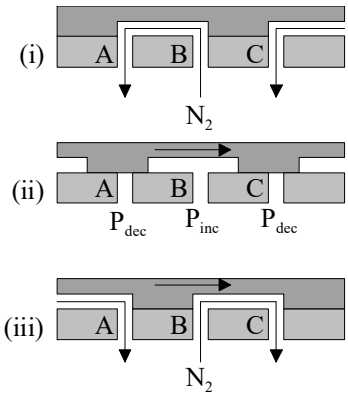

Figure 5.11: Two dimensional representation of sampling valve

In position (i) the nitrogen sweep gas flows from B to A, which leads directly to the detector, OUT position. When the valve is turned to the IN position (iii) the Teflon disc rotates and the nitrogen sweep gas flows from B to C, through the sample loop and then to the detector. As the valve is turned it is seen from the diagram that when position (ii) is reached the gas flow is temporally restricted. This causes a pressure decrease at A and C, and an increase in pressure at B. This pressure decrease causes a decrease in the output of the detector and a negative deflection. When position (iii) is reached, there is a surge of gas into the detector resulting in an increase of deflection. A typical output is shown in Figure 5.12.

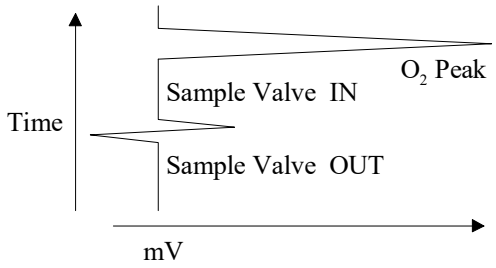

Figure 5.12: Typical output from chart recorder

When a column is inserted before the detector, it acts like a damper, reducing the effect of the gas surge. The drop in pressure is observed, but the surge of gas is not detected. If the oxygen sample reaches the detector before the baseline has reached equilibrium the response shown in Figure 5.13 is observed.

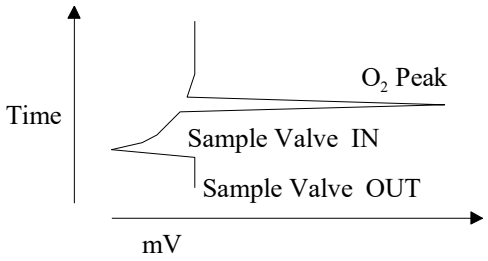

Figure 5.13: Effect of oxygen entering detector before baseline is reached

The sampling loops used for calibration contained tubing of varying internal diameters and lengths. The effect of this was that the gas flow was restricted to different extents when the sampling valve was turned to the IN position with different loops. The main consequence of this on detector output was a variation in the magnitude of the initially observed negative deflection. Generally the smaller the loop diameter, the greater the restriction of gas flow and the smaller the deflection.

5.5.6 CALCULATIONS

5.5.6.1 CONSTRUCTION OF THICKNESS VERSUS SATURATION CURVES

- **Calculation of sample thickness from experimental results data**

The average thickness, L, of a single sheet of separator paper was calculated using equation 5.9.

$$L = \frac{t}{21} \qquad (5.9)$$

Where: L = Separator thickness

t = Thickness of 21 samples

- **Calculation of weight (or volume) of water in sample from experimental results data**

The volume of water in the separator is obtained from the difference between the saturated and dry sample weights. The equation used is shown below:

$$V_{H_2O} = \frac{\left(W_{saturated} - W_{dry}\right)}{\rho_{H_2O} \cdot 21} \qquad (5.10)$$

Where: W= Weight of all 21 sheets of paper

ρ = density (1.00 for H_2O)

- **Percentage saturation of sample from experimental results data**

In order to obtain the percentage saturation it is first necessary to calculate the volume of fibres within the sample, this is done using the equation below.

$$V_{fibres} = A_{sample} \cdot \sum_{n} \frac{W_f \cdot P}{\rho_n} \qquad (5.11)$$

Where: W_f = Weight fraction of fibre type, n
P = Weight of paper per unit area (gcm^2)
ρ_n = Density of fibre type, n (gcm^{-3})
n = Fibre material
A_{sample} = Sample area

The percentage saturation is then calculated from equation 5.12.

$$\%\text{Saturation} = \frac{V_{H_2O}}{\left(A_{sample} \cdot L\right) - V_{fibres}} \cdot 100\% \qquad (5.12)$$

Graphs of V_{H2O} versus L, and V_{H2O} versus percentage saturation were constructed and used to obtain the thickness L, and percentage saturation, from the weight / or volume of water in the diffusion cell. Examples of these graphs are given in Figure 5.14 and Figure 5.15.

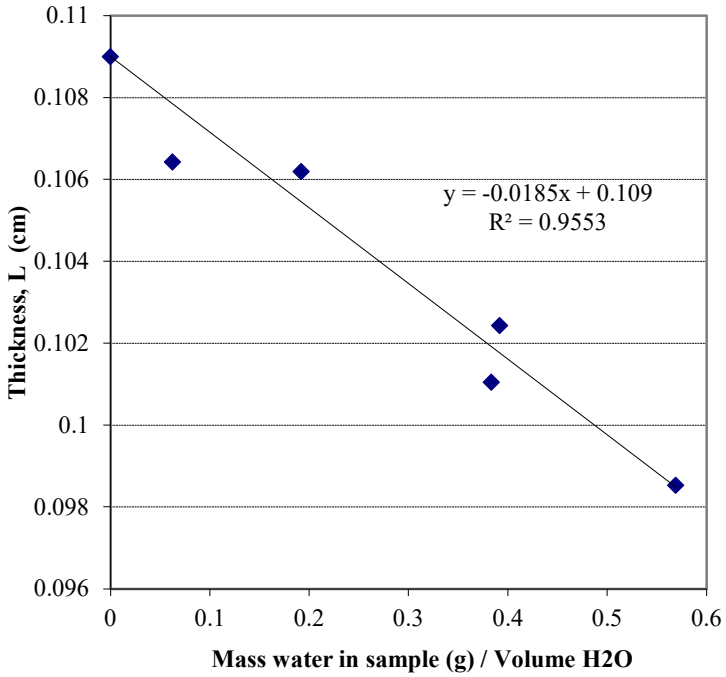

Figure 5.14: Graph of thickness versus volume of H_2O for H+V 140 separator paper

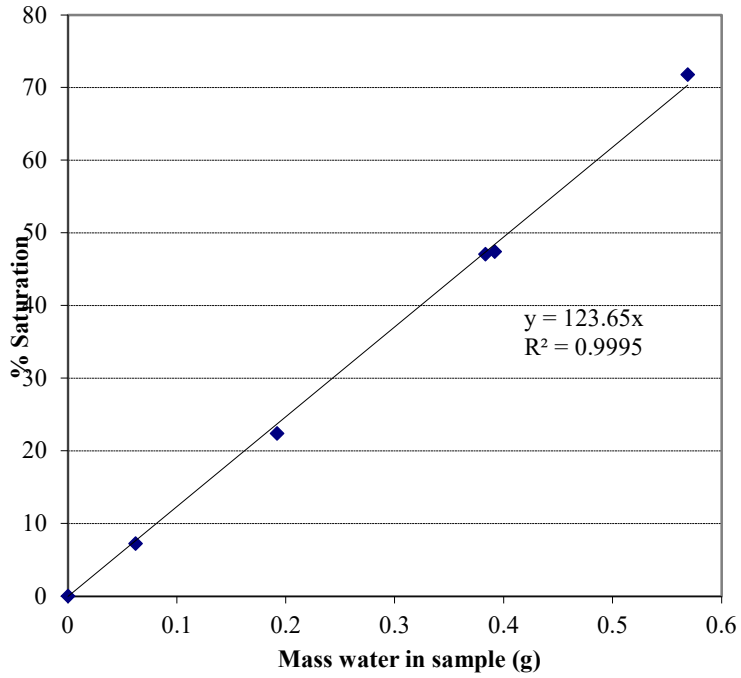

Figure 5.15: Graph of Percentage saturation versus volume of H_2O for H+V 140 separator paper

5.5.6.2 CALCULATION OF PERCENTAGE SATURATION OF PAPER IN DIFFUSION CELL.

To determine the percentage saturation of the sample in the diffusion cell it was necessary to calculate the volume of water in the sample. The weight of the samples was measured before and after saturation, and again after the test to allow the average volume of water in the sample to be calculated. The weight after the test was always less than that before due to evaporation within the diffusion cell. The following equation was used to calculate the volume of water.

$$V_{H_2O} = \frac{\left(\frac{M_{SI} + M_{SF}}{2}\right) - M}{\rho_{H_2O}} \qquad (5.13)$$

Where: M = Mass of sample

M_{SI} = Mass of saturated sample before test

M_{SF} = Mass of saturated sample after test

The separator percentage saturation was obtained from the graph of V_{H2O} versus %Saturation.

5.5.6.3 CALCULATION OF EFFECTIVE DIFFUSIVITY

To determine the effective diffusivity of the separator paper the mole fraction of oxygen on the nitrogen side of the cell must be calculated. This is obtained from the peak area, sample loop

volume and the gradient, m, and intercept, c, of the calibration curve using the following equation 5.14.

$$y_{O_2,L} = \frac{\left[\frac{PeakArea - c}{m}\right]}{SampleLoopVolume} \tag{5.14}$$

A diagram of the diffusion cell is shown in Figure 5.16.

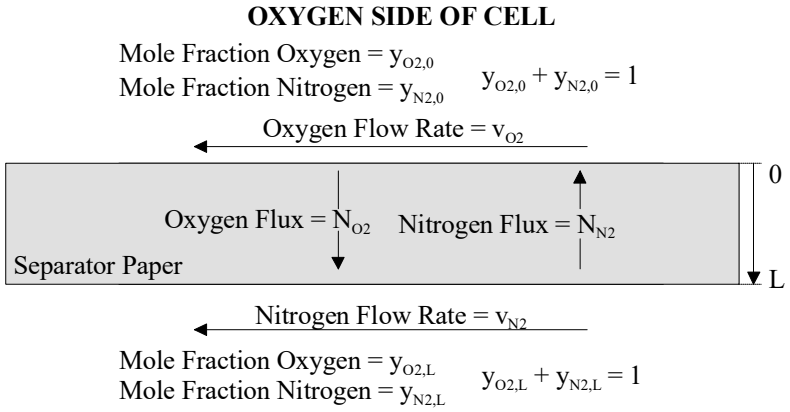

Figure 5.16: Diagram of diffusion cell

Oxygen flux across the separator is calculated from the mole fraction of oxygen on the nitrogen side of the cell, the flow rate of nitrogen in the cell and the area of the separator paper exposed by the hole in the gasket, A, using equation 5.15 below.

$$N_{O_2} = \frac{y_{O_2,L} \cdot v_{N_2}}{A} \tag{5.15 }$$

The ratio of the fluxes of two gases on each side of a membrane is equal to the square root of the ratio of atomic masses [6,7]. This relationship can be used to obtain the nitrogen flux from the oxygen flux as shown below

$$\frac{N_{N_2}}{N_{O_2}} = -\sqrt{\frac{M_{O_2}}{M_{N_2}}} = -\sqrt{\frac{32}{28}} = -1.07 \tag{5.16}$$

The mole fraction of nitrogen on the oxygen side of the diffusion cell is calculated using equation 5.17.

$$y_{N_2,0} = \frac{N_{N_2} \cdot v_{N_2}}{A} \tag{5.17}$$

And the mole fraction of oxygen from equation 5.18.

$$y_{O_2,0} = 1 - y_{N_2,0} \tag{5.18}$$

Since the gas is continuously being replaced on each side of the cell it is necessary to calculate the average mole fraction of oxygen on each side of the sample. On the oxygen side, oxygen is continuously being added therefore the concentration increases. On the nitrogen side, nitrogen is continuously being added therefore the concentration of oxygen decreases. Equations used to calculate the averages are shown below:

$$\bar{y}_{O_2,0} = \frac{1}{2}\left(1 + y_{O_2,0}\right) \tag{5.19}$$

$$\bar{y}_{O_2,L} = \frac{1}{2}\left(0 + y_{O_2,L}\right) \tag{5.20}$$

Ficks law states that the flux across a material is equal to the effective diffusivity multiplied by the concentration gradient, yielding:

$$\mathrm{N_{O_2}} = -\mathrm{D_{O_2,eff}} \cdot \frac{\mathrm{dC}}{\mathrm{dx}} \tag{5.21}$$

Concentration, C, can be related to pressure as shown below.

$$\mathrm{PV = nRT} \tag{5.22}$$

Where: P = Pressure
V = Volume
n = Moles
R = Gas constant
T = Temperature

$$\mathrm{C} = \frac{\mathrm{n}}{\mathrm{V}} = \frac{\mathrm{P}}{\mathrm{R} \cdot \mathrm{T}} \tag{5.23}$$

Equation 5.23 can be substituted into equation 5.21 to give flux in terms of pressure.

$$\mathrm{N_{O_2}} = -\frac{\mathrm{D_{O_2,eff}}}{\mathrm{R} \cdot \mathrm{T}} \cdot \frac{\mathrm{dP_{O_2}}}{\mathrm{dx}} \tag{5.24}$$

dP_{O2} is equal to the change in partial pressure of oxygen between the two sides of the separator paper and dx, is the thickness of the separator. Equation 5.24 can be modified to give:

$$N_{O_2} = -\frac{D_{O_2,eff} \cdot \left(P_{O_2,0} - P_{O_2,L}\right)}{R \cdot T \cdot L} \qquad (5.25)$$

Since both oxygen and nitrogen behave as ideal gases at room temperature the partial pressure of oxygen on each side of the cell is directly proportional to the molar fraction. This allows the effective diffusivity to be calculated by substituting pressures for mole fractions and rearranging equation 5.25, to give:

$$D_{eff} = \frac{N_{O_2} \cdot L \cdot R \cdot T}{P \cdot (\bar{y}_{O_2,0} - \bar{y}_{O_2,L})} \qquad (5.26)$$

5.6 REFERENCES TO CHAPTER 5

B. Culpin, Separator design for valve-regulated lead/acid batteries, Journal of Power Sources, Vol. 53, (1995), pp. 127-135

R. D. Laughlin, J. E. Davis, Text. Res. J., Vol. 31, (1961), pp. 904

Private communication, Hawker Energy, Newport, Gwent

G. J. Shugar, J. A. Dean, Chemist Ready Reference Handbook, McGraw Hill, (1990)

D. Rood, A Guide to the care, maintenance and trouble shooting of capillary G. C. systems, Hueting Pub. Ltd., Heidelberg: Nuting (1991)

D. S. Scott, F. A. L. Dullien, Diffusion of ideal gases in capillaries and porous solids, A.I.Ch.E. Journal, (1962), Vol. 8, No. 1, pp. 113-117

R. B. Evans, G. M. Watson, E. A. Manson, Gaseous Diffusion in Porous Media at Uniform Pressure, The Journal of Chemical Physics, Vol. 35, No. 6, Dec. (1961), pp. 2076-2083.

8 COULTER® Porometer II Reference Manual 9909858-D, Coulter Electronics Ltd., Northwell Drive, Luton, Beds, LU3 3RG, England, Section 3, p. 2.

6 Production of Test Batteries

6.1 INTRODUCTION

During the course of this project different designs of battery were examined using the experimental techniques described previously. In this section materials and manufacturing methods used for production of these batteries are described. A large number of the batteries examined were cycled to failure using different cycling regimes, details of which are also given.

6.2 MATERIALS AND MANUFACTURING PROCEDURE

6.2.1 BATTERY GRIDS

The battery grid production route can be described in two stages, the first of these being production of lead strip of suitable thickness, and the second, the punching out of the strip to form the grid. Two different grid types were used in the construction of the test batteries. These varied in composition and manufacturing method, a description of each method used is given below.

Stage 1. (a) **Production of Pure Lead Strip**

Lead grid was manufactured by firstly casting pure lead into a strip several centimetres thick. The lead strip was then rolled repeatedly until the desired thickness was obtained.

Stage 1. (b) **Production of Lead/Tin Strip**

Lead/tin grids were manufactured using Comminco casting machines. These have the ability to cast the grid to the desired thickness initially without the need for subsequent rolling.

Stage 2. **Manufacture of grids from lead strip**

Holes for the active material, of dimensions 4x13mm, were introduced into the lead strip using a punching machine thereby converting it into a grid. A band approximately 2cm wide on each side of the strip was left unpunched, this area provided the material to make the tab at the top of each electrode onto which the cast-on-strap was welded.

6.2.2 ACTIVE MATERIAL PRODUCTION

6.2.2.1 POSITIVE ACTIVE MATERIAL

Several compositions of positive active material were used in the construction of test batteries. Approximate compositions of the raw materials used are given below and commercial names have been employed where appropriate. The exact compositions of the paste mixes are unavailable due to commercial confidentiality.

Standard Grey Oxide Cyclic Paste

- 90% grey oxide (α-PbO, ≈29% lead)
- 10% red lead
- Sulphuric acid
- Distilled water

Tetrabasic Lead Sulphate Paste

- Grey oxide
- Tetrabasic lead sulphate
- Sulphuric acid
- Distilled water

Sulphated Grey Oxide Paste

- Grey oxide
- Sulphuric acid
- Distilled water

6.2.2.2 NEGATIVE ACTIVE MATERIAL

All test batteries contained negative electrodes manufactured from the same paste mix, the composition of which is given below. Exact ratios are again withheld due to commercial confidentiality.

Negative electrode paste mix

- Grey oxide
- Sulphuric acid
- Water
- Vanispersc* (lignosulphonates)
- Barium sulphate*
- Carbon black*
- Primafloc* (polyester fibres)

*expander

6.2.3 PLATE PRODUCTION

The positive and negative plates were both produced using the same manufacturing method. This involved mixing the lead oxides (and sulphates where appropriate), sulphuric acid, and distilled water in the correct quantities. In the case of the negative paste mix, expanders were also added. Once a paste of the correct consistency had been obtained, a pasting machine was used to push the paste into the holes of the battery grid. At this stage of manufacture, the paste was normally damp, so to improve the ease of handling a layer of thin paper manufactured from glass fibres was used the cover each side of the plate. Individual electrodes were cut from the pasted lead strip using a cylindrical cutter. A simplified diagram of this machine is shown in Figure 6.1 below.

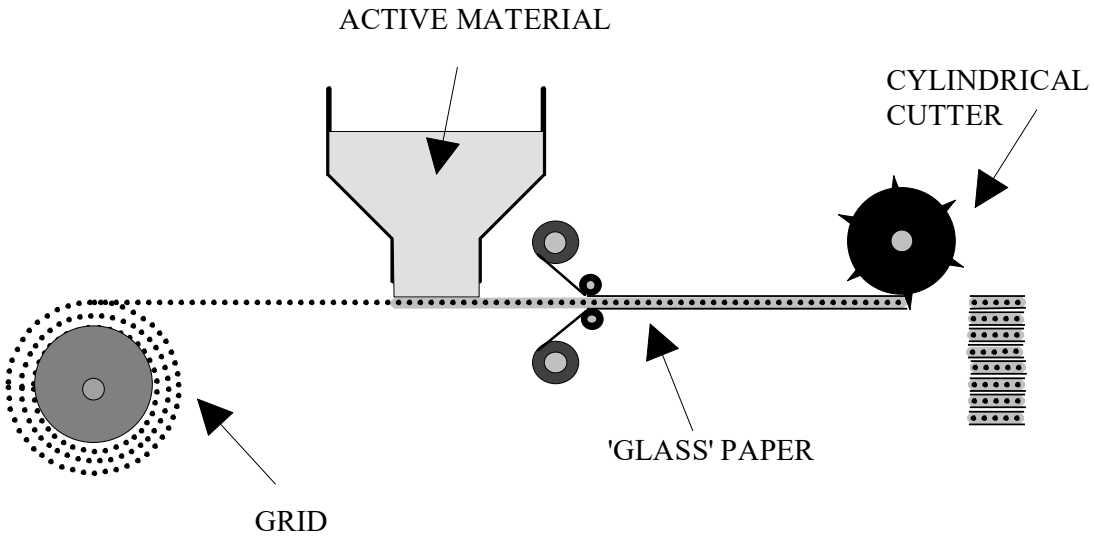

Figure 6.1: Pasting machine

6.2.4 CURING

Pasted plates were stacked into groups of 25 and put into metal baskets, before being placed into drying ovens. This allowed the plates to dry and the curing reactions within the paste to occur.

6.2.5 PRODUCTION OF MONOBLOCKS

Cells were constructed by wrapping sheets of separator paper around the positive plates. A 19-plate design was used consisting of 9 positive and 10 negative electrodes stacked alternately and connected in parallel to form each cell unit. Cells were inserted into a jig that compressed the plates while the cast-on-straps were attached to the tabs at the top of each positive and negative electrode. After removal from the jig, a thin polymer based paper was wrapped around

the bottom of the cell to ease insertion into the battery case. Cells were then connected by welding through pre cut holes in the battery case before the monoblock lid was plastic welded into position.

6.2.6 ACID FILL

KALLSTROM machines were used to fill the cell of each monoblock with the correct quantity of electrolyte. Due to the exothermic reactions that occur between sulphuric acid and unformed paste, it was necessary to firstly chill the acid to a few degrees centigrade. After this stage of manufacture the Bunsen valves could be added and the battery lid sealed.

6.2.7 FORMATION

The battery plates were formed after acid fill using a standard procedure. Again, the exact details of formation including voltage, current and duration are commercially sensitive and are thus omitted.

6.2.8 CYCLE LIFE TESTING OF BATTERIES

A small number of test batteries were examined after the formation stage. However, the majority were cycled to failure. This required the batteries to be repeatedly discharged and charged until the capacity had dropped below a predefined value, in the case of this study 80%.

At this point, cycling was stopped and the battery examined. In order to ascertain the battery capacity and state at the end of each cycle it is necessary to monitor the discharge voltage, current and time. Digatron charging units were used to serve this purpose, as they are capable of automatically cycling and monitoring the test batteries simultaneously, in addition they can also supply cycling data in real time as the tests proceed.

A number of different cycling regimes were used to cycle the batteries. Each cycle consists of a discharging and charging period. As many batteries vary in performance and properties the discharge part of the cycle is normally described as the number of hours required for the battery to reach 100% depth of discharge. This number is normally preceded by the letter c, so for example a C5 discharge would mean that the battery was discharged at a rate where it would be 100% discharged after 5 hours.

The charging phase of cycling was initiated when the monoblock voltage had dropped to a value of 10.2V. All charging was conducted at constant voltage for a set length of time. Details of the charging regime used in this study is described below.

- C5 Cycling Discharge - C5 rate 7.05A, to a voltage of 10.2V

  Charge - 2.45 volts per cell for 16 hours.

6.2.9 TEST BATTERIES EXAMINED

Details of the batteries examined are given in table 6.1 below.

Table 6.1: Test batteries examined

Battery ID	Positive Active Material type	Grid Type	Separator Type	Cycling Regime	Cycles to failure
Cycling Test – FF	Grey Oxide	Pure lead	H+V	N/A	N/A
Cycling Test – 10	Grey Oxide	Pure lead	H+V	C5	10
Cycling Test – 28	Grey Oxide	Pure lead	H+V	C5	28
Cycling Test – 42	Grey Oxide	Pure lead	H+V	C5	42
Cycling Test – 49	Grey Oxide	Pure lead	H+V	C5	49
Cycling Test – 65	Grey Oxide	Pure lead	H+V	C5	65
Cycling Test – 73	Grey Oxide	Pure lead	H+V	C5	73
Cycling Test – 92	Grey Oxide	Pure lead	H+V	C5	92
Cycling Test – 133	Grey Oxide	Pure lead	H+V	C5	133
Group 1 – FF	Grey Oxide & TTB	Pure lead	H+V	N/A	N/A
Group 1 – Cycled	Grey Oxide & TTB	Pure lead	H+V	C5	40
Group 2 – FF	Grey Oxide & TTB	Lead/Tin Alloy	H+V	N/A	N/A
Group 2 – Cycled	Grey Oxide & TTB	Lead/Tin Alloy	H+V	C5	29
Group 3 – FF	Sulphated Grey Oxide	Pure lead	H+V	N/A	N/A
Group 3 – Cycled	Sulphated Grey Oxide	Pure lead	H+V	C5	29
Group 4 – FF	Sulphated Grey Oxide	Lead/Tin Alloy	H+V	N/A	N/A
Group 4 – Cycled	Sulphated Grey Oxide	Lead/Tin Alloy	H+V	C5	27
Separator – H+V	Grey Oxide	Pure lead	H+V	C5	70
Separator – TFP	Grey Oxide	Pure lead	TFP	C5	160
Separator – Poly	Grey Oxide	Pure lead	Poly	C5	35

FF = Freshly formed; TTB = Tetrabasic lead sulphate; H+V = Hollingworth and Vose; TFP = Technical fibre products; Poly = H+V separator containing 8% polyester

7 RESULTS AND DISCUSSION: EFFECT OF CYCLING

7.1 INTRODUCTION

A large number of the batteries produced by Hawker Energy are for use in cyclic applications. They therefore have an interest in expanding their knowledge of how these batteries operate. An understanding of the compositional and structural changes that occur within a battery as the number of cycles increases is important if battery designs are to be improved.

Electrical testing results indicated that a batch of SBS (Sealed Battery System) 40 Amp hour batteries, constructed from 90% grey oxide / 10% red lead, positive active material, were failing after varying numbers of cycles. These batteries were manufactured using the same starting materials and processing techniques so were expected to show similar performance. Differences in performance can only be explained by the inherent variability of the manufacturing materials and process, that occur within each batch of batteries, that are not detectable from the normal quality control procedures. This observation provided an opportunity to study the effects of cycling on these batteries.

Freshly formed positive and negative active materials were examined to provide standard data to which the composition and structure of cycled samples could be compared.

7.2 ELECTRICAL TESTING OF BATTERIES

When a battery fails it can normally be attributed to failure of one or more cells. A GRANT Squirrel data logger was used to monitor the change in voltage with time of each cell during discharging of the battery as this allows the health of each cell to be assessed. This data has been represented as plots of voltage versus time for each cell. The line corresponding to the failed cell is red, the good cell blue and all other cells black.

The cell that reaches the lowest voltage during discharge is defined as the failed cell or bad cell. However, results show that all the cells within a battery degrade to a different extent. In some instances there is a clearly failed cell, with a very low potential, compared to the other cells in the battery which all have high potentials. In other batteries all the cells appear to fail to a certain extent and there is no clearly defined good or bad cell. Plots for batteries cycled 10, 28, 42, 49, 65, 73, 92 and 133 times are shown in Figure 7.1 to Figure 7.8, respectively. Figure 7.1 shows

a typical example of a battery with a single bad cell where all the other cells are good compared to Figure 7.5 where all the cells have failed to a certain extent.

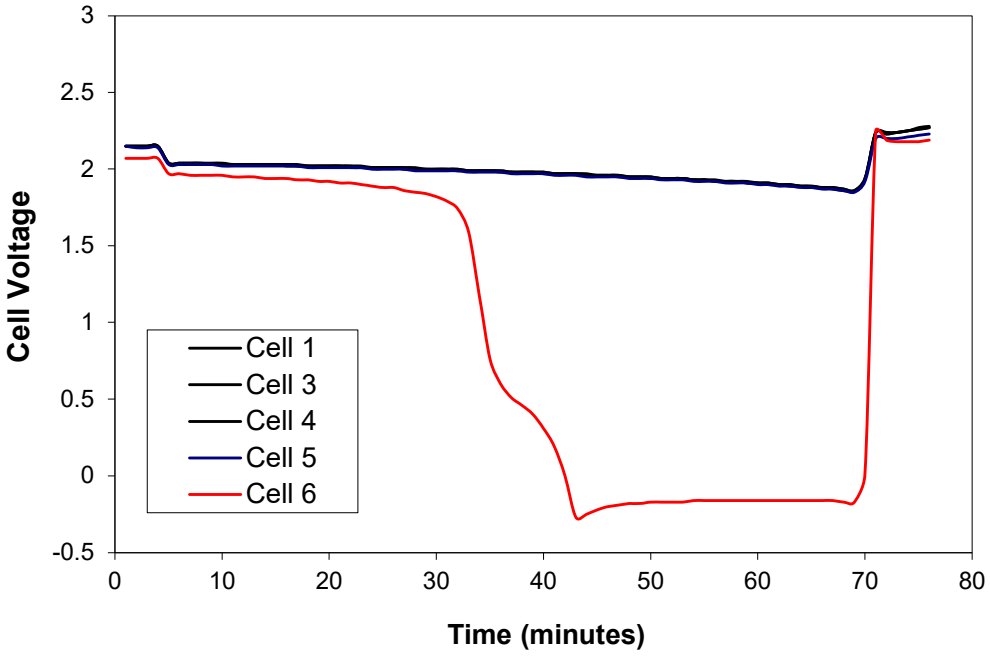

Figure 7.1: Plot of potential versus time for cells in battery cycled 10 times

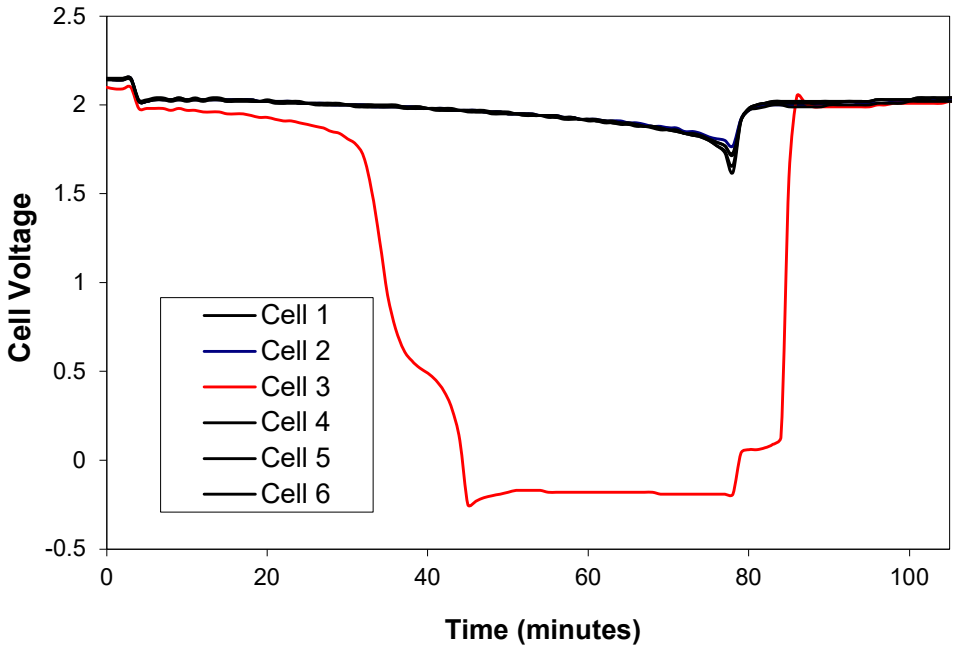

Figure 7.2: Plot of potential versus time for cells in battery cycled 28 times

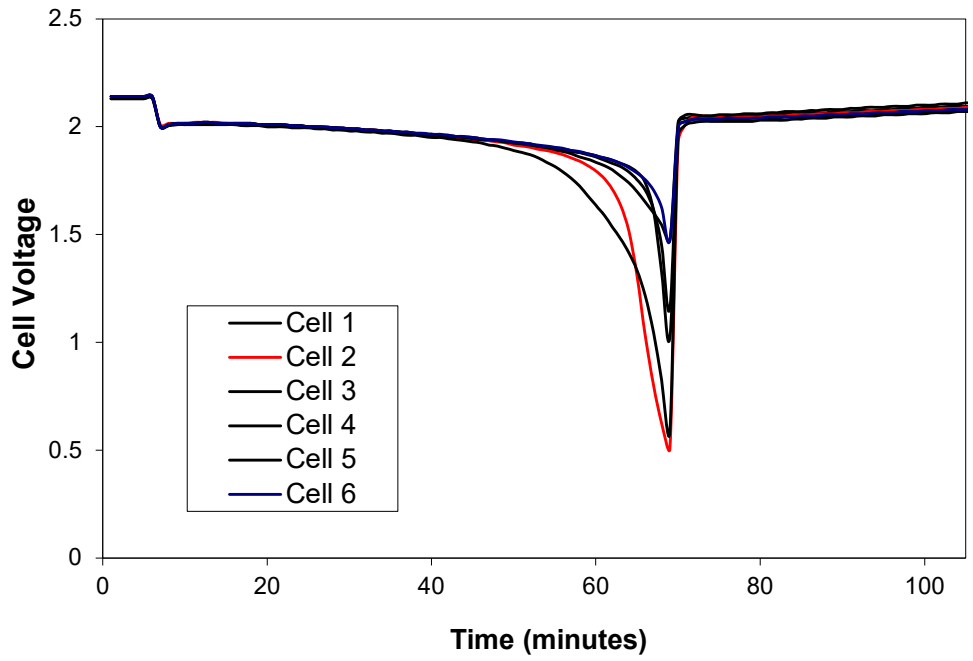

Figure 7.3: Plot of potential versus time for cells in battery cycled 42 times

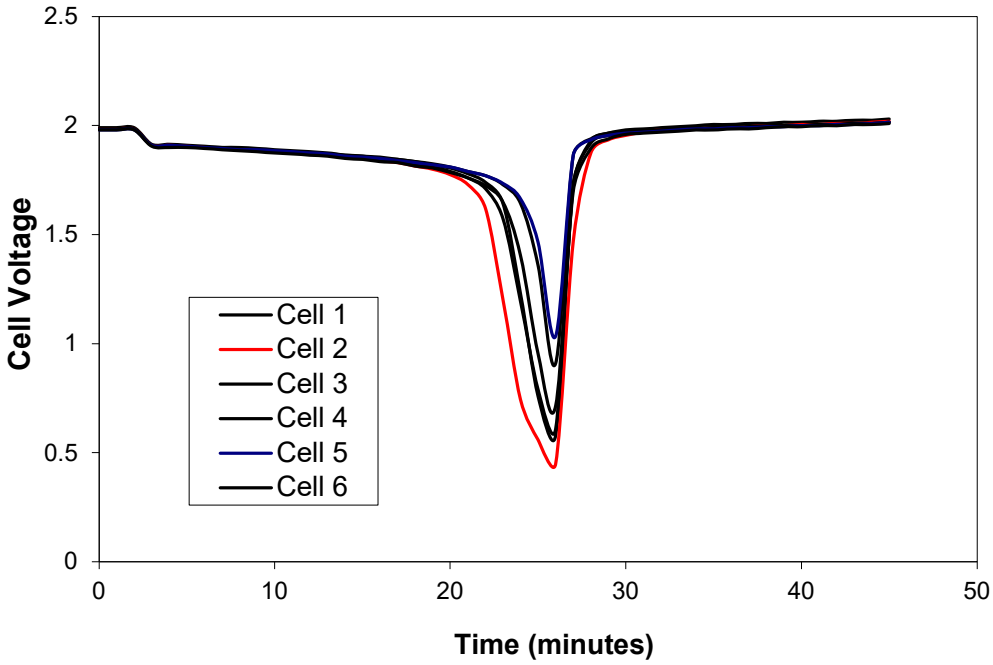

Figure 7.4: Plot of potential versus time for cells in battery cycled 49 times

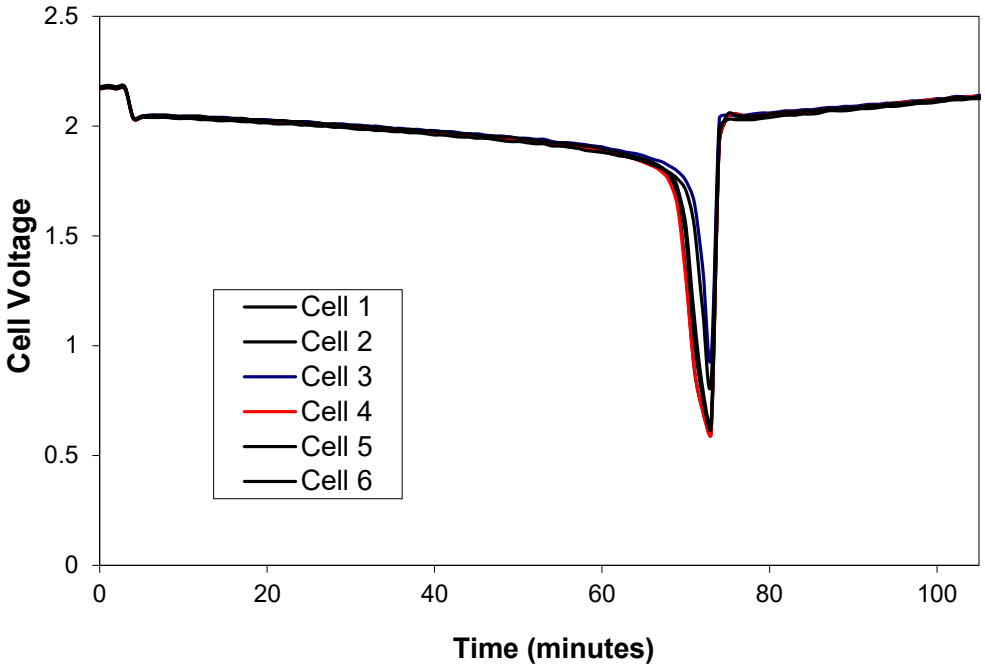

Figure 7.5: Plot of potential versus time for cells in battery cycled 65 times

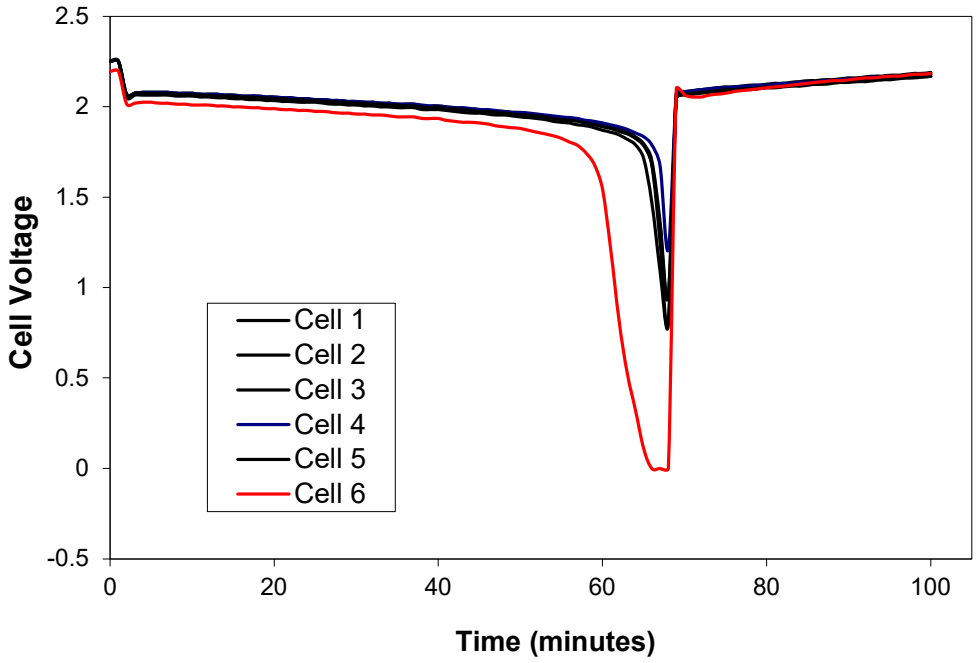

Figure 7.6: Plot of potential versus time for cells in battery cycled 73 times

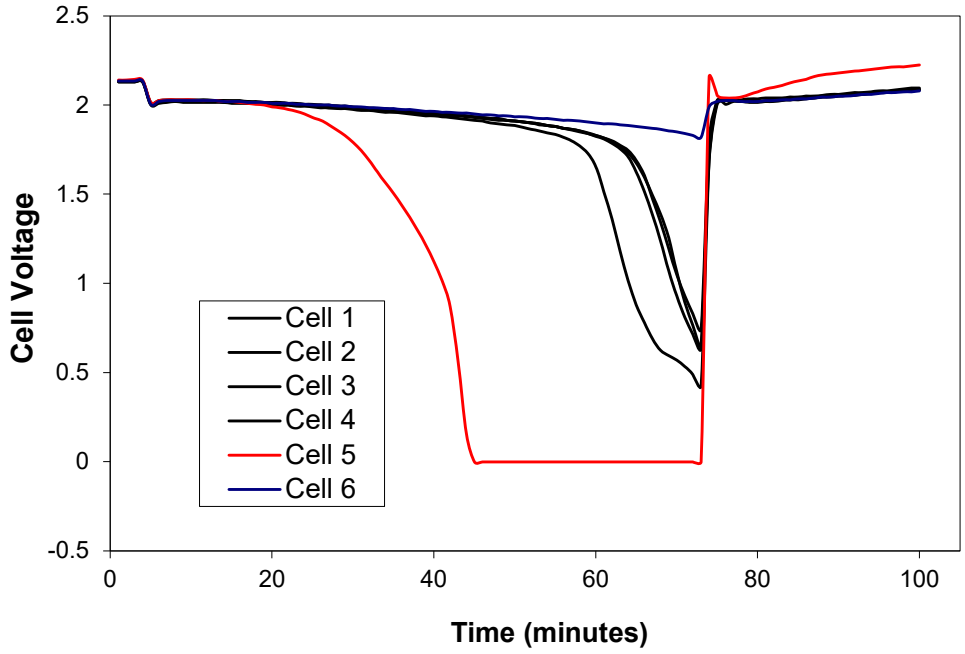

Figure 7.7: Plot of potential versus time for cells in battery cycled 92 times

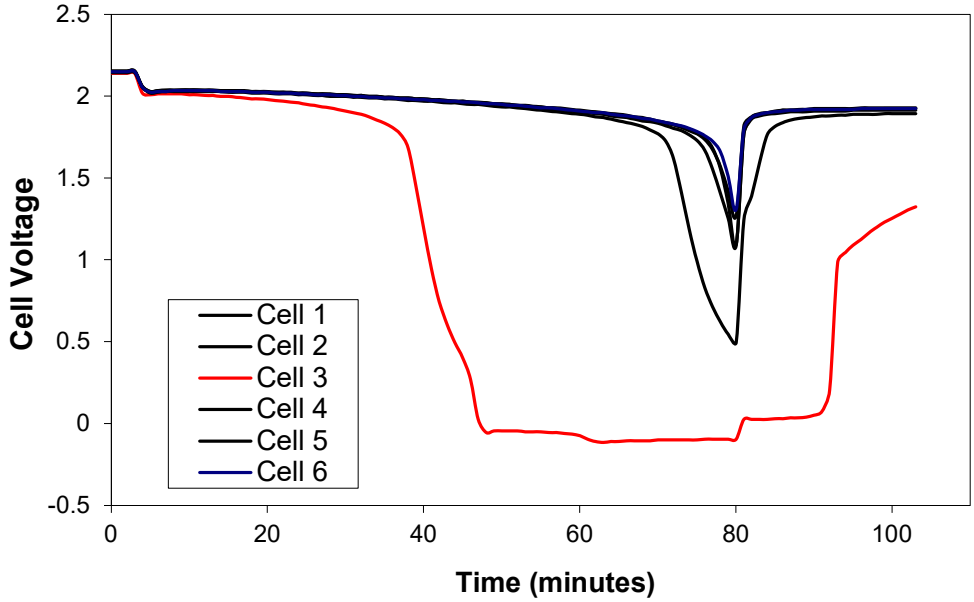

Figure 7.8: Plot of potential versus time for cells in battery cycled 133 times

7.3 ELECTROLYTE SPECIFIC GRAVITY

Acid stratification occurs when the acid concentration varies at different positions on the separator paper. Sulphuric acid concentration in the electrolyte is directly related to the specific gravity, which can be determined easily with a small sample of acid. For each of the cells examined the specific gravity was measured at the top and bottom. Values obtained are shown

in Table 7.1. The greater the difference between these two values the larger the amount of stratification.

Table 7.1: Specific gravity of electrolyte at top and bottom of separators in good and bad cells of cycled batteries.

Number of Cycles	Good Cell (x10^3)			Bad Cell (x10^3)		
	S.G. top	S.G. bottom	ΔS.G. (bottom – top)	S.G. top	S.G. bottom	ΔS.G. (bottom – top)
0	1315	1315	0	-	-	-
10	1325	1330	5	1275	1280	5
28	1330	1345	15	1295	1305	10
42	1330	1345	15	1330	1360	30
49	1310	1330	20	1315	1330	15
65	1310	1335	25	1285	1325	40
73	1315	1360	45	1285	1340	55
92	1315	1320	5	1315	1330	15
133	1345	1350	5	1330	1360	30

Acid stratification as a function of cycles is shown in Figure 7.9. The top of each bar represents the specific gravity at the bottom of the cell and the bottom of each bar the specific gravity at the top. Bar length therefore gives the amount of stratification. There is a general trend of greater stratification in the bad cell compared to the good. The only exception to this is in the batteries cycled 28 and 49 times.

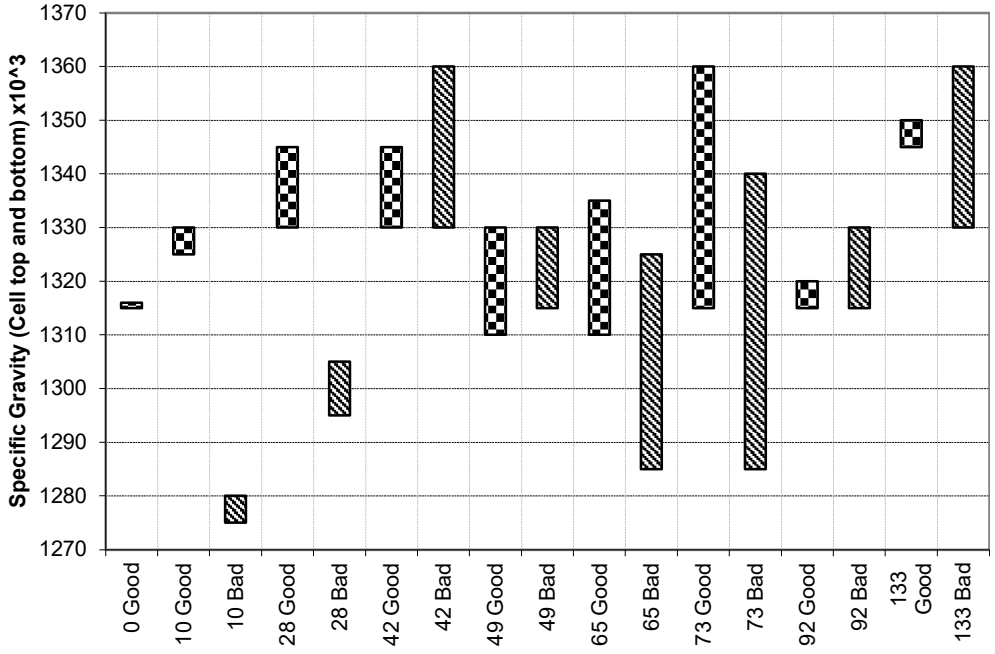

Figure 7.9: Difference in Specific gravity between top and bottom of separator papers in good and bad cells.

The batteries cycled between 0 and 73 times show an increase in stratification with number of cycles. This trend is not reflected in the results obtained from the batteries cycled 92 and 133 times. There is no obvious explanation for this trend.

7.4 POSITIVE ACTIVE MATERIAL

During battery cycling a number of compositional and structural changes occur within the positive active material. This is most apparent with reference to the compositional results obtained from the x-ray diffraction analysis. Figure 7.10 shows the composition of the positive active material from the good cells of the cycled batteries.

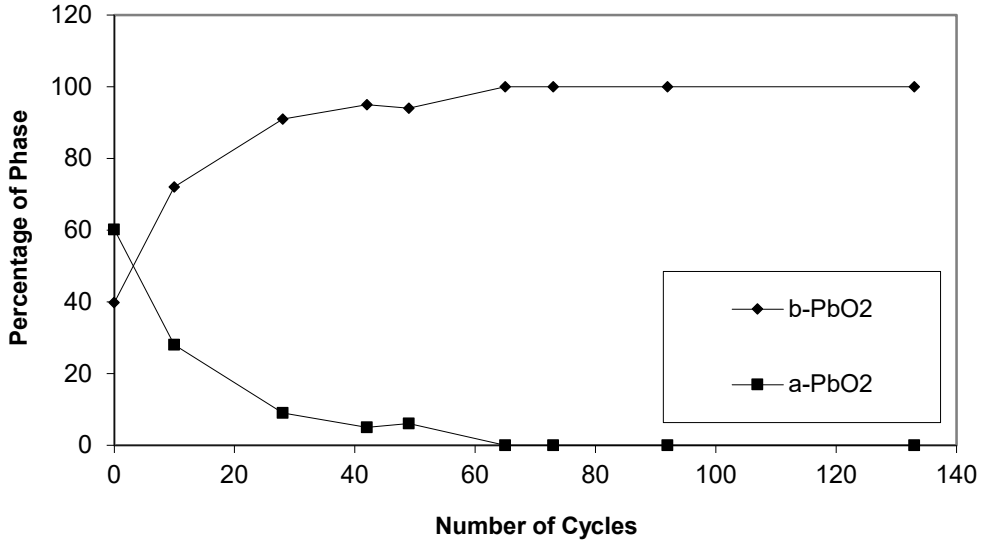

Figure 7.10: Composition of positive active material from good battery cells

The active material consists of a mixture of the alpha, (a-PbO2), and beta, (b-PbO2) forms of lead dioxide. As the battery is cycled the proportion of the alpha phase decreases. This phenomena is well documented, [1] and occurs because the alpha phase cannot be formed in acidic environments. The rate at which the alpha lead dioxide is converted to beta lead dioxide with cycles decreases. This is because as the number of cycles increases, the amount of the alpha phase available for conversion into lead sulphate decreases. Figure 7.11 shows the composition of the positive active material in the bad cells.

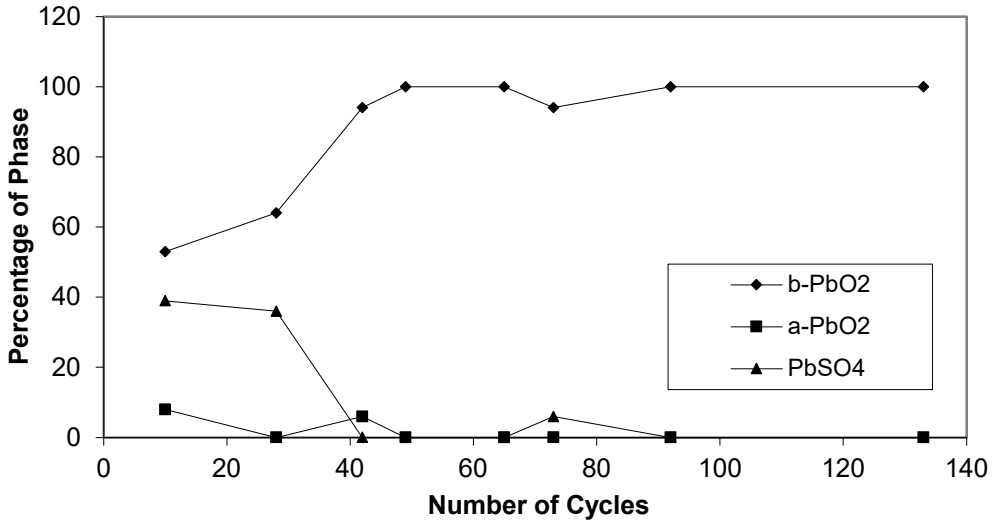

Figure 7.11: Composition of positive active material from bad battery cells

Figure 7.11 shows an increase in beta lead dioxide with number of cycles similar to that observed in the good cells, however the batteries cycled 10 and 28 times contain large amounts of lead sulphate. Lead sulphate is formed during discharge of the battery and is consequently converted back into lead dioxide on charging. This has not occurred in these cells and the lead sulphate remains. Examination using the scanning electron microscope identified large lead sulphate crystals in the battery cycled 28 times. These varied in size up to greater than 10μm, see Figure 7.12 a & b.

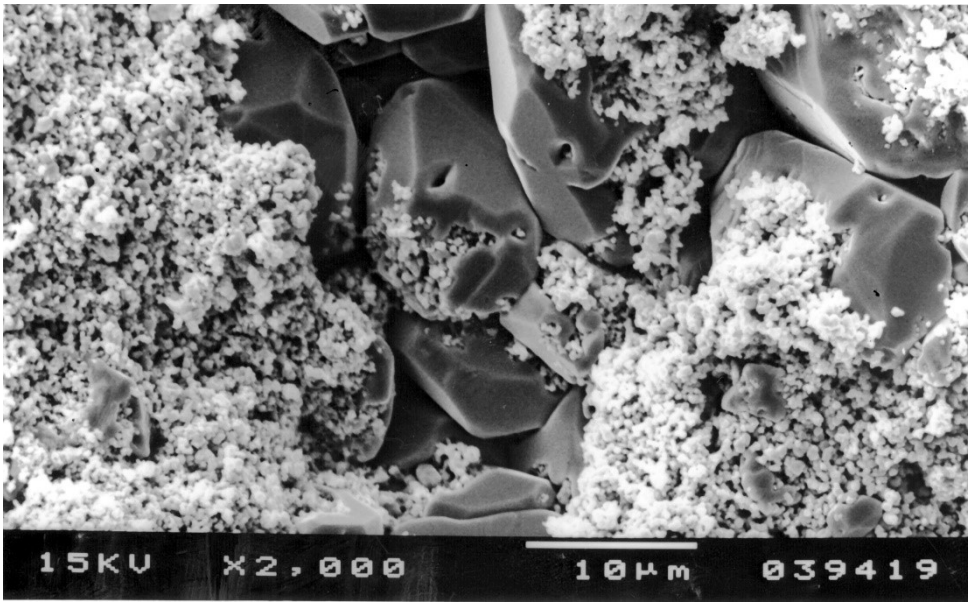

(a)

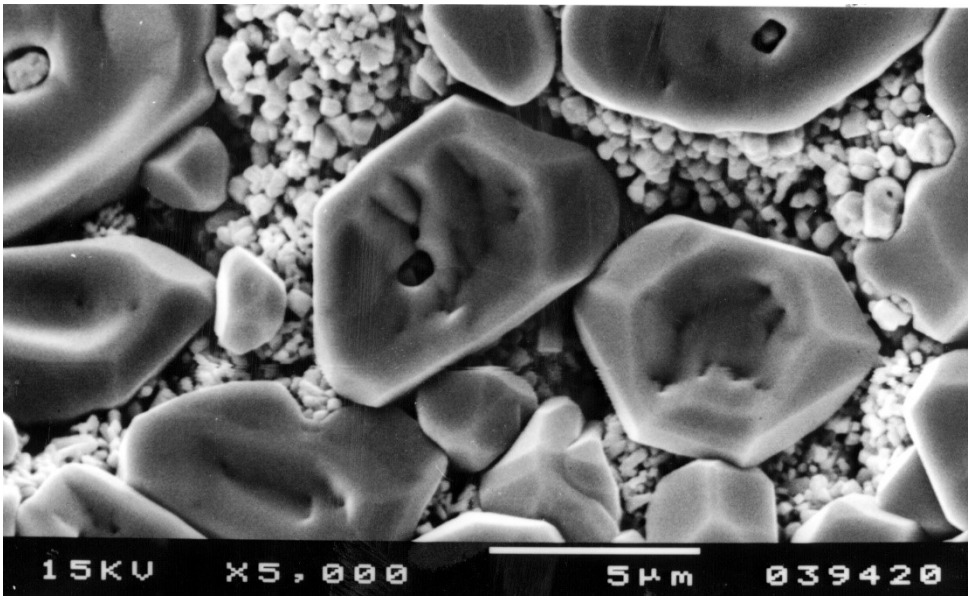

(b)

Figure 7.12 (a) & (b): Sulphate crystals in bad cell of battery cycled 28 times

From a kinetic standpoint once sulphate crystals of this size are formed it is unfavourable for them to react to form lead dioxide and sulphuric acid due to their high volume and low surface area. Given the amount of lead sulphate present it is not surprising that these cells have failed and it is almost certain that sulphation was the cause of capacity loss and eventual battery failure.

When a comparison is made between the quantities of alpha and beta lead dioxide in the good and bad cells of the batteries cycled 10 and 28 times the proportion of alpha lead dioxide is

reduced whereas the proportion of the beta phase is similar. This suggests that the lead sulphate in these batteries had formed mainly from alpha lead dioxide as opposed to beta lead dioxide.

Variations in BET surface area with cycles are shown in Figure 7.13 below.

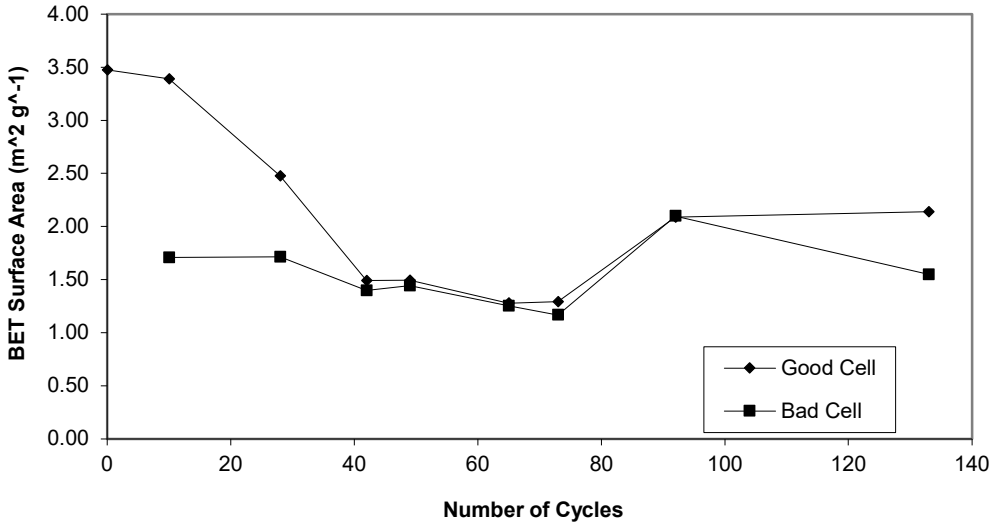

Figure 7.13: BET surface area of positive active material in cycled batteries

From the figure it can be seen that the BET surface area for the good cell in any battery is consistently higher than that in the corresponding bad cell. However there does not appear to be any consistent trend between BET surface area and number of cycles. The positive active material in the freshly formed battery has a surface area around 3.5, which then drops to a value comparable with that of the bad cell after approximately 40 cycles. This reduction in surface area with cycles is not observed in the bad cells (batteries cycled 10 and 28 times). Lead sulphate has a low surface area compared to lead dioxide and its presence is the most likely cause of the low surface areas of the plates in these batteries. Pycnometric density measurements of the positive active material from good and bad cells are shown in Figure 7.14.

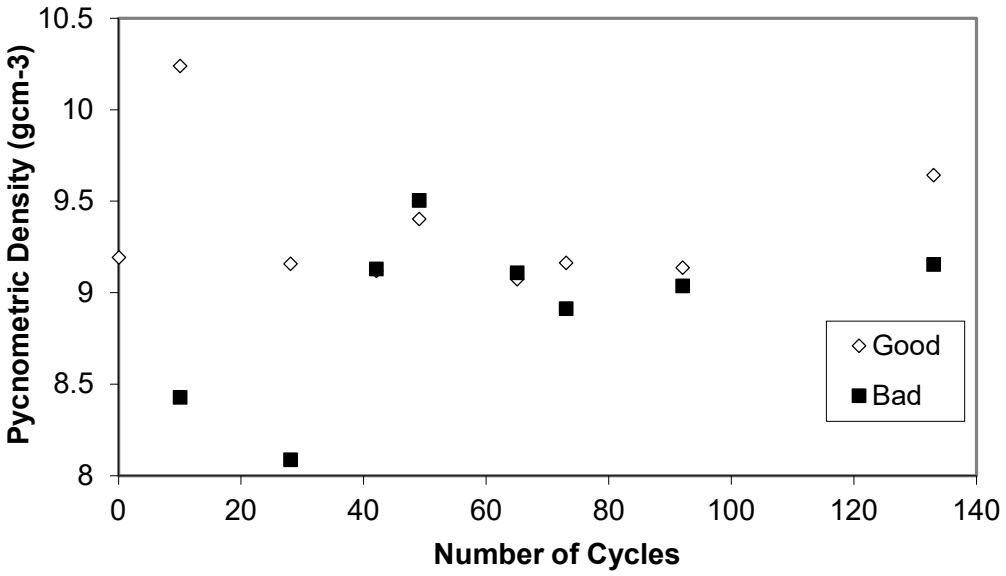

Figure 7.14: Pycnometric density measurements of positive active materials

The majority of the values lie between densities of 9 and 9.5, the same as in the freshly formed active material. This suggests that cycling has little effect on density. Lower density values were observed in the bad cells of batteries cycled 10 and 28 times, which is consistent with the presence of sulphate. An unusually high density of around 10.25 was recorded for the active material in the good cell of the battery cycled 10 times. The other results do not give any indication as to why this is the case.

7.5 NEGATIVE ACTIVE MATERIAL

Examination of the negative active material from cycled batteries using x-ray diffraction and wet chemical analysis revealed the presence of beta - lead monoxide, (b-PbO), in a number of the plates taken from both good and bad cells, Figure 7.15 and Figure 7.16.

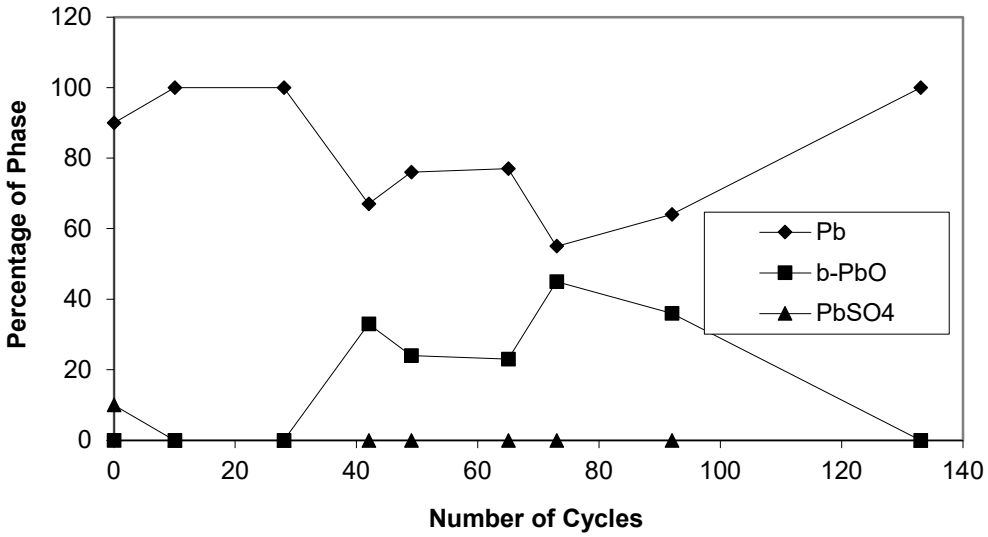

Figure 7.15: XRD analysis of negative active material from good cells

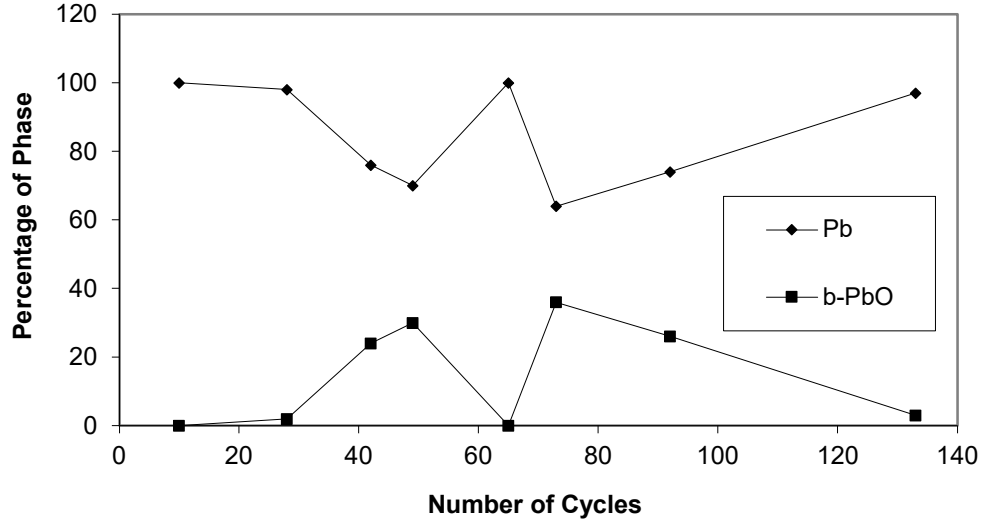

Figure 7.16: XRD analysis of negative active material from bad cells

There was also a corresponding increase in the BET surface area, as shown in Figure 7.17. This observation is consistent with the presence of lead monoxide, which has a greater surface area than lead.

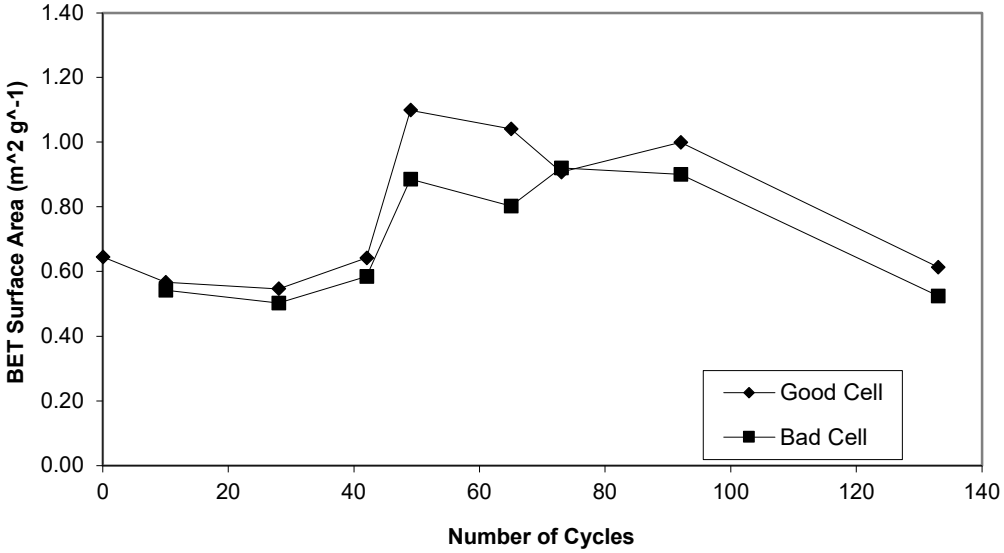

Figure 7.17: BET surface area of negative active materials from good and bad cells

Structural changes are visible in the scanning electron microscope images shown in Figure 7.18 and Figure 7.19. The morphology of the sample containing lead monoxide has particles with a much higher aspect ratio compared to the sample containing 100% lead.

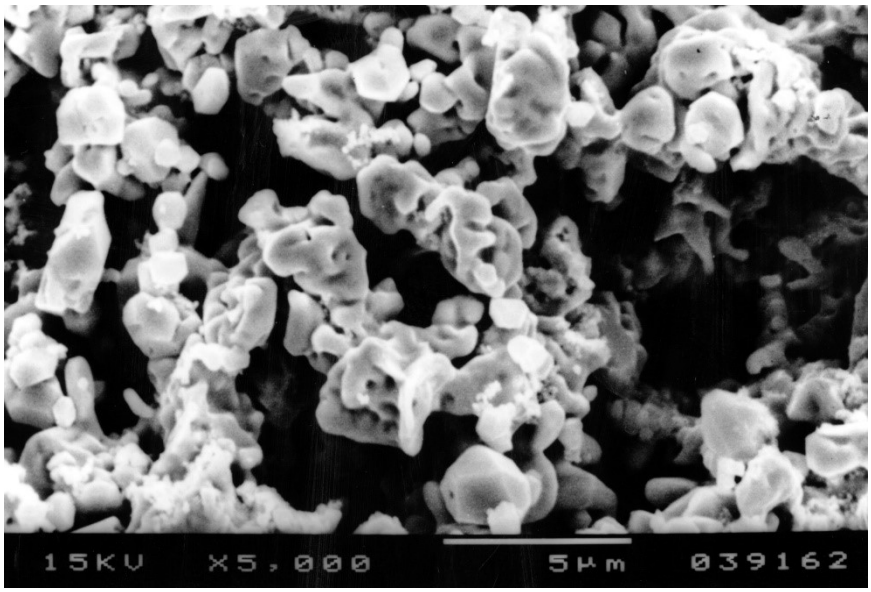

Figure 7.18: Negative active material containing 100% lead

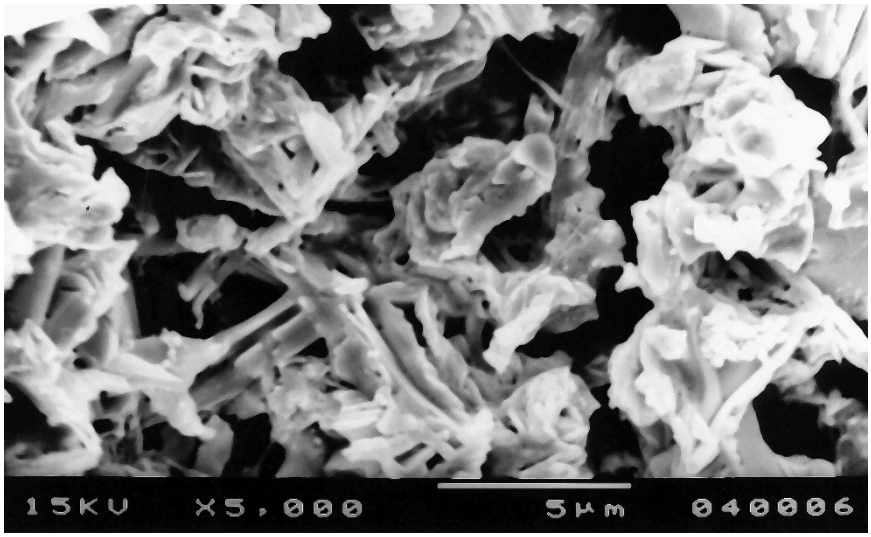

Figure 7.19: Negative active material containing 55% lead

The trends described in the results above are also reflected in the pycnometric density measurements shown in Figure 7.20 below. A decrease in density is observed in the plates containing lead monoxide.

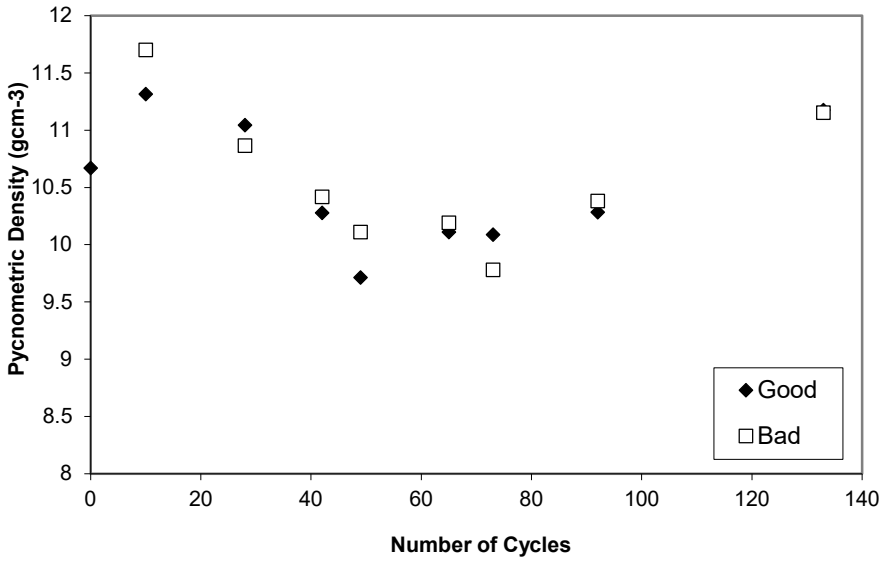

Figure 7.20: Pycnometric density measurements of negative active materials

Small quantities of lead monoxide in the range 0-3%, have been reported in the compositional analysis of negative electrodes previously [2], however the quantities reported in the batteries described above are significantly higher, very unusual and warrant further investigation. The formation of the lead monoxide could only have occurred by one of the routes described below.

1. **Formed in battery during cycling**

- This cannot be explained using any of the electrochemical processes currently used to describe battery operation.
- Theoretically the negative potential of the electrode should have reduced any lead monoxide to metallic lead before a significant proportion had formed.

2. **Formed after cycling during drying stage in tear-down procedure**

- Lead is known to oxidise easily therefore the oxide may have formed during plate drying in the vacuum oven, however there is a significant difference in the structure between the pure lead plates and plates containing oxide.
- All the negative plates were dried using the same procedure, however, only a number of the plates oxidised.
- The battery cycled 65 times showed significant amounts of oxide on the good cell, however none was present in the bad cell even though both plates were dried in the same oven at the same time.

From the observations above it is not possible to identify how the oxide formed. For this reason further investigations, described in the sections below, were conducted.

7.5.1 TRANSMISSION ELECTRON MICROSCOPY OF LEAD PARTICLES

Samples of negative active material were prepared for examination in the transmission electron microscope. The purpose of this being that if it could be shown that the electrode contained particles of oxide surrounded by lead this would provide an explanation as to why the oxide was not reduced. The active material containing the highest proportion of oxide and a sample of material consisting of 100% lead was examined. Pictures of typical particles from a freshly formed and cycled negative active material sample are shown in Figure 7.21 and Figure 7.22.

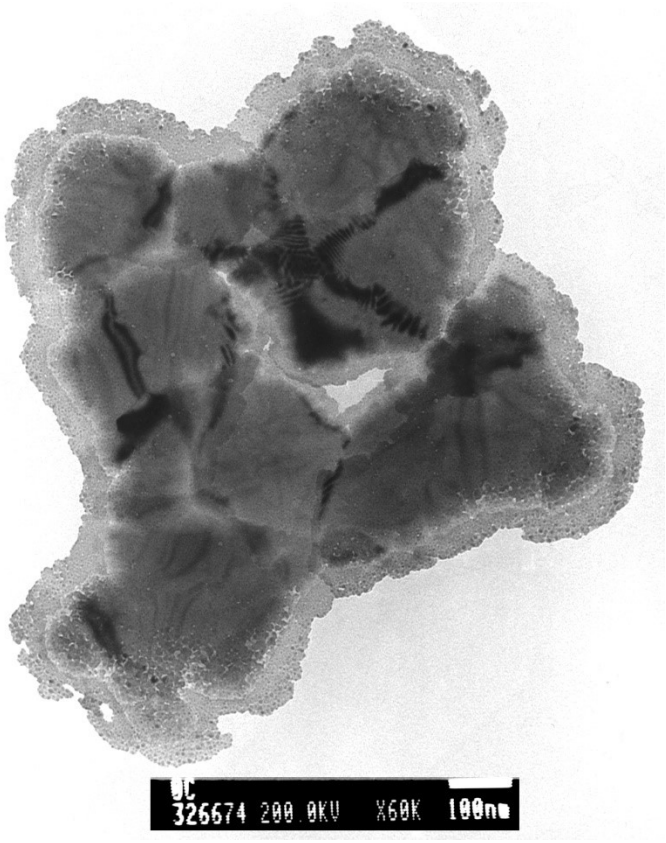

Figure 7.21: TEM picture of freshely formed particle from negative active material

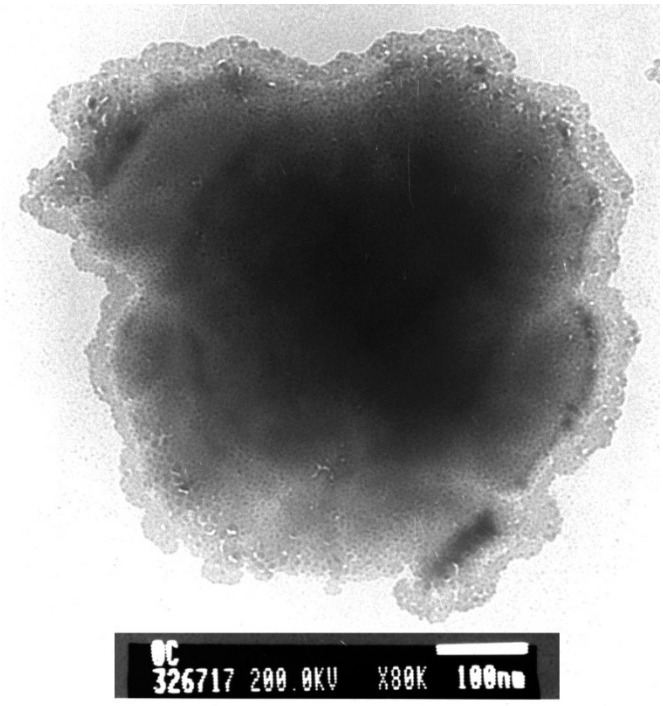

Figure 7.22: TEM picture of lead particle from negative active material cycled 73 times

There is no evidence in either sample of oxide surrounded by lead. This indicates that any oxide within the active material should have been reduced during charging. A surface layer is visible around the perimeter of each particle. Due to the thickness of this layer it was not

possible to obtain a compositional analysis, however it is likely to be a thin layer of lead monoxide as there are no other plausible alternatives.

A number of differences are visible between the particle from the freshly formed active material and the particle cycled 73 times. The freshly formed lead particle, Figure 7.21, consists of number of smaller lead grains with interference fringes visible at some of the boundaries where the grains meet. Figure 7.22 shows a cycled particle, it does not contain any fringes and the outer oxide layer is slightly different in appearance to that of the freshly formed. Close examination of the outer oxide layers indicates that they consist of a number of smaller particles of oxide.

7.5.2 RESISTIVITY MEASUREMENTS

The resistivity was measured for a number of negative active material samples cycled various numbers of times that contained different amounts of lead monoxide. This provided a means of determining the effect of lead monoxide on resistivity. Resistivities are plotted against the number of cycles the active material had sustained in Figure 7.23 below. The percentage of lead monoxide present is given next to each set of data points.

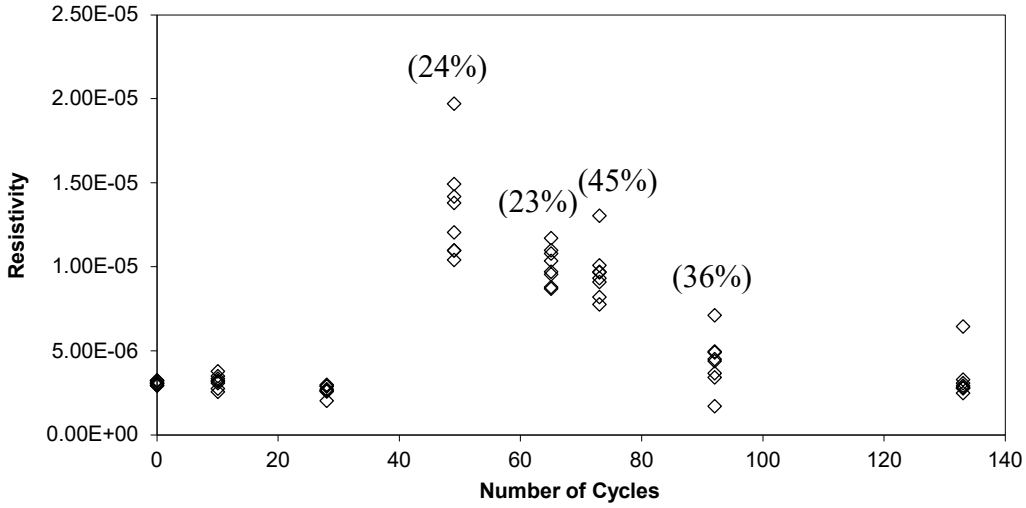

Number in brackets = % PbO in sample

Figure 7.23: Resistivity versus number of cycles of negative active material

From the active material samples examined the variance of resistivity values is greater in those containing oxide. This indicates the freshly formed active material has the most uniform structure and as the battery is cycled the uniformity decreases. The resistivity of the active material cycled 133 times is very similar to that of the freshly formed active material, suggesting cycling does not affect the negative active material structure significantly. The presence of

oxide within the active material increases the resistivity since the oxide is an insulator, however the amount of oxide does not appear to be correlated to the resistivity directly. The reason for this is unknown.

7.5.3 SCANNING ELECTRON MICROSCOPY OF LEAD PLATES DRIED IN HUMID ENVIRONMENT

In order to investigate the possibility that oxide formed during the drying process, due to the presence of higher than normal levels of humidity, an experiment was conducted to simulate drying in a high humidity environment. A sample of negative active material consisting of 100% lead was heated in the vacuum oven at a similar temperature to that used for drying whilst placed on a damp piece of separator paper, therefore exposing it to water vapour, for approximately 5 hours. The structure of the oxidised active material was then compared with the samples containing oxide, to determine if an unusually high humidity in the oven could have been the cause of oxidation. Figure 7.24 shows the structure of the negative active materials.

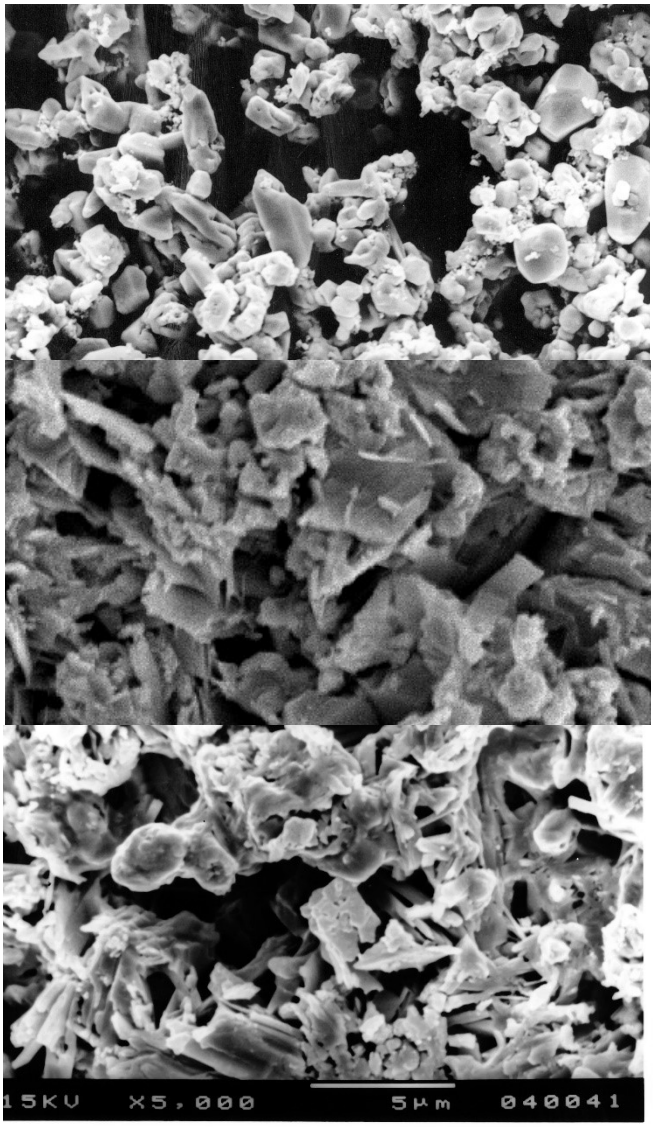

Top Picture – Pure lead negative active material
Middle Picture – Active material dried in humid environment (approx. 23% lead monoxide from XRD)
Bottom Picture – Active material sample cycled 65 times (23% lead monoxide)

Figure 7.24: Fracture surface images of negative active material samples after various treatments

From the structures shown in the figures above it is clear that drying in a humid environment produces structural as well as compositional changes. When comparing the structure of active material dried in a humid environment with that from the samples dried during the tear down procedure there are a number of similarities, although the structures do not resemble each other exactly. A comparison demonstrates that significant structural changes can occur if the moisture content is high during drying, but does not conclusively prove that a high moisture content during drying was responsible for the compositional and structural changes observed in the active materials.

7.5.4 SUMMARY OF RESULTS FROM ADDITIONAL TESTS

There is no evidence that the proportion of β-lead monoxide is linked to the number of cycles or resistivity, suggesting that its formation is unlikely to be due to a mechanism occurring during battery operation. It is possible that oxide formation occurred during plate drying. However, this cannot be confirmed from the current results. Due to similarities between the freshly formed and cycled active materials, which did not contain oxide, it is unlikely that battery failure was a result of negative plate failure. For this reason the presence of the oxide has not been investigated further.

7.6 EFFECT OF CYCLES ON CORROSION LAYER THICKNESS

During operation and overcharging of a battery, oxygen gas reacts with the positive grid forming a lead monoxide corrosion layer. This subsequently reacts electrochemically to form lead dioxide resulting in the formation of a corrosion layer containing both lead monoxide and dioxide. Corrosion layer thickness measurements were taken on the top, bottom, left and right hand sides of the grid wire in the good and bad cells of cycled batteries. Figure 7.25 shows the average corrosion layer thickness versus cycles for good and bad cells.

With the exception of the corrosion layer thickness measured on the battery cycled 49 times, which was significantly thicker than that on the other grids, the data appears to follow an exponential relationship.

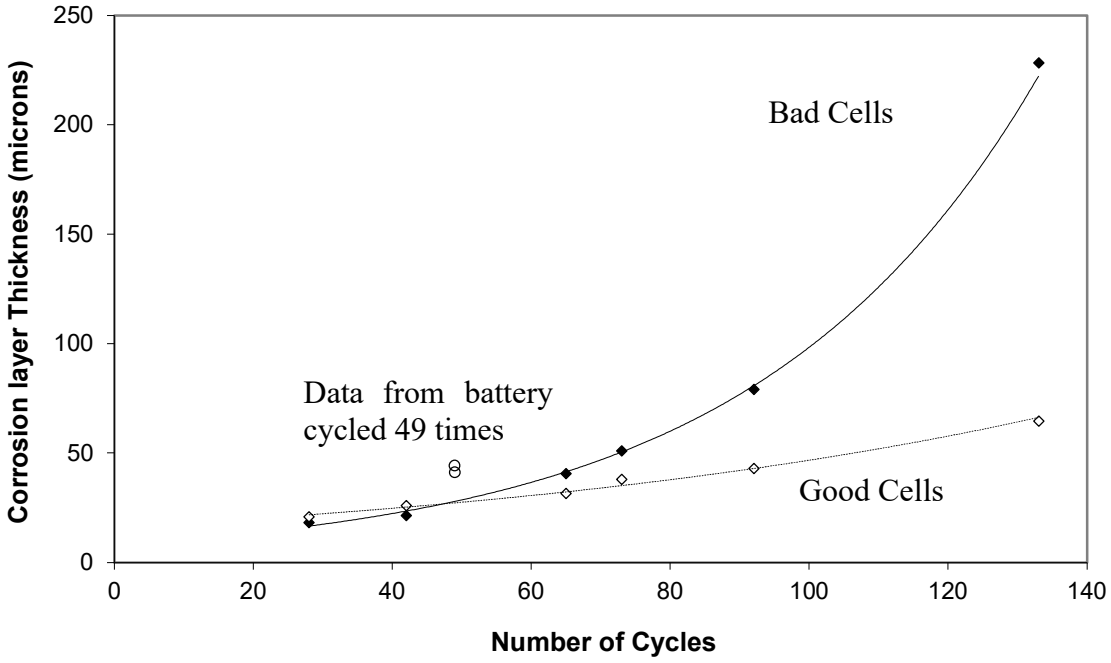

Figure 7.25: Corrosion layer thickness versus number of cycles for good cells

Equations of the curves in the above figure, assuming an exponential relationship, are shown below with corresponding R^2 values.

- Good cells $y = 16.4e^{0.0106x}$ $R^2 = 0.987$
- Bad cells $y = 8.3e^{0.0247x}$ $R^2 = 0.996$

From the above figure and equations it can be seen that, the rate of corrosion layer thickening increases with number of cycles and, is greatest in the bad cells. This observation can be explained by considering the processes that occur during cycling of the battery. Corrosion layer growth occurs during overcharging when oxygen evolved within the positive active material diffuses to the positive grid and reacts to form lead monoxide. It follows that corrosion layer growth rate and therefore thickness, must be related to overcharging time. The amount of overcharging that a battery cell sustains is a function of the charging time (16 hours for these batteries) and, the capacity or length of time needed to charge the cell. A consequence of battery cycling is a reduction in the capacity of the cells. It follows therefore that a reduced capacity cell, for example the bad cell, may charge more rapidly than the good cell in the same battery, effectively increasing the overcharging time. The increased corrosion layer thickening observed in the bad cells compared to the good cells could therefore be accounted for by the reduced capacity of the bad cells.

As discussed above the difference in corrosion layer thickness between the good and bad cells is a function of capacity. The thickness of the corrosion layers in the battery cycled 49 times was greater in both good and bad cells. This suggests that this battery failed due to a mechanism different to that present in the other batteries. From the current results it is not possible to be more specific with regard to this.

The structure and variations in thickness of the corrosion layer are discussed in greater detail in the proceeding chapters.

7.7 CONCLUSIONS

The following conclusions can be drawn from the results presented in this chapter.

1. When a battery fails the cells within the battery fail to different extents.
2. Sulphation of the positive plates is the most likely cause of failure in the batteries cycled 10 and 28 times. This suggests that if the cells have not failed due to sulphation, within the first 30 cycle's sulphation is unlikely to be the cause of failure.
3. Lead sulphate forms at the expense of α-lead dioxide rather than β-lead dioxide.
4. Resistivity of the negative active material does not vary significantly during battery cycling.
5. Cycling decreases the uniformity of the negative active material structure.
6. The corrosion layer thickness is greater in the bad cells.
7. Corrosion layer growth rate is greater in the bad cells.
8. Acid stratification is greater in the bad cells of a battery which indicates a lower capacity

7.8 REFERENCES

1. D. Berndt, Maintenance-Free Batteries, A handbook for battery technology, Second Ed., John Eiley and sons Inc., p. 314
2. F. A. Fleming, Phase III Analysis of cycled batteries, Hawker Energy Products Ltd.

8 RESULTS AND DISCUSSION: EFFECTS OF GRID ALLOY AND POSITIVE ACTIVE MATERIAL

8.1 INTRODUCTION

The previous chapter described changes that occur within a battery during cycling. In this chapter the influence of grid alloy composition and active material on battery performance is investigated. Cured, freshly formed and cycled positive and negative active materials from each battery design have been characterised allowing comparisons to be made.

8.2 DETAILS OF BATTERIES EXAMINED

The test batteries were produced using combinations of pure lead or lead/tin alloy positive grids, and grey oxide positive active materials containing either extra sulphuric acid (sulphated) or tetra-basic lead sulphate (TTB). The negative electrodes of all batteries were manufactured using a standard grey oxide paste mix. Four different battery designs were produced, named group 1-4, details of which are given in Table 8.1 below.

Table 8.1: Matrix of test batteries indicating positive active materials and grid alloy used in each group.

Positive active material type	Pure lead grid wire	Lead/tin alloy grid wire
Grey oxide with additional TTB PAM	Group 1	Group 2
Sulphated Grey Oxide PAM	Group 3	Group 4

Due to the practicality of testing a large enough number of batteries to enable comparisons of the actual performance, with respect to cycles to failure, to be made, it was decided to examine one of each battery. Although this approach does not allow a statistical estimation of the performance, it provides an opportunity to investigate the processes that occur in each design and predict how each of these may affect performance.

8.3 EXAMINATION OF CURED ELECTRODES

8.3.1 CURED POSITIVE ELECTRODES

X-ray diffraction and wet chemical analysis techniques were used to determine the composition of the positive active materials from each group. Compositions obtained are shown in Table 8.2.

Table 8.2: Compositional analysis of cured positive active materials

	α-PbO (%)	Pb (%)	4PbO.PbSO4 (%)
Group 1	65.4	3.8	30.8
Group 2	66.6	3.7	29.7
Group 3 *	95.1	4.9	0
Group 4 *	95.3	4.7	0

*Other compounds may be present but are not included as their abundance is negligible and cannot be entered into the PEAKS program for quantitative analysis.

The compositions obtained for groups 1 and 2, and groups 3 and 4 are almost identical. This is to be expected as these are essentially the same paste mixes on different grids. Groups 1 and 2 consist of α-lead monoxide with a small proportion of lead and approximately 30% tetra-basic lead sulphate, whereas groups 3 and 4 consist of almost 100% α-lead monoxide apart from a small proportion of lead.

Differences between the active materials are less noticeable in the fracture surfaces. Figure 8.1: Fracture surface of cured active material from group 1 to Figure 8.4: Fracture surface of cured active material from group 4 show fracture surfaces of each active material, taken in the scanning electron microscope. A number of 'rod shaped' particles can be seen in fracture surfaces of groups 1 and 2 which are not present in groups 3 and 4, these are tetra-basic lead sulphate crystals.

Tetra basic lead sulphate consists of high aspect ratio needle like crystals with a length of approximately 100 microns, see Figure 8.5: High aspect ratio tetra-basic lead sulphate crystals However, particles identified within the cured active material are shorter. The most likely explanation of this is that during the paste mixing and pasting stages of plate manufacture, tetra-basic lead sulphate crystals broke into shorter lengths.

BET surface areas of the active materials obtained for groups 1 to 4 were 1.48, 1.43, 2.19 and 1.48 m^2g^{-1} respectively. The BET surface area of the group 3 active material is unusually high. However, the sample of active material supplied for the analysis was noticeably damp and although dried for the analysis, may still have contained structural changes that would have

influenced results. Results suggest that there is no significant difference in surface area between the different active material types.

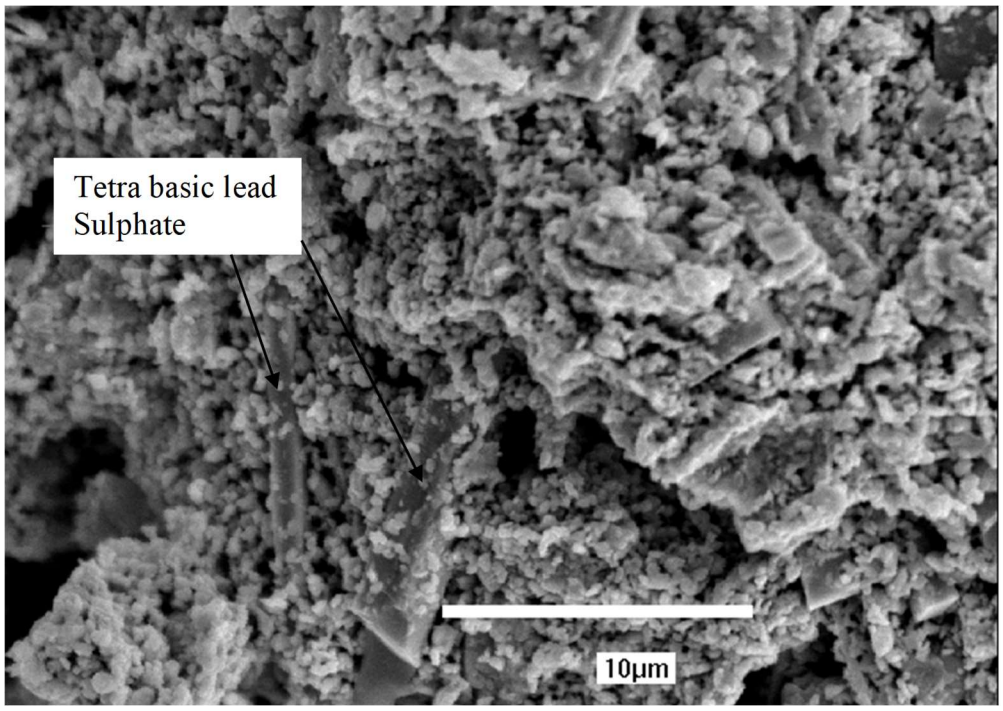

Figure 8.1: Fracture surface of cured active material from group 1

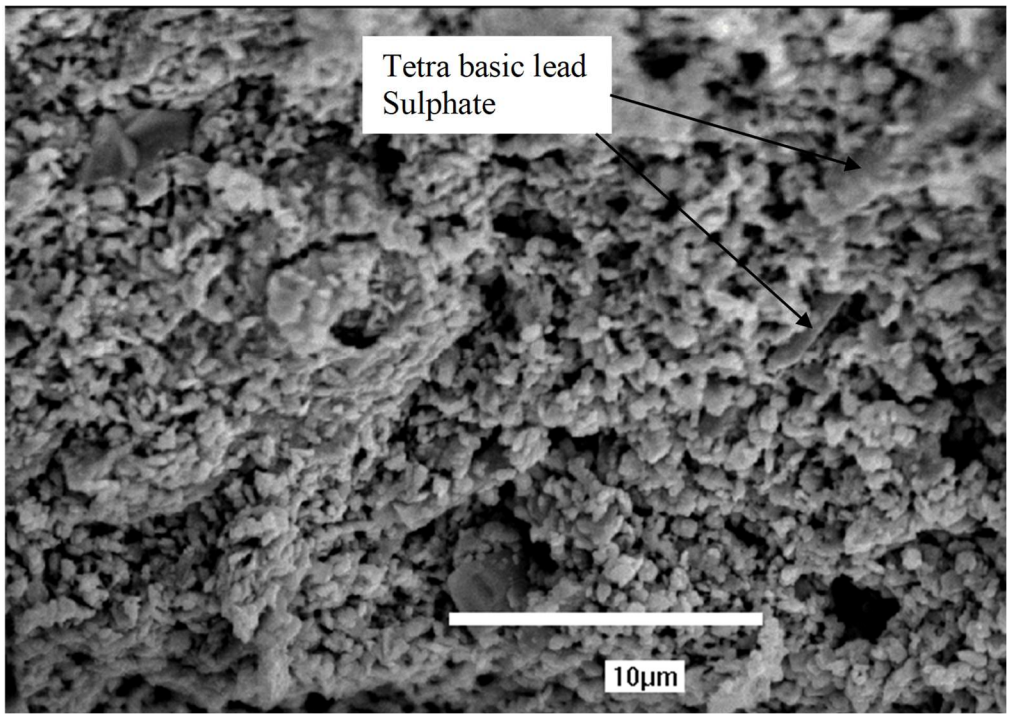

Figure 8.2: Fracture surface of cured active material from group 2

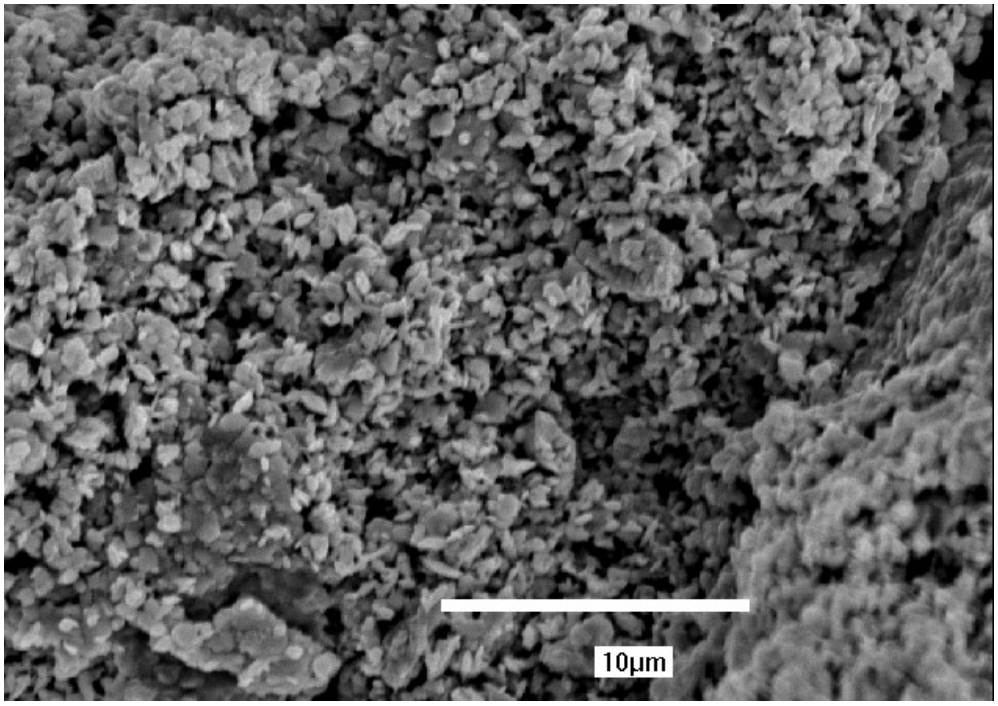

Figure 8.3: Fracture surface of cured active material from group 3

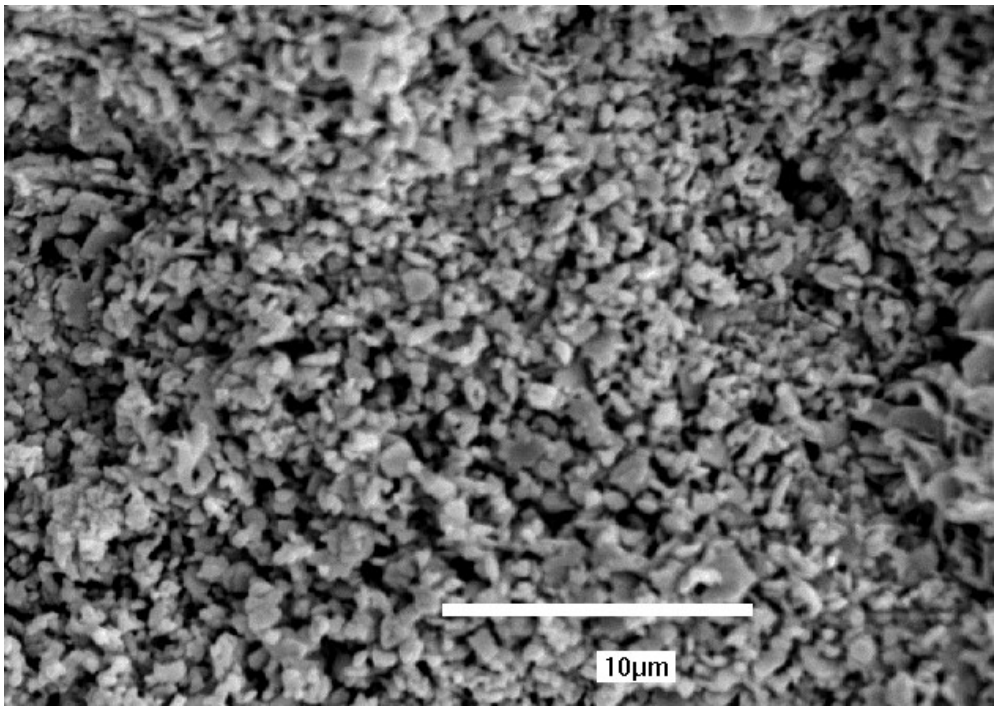

Figure 8.4: Fracture surface of cured active material from group 4

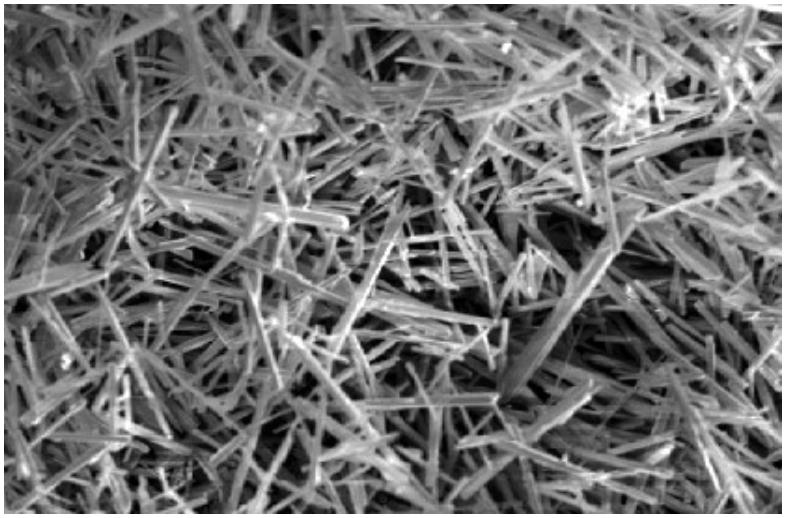

(Average crystal length = 100μm)

Figure 8.5: High aspect ratio tetra-basic lead sulphate crystals

Cross-sections of the cured electrodes were prepared using metallographic grinding and polishing techniques. Images of the grid wire and adjacent active material are shown in Figure 8.6 to Figure 8.9.

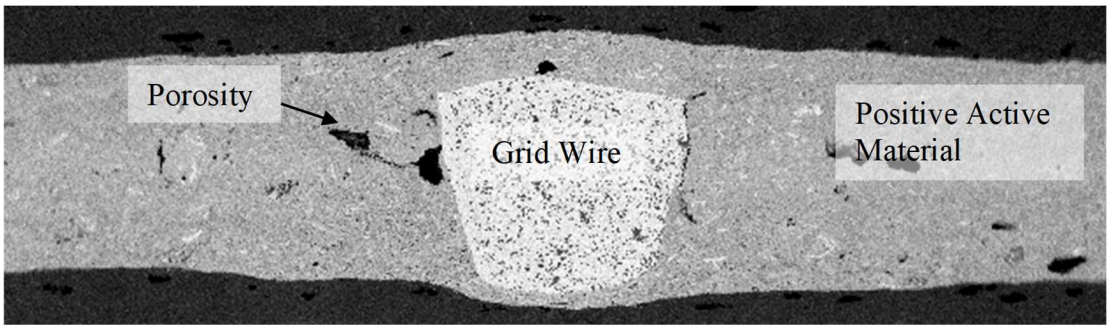

Figure 8.6: Group 1 cured electrode cross section

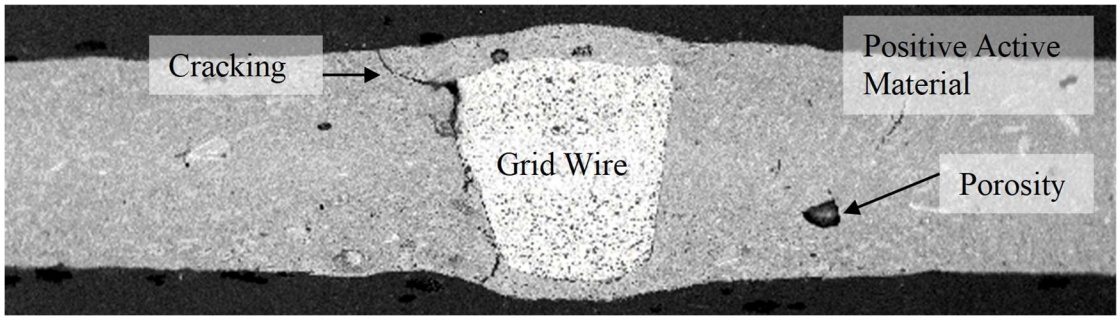

Figure 8.7: Group 2 cured electrode cross section

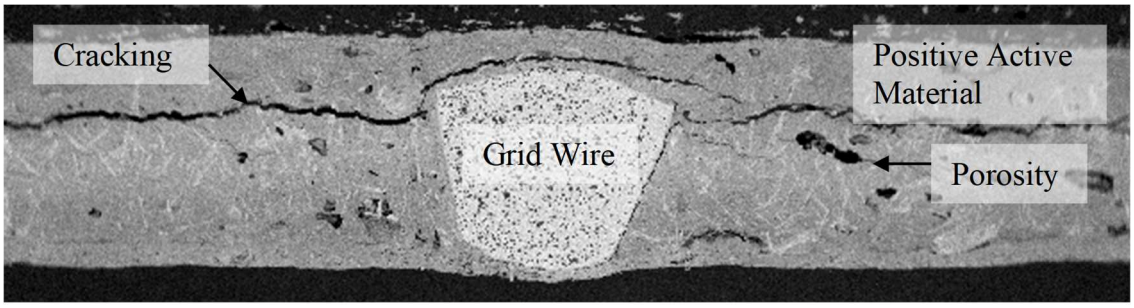

Figure 8.8: Group 3 cured electrode cross section

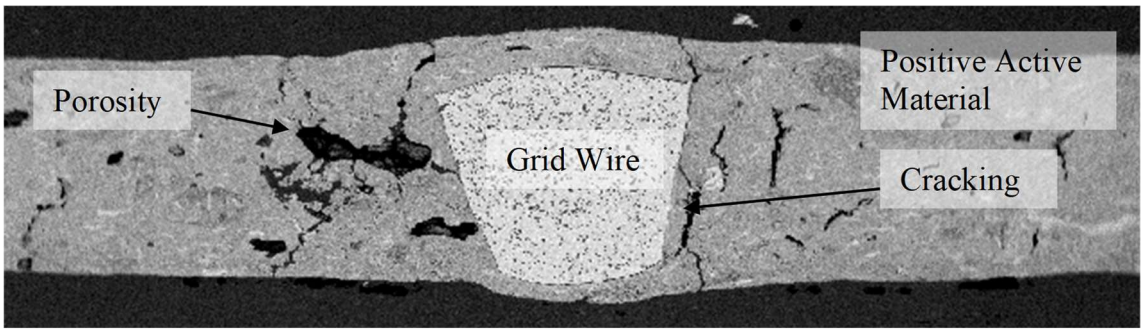

Figure 8.9: Group 4 cured electrode cross section

The influence of tetra-basic lead sulphate on the active material can be clearly seen in the figures above. Groups 3 and 4, which did not contain tetra-basic lead sulphate, have a significantly higher number of cracks. This suggests that even though SEM fracture surfaces do not show significant differences in structure, the tetra-basic lead sulphate does have an effect. It is

believed that the high aspect ratio of the tetra basic lead sulphate crystals help to consolidate the paste mix during drying and reduce the formation of cracks.

8.3.2 NEGATIVE ACTIVE MATERIAL

Quantitative compositional analysis of the cured negative active material indicated it consisted of approximately 100% α-lead monoxide with a small amount of lead present. No other compounds were identified in the analysis. A typical fracture surface is shown in Figure 8.10.

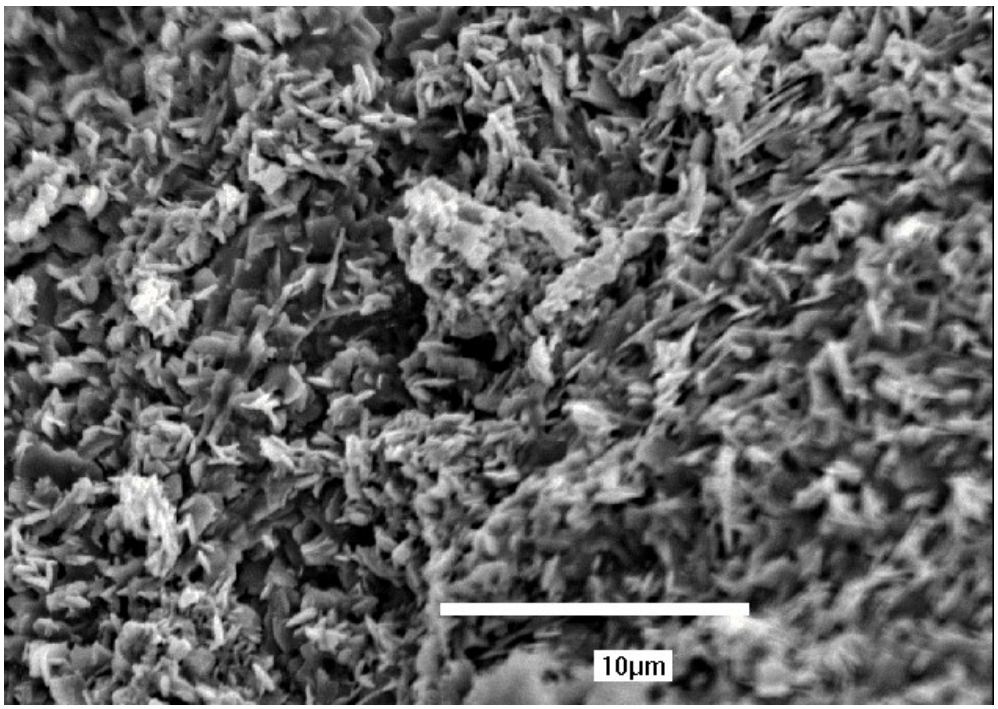

Figure 8.10: Fracture of negative active material used in the manufacture of batteries from groups 1 to 4

8.4 EXAMINATION OF FRESHLY FORMED BATTERIES

8.4.1 POSITIVE ACTIVE MATERIALS

Compositional analysis of the positive active materials from groups 1 to 4 using x-ray diffraction identified the alpha and beta polymorphs of lead dioxide. Lead sulphate was present in samples from groups 1, 2 and 4. Results from a quantitative analysis carried out using the Peaks program for each phase identified is given in Figure 8.11.

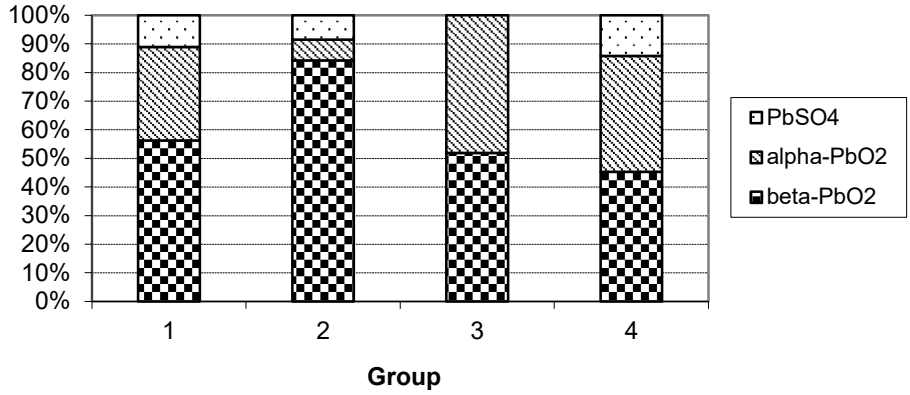

Figure 8.11: Compositional analysis of freshly formed positive active material

Recalling that groups 1 and 2, and 3 and 4 contain essentially the same positive active material, see Table 8.2, it is interesting to note the differences in composition between the two groups. This result highlights the inconsistencies that are present within freshly formed batteries. The most likely explanation for the differences in composition is local variations in acid concentration within the active material during the formation process. Acid concentration is an important factor in determining whether the alpha or beta polymorph of lead dioxide is formed. Fracture surfaces of the active materials are shown in Figure 8.12 to Figure 8.15 respectively.

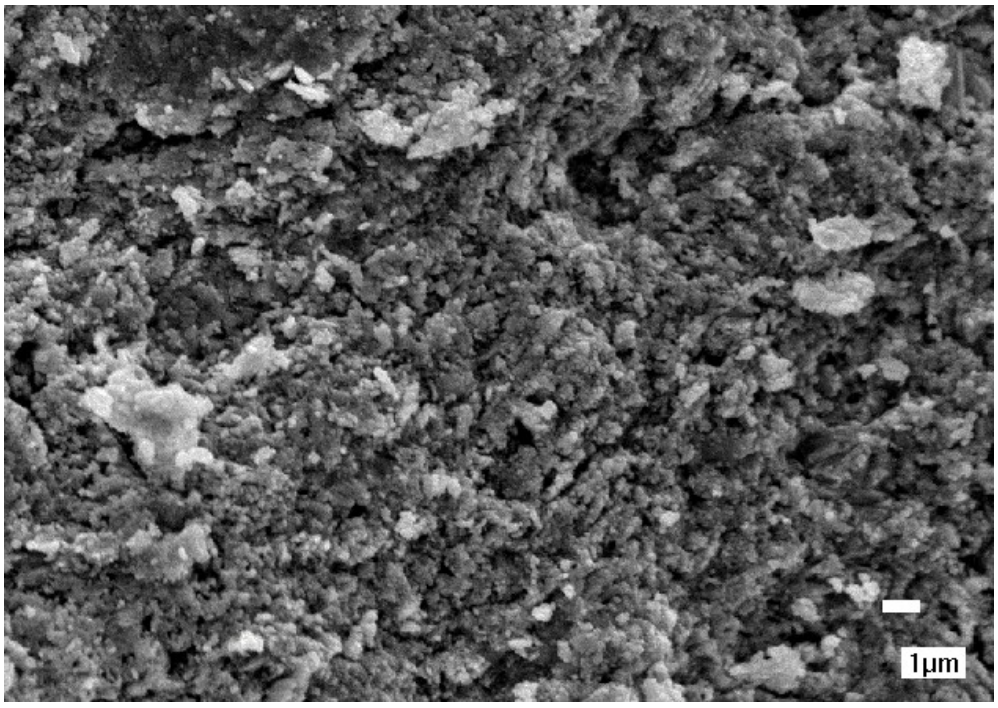

Figure 8.12: Fracture surface of freshly formed positive active material from group 1 (TTB).

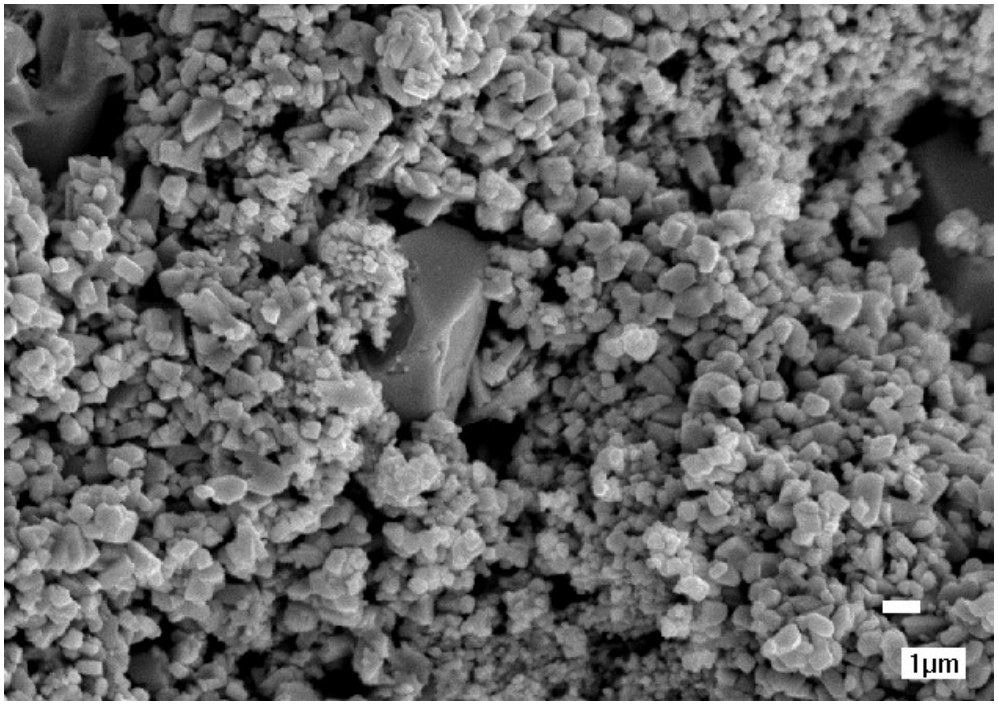

Figure 8.13: Fracture surface of freshly formed positive active material from group 2 (TTB)

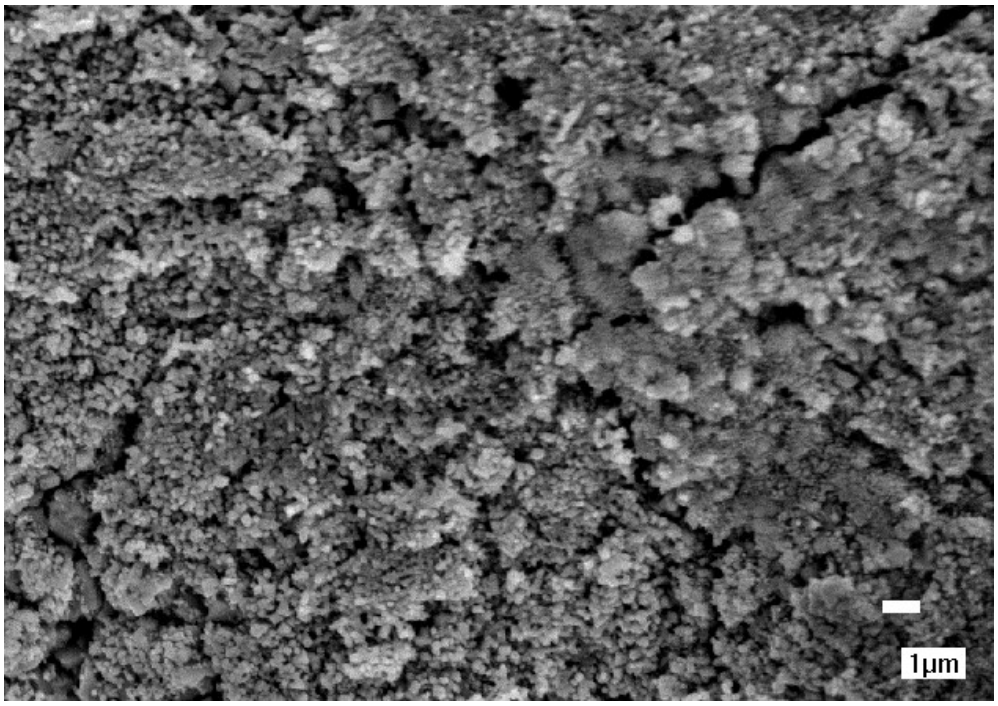

Figure 8.14: Fracture surface of freshly formed positive active material from group 3 (Sulphated)

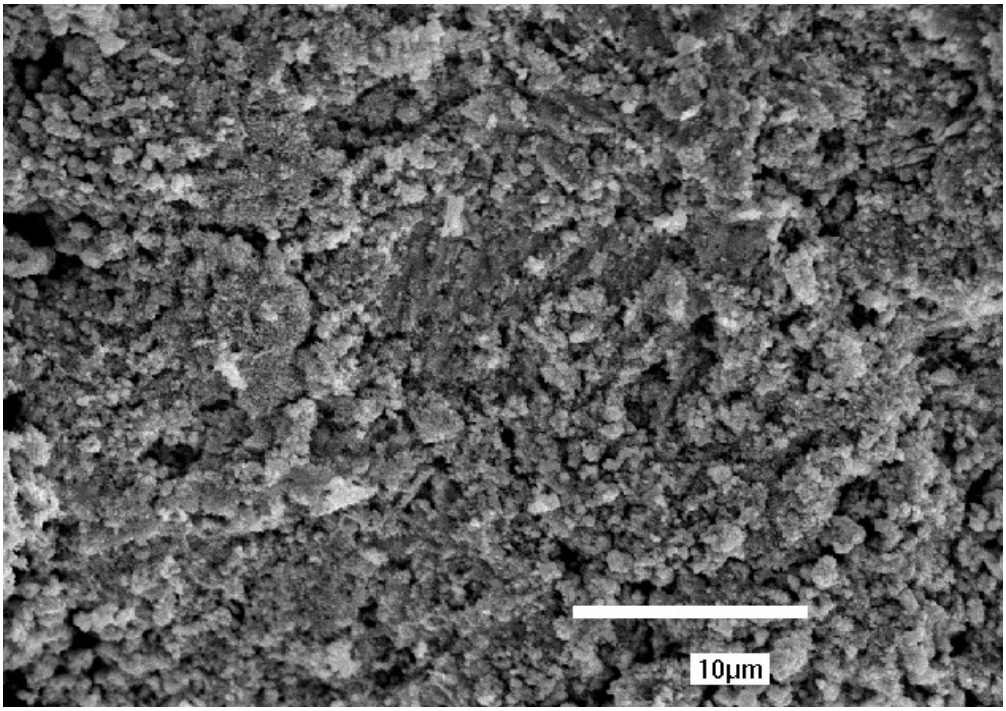

Figure 8.15: Fracture surface of freshly formed positive active material from group 4 (sulphated)

Comparison of the above figures shows that the structures of the positive active materials are very similar with the exception of that from group 2, Figure 8.13. The lead dioxide particles in this active material are noticeably greater in size compared to the others and a number of lead sulphate particles are also visible. This observation is corroborated by the BET surface area values obtained, 4.48, 1.63, 3.95 and 4.75 m^2g^{-1}, for groups 1 to 4 respectively. It can be seen that group 2 has a significantly lower surface area when compared to the others.

8.4.2 NEGATIVE ACTIVE MATERIALS

Qualitative analysis of the negative active materials using x-ray diffraction and wet chemical analysis yielded the results shown in Figure 8.16.

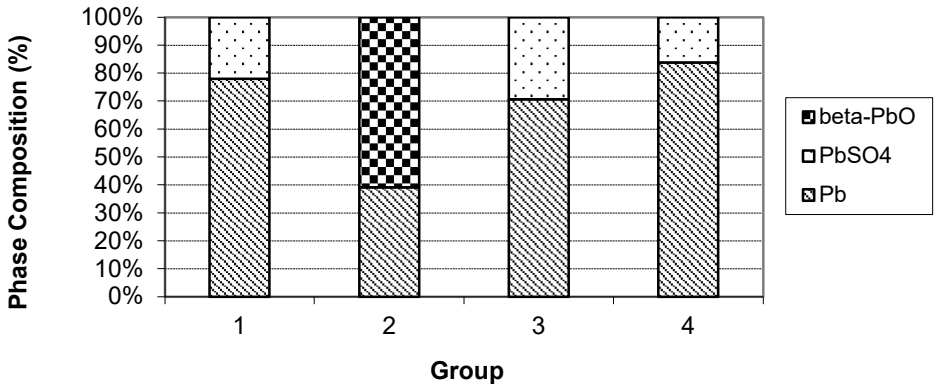

Figure 8.16: Compositional analysis of group 1 to 4 freshly formed negative active materials.

Figure 8.16 shows high levels of lead sulphate in all samples except that from group 2, which contains 60% beta-lead monoxide. High quantities of beta lead monoxide were identified in a number of the negative active materials from the cycled batteries described in the previous chapter. Battery operation would be highly unlikely if the negative plates contained this quantity of lead monoxide, therefore the most probable explanation is that the oxide formed during plate drying and is not linked to battery operation. The question of why the other plates do not contain oxide remains unanswered. The results described above are again reflected in the fracture surface micrographs shown in Figure 8.17 to Figure 8.20.

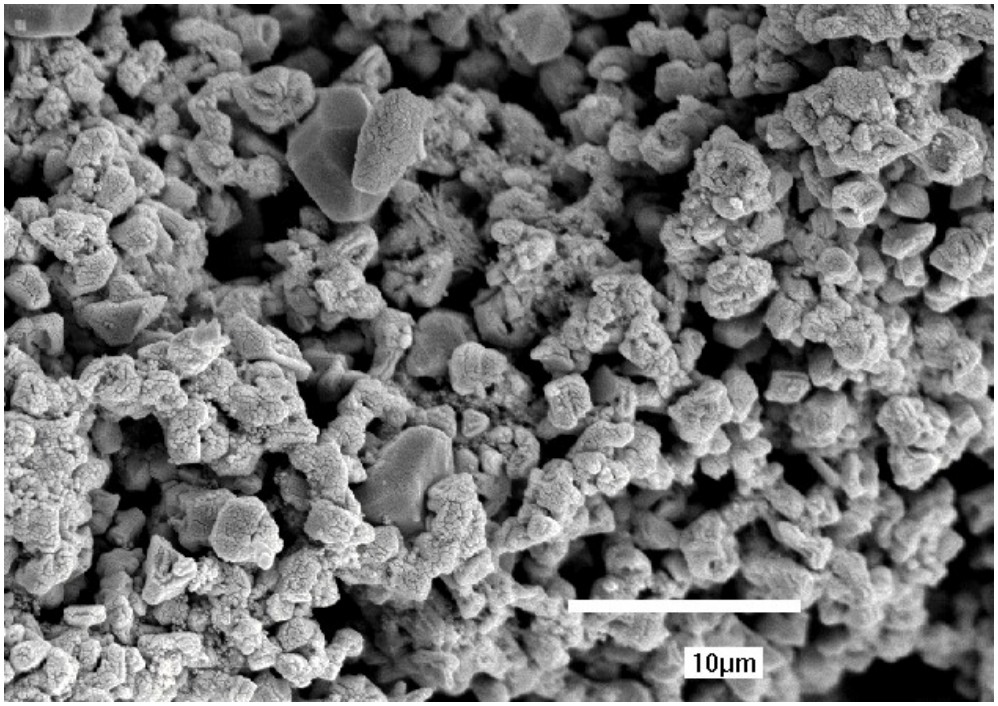

Figure 8.17: Fracture surface of freshly formed negative active material from group 1

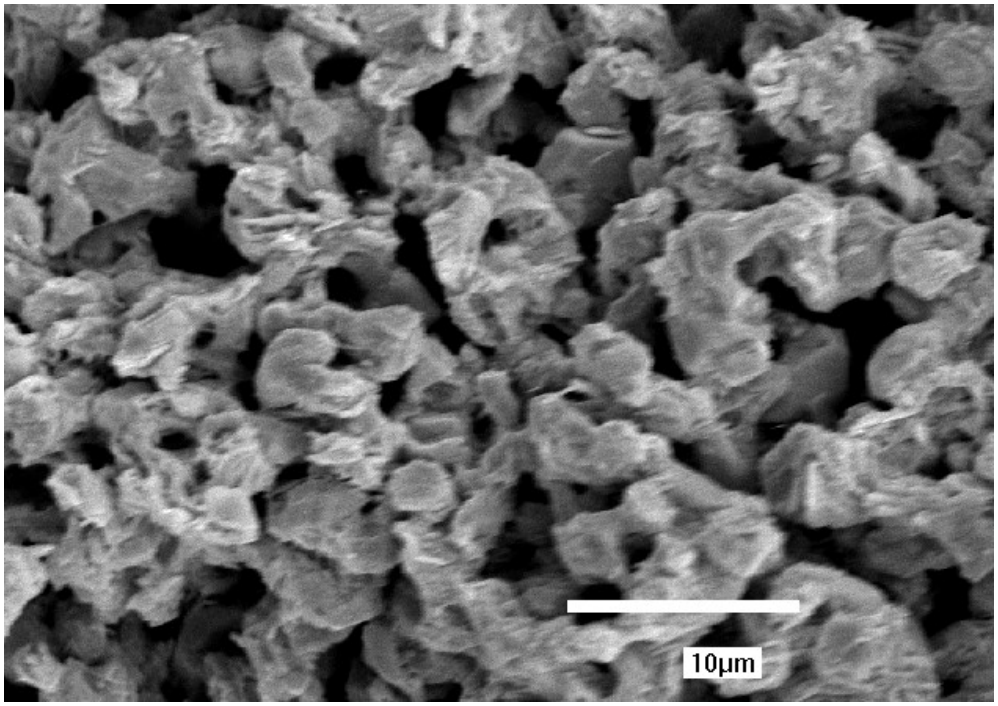

(Image is out of focus due to charging of the sample caused by the high proportion of lead monoxide, which is a non-conductor)

Figure 8.18: Fracture surface of freshly formed negative active material from group 2

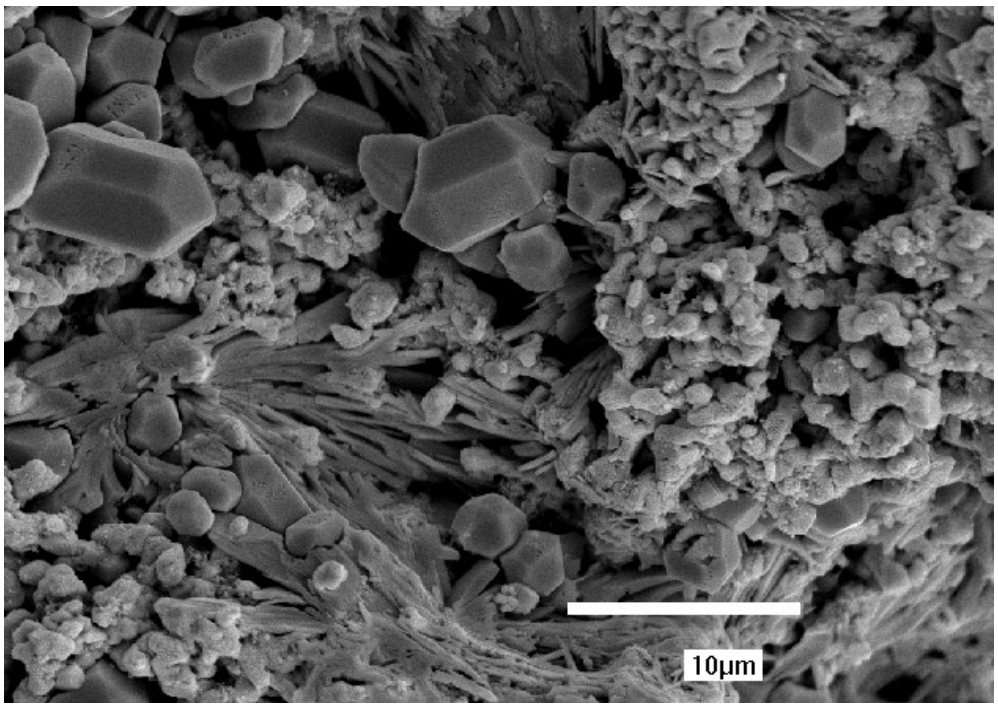

Figure 8.19: Fracture surface of freshly formed negative active material from group 3

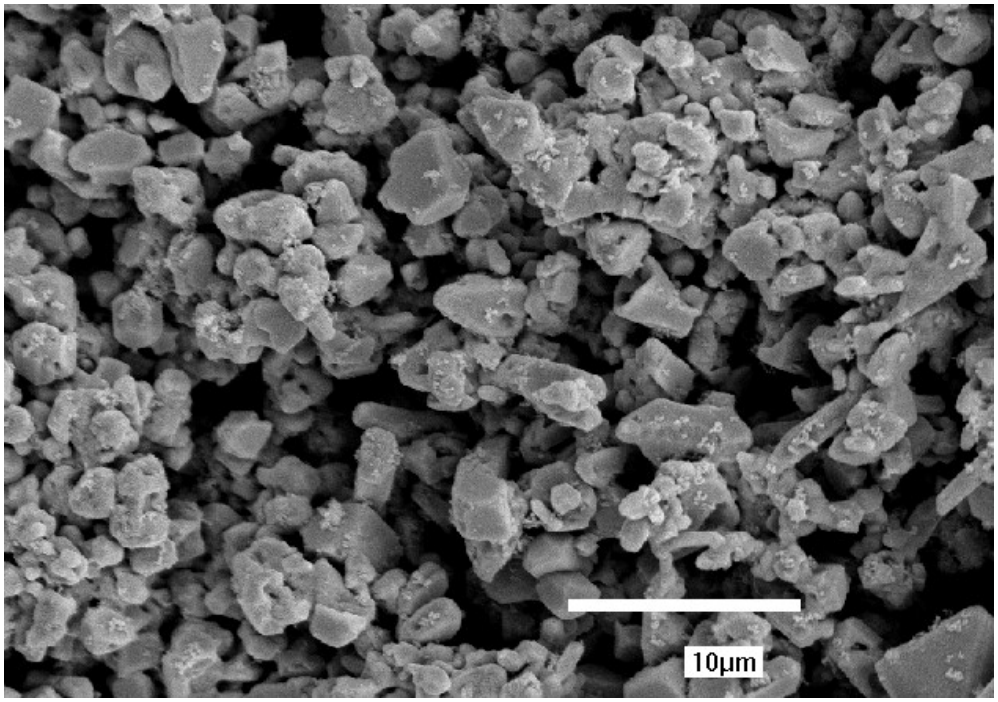

Figure 8.20: Fracture surface of freshly formed negative active material from group 4

BET surface areas obtained for the negative active materials were 0.59, 1.15, 0.57 and 0.68 for groups 1 to 4 respectively. The high surface area of the group 2 active material can be explained by the presence of lead monoxide. All other surface areas are around 0.6 which is comparable with that measured for the cycled batteries.

Lead sulphate crystals are clearly identifiable on the fracture surface of the group 3, negative active materials. Group 3 has the highest proportion of lead sulphate, and sulphate crystals are clearly visible. However, in addition to the flat faced lead sulphate crystals 'needle like' crystals are also visible that are not present on the fracture surfaces of the other groups. These are unlikely to be lead sulphate due to their morphology and are probably basic lead sulphates. They would not necessarily have been identified during the compositional analysis, using x-ray diffraction, as the majority of basic sulphate lines are the same as those produced by either lead sulphate or lead monoxide. This makes their identification in small quantities, amongst a mixture containing a high proportion of lead sulphate and lead monoxide, problematic.

8.5 EXAMINATION OF C5 CYCLED BATTERIES

A battery from groups 1 to 4 was cycled using a C5 cycling regime to failure and subsequently examined. The number of cycles sustained until failure for each battery is shown in Table 8.3.

Table 8.3: Cycles to failure for C5 cycled batteries (groups 1 to 4)

Group	Cycles to failure
1	40
2	29
3	29
4	27

From the table, the cycles to failure are all very similar except for the group 1 battery that achieved over 25% more cycles than the other batteries.

A good and bad cell was identified from each battery by monitoring the voltage of each cell during a C1 capacity discharge to 4V. Plots of voltage versus time are shown in Figure 8.21 to Figure 8.24 below.

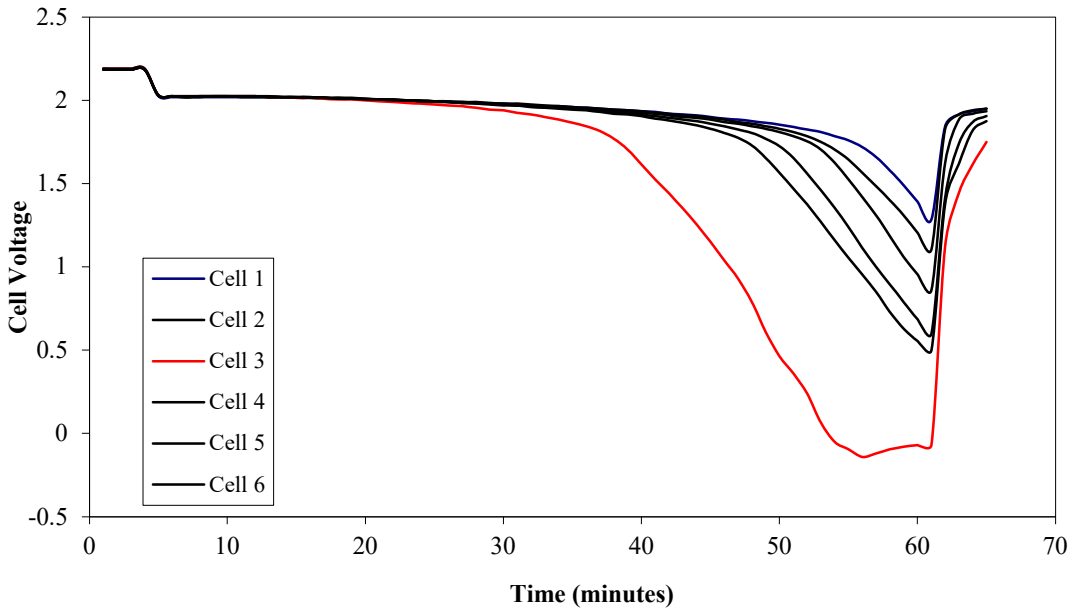

Figure 8.21: Plot of voltage versus time for cell in group 1 battery

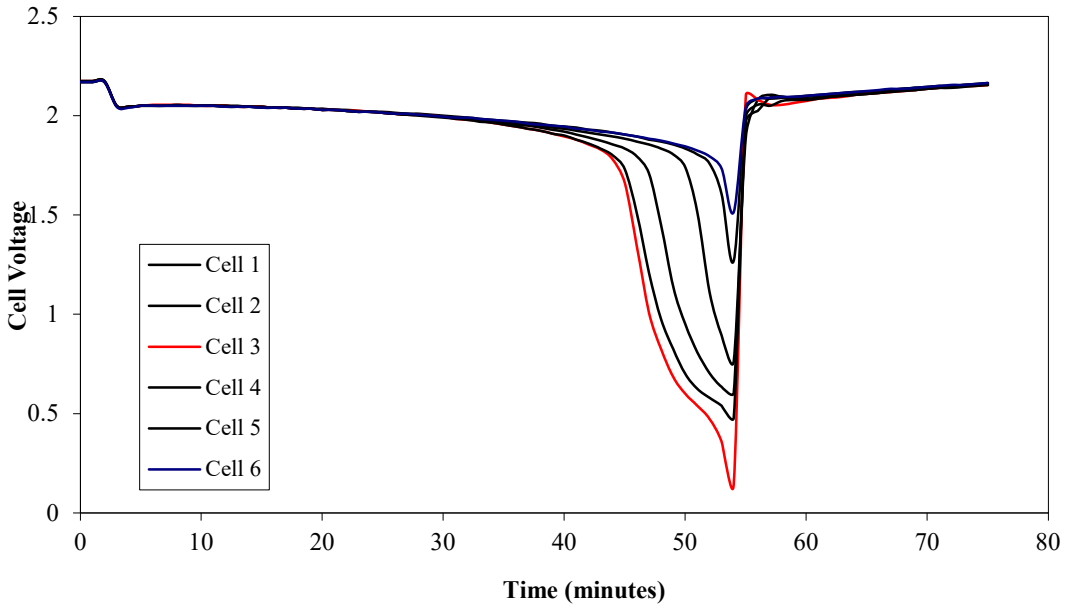

Figure 8.22: Plot of voltage versus time for cell in group 2 battery

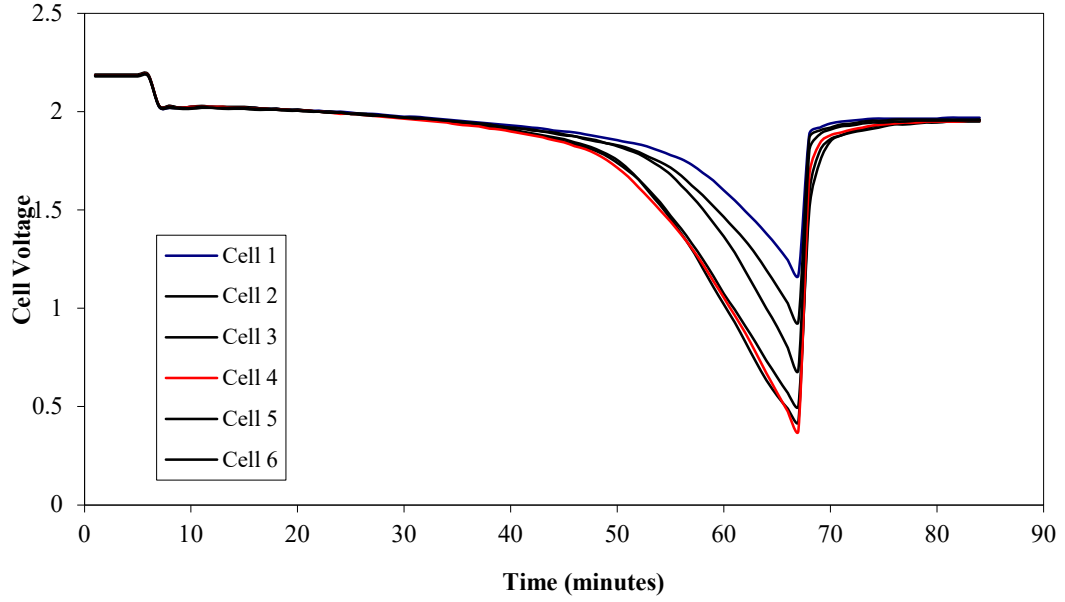

Figure 8.23: Plot of voltage versus time for cell in group 3 battery

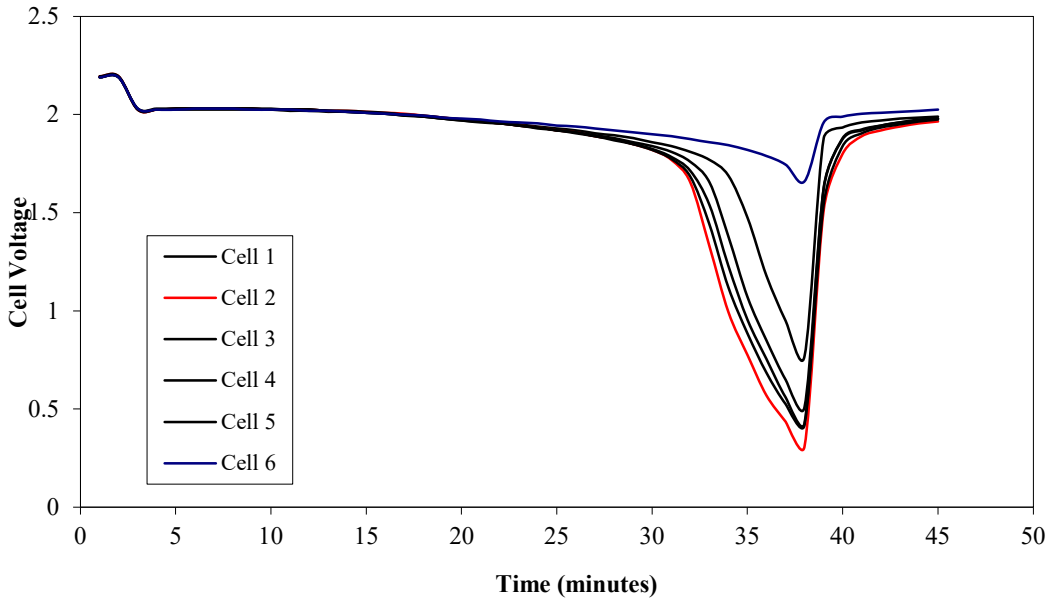

Figure 8.24: Plot of voltage versus time for cell in group 4 battery

From the figures it can be seen that all the cells failed to a certain extent.

8.5.1 POSITIVE ACTIVE MATERIAL

A compositional analysis of the positive active materials from group 1 to 4 batteries is given in Figure 8.25 below. Positive active material consists of alpha and beta lead dioxide, the only exception being lead sulphate in the good cells of group 2 batteries.

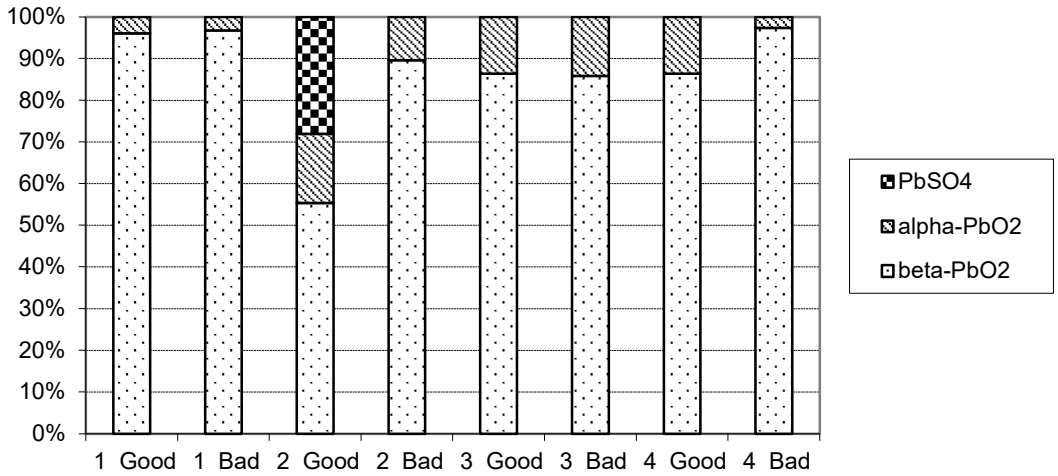

Figure 8.25: Analysis of positive plates from C5 cycled batteries

The BET surface areas of the active materials, Table 8.4, reflect the compositional results obtained. The batteries from the group 2 bad cell had the lowest surface area. Surface areas of the remaining samples were all in the range of 2.39 and 3.14, however the surface area of the active material in the good cell was always greater than that in the bad.

Table 8.4: BET surface area of positive active materials from C5 cycled batteries

Battery	BET Surface Area (m^2g^{-1})	
	Good	**Bad**
Group 1	2.72	2.39
Group 2	1.71	2.78
Group 3	2.87	2.69
Group 4	3.14	2.95

An initial examination of the fracture surfaces from the group 1 battery at low magnifications, Figure 8.26, from the good cell showed an increased porosity towards the edges of the tablet which was less evident at higher magnifications, Figure 8.27.

Figure 8.26: Low magnification fracture surface of group 1 good cell

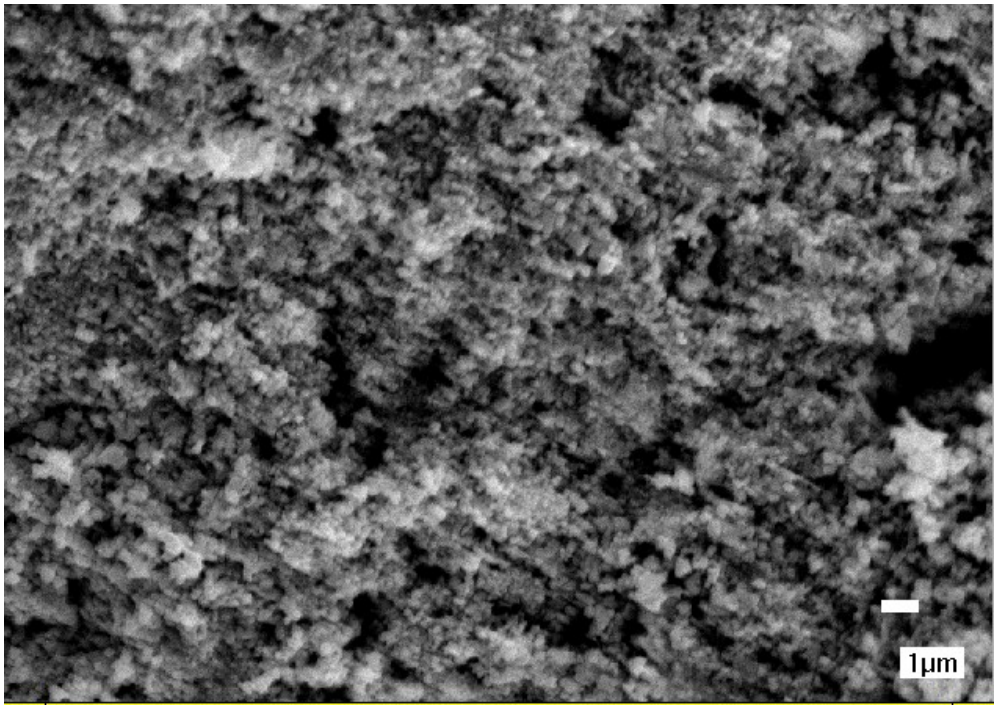

Figure 8.27: High magnification fracture surface of group 1 good cell

Examination of the bad cell indicated a similar effect with porosity on the outer edges being more apparent, see Figure 8.28. Figure 8.29 and Figure 8.30 show slightly higher magnification images of these regions, where the porosity on the outer edge of the tablet is clearly visible.

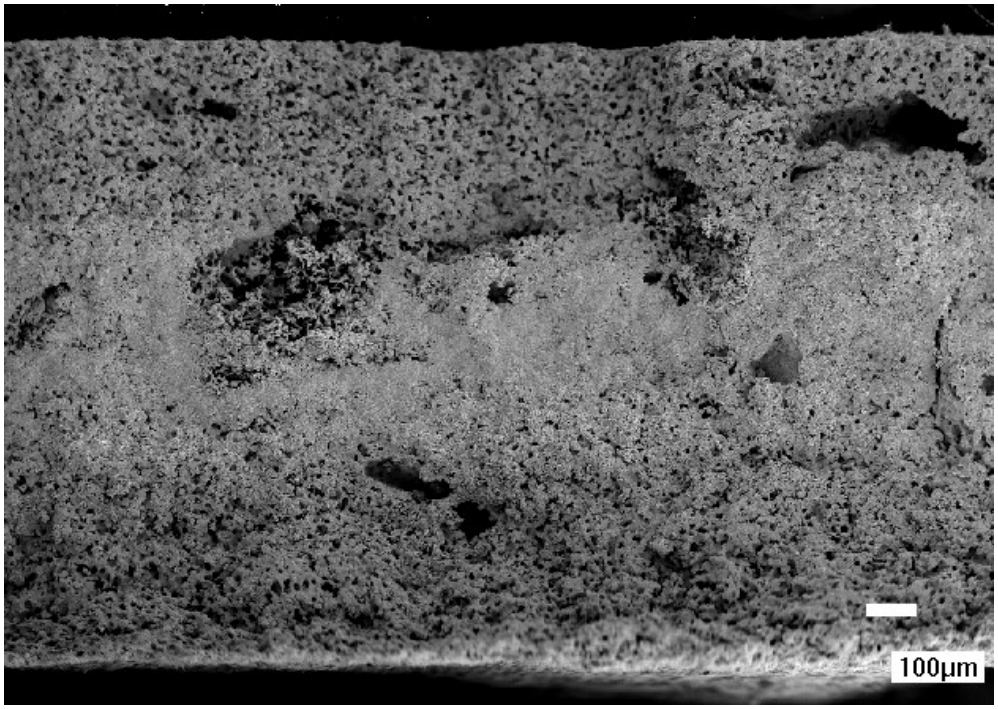

Figure 8.28: Low magnification fracture surface of group 1 bad cell

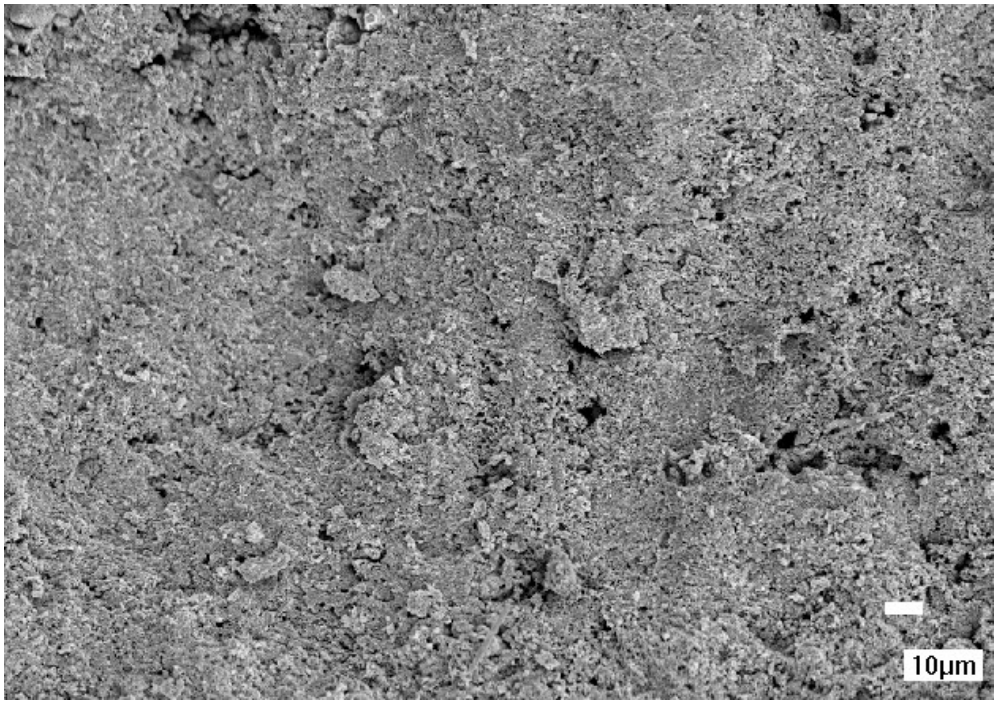

Figure 8.29: Low magnification fracture surface from group 1 bad cell taken from the central region of the tablet

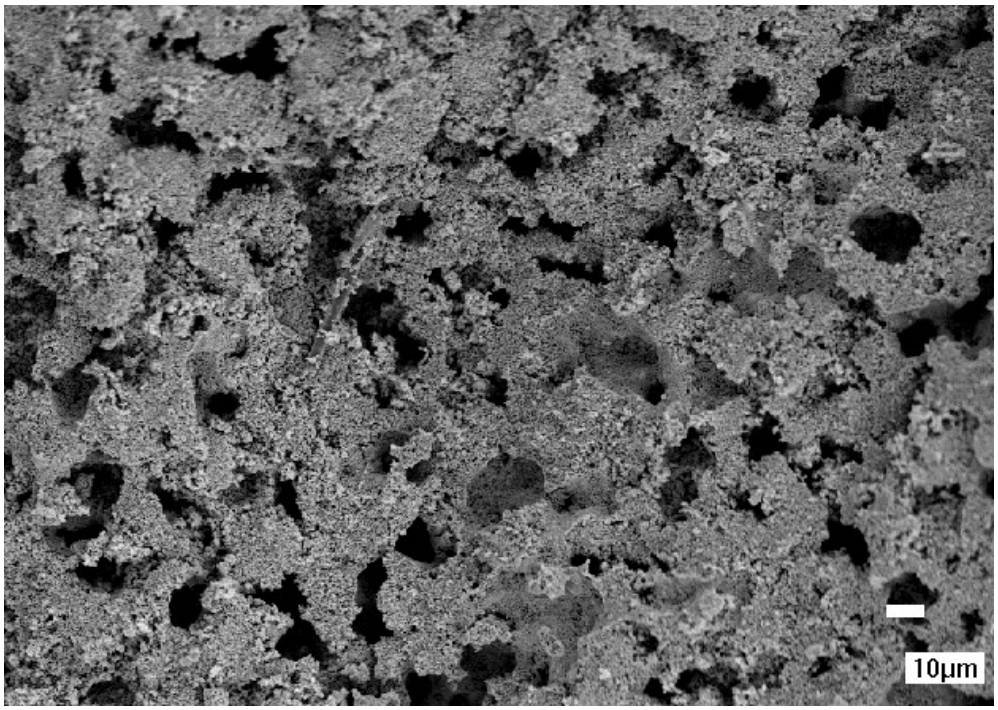

Figure 8.30: Low magnification fracture surface from group 1 bad cell taken from the outer region of the tablet

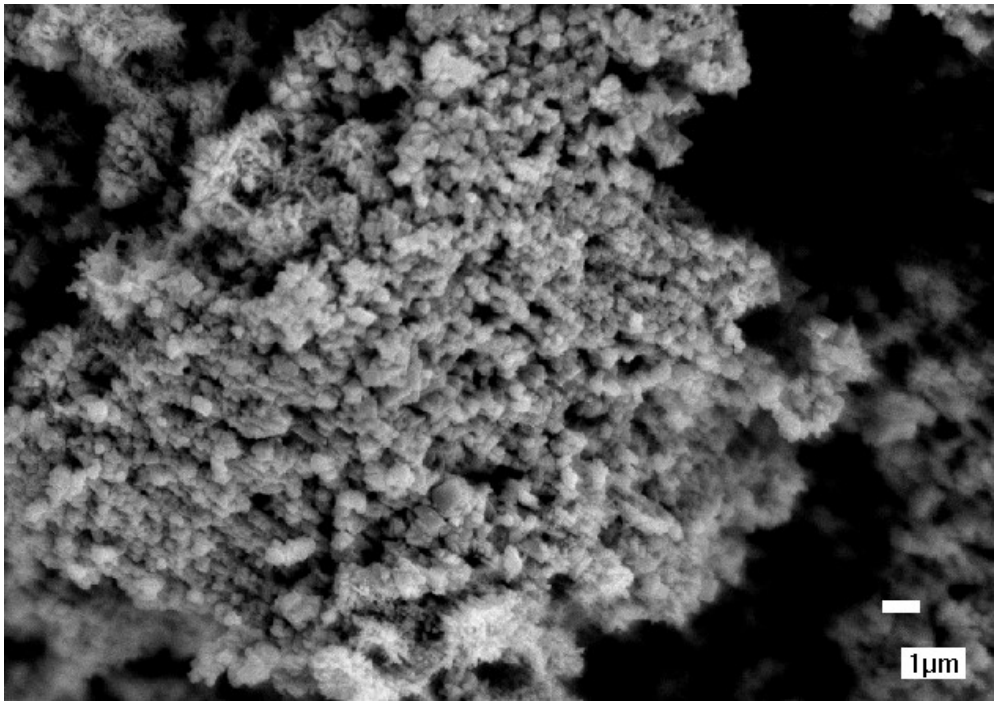

Figure 8.31: High magnification fracture surface from group 1 bad cell taken from the outer region of the tablet

High magnification images of the fracture surface in the central and outer regions are shown in Figure 8.31 and Figure 8.32 below. A comparison of the lead dioxide particles in each position concludes that there is no significant difference in size.

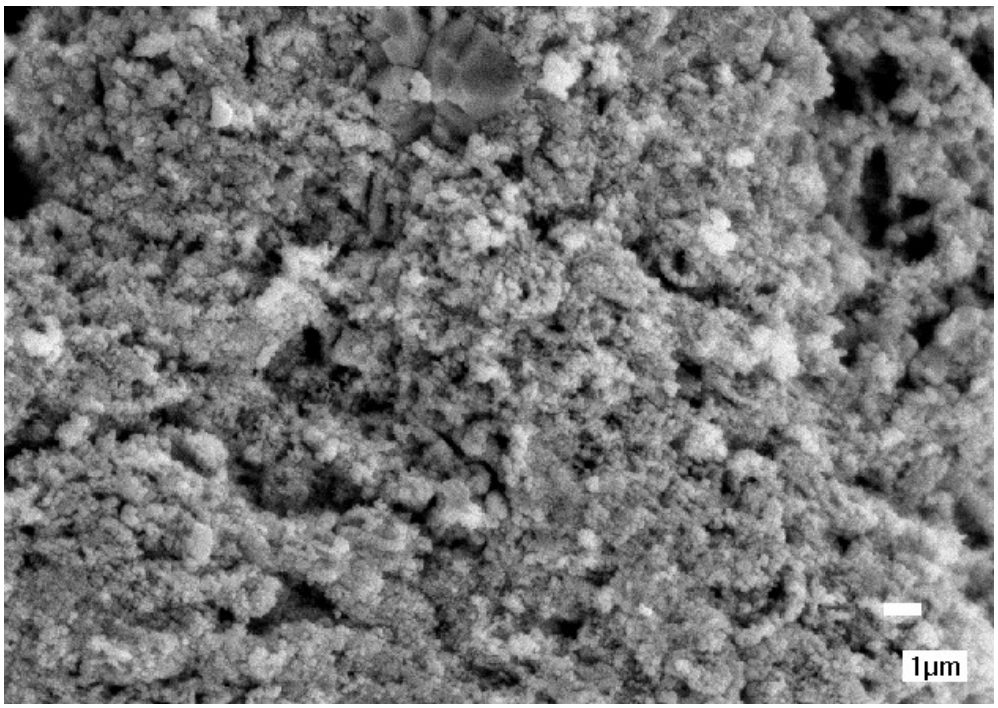

Figure 8.32: High magnification fracture surface from group 1 bad cell taken from the central region of the tablet

Positive electrodes constructed from group 2, 3 and 4 positive active materials showed similar trends in porosity distribution to that described above for the group 1 active material.

8.5.2 NEGATIVE ACTIVE MATERIAL

Results for the negative active material from the group 2 battery is not included, as these were not available. Compositional analysis of groups 1,3 and 4 are given in Figure 8.33 below. The active materials consist mostly of lead, with lead sulphate and beta lead monoxide in the good cell of the group 1 battery.

Figure 8.33: Analysis of negative plates from C5 cycled batteries

BET surface areas of the negative active materials do not correspond to the compositional analysis obtained. A typical anomaly within the results that demonstrates this is the group 1 active material from the good cell. This material contained lead monoxide and should theoretically have had the largest surface area, however it has the smallest.

Table 8.5: BET surface area of negative active materials from C5 cycled batteries

Battery	BET Surface Area (m^2g^{-1})	
	Good	Bad
Group 1	0.48	0.51
Group 2	*	*
Group 3	0.51	0.50
Group 4	0.51	0.52

*** Data Not Available**

Images of the fracture surfaces obtained in the scanning electron microscope indicate that there is no real difference in structure of the negative active material from the batteries except for that from group 1, which contained the lead monoxide and lead sulphate. Lead monoxide and lead sulphate crystals were identified in this active material. However, they appear to be

concentrated towards the middle of the tablet rather than uniformly throughout it. A typical fracture surface of a negative active material containing 100% lead is shown in Figure 8.34 below. Figure 8.35 and Figure 8.36 show the fracture surfaces at the edge and centre of the group 1 negative active material.

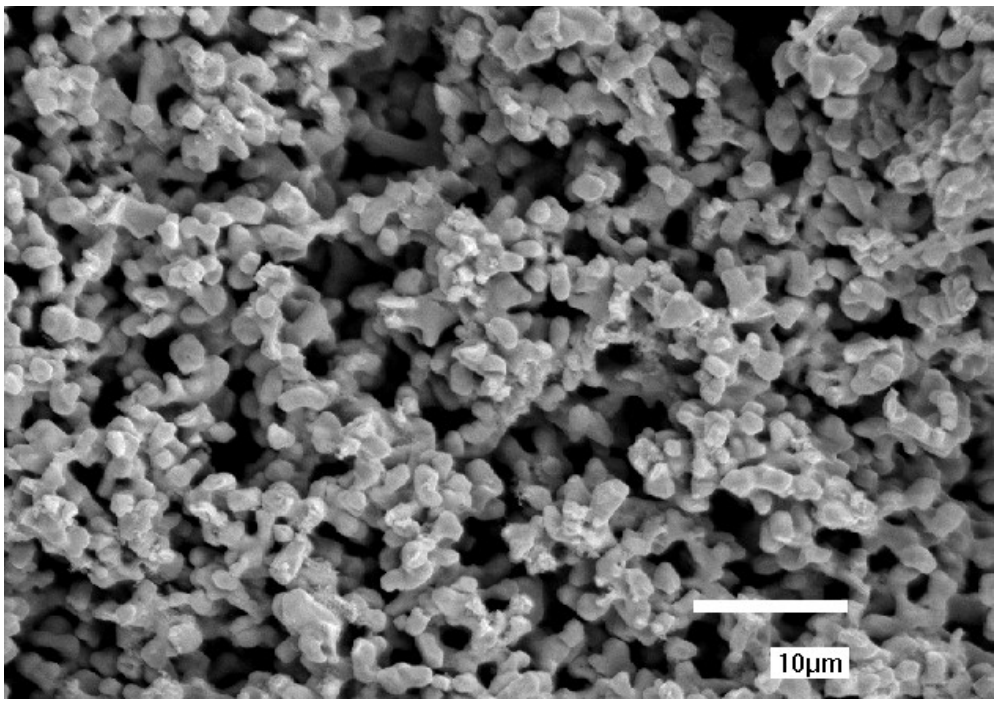

Figure 8.34: Fracture surface of group 4 negative active material from bad cell

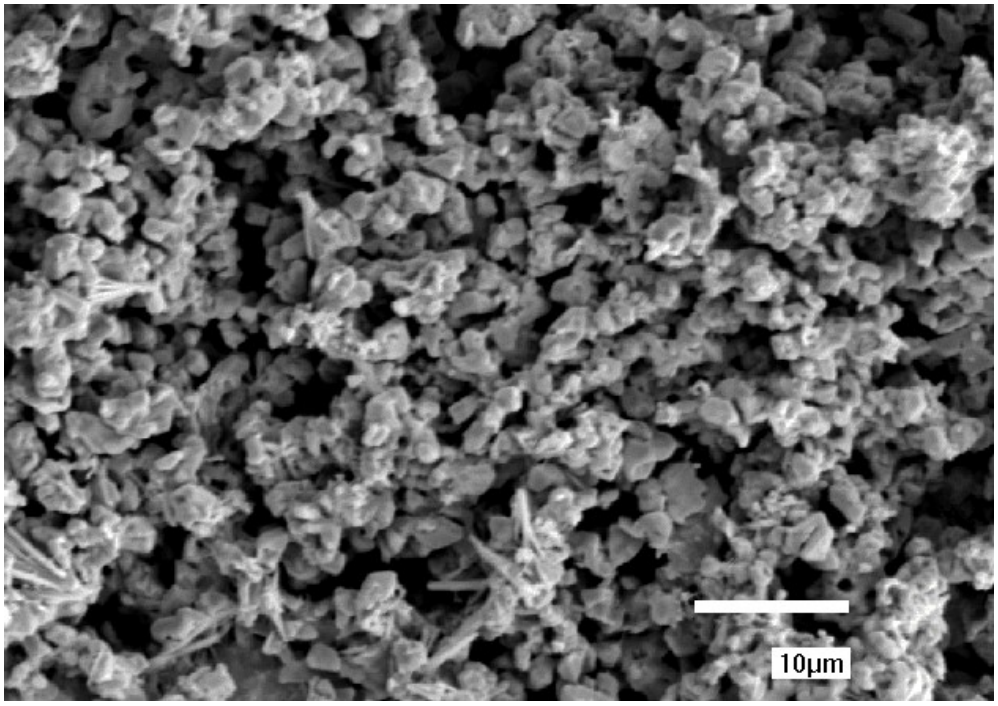

Figure 8.35: Fracture surface of group 1 negative active material from good cell taken from the edge of the tablet.

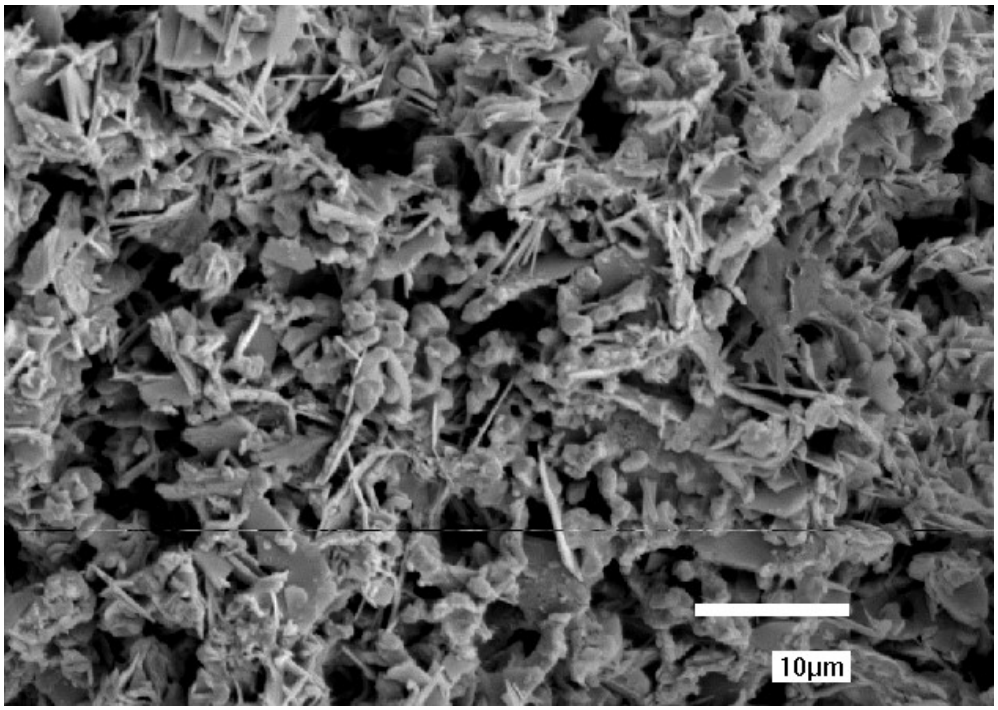

Figure 8.36: Fracture surface of group 1 negative active material from good cell taken from the centre of the tablet.

Further examination of additional tablets did not indicate the presence of lead monoxide or sulphate crystals concentrated in the central region. This suggests that the in-homogeneity only occurs in isolated tablets or at specific positions within the electrode.

8.6 CONCLUSIONS

The following conclusions can been drawn from the results reported in this chapter.

1. The BET surface areas of the positive active material is generally greater in the good cells.
2. Tetra basic lead sulphate crystals break into shorter lengths during the electrode pasting procedure.
3. Cured positive active materials containing tetra basic lead sulphate crystals have smaller number of internal cracks compared to the equivalent paste containing no tetra basic lead sulphate.
4. The unexpected presence of lead sulphate in some positive active materials, where the same positive active material in the battery containing a different grid wire did not contain sulphate, highlights the variability that can occur between electrodes.
5. The group 1 battery sustained >25% more cycles compared to the others groups tested.
6. The failure of all batteries in the test can be attributed to the degradation of each of the cells to varying extents rather than total failure of a single cell.

9 RESULTS AND DISCUSSION: CORROSION LAYER CHARACTERISATION

9.1 INTRODUCTION

In previous chapters results from examining different battery designs with various grid alloys and active materials were described. One of the major processes influenced by grid alloy and positive active material is corrosion layer growth. An analysis of the corrosion layers produced by each battery type investigated is presented in this chapter. Battery types include that used to study cycling, and groups 1 to 4. The structural and chemical composition of each corrosion layer was analysed using a number of different techniques, the results of which are presented in the following sections.

9.2 VISUAL EXAMINATION OF CORROSION LAYERS USING LIGHT MICROSCOPY

Samples were prepared using the polishing method described previously. From the total number of batteries examined five different designs containing variations in positive active material or grid wire were examined.

9.2.1 FEATURES IDENTIFIED IN BATTERIES CYCLED >90 TIMES

In general the corrosion layers in batteries that survived >90 cycles to failure were found to exhibit features which did not appear as frequently in batteries that failed earlier i.e. <90 cycles. The most prominent of these were cracks, most commonly occurring adjacent to grid-wire corners although a number were identified on the edge of the wire. A typical grid wire cross section exhibiting these features is shown in Figure 9.1. The corrosion layer extends around the whole perimeter of the wire. Pores are visible at a number of locations within the positive active material. There is no evidence that the presence of a pore promotes or reduces the probability of a defect occurring in the adjacent region of corrosion layer.

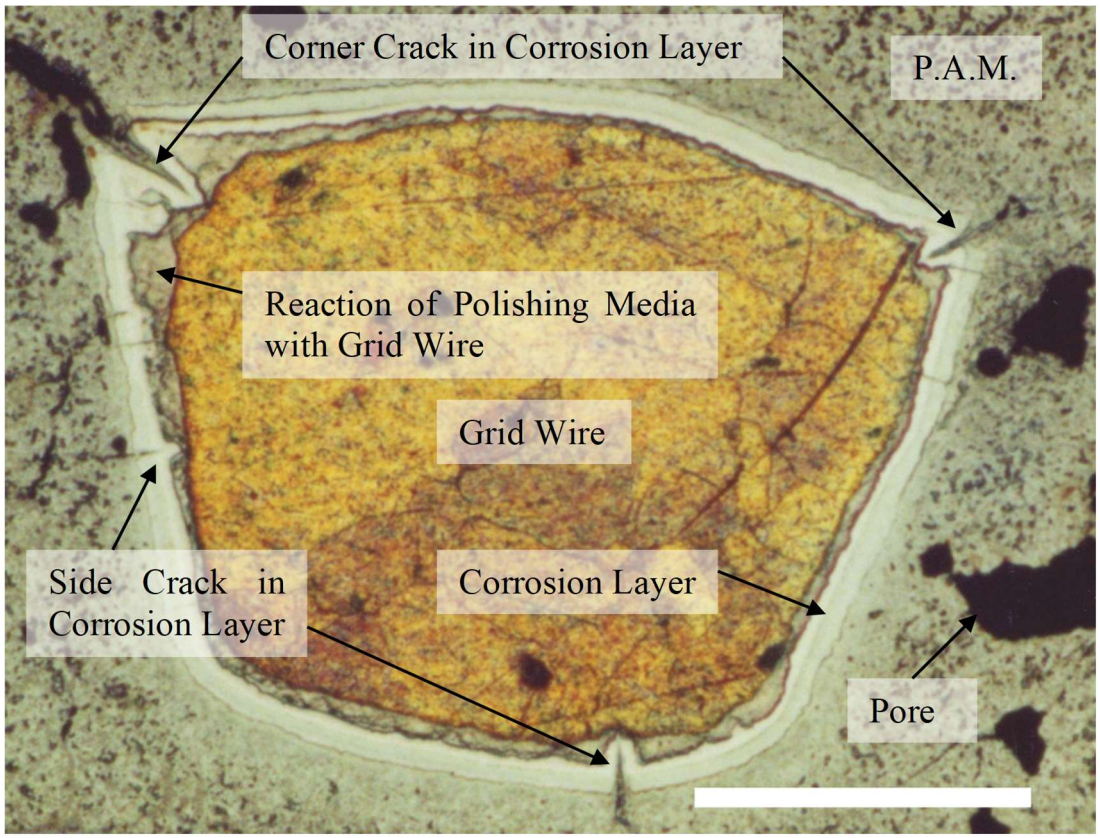

Figure 9.1: Positive grid wire showing corrosion layer and cracks (Scale bar: 500µm)

A higher magnification image of a crack observed in the corrosion layer on the side of a grid wire is given in Figure 9.2. The layer consists of two sub-layers separated by an internal boundary. Cracking has occurred through both layers and a short distance into the underlying lead grid. A reaction between the polishing media and lead grid adjacent to the corrosion layer produces an additional feature that should not be confused with the lead oxide corrosion layer produced during battery operation. Positive active material is visible on both sides of the crack walls as far as the crack tip. This is likely to have formed by the movement of small particles of lead oxide and/or lead sulphate into the crack that subsequently reacted to form a rigid, porous active material. Movement of the electrolyte during overcharging, when gases are produced, would promote the movement of particles into cracks. The crack centre contains the resin used for sample mounting during polishing indicating that during battery operation this region would have been filled with either electrolyte or gas.

Closer examination of the corrosion layer revealed the presence of cracks at the internal boundary within the corrosion layer, Figure 9.3. Formation of a crack in this location suggests a difference in properties of these layers and indicates that the bond between them is not as strong as the layers themselves.

Smaller fissure cracks were also observed in the lower corrosion layer, Figure 9.4. They appear to be propagating in an outward direction since cracks only grow under a tensile stress. The formation of cracks such as these could be a result of either (i) internal stresses within the layer caused by geometrical effects or, (ii) stresses caused by gas pressure produced during battery operation, especially during overcharging.

A number of smaller cracks and oxide fingers penetrating the grid were observed on the sides of some wires, shown in Figure 9.5. Examination of the oxide finger at higher magnification, Figure 9.6, revealed a small crack or fissure running down the centre. Whether this is a genuine crack, or the point at which the layers growing out from each side of the crack join up is unknown. Formation of a finger such as this could be an initial stage in the formation of the larger cracks discussed previously. The crack featured on the right hand side of the photograph appears to be growing in an inward direction, suggesting there is more than one mechanism for crack initiation and growth.

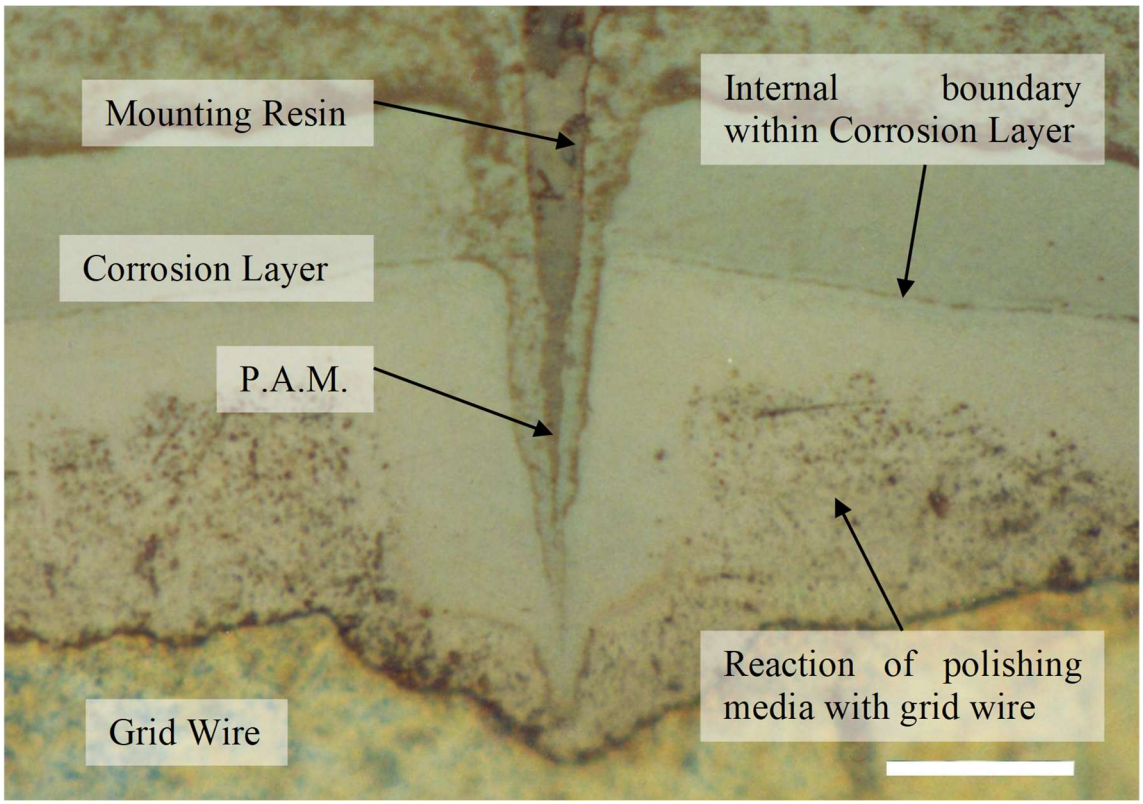

Figure 9.2: Typical crack observed in corrosion layer (Scale bar: 50µm)

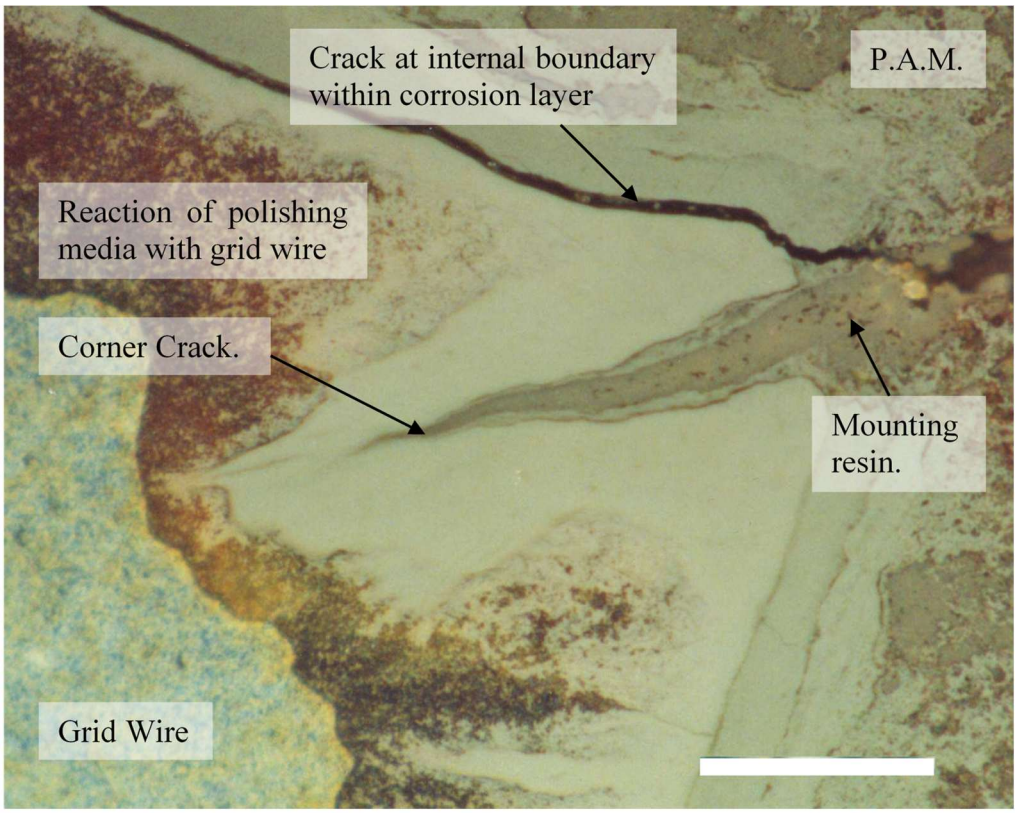

Figure 9.3: Crack observed on corner of grid wire (Scale bar: 50µm)

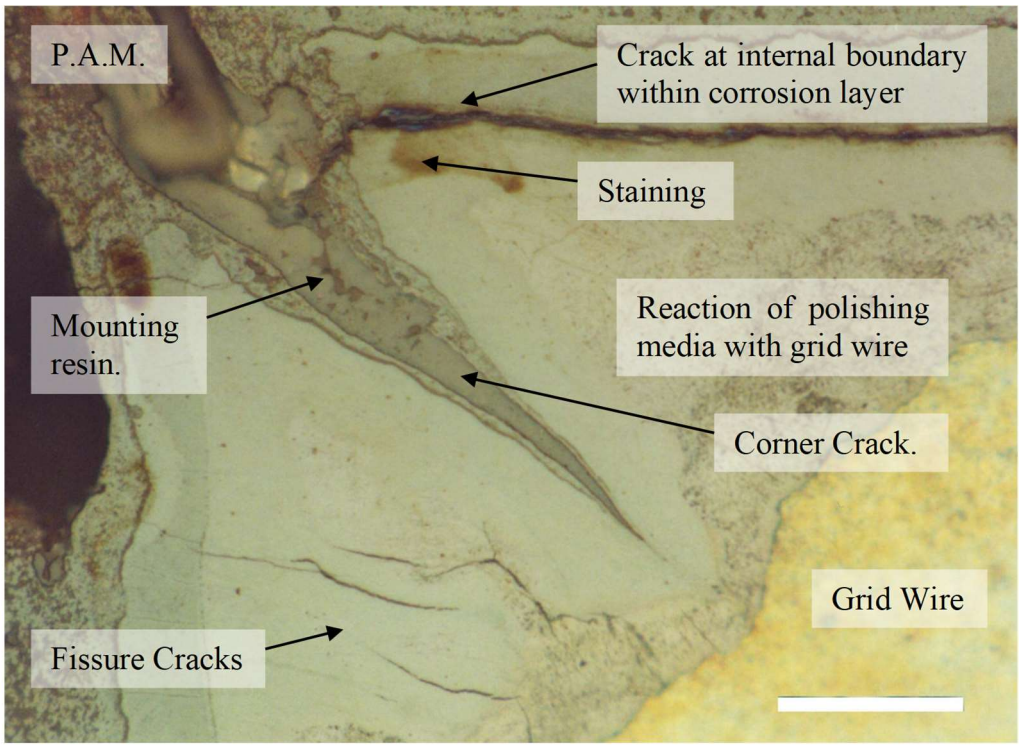

Figure 9.4: Fissures within corrosion layer adjacent to corner crack (Scale bar: 50µm)

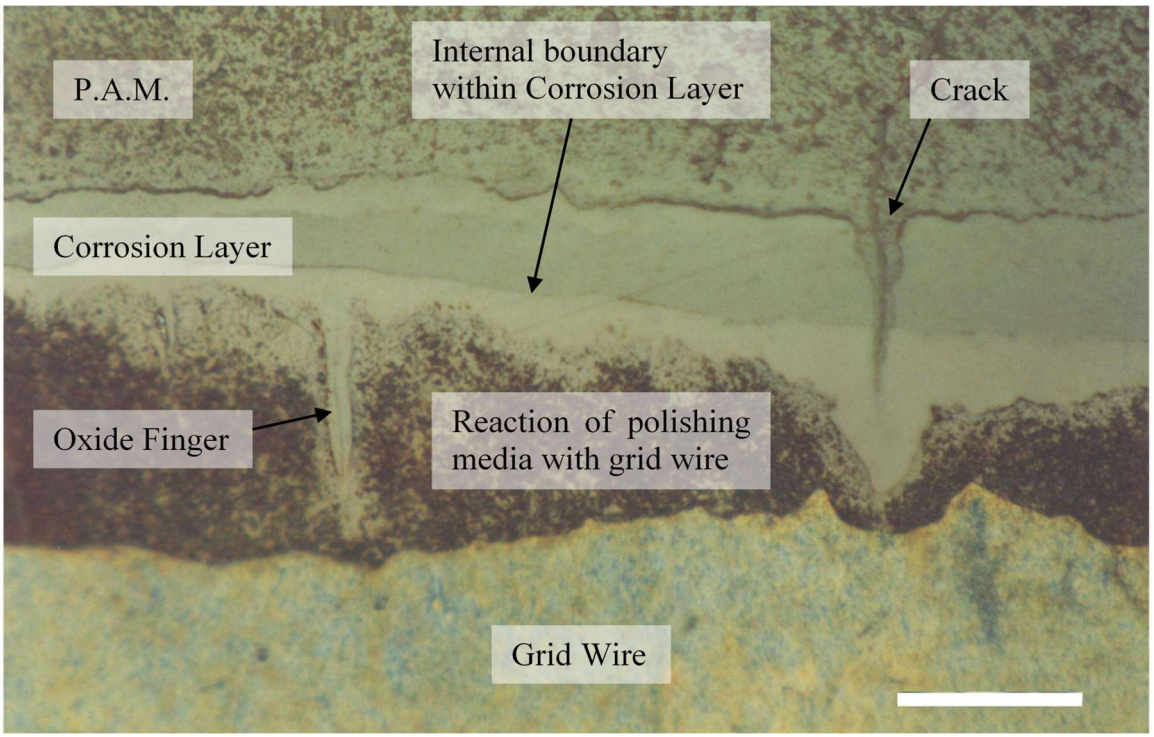

Figure 9.5: Crack observed on edge of grid wire (Scale bar: 50μm)

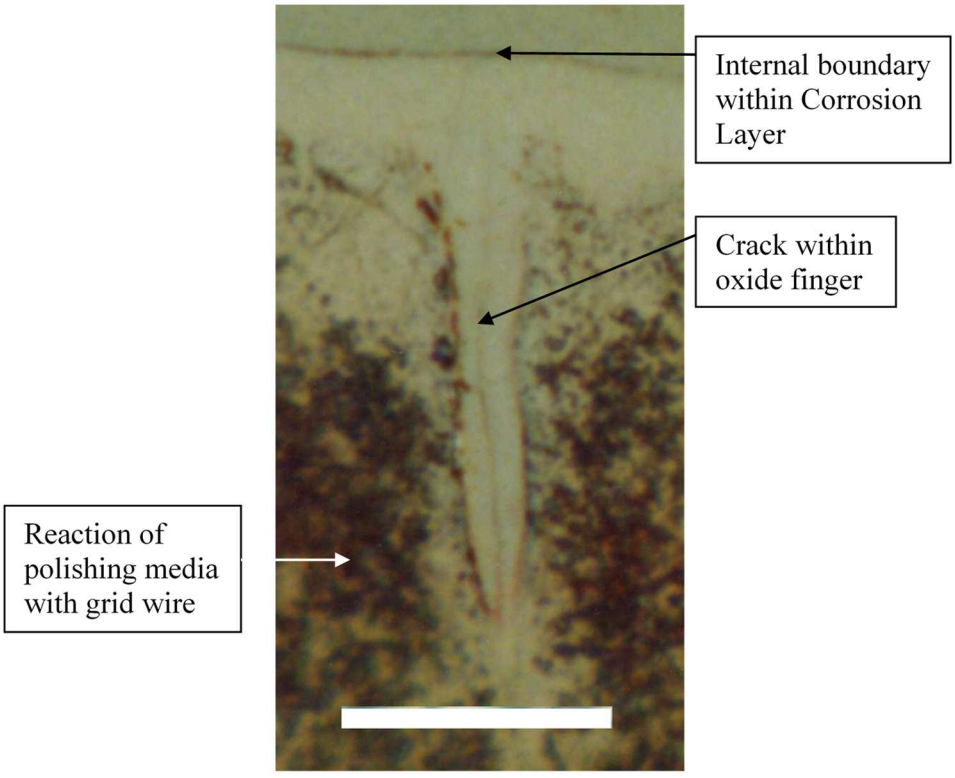

Figure 9.6: High magnification of oxide finger (Scale bar: 50μm)

Positive active material on the inner surfaces of a crack will affect the propagation rate. When positive active material is discharged the lead oxide is reduced to form lead sulphate with a

consequential increase in volume. This change will produce a force perpendicular to the crack direction effectively pushing the crack walls outwards and increasing the stress concentration around the crack tip, therefore promoting propagation. It should also be noted that cracks provide effective routes for the transport of oxygen to the grid / corrosion layer interface where the brittle oxide, which is prone to cracking, can be formed.

9.2.2 COMPARISON OF CORROSION LAYERS FROM DIFFERENT BATTERY TYPES

Examination of the corrosion layers of each battery type examined indicated variations in structure and morphology. A typical corrosion layer, from one of the batteries used to study the effects of cycling, is shown in Figure 9.7. The lead grid is out of focus in the photograph, however this is an unavoidable consequence of the preparation method used. Cracking can be seen parallel to the grid surface running along the 'grid side' of the corrosion layer. No porosity is visible within the corrosion layer. An internal boundary within the corrosion layer is visible in the central region.

The corrosion layer observed on the group 1 battery grid, Figure 9.8, is very similar in appearance to the previous one except that the internal boundary within the layer is closer to the positive active material and lighter in colour.

Figure 9.9 shows the corrosion layer from the group 2 battery. No internal boundary is visible in this layer and a number of black spots are visible which are believed to be pores.

A much higher amount of porosity is visible in the corrosion layer from the group 3 battery, Figure 9.10. A large number of cracks are visible in the corrosion layer and positive active material. Large pores are also visible in the positive active material adjacent to the corrosion layer.

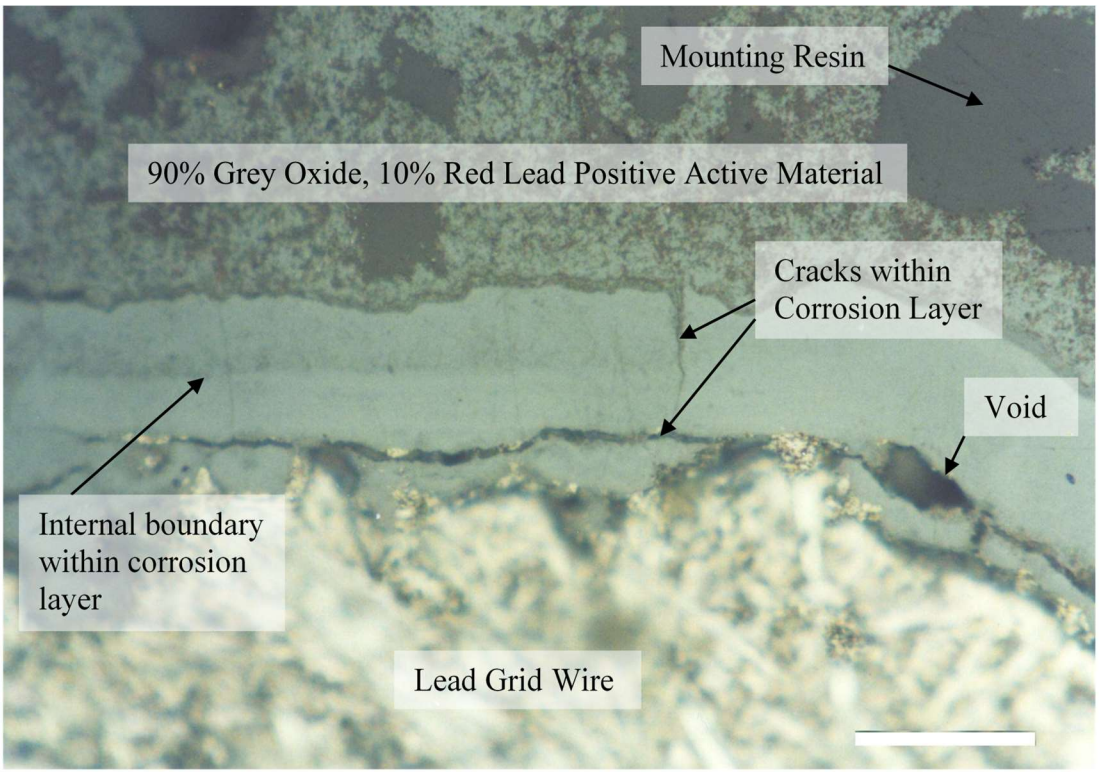

Figure 9.7: Corrosion layer from cycled battery (Scale bar: 50μm)

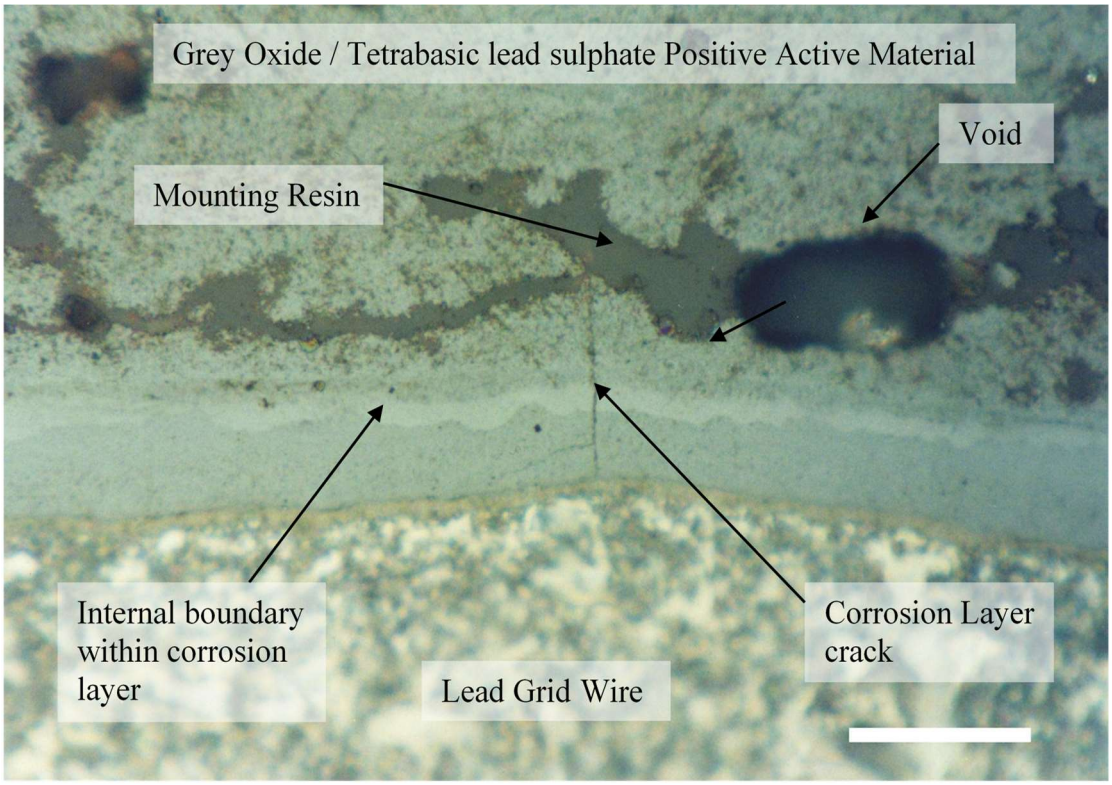

Figure 9.8: Corrosion layer from group 1 battery (Scale bar: 50μm)

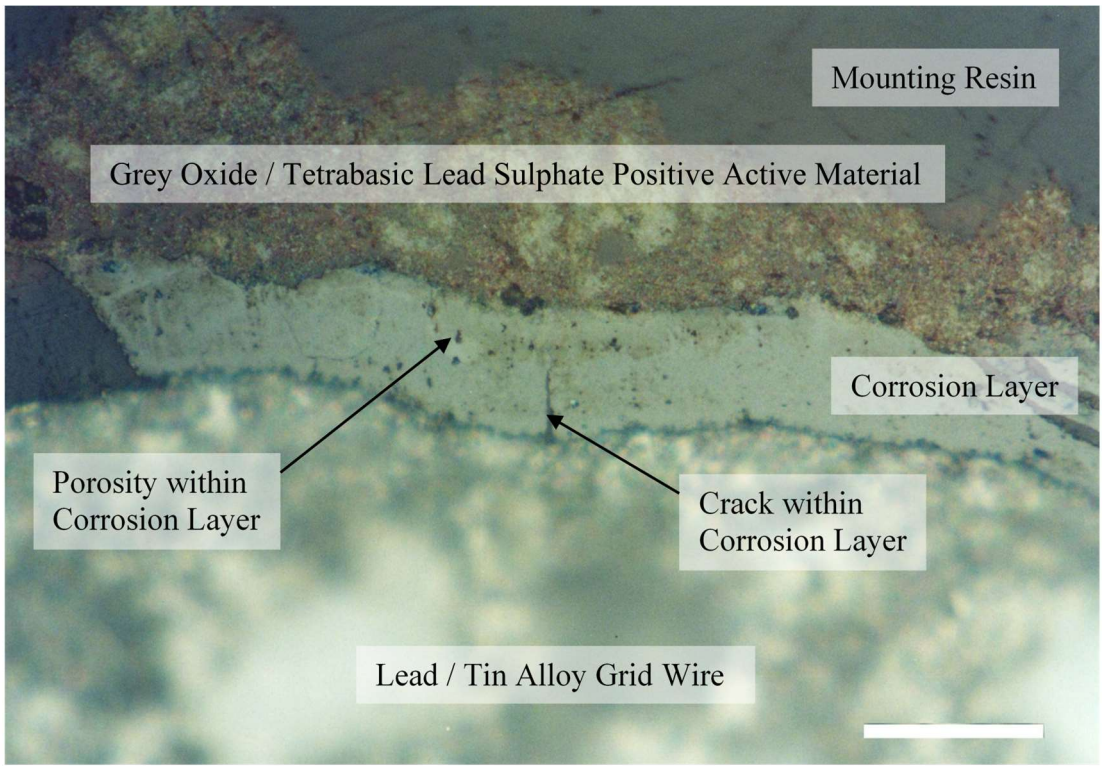

Figure 9.9: Corrosion layer from group 2 battery (Scale bar: 50μm)

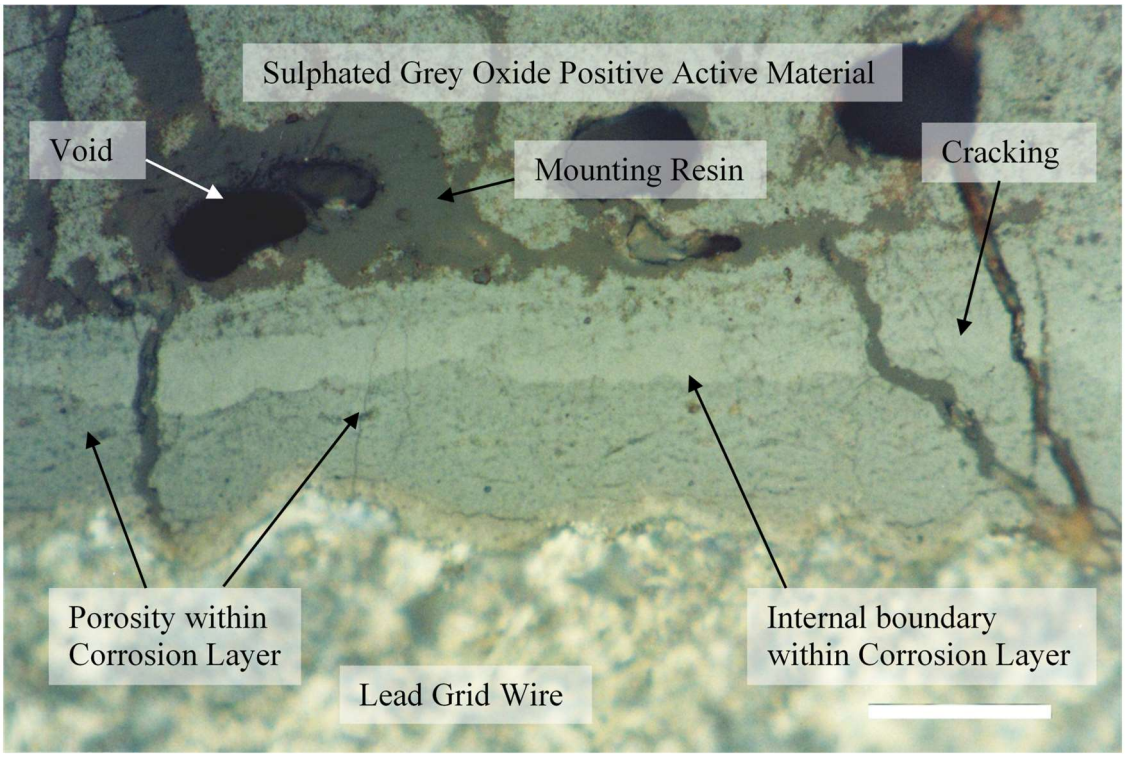

Figure 9.10: Corrosion layer from group 3 battery (Scale bar: 50μm)

A typical corrosion layer from a group 4 battery is shown in Figure 9.11. A large amount of fine porosity is visible across the width of the layer and a number of larger pores are also present. A lighter band in the corrosion layer is visible adjacent to the positive active material.

Corrosion layer thickness measurements taken on the good and bad cells of the batteries examined are shown in Table 9.1.

Table 9.1: Oxide thickness measurements

	Cycles	Good (μm)		Bad (μm)	
		Average	Standard Deviation	Average	Standard Deviation
Cycling*	28 and 42	23.5	6.6	19.8	3.1
Group 1	40	47.7	12.7	40.0	11.0
Group 2	29	28.1	5.3	25.5	5.8
Group 3	29	47.5	8.8	50.8	5.9
Group 4	27	89.4	12.6	88.1	14.4

* Data averaged for batteries cycled 28 and 42 times.

There is no significant difference between the corrosion layer thickness measurements for the good and bad cells. The thickest layers occurred on batteries from groups 3 and 4 (ignoring group 1 due to higher cycles). These layers contained the most pores and therefore would have allowed oxygen gas to diffuse to the grid / corrosion layer interface readily. When a comparison is made between group 3 and 4 batteries, group 4 which contained the lead / tin grid has a thicker layer. This suggests that tin promotes an increase in corrosion layer thickness. The same conclusion cannot be drawn from the batteries from groups 1 and 2 since the group 1 battery sustained significantly more cycles. The thinnest corrosion layer occurred on the battery type used to study the effects of cycling.

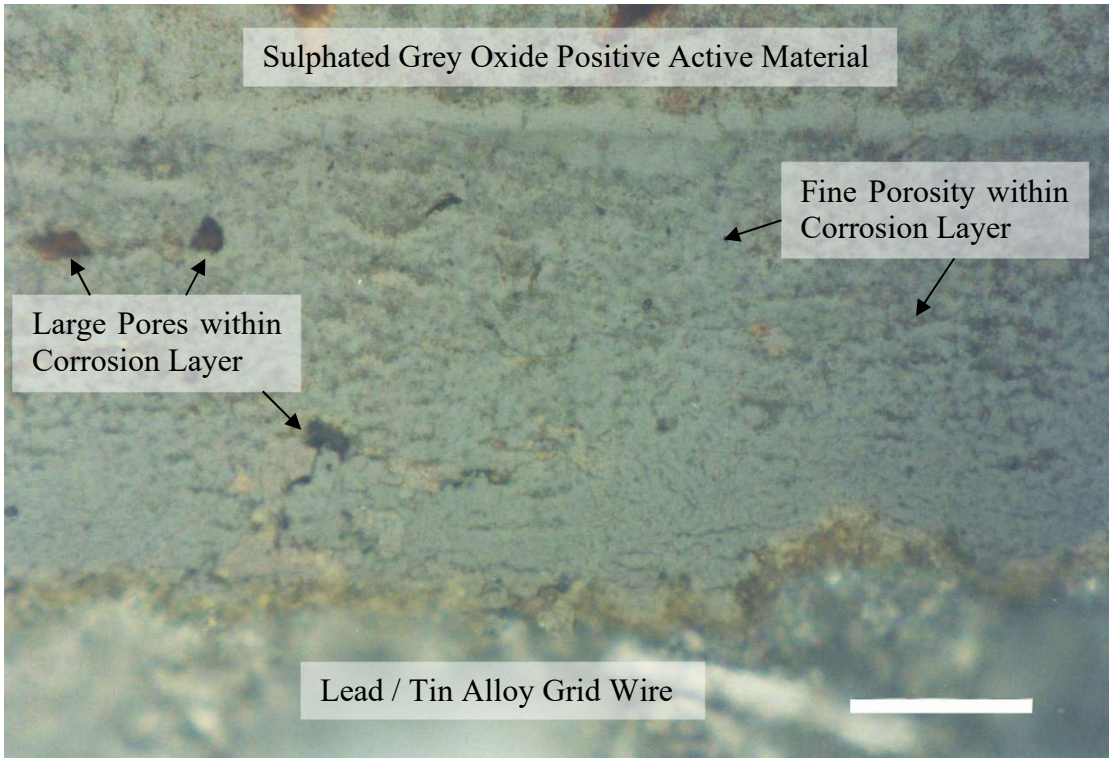

Figure 9.11: Corrosion layer from group 4 battery (Scale bar: 50μm)

9.3 ANALYSIS OF CORROSION LAYERS USING ELECTRON MICROSCOPY AND ANALYSIS

A compositional analysis of the corrosion layer was carried out using electron probe microanalysis. This involved obtaining electron images of the corrosion layers, which proved useful in providing additional information on layer porosity.

The results of main interest are quantitative, however, the qualitative results will be considered first. Lead, oxygen and sulphur were identified in all corrosion layers with the addition of tin in the case of those attached to a grid wire alloyed with tin. This shows that tin contained within the grid is incorporated into corrosion layers during growth. The fact that no other elements were identified, with the exception of carbon, which was used as a conductive coating, indicates that the materials used to manufacture the battery were pure and did not contain detectable amounts of any other element.

Initial spot quantitative analyses on the corrosion layers examined showed a large variation in compositional values obtained due to the presence of porosity and surface roughness. The surface roughness is clearly visible in the scanning electron images and porosity in the back-scattered electron images. This can be explained by considering the interactions of the electrons with the sample and method used to calculate the quantity of each element present.

Calibration of the electron probe microanalyser was achieved with the use of standards. However, with this approach the accuracy of the analysis is dependent on the unknown sample and standards having similar densities. Porosity within the corrosion layers effectively reduces their effective density and introduces errors into the results.

When x-rays from the sample are counted the analysis software automatically assumes that the sample is 100% dense, if a pore is present, the number of x-rays emitted is reduced and the calculation of the composition altered. This is demonstrated by the typical analysis given in Table 9.2.

Table 9.2: Typical EPMA compositional analysis

Atom %	Pb	43.4
	O	56
	S	0.6
	Sn	0.1
Total Wt%		**96.1**

The accuracy of an analysis can be determined by considering the total weight percent, the closer it is to 100%, the more accurate the analysis. For the purposes of this study all analyses with a total weight percent of less than 90% were ignored as this indicated that region of sample excited by the electron beam contained an unacceptable level of porosity or surface roughness.

In order to obtain an accurate value for the oxide stoichiometry, a large number of quantitative analyses were conducted. As variations in oxide stoichiometry between the inner and outer edges of the corrosion layer are of interest, a quantitative line scan between these two positions was the most appropriate option.

Analyses were conducted at one-micron intervals along the scan line. This provided the maximum number of practical analysis points considering that the minimum area that can be analysed is approximately one micron in diameter. The maximum number of analysis points was used since for the more porous samples a large number of the analyses were rejected because the total weight percent was less than 90%. To calculate the stoichiometry of the oxide in the corrosion layer it is necessary to make a number of assumptions for each analysis. These are summarised below:

- The only elements present in the corrosion layer are lead, oxygen, tin and sulphur.
- All sulphur present within the corrosion layer is in the form of a metal sulphate.

- Lead and tin within the corrosion layer are either in the form of an oxide or sulphate
- Oxide stoichiometry for a given analysis point is always the same regardless of metal e.g. lead or tin.

From these assumptions a number of expressions have been derived to obtain values for the total metal and oxygen atoms available for incorporation into oxide. This allows the stoichiometry of the oxide to be calculated.

Total metal atoms forming oxide, $T_M = P + T - S$ (9.1)

Total oxygen atoms forming oxide, $T_O = O - (4 \times S)$ (9.2)

Oxide stoichiometry ratio, MO_n, $n = T_O / T_M$ (9.3)

Where: P = Number of lead atoms identified in analysis

T = Number of tin atoms identified in analysis

S = Number of sulphur atoms identified in analysis

O = Number of oxygen atoms identified in analysis

Secondary and back scattered electron images and plots of oxygen/lead ratio versus distance across corrosion layer for each of the battery types examined are shown in Figure 9.12 to Figure 9.16.

The scanning process resulted in a layer of contamination being deposited on the corrosion layer surface. This provided a means to identify the exact position of the scan line. For all plots the scan direction is from the active material towards the grid wire.Variations in ratio occur with distance across the corrosion layer and also between the different battery designs. There is a general trend of a decrease in oxygen content towards the grid wire. When comparing the scan lines and plots, variations in oxygen/lead ratio do not always correspond to the positions of internal boundaries within the corrosion layer.

Scatter in some of the plots is caused by errors introduced by variations in surface roughness and porosity. Despite these factors it is still possible to identify general trends within the corrosion layer of each battery design.

Internal boundaries within the corrosion layers can be identified in both back-scattered and secondary electron images by darker and lighter regions. The darker regions correspond to lower atomic mass areas and the light regions to high. This can be used to explain the light shade of the grid wire, which has a high average atomic mass and is therefore efficient at back-scattering electrons.

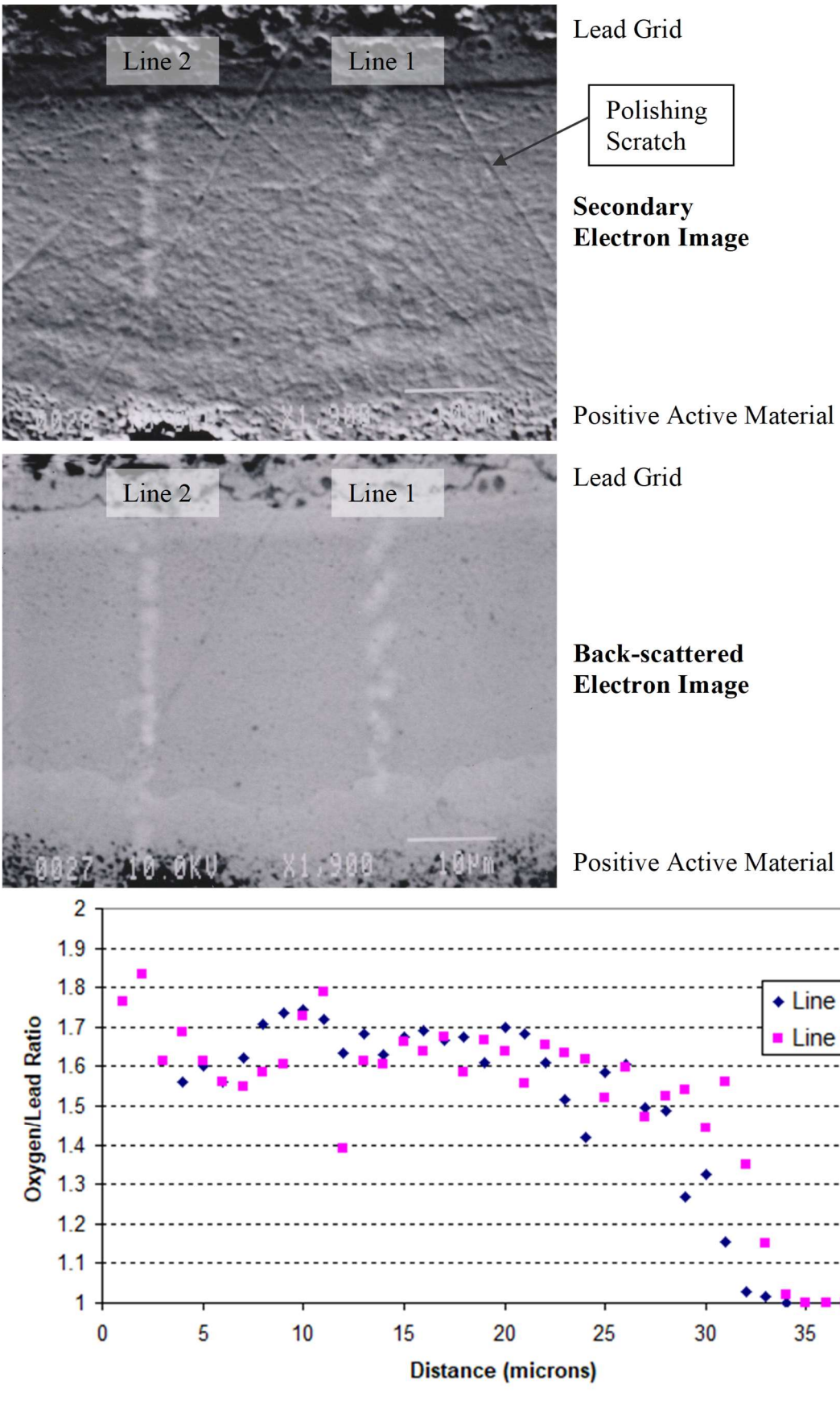

Figure 9.12: Analysis of Corrosion Layer from battery used to study cycling (Scan direction from PAM to Grid)

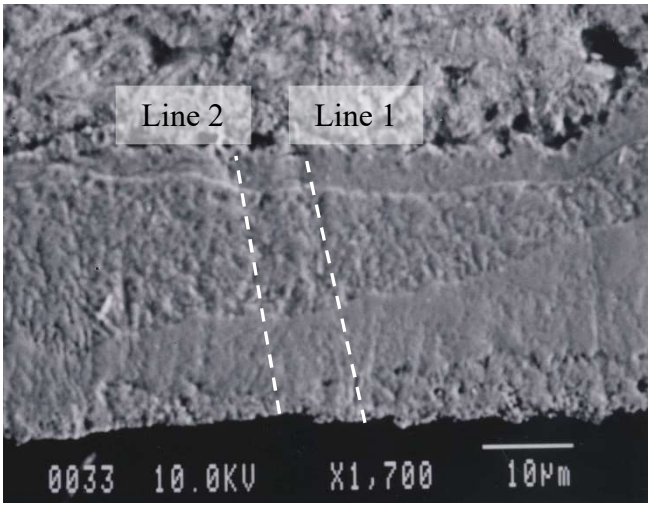

Grid Wire

Secondary Electron Image

Positive Active Material

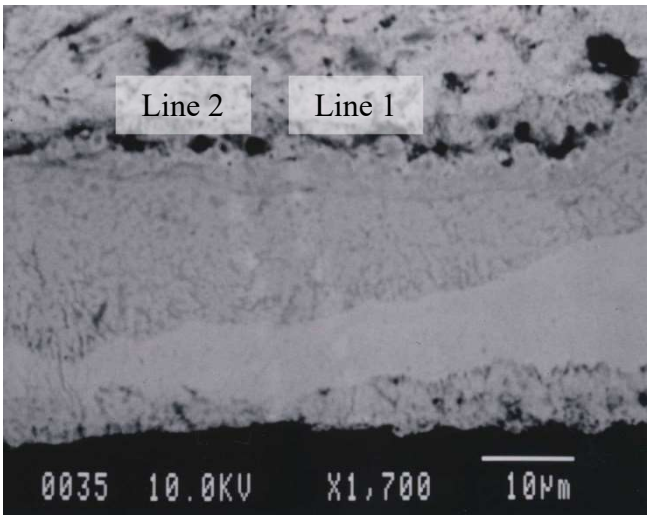

Lead Grid

Back-scattered Electron Image

Positive Active Material

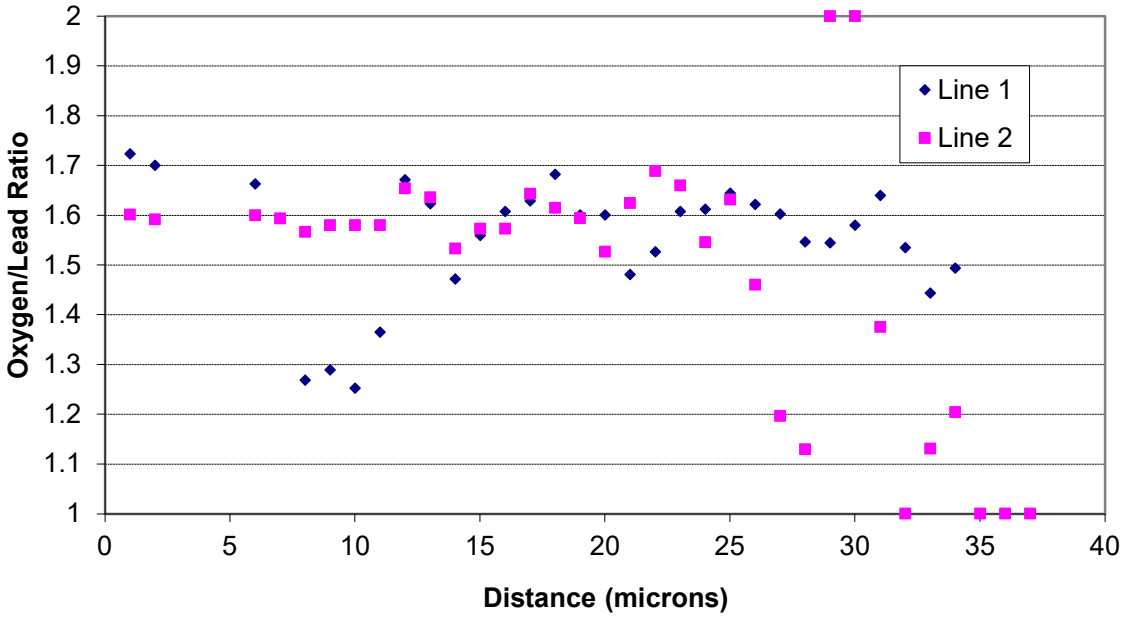

Figure 9.13: Analysis of Group 1 Corrosion Layer (Scan direction from PAM to Grid)

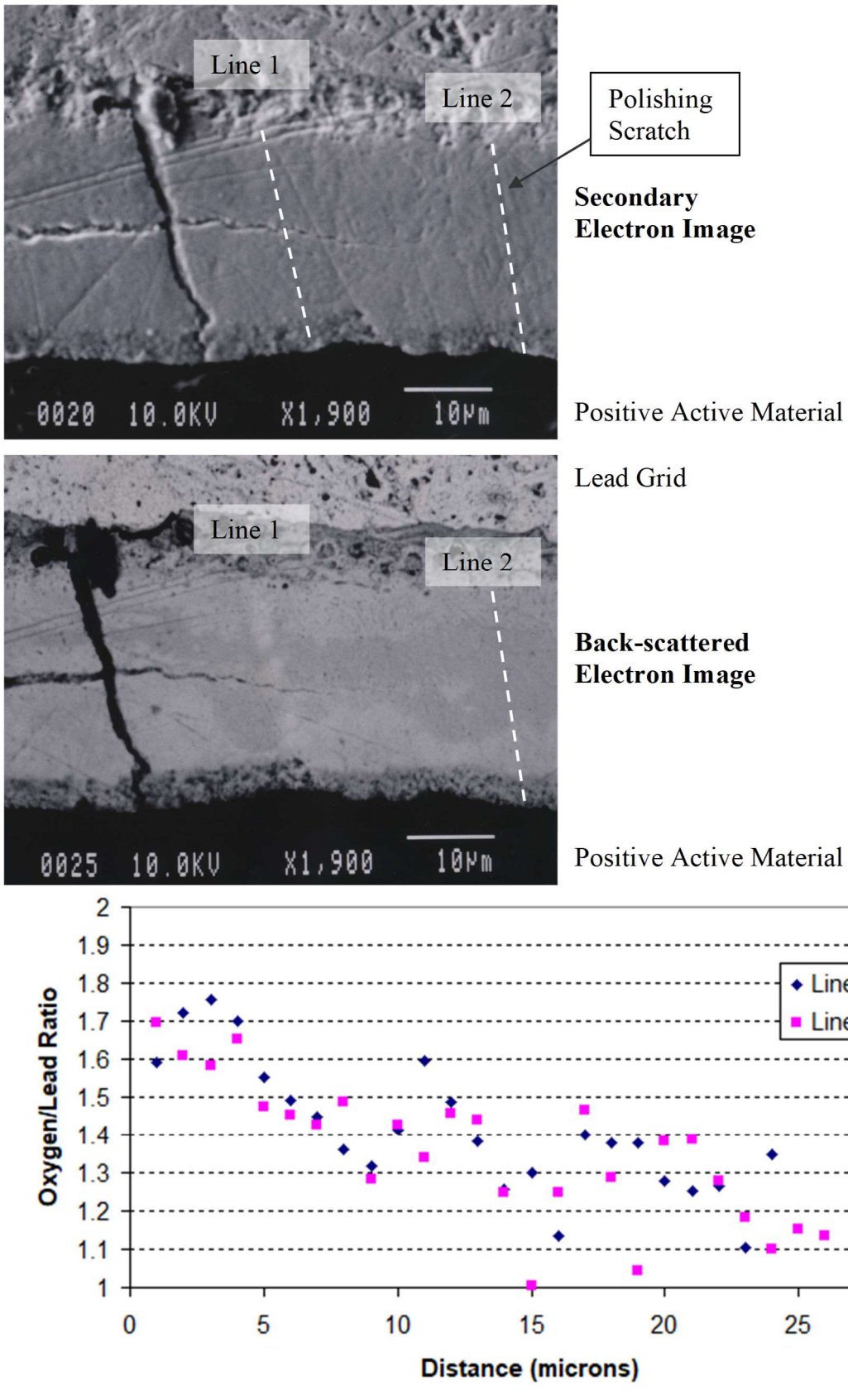

Figure 9.14: Analysis of Group 2 Corrosion Layer (Scan direction from PAM to Grid)

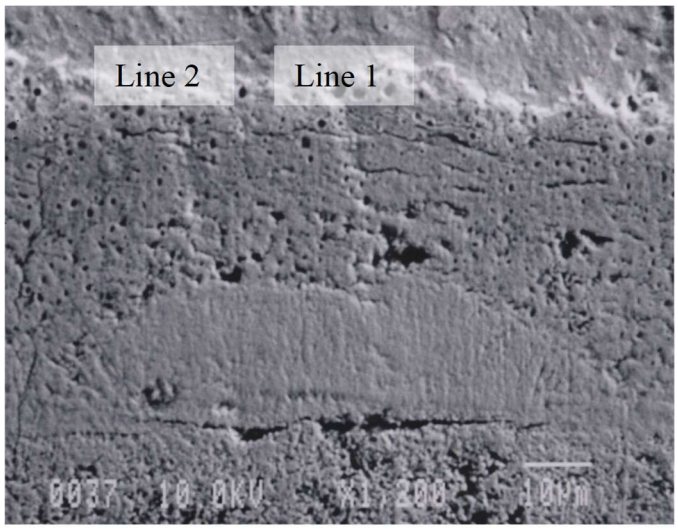

Lead Grid

Secondary Electron Image

Positive Active Material

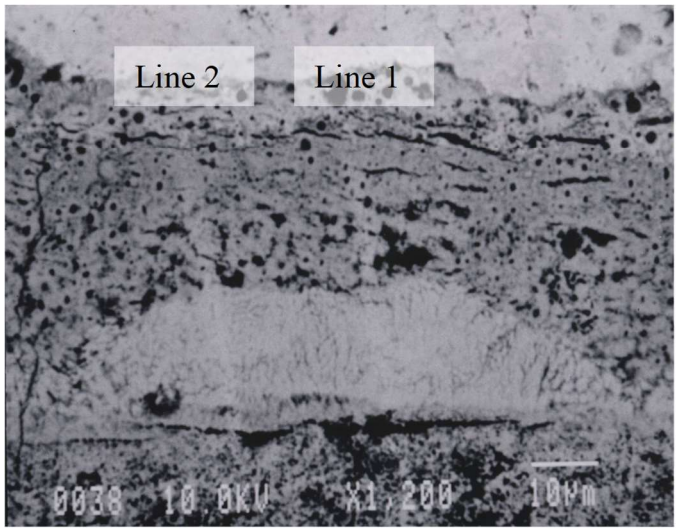

Lead Grid

Back-scattered Electron Image

Positive Active Material

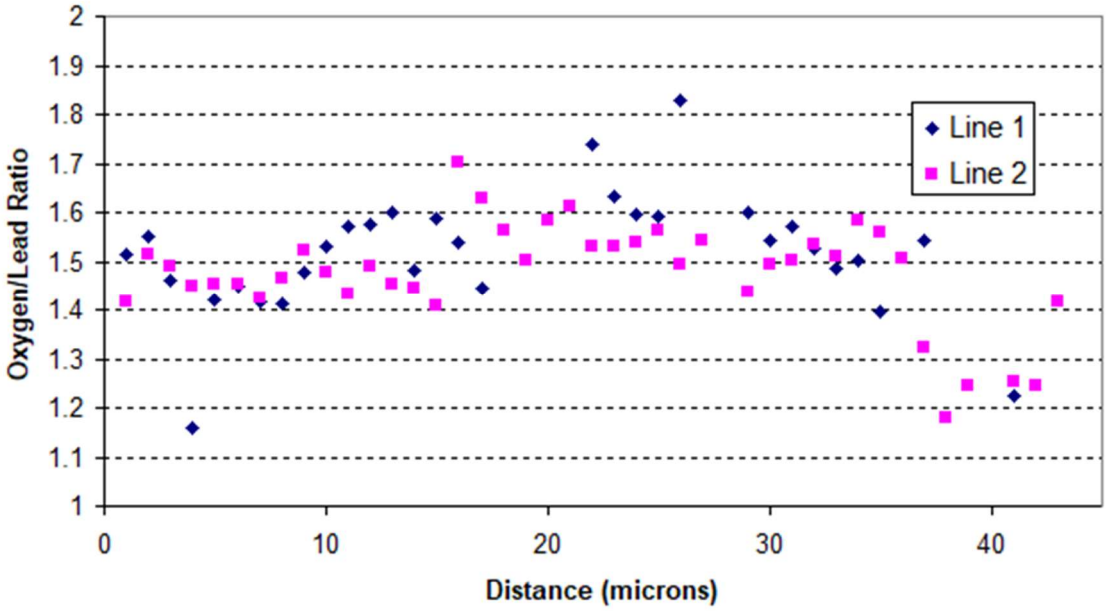

Figure 9.15: Analysis of Group 3 Corrosion Layer (Scan direction from PAM to Grid)

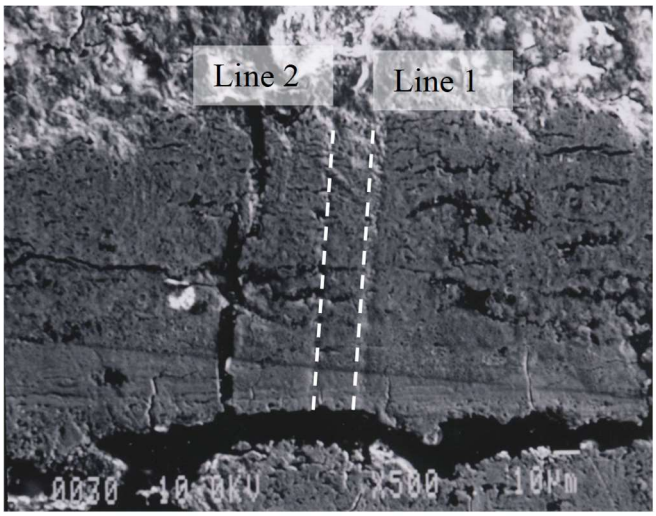

Lead Grid

Secondary Electron Image

Positive Active Material

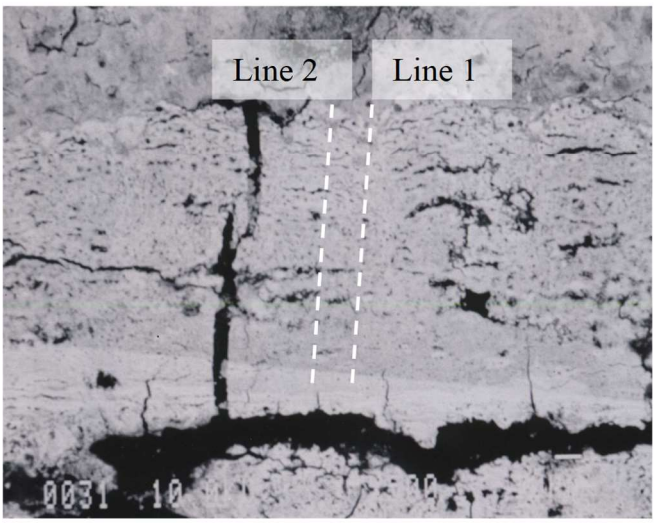

Lead Grid

Back-scattered Electron Image

Positive Active Material

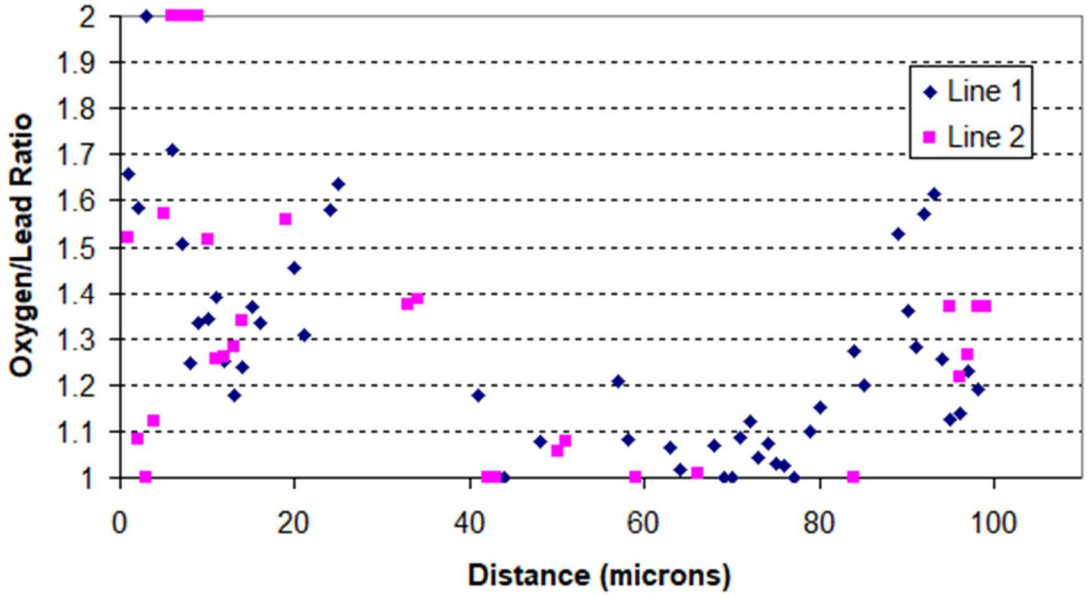

Figure 9.16: Analysis of Group 4 Corrosion Layer (Scan direction from PAM to Grid)

From an examination of the images it can be seen that the lighter band within the corrosion layer is positioned adjacent to the positive active material and the darker band to the grid wire. This observation suggests an increased lead content in the corrosion layer adjacent to the positive active material. This cannot be explained when it is considered that the oxygen concentration is considered to be higher in these regions.

For oxidation of a metal to occur, oxygen must diffuse to the metal surface where it reacts to form oxide resulting in the build up of a layer on the surface. Subsequent oxidation therefore requires oxygen to diffuse through the existing oxide to the metal surface interface. The type of oxide layer formed governs the efficiency of this process and is predicted using the Pilling Bedworth ratio, R, which is shown in equation 9.4 below.

$$R = \frac{\text{Oxide volume per metal atom}}{\text{Metal volume per metal atom}} \qquad (9.4)$$

If R<1 then the oxide takes up less volume than the metal and a porous oxide layer is formed, resulting in rapid oxidation. For, 1<R<2, the oxide takes up slightly more volume than the metal and an adherent non porous protective layer is formed, however if the volume of the oxide is too large, R>2, spalling occurs resulting in an increased oxidation rate.

Values for 'oxide volume per metal atom' and 'metal volume per metal atom' can be calculated from crystallographic information, namely the size of the unit cell and the number of atoms contained within it.

Pilling Bedworth ratios for a number of lead oxides are given in Table 9.3.

Table 9.3: Pilling Bedworth Ratios for different lead oxides

Oxide	Structure	Pilling Bedworth ratio
a-Lead Monoxide (PbO)	Pseudo tetragonal	*1.31*
b-Lead Monoxide (PbO)	Orthorhombic	*1.27*
Minium	Tetragonal	*1.40*
a-Lead Dioxide (PbO_2)	Orthorhombic	*1.34*
b-Lead Dioxide (PbO_2)	Tetragonal	*1.37*

The Pilling Bedworth values calculated all lie in the range 1<R<2, therefore the oxide should be adherent and non porous, however cracks are observed within the corrosion layers of a number of samples. An explanation for this may be the unexpectedly high value obtained for Minium (Pb_3O_4). Corrosion layers consist of a lead monoxide layer adjacent to the grid wire. An increase in oxygen content is observed towards the corrosion layer / positive active material

interface where the oxygen concentration is higher. A simplified corrosion layer structure might be represented as shown in Figure 9.17 below.

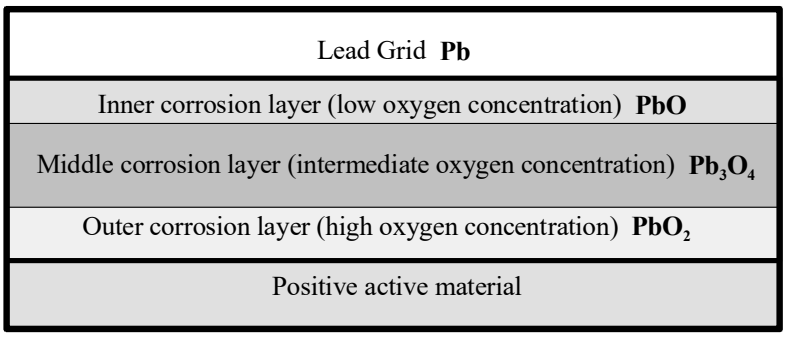

Figure 9.17: Simplified representation of corrosion layer

If the ratios of oxygen volume per metal atom are calculated for the interfaces shown in the diagram the following Pilling Bedworth ratios are obtained, values range due to different forms (structures) of the same stoichiometry oxide.

Interface (1)	Pb/PbO	1.27 – 1.31
Interface (2)	PbO/Pb_3O_4	1.07 – 1.11
Interface (3)	Pb_3O_4/PbO_2	0.95 – 0.98

From the values obtained the ratio at interface (3) has a value less than 1, a decrease in the volume of the oxide and increased porosity would therefore be expected. This could be used to explain the formation of cracks in the plane of the oxide between layers. However, an argument against this is that the oxide stoichiometry changes gradually throughout the thickness of the corrosion layer, which would eliminate the sudden change present at a metal / oxide interface. An additional factor which would favour the formation of cracks is variation in thermal expansion coefficient between layers.

9.4 ANALYSIS OF CORROSION LAYER / GRID INTERFACE

Corrosion layer preparation using grinding and polishing techniques produced a high quality surface finish for electron microscopy and analysis. However, the differences of material removal rate between the soft lead grid and hard ceramic corrosion layer make examination of this interface almost impossible. For this reason, the alternative technique of ultra micro-toming was used. This not only provided a flat section, but the disruption to the interface was negligible making detailed examination feasible.

Samples were prepared from the freshly formed positive electrodes of battery groups 1 to 4. Secondary electron images of the sections taken are shown in Figure 9.18 to Figure 9.21. From

the figures it can be seen that this technique provides high definition pictures of both corrosion layer and interface morphology.

A feature observed in the photographs is the presence of ‘fingers’ of oxide growing into the lead/tin grids but not into the pure lead. Corrosion layers produced from lead grids have a smooth grid / corrosion layer interface, however those growing from lead tin grids do not.

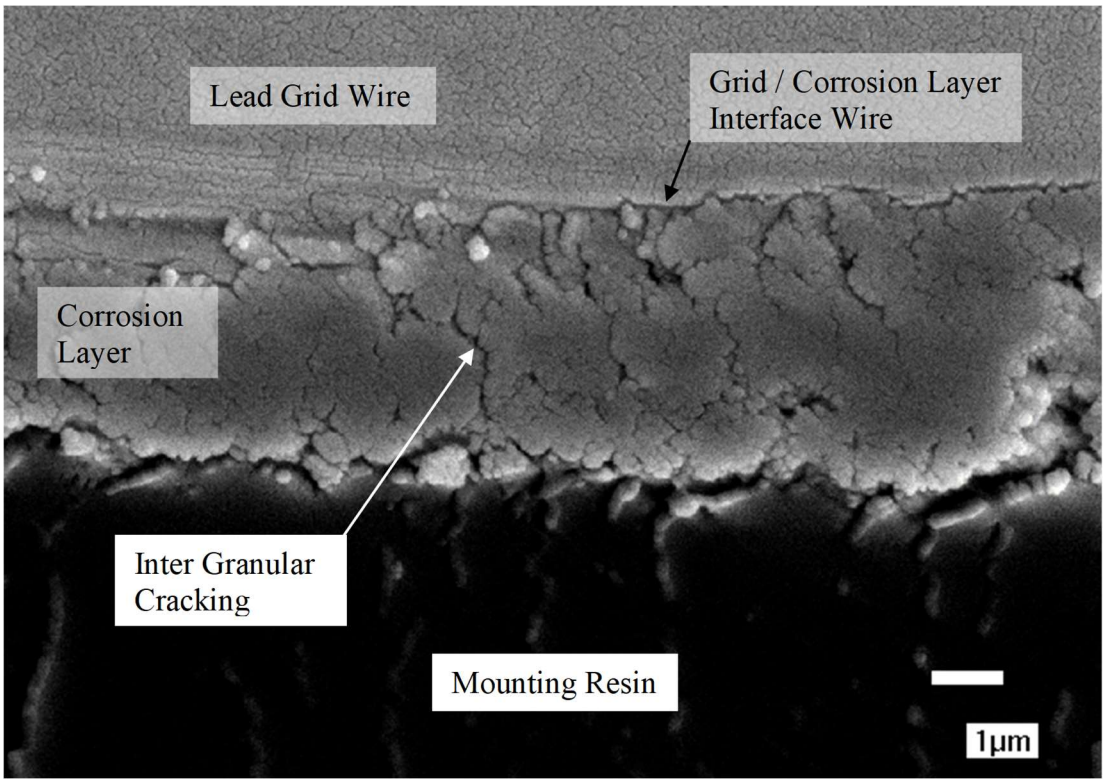

Figure 9.18: Grid Corrosion Layer interface from group 1 battery

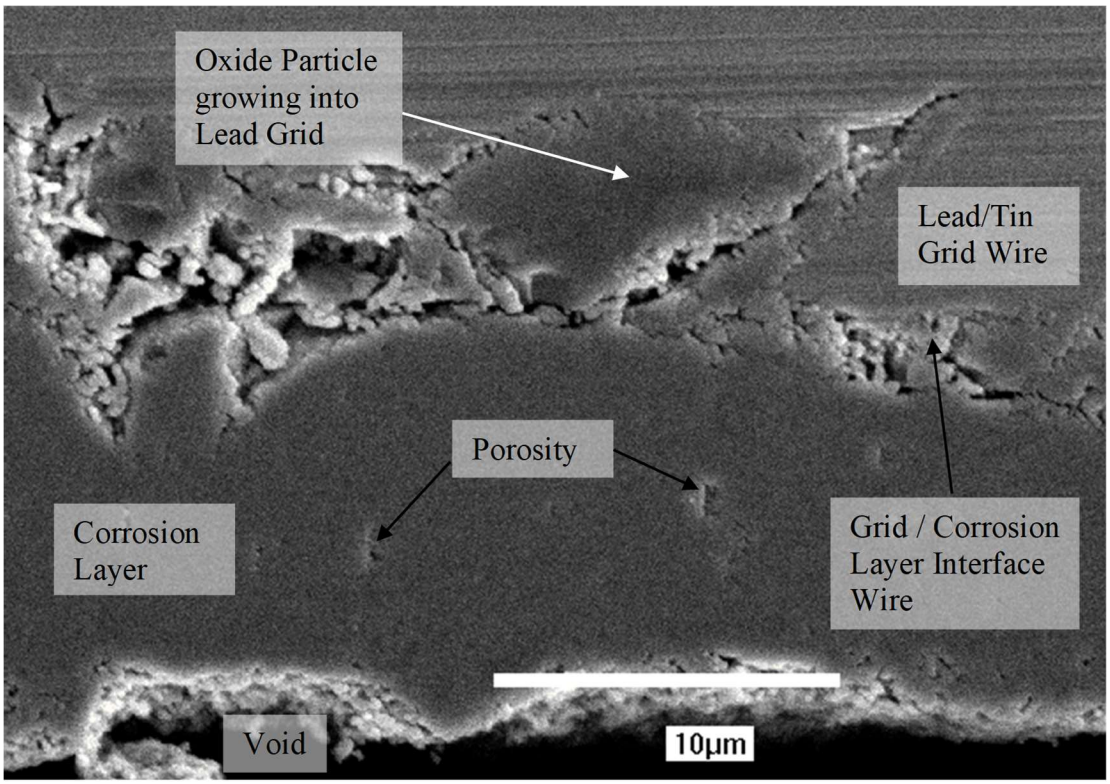

Figure 9.19: Grid Corrosion Layer interface from group 2 battery

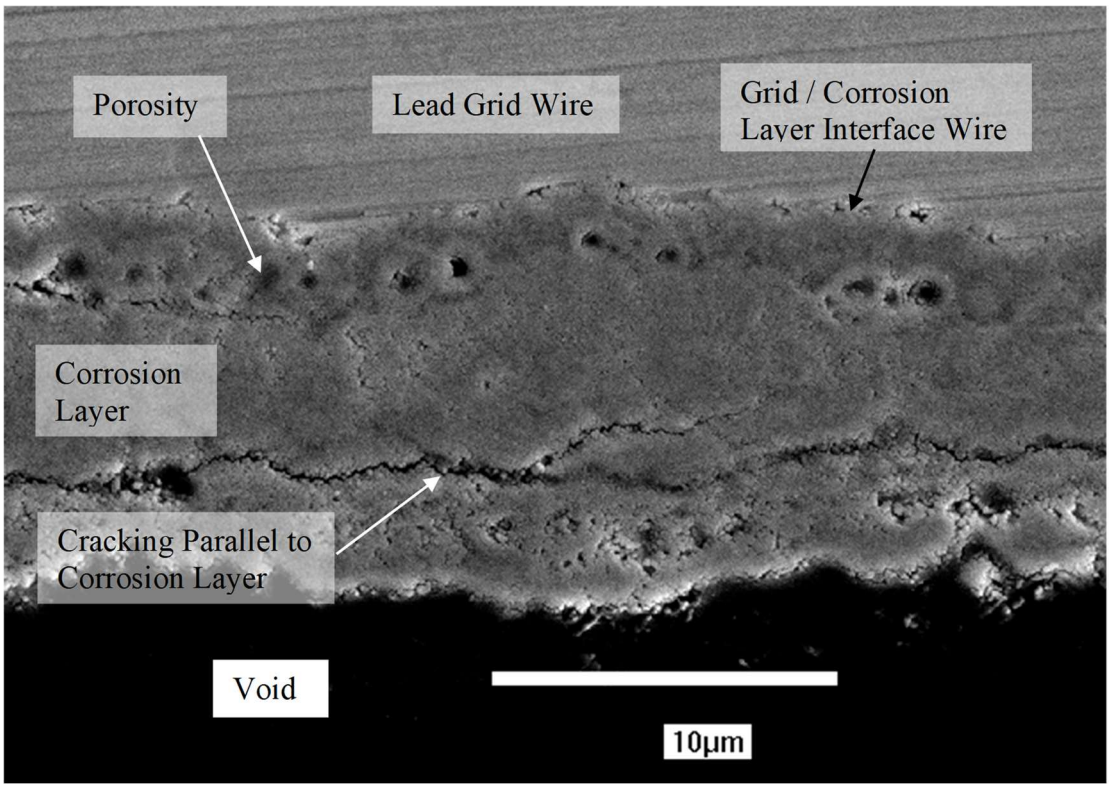

Figure 9.20: Grid Corrosion Layer interface from group 3 battery

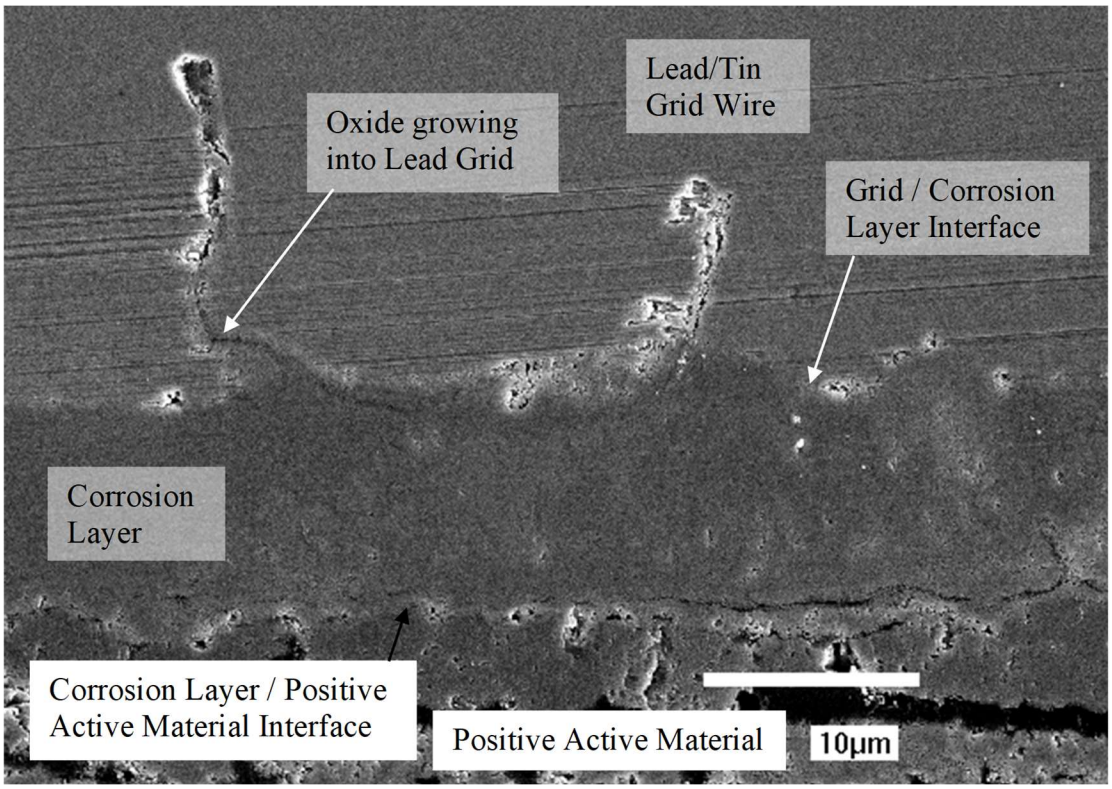

Figure 9.21: Grid Corrosion Layer interface from group 4 battery

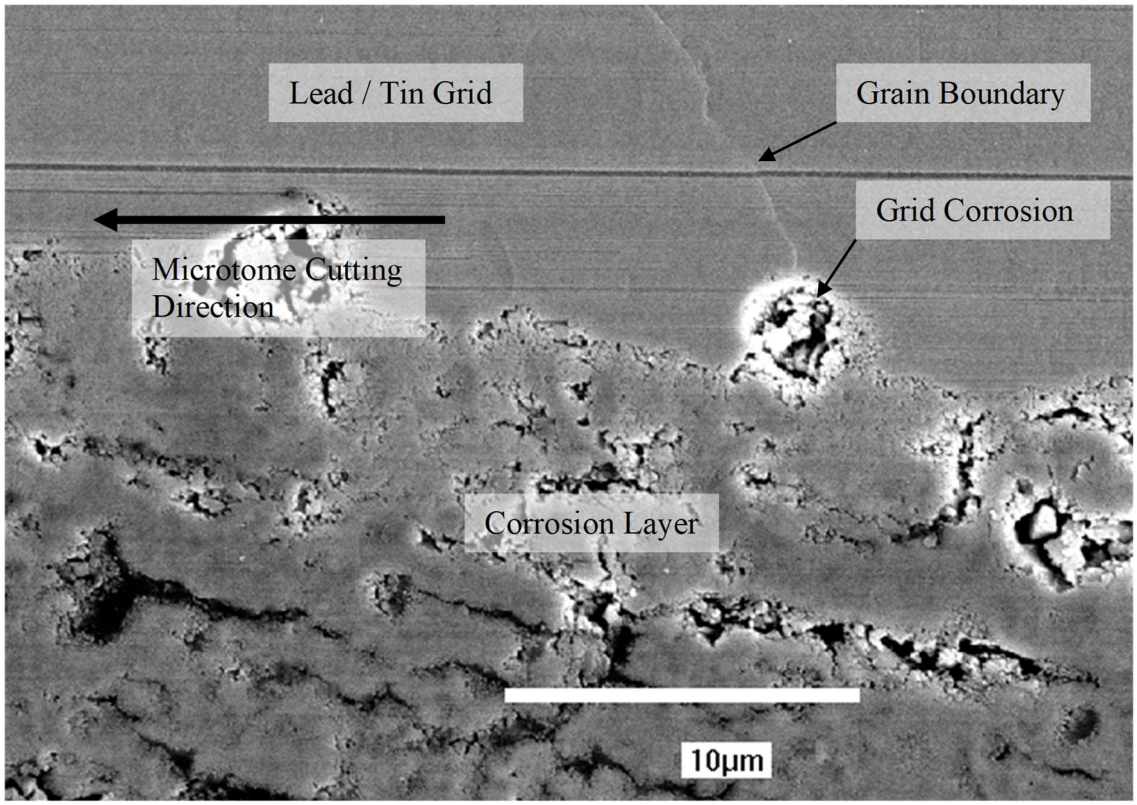

Figure 9.22: Corrosion propagating along grain boundary

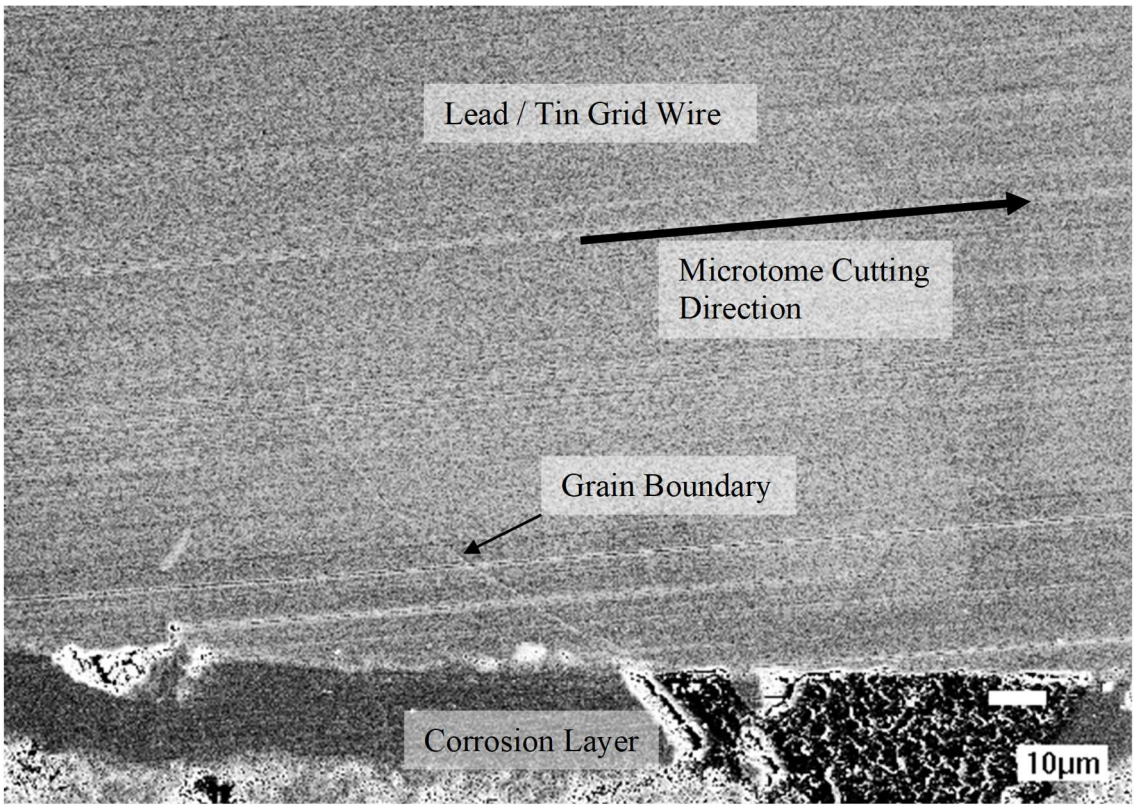

Figure 9.23: Microtomed grid indicating position of grain boundary

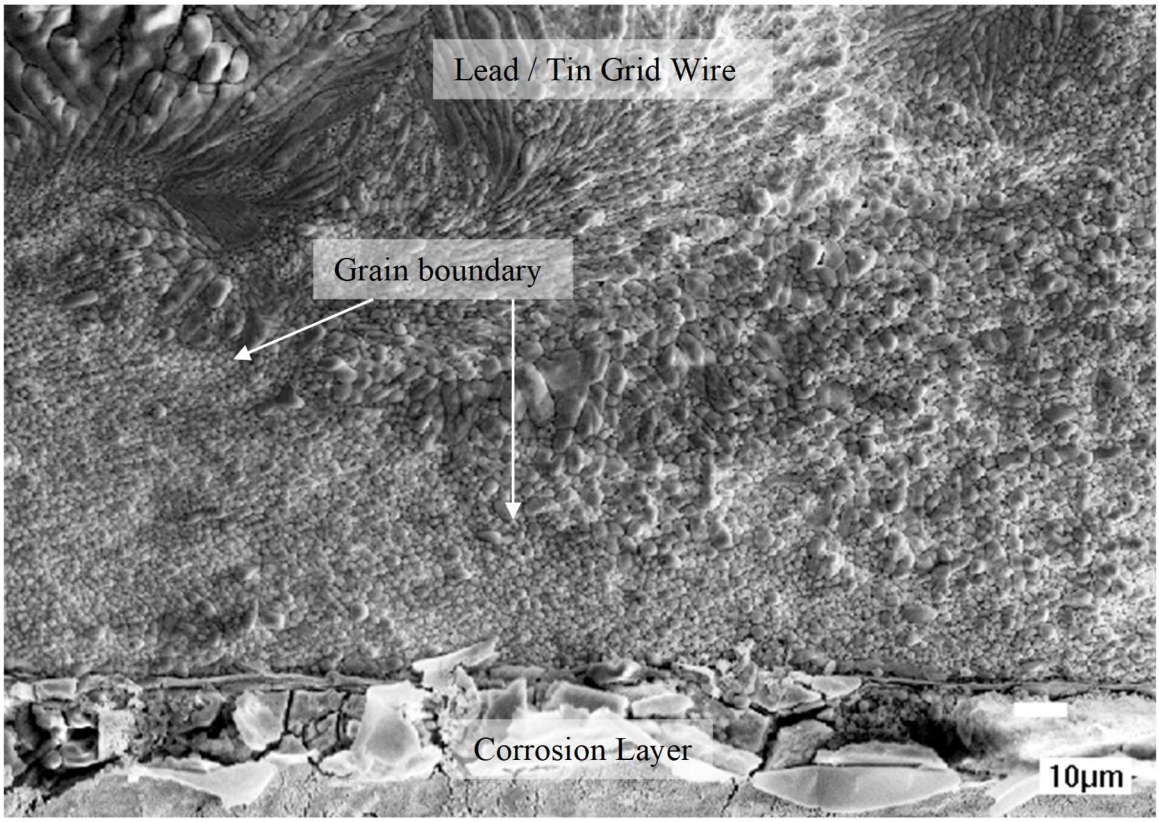

Figure 9.24: Etched grid indicating position of grain boundary

A more detailed examination of a lead/tin grid corrosion layer identified what was believed to be corrosion initiating in the region of a grain boundary, Figure 9.22. Closer examination of the grain boundary showed a small step. A likely explanation is that the shearing action of the microtome's knife as it cuts a section from the alloy surface produces a force at the grain boundaries high enough to cause a displacement, and the resulting step. The 'step' was confirmed as a grain boundary by etching a section and comparing the location of the step with that of the grain boundary revealed by etching, Figure 9.23 and Figure 9.24.

Electron probe microanalysis was used to obtain values of the tin content within the grain and at the grain boundaries by taking 17 randomly distributed analysis points at each position. Average percentage tin values obtained from the data for the grain and grain boundary regions were 0.75 and 0.96% respectively. An analysis using the students t-test confirmed that there was a difference between the two sample means obtained to a 0.2 per cent significance level.

The higher tin concentration observed at the grain boundary is due to the precipitation of tin in these regions during solidification of the alloy. This can be expressed by the following phase reaction obtained from the appropriate position on the lead tin phase diagram shown in Figure 9.25.

$$\mathbf{L} \rightarrow \alpha \rightarrow \alpha + \beta$$

L = Liquid

α = Lead

β = Tin

As the molten alloy cools during the casting procedure the α-phase solidifies. At very low temperatures, <50°C the $\alpha+\beta$ region of the diagram is entered and the β phase, tin, precipitates at the grain boundaries.

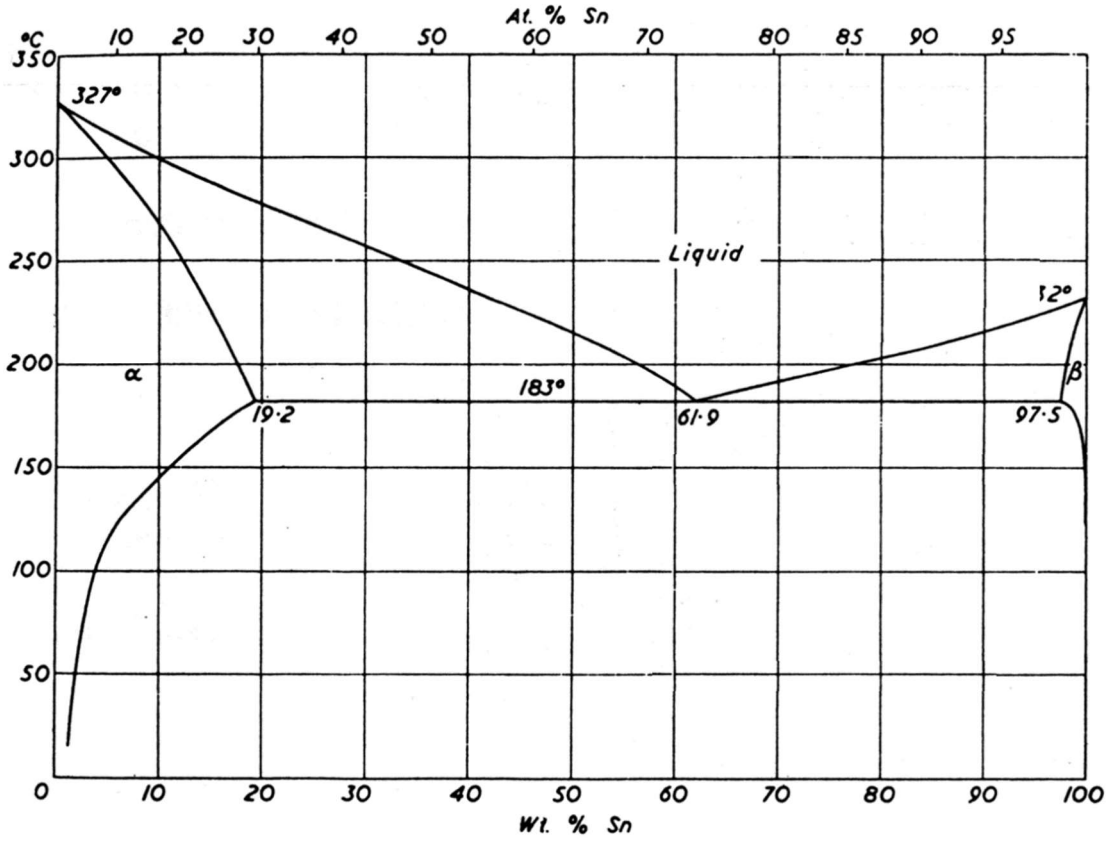

Figure 9.25: Lead – Tin phase diagram (α=lead, β=tin)

Corrosion is more likely to occur in the vicinity of the tin precipitates, as the higher concentration of tin will cause enhanced galvanic corrosion to occur, due to the different electrode potentials of lead and tin.

9.5 CONCLUSIONS

The following conclusions can be drawn from the data presented in this chapter.

1. A typical corrosion layer consists of a number of layers where the mechanical strength of the interface is less than that of the individual layers.
2. A number of different crack types occur within the corrosion layer including: corner cracks, side cracks, fissure cracks, oxide finger containing crack and internal boundary cracks.
3. Crack initiation is considered to be a result of more than one mechanism. These are: stresses due to heating, geometrical effects and internal pressure caused by the evolution of gas.
4. Oxygen concentration within the oxide across the corrosion layer decreases towards the grid wire.
5. Corrosion layers formed from lead tin alloy grids contained elemental tin.
6. Corrosion layers formed from sulphated grey oxide positive active material have higher porosity and are thicker compared to the non-sulphated active materials.

7. Corrosion layers formed from non-sulphated grey oxide positive active material tend not to contain pores.
8. Corrosion is promoted in lead/tin grids by crack and corrosion growth along tin rich grain boundaries.

10 RESULTS AND DISCUSSION: FINITE ELEMENT (FE) MODELLING OF CURRENT DENSITY ON THE POSITIVE BATTERY GRID

10.1 INTRODUCTION

A battery electrode consists of a lead grid, which acts as a current collector, surrounded by either positive or negative active material. During battery operation electrons must pass from the surface of the active material to the surface of the grid wire. Due to the geometrical arrangement of the active material and grid wires in a battery electrode, the current flowing into the surface of the grid may vary. A model proposed by Pavlov [1] suggests that the cycle life of positive plates depends on the variations in current density on the grid surface, as this determines the intensity of the destructive processes in the positive active mass during operation.

Due to the complex geometry of the grid wire shapes, calculating the variation in current density using an analytical method would be extremely complicated and practically impossible. A more practical approach is to use a finite element method to solve the problem. The package chosen to obtain a solution was Ansys [2]. Ansys is a multi-purpose finite element program that can be used to solve a number of physical problems including current flow in a material.

10.2 CALCULATION OF HEAT AND ELECTRON FLOW IN A MATERIAL

To use Ansys to solve current conduction problems it is first necessary to make the analogy with heat transfer problems. Ansys solves electrical problems as a heat flow problem and substitutions must be made for the input and output variables. The quantity of heat flowing, Q, within a material is proportional to the length of time, t, cross-sectional area, A, and temperature gradient, as shown in Figure 10.1 below.

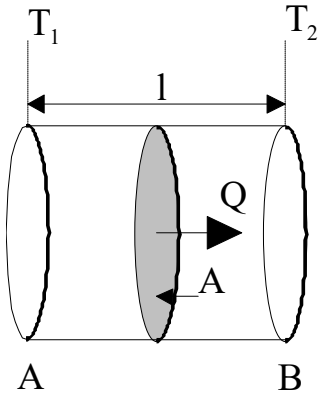

Figure 10.1: Heat flow in a material

The temperature gradient, between points A and B in figure 10.1, can be expressed in terms of the two temperatures T_1, T_2 and the length, as shown in equation 10.1 below.

$$\frac{T_1 - T_2}{l} \tag{10.1}$$

As the heat flow, Q, is proportional to these quantities it can be expressed as:

$$Q \propto tA\frac{T_1 - T_2}{l} \tag{10.2}$$

Therefore by incorporating the thermal conductivity, K, equation 10.2 becomes:

$$Q = KtA\frac{T_1 - T_2}{l} \tag{10.3}$$

When considering the electrical problem the current flow, I, is equal to the quantity of electrons flowing, Q, with time, t, as shown in equation 10.4.

$$I = \frac{Q}{t} \tag{10.4}$$

Current flow can also be related to potential difference, V, and resistance, R, by ohms law:

$$I = \frac{V}{R} = \frac{V_1 - V_2}{R} \tag{10.5}$$

And resistance can be written in terms of resistivity, ρ, length and area by,

$$R = \frac{\rho l}{A} \tag{10.6}$$

Therefore by combining equations 10.4, 10.5 and 10.6, equation 10.7 is obtained:

$$Q = \frac{1}{\rho} tA \frac{V_1 - V_2}{l} \qquad (10.7)$$

From the thermal, 10.3, and electrical, 10.7, equations thermal conductivity, K, is seen to be analogous to the electrical conductivity 1/ρ. This allows an electrical problem to be solved in a thermal context if the mental substitution of input and output variables shown in Table 10.1 is made:

Table 10.1: Substitution of input and output variables.

	Thermal (ANSYS)	**Electrical Equivalent**	**Symbol**
Input Variable	Temperature	Potential (Voltage)	Φ
	Heat generation	Current influx	Q
	Thermal conductivity	Electrical conductivity	K
Output Variable	Sum of thermal flux	Current density	TF

10.3 DESCRIPTION OF THE FINITE ELEMENT PROGRAM ANSYS

The equations stated above for electrical and heat conduction are for one-dimensional cases only, however Ansys is capable of solving two and three-dimensional problems. A large number of physical processes are governed by the general 'quasi-harmonic' equations [3]. One such equation, which is used by Ansys for solving heat conduction problems in three-dimensions, is the Laplace equation. This equation can be used for solving a wide range of physical processes including, heat conduction and distribution of electric potential. The equation can be written in its most basic form as shown below.

$$\frac{\partial}{\partial x}\left(k_x \frac{\partial \phi}{\partial x}\right) + \frac{\partial}{\partial y}\left(k_y \frac{\partial \phi}{\partial y}\right) + \frac{\partial}{\partial z}\left(k_z \frac{\partial \phi}{\partial z}\right) + Q = 0 \qquad (10.8)$$

The use of this equation for solving this type of problem is widely accepted. Ansys solves this equation using complex mathematical techniques, which are beyond the scope of this project and therefore will not be described.

10.4 MESHING OF GEOMETRY

In order to find the finite element solution to a problem it is firstly necessary to input the geometry of the component to be analysed into the package. After this step has been completed, the geometry is divided into smaller areas, called elements, which form a mesh. The mesh size and element shape, are predefined before the geometry is meshed. A finer mesh with smaller

elements provides a more accurate solution compared to a coarser mesh. This is illustrated in Figure 10.2 below.

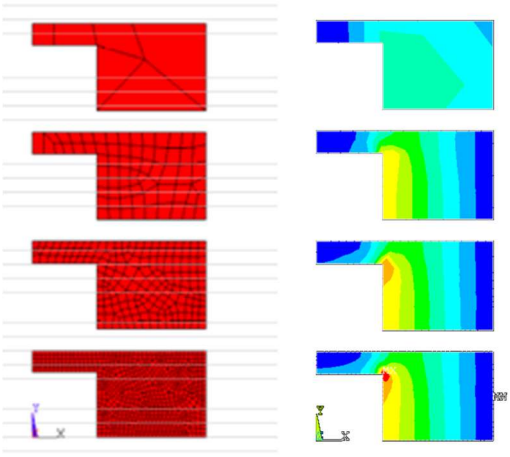

Figure 10.2: Effect of mesh size on finite element solution (coarse mesh - top / fine mesh - bottom)

Solution accuracy is also influenced by element type. Generally elements can be defined in terms of their shape and the number of nodes or integration points. Larger numbers of integration points allow a more accurate solution for a given size of element. For the purposes of this project, a two-dimensional model utilising two-dimensional flat elements was used.

An advantage of using a coarse mesh and simple element is to reduce the time taken by the computer to calculate the solution. For the size of the geometries modelled in this project even the most finely meshed only took Ansys seconds to calculate an answer, therefore there was no advantage to using a coarser mesh. The element type used was a two-dimensional 4 node quadrilateral solid element, referred to in the Ansys guide as *PLANE55*. In order to ensure consistency of results element and mesh size were kept the same for all calculations.

10.5 ANSYS OUTPUT

Once the solution to a problem has been obtained, Ansys is capable of calculating the thermal flux, TF, in each direction. This can be calculated at the centre of each element or at the nodes. The output command used was *'sum of thermal flux'* which is calculated using the values of thermal flux in each of the three directions, x, y and z, using equation 10.9. Since the model of the grid is two dimensional, TF_z, can be assumed to be zero.

$$TF_{SUM} = \sqrt{\left(|TF_x|^2 + |TF_y|^2 + |TF_z|^2 \right)} \qquad (10.9)$$

The net sum of thermal flux, TF_{SUM}, is represented in the form of a contour plot. Positions of contour lines are determined from the flux gradient of the surrounding area and do not correspond to the positions of elements or nodes where the fluxes are calculated.

10.6 APPLICATION OF INPUT VARIABLES INTO MODEL

After the component geometry is defined and meshed, temperatures and heat generation rates are applied onto the nodes. Nodes defining the edge of the grid wire are set at a constant temperature (potential), while heat generation (electron flux) is applied to the remaining nodes. This is shown diagrammatically in Figure 10.3 below.

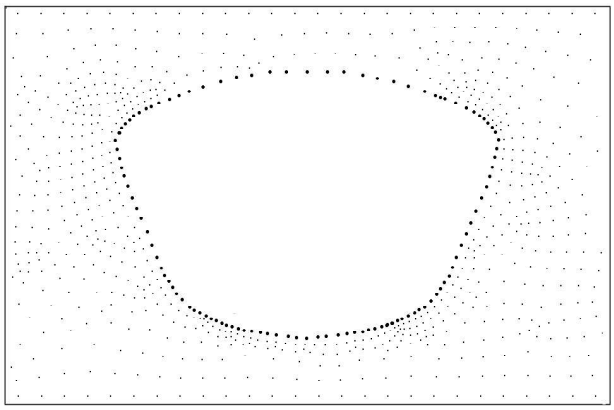

Positions of nodes are represented by dots on the diagram
Large dot (•) = Node where a constant temperature (or potential) is applied
Small dot (·) = Node where constant heat generation rate (or current influx) is applied

Figure 10.3: Application of loads onto nodes of meshed geometry

For this analysis, the properties of the active material are assumed to be isotropic, requiring the *'isotropic material properties'* option within Ansys to be used when inputting a value for conductivity.

10.7 ASSUMPTIONS

The flow of electrons between the positive active material and lead grid during the operational life of a battery is influenced by a number of factors. It would be impractical to include these within the finite element model therefore it is necessary to make a number of assumptions, details of which are given below.

- **Active material conductivity**

  During discharge of the positive electrode lead dioxide is converted into lead sulphate. Lead sulphate is an insulator, therefore the proportion of the plate consisting of lead dioxide reduces during discharge and the resistance of the active material increases accordingly. However, this reaction does not occur uniformly throughout the bulk of the active material

so variation of conductivity with position relative to the grid wire and electrode surface may also occur. An attempt to incorporate these changes into the model would prove to be highly problematic and for this reason it is assumed that the conductivity of the active material is constant and uniform throughout the electrode.

- **Active material cracking**

  Cracks are often observed within the bulk of the active material and at the grid/corrosion layer and corrosion layer/active material interfaces. Cracking will influence current density, as current flow will concentrate in areas of good electrical contact adjacent to cracked regions. Cracks form between the grid and positive active material during curing, or as a result of stresses caused by the changing dimensions of the active material while cycling. The geometry of the grid will influence the formation of cracks to a certain extent as sharp corners can act as areas of stress concentration, however, variations in current density are unlikely to be a significant contributor to the formation of cracks. It would be extremely hard to reliably predict where cracks may form on a grid wire and for this reason they are not included in the model.

- **Corrosion layer**

  The corrosion layer is not included in the model. When the corrosion layer is uniform it will not influence current density and can therefore be excluded. Variations in corrosion layer thickness will influence current density. However obtaining reliable values to enter would be extremely difficult and would not contribute significantly in determining the best grid design.

10.8 SELECTION OF INPUT VARIABLES

The fundamental difference between the model and battery electrode is that the input variables entered in the model are constants where as in the battery they vary depending on parameters such as discharge rate and depth of discharge. This makes quantitative estimations of actual current density values extremely difficult. However, the aim of this investigation is to evaluate different grid designs and this can be done if variables are kept constant. For this reason all grid geometry of the grids analysed are to the same scale and have the same loads applied, meaning that all variations in the solutions are a result of geometrical differences alone. The actual quantities entered into the Ansys model are shown in Table 10.2 below.

Table 10.2: Quantities inputted into Ansys model

Variable	Variable value entered into model
Constant temperature node	0
Constant heat generation	1
Isotropic conductivity	1

10.9 CONSIDERATIONS REQUIRED FOR USING A 2-D MODEL TO REPRESENT A 3-D PROBLEM

The positive electrode is a three-dimensional component of the battery consisting of a lead grid surrounded by current producing positive active material. The task of inputting the geometry of the grid and active material into Ansys can be simplified by considering the problem in two dimensions only. Two-dimensional sections of the electrode can be taken, in the plane, or perpendicular to the orientation of the electrode. Figure 10.4 shows a three-dimensional representation of a small section of positive electrode with the sections marked.

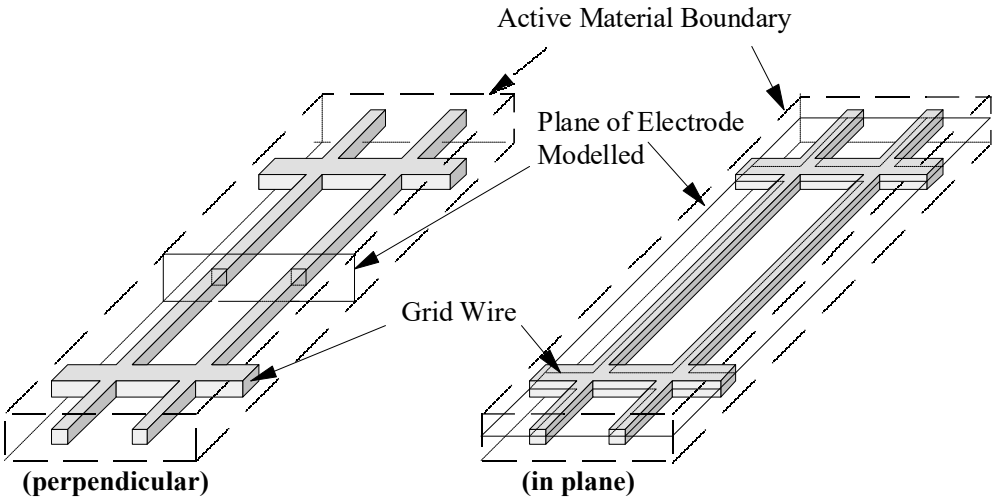

Figure 10.4: Sections taken when modelling positive electrode

The actual cross-sectional shape of the grid wire is not square, as shown in the diagram above, but a trapezoidal shape with curved edges. It is therefor symmetrical in the vertical plane but not in the horizontal. If the 'in-plane' section is modelled a certain amount of flux would flow in the 'z' direction (out of the paper), however the flux in the x and y directions can be predicted. Figure 10.5 below shows the variations in current density for a grid hole.

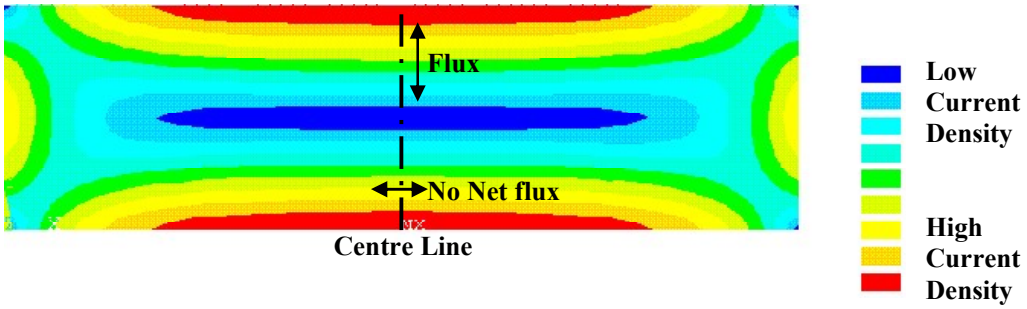

Figure 10.5: Variations in current density for a grid hole

The current density pattern shown in the diagram is symmetrical about the centre line, indicating that on this line there is a flow of flux in the vertical direction but not in the horizontal. It follows that if a perpendicular slice of the electrode is modelled in this position the net flow of flux in the z direction will be zero and the model will be accurate.

10.10 EVALUATION OF CURRENT GRID DESIGN

Dimensions of the grid design, currently in use by Hawker Energy, are shown in Figure 10.6a. The design consists of a rectangular grid with a curved trapezoidal shaped grid wire cross section. The grid is produced from a lead strip which has the rectangular grid holes punched out automatically. The cross section of the grid wires changes to a more square shape towards the regions where the wires cross. The section shown in Figure 10.6b is taken from a mid-point and is therefore representative of the majority of wire cross-section.

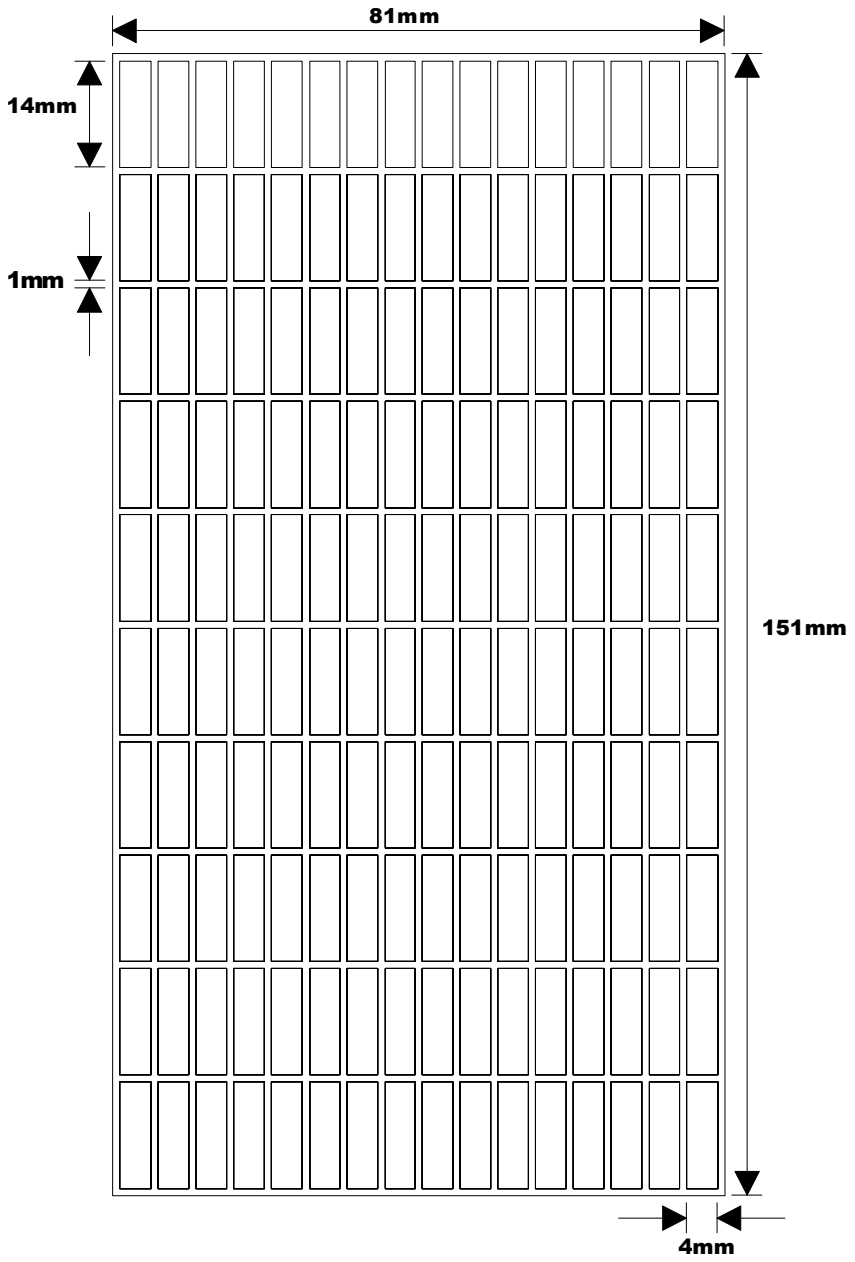

(Note: 'Tab' used to attach cast-on-strap is not shown)

(a)

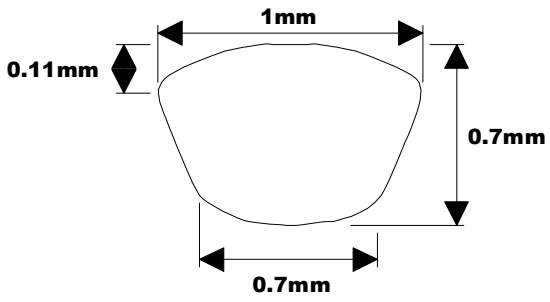

(b)

Figure 10.6: Dimensions of Cross section of the Positive electrode

During pasting the grid is coated in a layer of positive active material. For the purposes of this study an electrode thickness of 1mm was used. In order to model a component it is only necessary to enter a single repeating unit of the structure, represented by the shaded area in Figure 10.7 below. This area was chosen as it allows a non-symmetrical grid wire shape to be modelled.

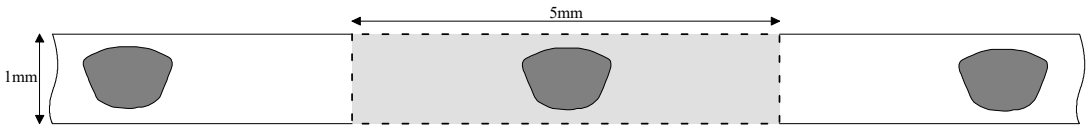

Figure 10.7: Positive electrode cross-section showing area modelled

A typical cross-section from the bad cell of a battery cycled 92 times is shown in Figure 10.8. A uniform corrosion layer is visible around the top and bottom surfaces of the wire, however, substantial thickening of the layer has occurred on the upper part of the sides.

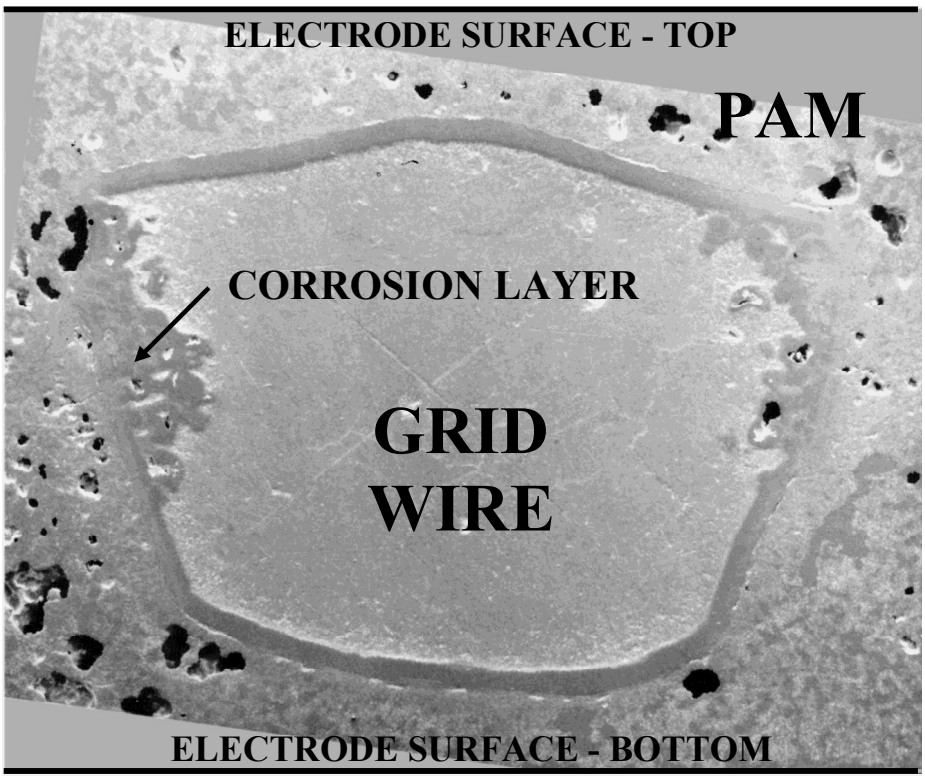

Figure 10.8: Cross-section of grid wire showing thickening of corrosion layer

The variation in current density produced when the geometrical arrangement of the grid wire shown in Figure 10.8 is entered into Ansys is shown in Figure 10.9a and b. Figure 10.9a shows a cross-section of grid wire with surrounding positive active material and Figure 10.9b is a close-up of the grid wire showing the current density around the surface of the grid wire.

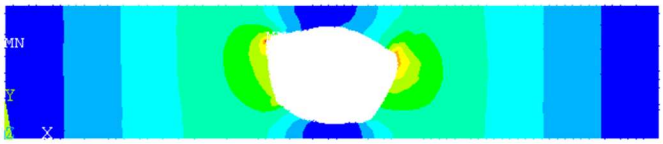

(a)

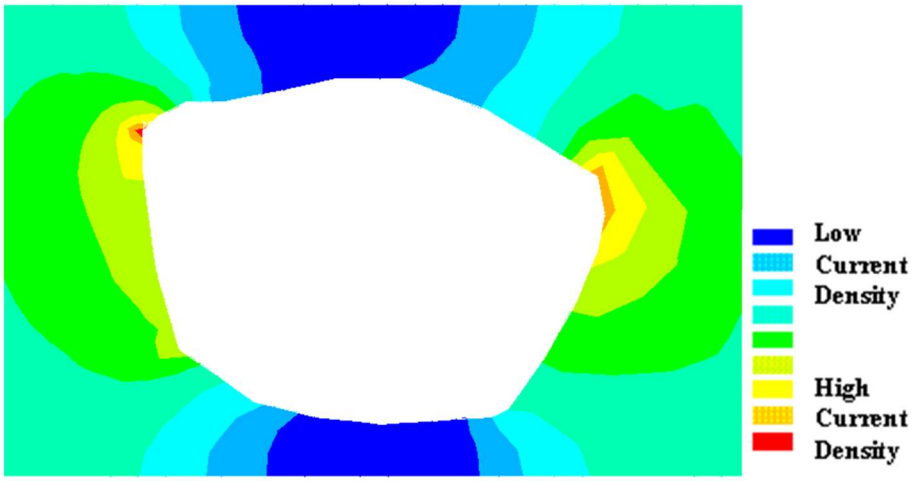

(b)

Figure 10.9: Current density distribution around a battery grid wire.

The areas of high corrosion layer thickness in figure 10.8 correspond to the areas of high current density shown in

10.11 EFFECT OF GRID WIRE ORIENTATION ON CURRENT DENSITY DISTRIBUTION

During the grid production and pasting processes of battery manufacture, grid wires can sometimes become rotated about their central axis. This can result in a variation in current density distribution around the grid wire surface. Figure 10.10 shows the current density distribution around two grid wires, orientated at 0° and 40° respectively.

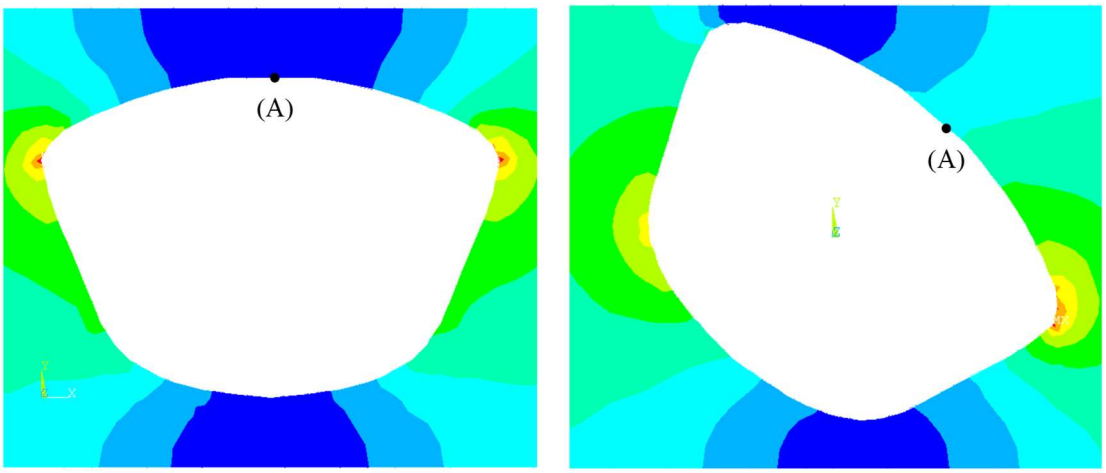

Figure 10.10: Effect of grid wire rotation on current density

The variations in current density distribution can be compared more easily if the normalised current density is plotted against distance around the grid wire. This is shown in Figure 10.11 below.

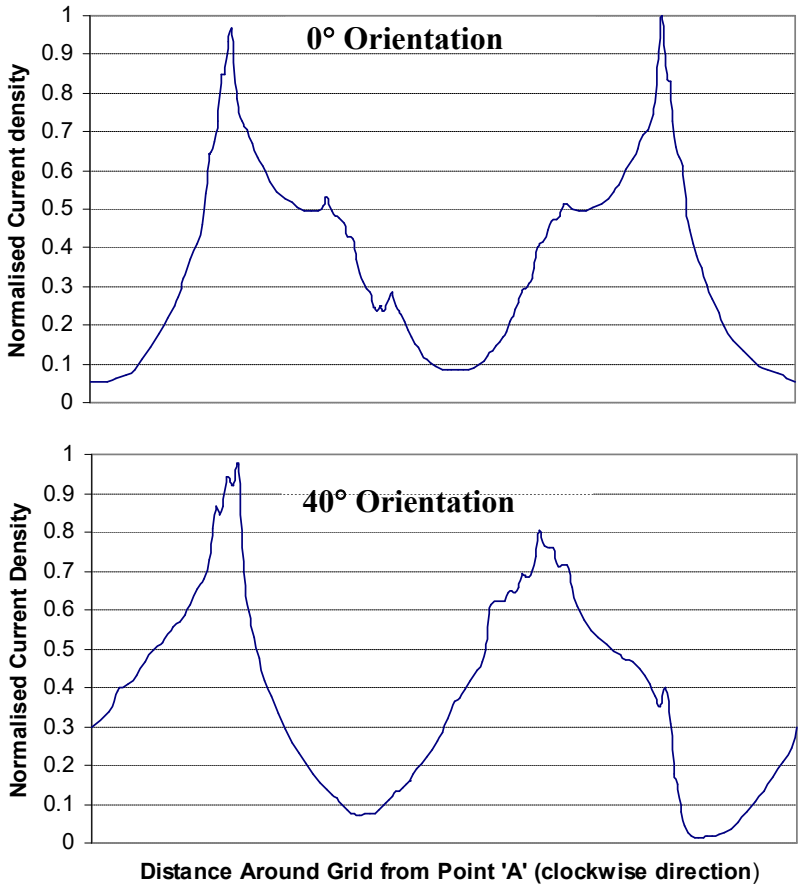

Figure 10.11: Current density versus position around grid wire

Theoretically, the curves shown in Figure 10.11 above would be smooth, however, they each contain a number of perturbations. This is caused by inconsistencies due to the mesh size and

can be ignored. In comparing the curves, the effect of rotating the grid wire is to reduce the maximum current densities on each side. Grid wire orientation is therefore not an important factor and would not be expected to affect battery performance in terms of corrosion layer growth adversely.

10.12 GRID WIRE MODIFICATION

In order to reduce the probability of a thick corrosion layer forming on the surface of the positive electrode grid, the current density on the surface must be as low as possible. This can be achieved by modifying the electrode to produce as uniform and low a current density distribution as possible. The obvious way to achieve this is to modify the geometrical arrangement of the grid and active material. However, the points listed below must be considered when proposing new electrode designs.

- **Mechanical Strength**

  During manufacture the grid is rolled, pasted and cut into individual electrodes. These processes put the grid under mechanical stresses unlike those experienced during battery operation and any grid design must be able to withstand these.

- **Mechanical stability during corrosion**

  As a battery grid corrodes the lead is converted into lead oxides of varying oxygen content. The consequential reduction of the grid wire cross-section, results in a decrease of mechanical strength and conductivity. Consideration must therefore be given to the strength of the grid wire after a certain amount of surface corrosion has occurred.

- **Grid Weight**

  For many batteries weight is an important factor and it is advantageous to have as light a grid as possible.

When comparing different electrode designs any variation in current density must be a consequence of grid design only and not of size. To ensure all designs could be compared with each other the grid and active material cross-sectional areas were kept the same as that of the original electrode. Dimensions of the grid designs investigated are given in Table 10.3 below.

Table 10.3: Dimensions of grid designs investigated

Design	Dimensions (mm)	C.S.A. (mm2)	Circumference (mm)	Normalised circumference
Circle	Diameter = 0.82	0.54	2.58	0.95
Square	Width = 0.74	0.54	2.94	1.08
Hexagon – 0	Width = 0.79	0.54	2.74	1.01
Hexagon – 30	Width = 0.79	0.54	2.74	1.01
Hawker Energy Design	Height = 0.7 Width = 1	0.54	2.71	1

The current density distributions around the grid wire for each of the designs in table 10.3 are shown in Figure 10.12.

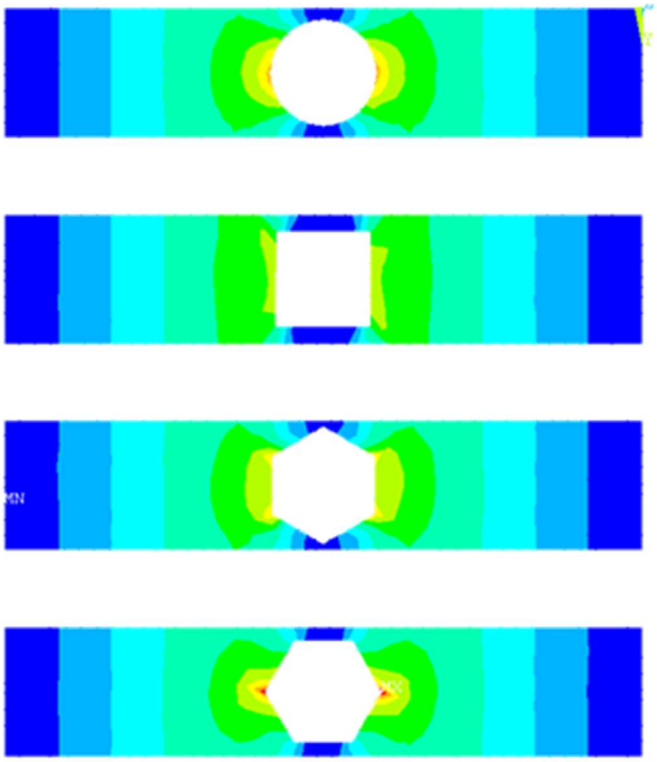

Figure 10.12: Current density around new grid cross-sections

Plotting the normalised current density against distance around the grid allows the magnitude of the current densities to be compared more easily. This is shown in Figure 10.13.

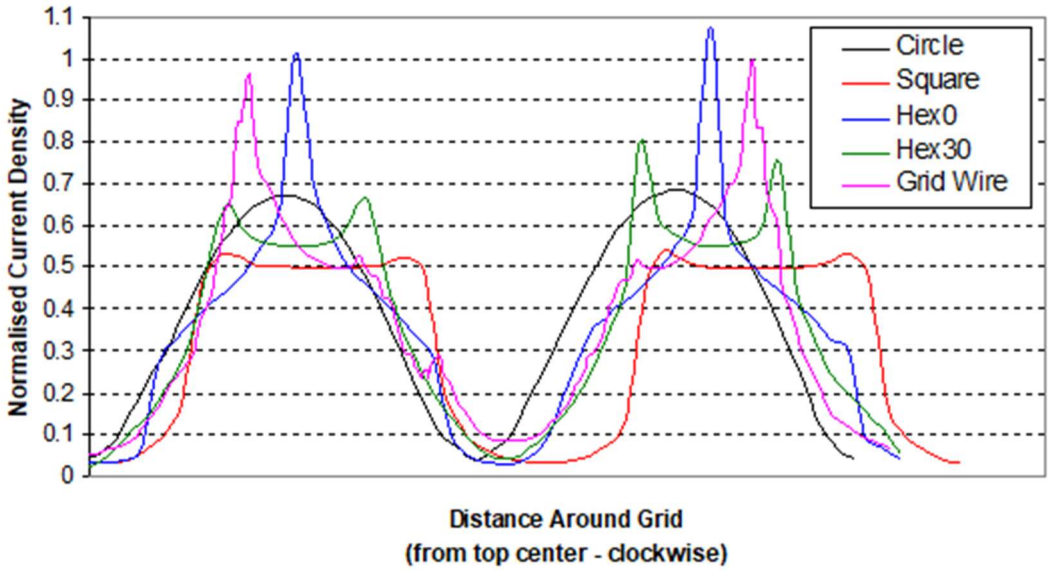

Figure 10.13: Variations in current density on surface of different grid designs

From Figure 10.13 it can be seen that there are differences in the value of current density obtained on each side of the wire. These can be accounted for by variations in the meshing generated by the computer.

The maximum current density was obtained from the 0-degree orientated hexagon, followed by the original grid design, 30-degree orientated hexagon, circle and then square. This is an interesting result as the relatively 'pointed' corners of the square do not appear to affect the current density significantly and the circle, which does not contain any 'pointed' surfaces, produces a higher maximum current density. This result highlights the influence of the amount of active material that surrounds the grid surface and suggests that re-arranging the geometry of the active material could be a much more effective method of reducing current density.

10.13 EFFECT OF CHANGING POSITIVE ACTIVE MATERIAL GEOMETRY

To investigate the effect of modifying the active material distribution around the grid wire a series of models were set up where these changes were represented. Contour plots for a range of positive active material distributions are shown in Figure 10.14.

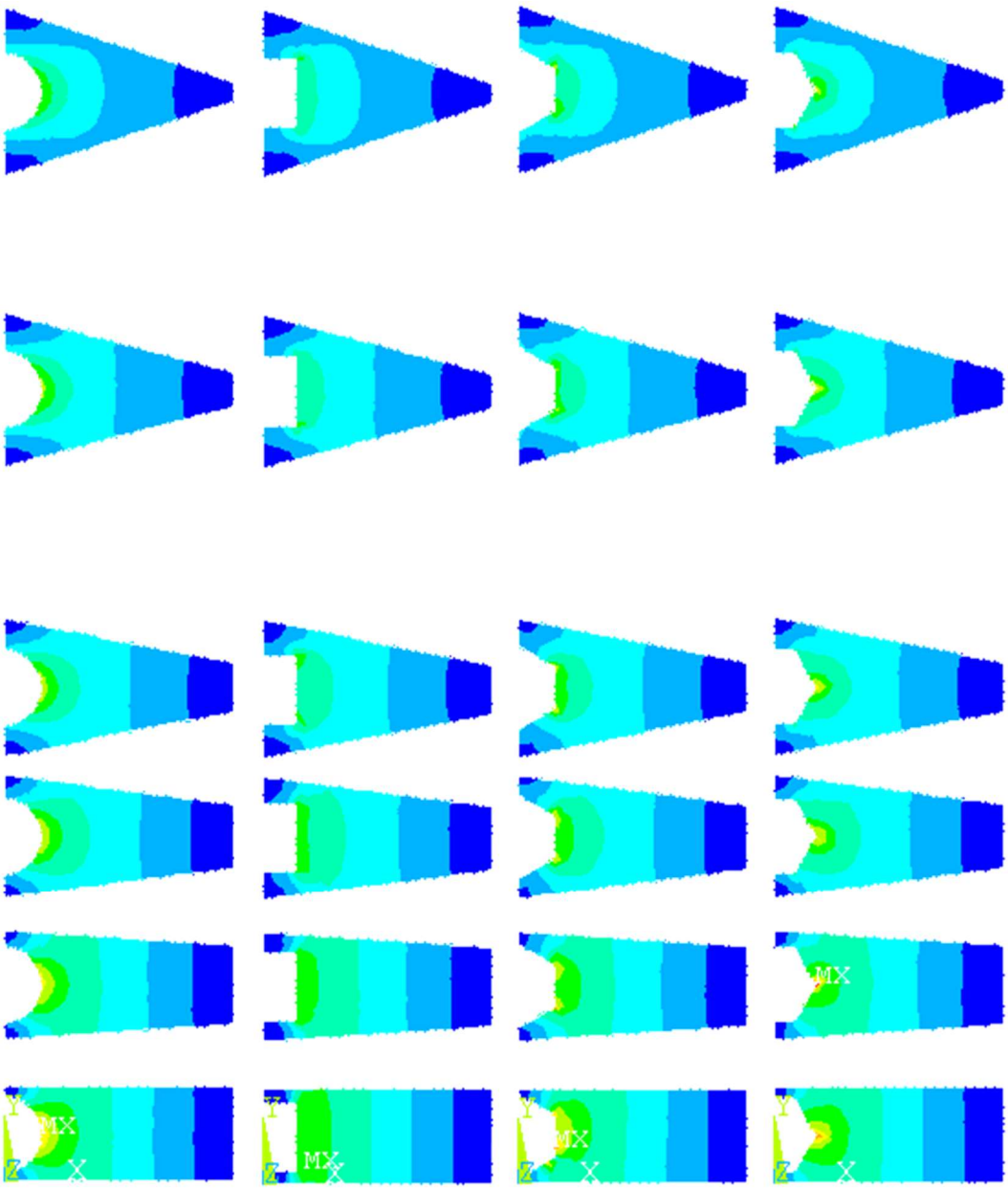

Figure 10.14: Effect of positive active material geometry on current density distribution around grid wire.

The effect of increasing the amount of active material on the top and bottom of the grid wire is clearly evident. It can be seen that increasing the amount of active material in this way proportionally increases the current density in these regions resulting in a decrease of the peak current density at the sides of the grid wire, where the maximum values was formerly seen to occur.

A cross section through a hypothetical battery design implementing this principle is shown in Figure 10.15.

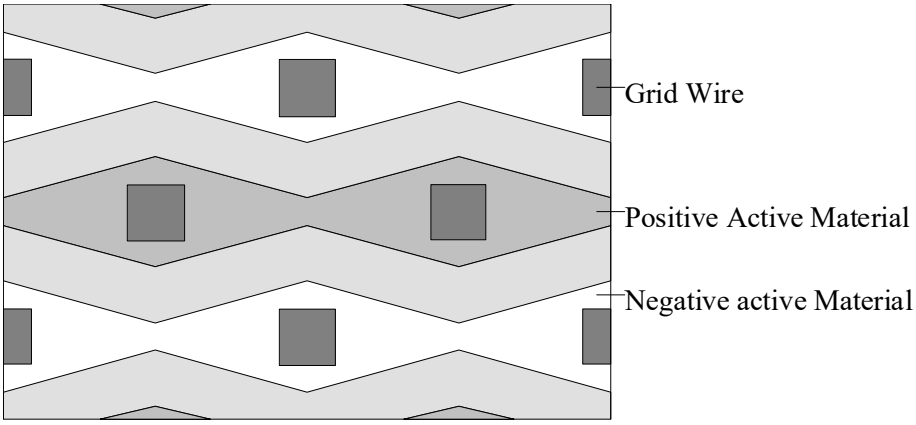

Figure 10.15: Cell design to reduce current density

In order to implement this arrangement it can be seen that it is necessary to offset the grid wires in the positive and negative electrodes relative to each other. Although there would be clear advantages, as described, in adopting this arrangement, there are likely to be practical problems in implementing this concept where grid wires run in an orthogonal arrangement. One possible solution would be the construction of a battery where the grid wires ran in one direction only. The effect of this on the assembled electrode stiffness and strength, and the implications for a completed battery would need to be assessed. Intuition suggests that considerable stiffness will be lost.

10.14 CONCLUSIONS

The following conclusions can be drawn from the investigations.

1. Grid wire and positive active material geometry affect corrosion layer thickness.
2. Rotation of grid wires does not result in an increased current density distribution on the wire surface.
3. Current density distribution is greatly affected by grid shape
4. Due to the uneven distribution of positive active material around the grid wire a design with sharp edges, such a square, does not necessarily have a lower current density distribution compared to a circle.
5. Changing the geometry of the positive active material surrounding the grid wire can have a significant effect on reducing the current density distribution.

10.15 REFERENCES

1. D. Pavlov, A theory of the grid/positive active-mass (PAM) interface and possible methods to improve PAM utilisation and cycle life of lead/acid batteries, Journal of Power Sources, Vol. 53, (1995), pp. 9-21

2. ANSYS, Inc. Southpointe 275 Technology Drive, Canonsburg, PA 15317, ANSYS Theory Reference. 000855. Eighth Edition. SAS IP, Inc©
3. O.C.Zienkiewicz, The Finite Element Method in Engineering Science, McGraw-Hill.London

11 RESULTS AND DISCUSSION: SEPARATOR STUDY

11.1 INTRODUCTION

Battery performance is influenced by the separator type specified in the design. Hawker Energy currently use separator papers manufactured by Hollingworth and Vose (H+V) for the construction of their batteries. In this chapter results from a study to investigate the use of alternative separator types is described.

The approach adopted was to build a number of batteries of similar design using the same active materials but with different separator papers. Each battery was tested using a C5 cycling regime until the failure point, at 80% of the original capacity, was reached. Three different separator papers were compared in the study, details of which are given in Table 11.1. Due to difficulties in acquiring sufficient samples of Hollingworth and Vose 8% polyester separator paper it was not possible to conduct all the tests described in this chapter on this paper type.

Table 11.1: Types of separator paper used in the construction of test batteries

Separator Type	**Weight** (g/m^2)**	**Composition (%)*****	
		Glass	**Polyester**
Hollingworth & Vose	146.56	100	0
Hollingworth & Vose 8% Polyester *	181.96	92	8
Technical Fibre Products	144.44	100	0

*Due to shortage it was not possible to conduct all the tests carried out on this separator type.
**Measured value
***Manufacturers value

11.2 CHARACTERISATION OF BATTERIES MANUFACTURED USING DIFFERENT SEPARATOR PAPERS

The performance of each battery type was compared by plotting the discharge time against cycle number, as shown in Figure 11.1.

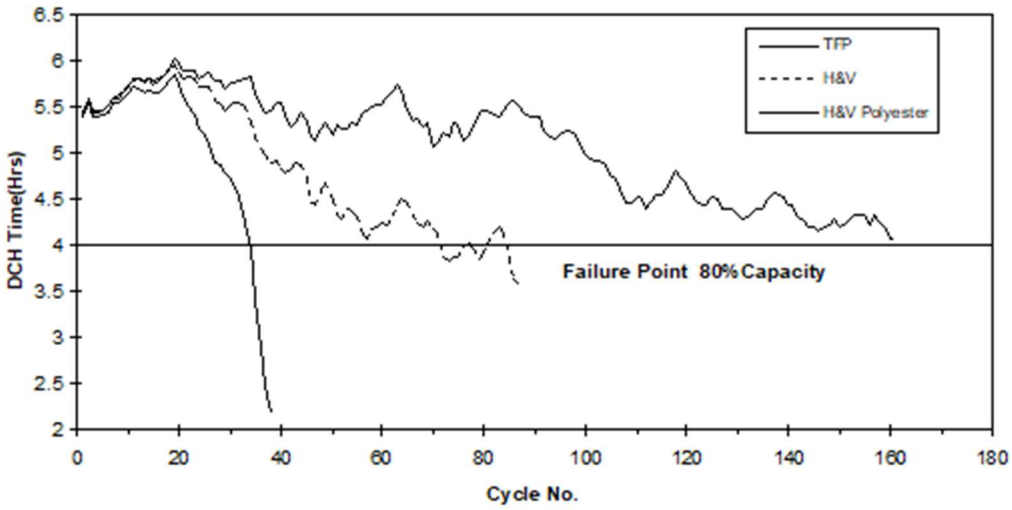

Figure 11.1: Discharge time versus cycle number for separator types used in the manufacture of test batteries [1]

From the figure it can be seen that there is a significant difference in performance between the batteries containing each separator type. The battery containing Hollingworth and Vose (8% polyester) separator paper was the first to fail at approximately 35 cycles. The second to fail was the battery containing Hollingworth and Vose (glass) separator paper at approximately 70 cycles. The final battery to fail was that containing Technical Fibre Products (glass) separator paper at over 160 cycles. Previous tests carried out by Hawker Energy, Newport, on batteries manufactured from these separator types indicated similar trends in performance to those described above [2].

Voltages of the cells in each battery type were monitored during a C1 capacity discharge to 4V in order to identify the good and bad cells. Results indicated that all batteries failed due to the degradation of a number of cells rather than a single failed cell.

11.2.1 ELECTRICAL TESTING OF INDIVIDUAL BATTERY ELECTRODES

During battery operation the potential of the positive and negative electrodes can vary, depending on the diffusion of ions through the electrolyte and oxygen gas through pores in the separator. The potential of the positive and negative plates in the good and bad cells of each battery examined, were measured relative to a mercury sulphate reference electrode for a discharge (7.05A to 6V)/charge cycle. Variations in potential of the electrodes in each cell examined are given in Figure 11.2 to Figure 11.4.

It can be seen that as the batteries are discharged the cell potentials decrease until the failure point is reached. This reduction in cell potential is a result of a decrease in the potential of the positive electrode and an increase in the potential of the negative electrode.

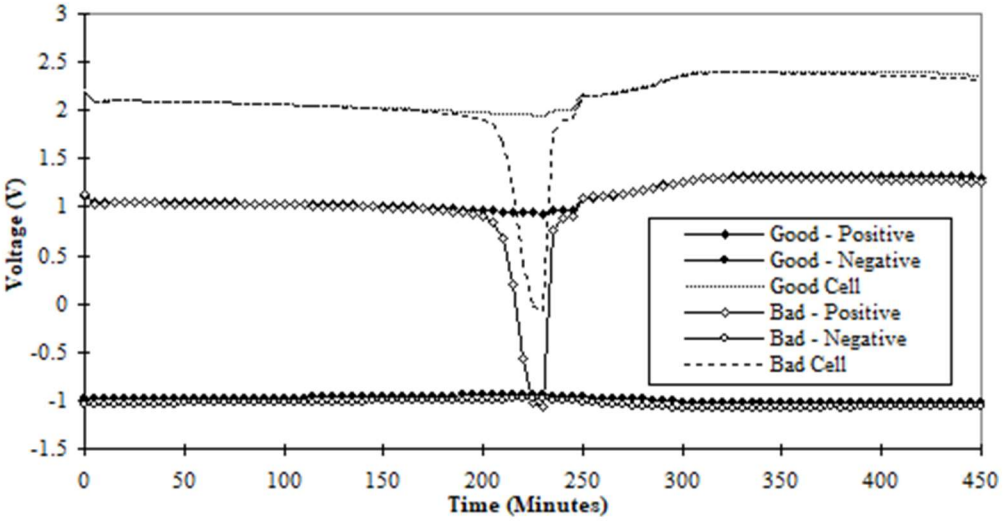

Figure 11.2: Potential of electrodes in good and bad cells of the battery containing Technical Fibre Products Separator Paper

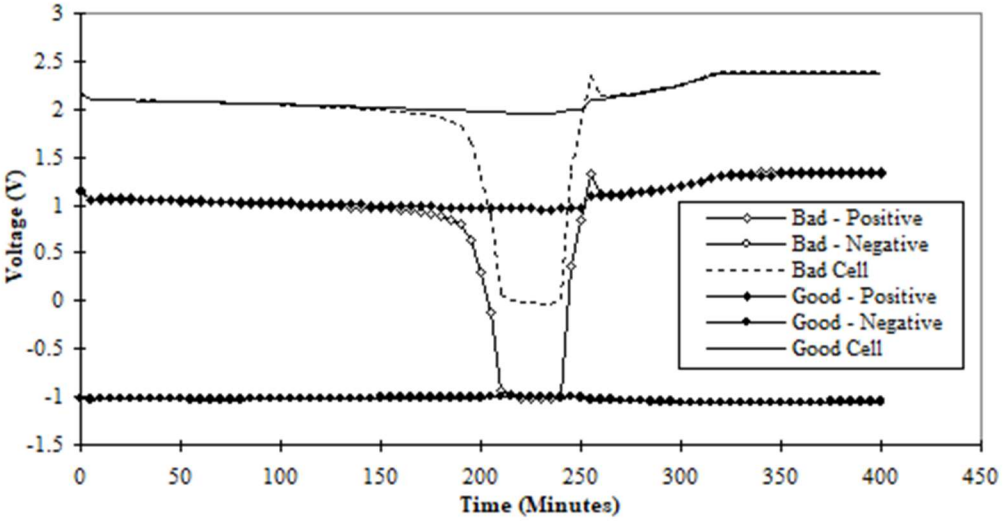

Figure 11.3: Potential of electrodes in good and bad cells of the battery containing Hollingworth and Vose (100% glass) Separator Paper

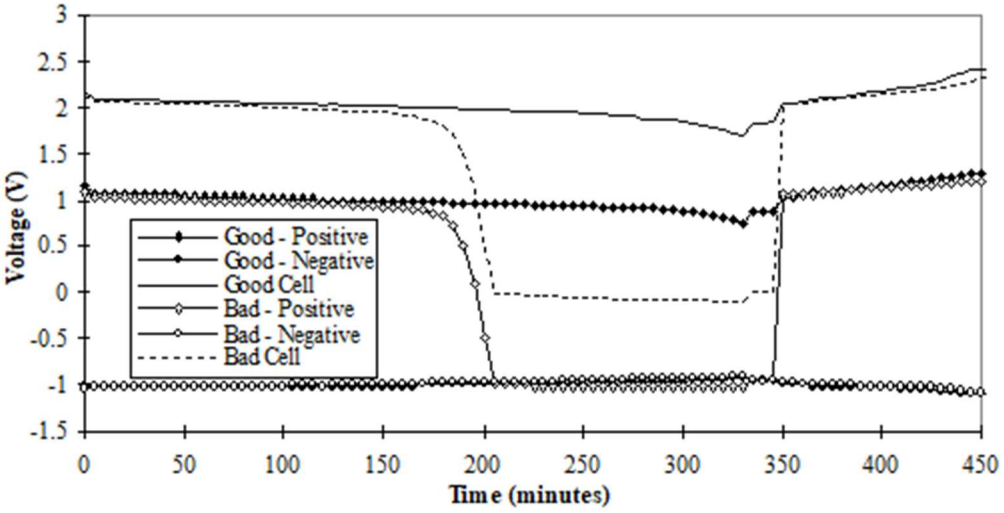

Figure 11.4: Potential of electrodes in good and bad cells of the battery containing Hollingworth and Vose (8% polyester) Separator Paper

From Figure 11.2, 11.3 and 11.4 it can be seen that the time between the start of reduction in potential of the bad cell and recharging of the battery varies for each of the batteries tested. The greatest time is observed for the battery containing Hollingworth and Vose 8% polyester separator paper, which sustained 35 cycles to failure, and the least time, for the battery containing Technical Fibre Products separator paper, which sustained 160 cycles.

The reduction in cell voltage observed in the bad cells from each of the batteries tested is a result of a reduction in potential of the positive electrode. No significant increase in potential of the negative electrode was observed for any of the batteries. This indicates that failure is due to the positive rather then negative electrode.

11.2.2 ANALYSIS OF ACTIVE MATERIALS

An analysis of the composition and BET surface area was carried out on the active materials from all batteries tested. This was done to determine whether any significant changes were present which would suggest different failure mechanisms.

Composition of the active materials was determined using x-ray diffraction and wet chemical analysis. This was done for both positive and negative plates from good and bad cells.

A compositional analysis of the positive electrodes from the good and bad cells examined is given in Figure 11.5.

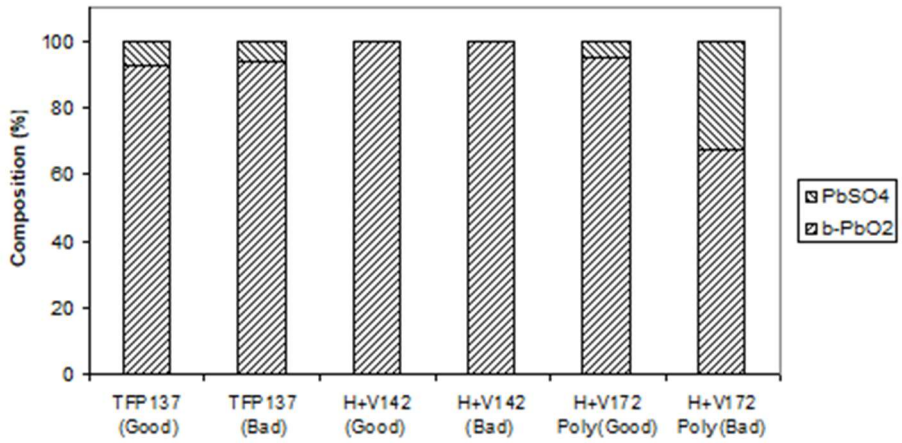

Figure 11.5: Composition of positive active material from good and bad cells

Examination of the positive electrodes revealed the presence of a small amount of sulphation in the positive plates from the batteries containing Hollingworth and Vose 8% polyester and Technical Fibre Products separator paper. This was less than 10%, except for the bad cell of the battery containing Hollingworth and Vose 8% polyester separator paper, which contained approximately 30% lead sulphate. These results correlated with the BET surface areas, Figure 11.6 which show a reduction where the larger amounts of sulphate are present.

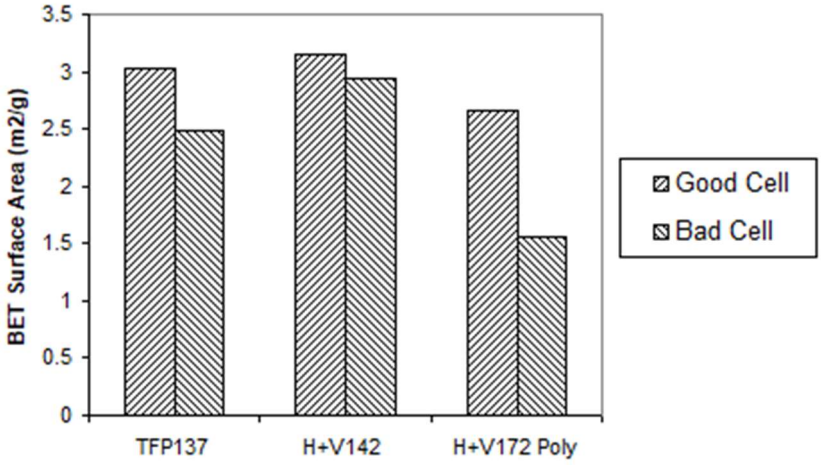

Figure 11.6: BET surface areas of positive active materials in good and bad cells

Analysis of all negative active materials revealed that the composition was 100% lead. Measurements of BET surface area for these materials are given in Figure 11.7. These results do not show any significant variation in the negative active materials from the batteries tested.

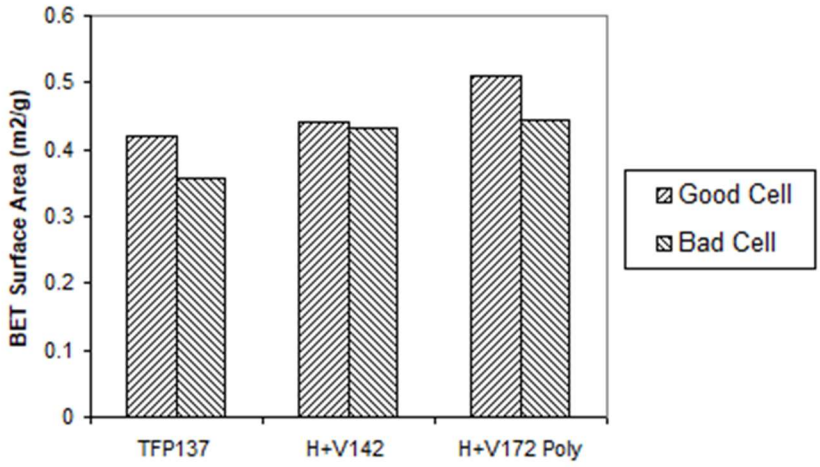

Figure 11.7: BET surface areas of positive active materials in good and bad cells

11.2.3 VARIATION IN ACID SPECIFIC GRAVITY AND SEPARATOR SATURATION WITHIN CELL

During operation of a lead acid battery variations in acid concentration are observed at different positions within the cell. This phenomenon is commonly referred to as acid stratification and can be determined by measuring specific gravity. There are several mechanisms, which contribute to stratification such as uneven discharge of the active material throughout the electrodes and the force of gravity.

Gases produced during charging can cause the movement of acid around the separator and electrodes thereby reducing the extent of stratification. The effectiveness of this process is influenced by the separator properties and for this reason stratification measurements have been taken for the cells examined in the test batteries.

The electrolyte specific gravity in five equally spaced strips positioned between the top and bottom of the cells taken from the batteries containing Hollingworth and Vose 100% glass and Technical Fibre Products 100% glass separator paper was measured. Results obtained are shown in Figure 11.8 and Figure 11.9.

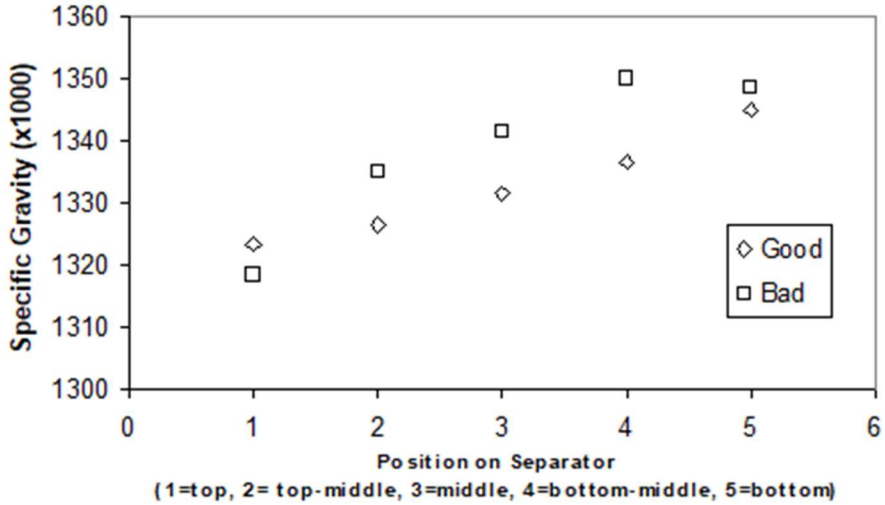

Figure 11.8: Variation in acid specific gravity with height for Hollingworth and Vose separator paper

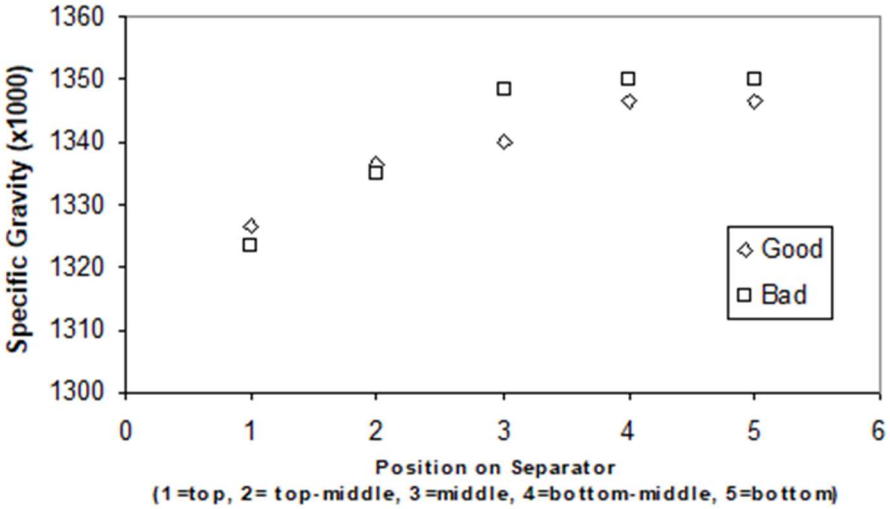

Figure 11.9: Variation in acid specific gravity with height for Technical Fibre Products separator paper

From the figures it can be seen that the specific gravity of the electrolyte decreases with cell height. The smallest stratification was observed in the battery containing Technical Fibre Products separator paper, which achieved the greatest number of cycles. This battery also showed the smallest difference in acid specific gravity between the good and bad cells.

To determine separator saturation, the weight of acid in five equally spaced strips positioned between the top and bottom of the cell was measured. The acid specific gravity at the corresponding positions was then used to determine the volume of acid and therefore saturation. Measurements of percentage saturation versus separator height for Technical Fibre Products 100% glass and Hollingworth and Vose 100% glass separator papers are shown in Figure 11.10 and Figure 11.11 below.

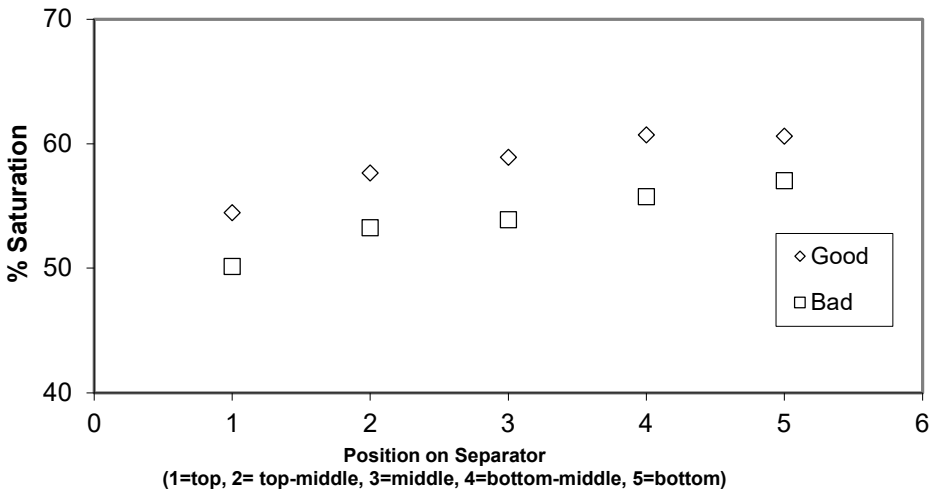

Figure 11.10: Variation in saturation with height for Hollingworth and Vose separator paper

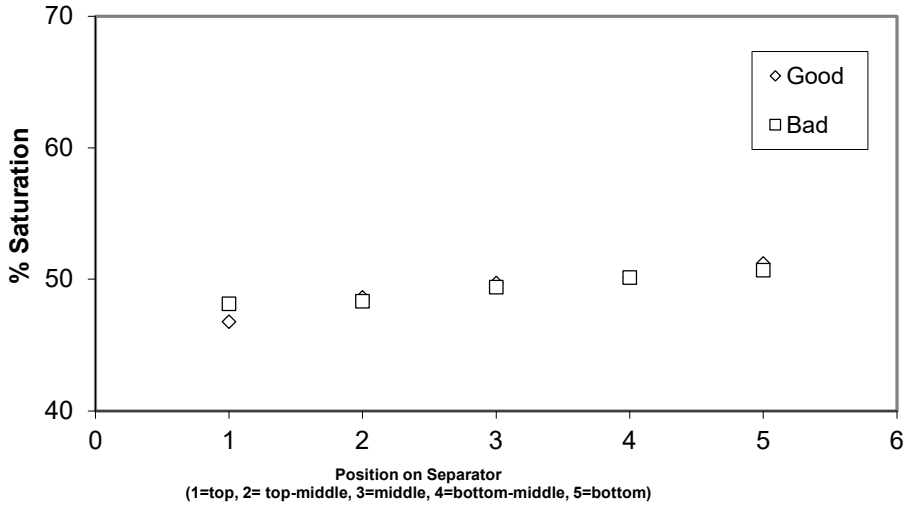

Figure 11.11: Variation in saturation with height for Technical Fibre Products separator paper

Both figures show an increase in separator saturation towards the bottom of the cell. This is likely to be due to gases escaping through the top of the cell during charging. The Technical fibre Products separator paper has a lower saturation compared to the Hollingworth and Vose. However, this is to be expected as the battery sustained the greatest number of cycles and would therefore have lost the greatest amount of water from the electrolyte. Differences in saturation with height between separators taken from the good and bad cells are greater in the battery containing Hollingworth and Vose separator paper. The implication of this is that, during battery operation, the bad cell sustained a greater amount of water loss.

11.3 CHARACTERISATION OF SEPARATOR PAPERS USED IN THE MANUFACTURE OF TEST BATTERIES

In this section results obtained from characterisation of the separator paper types used in the manufacture of the test batteries is described. A number of analytical techniques were used to characterise the papers in order to establish any connection between separator properties and performance within the battery.

11.3.1 SCANNING ELECTRON MICROSCOPY

Examination of the separator paper samples showed that each paper had a rough and smooth side. Subsequent examination in the scanning electron microscope indicated that the best representation of fibre size and orientation was obtained from the images taken from the smooth side, as more fibres were within the depth of field of the microscope.

Figure 11.12 and Figure 11.13 show low and high magnification images of Hollingworth and Vose 8% polyester separator paper respectively. Polyester fibres are visible in Figure 11.13 and are identified by their thickness, which is significantly larger then that of the glass. The polyester fibres are approximately 20 microns in diameter, and the glass fibres range in size between <1 to approximately 3.5 microns. A number of the glass fibres appear to be permanently attached to the polyester fibres. Both polyester and glass fibres show random orientation in both figures.

Hollingworth and Vose 100% glass separator paper is shown in Figure 11.14 and Figure 11.15 at low and high magnifications respectively. Glass fibres range in diameter between <1 and approximately 3.5 microns. A larger proportion of the thicker fibres appear to be orientated in the machine direction (horizontal in figure) compared to the thinner fibres.

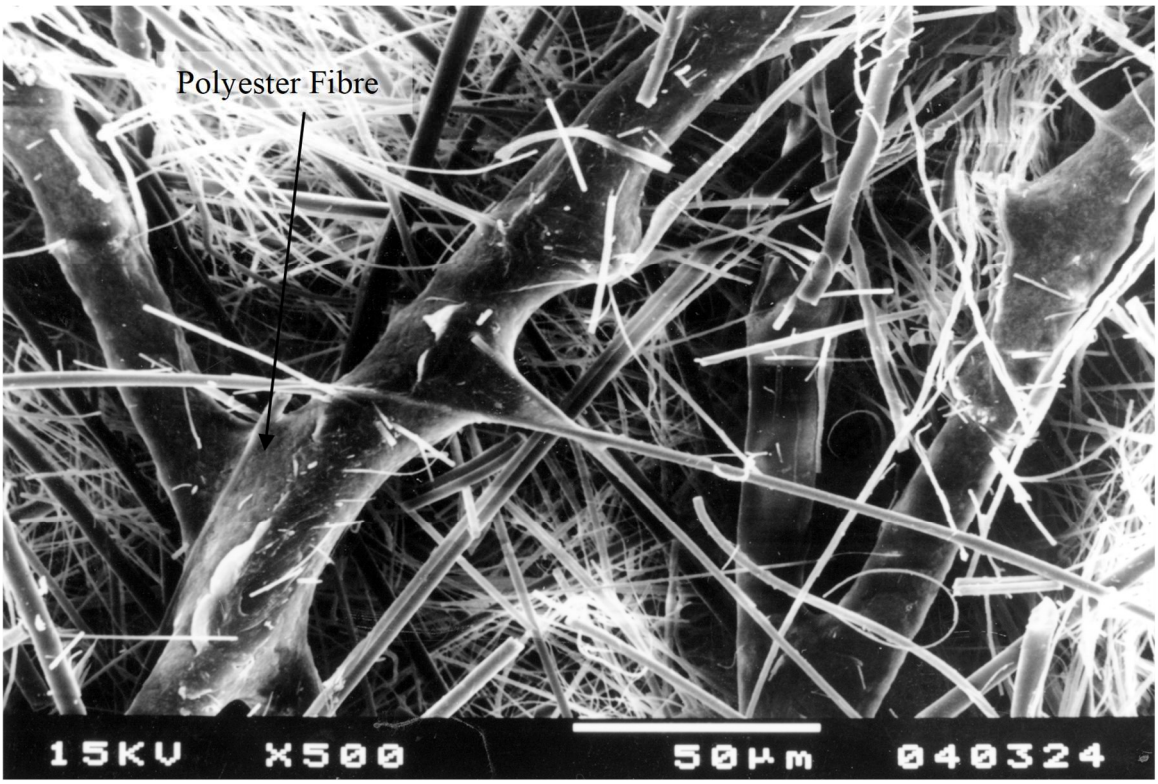

Figure 11.12: Hollingworth and Vose (8% Polyester) Separator Paper – Low magnification

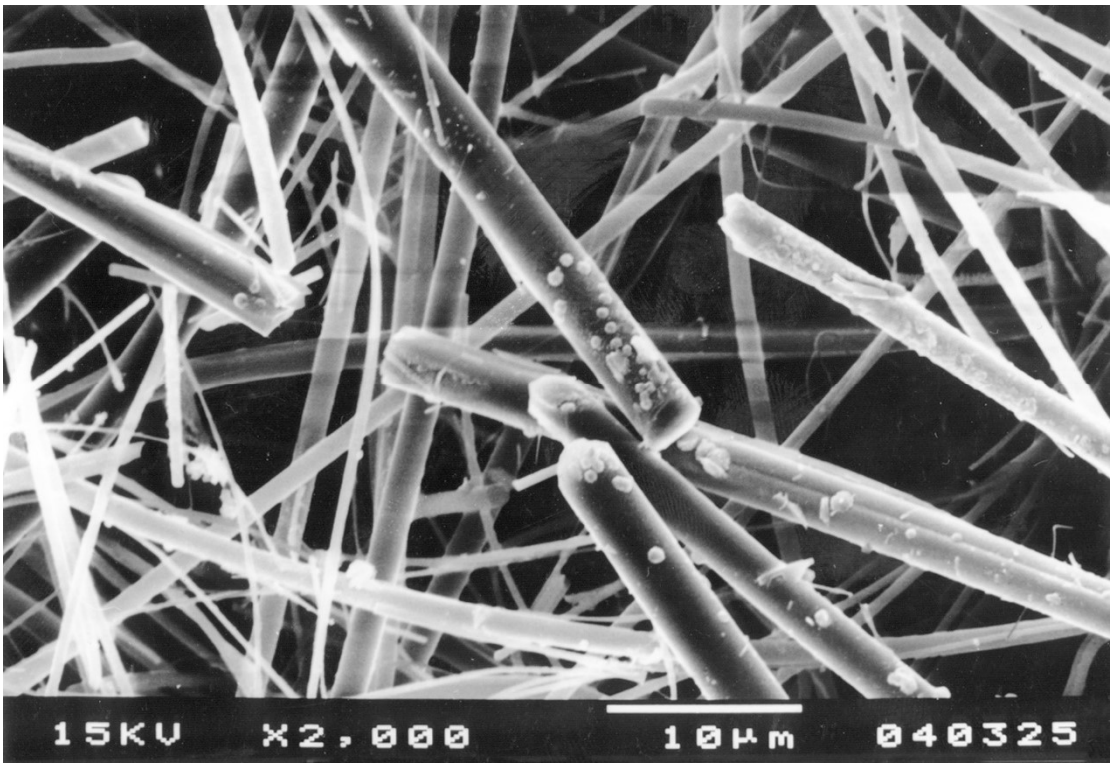

Figure 11.13: Hollingworth and Vose (8% Polyester) Separator Paper – High magnification

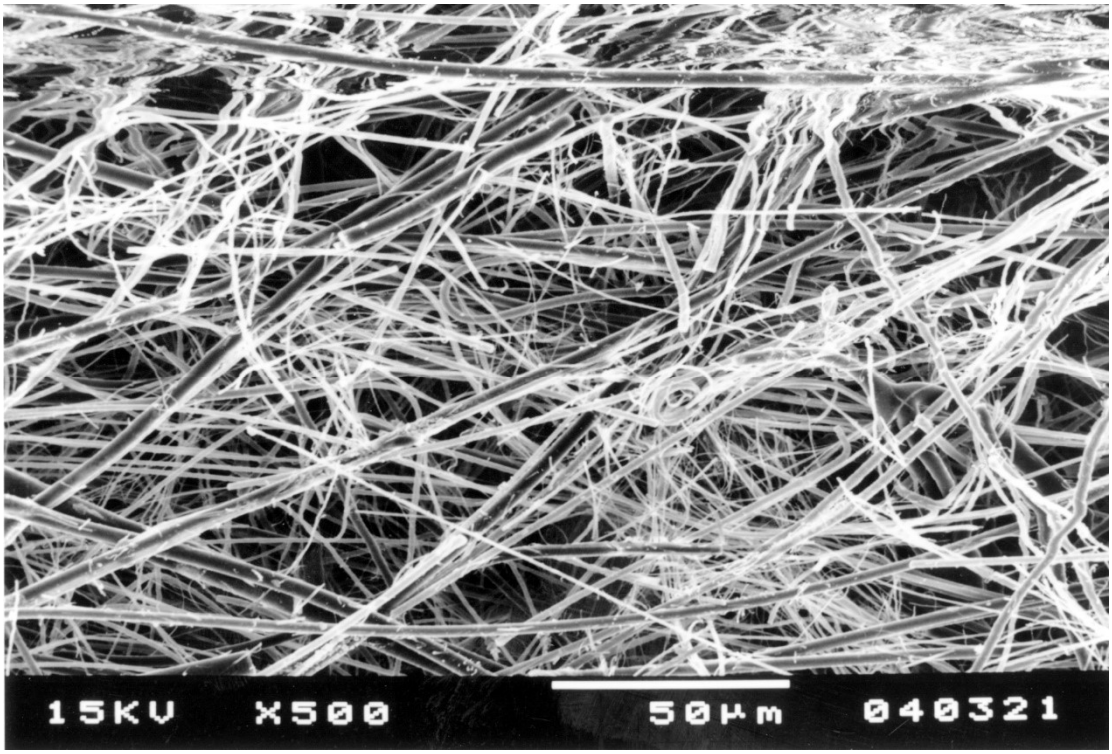

Figure 11.14: Hollingworth and Vose (100% Glass) Separator Paper – Low magnification

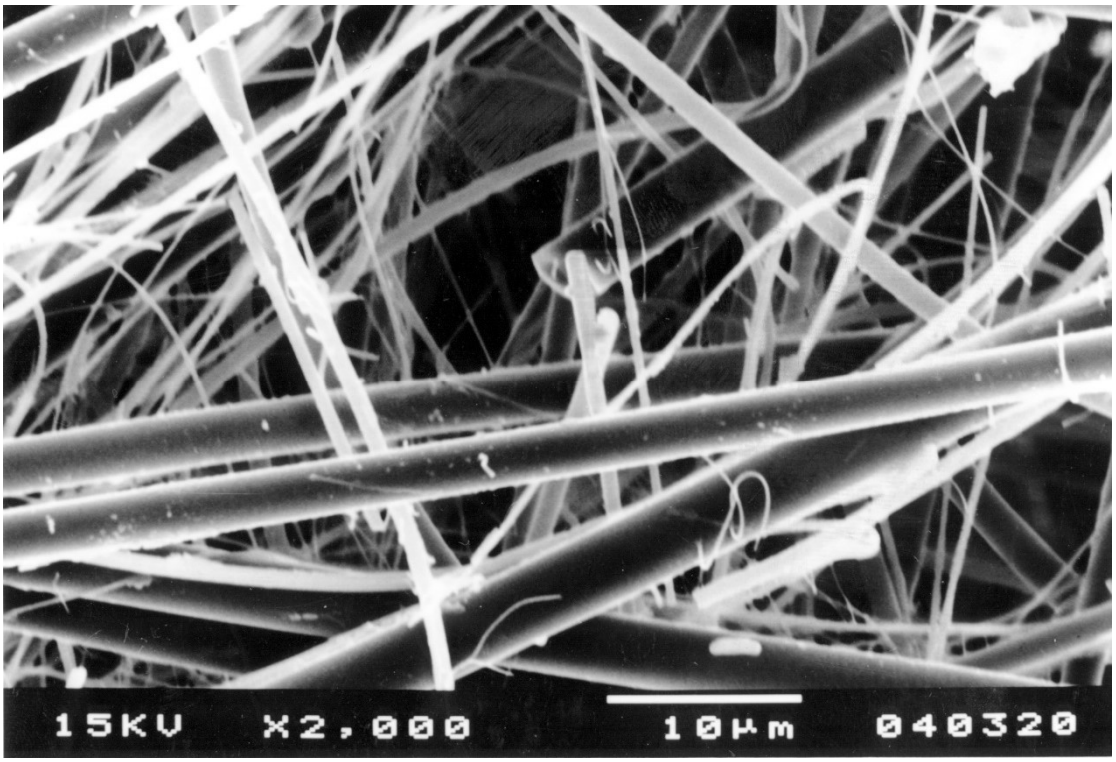

Figure 11.15: Hollingworth and Vose (100% Glass) Separator Paper – High magnification

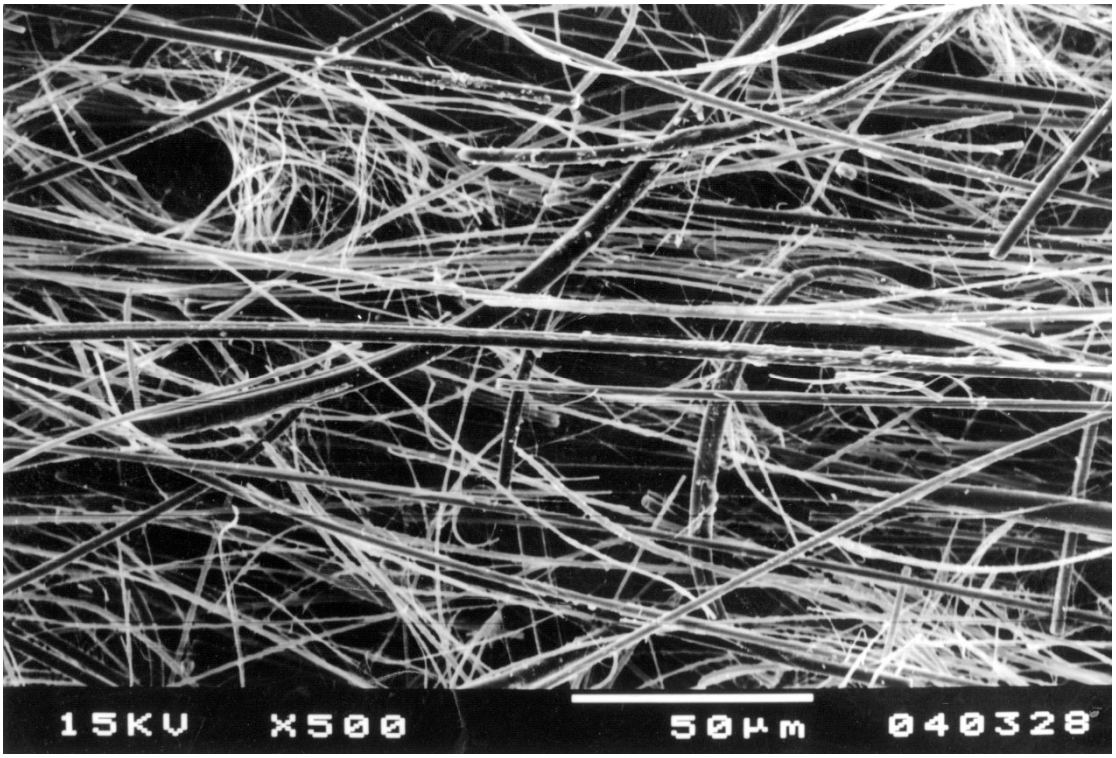

Figure 11.16: Technical Fibre Products (100% Glass) Separator Paper – Low magnification

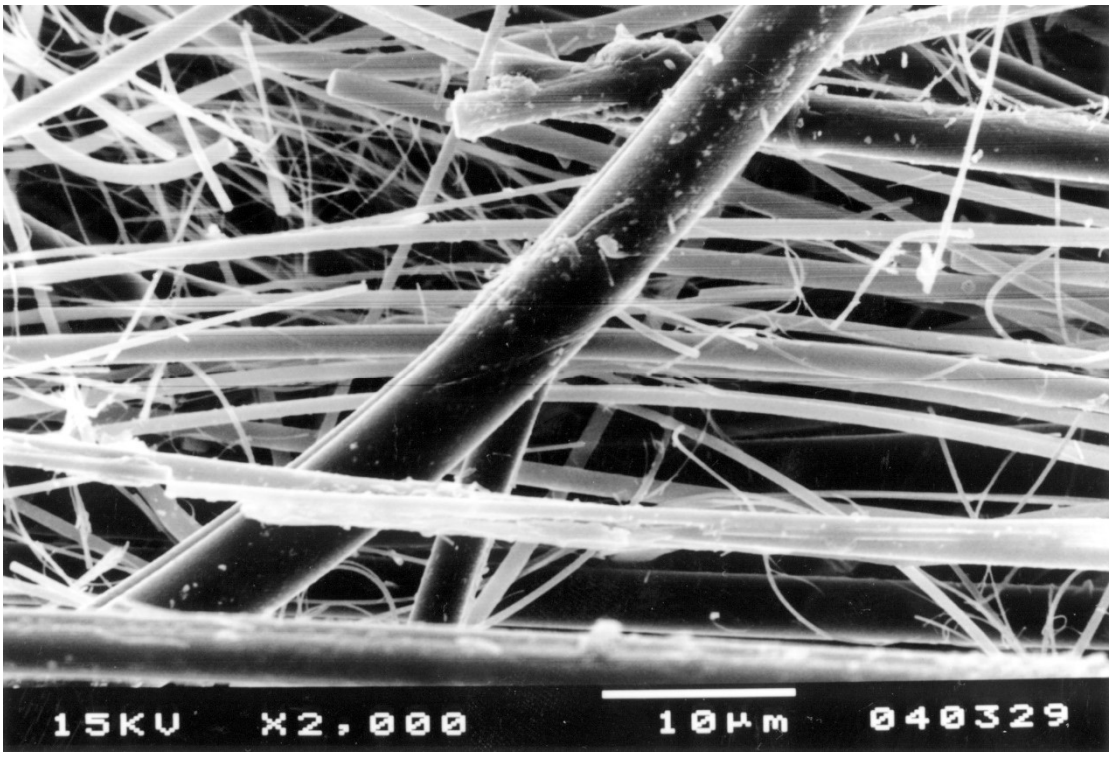

Figure 11.17: Technical Fibre Products (100% Glass) Separator Paper – High magnification

Images of the Technical Fibre Products separator paper are given in Figure 11.16 and Figure 11.17 at low and high magnifications respectively. Fibre diameters range between <1 micron to approximately 5 microns. A larger proportion of the fibres are orientated in the machine direction, compared to the other separator papers examined.

11.3.2 WICKING TESTS

Within a battery cell wicking rate will influence the time taken for the electrolyte to penetrate all areas after the initial acid fill. During subsequent operation the separator papers are not completely saturated allowing electrolyte to move between areas of differing saturation within the paper. Wicking tests were used to measure the speed at which electrolyte moves through the various separator papers by capillary flow.

Plots of time versus height squared for the separator types examined are shown in

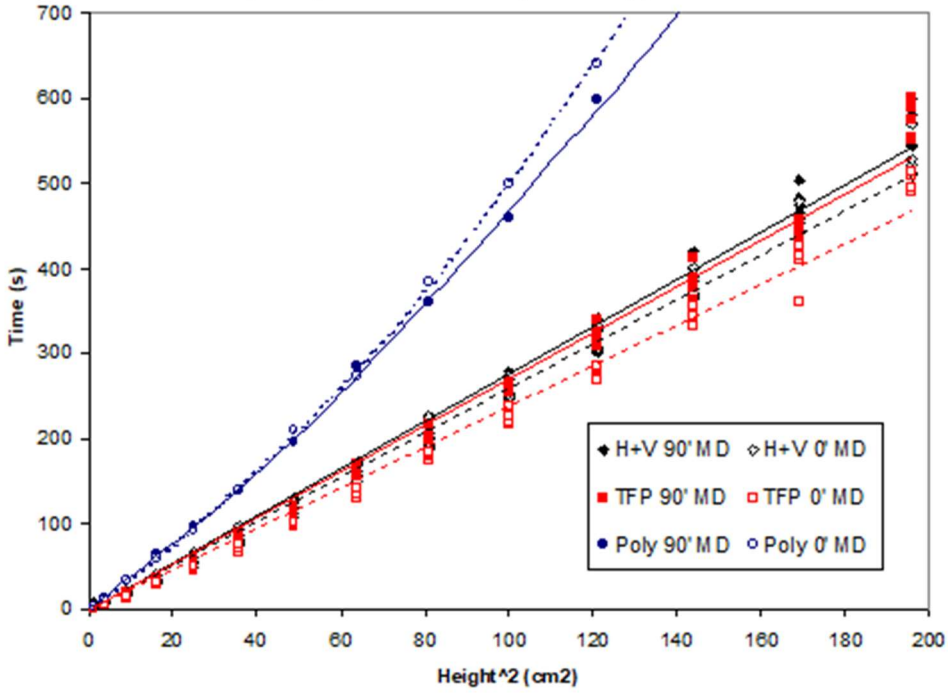

Figure 11.18. When wicking height, h, is much less than the maximum wicking height h_m, a linear relationship is observed allowing linear regression lines to be plotted between each set of data points [4]. A linear relationship is obtained for both separators containing 100% glass, however a non-linear relationship is obtained for the separator containing polyester fibres. This is because the polyester fibres have a higher contact angle with sulphuric acid compared to the glass. This results in a lower value of h_m and the linear t versus h^2 relationship is no longer valid.

Both 100% glass separator papers have the highest wicking rate in the machine direction. Wicking rate will be influenced by a number of parameters such as the range of fibre diameters'

[3] and fibre orientation. The average wicking rate from the two directions is greatest for the Technical Fibre Products separator, suggesting it may have a greater proportion of finer fibres. The difference between the wicking rates in the 0 and 90° directions is greatest for the Technical Fibre Products separator paper. This is a likely consequence of the higher proportion of orientated fibres identified by examination in the scanning electron microscope.

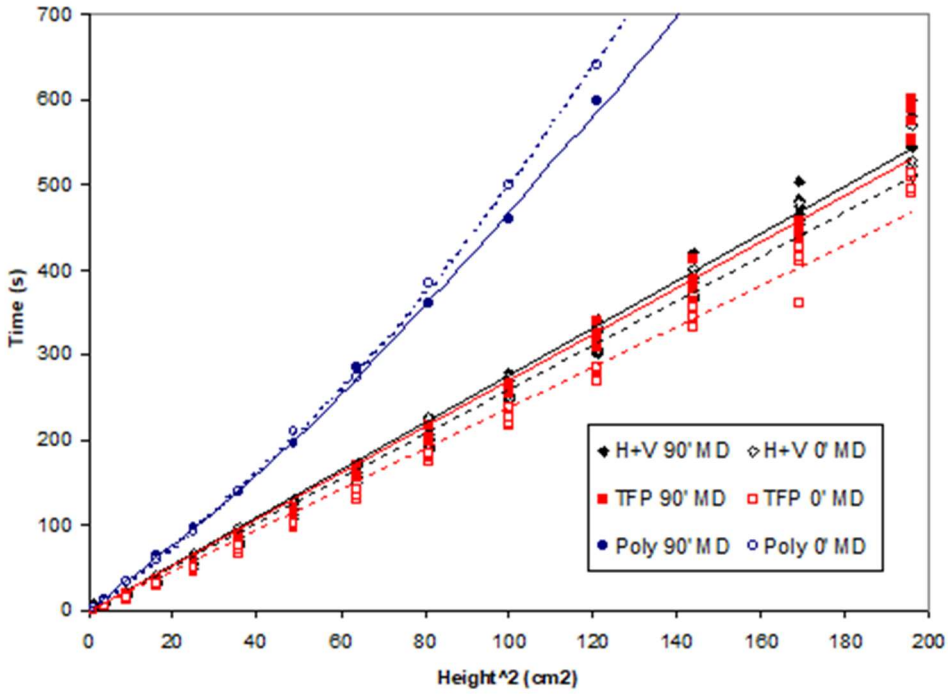

Figure 11.18: Wicking rates of separator papers used in the manufacture of test batteries

11.3.3 PERMEABILITY MEASUREMENTS

Permeability and porosity measurements are shown in table 11.2 below.

Table 11.2: Porosity and Permeability measurements

	Porosity (µm)			Permeability (L/min/cm²)
	Minimum	Maximum	Mean	
H+V 142	3.9	14.4	5.8	13.2
H+V 8% Polyester	3.0	9.0	4.6	7.9
TFP	4.5	14.6	6.7	14.7

The lowest permeability was obtained for the separator containing polyester fibres, which was just over half the value obtained for the 100% glass separators. The values obtained for the two 100% glass separators are very similar although the Technical Fibre Products separator has a larger maximum pore size and a higher permeability compared to the Hollingworth and Vose separator material.

11.3.4 DIFFUSIVITY MEASUREMENTS

During the cycle life of a lead acid battery water loss from the electrolyte results in the battery cell operating at varying levels of saturation. Total water loss increases with the number of cycles, therefore saturation will decrease. Separator saturation will affect battery operation by influencing the diffusion of gases and ions between the positive and negative electrodes. At high saturation levels ionic conduction through the electrolyte will be high and diffusion of gases low and at low saturation levels diffusion of gases will be high and ionic conduction low. The effect of saturation on the flow of gases across the separator paper has been determined by measuring the separator diffusivity at varying saturation levels.

Diffusivity measurements have not been made for the Hollingworth and Vose 8% polyester separator due to its unavailability, however measurements have been taken on the two 100% glass separator papers. Plots of diffusivity versus saturation for Hollingworth and Vose and Technical Fibre Products separator papers are given in Figure 11.19 and Figure 11.20 below.

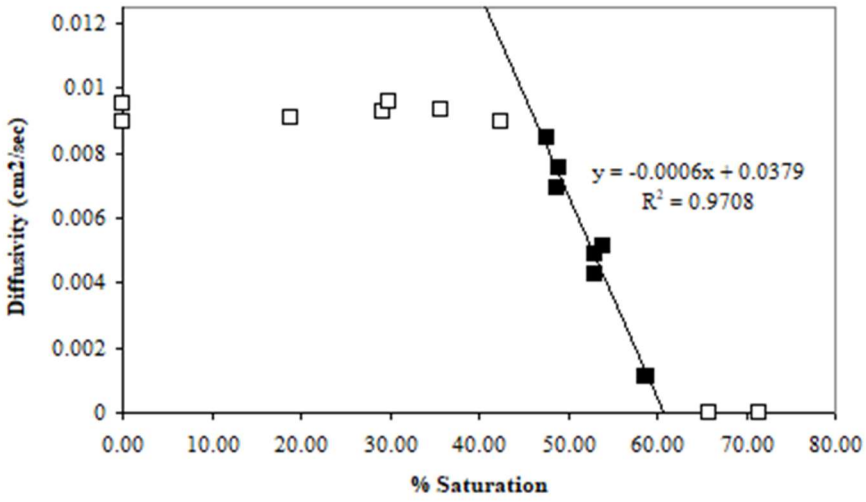

Figure 11.19: Diffusivity versus saturation for Hollingworth and Vose 100% glass separator paper

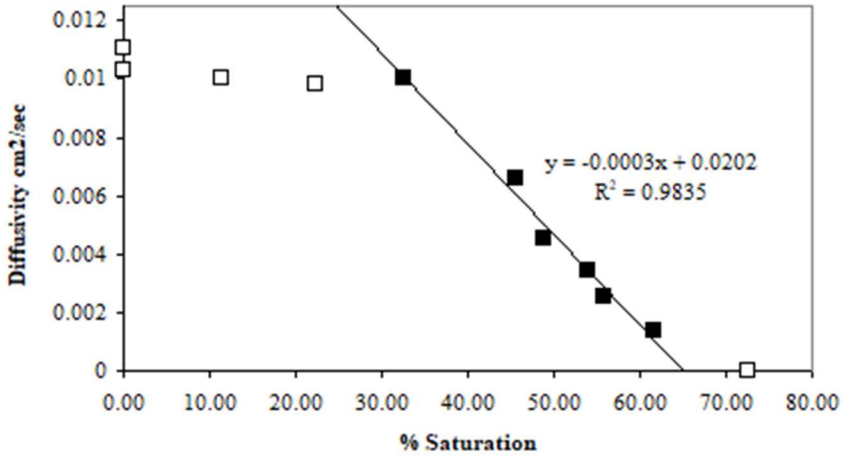

Figure 11.20: Diffusivity versus saturation for Technical Fibre Products 100% glass separator paper

It can be seen that both figures exhibit a similar trend. Each plot can be divided into three distinct sections. The first section consists of a horizontal plateau along which the diffusivity remains relatively constant up to a break point. The saturation at which this point occurs is different for the two separators examined. At saturation levels above the break point there is a steady decrease in diffusivity, which continues linearly until a diffusivity of zero is reached. Above this saturation the diffusivity remains at zero.

Diffusivity of the dry separator papers is similar, around 0.01 cm^2/s with the Technical Fibre Products separator just above this value, and the Hollingworth and Vose just below. As the saturation of the separator papers increases greater numbers of the gaps or pores between the fibres fill with electrolyte. At low saturation levels this has little effect on diffusivity. However, at higher saturation levels distinct paths through the separator are formed. As saturation increases further individual paths are blocked therefore reducing the diffusivity. This process continues until all paths through the paper are blocked and the diffusivity reaches a value of zero.

R^2 values of lines plotted using a least squares fit, between the break point and zero saturation (filled points on figures), are 0.97 and 0.98 for the Hollingworth and Vose and Technical Fibre Products separator papers respectively. This suggests that the relationship is linear. The gradient of the line corresponding to the Technical Fibre Products separator paper is half that of the Hollingworth and Vose paper. This shows that as saturation increases the paths become blocked at a lower saturation level in the Technical Fibre Products separator paper compared to the

Hollingworth and Vose. There is little difference between the saturation levels at which the diffusivity becomes zero for both papers.

11.3.5 SEPARATOR PAPER COMPRESSION TESTS

Compression tests, described in the experimental methods chapter, were carried out on Hollingworth and Vose and Technical Fibre Products 100% glass separator papers in order to determine how the force that is exerted by each paper varies with electrolyte saturation. In order to do this it was necessary to compress the papers and add electrolyte in stages taking measurements at each saturation level.

After the initial compression of both separator types in the dry condition, 0% saturation, a steady drop in force was observed. This indicated that the papers exhibit viscoelastic behaviour. Initial results showed that this produced negligible variations when readings were taken after a predefined relaxation time. There are a number of possible mechanisms that could explain this behaviour.

Since the viscoelastic behaviour of glass, below the glass transition temperature, is insignificant within the time scales of this investigation the behaviour of the separator papers is primarily influenced by the structure rather than the compositional or material properties of glass.

Separator paper consists of a mass of fine glass fibres inter-linked in various orientations shown diagrammatically in Figure 11.21.

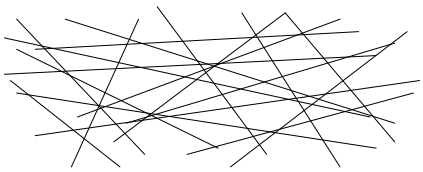

Figure 11.21: Simplified structure of separator paper

Glass is a brittle material and does not exhibit plastic deformation characteristics. During compression of separator paper the fibres will bend until they reach their elastic limit, after which fibre fracture occurs. In addition to fracture, the only way in which the fibres can release the elastic strain energy stored within them is to move into a position where the bending force is reduced. The time taken for the fibres to move is the mechanism believed responsible for the paper's viscoelastic behaviour. In practice this will be a cumulative effect of a large number of fibres moving synchronously together. The situation of two fibres acting on each other is represented diagrammatically in Figure 11.22.

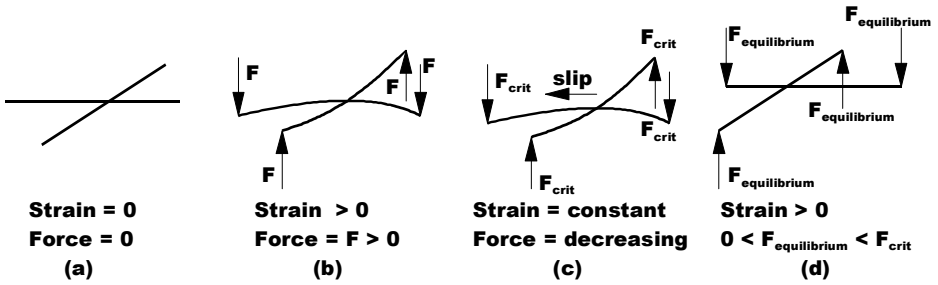

Figure 11.22: Representation of fibre movement within a separator paper during compression.

Separator papers consist of many fibres crossing each other, a pair of which is shown in Figure 11.22(a). When a load is applied to the fibres elastic deformation occurs and the fibres deform as shown in Figure 11.22(b). As the strain increases a critical force is reached at which point the fibres are able to slip past each other, resulting in a decrease in their deformation, Figure 11.22(c). The effect of this is a reduction in the force exerted by the fibres, whilst maintaining the same overall separator strain. At a particular point the sliding fibres will reach an equilibrium force condition at which the sliding will stop, Figure 11.22(d). The result is a decrease, from the initial force exerted by the compressed separator with time. Alternatively, if the fibres are unable to slip to a position of lesser strain, fibre breakage will occur when the force exceeds that for fracture.

In practice the mechanism described above will be influenced by other factors such as the surface tension and lubrication effects of the electrolyte. A plot of load versus saturation for both separator papers consisting of 100% glass is shown in Figure 11.23 below.

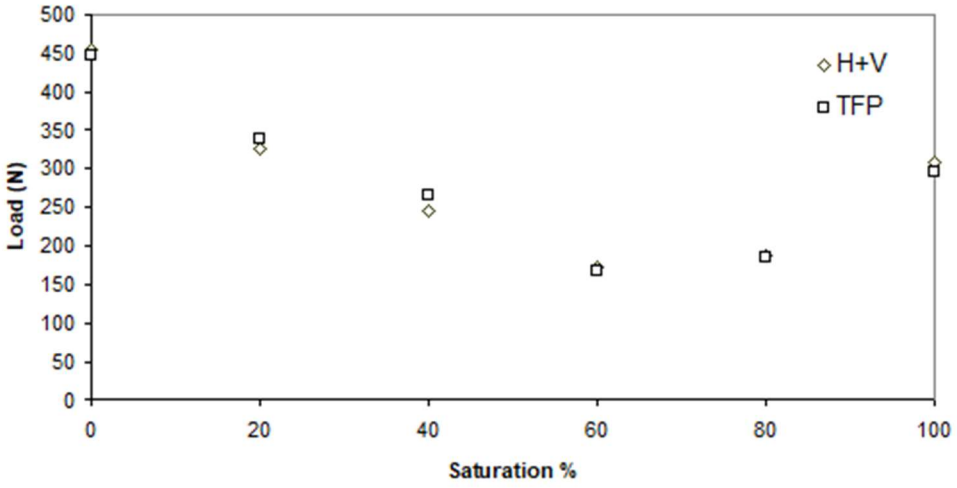

Figure 11.23: Load versus saturation for Hollingworth and Vose and Technical Fibre Products 100% glass separator papers

From the figure it can be seen that there is no significant difference in the behaviour exhibited by both separator types. A decrease in force occurs between 0 and 60% saturation, followed by

an increase between 60 and 100%. Investigations by Nakamura [4] *et. al.* indicate a similar trend when contraction percentage is plotted against amount of electrolyte added to the separator sample. This can be explained by considering the interaction between the electrolyte and fibres, shown diagrammatically in Figure 11.24. From the figure it can be seen that there is no force acting between the fibres at 0 and 100% saturation. However, at an intermediate level of saturation a drop of electrolyte can sit between the fibres. The surface tension of the electrolyte causes the fibres to bend towards each other reducing any force at the ends of the fibres.

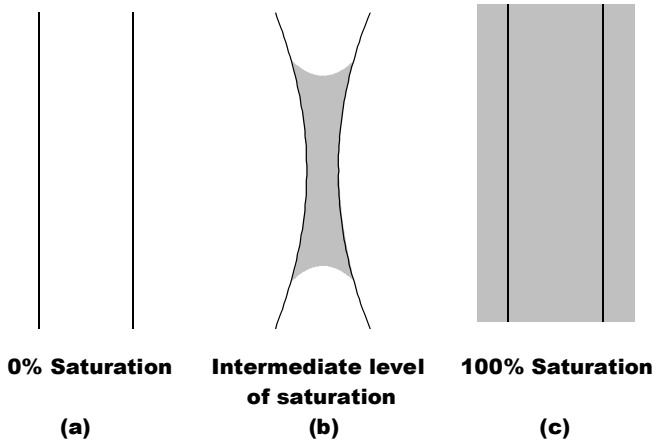

Figure 11.24: Influence of electrolyte between glass fibres

As the separator saturation increases, the ratio of each interaction type between fibres, either (a), (b), or (c) as shown in Figure 11.24, will vary and influence the total force exerted by the paper therefore explaining the U shape curve. Intuition suggests that the drop in force observed between the values at 0% and 100% saturation is a combination of the paper relaxation throughout the time of the experiment, lubrication of the fibres with electrolyte and surface tension effects of the electrolyte.

11.4 FINAL DISCUSSION

From the results of this study it is clear that battery cycle life is greatly affected by the choice of separator paper. The low cycle life exhibited by the polymer-containing separator may be a consequence of the lower permittivity and wicking rates observed. The most influential contributing factor to this, is most likely to be the high contact angle between the electrolyte and fibre surface.

The variation in cycle life performance between the Hollingworth and Vose and Technical Fibre Products 100% glass separators is harder to explain. Both separators gave very similar results in all tests. The only differences were in the fibre orientation and variation in diffusivity with saturation. This suggests that these factors are important in determining cycle life as they

influence the movement of electrolyte through the paper and therefore also the flow of gases and ions between electrodes.

11.5 CONCLUSIONS

A list of general conclusions that can be drawn from the results obtained is given below.

- Failure of all batteries tested was due to the positive electrode.
- Acid stratification was less in the battery that sustained the most cycles.
- 100% glass fibre separators have a higher wicking rate compared to separators containing polyester fibres.
- Wicking rates are higher in the machine direction for separators consisting of 100% glass.
- Wicking rates are greater in the direction of fibre orientation of a separator paper.
- Separator paper permittivity appears to be an important factor in determining the cycle life of a battery.

11.6 REFERENCES

1. Figure supplied by Hawker Energy Ltd, Newport.
2. Verbal communication, Dr Raju Kurian, Hawker Energy, Newport.
3. K. Nakamura, M. Shiomi, K. Takahashi, M. Tsubota, Failure modes of valve-regulated lead / acid batteries, Journal of Power Sources, vol. 59, (1996), pp. 153-157
4. B. Culpin, Separator design for valve-regulated lead/acid batteries, Journal of Power sources, Vol. 53, (1995), pp. 127-135.

12 GENERAL CONCLUSIONS AND SUGGESTIONS FOR FUTURE WORK

12.1 INTRODUCTION

Throughout the course of this work a wide range of the components and materials used to construct valve regulated lead acid batteries have been studied. In the majority of instances this has been done in the context of the battery as a whole. The alternative approach of characterising materials outside of the battery, as in the case of the separator papers has also been done. In the following chapter the most significant results are discussed.

12.2 PREPARATION AND DRYING OF BATTERY ELECTRODES

All electrodes removed from test batteries were dried in a vacuum oven to remove moisture and stabilise the active materials prior to further analysis. However, on a number of the negative active material samples, large amounts of beta-lead monoxide were identified in x-ray diffraction patterns. This was first observed in the initial set of batteries examined in order to determine the effects of cycling. More detailed analyses of the active materials were inconclusive in identifying the cause or origin of the oxide. A negative active material sample containing approximately 60% lead monoxide was obtained from the second set of batteries examined containing different active materials and grid wires. Intuition suggests that it is almost certain that this quantity of oxide must have formed at some point after the cycling phase of analysis had ceased and most likely during the drying stage of the tear down procedure. This conclusion strongly suggests that lead monoxide observed in the negative plates from the initial set of batteries used to study cycling, formed during the drying stage. These results are of concern, and suggest that the currently used drying procedure should be improved. A likely explanation as to why only a number of the plates were affected is the presence of non-uniform temperature and humidity within the oven during drying. An investigation should be carried out in order to determine the magnitude and influences of these changes on the negative active material. It would also be interesting to investigate the drying of plates in the presence of an inert gas flowing through the oven, which would increase the rate of water vapour removal and also allow plate heating by convection as well as radiation from the oven walls.

12.3 CYCLED BATTERIES

The work conducted to investigate the effects of cycling on the battery can be divided into a number of principal stages; (i) the initial cycling and testing of the batteries, (ii) examination of the positive and negative active materials, (iii) examination of the positive grid corrosion layer. Examination of the active materials did not identify any abnormal changes in structure and composition as a result of cycling. Identification of known failure mechanisms such as sulphation of the positive plates was observed in a number of instances.

Compositional analysis showed a steady decrease in the quantity of alpha-lead dioxide with number of test cycles. This phenomenon is well documented, and of importance to battery operation, as the ratio of the alpha and beta phases can influence plate capacity. It is suggested that the formation and conversion of alpha into beta lead dioxide during battery operation should be investigated in further detail.

Measurement of oxide thickness showed a corrosion layer growth, which appeared to follow an exponential relationship, and had a higher growth rate in the bad cells. Corrosion layer thickening could be investigated in greater detail by taking thickness measurements in situ using a non destructive technique such as electrochemical impedance analysis.

12.4 EFFECTS OF GRID ALLOY AND POSITIVE ACTIVE MATERIAL

A number of interesting conclusions were drawn from the results obtained from batteries containing different active materials and grid wires. Some differences in active material compositions were observed in samples that could only be explained by variability of the samples or in the testing procedures.

Variations in the porosity of the positive electrode across its width were observed in all cycled battery samples in groups 1-4. Further investigations should be carried out in order to determine the exact cause of these changes. A possible approach would be to construct a battery with only one side of the electrode exposed to the electrolyte.

The strength and durability of a positive active material can influence the formation of cracks within the active material structure. Investigations to determine the strength of various active materials studied would be useful it assessing the likelihood of cracking occurring during battery operation that would lead to an increase in resistance.

12.5 CORROSION LAYER CHARACTERISATION

Corrosion layers on the positive grids from the various battery designs examined in this project were characterised using a number of different techniques. Examination of polished sections using light microscopy revealed significant differences in both corrosion layer thickness and structure. The most common features identified were cracks and porosity, the severity of which was found to be dependent on the type of grid and positive active material utilised in the design.

Sulphation of positive paste results in a corrosion layer which is significantly more porous than the unsulphated equivalent. Sulphated pastes tend to produce thicker corrosion layers as a result of faster oxygen diffusion through the network of pores to the grid/corrosion layer interface, however the relationship between amount of sulphation and extent of porosity has not been investigated and is not known.

Corrosion layers formed in batteries that have sustained a large number of cycles are more prone to the formation of cracks and features less common at lower cycles. These include cracks at various orientations within the corrosion layer and fingers of oxide, which appear to accelerate the growth of the corrosion layer into the grid. Results suggest that these features are a consequence of a number of different formation mechanisms. In addition to material characteristics the features are also likely to be influenced by factors such as charging regime and rate of discharge. These will influence the heat generated internally within the battery which will lead to cracking due to differential thermal expansion effects for different phases of material in the structure. Corrosion layer resistance is an important property and should be investigated with respect to structural morphology.

It has been demonstrated that tin has an influence on the mechanism by which the corrosion layer propagates into the grid. Results indicated that precipitation of tin, resulting in higher concentrations at grain boundaries, induced enhanced galvanic corrosion in these regions. The effect of various heat treatments and methods for grain modification should be investigated and their influence on corrosion layer growth and propagation into the grid characterised.

12.6 GEOMETRICAL DESIGN OF GRIDS

The geometry of the positive grid and active material has been shown to influence the corrosion layer formation. A finite element model using ANSYS was used to model variations in current density around the parameter of a grid wire cross section. A correlation was observed between areas of high current density in the model and thickening of the corrosion layer on the battery grids examined. The model was later used to predict current density on alternative grid designs.

However, within the current scope of this programme it was not possible to validate these results experimentally. It is recommended that positive electrodes should be constructed using the alternative geometrical arrangements of grid and positive active material in order to validate the model.

12.7 SEPARATOR PAPER

Investigations have demonstrated that separator paper structural characteristics have an influence on battery cycle life. Fibre material and orientation affect separator properties, which in turn influence battery operation in a number of different ways. Separator compressive properties will influence the efficiency of battery charging by affecting the contact between loose positive active material particles. Separator diffusivity during overcharging will determine the flow of gas to the negative electrode and thereby the amount that reaches the positive grid and is available to react to form the corrosion layer. Both the properties described above are a function of separator electrolyte saturation, which itself decreases during the life of a battery due to electrolyte water loss. Tests should be conducted to determine the effects of separator saturation on overall battery performance. This would allow material properties of separator papers to be related directly to battery performance.

12.8 SUMMARY OF THE SUGGESTIONS FOR FUTURE WORK

12.8.1 EXPERIMENTAL METHODS

Investigation of …

- The drying of plates in an oven whilst under a constant flow of an inert gas.

12.8.2 POSITIVE ACTIVE MATERIAL

Investigations of …

- The reduction in alpha-lead dioxide content in positive active material with number of cycles and depth of discharge.
- The effect of positive paste mix on the number and distribution of cracks formed, after curing and during varying modes of operation and how this affects the strength of the positive active material.
- The porosity distribution within the positive active material across the width of the positive electrode.

12.8.3 POSITIVE ELECTRODE GRID CORROSION LAYER

Investigations of …

- The relationship between corrosion layer thickness and number of cycles.
- The influence of corrosion layer porosity on resistance.
- The effect of current density on corrosion layer growth rate.
- The effect of sulphation on corrosion layer porosity.
- The effect of charging regime on the formation of cracks within the corrosion layer.
- The effect of positive grid grain structure modification of corrosion layer propagation and growth.
- The relationship between predicted current density using ANSYS and experimental results for alternative grid designs.

12.8.4 SEPARATOR

Investigations of …

- The effect of separator compression on diffusivity at varying saturation levels.
- The influence of separator saturation on battery charge and discharge efficiency.
- The effect of separator fibre orientation on battery operation.

13 Journal Publications

1- R. J. Ball, R. Evans, M. Devan, R. Stevens, Characterisation of defects observed within the positive grid corrosion layer of the valve regulated lead/acid battery, Journal of Power Sources, Vol. 103 (2002), pp. 207-212

2- R. J. Ball, R. Evans, R. Stevens, Finite element (FE) modelling of current density on the valve regulated lead/acid battery positive grid, Journal of Power Sources, Vol. 103 (2002), pp. 213-222

3- R. J. Ball, R. Evans, R. Stevens, Characterisation of separator papers for use in valve regulated lead/acid batteries, Journal of Power Sources, Vol. 104 (2002), pp. 208-220

4- R. J. Ball, R. Kurian, R. Evans, R. Stevens, Study of valve-regulated lead/acid batteries manufactured with different separator papers, Journal of Power Sources, Vol. 104 (2002), pp. 234-240

5- R. J. Ball, R. Kurian, R. Evans, R. Stevens, Failure mechanisms in valve regulated lead/acid batteries for cyclic applications, Journal of Power Sources, Vol. 109 (2002), pp. 189-202

6- R. J. Ball, R. Kurian, R. Evans, R. Stevens, Influence of positive active materials type and grid alloy on corrosion layer structure and composition in the valve regulated lead/acid battery, Journal of Power Sources, Vol. 111 (2002), pp. 23-38

7- R. J. Ball, R. Stevens, Design aspects of the valve regulated lead/acid battery positive electrode, Journal of Power Sources, Vol. 113 (2002), pp. 228-232

ELSEVIER

Journal of Power Sources 103 (2002) 207–212

JOURNAL OF POWER SOURCES

www.elsevier.com/locate/jpowsour

Characterisation of defects observed within the positive grid corrosion layer of the valve regulated lead/acid battery

R.J. Ball[a,*], R. Evans[b], M. Deven[c], R. Stevens[a]

[a]*Department of Engineering and Applied Science, University of Bath, Bath BA2 7AY, UK*
[b]*Invensys, Westinghouse site, Chippenham, Wiltshire SN15 1SJ, UK*
[c]*University of Warwick Science Park, Buehler/Krautkramer, Nillburn Hill Road, Coventry CV4 7HS, UK*

Received 30 March 2001; received in revised form 25 June 2001; accepted 29 June 2001

Abstract

An investigation into the failure of a series of cycled 40 Ah valve regulated lead acid batteries, identified a number of different defect types present in the corrosion layer. In this paper, a detailed description of the materialographic preparation method used to produce cross-sections of the corrosion layer is given. Each of the defect types identified is described and illustrated in an appropriate micrograph. Variations between the defect types suggest that there is more than one mechanism for defect initiation and growth. Possible mechanisms for sources of the defects and their subsequent growth are proposed. © 2002 Elsevier Science B.V. All rights reserved.

Keywords: VRLA; Corrosion layer

1. Introduction

During operation of a valve regulated lead acid battery a corrosion layer forms on the surface of the positive grid [1]. This layer acts as an interface between the current collecting grid and current producing positive active material. Characteristics of the corrosion layer are important in determining battery efficiency, as electrons must flow across the layer during battery operation [2].

Corrosion layer properties such as structure and composition have an influence on the flow of electrons and, therefore, efficiency of battery operation [3]. An additional factor that can affect performance by altering the corrosion layer properties is the formation of defects within the corrosion layer. The defects observed are normally in the form of cracks and pores, which have two main effects. Firstly, they act to reduce the effective electrical conductivity of the layer, as electrons cannot flow across cracks, and secondly, to increase diffusion rates of gases, such as oxygen, and electrolyte, through the corrosion layer by provision of an easy pathway.

During examination of positive grid corrosion layers from valve regulated lead/acid batteries a number of different types of defect were observed. A summary of the defect types found is presented in this paper.

* Corresponding author. Tel.: +44-1225-826826; fax: +44-1225-826098.
E-mail address: r.j.ball@bath.ac.uk (R.J. Ball).

2. Experimental methods

2.1. Production of test batteries

The batteries examined in this study were all constructed using identical materials and the same design. A 40 A, 12 V monobloc unit was used. Positive electrodes were produced using a standard grey oxide positive paste. The negative paste mix was also manufactured from grey oxide. Positive and negative grids were produced from pure lead strip. Glass microfibre separators were used in the design, 70% coarse, 30% fine fibre.

2.2. Battery cycling

Cycling was carried out automatically using Digitron charging units. Each cycle consisted of a constant current discharge at 7.05 A to 10.2 V followed by a constant voltage recharge at 14.7 V for 16 h. This was repeated until the capacity after charging was <80% of the starting capacity. The cell that showed the greatest voltage difference between end of discharge and end of charge was examined as this cell exhibited the thickest positive grid corrosion layer.

2.3. Preparation of corrosion layers for microscopy

The corrosion layer structure on the positive grid bars of a battery can provide important information as to why a

0378-7753/02/$ – see front matter
PII: S0378-7753(01)00856-4

battery cell has failed. An effective way to study these features is to examine a polished cross section using optical microscopy.

Dried battery plates consist of a soft lead grid, which has very low stiffness, surrounded by friable, brittle active material. When handling plates great care must be taken to avoid unnecessary bending as this can lead to the formation of additional cracks in the active material. After removal of the plates from the battery they were washed in distilled water to remove acid and dried in a vacuum oven for approximately 24 h. In order to minimise the risk of causing further damage to the plates after drying, they were quickly stabilised by encapsulation in resin. This was achieved by laying the plates horizontally, jacked up on small plastic blocks approximately 3 mm high, within a specially made latex mould. Resin was then poured into the mould to a height of approximately 7 mm, thus, surrounding each side of the plate with several millimetres of resin.

In order to ensure consistency of results, cross-sections of the electrodes were always taken from the middle position of the plate. However, exceptions to this procedure were made if this area contained cracked active material caused by post tear down damage. Samples were normally taken by cutting a strip of electrode approximately 15 mm in width from the centre of the plate. This strip was then cut into smaller sections and remounted in smaller cylindrical moulds suitable for polishing.

2.4. Polishing procedure

The procedure used for polishing the sections consisted of a number of different stages. Although some polishing was done automatically, it was found that the best results were achieved by hand. A common problem encountered when polishing a multi-phase material, such as a battery plate, is the risk of a particle of a hard phase such as the oxide, becoming dislodged and consequently, damaging the softer lead phase. Little can be done to prevent this. However, damage can be minimised in two ways. Firstly, by having a small sample of electrode and secondly, by holding the sample so that its length is in the same orientation as that of the polishing wheel. Due to the variation in properties, no two samples behaved in the same way when being polished. For this reason, it was necessary to periodically check the sample at the end of each stage of preparation using light microscopy to ensure the next stage could be started without having induced extrinsic damage.

2.4.1. Planar grinding stage

Samples were initially ground using silicon carbide paper. However, a problem with this approach occurs when small particles of carbide break off or become dislodged. If this occurs, particles often become embedded in the soft lead grid. This proved to be unavoidable. However, the severity and quantity of embedded carbide could be reduced in two ways. Firstly, a bar of steel was rubbed against each fresh sheet of silicon carbide paper, with a generous amount of water flowing, for a few seconds before the sample was ground. The purpose of this was to remove any loose carbide particles and to break off and remove any sharp spikes of carbide that were likely to become attached to and break inside the lead. Secondly, a layer of candle wax was applied to the paper. This acted, as a soft medium to which any loose particle would become attached, rather than become embedded in the lead. A series of different grades of silicon carbide material were used ranging from 300 to 1200 grit and a platen speed of 150 rpm was used. Water was used as a lubricant and only a light pressure was applied when grinding the sample. The papers were replaced after 30 s to 1 min of grinding.

2.4.2. Polishing stage

The polishing stages of preparation were conducted using a Texmet polishing cloth loaded with alumina suspension. A platen speed of 100 rpm was used and normally a good sample finish was achieved after polishing with 5 and 0.3 μm alumina. Polishing was again conducted by hand and periodic checks of the surface using light microscopy were required to identify the point at which the next stage of the sample preparation route could be initiated.

2.4.3. Finishing stage

The finishing stage was conducted using a Buehler Vibromet 2. Buehler Masterpolish was used as a polishing media on a Texmet cloth. A polishing time of 30 min was found to produce the best results.

2.5. Light microscopy

Samples were examined using a ZEISS ICM405 optical microscope. When examining the polished samples care must be taken in the interpretation of the image, especially at the interface between the lead and positive active material. Even after vibratory polishing slight differences in height between the lead and corrosion layer were noticeable. However, at higher magnifications, this effect is less obvious and a shadowing effect is often observed, which could easily be mistaken as an interface or feature of the sample. Another phenomenon was reaction of polishing media with the lead grid. The most misleading effect was a reaction of the polishing media with the lead grid adjacent to the corrosion layer. On certain samples this reaction layer looked convincingly like an additional phase of the grid corrosion layer and to avoid confusion is labelled accordingly in all figures.

3. Results and discussion

In general, the corrosion layers in batteries that survived >90 cycles to failure were found to exhibit features which did not appear as frequently in batteries that had failed earlier, i.e. <90 cycles. The most prominent of these were

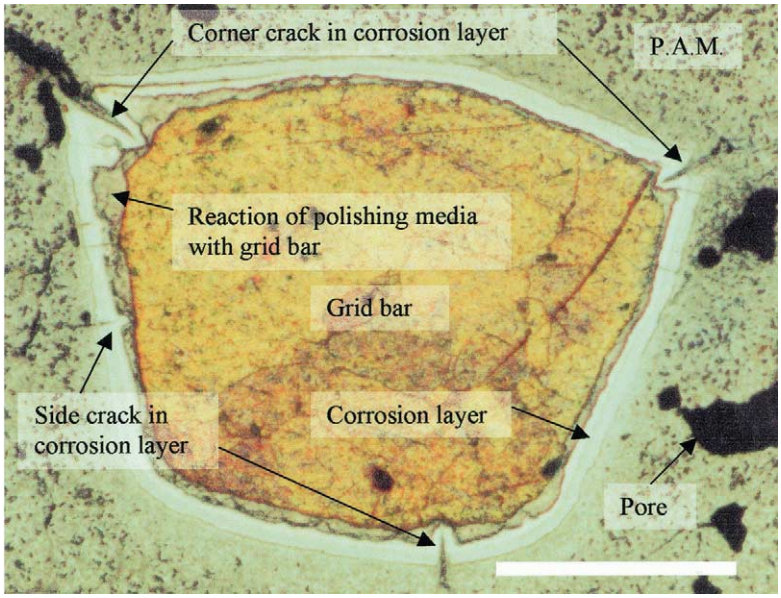

Fig. 1. Positive grid bar showing corrosion layer and cracks (scale bar: 500 μm).

cracks, most commonly occurring adjacent to grid-bar corners although a number were identified on the edge of the bar. A typical grid bar cross-section exhibiting these features is shown in Fig. 1. The corrosion layer extends around the whole perimeter of the bar. Pores are visible at a number of locations within the positive active material. There is no evidence that the presence of a pore promotes or reduces the probability of a defect occurring in the adjacent region of corrosion layer.

A higher magnification image of a crack observed in the corrosion layer on the side of a grid bar is given in Fig. 2. The layer consists of two sub-layers separated by an internal boundary. Cracking has occurred through both layers and a short distance into the underlying lead grid. A reaction between the polishing media and lead grid adjacent to the corrosion layer produces an additional feature that should not be confused with the corrosion layer of intermediate stoichiometry produced during battery operation. Positive active material is visible on both sides of the crack walls as far as the crack tip. This is likely to have formed by the movement of small particles of lead oxide and/or lead sulphate into the crack that subsequently reacted to form a rigid, porous active material. Movement of the electrolyte during overcharging, when gases are produced, would promote the movement of particles into cracks. The crack centre contains the resin used for sample

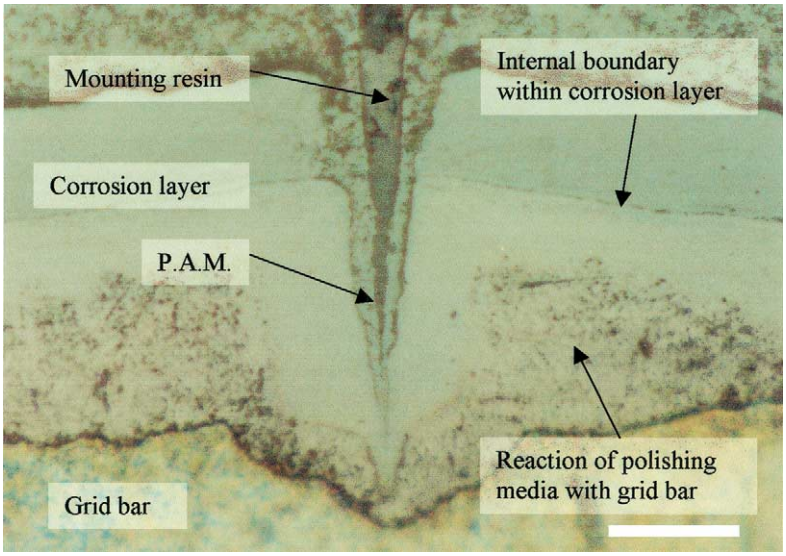

Fig. 2. Typical crack observed in corrosion layer (scale bar: 50 μm).

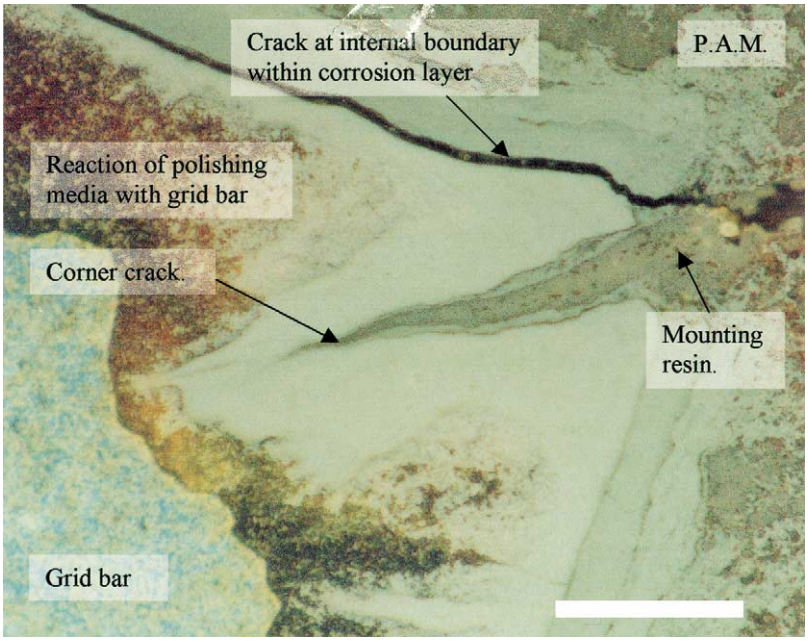

Fig. 3. Crack observed on comer of grid bar (scale bar: 50 μm).

mounting during polishing, suggesting that during battery operation this region could well have been filled with either electrolyte or gas.

Closer examination of the corrosion layer revealed the presence of cracks at the internal boundary within the corrosion layer, Fig. 3. Formation of a crack in this location suggests a difference in properties of these layers and indicates that the bond between them is not as strong as either of the individual layers.

Smaller fissure cracks were also observed in the lower corrosion layer, Fig. 4. They appear to be propagating in an outward direction, since cracks only grow under a tensile stress. The formation of cracks such as these could be a result of either (i) internal stress within the layer, caused by geometrical effects or (ii) stress caused by gas pressure produced during battery operation, especially during overcharging.

A number of smaller cracks and oxide fingers penetrating the grid were observed on the sides of some bars, shown in Fig. 5. Examination of the oxide finger at higher magnification, Fig. 6, revealed a small crack or fissure running down the centre. Whether this is a genuine crack, or the point at

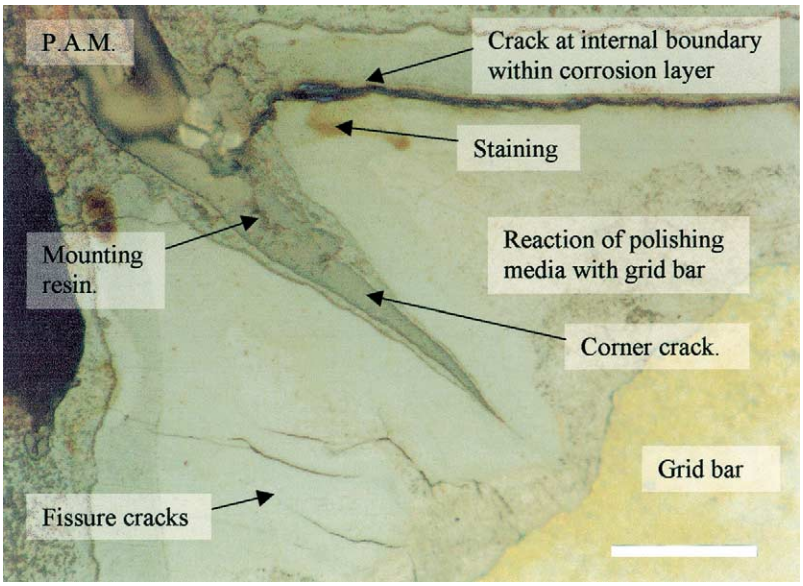

Fig. 4. Fissures within corrosion layer adjacent to corner crack (scale bar: 50 μm).

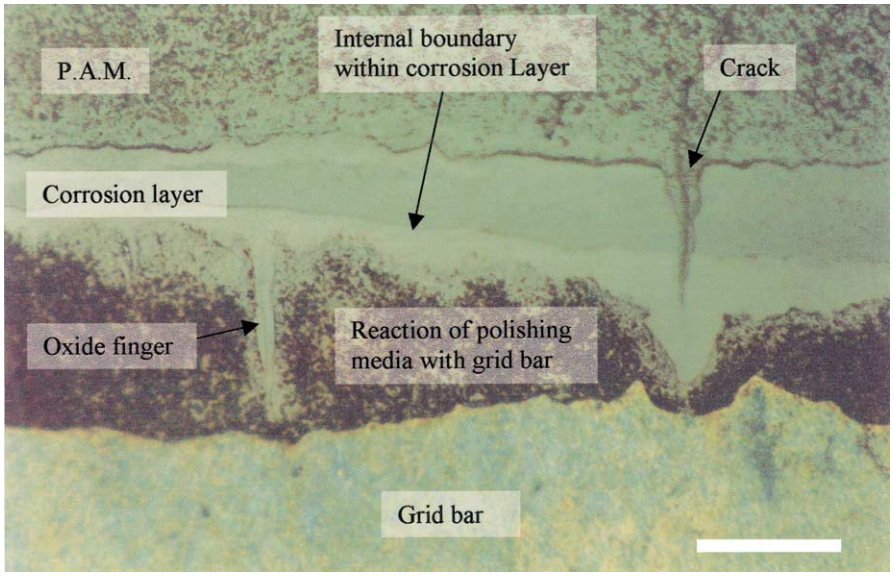

Fig. 5. Crack observed on edge of grid bar (scale bar: 50 μm).

which the layers growing out from each side of the crack join up is unknown. Formation of a finger such as this could be an initial stage in the formation of the larger cracks discussed previously. The crack featured on the right hand side of the photograph appears to be growing in an inward direction, suggesting there is more than one mechanism for crack initiation and growth.

Positive active material on the inner surfaces of a crack will affect the propagation rate. When positive active material is discharged the lead dioxide is reduced to form lead sulphate with a consequential increase in volume. This change will produce a force perpendicular to the crack direction effectively pushing the crack walls outwards and increasing the stress concentration around the crack tip, therefore, promoting propagation. It should also be noted that cracks provide effective routes for the transport of oxygen to the grid/corrosion layer interface where the brittle oxide, which is prone to cracking, can be formed.

The probability of defects initiating within the battery can be reduced by taking measures such as (i) designing grids to reduce stresses in the corrosion layer caused by geometrical factors such as sharp corners, and (ii) keeping the battery

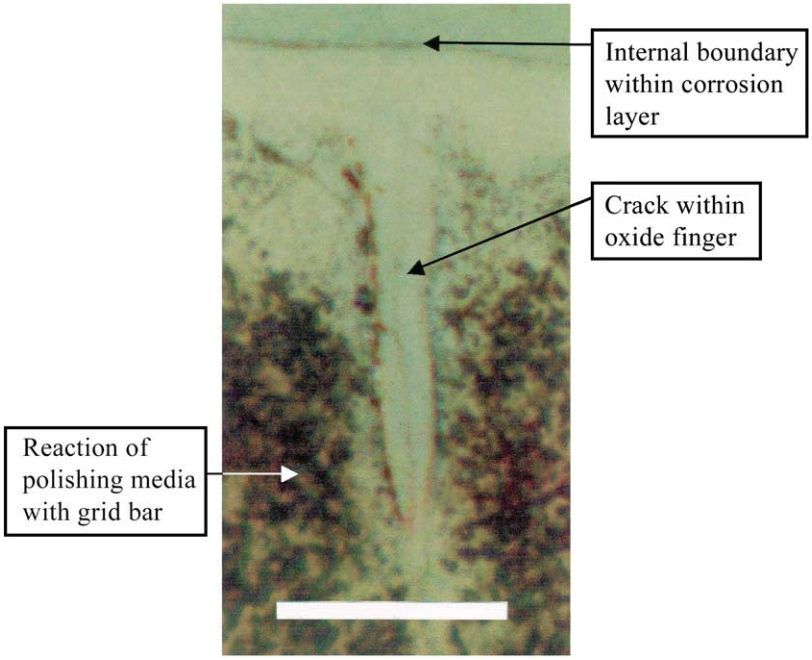

Fig. 6. High magnification of oxide finger (scale bar: 50 μm).

well ventilated to reduce heat build-up. Defects such as cracking between different phases of the corrosion layer can only be avoided by changing the nature of corrosion layer structure. This is a more difficult problem to address as structure is influenced by the reaction changes taking place in the positive active material, the composition and microstructure of the grid alloy and the battery operating conditions.

4. Conclusions

Examination of the corrosion layer has allowed a number of different types of defect to be identified. Principally these were

- cracking adjacent to grid bar corners;
- internal boundary cracks within the corrosion layer;
- small fissure cracks;
- small penetrating cracks and oxide fingers.

The variation in different types of defect suggests there is more than one mechanism for defect initiation and growth. Defects will often occur due to stresses within the corrosion layer. These can arise for the following reasons:

- thermal cycling of the oxide due to changing heat generation rates at different periods of the discharge/charge cycle;
- geometrical (volume) changes associated with the conversion of lead oxide to sulphate during cycling;
- oxygen gas evolved during overcharging pressurising and escaping through the oxide corrosion layer.

References

[1] D.A.J. Rand, L.S. Holden, G.J. May, R.H. Newman, K. Peters, Valve-regulated lead/acid batteries, J. Power Sources 59 (1996) 191–197.
[2] D. Pavlov, A theory of the grid/positive active-mass (PAM) interface and possible methods to improve PAM utilization and cycle life of lead/acid batteries, J. Power Sources 53 (1995) 9–21.
[3] A.F. Hollenkamp, K.K. Constanti, M.J. Koop, L. Apateanu, M. Calabek, K. Micka, Effects of grid alloy on the properties of positive-plate corrosion layers in lead/acid batteries. Implications for premature capacity loss under repetitive deep-discharge cycling service, J. Power Sources 48 (1994) 195–215.

ELSEVIER

Journal of Power Sources 103 (2002) 213–222

JOURNAL OF POWER SOURCES

www.elsevier.com/locate/jpowsour

Finite element (FE) modelling of current density on the valve regulated lead/acid battery positive grid

R.J. Ball[a,*], R. Evans[b], R. Stevens[a]

[a]*Department of Engineering and Applied Science, University of Bath, Bath BA2 7AY, UK*
[b]*Invensys, Westinghouse Site, Chippenham, Wiltshire SN15 1SJ, UK*

Received 30 March 2001; received in revised form 25 June 2001; accepted 29 June 2001

Abstract

During operation of the valve regulated lead/acid (VRLA) battery, a mixed stoichiometry lead oxide corrosion layer is formed on the surface of the positive electrode. The formation of this layer has a number of consequences including increased electrode resistance and decreased strength. Experimental results obtained from cycling 40 A h VRLA batteries revealed an increase in corrosion layer thickness on the sides of the grid bars compared to the top and bottom. It is suggested that the areas of increased corrosion layer thickness corresponded to the areas of high current density on the surface of the grid. In order to investigate this observation the finite element package ANSYS was used to produce qualitative estimates of the values in current density, which would be expected on the tested grid design. Results suggest that corrosion layer thickening is related to current density. The model was then used to predict the expected current distribution around a number of hypothetical electrode designs. These incorporated changes in both grid bar cross-section and positive active material. Results showed that improvements could be made to existing grid designs with respect to lowering current densities.

Keywords: VRLA battery; Grid; Finite element analysis; ANSYS

1. Introduction

Valve regulated lead/acid (VRLA) battery cells, constructed using a flat plate design, consist of a number of interleaved electrodes, each comprising a lead grid surrounded by either positive or negative active material. The grid bar gives support to the active material, however, its primary function is to act as a current collector.

A large segment of the VRLA battery market is for cyclic applications; consequently cycle life is an important factor to consider when designing a battery. Electrode design can affect cycle life by determining the current profile during charge and discharge, which is related to efficiency. Battery designers have been aware of this for many years and inclusion of features such as additional grid bars directed towards the lug can be seen on many designs as a method of improving the efficiency of current collection in the plane of the electrode.

During battery operation electrons flow between the electrode grid and positive active material. The difference in surface area between the active material, approximately 500 m^2 and grid, approximately 50 cm^2, results in a large increase in current density at the grid/positive active material interface. Pavlov [1] has suggested that grid bar shape and plate design will influence the uniformity of current distribution on the grid surface. As a basic electrode design principle it is advantageous to have as low and uniform a current density as is practically possible. A model proposed by Pavlov suggests that the cycle life of positive plates depends on the variations in current density on the grid surface, as this determines the intensity of the destructive processes in the positive active mass during operation.

Unpublished work by the authors into the affects of cycling on positive grid/corrosion layer growth showed a thicker corrosion layer on the surfaces of the grid bar, where the maximum current density was expected. It is believed that a higher current density can lead to a raised temperature resulting from resistance heating.

Due to the complex geometry of the grid bar, calculating the variation in current density using an analytical method would be extremely complicated and practically impossible. A more practical approach is to use a finite element (FE) method to solve the problem. The package chosen to obtain a solution was ANSYS [2]. ANSYS is a multi-purpose FE

* Corresponding author. Tel.: +44-1225-826826; fax: +44-1225-826098.
E-mail address: r.j.ball@bath.ac.uk (R.J. Ball).

0378-7753/02/$ – see front matter
PII: S0378-7753(01)00857-6

program that can be used to solve a number of physical problems including current flow in a material.

2. Battery manufacture and testing

The results presented in this paper are based on observations of corrosion layer thickness made on a number of test batteries. The battery design used is a 40 A h VRLA product, manufactured using grey oxide positive active material and grey oxide negative active material. 100% glass microfibre separators were used consisting of 70% coarse and 30% fine fibres.

Cycling was carried out automatically using Digitron charging units. Each cycle consisted of a constant current discharge at 7.05 A to 10.2 V followed by a constant voltage recharge at 14.7 V for 16 h. This was repeated until the capacity after charging reduced to less than 80% of the starting capacity. The cell that showed the greatest voltage difference between end of discharge and end of charge was examined as this cell exhibited the thickest positive grid/corrosion layer. In order to determine the positive grid/corrosion layer thickness plates were removed from the battery case, washed in distilled water, dried in a vacuum oven and then encapsulated in resin. Cross-sections of the grid bars were then prepared using standard materialographic grinding and polishing techniques. Images of the cross-sections were obtained using a Jeol 6310 scanning electron microscope after a thin layer of gold had been sputter coated onto the sample surface to prevent charging.

Examination of a range of batteries which failed after varying numbers of cycles, between 10 and 133 times, indicated that there was a greater thickening of the corrosion layer on the edge of the grid bars compared to the top and bottom. This observation was most clearly illustrated on the bad cell of the battery that sustained 92 cycles to failure. A photomicrograph showing the grid/corrosion in this cell is recorded later in this paper, for comparative purposes with the FE model.

3. Calculation of electron flow in a material

In order to use ANSYS to solve current conduction problems it is necessary to make the analogy with the heat transfer problems. ANSYS solves electrical problems as a heat flow problem and substitutions must be made for the input and output variables. The quantity of heat flowing, Q, within a material is proportional to the length of time, t, cross-sectional area, A, and temperature gradient, as shown in Fig. 1. The temperature gradient, between points A and B in the figure, can be expressed in terms of the two temperatures T_1, T_2 and the length, l, as shown in Eq. (1).

$$\frac{T_1 - T_2}{l} \tag{1}$$

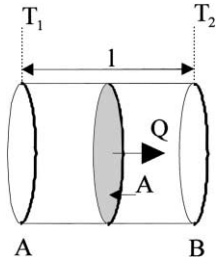

Fig. 1. Heat flow in a material.

As the heat flow, Q, is proportional to these quantities it can be expressed as

$$Q \propto tA\frac{T_1 - T_2}{l} \tag{2}$$

Therefore incorporating the thermal conductivity, K, Eq. (2) becomes

$$Q = KtA\frac{T_1 - T_2}{l} \tag{3}$$

When considering the electrical problem the current flow, I, is equal to the quantity of electrons flowing, Q, with time, t, as shown in Eq. (4).

$$I = \frac{Q}{t} \tag{4}$$

Current flow can also be related to potential difference, V, and resistance, R, by Ohm's law.

$$I = \frac{V}{R} = \frac{V_1 - V_2}{R} \tag{5}$$

And resistance can be written in terms of resistivity, ρ, length and area by

$$R = \frac{\rho l}{A} \tag{6}$$

Therefore by combining Eqs. (4)–(6), Eq. (7) is obtained:

$$Q = \frac{1}{\rho}tA\frac{V_1 - V_2}{l} \tag{7}$$

From the equations describing thermal (3) and electrical (7) behaviour, the thermal conductivity, K, is seen to be analogous to the electrical conductivity $1/\rho$. This allows an electrical problem to be solved in a thermal context if the substitution of input and output variables shown in Table 1 is made. The equations stated above for electrical and heat conduction are for one-dimensional (1-D) cases, however, in

Table 1
Substitution of input and output variables

	Thermal (ANSYS)	Electrical equivalent	Symbol
Input variable	Temperature	Potential (voltage)	Φ
	Heat generation	Current influx	Q
	Thermal conductivity	Electrical conductivity	K
Output variable	Sum of thermal flux	Current density	TF

the instance of the battery electrode it is necessary to generate a solution for 2-D or 3-D problems. ANSYS solves 2-D and 3-D problems by applying the Laplace equation [3]. This equation can be used for solving a wide range of continuous physical processes including, heat conduction and the distribution of electric potential. The equation can be written in its most basic form as shown below:

$$\frac{\partial}{\partial x}\left(k_x \frac{\partial \Phi}{\partial x}\right) + \frac{\partial}{\partial y}\left(k_y \frac{\partial \Phi}{\partial y}\right) + \frac{\partial}{\partial z}\left(k_z \frac{\partial \Phi}{\partial z}\right) + Q = 0 \qquad (8)$$

where Φ is an unknown function assumed to be a single value within the region and k_x, k_y, k_z, and Q are known specified functions of x, y and z, respectively. For more detailed information on the solution techniques used to solve this equation the ANSYS guides [4] should be consulted.

4. Meshing of the geometry

In order to find the FE solution to a problem, it is first necessary to input the geometry of the component to be analysed into the package. After this step has been completed, the geometry is divided into smaller sections, called elements, which form a mesh. The mesh size and element shape, are predefined before the geometry is meshed. A finer mesh with smaller elements provides a more accurate solution compared to a coarser mesh as is illustrated in Fig. 2.

Solution accuracy is also influenced by element type. Generally elements can be defined in terms of their shape and the number of nodes or integration points. Larger numbers of integration points allow a more accurate solution for a given size of element. For the purposes of this analysis, a 2-D model utilising 2-D flat elements was used.

An advantage of using a coarse mesh and simple element is a reduction in the time taken by the computer to calculate the solution. For the size of the geometries modelled in this instance, even the most finely meshed condition only took ANSYS seconds to calculate an answer, therefore there was little advantage to using a coarser mesh. The element type used was a 2-D four-node quadrilateral solid element, referred to in the ANSYS guide as PLANE55. In order to ensure consistency of results, element and mesh size were kept the same for all calculations.

5. ANSYS output

Once the solution to a problem is obtained, post processing in ANSYS allows calculation of thermal flux (TF) in each direction. This can be calculated at the centre of each element or at the nodes. The output command used was 'sum of TF' which is calculated using the values of TF in each of the three directions: x, y and z, using Eq. (9). Since the model of the grid is 2-D, TF_z, can be assumed to be zero.

$$TF_{SUM} = \sqrt{|TF_x|^2 + |TF_y|^2 + |TF_z|^2} \qquad (9)$$

The net sum of TF, TF_{SUM}, is represented in the form of a

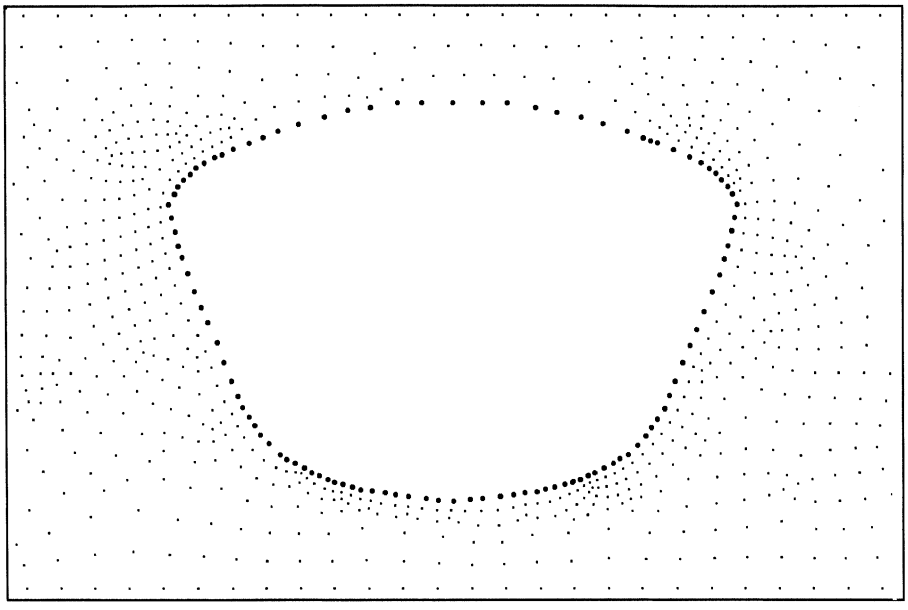

Fig. 3. Application of loads onto nodes of meshed geometry (positions of nodes are represented by dots on the diagram: large dot (•), node where a constant temperature (or potential) is applied; small dot (·), node where constant heat generation rate (or current influx) is applied).

contour plot. Positions of contour lines are determined from the flux gradient of the surrounding area and do not correspond to the positions of elements or nodes where the fluxes are calculated.

6. Application of Input variables into the model

When the component geometry is defined and meshed, temperatures and heat generation rates are applied onto the nodes. Nodes defining the edge of the grid bar are set at a constant temperature (potential), while heat generation (electron flux) is applied to the remaining nodes. This is shown diagrammatically in Fig. 3. For the analysis, properties of the active material are assumed to be isotropic, requiring the 'isotropic material properties' option within ANSYS to be used when inputting a value for conductivity.

7. Assumptions

The flow of electrons between the positive active material and lead grid, during operational life of a battery, is influenced by a range of factors. It is neither necessary nor practical to include all of these in the model. However, in order to exclude these a number of assumptions need to be made, details of which are given in the following paragraphs.

- Active material conductivity

  During discharge of the positive electrode lead dioxide is converted into lead sulphate. Lead sulphate is an insulator, therefore the proportion of the plate consisting of lead dioxide reduces during discharge and the resistance of the active material increases accordingly. However, this reaction does not occur uniformly throughout the bulk of the active material, so variation of conductivity with position relative to the grid bar and electrode surface may also occur. Any attempt to incorporate these changes into the model would prove to be highly problematic and for this reason it is assumed that the conductivity of the active material is constant and uniform throughout the electrode.
- Active material cracking

  Cracks are often observed within the bulk of the active material and at the grid/corrosion layer and corrosion layer/active material interfaces. Cracking will influence current density, as current flow will concentrate in areas of good electrical contact adjacent to a cracked region. Cracks form between the grid and positive active material during curing, or as a result of stresses caused by the changing dimensions of the active material while cycling. The geometry of the grid will influence the formation of cracks to a certain extent as sharp corners can act as areas of stress concentration, however, variations in current density are unlikely to be a significant contributor to the formation of cracks. It would be extremely hard to reliably predict where cracks may form relative to the grid bar and for this reason they are not included in the model.
- Corrosion layer

  The corrosion layer is not integral to the model. When the corrosion layer is uniform it will not influence current density and can therefore be excluded. However, variations in corrosion layer thickness will influence current density. Obtaining reliable values of the thickness in order to enter would be extremely difficult and would not contribute significantly in determining the best grid design.

Table 2
Quantities inputted into ANSYS model

Variable	Variable value entered into model
Constant temperature node	0
Constant heat generation	1
Isotropic conductivity	1

8. Selection of input variables

The fundamental difference between the model and battery electrode is that the input variables entered in the model are constants, whereas in the battery they vary depending on parameters such as discharge rate and depth of discharge. This makes quantitative estimation of actual current density values extremely difficult. However, the aim of this investigation is to evaluate the relative performance of different grid designs and this can be done if variables are kept constant. For this reason all geometries of the grids analysed are to the same scale and have the same loads applied, with the result that all variations in the solutions are a consequence of geometrical differences alone. The actual values entered into the ANSYS model are shown in Table 2.

9. Interpretation of a 2-D model representing a 3-D problem

The positive electrode is a 3-D component of the battery consisting of a lead grid surrounded by current producing positive active material. The task of inputting the geometry of the grid and active material into ANSYS can be simplified by considering the problem in two dimensions only. The 2-D sections of the electrode can be taken, in the plane of, or perpendicular to the orientation of the electrode. Fig. 4 shows a 3-D representation of a small section of positive electrode with the sections marked.

The actual cross-sectional shape of the grid bar is not square, as shown in the diagram above, but is a trapezoidal shape with curved edges. It is therefore symmetrical in the vertical plane but not in the horizontal. If the 'in-plane' section is modelled a certain amount of flux would flow in the z-direction (out of the paper), however, the flux in the

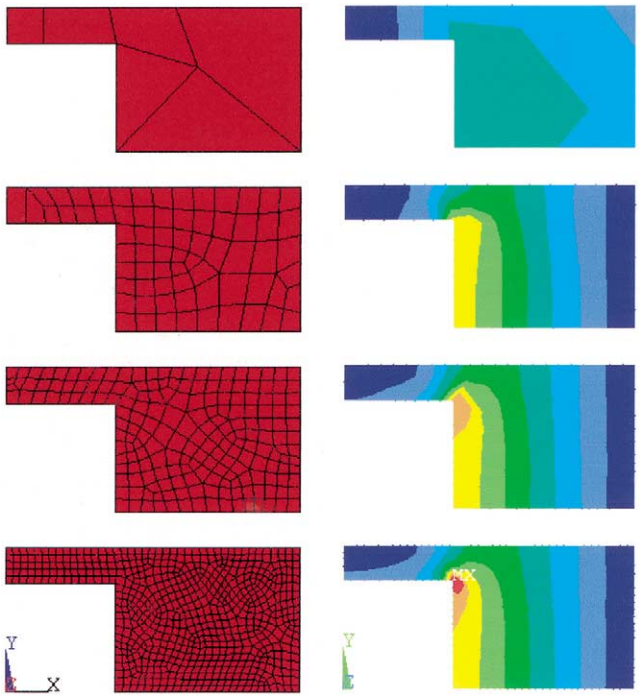

Fig. 2. Effect of mesh size on FE solution (coarse mesh, top/fine mesh, bottom).

x- and y-directions can be predicted. Fig. 5 shows the variations in current density for a grid hole.

The current density pattern shown in the diagram is symmetrical about the centre line, indicating that on this line there is a flux in the vertical direction but not in the horizontal. It follows that if a perpendicular slice of the electrode is modelled in this position the net flux in the z-direction will be zero and the model will be representative.

10. Evaluation of current grid design

During electrode manufacture the grid is coated in a layer of positive paste which is transformed to positive active material during battery formation. For the purposes of this study an electrode thickness of 1 mm was used. In order to model a component it is only necessary to enter a single repeating unit of the structure. The shaded area in Fig. 6 represents a suitable unit for the current grid design. This area was chosen as it allows a non-symmetrical shape of grid bar to be modelled.

A typical cross-section from the bad cell of a battery cycled 92 times is shown in Fig. 7. A uniform corrosion layer is visible around the top and bottom surfaces of the bar,

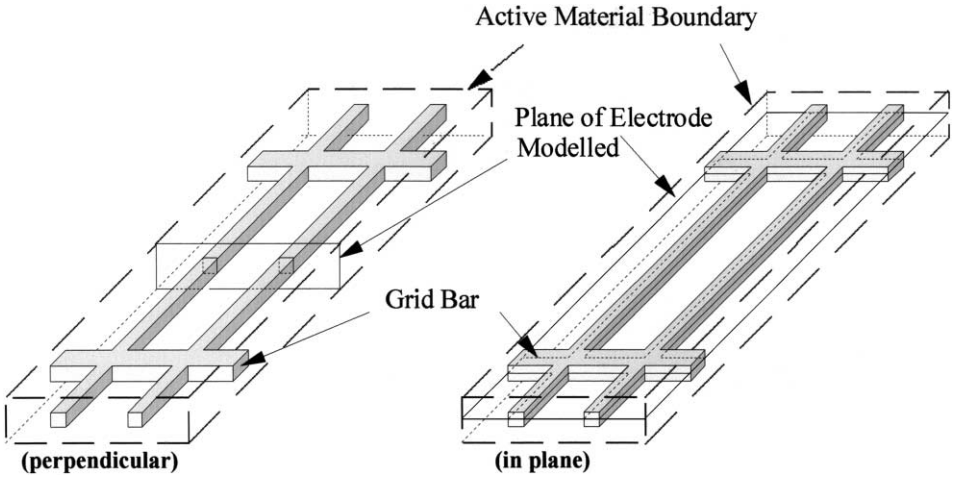

Fig. 4. Sections taken when modelling positive electrode.

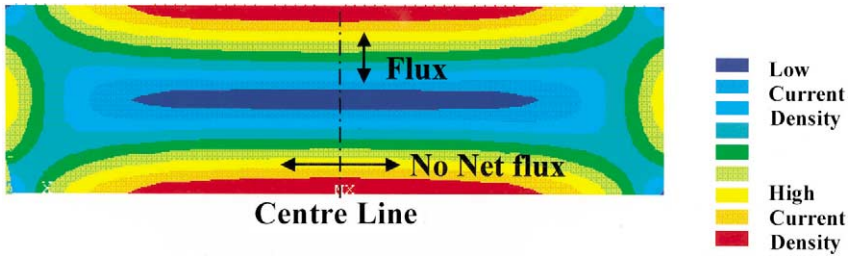

Fig. 5. Variations in current density for a grid hole.

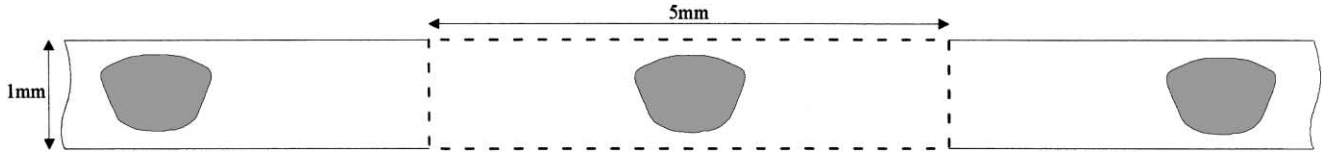

Fig. 6. Positive electrode cross-section showing area modelled.

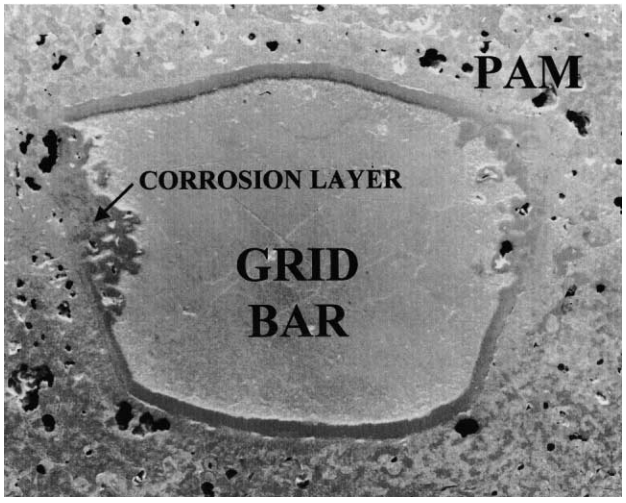

Fig. 7. Cross-section of grid bar showing thickening of corrosion layer.

however, substantial thickening of the layer has occurred on the upper section of the sides.

The variation in current density produced when the geometrical arrangement of the grid bar shown in Fig. 7 is entered into ANSYS is shown in Fig. 8a and b. Fig. 8a shows a cross-section of grid bar with surrounding positive active material and Fig. 8b is a close-up of the grid bar showing the current density around the surface of the grid bar. It is apparent that the areas having high values of the corrosion layer thickness in Fig. 7 correspond to the areas of high current density shown in Fig. 8.

11. Effect of grid bar orientation on current density distribution

During the grid production and pasting processes involved in battery manufacture, grid bars can sometimes become rotated about their central axis. This can result in a variation in current density distribution around the grid bar surface. Fig. 9 shows the current density distribution around two grid bars, orientated at 0 and 40°, respectively.

The variations in current density distribution can be compared more easily if the normalised current density is plotted against distance around the grid bar, shown diagrammatically in Fig. 10.

On the basis of current theory the curves shown in Fig. 10 would be expected to be smooth, however, they each contain a number of perturbations. This is caused by inconsistencies due to the mesh size and can be ignored. In comparing the curves, the effect of rotating the grid bar is to reduce the maximum current densities on each side. Grid bar orientation is therefore not an important factor and would not be expected to affect adversely battery performance in terms of corrosion layer growth.

12. Grid bar modification

In order to reduce the probability of a thick corrosion layer forming on the surface of the positive electrode grid, the current density on the surface must be as low as possible. This can be achieved by modifying the electrode to produce a uniform distribution and as low a current density as possible. One approach to achieve this is to modify the geometrical arrangement of the grid and active material. However, geometrical alterations to the design will have implications with regard to battery manufacturing method, performance and cycle life, etc. In addition to current density a number of additional conditions must be considered, details of which are given in the following section.

- Mechanical strength

  During manufacture the grid is rolled, pasted and cut into individual electrodes. These processes put the grid under mechanical stresses unlike those generated during battery operation. Any grid design must be able to withstand such stresses.
- Mechanical stability during corrosion

  As a battery grid corrodes the lead is converted into lead oxides of varying oxygen content. The consequential reduction of the grid bar cross-section, results in a decrease of mechanical strength and electrical conductivity. Consideration must therefore be given to the remnant strength of the grid bar after a certain amount of surface corrosion has occurred.
- Grid weight

  For many batteries weight is an important factor and it is advantageous to have as light a grid as possible.

When comparing different electrode designs any variation in current density must be a consequence of grid design only and not of size. To ensure all designs could be compared with each other the grid and active material cross-sectional areas were kept the same as that of the original electrode.

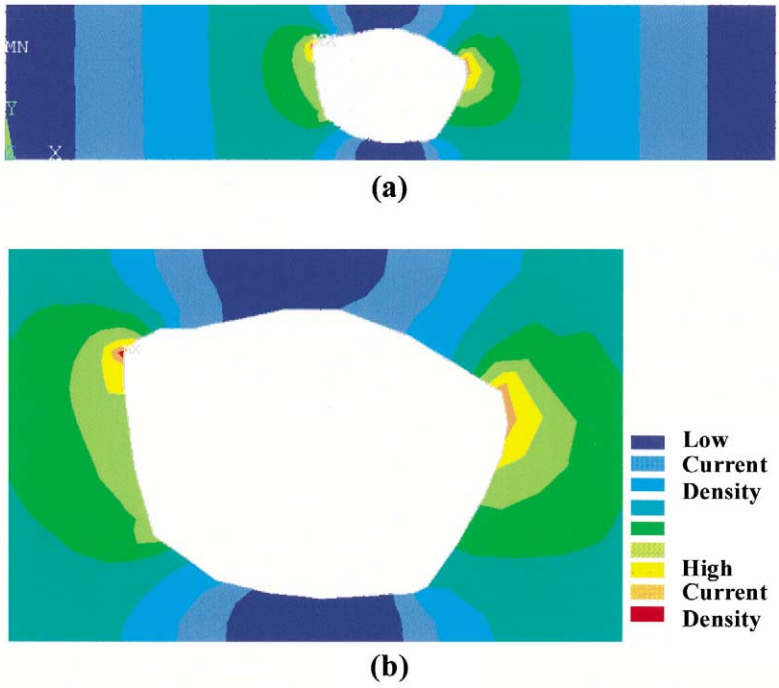

Fig. 8. Current density distribution around a battery grid bar.

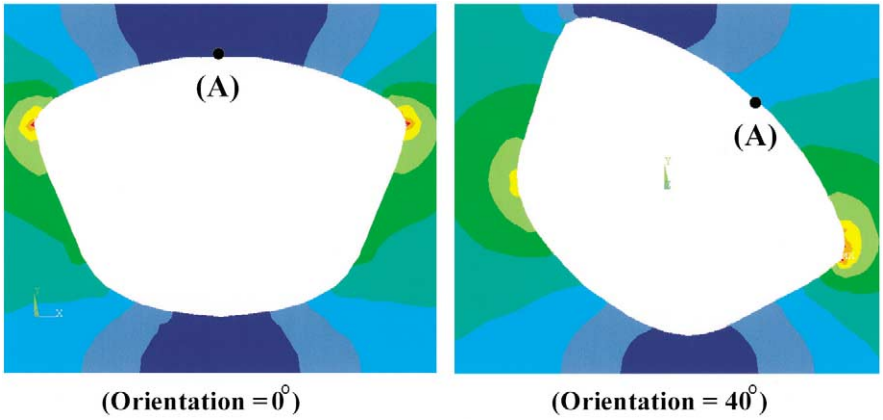

Fig. 9. Effect of grid bar rotation on current density.

Dimensions of the grid designs used in the investigation are given in Table 3.

Current density distributions around the grid bar for each of the designs in Table 3 are shown in Fig. 11. Plotting the normalised current density against distance around the grid allows the magnitude of the current densities to be compared more easily, as shown in Fig. 12. From the figure it can be seen that there are differences in the value of current

Table 3
Dimensions of grid designs investigated

Design	Dimensions (mm)	CSA (mm^2)	Circumference (mm)	Normalised circumference
Circle (diameter)	0.82	0.54	2.58	0.95
Square (width)	0.74	0.54	2.94	1.08
Hexagon 0 (width)	0.79	0.54	2.74	1.01
Hexagon 30 (width)	0.79	0.54	2.74	1.01
Hawker energy (height)	0.7	0.54	2.71	1
Design (width)	1			

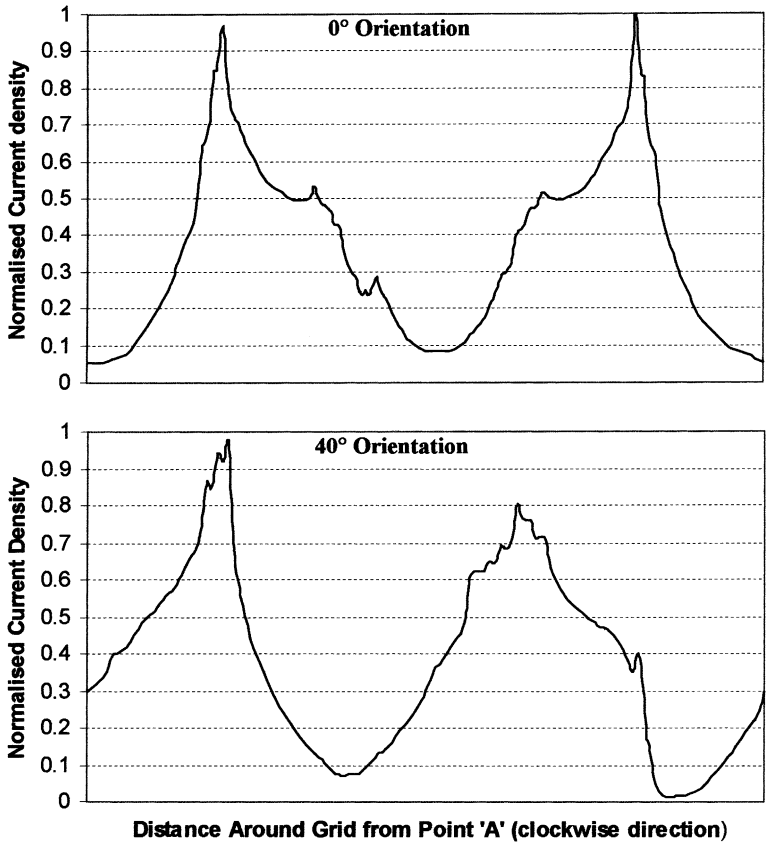

Fig. 10. Current density vs. position around grid bar.

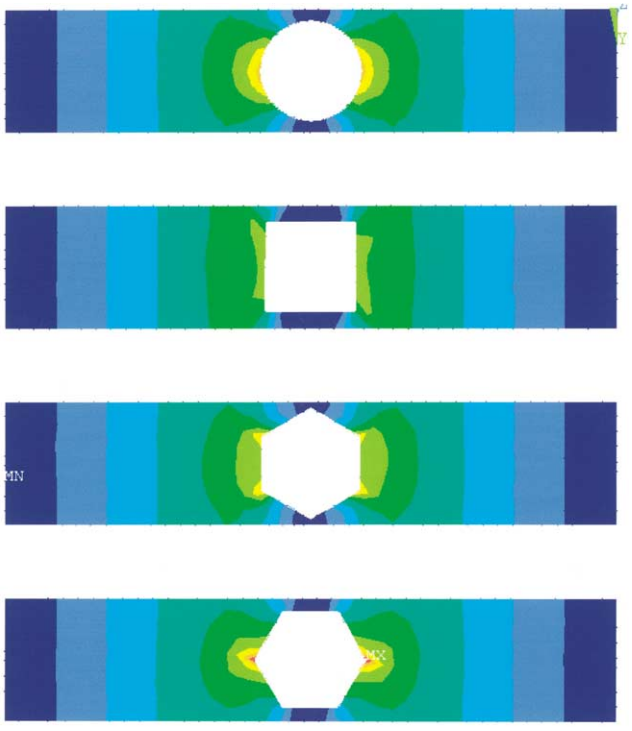

Fig. 11. Current density around new grid cross-sections.

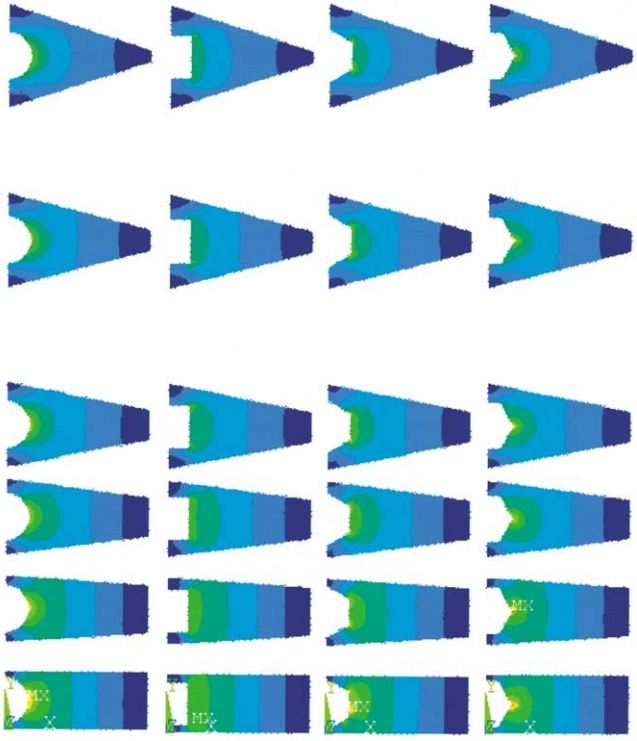

Fig. 13. Effect of positive active material geometry on current density distribution around grid bar.

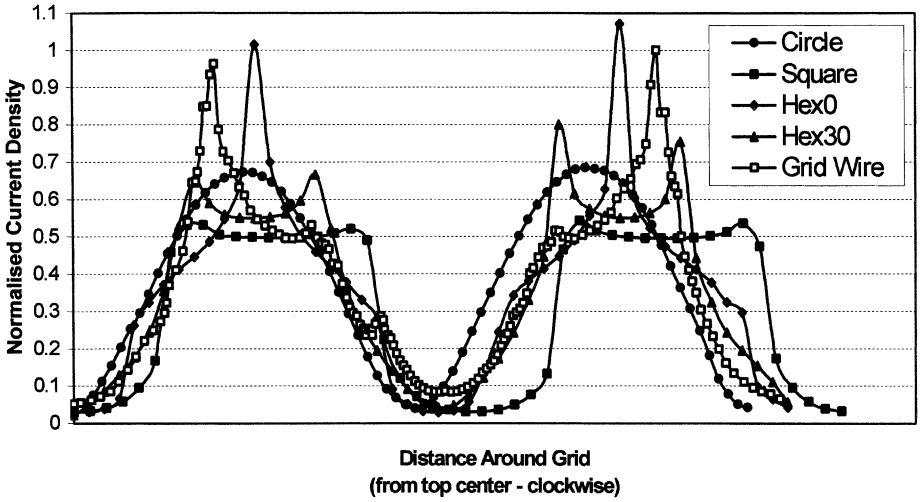

Fig. 12. Variations in current density on surface of different grid designs.

density obtained on each side of the bar. These can be accounted for by variations in the meshing generated by the computer. The maximum current density was obtained from the 0° orientated hexagon, followed by the original grid design, 30° orientated hexagon, circle and square. This is an interesting result as the relatively 'pointed' corners of the square do not appear to affect the current density significantly and the circle, which does not contain any 'pointed' surfaces, produces a higher maximum current density. This result highlights the influence of the amount of active material that surrounds the grid surface and suggests that re-arranging the geometry of the active material could be a much more effective method of reducing current density.

13. Effect of changing positive active material geometry

To investigate the effect of modifying the active material distribution around the grid bar a series of models were set-up where these changes were represented. Contour plots for a range of positive active material distributions are shown in Fig. 13.

The effect of increasing the amount of active material on the top and bottom of the grid bar is clearly evident. It can be seen that increasing the amount of active material in this way increases proportionally the current density in these regions, resulting in a decrease of the peak current density at the sides of the grid bar where the maximum values formerly occurred.

A cross-section through a hypothetical battery design implementing this principle is shown in Fig. 14. In order to implement this arrangement it can be seen that it is necessary to offset the grid bars in the positive and negative electrodes relative to each other. Although there would be clear advantages, as described, in adopting this arrangement, there are likely to be practical problems in implementing this concept where grid bars run in an orthogonal arrangement. One possible solution would lie in the construction of a battery where the grid bars ran in one direction only. The effect of this on the assembled electrode stiffness and strength, and the implications for a completed

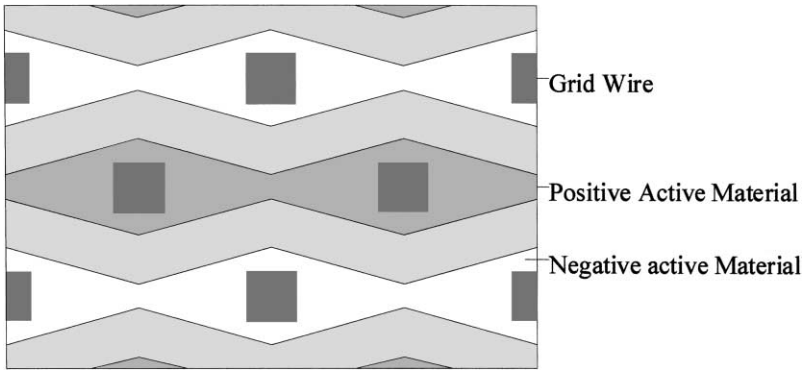

Fig. 14. Cell design to reduce current density.

battery would need to be assessed. It is suggested that considerable mechanical stiffness would be lost with this configuration.

14. Conclusions

The following conclusions can be drawn from the investigations.

1. Grid bar and positive active material geometry affect corrosion layer thickness.
2. Rotation of grid bars does not result in an increased current density distribution on the bar surface.
3. Current density distribution is greatly affected by grid shape.
4. Due to the uneven distribution and thickness of positive active material around the grid bar, a design with sharp corners such as a square section, does not necessarily result in the maximum current density distribution occurring at the corner of the square.
5. Changing the geometry of the positive active material surrounding the grid bar can have a significant effect on reducing the current density distribution.

Acknowledgements

Engineering and Physical Sciences Research Council support in the form of a studentship is acknowledged.

References

[1] D. Pavlov, A theory of the grid/positive active-mass (PAM) interface and possible methods to improve PAM utilisation and cycle life of lead/acid batteries, J. Power Sources 53 (1995) 9–21.
[2] ANSYS Inc., Southpointe 275 Technology Drive, Canonsburg, PA 15317.
[3] O.C. Zienkiewicz, The Finite Element Method in Engineering Science, McGraw-Hill, London.
[4] ANSYS Theory Reference, 8th Edition, SAS IP Inc.©, 000855, Chapter 6.

ELSEVIER

Journal of Power Sources 104 (2002) 208–220

JOURNAL OF POWER SOURCES

www.elsevier.com/locate/jpowsour

Characterisation of separator papers for use in valve regulated lead/acid batteries

R.J. Ball[a,*], R. Evans[b], R. Stevens[a]

[a]*Department of Engineering and Applied Science, University of Bath, Bath BA2 7AY, UK*
[b]*Invensys, Westinghouse site, Chippenham, Wiltshire SN15 1SJ, UK*

Received 2 July 2001; received in revised form 3 September 2001; accepted 3 September 2001

Abstract

Separator papers are an essential component of a valve regulated lead/acid (VRLA) battery. In addition to separating the positive and negative electrodes, they provide a constant pressure on the active materials thereby reducing the rate of degradation during cycling. Dendrites formed from the negative active material are also less likely to cause short circuits in batteries where a separator is employed. The level to which a separator will influence the performance of a VRLA battery it strongly dependent on its properties. This paper describes the results from a series of tests used to characterise the properties of separators most influential to battery performance. These properties include, the macroscopic structure, permittivity and wicking rates. During the operational life of a VRLA battery the volume of electrolyte will decrease, due mainly to the electrolysis of water during overcharging. The consequence of this process is a variation of acid saturation during the life of the battery, which will have a direct influence on the compressive and diffusive properties of the separator. Compressive and diffusive characteristics were therefore measured over a range of saturation levels. Characterisation was conducted on three separator types. Types A and B were 100% glass but had slightly different structures and type C contained 8% polyester fibres mixed with glass.

Keywords: Separator paper; Diffusivity; VRLA

1. Introduction

Separator papers play an important role in the operation of a valve regulated lead/acid (VRLA) battery in several ways. In addition to providing a means by which to immobilise the electrolyte and prevent positive and negative plates from coming into contact with each other, they can influence the reactions occurring within the battery. The behaviour of a separator paper in the environment of a battery is directly related to its structure. Battery separator structures are complex and characterised using a wide range of different techniques. Currently used methods can be divided into two groups, each concerned with a different aspect of the influence of separators on battery operation.

The first of these is concerned with the flow of liquid or gas through the paper, which include wicking, drainage and diffusion tests. Culpin [1] has examined these characteristics in some detail. He investigated the drainage characteristics of separators in both the free and compressed state. Testing in the compressed state simulates the forces exerted by the cell walls through the electrodes on the separator. Paper saturation was calculated from the dimensions and weight difference of the papers between the saturated and dry state.

The second type of test evaluates the behaviour of the separator whilst under a compressive load [2,3]. This is normally combined with measurement of the change in force or strain associated with variations in paper saturation. This is relevant as changes in saturation occur as a result of electrolyte water loss during cycling.

There is no universally agreed standard method for the determination of a simple parameter such as separator thickness. Both 'The Battery Council International' (BCI) and 'The Japanese Industrial Standards' (JIS) propose different methods. The BCI utilise a 29 mm anvil and 10.34 kPa load, whereas the JIS use 10 cm × 10 cm samples with a 20 kPa load [4]. These different test methods can give variations in measured parameters of up to 20% for the same material. It is therefore important to only use one test protocol when designing batteries. The compressive force exerted on the battery plates by the separator will be

* Corresponding author. Tel.: +44-01225-826826; fax: +44-01225-826098.
E-mail address: r.j.ball@bath.ac.uk (R.J. Ball).

0378-7753/02/$ – see front matter
PII: S0378-7753(01)00925-9

influenced by a number of factors, which must be taken into account in battery design. The most significant of these are as follows [5]:

- how thickness is measured;
- variation in separator materials;
- variation of the plate dimensions;
- draught on battery case;
- separator compression used (restrained thickness/unrestrained thickness);
- acid saturation level;
- density of separator;
- surface area of separator;
- case material used;
- uniformity of compression between plates.

When considering the problem of characterising a more complex property such as behaviour under compressive loading, whilst saturated with electrolyte, there is even more opportunity to vary procedures. For example, the viscoelastic properties of the paper will influence results depending on what load rate is used. Sample dimensions can also affect results.

Nakamura et. al. [2] have studied the compressive properties of separators using a jig, where a stack of five separator papers are mounted horizontally between two plates. The distance between the plates is variable and measurements of the load were taken via a load cell. Samples were compressed to a specified load and then the acid added after a period of 1 hour had elapsed. In comparison, an alternative approach adopted by McGregor [3] utilised a specially designed piston cell. This consisted of a normal battery cell with one of the walls connected to a piston therefore allowing variations in cell compression to be made. Separator papers were held in the vertical position and dividing plates inserted between the papers. Compressive loads were applied and measured using a pressure gauge attached to a regulated gas supply and the cell piston.

Results from both researchers indicated the general trend of a reduction in thickness or force applied by the paper as saturation was increased from 0%. However, results from Nakamura, suggest a reversal of this trend and an increase in force after a saturation of approximately 50% is reached.

This paper describes results obtained from the characterisation of three separator paper types using a range of techniques.

2. Experimental methods

2.1. Scanning electron microscopy

Samples of each separator type studied were examined in a JEOL 6310 scanning electron microscope. In order to prevent charging of the glass fibres a thick layer of gold was applied using an Edwards sputter coater.

2.2. Wicking measurements

The rate at which an electrolyte rises up a sample of separator paper by capillary action will be influenced by both separator structure and material. It is extremely difficult to model the flow of electrolyte through a fibrous material such as a separator; however, if the pores are assumed to be round in cross-section the wicking characteristics can be described using the Washburn equation. The equation relates the velocity of the liquid, v ($\mathrm{d}h/\mathrm{d}t$), at a given height, h, to pore radius, r, surface tension, γ, contact angle between liquid and solid surface, θ, viscosity, η, density, ρ, and the gravitational constant, g. The equation is generally written in the following form [1]:

$$v = \frac{\mathrm{d}h}{\mathrm{d}t} = \frac{2r\gamma\cos\theta}{8\eta h} - \frac{r^2\rho g}{8\eta} \quad (1)$$

integration of Eq. (1) ignoring the gravity term yields Eq. (2), where K is tortuosity [1].

$$h^2 = \frac{\gamma r t\cos\theta}{K^2 2\eta} \quad (2)$$

Eq. (2) predicts that for values of $h \ll h_\mathrm{m}$, where h_m is the maximum height reached, at infinite time, the relationship between h^2 and t is linear [6]. Wicking characteristics of different separator papers were compared by plotting height squared, h^2, versus time, t, within the saturation range where the gradient is proportional to the wicking rate.

Wicking tests were conducted using separator paper strips of 20 mm × 155 mm. Separator paper is manufactured as strip (or roll) using a continuous process. Samples were cut at 0 degrees and at 90 degrees to the manufacturing direction of the paper. Dots of saturated methyl red indicator solution in ethanol were applied at 10 mm intervals along the length of the strip, starting 5 mm from one end. Methyl red is orange when neutral and turns to a deep red on contact with acid thus allowing the electrolyte front to be clearly visible.

Each strip was suspended in electrolyte so that the meniscus was level with the first dot 5 mm from the strip end. The time the electrolyte front reached each dot was then recorded until the strip was totally saturated and all the dots had changed colour.

2.3. Permeability

The pore size distribution of the materials was determined using a liquid displacement method. This method relies on the principle that there is a rise of liquid in a capillary due to surface tension. At equilibrium, the following expression can be written for liquid rising up a capillary.

$$2\pi r\gamma\cos\theta = r^2\pi h\rho g \quad (3)$$

Capillary or pore radius, r is expressed in terms of the height reached by the liquid, h, surface tension of liquid, γ, density of liquid, ρ, contact angle between the liquid and capillary wall, θ, and gravitational constant, g. By making

the substitution of pressure, $P = h\rho g$, into equation 3, equation 4 is obtained.

$$Pr = 2\gamma\cos\theta \tag{4}$$

Where, $\gamma\cos\theta$ is equal to the Wilhelmy surface tension. If the wetting liquid is assumed to have a contact angle of 0 then Eq. (4) can be re-arranged in terms of the pore diameter (d), thus allowing the porosity distribution to be obtained.

$$d = \frac{4\gamma}{P} \tag{5}$$

Porosity distribution and permeability values were obtained for each of the separator papers characterised. Data was collected using a Coulter Porometer II. A sample comprising of a separator paper disc 25 mm in diameter was cut from a larger sheet using a punch. The sample was then submerged in the wetting liquid for a minimum of 2 min to allow total saturation of the pores. The wetted sample was subsequently placed into the machine, which measures flow rate with change in pressure, and measurements taken. Permeability was measured after porosity since a dry separator is required. Measurements were repeated several times for each sample and an average taken.

2.4. Diffusion

The diffusivity of battery separator papers at varying amounts of saturation was measured using a specifically designed diffusion rig. The diffusion rig consisted of three principal components, the diffusion cell, sampling valve and gas chromatograph. Fig. 1 shows a schematic diagram of the apparatus. During diffusion measurements nitrogen and oxygen flow on each side of the sample held within the diffusion cell. The oxygen side of the cell is vented to atmosphere while the nitrogen side is connected to a sampling valve. Switching the sampling valve allows gas in the sample loop, from the nitrogen side of the cell, to be directed into the gas chromatograph. The quantity of oxygen that had passed through the separator paper in the diffusion cell was determined from the detector response.

The diffusion cell was manufactured from stainless steel and is shown diagrammatically with dimensions in Fig. 2. A gas tight seal was achieved using two PTFE gaskets, which the disk of separator paper being examined was clamped between.

Four interchangeable sampling loops were used in total, one for measurements and an additional three having various

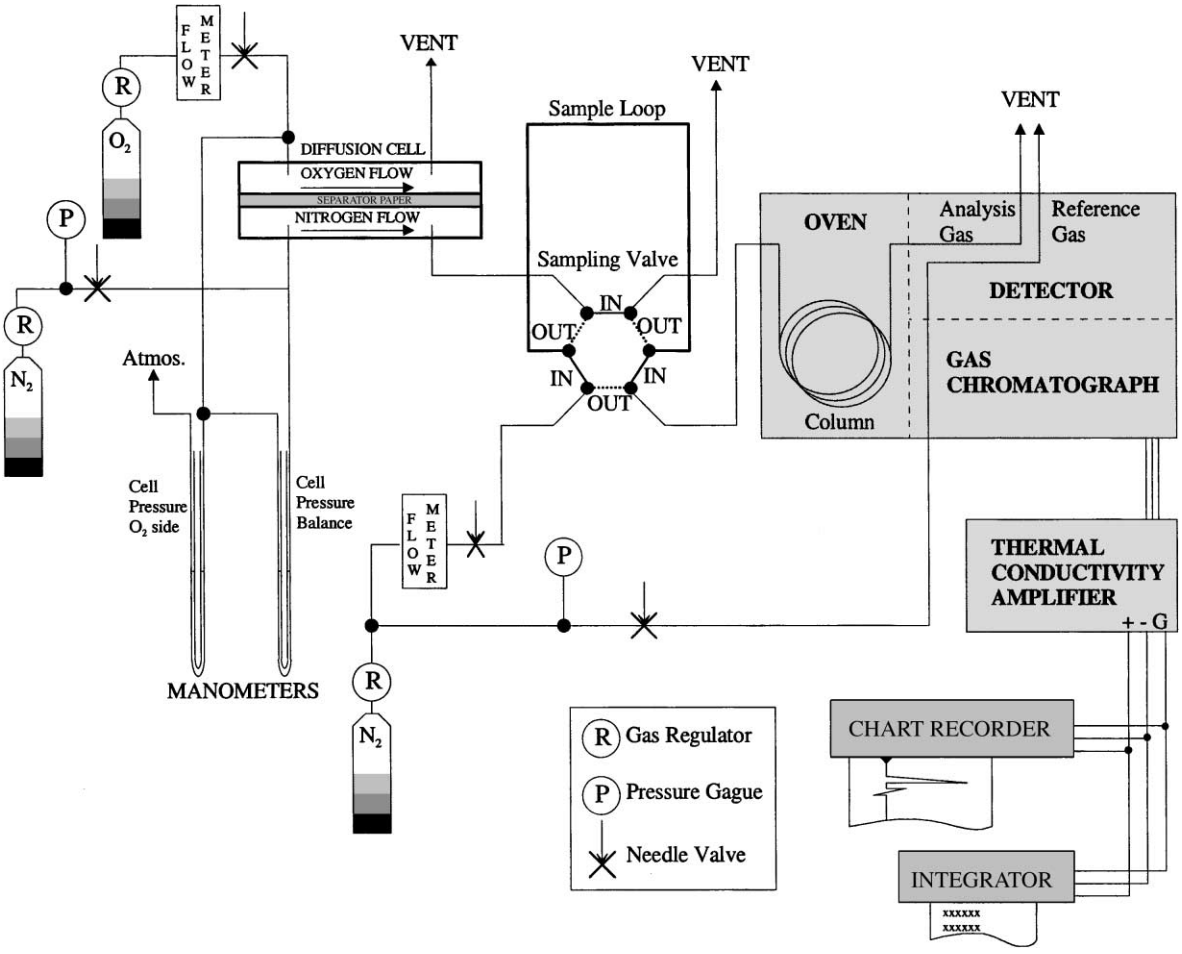

Fig. 1. Diagram of apparatus used to measure diffusivity of separator paper.

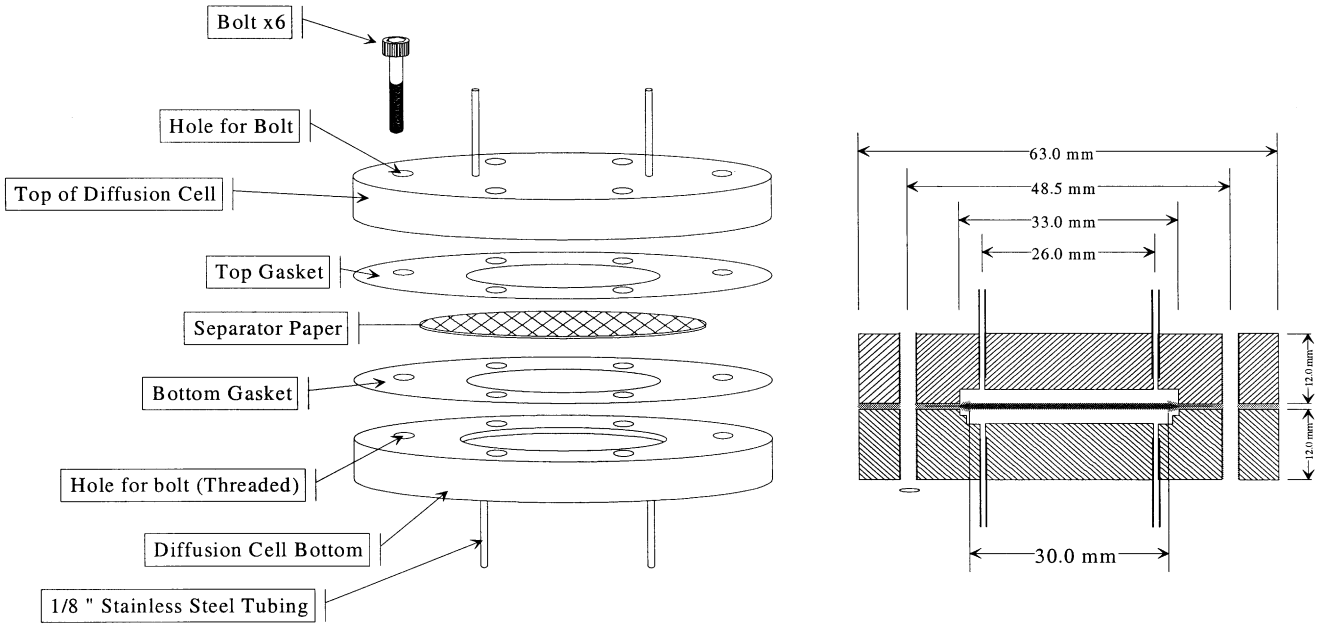

Fig. 2. Schematic diagram of diffusion cell.

Table 1
Sample loop details

Sample loop	Application	Volume (μl)
1	Measurement and calibration	490
2	Calibration	283
3	Calibration	163
4	Calibration	87

volumes for calibration purposes. Loop details are given in Table 1. Sample loops were constructed to the volumes given in the table, as these covered the range of oxygen samples expected during experimentation. The sample loop volume for measurement was 490 μl, therefore 50% is approximately 283 μl, which corresponds to the maximum theoretical volume of oxygen which could pass into the detector for an infinitely permeable sample or membrane. The 163 and 87 μl loops are approximately 66 and 33% of 283, therefore giving evenly spaced points on a calibration curve of volume of oxygen versus detector response.

A Philips PU4500 gas chromatograph was used to determine the volume of oxygen in the sample of gas. An Alltech Porapak®S washed molecular sieve column was used to separate water vapour within the sample gas which had evaporated from the sample surface. This column is traditionally used for the analysis of flue gases, but proved suitable for this application. The volume of oxygen in each sample of gas was determined using a Philips thermal conductivity detector. Due to the susceptibility of the detector filaments to oxidation the detector was operated at its minimum temperature setting. The output from the thermal conductivity amplifier was recorded using a Philips 8251 single pen chart recorder and Hewlett-Packard 3390A Integrator.

Due to sensitivity of the detector to flow rate and temperature it was necessary to calibrate the rig before each set of readings was taken. This was achieved by measuring the detector response when different volumes of oxygen gas were passed into the detector. In practice this was achieved using different sized sampling tubes and passing oxygen gas directly into the sampling valve thus bypassing the diffusion cell. Once calibrated, measurements of oxygen diffusion through the paper could be made.

2.4.1. Calculations

Due to the diffusion cell design it was not possible to constrain the surfaces of the separator once it had been inserted. A consequence of this was that the thickness of the sample could not be determined directly. When a separator paper is wetted with a liquid the surface tension causes the fibres to move together thus reducing the effective paper thickness. Because of this, the thickness of the samples whilst in the diffusion cell could only be predicted from experimental results. Measuring the thickness of a stack of each of the separator paper types examined, at varying saturations, under a constant load, allowed the separator thickness and percentage saturation of the samples in the diffusion cell to be calculated from the weight of water in the sample.

Results for each separator type examined are represented as plots of diffusivity versus percentage saturation. The volume of water in the sample, V_{H_2O}, is obtained from the weight of water in the sample using, Eq. (6). The volume of glass fibres in the sample, W_f, is obtained using Eq. (7). Percentage saturation is then calculated from the volume of water in the sample, the volume of fibres in the sample and the sample dimensions using Eq. (8). The terms used in Eqs. (6)–(8) are as follows: mass of sample, M; mass of

saturated sample before test, M_{SI}; mass of saturated sample after test, M_{SF}; weight fraction of fibre type, W_f; weight of paper per unit area (g cm^{-2}), P; density of fibre type, n (g cm^{-3}), ρ_n; sample area, A_{sample} and sample thickness obtained from experimental results, L.

$$V_{H_2O} = \frac{(M_{SI} + M_{SF}/2) - M}{\rho_{H_2O}} \quad (6)$$

$$V_{fibres} = A_{sample} \sum_n \frac{W_f P}{\rho_n} \quad (7)$$

$$\text{saturation}\,(\%) = \frac{V_{H_2O}}{(A_{sample} L) - V_{fibres}} 100 \quad (8)$$

2.4.2. Determination of separator effective diffusivity

To determine the effective diffusivity of the separator paper the mole fraction of oxygen on the nitrogen side of the cell must be calculated. The mole fraction of oxygen is obtained from the peak area, sample loop volume, and gradient, m, and intercept, c, of the calibration curve of volume of oxygen versus detector response, using Eq. (9). A diagram of the diffusion cell is shown in Fig. 3.

$$y_{O_2,L} = \frac{[(\text{peak area} - c)/m]}{\text{sample loop volume}} \quad (9)$$

Oxygen flux through the separator is calculated from (i) the mole fraction of oxygen on the nitrogen side of the cell, $y_{O_2,L}$, (ii) the flow rate of nitrogen in the cell, v_{N_2}, and (iii) the area of the separator paper exposed by the hole in the gasket, A, using Eq. (10).

$$N_{O_2} = \frac{y_{O_2,L} v_{N_2}}{A} \quad (10)$$

The ratio of the fluxes, N, of two gases on each side of a membrane is equal to the square root of the ratio of atomic masses, M [7,8]. This relationship can be used to obtain the nitrogen flux from the oxygen flux as shown in Eq. (11).

$$\frac{N_{N_2}}{N_{O_2}} = -\sqrt{\frac{M_{O_2}}{M_{N_2}}} = -\sqrt{\frac{32}{28}} = -1.07 \quad (11)$$

The mole fraction of nitrogen on the oxygen side of the diffusion cell is calculated using Eq. (12).

$$y_{N_2,0} = \frac{N_{N_2} A}{v_{O_2}} \quad (12)$$

And the mole fraction of oxygen from Eq. (13).

$$y_{O_2,0} = 1 - y_{N_2,0} \quad (13)$$

Since the gas is continuously being replaced on each side of the cell it is necessary to calculate the average mole fraction of oxygen on each side of the sample. On the oxygen side, oxygen is continuously being added, therefore the concentration increases. On the nitrogen side, nitrogen is continuously being added, consequently the concentration of oxygen decreases. Eqs. (14) and (15) are used to calculate the averages.

$$\overline{y}_{O_2,0} = \tfrac{1}{2}(1 + y_{O_2,0}) \quad (14)$$

$$\overline{y}_{O_2,L} = \tfrac{1}{2}(0 + y_{O_2,L}) \quad (15)$$

Fick's law, Eq. (16), states that the flux across a material is equal to the effective diffusivity, D_{eff}, multiplied by the concentration gradient (dC/dx).

$$N_{O_2} = -D_{O_2,eff} \frac{dC}{dx} \quad (16)$$

Concentration, C, can be related to pressure, P, by rearranging Eq. (17) to give, C in terms of, volume, V, moles, n, gas constant, R, and, temperature, T as shown in Eq. (18).

$$PV = nRT \quad (17)$$

$$C = \frac{n}{V} = \frac{P}{RT} \quad (18)$$

Eq. (18) can be substituted into Eq. (16) to give flux in terms of pressure, shown in Eq. (19).

$$N_{O_2} = -\frac{D_{O_2,eff}}{RT} \frac{dP_{O_2}}{dx} \quad (19)$$

dP_{O_2} is equal to the change in partial pressure of oxygen between the two sides of the separator paper where dx is the

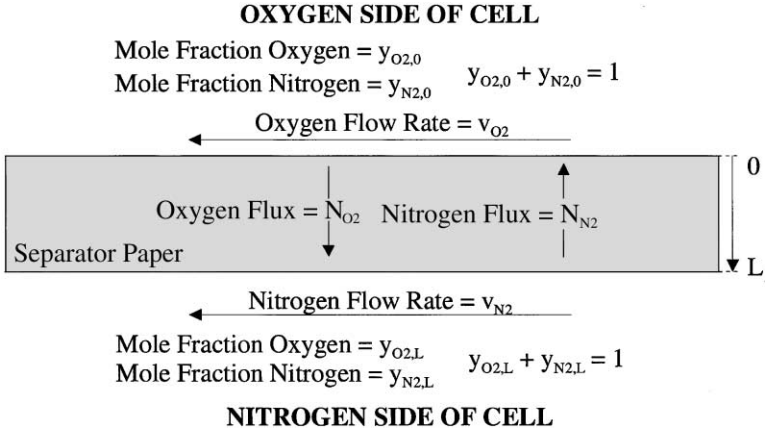

Fig. 3. Diagram of gas flows during measurement of diffusivity.

thickness of the separator, Eq. (19) can therefore be modified to give Eq. (20).

$$N_{O_2} = -\frac{D_{O_2,\text{eff}}(P_{O_2,0} - P_{O_2,L})}{RTL} \quad (20)$$

Since both oxygen and nitrogen behave as ideal gases at room temperature the partial pressure of oxygen on each side of the cell is directly proportional to the molar fraction. This allows the effective diffusivity to be calculated by substituting pressures for mole fractions and rearranging Eq. (20) to give Eq. (21).

$$D_{\text{eff}} = \frac{N_{O_2} LRT}{P(\bar{y}_{O_2,0} - \bar{y}_{O_2,L})} \quad (21)$$

2.5. Compression tests

The apparatus used to characterise the separator papers consisted of a horizontal jig mounted in an Instron mechanical testing machine. Loads were monitored using a load cell with range 0–500 N. The load cell output was recorded using a chart recorder. A diagram of the apparatus is shown in Fig. 4.

A stack of 20 sheets, each 10 cm × 10 cm, was used for each test. These dimensions were chosen since they are similar in size to the sheets of separator paper used in commercially available batteries. Separator paper was provided in the form of a roll and samples were taken in a line along the centre of the paper. Once inserted into the testing machine the stack of papers was compressed until a force equivalent to a pressure of 25 kPa was measured. This load is comparable in magnitude to that used in the manufacture of commercially available batteries. There was no significant difference in the thickness of the papers tested when under this load.

Separator papers exhibit viscoelastic behaviour, the consequence of this being a steady decrease in the force applied by the paper with time after compression had ceased. The rate of the decrease in force is directly proportional to the compression rate. For this reason a slow cross-head (loading) rate of 1 mm min^{-1} was used as this minimised the rate of reduction in force due to paper relaxation.

Following compression of the separator papers an amount of electrolyte equivalent to one-fifth of the total pore volume was added. After the electrolyte had been adsorbed into the separator paper a reading of the force was taken. Initial measurements indicated that steady state conditions were not reached after a period of more than 6 h. Waiting for this period of time has a number of disadvantages such as electrolyte evaporation. However, approximately 90% of the total change in force measured after a period of 30 min from the addition of acid occurred in the first 10 min. It was therefore decided to take measurements of force after a set time of 30 min, since after this length of time, the majority of the change in force had been observed and changes due to evaporation would be insignificant. This step was repeated allowing the force to be monitored at saturation levels of 0, 20, 40, 60, 80, and 100%.

3. Results and discussion

3.1. Scanning electron microscopy

Examination of each separator paper type showed that the papers had a rough and smooth side. Subsequent examination in the scanning electron microscope indicated that the best representation of fibre size and orientation was obtained from the images taken from the smooth side, as more fibres were within the depth of field of the microscope.

Type A glass separator paper is shown in Figs. 5 and 6 at low and high magnifications, respectively. Glass fibres range in diameter between <1 and approximately 3.5 μm. A larger proportion of the thicker fibres appear to be orientated in the

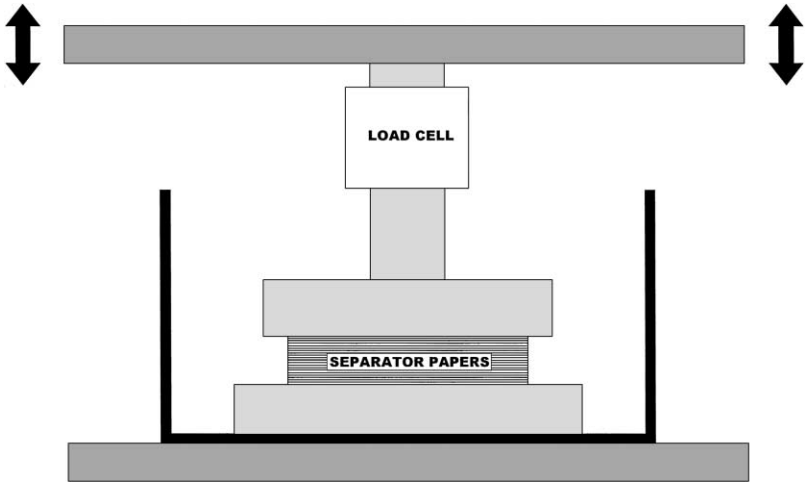

Fig. 4. Diagram of apparatus used to measure compressive properties of separator paper.

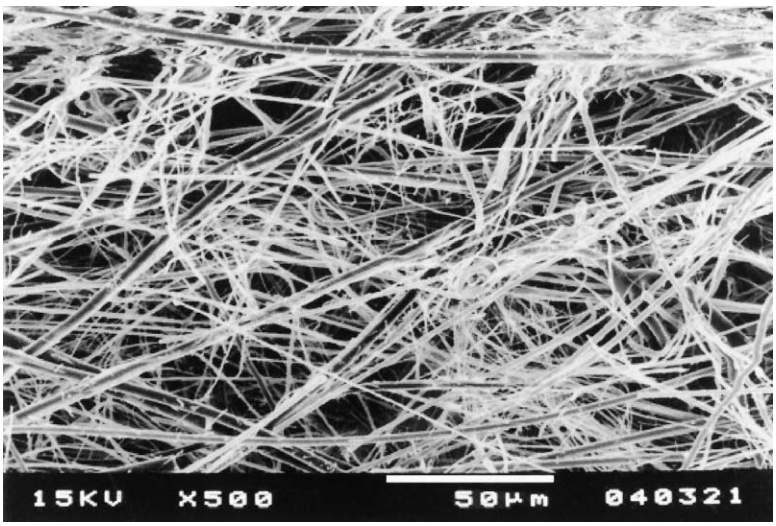

Fig. 5. Separator paper type A—low magnification.

machine direction (horizontal in figure) compared to the thinner fibres.

Images of the type B separator paper are given in Figs. 7 and 8 at low and high magnifications, respectively. Fibre diameters range between <1 and approximately 5 μm. A larger proportion of the fibres are orientated in the machine direction, compared to the other separator papers examined.

Figs. 9 and 10 show low and high magnification images of type C separator paper. Polyester fibres are visible in Fig. 10 and are identified by their thickness, which is significantly larger then that of the glass. The polyester fibres are approximately 20 μm in diameter, and the glass fibres range in size between <1 to approximately 3.5 μm. A number of the glass fibres appear to be permanently attached to the polyester fibres. Both polyester and glass fibres show random orientation in both figures.

3.2. Wicking tests

Within a battery cell, wicking rate will influence the time taken for the electrolyte to penetrate all areas after the initial acid fill. During subsequent operation the separator papers are not completely saturated allowing electrolyte to move between areas of differing saturation. Wicking tests were used to measure the speed at which electrolyte moves through the various separator papers by capillary flow.

Plots of time versus "height squared" for the separator types examined are shown in Fig. 11. When wicking height, h, is much less than the maximum wicking height h_m, a linear relationship is observed, allowing linear regression lines to be plotted between each set of data points [1]. A linear relationship is obtained for both separators containing

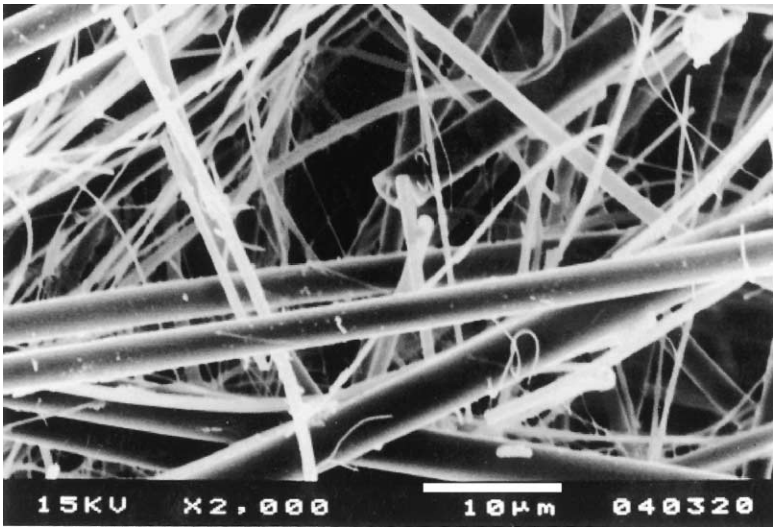

Fig. 6. Separator paper type A—high magnification.

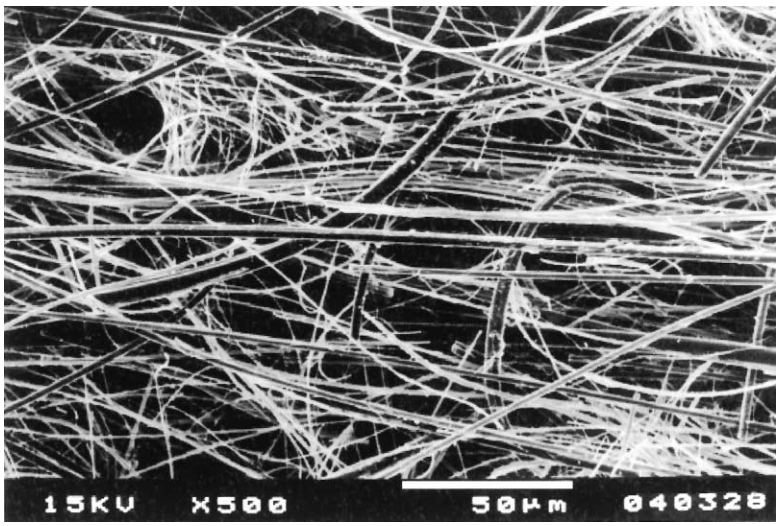

Fig. 7. Separator paper type B—low magnification.

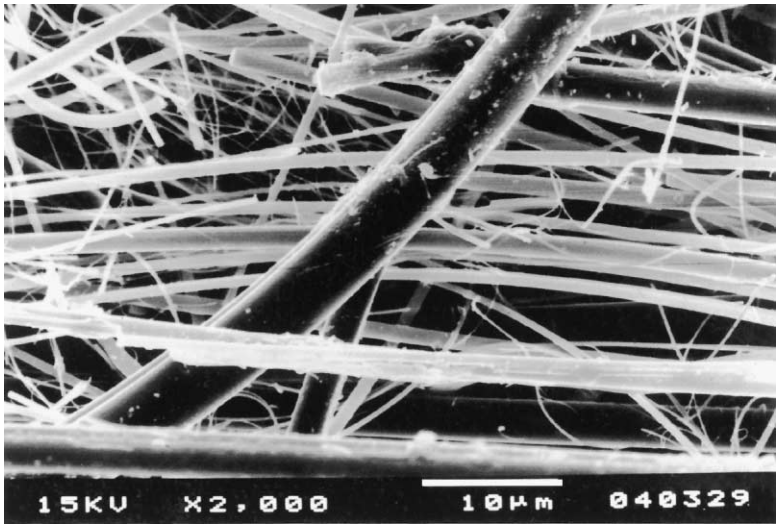

Fig. 8. Separator paper type B—high magnification.

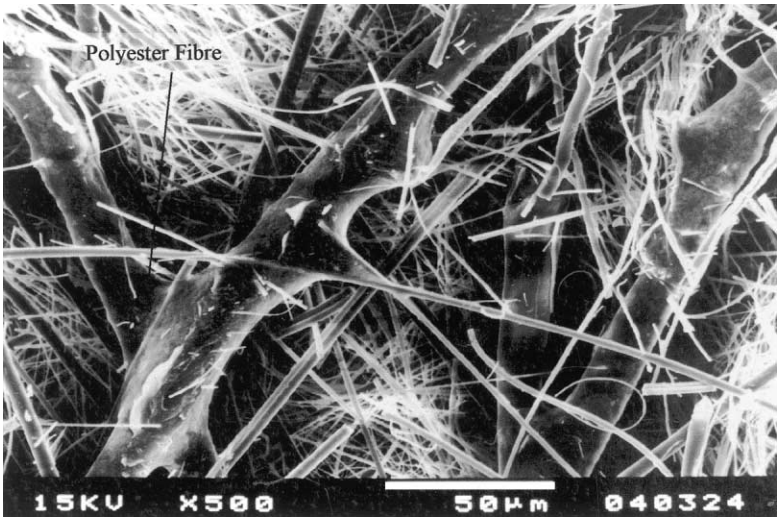

Fig. 9. Separator paper type C—low magnification.

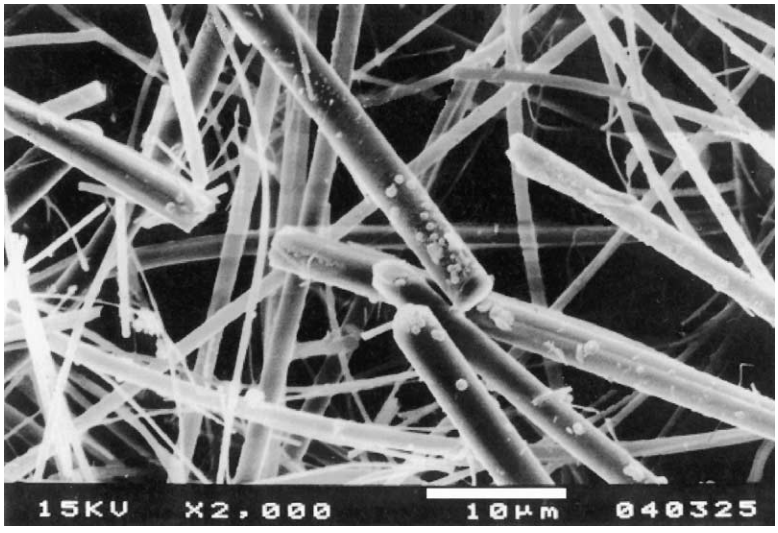

Fig. 10. Separator paper type C—high magnification.

100% glass, however a non-linear relationship is obtained for the separator containing polyester fibres. This is because the polyester fibres have a higher contact angle with sulphuric acid compared to the glass. A lower value of h_m results and the linear t versus h^2 relationship is no longer valid.

Both of the 100% glass separator papers have the highest wicking rate in the machine direction. Wicking rate will be influenced by a number of parameters such as the range of fibre diameters' [2] and fibre orientation. The average wicking rate from the two directions is greatest for the type B separator, suggesting that when saturated and unrestrained it has a larger, average pore radius, or number of pores, compared to the other papers therefore allowing maximum flow of electrolyte. The difference between the wicking rates in the 0° and 90° directions is greatest for the type B separator paper. This is a likely consequence of the higher proportion of orientated fibres, as identified by examination in the scanning electron microscope.

3.3. Permeability measurements

Permeability and porosity measurements are shown in Table 2. The lowest permeability was obtained for the separator containing polyester fibres, type C, which was just over half the value obtained for the 100% glass separators. The values obtained for the two 100% glass separators, type A and B, are very similar although the type B separator has a larger maximum pore size and a higher permeability compared to the type A separator material.

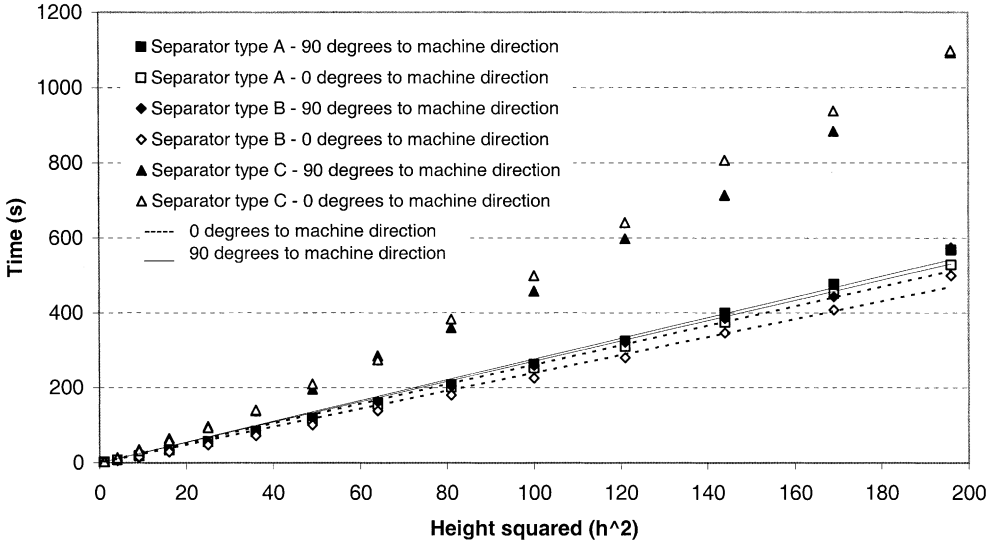

Fig. 11. Wicking rates of separator types A, B and C.

Table 2
Porosity and permeability measurements

Separator type	Porosity (μm)			Permeability (l min^{-1} cm^{-2})
	Minimum	Maximum	Mean	
A	3.9	14.4	5.8	13.2
B	4.5	14.6	6.7	14.7
C	3.0	9.0	4.6	7.9

3.4. Diffusivity measurements

During the life of a VRLA battery, water loss from the electrolyte caused by repeated charging during cycling results in the battery cell operating at an ever-decreasing level of saturation. Separator saturation will affect battery operation by influencing the diffusion of gases and ions between the positive and negative electrodes. At high saturation levels ionic conduction through the electrolyte will be high and diffusion of gases low and at low saturation levels diffusion of gases will be high and ionic conduction low. The effect of saturation on the flow of gases across the separator paper has been determined by measuring the separator diffusivity at varying saturation levels.

Diffusivity measurements have not been made for the type C polyester separator due to its unavailability, however measurements have been taken on the two 100% glass separator papers. Plots of diffusivity versus saturation for type A and type B separator papers are given in Figs. 12 and 13 below.

It can be seen that both graphs exhibit a similar trend. Each plot can be divided into three distinct sections. The first section consists of a horizontal plateau along which the diffusivity remains relatively constant up to a break point. The saturation at which this point occurs is different for the two separator papers examined. At saturation levels above the break point there is a steady decrease in diffusivity, which continues linearly until a diffusivity of zero is reached. Above this saturation the diffusivity remains at zero. This trend is similar to that observed by Culpin [9], where a rapid decrease in diffusivity was observed between saturation levels of approximately 70 and 90%.

Diffusivity of the dry separator papers is similar, around 0.01 cm^2 s^{-1} with the type B separator just above this value, and the type A below. As the saturation of the separator papers increases greater numbers of the gaps or pores between the fibres fill with electrolyte. At low saturation levels this has little effect on diffusivity. However, at higher saturation levels distinct paths through the separator are formed. As saturation increases further individual paths are blocked therefore reducing the diffusivity. This process continues until all paths through the paper are blocked and the diffusivity reaches a value of zero. Culpin [9] suggests that this trend may be a result of the anisotropic structure of the separator paper and the fact that pores in the plane of the paper are generally larger than those in the transverse direction.

Correlation coefficient values of lines plotted using a least squares fit, between the break point and zero saturation (filled points on figures), are 0.97 and 0.98 for the type A and type B separator papers, respectively. This strongly implies that the relationship is linear. The gradient of the line corresponding to the type B separator paper is half that of the type A paper, which suggests that as saturation increases the paths become blocked at a lower saturation level in the type B separator paper compared to the type A. There is little difference between the saturation levels at which the diffusivity becomes zero for both papers.

3.5. Separator paper compression tests

Compression tests, described in the experimental methods chapter, were carried out on type A and type B 100% glass separator papers in order to determine how the force that is exerted by each paper varies with electrolyte saturation. In order to do this it was necessary to compress the papers and

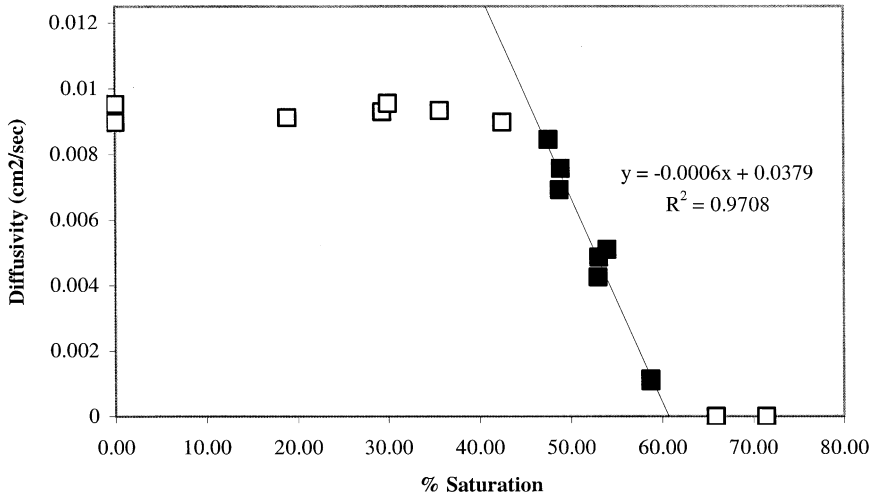

Fig. 12. Diffusivity vs. saturation for separator type A.

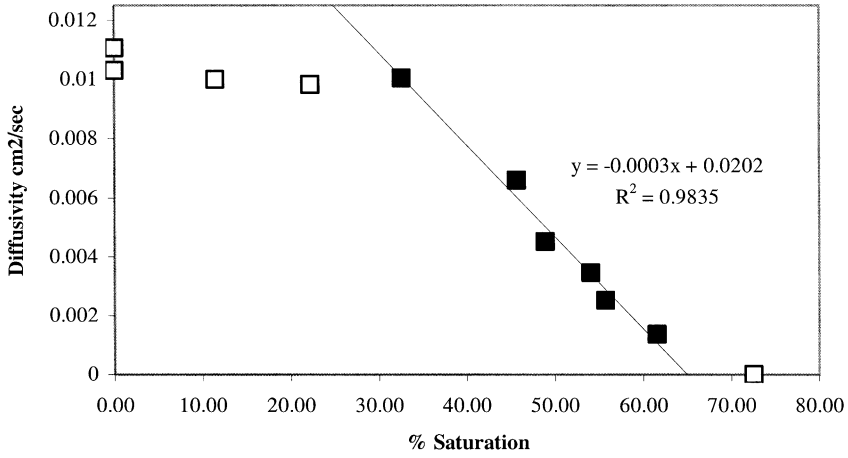

Fig. 13. Diffusivity vs. saturation for separator type B.

add electrolyte in stages taking measurements at each saturation level.

After the initial compression of both separator types in the dry condition, 0% saturation, a steady drop in force was observed. This indicated that the papers exhibit viscoelastic behaviour. Initial results showed that this produced negligible variations when readings were taken after a predefined relaxation time. There are a number of possible mechanisms that could explain this behaviour.

Since the viscoelastic behaviour of glass, below the glass transition temperature, is insignificant within the time scales of this investigation, the behaviour of the separator papers is primarily influenced by the structure rather than the compositional or material properties of glass.

Separator paper consists of a mass of fine glass fibres inter-linked in various orientations shown diagrammatically in Fig. 14. Glass is a brittle material and does not exhibit plastic deformation characteristics. During compression of separator paper the fibres will bend until they reach their elastic limit, after which fibre fracture occurs. In addition to fracture, the only way in which the fibres can release the elastic strain energy stored within them is to move into a position where the bending strain is reduced. The time response for the fibres to move is the mechanism believed responsible for the paper's viscoelastic behaviour. In practice this will be a cumulative effect of a large number of fibres moving synchronously together. The situation of two fibres acting on each other is represented diagrammatically in Fig. 15.

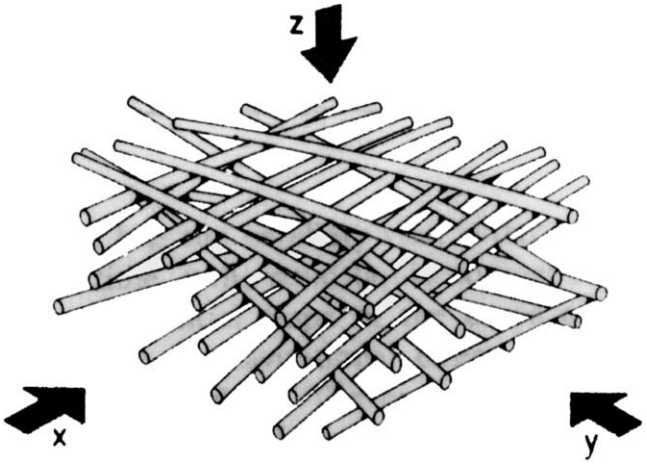

Fig. 14. Simplified structure of separator paper.

Separator papers consist of many fibres crossing each other, a pair of which is shown in Fig. 15(a). When a load is applied to the fibres, elastic deformation occurs and the fibres deform as shown in Fig. 15(b). As the strain increases

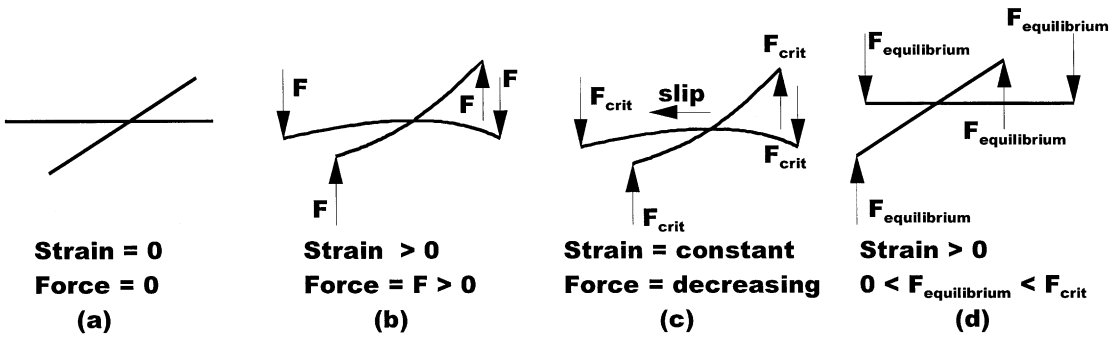

Fig. 15. Representation of fibre movement within a separator paper during compression.

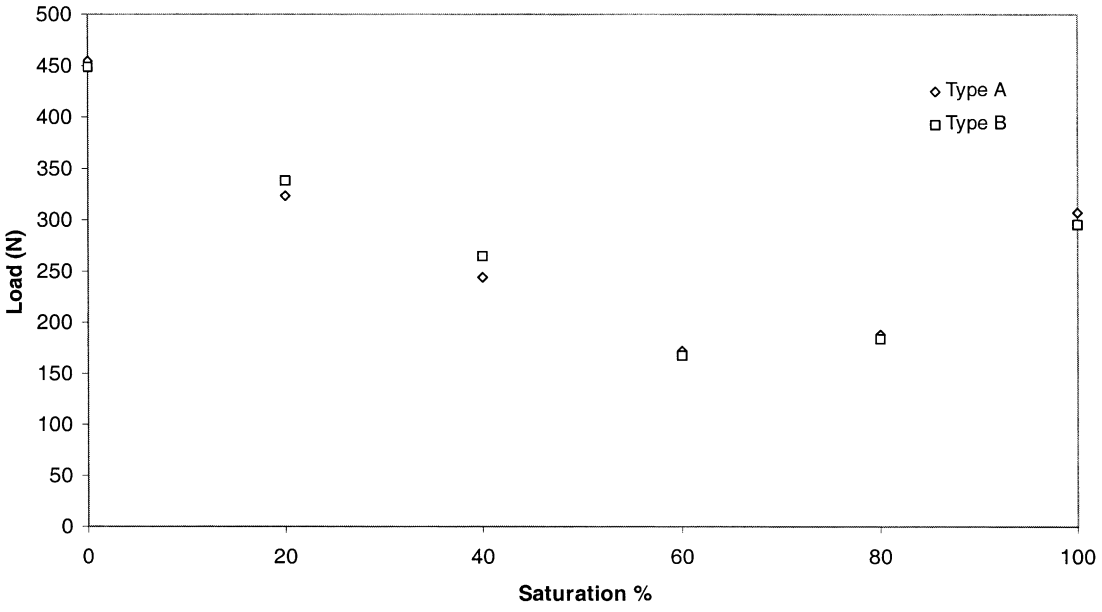

Fig. 16. Load vs. saturation for separator types A and B.

a critical force is reached at which point the fibres are able to slip past each other, resulting in a decrease in their deformation, Fig. 15(c). The effect of this is a reduction in the force exerted by the fibres, whilst maintaining the same overall separator strain. At a particular point the sliding fibres will reach an equilibrium force condition at which the sliding will stop, Fig. 15(d). The result is a decrease, from the initial force exerted by the compressed separator with time. Alternatively, if the fibres are unable to slip to a position of lesser strain, fibre breakage will occur when the force exceeds that for fracture.

In practice the mechanism described above will be influenced by other factors such as the surface tension and lubrication effects of the electrolyte. A plot of load versus saturation for both separator papers consisting of 100% glass is shown in Fig. 16.

From the figure it can be seen that there is no significant difference in the behaviour exhibited by both separator types. A decrease in force occurs between 0 and 60% saturation, followed by an increase between 60 and 100%. Investigations by Nakamura et. al. [2] indicate a similar trend when contraction percentage is plotted against amount of electrolyte added to the separator sample. This can be explained by considering the interaction between the electrolyte and fibres, shown diagrammatically in Fig. 17. From the figure it can be seen that there is no force acting between the fibres at 0 and 100% saturation. However, at an intermediate level of saturation a drop of electrolyte can sit between the fibres. The surface tension of the electrolyte causes the fibres to bend towards each other reducing any force at the ends of the fibres.

As the separator saturation increases, the ratio of each interaction type between fibres as shown in Fig. 17(a)–(c), will vary and influence the total force exerted by the paper

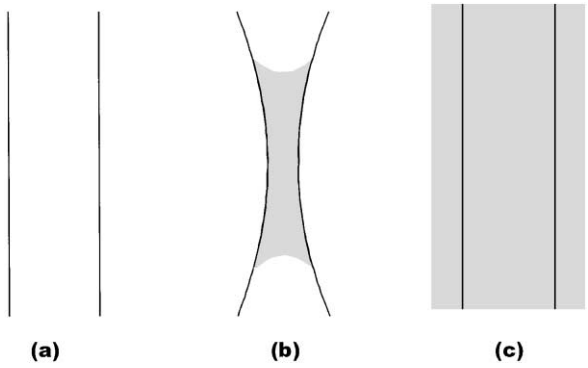

Fig. 17. Influence of electrolyte between glass fibres at 0% saturation (a), intermediate level of saturation (b), 100% saturation (c).

therefore explaining the U shape curve. It is suggested that the drop in force observed between the values at 0 and 100% saturation is due to a combination of the paper relaxation throughout the time of the experiment, lubrication of the fibres with electrolyte and surface tension effects of the electrolyte.

4. Conclusions

Scanning electron microscopy is an effective method for the examination of separator papers and allows glass and polyester fibres to be distinguished from each other. Fibre orientation has an influence on the diffusivity characteristics of partly saturated separator papers in the range 30–70% saturation. However, fibre orientation had little effect on the wicking rates and compression characteristics of the paper. The presence of polyester fibres within the paper reduced the wicking rate due to its larger contact angle compared to glass.

References

[1] B. Culpin, Separator design for valve regulated lead/acid batteries, J. Power Sources 53 (1995) 127–135.
[2] K. Nakamura, M. Shiomi, K. Takahashi, M. Tsubota, Failure modes of valve regulated lead/acid batteries, J. Power Sources 59 (1996) 153–157.
[3] K. McGregor, Effects of compression on recombant battery separator mats in valve regulated lead/acid batteries, J. Power Sources 73 (1998) 65–73.
[4] G.C. Zguris, Absorptive glass-mat separators for valve regulated lead/acid batteries—thoughts on compression, J. Power Sources 67 (1997) 307–313.
[5] G.C. Zguris, A broad look at separator material technology for valve regulated lead/acid batteries, J. Power Sources 73 (1998) 60–64.
[6] R.D. Laughlin, J.E. Davis, Text. Res. J. 31 (1961) 904.
[7] D.S. Scott, F.A.L. Dullien, Diffusion of ideal gases in capillaries and porous solids, Am. Inst. Chem. Eng. J. 8 (1) (1962) 113–117.
[8] R.B. Evans, G.M. Watson, E.A. Manson, Gaseous diffusion in porous media at uniform pressure, J. Chem. Phys. 35 (6) (1961) 2076–2083.
[9] B. Culpin, J. Hayman, Transport and wetting phenomena recombination separator systems, J. Power Sources 11 (1986).

ELSEVIER

Journal of Power Sources 104 (2002) 234–240

JOURNAL OF POWER SOURCES

www.elsevier.com/locate/jpowsour

Study of valve-regulated lead/acid batteries manufactured with different separator papers

R.J. Ball[a,*], R. Kurian[b], R. Evans[c], R. Stevens[a]

[a]*Department of Engineering and Applied Science, University of Bath, Bath BA2 7AY, UK*
[b]*Hawker Ltd., Stephenson St, Newport NP9 OXJ, UK*
[c]*Invensys, Westinghouse Site, Chippenham, Wiltshire SN15 1SJ, UK*

Received 2 July 2001; received in revised form 3 September 2001; accepted 18 September 2001

Abstract

The separator paper is a key component within a valve-regulated lead/acid (VRLA) battery. Here we describe an experimental program aimed at elucidating how separator papers influence battery performance. Identical batteries were manufactured using three different types of separator paper and subsequently cycled to failure. The failed batteries were then subjected to a series of tests, which included measurements of electrode potentials, compositional analysis of active materials, separator paper saturation and stratification measurements. Results indicated that separator paper type significantly influences battery performance. It is believed that subtle changes in the separator structure caused changes in the rate at which imbalances between the cells in each test battery developed, which led to subsequent changes in failure.

Keywords: Valve regulated lead acid (VRLA) battery; Separator paper; Cycle life

1. Introduction

In a battery, the individual electrodes must be physically separated so that the electrolyte forms the only conduction path between them. In order to ensure separation of the electrodes in valve-regulated lead/acid (VRLA) batteries, a separator material is used. Separators need to be porous in order to allow the penetration of electrolyte and movement of gases produced during battery operation [1]. Over recent years, development has led to the wide acceptance of an absorptive borosilicate glass microfibre separator material [2]. This material has a very high porosity, approximately 95% is inert, and has a contact angle of 0° with sulphuric acid [3]. It was originally used by the Gates Rubber Company in 1972 with a flat plate design [4]. In addition to the above functions, separators also absorb excess electrolyte and reduce the risk of dendrite formation, which can develop short circuits between plates resulting in a damaged cell.

Although battery separator papers do not themselves react chemically during battery operation, they have a significant influence over the charge and discharge reactions and are not inactive barriers, as is the case for flooded cells. In recent years, research has been conducted on separators in order to investigate how they influence battery operation [2,3].

In addition to their obvious role as a material to absorb and immobilise electrolyte, subtle changes in porosity and compression characteristics can have significant effects on battery performance. The importance of the various separator properties is dependent on operational characteristics such as the depth of discharge and number of cycles to which the battery will be subjected.

A number of properties that are desirable in a good separator have been identified by Zguris [5]. In addition to immobilising the electrolyte and allowing the battery to operate at an angle, a separator that applies a consistent and uniform compression on the plates during the life of the battery is required. A number of key points, which must be considered when designing a separator, are summarised as follows.

- Retention of separator thickness during saturation is important as this maintains plate compression when the separator is wetted.
- As variations in temperature have been observed to result in changes in compression force of up to 10%, it is important that the separator is insensitive to the

* Corresponding author. Tel.: +44-1225-826826; fax: +44-1225-826098.
E-mail address: r.j.ball@bath.ac.uk (R.J. Ball).

0378-7753/02/$ – see front matter
PII: S0378-7753(01)00924-7

effects of draughts impinging on the outside of the battery case.
- Resiliency of the separator, when subject to a crushing force is important, as failure to recover can lead to changes in the active material pore structure, resulting in a decline in battery performance.
- Studies have shown that as a stack of plates is compressed into a cell, not all separators deform equally. Uniform stack compression is important to ensure active mass consistency between plates.

This paper describes work to identify the effect of separator type on battery operation. The approach adopted was to build a number of batteries of similar design using the same components such as electrodes, case, etc., but with different separator materials. Each battery was cycled to failure and subsequently examined using a range of techniques.

2. Construction of test batteries

The batteries used in this study were all 40 Ah, 12 V monoblocs. Pure lead grids were used for both positive and negative electrodes. The positive and negative active materials were formed from a paste containing grey oxide. Batteries containing the different separator materials were manufactured for testing. In this study three different separator materials were compared, details of which are given in Table 1.

3. Cycling of test batteries

Cycling was carried out automatically using Digitron charging units. Each cycle consisted of a constant current discharge at 7.05 A to 10.2 V followed by a constant voltage recharge at 14.7 V for 16 h. This was repeated until the capacity after charging reduced to less than 80% of the starting capacity. The cells that showed the greatest and least voltage difference between end of discharge and end of charge were examined, these are referred to as the ''bad'' and ''good'' cells, respectively.

Table 1
Types of separator paper used in the construction of test batteries

Separator type	Weight (g/m^2)[a]	Composition (%)[b]	
		Glass	Polyester
A	146.56	100	0
B	144.44	100	0
C[c]	181.96	92	8

[a] Measured value.
[b] Manufacturers value.
[c] Due to shortage, it was not possible to conduct all the tests carried out on this separator type.

4. Experimental methods

4.1. Examination of separator material

Data on separator saturation and acid specific gravity at different heights within the battery cell was obtained using the following procedure. After the cell had been removed from the battery case, it was split exposing a sheet of separator paper. The paper was cut into five horizontal strips, each approximately 1 in. in width, and each strip was then weighed to an accuracy of 0.0001 g. Distilled water was used to remove residual acid from the strips before drying in an oven. After the strips had been washed and dried, they were re-weighed allowing the weight of acid in each strip to be calculated. This procedure was then repeated on a new separator sheet, except that instead of weighing the strips, the specific gravity was measured. Three sets of five strips were examined using this method from a good and bad cell from each test monobloc. Care was taken to weigh the strips as quickly as possible to reduce the errors caused by evaporation and the strips being held in the horizontal position, i.e. cell on its side. After cutting, the order in which the strips were weighed was randomised to remove the possibility of introducing systematic errors into the results. Finally, the area of each strip was measured to allow the separator saturation to be calculated. Separator thickness was calculated from the electrode thickness and cell dimensions of the experimental batteries.

4.2. Examination of active materials

Active materials obtained from the ''good'' and ''bad'' cells of batteries were characterised using a number of techniques. However, before tests could be conducted, it was necessary to stabilise the active materials by soaking in distilled water for 30 min to remove the acid and then drying in a vacuum oven at 70 °C for 15 h, or until dry.

Values for BET surface area were obtained using a Micromeritics Gemini 2360 VS.OO. analyser. The stabilised active material was broken into small pieces prior to the analysis to allow insertion into the sample tube.

Compositional information was obtained using X-ray diffraction (XRD) and a wet chemical analysis technique. Wet chemical analysis was used to determine the amount of lead in the sample, as this cannot be obtained accurately using XRD. The analysis technique used a solution of sodium hydroxide, mannitol sugar and hydrazine sulphate, commonly referred to as mannitol solution. When a sample of active material is boiled in the solution, all lead compounds are dissolved leaving only metallic lead. By measuring the sample weight before and after reaction, the weight percentage of metallic lead can be determined.

XRD was conducted on a Philips PW1730/00 diffractometer using Cu Kα radiation. Samples were scanned over a range of 5–90° at a speed of 0.5 s per step with a step size of 0.01°.

A quantitative analysis of the active materials was determined by entering the results from the wet chemical analysis and XRD into the PEAKS program. The PEAKS program was developed by the CSIRO in the Division of Mineral Products under sponsorship from Pasminco Metals Ltd. [6]. PEAKS is capable of determining the relative abundance of the lead phases commonly found at different stages of lead acid battery manufacture and service. Characteristic intensities from the XRD patterns are entered into the "input screen" of the program and the relative abundance of each phase is calculated. Initial corrections are made for background radiation and peak overlap before average intensities are calculated for up to three of the peaks from each phase present. Data is then normalised for differences in scattering power using pre-determined calculated reference intensity ratios [7].

5. Results and discussion

5.1. Electrical testing of batteries

Plotting the discharge time against cycle number (Fig. 1), allows the performance of each battery type to be compared. From the figure it can be seen that there is a significant difference in performance between the batteries containing each separator type. The battery containing type C separator paper was the first to fail at approximately 35 cycles. The second to fail was the battery containing type A separator paper at approximately 70 cycles. The final battery to fail was that containing type B separator paper at over 160 cycles. Previous tests indicated similar trends in performance to those described above with respect to separator type [8].

Voltages of the cells in each battery type were monitored during a C1 capacity discharge to 4 V in order to identify the good and bad cells. Results indicated that all the batteries failed due to the degradation of a number of cells rather than a single failed cell.

During battery operation, the potential of the positive and negative electrodes can vary depending on the diffusion of ions through the electrolyte and oxygen gas through pores in the separator. The potential of the positive and negative plates in the good and bad cells of each battery examined were measured relative to a mercury sulphate reference electrode for a discharge (7.05 A to 6 V) per charge cycle. Variations in potential of the electrodes in each cell examined are given in Figs. 2–4.

It can be seen that as the batteries are discharged, the cell potentials decrease until the failure point is reached. This reduction in cell potential is the result of a decrease in the potential of the positive electrode and an increase in the potential of the negative electrode.

From Figs. 2–4, the time between the start of reduction in potential of the bad cell and recharging of the battery varies for each of the batteries tested. The greatest time is observed for the battery containing type C separator paper, which sustained 35 cycles to failure, and the least time for the battery containing type B separator paper, which sustained 160 cycles.

The reduction in cell voltage observed in the bad cells from each of the batteries tested is a result of a reduction in potential of the positive electrode. No significant increase in potential of the negative electrode was observed for any of the batteries. This indicates that failure is due to the positive rather then the negative electrode.

5.2. Analysis of active materials

Compositional analysis and BET surface area measurements were carried out on the active materials from all batteries tested. This was done to determine whether any significant changes were present which would suggest different failure mechanisms.

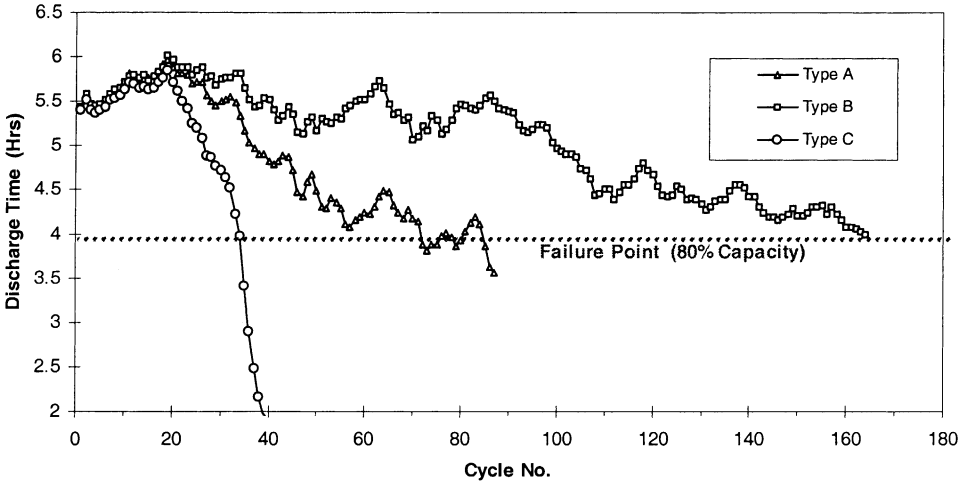

Fig. 1. Discharge time vs. cycle number.

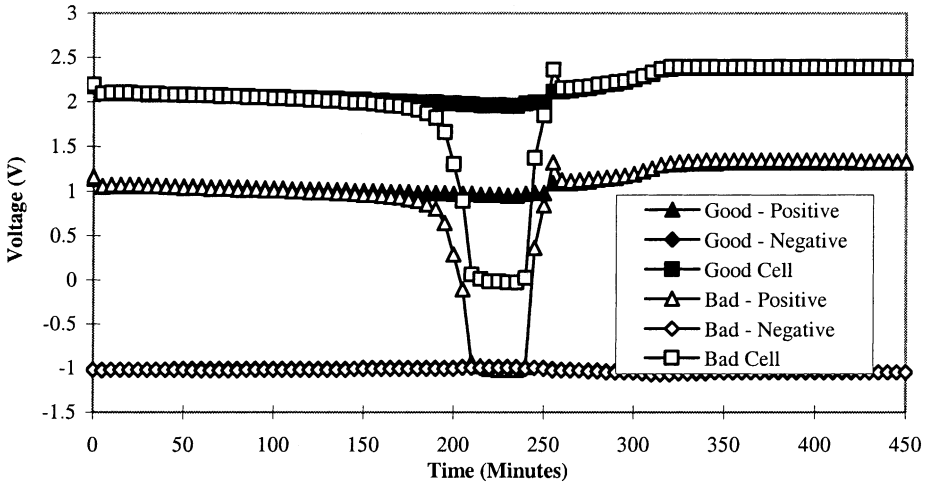

Fig. 2. Potential of the individual electrodes in the battery containing type A separator.

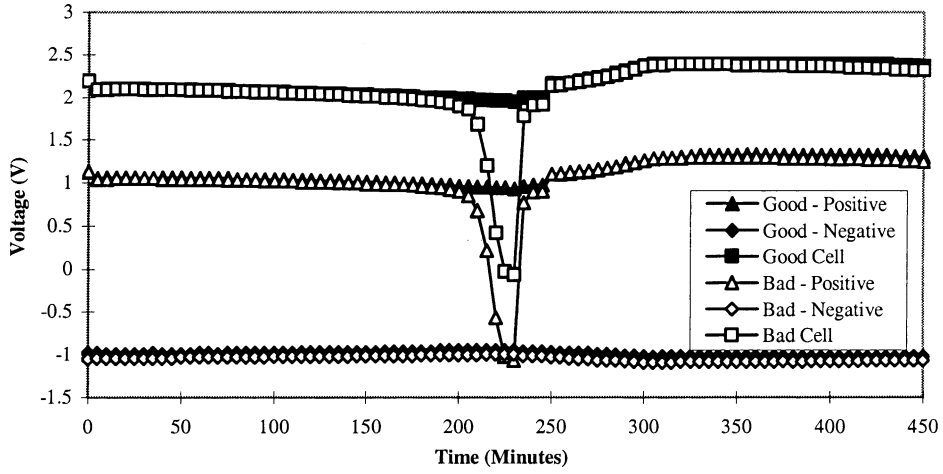

Fig. 3. Potential of the individual electrodes in the battery containing type B separator.

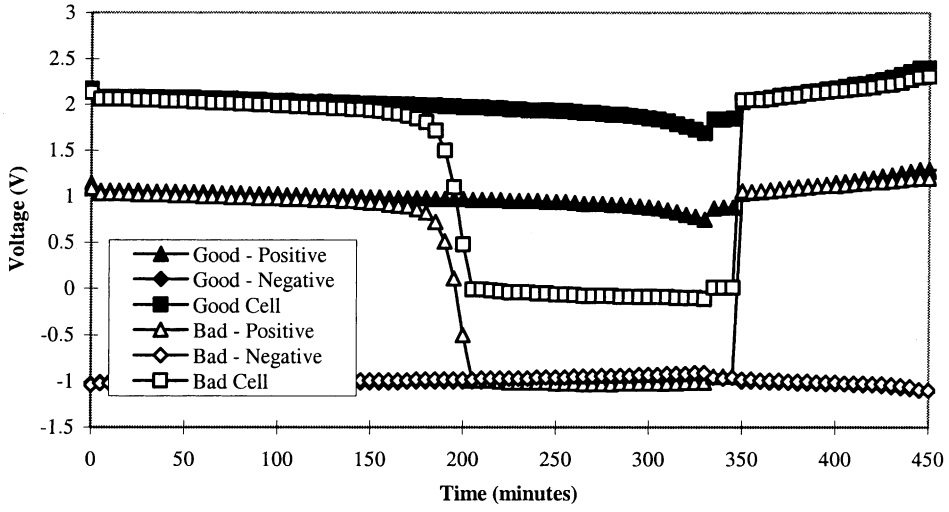

Fig. 4. Potential of the individual electrodes in the battery containing type C separator.

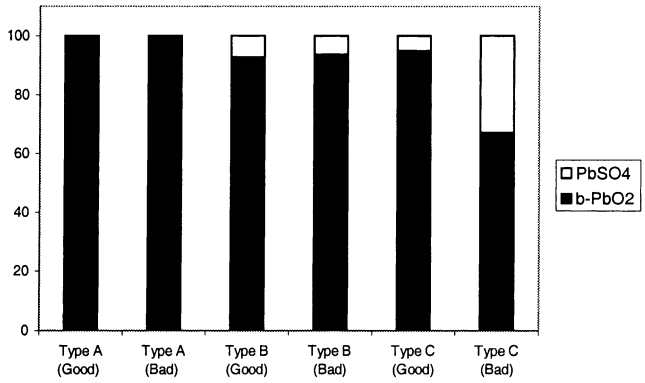

Fig. 5. Composition of positive active materials in all test batteries.

Composition of the active materials was determined using XRD and wet chemical analysis. This was done for both positive and negative plates from good and bad cells. A compositional analysis of the positive electrodes from the good and bad cells examined is given in Fig. 5.

Examination of the positive electrodes revealed the presence of a small amount of sulphation in the positive plates from the batteries containing separator types B and C. This was less than 10%, except for the bad cell of the battery containing type C separator paper, which contained approximately 30% lead sulphate. These results correlated with the values of BET surface area (Fig. 6), which show a reduction in surface area where lead sulphate is present.

Analysis of all negative active materials revealed that the composition was 100% lead. Measurements of BET surface area for these materials are given in Fig. 7. These results do not show any significant variation in the negative active materials from the batteries tested.

5.3. Separator saturation and specific gravity measurements

During operation of a lead acid battery, variations in acid concentration are observed at different positions within the cell. This phenomenon is commonly referred to as acid stratification and can be determined by measuring specific gravity. There are several mechanisms which contribute to stratification, such as uneven discharge of the active material throughout the electrodes and the force of gravity.

Gases produced during charging can cause the movement of acid around the separator and electrodes, thereby reducing the extent of stratification. The effectiveness of this process is influenced by the separator properties and for this reason stratification measurements have been taken for the cells examined from the test batteries.

The specific gravity of the electrolyte in five equally spaced strips positioned between the top and bottom of the cells taken from the batteries containing separator paper types A and B was measured. Results obtained are shown in Figs. 8 and 9.

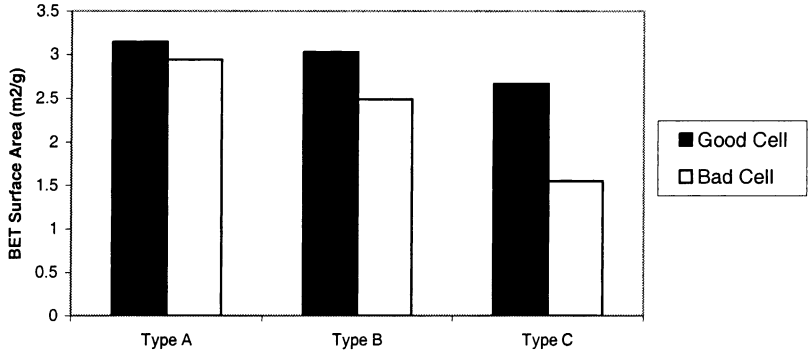

Fig. 6. BET surface areas of positive active materials in all test batteries.

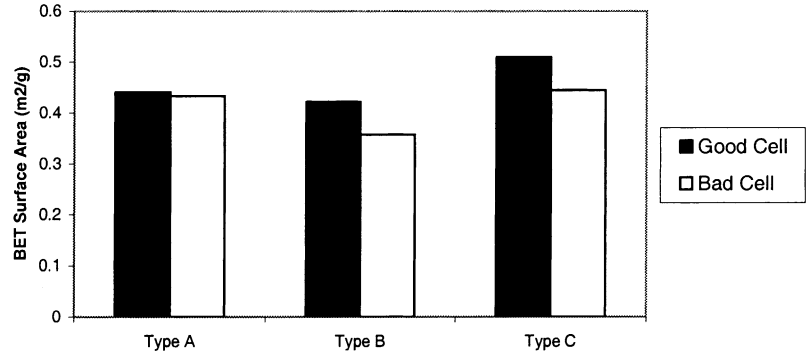

Fig. 7. BET surface areas of negative active materials in all test batteries.

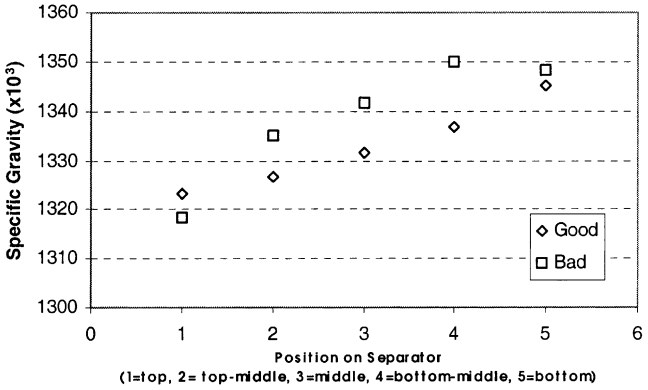

Fig. 8. Variation of electrolyte specific gravity with cell height for separator type A.

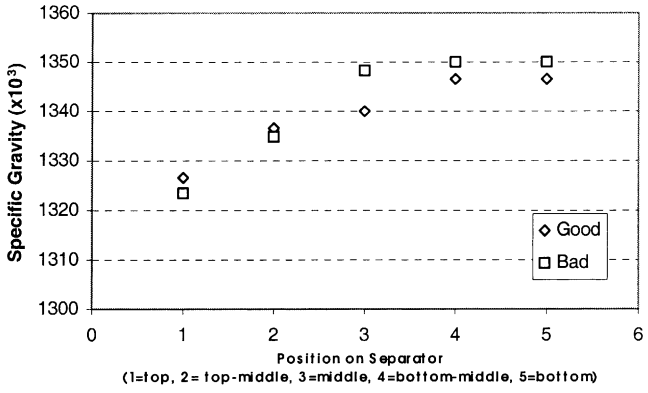

Fig. 9. Variation of electrolyte specific gravity with cell height for separator type B.

The results in Figs. 8 and 9 show the specific gravity of the electrolyte decreases with cell height. The smallest stratification was observed in the battery containing type B separator paper, which achieved the greatest number of cycles. This battery also showed the smallest difference in acid specific gravity between the good and bad cells.

To determine separator saturation, the weight of acid in five equally spaced strips positioned between the top and bottom of the cell was measured. The acid specific gravity at the corresponding positions was then used to determine the volume of acid and therefore saturation. Measurements of percentage saturation versus separator height for batteries containing types A and B separator papers are shown in Figs. 10 and 11. Average saturations for the total cell for batteries containing separator types A, B and C are given in Table 2.

Both figures show an increase in separator saturation towards the bottom of the cell. This is likely to be due to the gravitational forces and gases escaping through the top of the cell during charging. The presence of a separator paper decreases the gravitational effect significantly compared to a flooded cell without the separator paper. From Table 2, separator paper type B has a lower saturation compared to types A and C. However, this is to be expected as this battery sustained the greatest number of cycles and

Fig. 10. Variation of electrolyte saturation with cell height for separator type A.

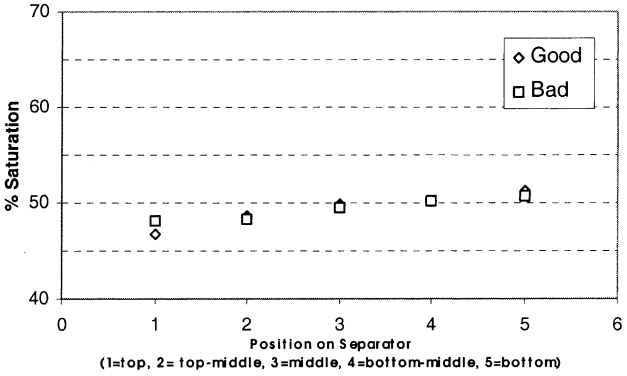

Fig. 11. Variation of electrolyte saturation with cell height for separator type B.

Table 2
Average separator saturations for cells from batteries containing separator types A, B and C

Separator type	Separator saturation (vol.%)	
	Good cell	Bad cell
A	58.42	54.02
B	49.33	49.34
C	57.57	40.75

would therefore have lost the greatest amount of water from the electrolyte. Differences in total cell saturation between the good and bad cells is least in the battery containing type B separator paper compared to types A and C. The implication of this is that, during battery operation, the bad cells in batteries containing separator types A and C sustained a greater amount of water loss.

6. General discussion

This study shows that battery cycle life is influenced by the choice of separator paper. The low cycle life exhibited by the battery containing type C separator is probably a consequence of lower wicking rates. This is a result of the higher

contact angle between the electrolyte and polyester fibre surface compared to the other separator papers.

Separator types A and B were very similar in weight and composition, both containing 100% glass fibres, however, a significant difference in cycle life was observed. Subtle differences in the separator papers' structures resulted in variations in acid stratification and saturation between the different test batteries. The separator papers influenced the rate at which variations in specific gravity and saturation between cells within a battery developed, which inevitably resulted in the monobloc, becoming unbalanced and premature failure resulting. Consequently, the results in this paper have been able to highlight the importance of choice of separator when designing a battery and the need for consistency of saturation and stratification between cells on cycle life.

Acknowledgements

The authors would like to thank Hawker Ltd., Newport, for manufacturing and cycling all test batteries included in this paper and for supplying samples of separator paper for analysis.

References

[1] W. Bohnstedt, Challenges for automotive battery separator development, J. Power Sources 67 (1997) 299–305.
[2] K. Peters, Influence of separator structure on the performance of valve-regulated batteries, J. Power Sources 42 (1993) 155–164.
[3] B. Culpin, Separator design for valve-regulated lead/acid batteries, J. Power Sources 53 (1995) 127–135.
[4] R.H. Newnham, Advantages and disadvantages of valve-regulated lead/acid batteries, J. Power Sources 52 (1994) 149–153.
[5] G.C. Zguris, A review of physical properties of separators for valve-regulated lead/acid batteries, J. Power Sources 59 (1996) 131–135.
[6] D.A.J. Rand, R.J. Hill, M. McDonagh, Improving the curing of positive plates for lead/acid batteries, J. Power Sources 31 (1990) 125–203.
[7] K. Harris, R.J. Hill, D.A.J. Rand, Crystalline phase composition of positive plates in lead/acid traction batteries under simulated electric vehicle service, J. Power Sources 8 (1982) 175–196.
[8] R. Kurian, Private communication, Hawker Ltd., Newport.

ELSEVIER

Journal of Power Sources 109 (2002) 189–202

JOURNAL OF POWER SOURCES

www.elsevier.com/locate/jpowsour

Failure mechanisms in valve regulated lead/acid batteries for cyclic applications

R.J. Ball[a,*], R. Kurian[b], R. Evans[c], R. Stevens[a]

[a]*Department of Engineering and Applied Science, University of Bath, Bath BA2 7AY, UK*
[b]*Hawker Ltd., Stephenson St., Newport NP9 OXJ, UK*
[c]*Invensys, Westinghouse site, Chippenham, Wiltshire SN15 1SJ, UK*

Received 9 September 2001; received in revised form 17 January 2002; accepted 22 January 2002

Abstract

Valve regulated lead/acid (VRLA) batteries are used in a variety of different applications, one of which is cycling. Cycle life testing of a batch of 40 Ah VRLA batteries showed a large variation in the cycles to failure ranging from 10 to 133 cycles. Further testing and the destructive examination of these batteries provided information on the likely causes of failure. Results from monitoring reduction in cell voltage during a final discharge/charge cycle, scanning electron microscopy (SEM), BET surface area analysis, X-ray diffraction, interfacial analysis and electron probe analysis, were used to identify the failure mechanisms occurring within the batch. Batteries that failed after a low number of cycles, 10 and 28, were believed to have done so due to sulphation of the positive plate. Thick corrosion layers were shown to be the cause of failure in the batteries that sustained high numbers of cycles, 92 and 133. Results suggested that batteries failing at intermediate numbers of cycles, 42, 49, 65 and 73, failed due to degradation of the cells simultaneously and a single failure mechanism could not be identified.

Keywords: VRLA; Cycle life; Positive electrode

1. Introduction

A significant proportion of the valve regulated lead/acid (VRLA) batteries currently produced are for use in cyclic applications. An understanding of the compositional and structural changes that occur within a battery during repeated cycling is important if failure mechanisms are understood and battery designs to be improved.

Cycling data obtained from a single batch of 40 Ah VRLA batteries, indicated that they were failing after different numbers of cycles. These batteries were manufactured using the same starting material and processing technique, so were expected to show similar cycle lives. Differences in cycle life can only be explained by the inherent variability of the materials and processes that occur within each batch of batteries during manufacture, that are not detectable from the usual quality control procedures. Care was taken in the production of the cells and batteries to ensure standard procedures, thereby producing a product as uniform as possible. Details of the production process are of necessity confidential. In this paper, results obtained from the examination of a number of batteries from the same batch that failed after different numbers of cycles is discussed.

2. Production of test batteries

The batteries examined in this study were all 40 Ah, 12 V monobloc units of the same design and constructed using identical materials. Positive electrodes were produced using a standard grey oxide positive paste. The negative paste mix was also manufactured from grey oxide. Positive and negative grids were produced from a proprietary lead alloy. Glass microfibre separators were used, consisting of 70% coarse and 30% fine fibres. Assembled batteries were filled with electrolyte of specific gravity (SG) 1.290 at 15.5 °C prior to formation.

3. Cycling of test batteries

Cycling was carried out automatically using Digitron charging units. Each cycle consisted of a constant current discharge at 7.05 A to 10.2 V followed by a constant voltage

* Corresponding author. Tel.: +44-1225-826826; fax: +44-1225-826098.
E-mail address: r.j.ball@bath.ac.uk (R.J. Ball).

0378-7753/02/$ – see front matter
PII: S0378-7753(02)00071-X

recharge at 14.7 V for 16 h. This was repeated until the capacity after charging was less than 80% of the starting capacity.

4. Experimental methods

4.1. Characterisation of cells

The reduction in capacity of all cycled batteries can be attributed to changes that have occurred in the individual cells. However, the extent to which these destructive processes have developed in each cell is often different. Any variations can be quantified by measuring the reduction in voltage of each cell with time.

A series 1200 GRANT Squirrel data logger, was used to log individual cell voltages with time. Connections from each cell to the data logger were made by inserting nails through the battery case lid into the underlying cast-on straps. Each cell was connected to a different channel of the data logger prior to the battery being subjected to a C1 (100% depth of discharge in 1 h) capacity discharge to 6 V. The discharge current was 27.6 A and recharge voltage 14.7 V. Voltages were logged at 1 min intervals. After discharge, the battery was recharged and squirrel data downloaded into a PC and displayed on an Excel spreadsheet. Connections made between the cells of the battery and data logger are shown diagrammatically in Fig. 1. The cells which had the greatest and least reduction in voltage were removed for examination and referred to as the bad and good cells, respectively.

4.2. Destructive examination of test batteries

All batteries were destructively examined, in the charged state, to allow detailed analysis of individual electrodes. In order to remove the battery cells for examination, it was necessary to gain access to the interior of the battery. This was done by firstly removing the polypropylene battery lid as shown in Fig. 2. The good and bad cells were then removed from the battery case for further examination by cutting the connecting weld and pulling the cell directly upwards, out of the battery case.

Once the cells had been removed from the battery case, the positive electrodes were separated for examination. This was achieved by pulling off the cast-on straps with a pair of pliers, which conveniently doubled as an integrity check for the welds between the electrode and cast-on strap. A cell with one cast-on-strap partly removed is shown in Fig. 3.

Measurements of the SG of the electrolyte were taken, using a surface tension method, at the top and bottom of each cell, to allow the extent of acid stratification to be assessed. Electrolyte was obtained by squeezing it out from a sample of the separator paper taken from a representative position within the cell.

Representative positive plates, from both good and bad cells, were placed in a beaker of distilled water for approximately 30 min to dilute and remove acid. Plates were rinsed with industrial methylated spirits and placed in a vacuum oven at 60 °C for 24 h or until totally dried. After the plates had dried, the oven heater was switched off and the plates were allowed to cool down to room temperature whilst still under vacuum to prevent oxidation. Dried plates were then

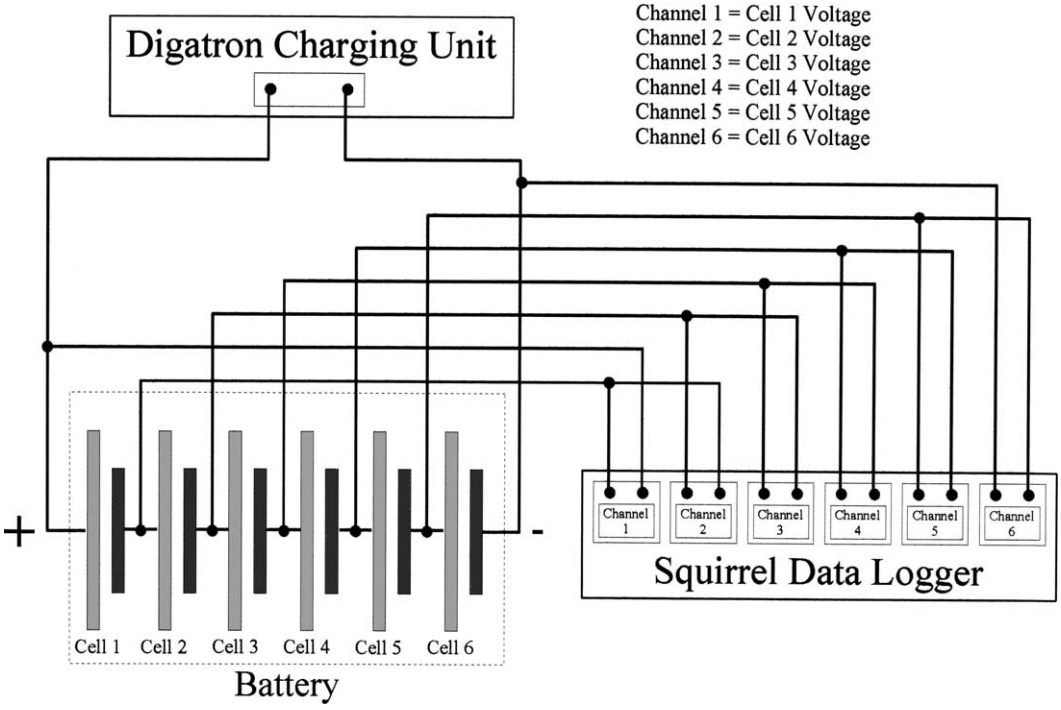

Fig. 1. Circuit used to monitor voltages of individual cells during a discharge/charge cycle.

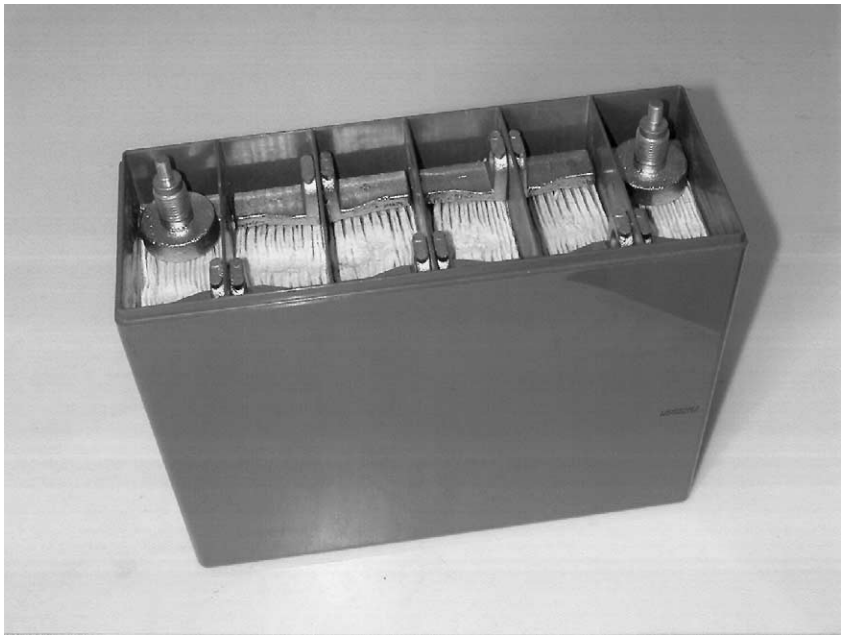

Fig. 2. A 12 V six cell monobloc with lid removed.

stored in a dessicator, containing silica gel, before further examination and analysis. It should be noted that despite the care taken to preserve the plates lead oxide is prone to self decomposition, whereby oxygen is evolved [1]. For this reason, results indicating oxide stoichiometry of the corrosion layer should be viewed as being pessimistic in terms of oxygen concentration. Negative plates were not examined, as the high surface area sponge lead of which they consist is highly reactive and it was practically impossible to remove the plates without the formation of oxide on their surface.

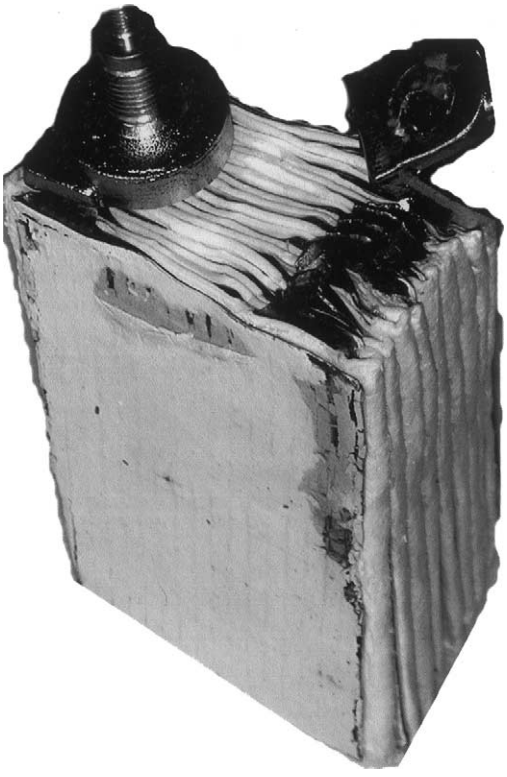

Fig. 3. Cell removed from battery showing cast-on strap partly removed.

4.3. Scanning electron microscopy (SEM) of active material fracture surfaces

An effective method of determining the structure of the active material is to examine fracture surfaces in a scanning electron microscope. This can give valuable information on the composition and structural properties such as particle size, shape and porosity.

Samples were made by attaching a small piece of positive active material to a planchette with araldite adhesive. A thin layer of gold was applied using an Edwards sputter coater to improve conductivity and reduce charging. A coating time of 5 min was used. Samples were stored in a desiccator, until required for examination in the SEM, to prevent the adsorption of moisture and contamination.

All images were produced with secondary electrons using a JEOL 6310 scanning electron microscope. At high magnifications, the smallest spot size that could be used easily was selected. Working distances were reduced as much as possible to enhance image quality and a beam voltage of 15 kV was found to give good quality images.

4.4. BET surface area analysis

It is important to consider the surface area of the positive active material when studying batteries. It will have a direct influence on the way in which the battery operates since all electrochemical reactions that occur within a battery during operation, do so on the surface of the active materials.

Values of surface area are obtained by measuring the volume of gas required to form a monolayer on the sample surface (BET method). The gas used was nitrogen, which has a cross sectional area of 1.62×10^{-20} m^2.

The analysis was performed using a Micromeritics Gemini 2360 VS.OO. This equipment is used to measure the volume of gas adsorbed with change in pressure. BET surface area analysis was conducted on samples of positive active material after removal from the battery. Active material was removed from the battery grid and broken into pieces, small enough to fit into the sample tube. Care was taken not to break the pieces more than necessary, as this artificially increases the surface area and therefore the measured value.

4.5. X-ray diffraction (XRD)

XRD was used to determine the composition of the samples of positive active material from the cells examined. Standard data files from the Joint Committee for Powder Diffraction Standards (JCPDS) [2] were used to initially identify the phases present.

Quantitative analysis of a mixture can be obtained as the intensity of the peaks on a diffraction pattern, corresponding to a particular phase, are related to the proportion of that phase [3].

For the purposes of this study the computer program PEAKS, specifically designed for the quantitative analysis of materials, commonly found in the lead acid battery, was used [4]. The program is capable of determining the relative abundance of the lead phases commonly found at the different stages of lead acid battery manufacture and service. Peak intensities from the XRD patterns are entered into the ''input screen'' of the program and the relative abundance of each phase is calculated. Initial corrections are made for background radiation and peak overlap before average intensities are calculated for up to three of the peaks from each of the phases present. Data is then normalised for differences in scattering power using pre-determined calculated reference intensity ratios [5].

XRD samples were prepared from the dried plates by pushing a number of tablets from the centre of the grid and then grinding to a fine powder using a pestle and mortar. The ground powder was placed in an aluminium XRD holder with a glass slide back. This was then inserted into the X-ray diffractometer for analysis.

A Philips PW1730/00 diffractometer using Cu Kα radiation, was used for all analyses. Samples were scanned over a range of 5–90° in order to obtain background values at 9 and 19 for quantitative analysis using the PEAKS program. A scan speed of 0.5 s per step and a step size of 0.01° was used.

4.6. Interfacial analysis

The thickness and structure of the positive grid corrosion layer can provide important information as to why a battery cell has failed. An effective way to study these features is to examine a polished cross section using optical or electron microscopy.

Dried battery plates consist of a soft lead grid, having very low stiffness, surrounded by friable active material. When handling plates, great care must be taken to avoid unnecessary bending as this can lead to the formation of additional cracks in the active material and corrosion layer. To reduce the risk of damaging the plates after removal from the battery, they were initially encapsulated in resin in order to increase their durability. After encapsulation, the plates were cut and remounted into suitable sizes for polishing.

Several polishing stages were used to prepare the samples. Initially, they were flattened using 300–1200 grit size silicon carbide paper with a platen speed of 150 rpm. Water was used as a lubricant and only light pressure was applied to the sample. Texmet polishing cloth loaded with five and then 0.3 μm alumina suspension was used for the second stage. Finally, a texmet cloth with masterpolish was used on a Buehler Vibromet vibratory polisher, for approximately 30 min.

4.7. Measurement of corrosion layer thickness

An optical microscope with camera attachment was used to record images of grid wires showing the corrosion layer. The thickness of the corrosion layer was measured at various positions on the grid wire using Optimas 6 image analysis software [6].

4.8. Electron probe microanalysis

A Jeol JXA-8600 superprobe was used to determine the composition of the corrosion layer on the good cell of the battery cycled 92 times, as this was of a reasonable thickness and a typically representative structure of the layer observed on the other batteries. Readings were taken in a line across the corrosion layer at 1 μm intervals. An initial qualitative analysis indicated that the corrosion layer consisted of lead, oxygen and sulphur. Results were used to calculate the oxygen to lead ratio for each analysis. To prevent charging effects, the samples were coated with a thin layer of carbon, using an Edwards sputter coating unit. Samples and standards were coated simultaneously to reduce errors caused by adsorption of X-rays by the coating layer.

5. Results and discussion

5.1. Cycling of batteries

The batteries examined in this study were all cycled until their capacity reached a value of 80% of the starting capacity. The number of cycles required for this state to be reached varied between individual batteries. The results presented are based on eight batteries from the same batch,

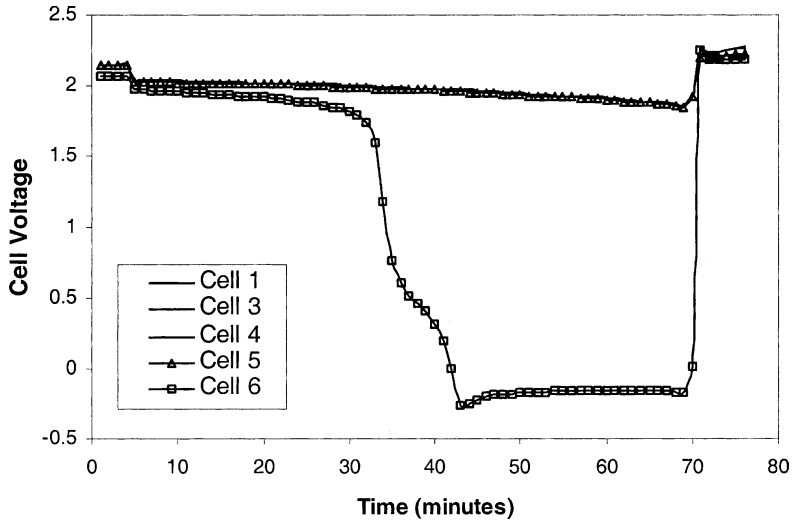

Fig. 4. Plot of potential vs. time for cells in battery cycled 10 times.

which failed after 10, 28, 42, 49, 65, 73, 92 and 133 cycles. An additional battery from this batch was examined in the freshly formed state for comparison with the cycled batteries.

5.2. Electrical testing of batteries

When a battery is cycled, its capacity will gradually reduce to a lower value at the end of each discharge/charge cycle. This is caused by degradation of the electrodes within the battery. The test batteries consisted of a 12 V monobloc containing six cells, each producing just over 2 V. The reduction of the capacity of a battery during charging is caused by a reduction in capacity of the individual cells. However, the degree to which the capacity has reduced in each cell generally varies. The capacity of a cell is directly related to its drop in voltage during discharge. Figs. 4–11 show plots of cell voltage versus time for a final discharge/charge cycle after the battery had reached its failure point.

In Figs. 4–11, the variation in potential of the good cells is plotted with triangles, the bad cells with squares, and the intermediate cells with a plane line. The plots demonstrate that the cells within each battery have degraded by varying amounts. In some instances, there is a clear example of a failed cell, with a very low potential, compared to the other cells in the battery which all have high potentials. In other batteries, all the cells appear to fail to a certain extent and there is no clearly defined good or bad cell. Fig. 4 shows a typical example of a battery with a single bad cell where all the other cells are good, in comparison Fig. 8 is from a battery where all the cells have, to a certain extent failed. Previous research on batteries with similar plates [7] indicated that the positive, as opposed to the negative plates, were the capacity limiting factor.

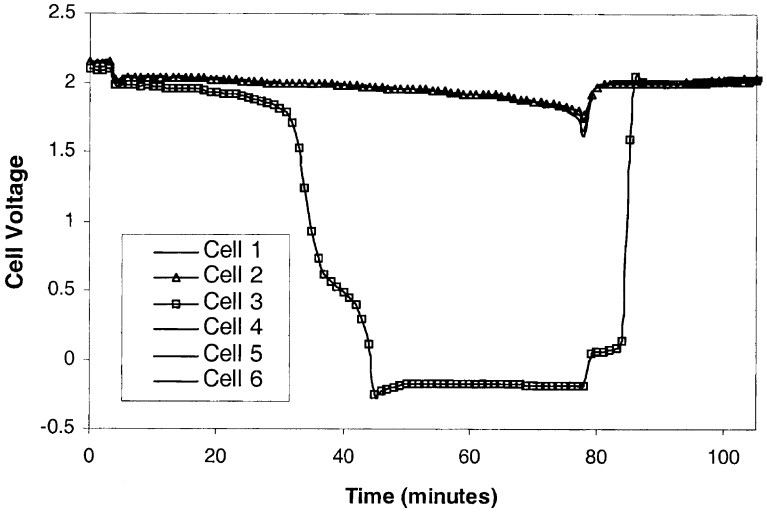

Fig. 5. Plot of potential vs. time for cells in battery cycled 28 times.

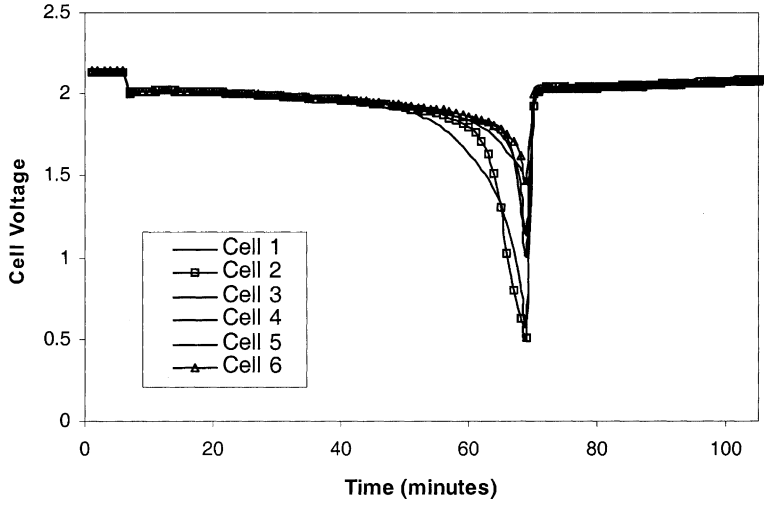

Fig. 6. Plot of potential vs. time for cells in battery cycled 42 times.

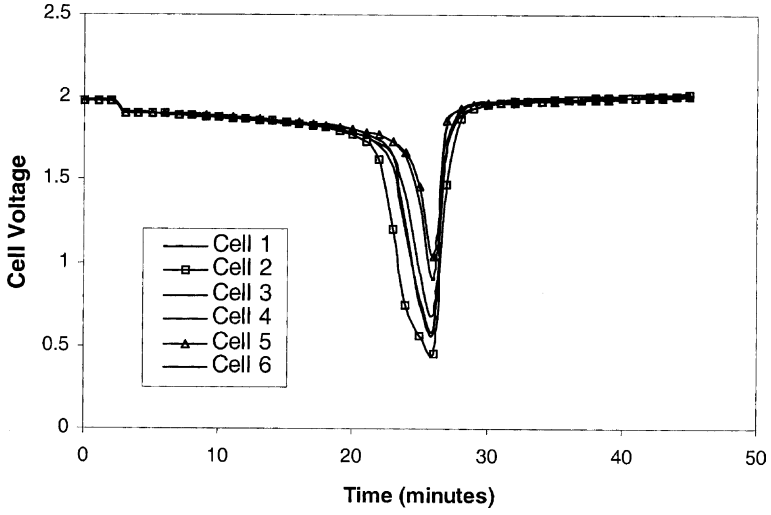

Fig. 7. Plot of potential vs. time for cells in battery cycled 49 times.

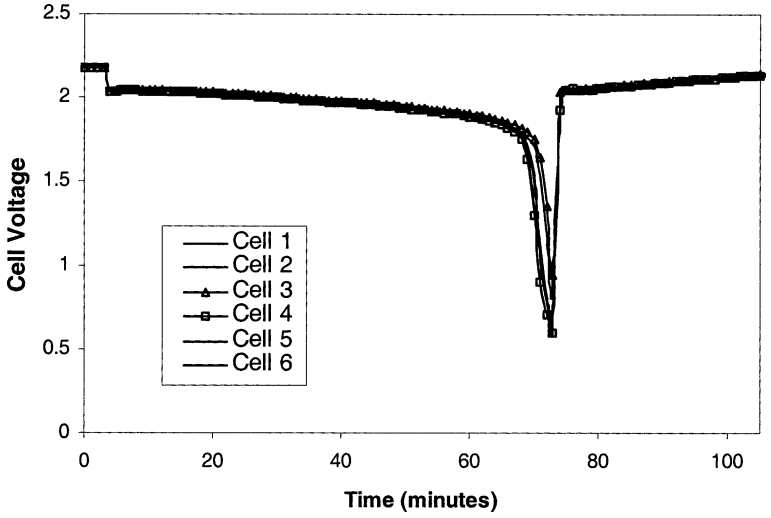

Fig. 8. Plot of potential vs. time for cells in battery cycled 65 times.

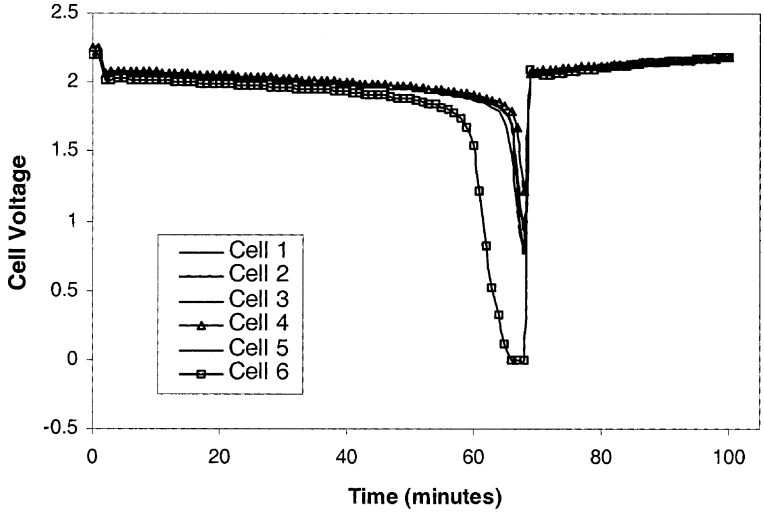

Fig. 9. Plot of potential vs. time for cells in battery cycled 73 times.

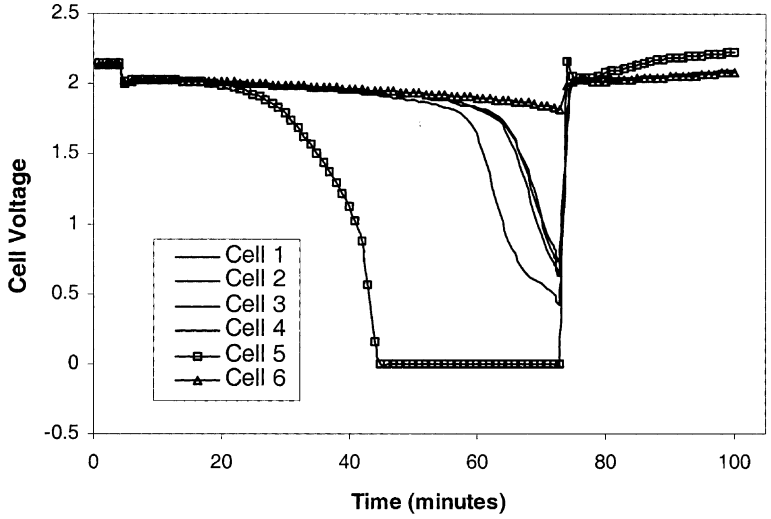

Fig. 10. Plot of potential vs. time for cells in battery cycled 92 times.

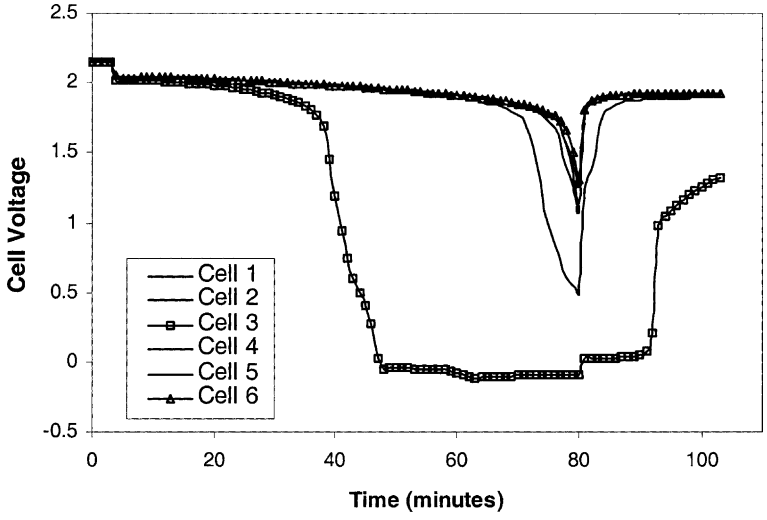

Fig. 11. Plot of potential vs. time for cells in battery cycled 133 times.

Table 1
Specific gravity of electrolyte at top and bottom of separators in good and bad cells of cycled batteries

Number of cycles	Good cell ($\times 10^3$)			Bad cell ($\times 10^3$)		
	SG top	SG bottom	ΔSG (bottom–top)	SG top	SG bottom	ΔSG (bottom–top)
0	1315	1315	0	–	–	–
10	1325	1330	5	1275	1280	5
28	1330	1345	15	1295	1305	10
42	1330	1345	15	1330	1360	30
49	1310	1330	20	1315	1330	15
65	1310	1335	25	1285	1325	40
73	1315	1360	45	1285	1340	55
92	1315	1320	5	1315	1330	15
133	1345	1350	5	1330	1360	30

5.3. Electrolyte SG

Acid stratification occurs when the acid concentration varies at different positions on the separator paper. Sulphuric acid concentration in the electrolyte is directly related to the SG, which can be determined easily with a small sample of acid. For each of the cells examined, the SG was measured at the top and bottom of the separator. Values obtained are shown in Table 1. The greater the difference between these two values the larger the amount of stratification.

Acid stratification as a function of number of cycles is shown in Fig. 12. The top of each bar represents the SG at the bottom of the cell and the bottom of each bar, the SG at the top. Bar length therefore gives the degree of stratification. There is a general trend demonstrating greater stratification in the bad cell compared to the good. The only exception to this is in the batteries cycled 28 and 49 times.

The batteries cycled between 0 and 73 times show an increase in stratification with number of cycles. This trend is not reflected in the results obtained from the batteries cycled 92 and 133 times. There is no obvious explanation for this trend.

It should also be noted that the majority of cells have electrolyte specific gravities greater than that of the freshly formed battery. This increase in sulphuric acid concentration suggests water loss, which may contribute to a decrease in battery capacity.

5.4. Positive active material

5.4.1. Compositional analysis

During battery cycling, a number of compositional and structural changes occur within the positive active material. This is most apparent with reference to the compositional

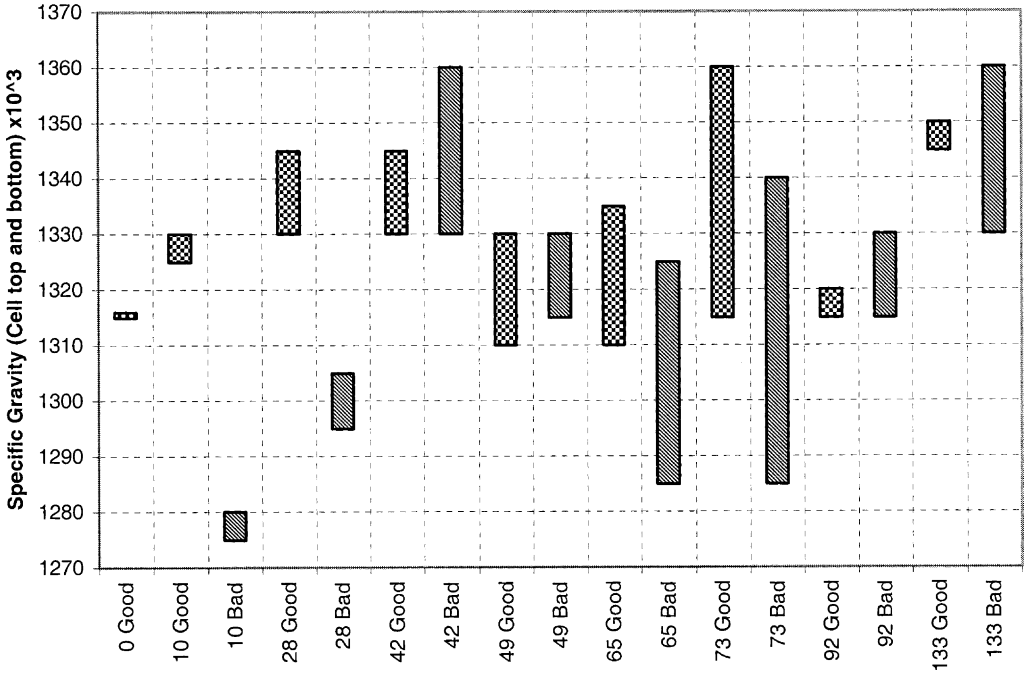

Fig. 12. Difference in specific gravity between top and bottom of separator papers in good and bad cells.

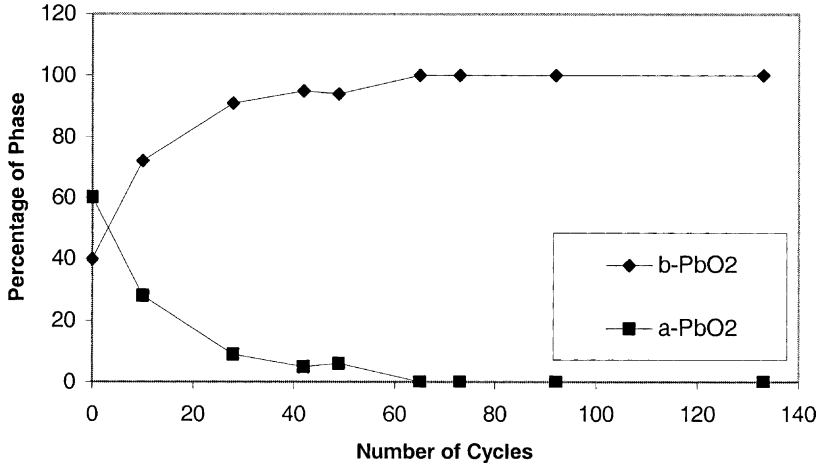

Fig. 13. Composition of positive active material from good battery cells.

analysis obtained from the X-ray diffraction patterns. Fig. 13 shows the composition of the positive active material from the good cells of the cycled batteries.

The active material consists of a mixture of alpha-lead dioxide (α-PbO_2, orthorhombic), and beta-lead dioxide (β-PbO_2, tetragonal). As the battery is cycled, the proportion of the alpha phase decreases. This phenomenon is well documented, [8] and occurs because the alpha phase cannot be formed in acidic environments. The rate at which the alpha lead dioxide is converted to beta lead dioxide reduces with number of cycles due to the diminishing fraction of alpha phase.

The composition of the positive active material in the bad cells is shown in Fig. 14. Increase in beta lead dioxide with number of cycles similar to that observed in the good cells is shown in Fig. 14. However, the batteries cycled 10 and 28 times contain large amounts of lead sulphate. Lead sulphate is formed during discharge of the battery and is consequently converted back into lead dioxide on charging. This has not occurred in these cells and the remnant lead sulphate is present. Examination using the scanning electron microscope identified large lead sulphate crystals in the battery cycled 28 times. These varied in size from a few microns to greater than 10 microns, see Figs. 15 and 16.

From a kinetic standpoint, once sulphate crystals of this size are formed, it is unfavourable for them to react to form lead dioxide and sulphuric acid due to their high volume and low surface area. Given the amount of lead sulphate present, it is not surprising that these cells have failed and it is almost certain that sulphation was the cause of capacity loss and eventual battery failure. This is reflected by the very low SG measured in these cells, which suggest incomplete charging.

When a comparison is made between the quantities of alpha and beta lead dioxide in the good and bad cells of the batteries cycled 10 and 28 times, the proportion of alpha lead dioxide is reduced whereas the proportion of the beta phase is similar. This suggests that the lead sulphate in these batteries had formed mainly from alpha lead dioxide as opposed to beta lead dioxide.

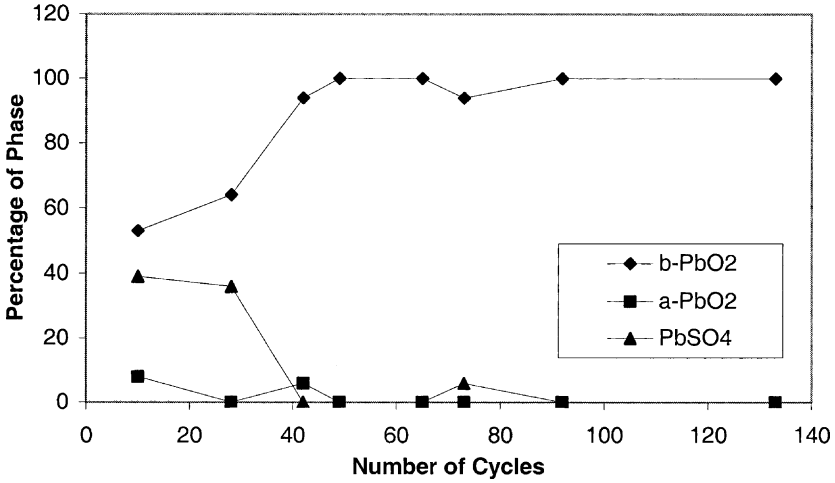

Fig. 14. Composition of positive active material from bad battery cells.

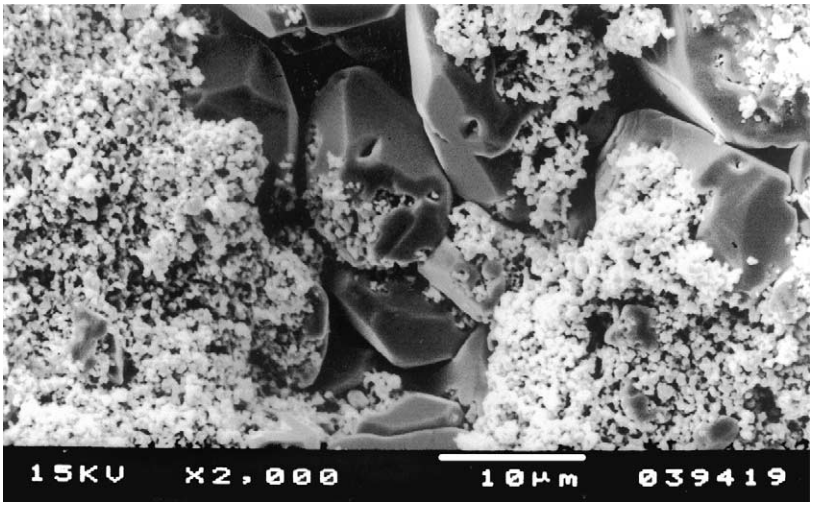

Fig. 15. Sulphate crystals in bad cell of battery cycled 28 times (2000×).

5.4.2. Surface area analysis

Variations in BET surface area with number of cycles are shown in Fig. 17. BET surface area for the good cell in every battery is consistently higher than that in the corresponding bad cell, as shown in Fig. 17. However, there does not appear to be any consistent trend between BET surface area and number of cycles. The positive active material in the freshly formed battery has a surface area around 3.5, which then drops to a value comparable with that of the bad cell after approximately 40 cycles. This reduction in surface area with cycles is not observed in the bad cells (batteries cycled 10 and 28 times). Lead sulphate has a low surface area compared to lead dioxide and its presence is the most likely cause of the low measured surface areas of the plates in these batteries.

5.5. Corrosion layer thickness measurements

During operation and overcharging of a battery, oxygen gas reacts with the positive grid forming a lead monoxide corrosion layer. This subsequently reacts electrochemically to form lead dioxide resulting in the formation of a corrosion layer containing both, lead monoxide and lead dioxide. Corrosion layer thickness measurements were taken on the top, bottom, left and right hand sides of the grid wire in the good and bad cells of cycled batteries. The average corrosion layer thickness versus the number of cycles for good and bad cells is shown in Fig. 18.

With the exception of the corrosion layer thickness measured on the battery cycled 49 times, which was significantly thicker than that on the other grids, the data appears to follow an exponential relationship. Equations of the curves in Fig. 18, assuming an exponential relationship, are shown with corresponding "best fit" R^2 values.

- Good cells $y = 16.4\,e^{0.0106x}$ $R^2 = 0.987$
- Bad cells $y = 8.3\,e^{0.0247x}$ $R^2 = 0.996$

From the figure and equations, it can be seen that the rate of corrosion layer thickening increases with number of cycles and is greatest in the bad cells. This observation

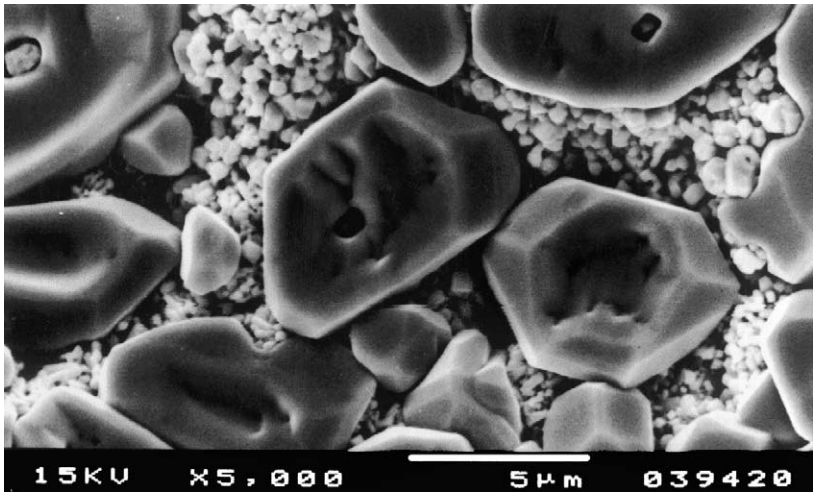

Fig. 16. Sulphate crystals in bad cell of battery cycled 28 times (5000×).

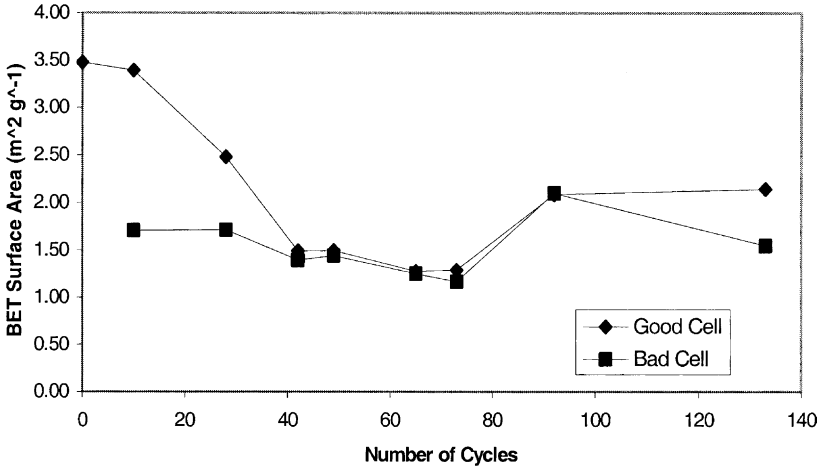

Fig. 17. BET surface area of positive active material in cycled batteries.

can be explained by considering the processes that occur during cycling of the battery. Corrosion layer growth occurs during overcharging when oxygen evolved within the positive active material diffuses to the positive grid and reacts to form lead oxide. This is shown by Eqs. (1)–(3).

$$2Pb + O_2 \rightarrow 2PbO \quad (1)$$

$$PbO + (n-1)O \rightarrow PbO_n (1 < n < 2) \quad (2)$$

$$PbO_n + (2-n)O \rightarrow PbO_2 \quad (3)$$

It follows that corrosion layer growth rate and therefore its thickness is related to overcharging time. The amount of overcharging, that a battery cell sustains, is a function of the charging time (16 h for these batteries) and the capacity or length of time needed to charge the cell. A consequence of battery cycling is a reduction in the capacity of the cells. It follows therefore that a reduced capacity cell, for example the bad cell, may charge more rapidly than the good cell in the same battery, effectively increasing the overcharging time. The increased corrosion layer thickening observed in the bad cells compared to the good cells could therefore be accounted for by the reduced capacity of the bad cells. The process of thickening of the corrosion layer is thus one of cumulative damage. It should be noted however, that the recharge potential of 14 V, although relatively high, was the standard potential used throughout the experiments. It is recognised that recharging at a lower potential for a longer period could reduce the rate of positive corrosion layer thickening, possibly extending the cycle life of the battery.

It is apparent from the results that the battery cycled 49 times behaved in a different manner as compared to all other batteries tested. Additionally, the corrosion layer thickness in both the good and bad cells of this battery were unusually thick. It is therefore not unreasonable to suggest that a different failure mechanism or combination of failure mechanisms has been operative in this battery. Further work would be required to understand the actual mechanisms of failure.

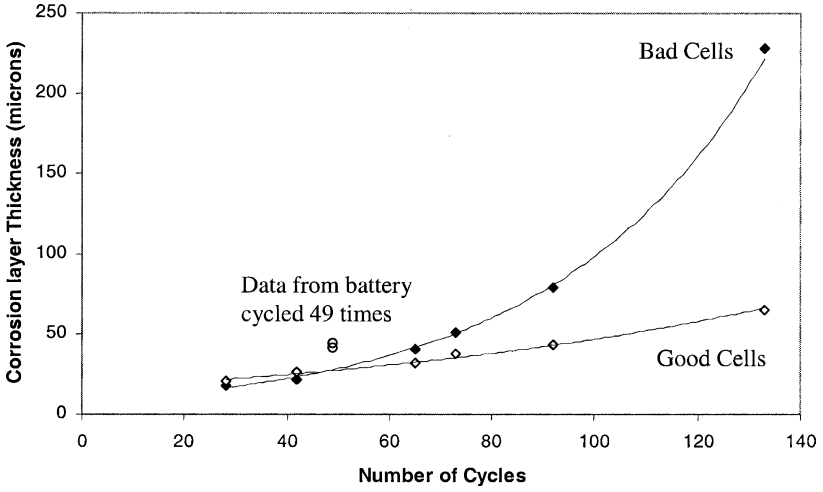

Fig. 18. Corrosion layer thickness vs. number of cycles for good cells.

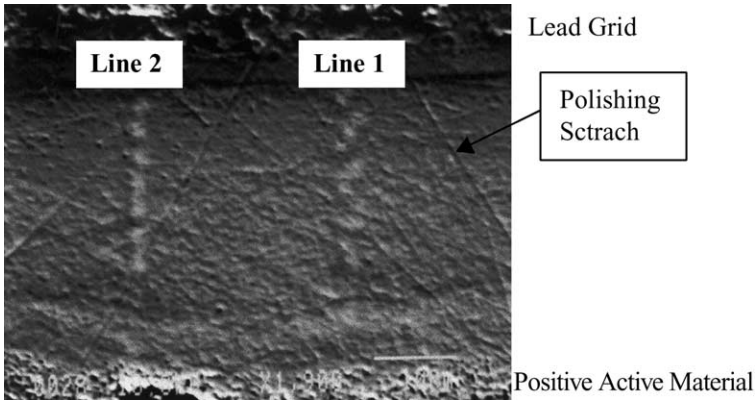

Fig. 19. Secondary electron image showing area of corrosion layer analysed using EPMA.

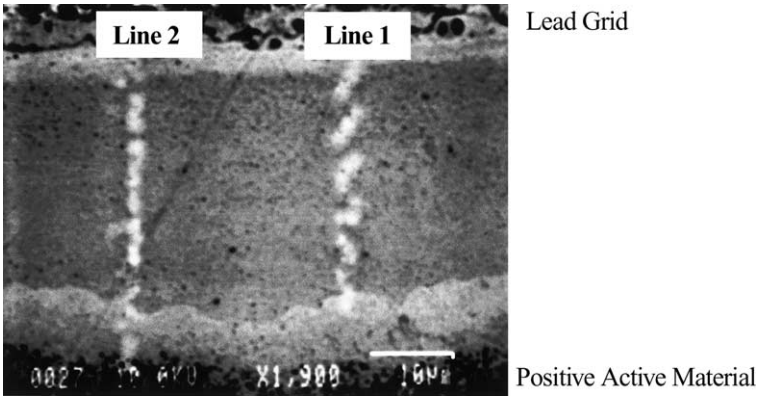

Fig. 20. Backscattered electron image showing area of corrosion layer analysed using EPMA.

5.6. Electron probe microanalysis

Quantitative analysis of the positive grid corrosion layer using electron probe microanalysis revealed a variation in the concentration of oxygen with distance across the corrosion layer section. Secondary and backscattered electron images of the position of each trace where the concentration of oxygen was measured is shown in Figs. 19 and 20. The thickness of the corrosion layer is approximately 40 μm.

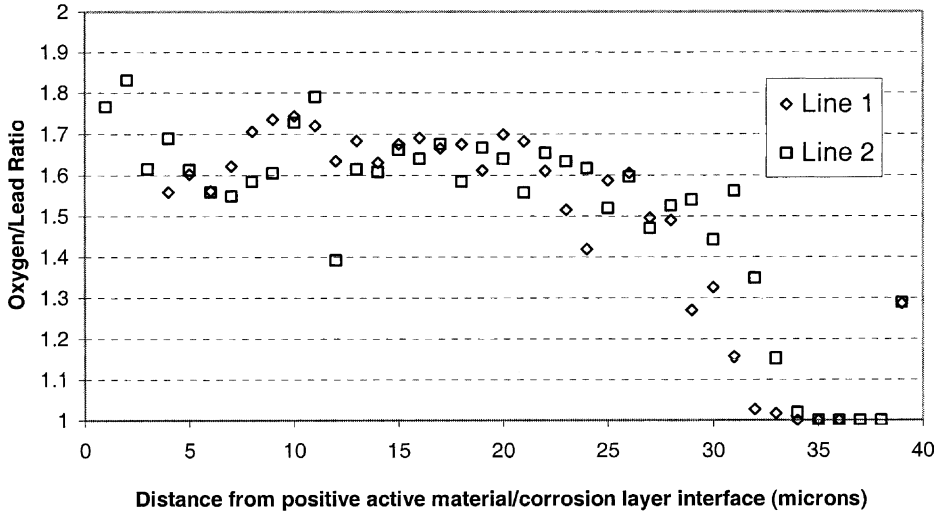

Fig. 21. Compositional analysis of corrosion layer from battery used to study cycling performance.

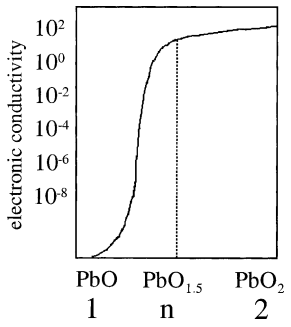

Fig. 22. Variation in electronic conductivity of lead oxide with oxygen concentration [7].

From Fig. 19, it is apparent that the corrosion layer section has a reasonably flat surface. This is important as the accuracy of electron probe microanalysis is sensitive to surface roughness. The backscattered image, Fig. 20, does not indicate the presence of any porosity, which can contribute to errors in the compositional analysis.

The variation in oxygen/lead ratio for two line scans across the corrosion layer section is shown in Fig. 21. A consequence of the variation in concentration of oxygen, or stoichiometry of the oxide, is a change in conductivity. It has been shown that the conductivity of the oxide decreases dramatically with oxygen concentration, this is shown diagrammatically in Fig. 22 [9].

Oxygen to lead ratio greater than 1.5, for the majority of the corrosion layer thickness as shown in Fig. 21, suggests high conductivity. However, this value drops to between 1 and 1.5 for a band of the corrosion layer approximately 10 μm in thickness adjacent to the lead grid. It is suggested that the reduction in oxygen concentration is caused because the oxygen must diffuse through the outer regions of the corrosion layer before reaching this position. Low oxygen concentrations are consistent with the formation of a thin passivating layer of lead monoxide adjacent to the corrosion layer which has been reported in previous literature [10]. The presence of lead monoxide is normally associated with the reaction of lead dioxide with lead during self discharge, according to Eq. (4).

$$PbO_2 + Pb \rightarrow 2PbO \quad (4)$$

6. General discussion

A number of possible causes for failure have been identified. For the batteries, which sustained the least numbers of cycles, 10 and 28, the most likely cause of failure is sulphation of the positive electrode, Figs. 14–16. The sulphation was restricted to the bad cells of the battery, which showed a rapid reduction in voltage, and therefore capacity, Figs. 4 and 5, during the final discharge/charge cycle compared to the remaining five cells which all showed similar performance.

Failure of the batteries that sustained a high number of cycles, 92 and 133, is considered to be due to the large corrosion layer thickness observed on the bad cells, Fig. 18. The plots of cell voltage versus time, Figs. 10 and 11 indicate that these cells showed a reduction in voltage much earlier than the remaining cells.

The batteries that failed at an intermediate number of cycles, 42, 49, 65 and 73, did not have component cells which exhibited significantly different behaviour, Figs. 6–9. This suggests that all the cells failed gradually, at the same rate, during cycling. Failure was due to a continuous degradation of the active materials rather than as a consequence of a particular failure mechanism affecting one specific aspect of battery performance. BET surface areas, Fig. 17, are similar for both good and bad cells, which is consistent with this observation. This type of failure is commonly referred to as premature capacity loss [11].

7. Conclusions

The following conclusions can be drawn from the results and discussion:

1. When a battery fails, the cells within the battery degrade to different levels.
2. Sulphation of the positive plates is the most likely cause of failure in the batteries cycled 10 and 28 times. This suggests that if the cells have not failed due to sulphation, within the first 30 cycles, sulphation is unlikely to be the cause of subsequent failures.
3. Lead sulphate forms more readily at the expense of α-lead dioxide rather than β-lead dioxide.
4. Resistivity of the negative active material does not vary significantly during battery cycling.
5. Acid stratification is greater in the bad cells of a battery that indicates a lower capacity.
6. The corrosion layer thickness is greater in the bad cells.
7. Corrosion layer growth rate is greater in the bad cells.
8. The battery formed a passivating lead monoxide corrosion layer adjacent to the positive grid.

References

[1] W. Mindt, Electrical properties of electrodeposited PbO_2 films, J. Electrochem. Soc. 116 (8) (1969) 1076–1080.
[2] Joint committee for powder diffraction standards, PDF-2 Database Sets 1–45, International Centre for Diffraction Data, 12 Campus Boulevard, Newtown Square, PA, USA, 1995, pp. 19073–3273.
[3] R. Jenkins, J.L de Vries, An introduction to X-ray powder diffraction, in: N.V. Philips (Ed.), Gloeilampenfabrieken, Eindhoven, Holland, The Netherlands.
[4] D.A.J. Rand, R.J. Hill, M. McDonagh, Improving the curing of positive plates for lead/acid batteries, J. Power Sources 31 (1990) 203–225.
[5] K. Harris, R.J. Hill, D.A.J. Rand, Crystalline phase composition of positive plates in lead/acid traction batteries under simulated electric vehicle service, J. Power Sources 8 (1982) 175–196.
[6] OPTIMAS 6.1, Optimas UK Ltd., West Maling, Kent, UK.

[7] R.J. Ball, R. Kurian, R. Evans, R. Stevens, Study of valve regulated lead/acid batteries manufactured with different separator papers, J. Power Sources 104 (2) (2002) 234–240.
[8] D. Berndt, Maintenance-Free Batteries, A handbook for battery technology, 2nd Edition, Wiley, p. 314.
[9] F. Lappe, Some physical properties of sputtered PbO_2 films, J. Phys. Chem. Solids 23 (1962) 1563–1572.
[10] D. Pavlov, A theory of the grid/positive active-mass (PAM) interface and possible methods to improve PAM utilization and cycle life of lead/acid batteries, J. Power Sources 53 (1995) 9–21.
[11] K.K. Constanti, A.F. Hollenkamp, M.J. Koop, K. McGregor, Physical change in positive-plate material—an underrated contributor to premature capacity loss, J. Power Sources 55 (1995) 269–275.

ELSEVIER

Journal of Power Sources 111 (2002) 23–38

JOURNAL OF POWER SOURCES

www.elsevier.com/locate/jpowsour

Influence of positive active material type and grid alloy on corrosion layer structure and composition in the valve regulated lead/acid battery

R.J. Ball[a,*], R. Kurian[b], R. Evans[c], R. Stevens[a]

[a]*Department of Engineering and Applied Science, University of Bath, Bath, BA2 7AY, UK*
[b]*Hawker Ltd., Stephenson St. Newport NP9 0XJ, UK*
[c]*Invensys, Westinghouse site, Chippenham, Wiltshire, SN15 1SJ, UK*

Received 9 September 2001; received in revised form 4 March 2002; accepted 11 March 2002

Abstract

Performance of a valve regulated lead/acid battery is affected by the properties of the positive grid corrosion layer. An investigation has been carried out using a range of experimental techniques to study the influence of corrosion layer composition and structure on cyclic performance. A number of designs of battery were manufactured with different grids and positive active materials (PAMs). Two grid types were used consisting of either pure lead or a lead/tin alloy. Variations in PAM composition and structure were obtained by forming electrodes from grey oxide pastes containing additions of, red lead, tetrabasic lead sulphate, or sulphuric acid (sulphated). Results indicated that both grid alloy composition and PAM type affect the corrosion layer properties. Ultra-microtoming was used to prepare sections of the grid/corrosion layer interface. Results showed that corrosion propagated along tin rich grain boundaries.

Keywords: VRLA; Corrosion layer; EPMA; Ultra-microtoming

1. Introduction

The corrosion layer is one of the most important components of the positive electrode. Its properties will influence battery operation since electrons generated must flow through it. The ease with which electrons can flow is dependant on geometry, composition, structure and thickness. High currents can be generated as a result of the large difference in surface area between the positive active material (PAM) and grid. For a typical grid with a surface area of around 50 cm^2 the corresponding PAM area will be in the region of 500 m^2 [1].

The corrosion layer is first formed during plate curing and then increases in thickness as the battery is cycled. Thickness will be influenced by curing parameters such as temperature, humidity and oxygen concentration. Corrosion layers commonly consist of a multi-layered structure comprising of lead oxides of different stoichiometry. Normally the concentration of oxygen within the corrosion layer increases with distance away from the grid. This is because oxygen must diffuse from the outer surface of the layer towards the grid.

The change in molar volume that occurs when Pb is oxidised to PbO_2 is >38%. A consequence of this is the generation of internal stresses, which cause cracks to form, when the corrosion layer reaches a critical thickness. This process occurs within the corrosion layer and at the corrosion layer/PAM interface. Non-uniform heating of the corrosion layer is another cause for the formation of cracks. Crack formation is undesirable as it reduces the strength and conductivity of the material. However, elastically compliant elements present within the corrosion layer and PAM offset this effect; these are commonly referred to as gel zones and allow stresses to be relieved and help in reducing the incidence of cracking [2,3]. The formation of gel zones is dependent on the state of hydration of the corrosion layer, which is influenced by the alloying elements present within the grid.

Lappe [4] investigated the relationship between electronic conductivity and stoichiometric coefficient of the lead oxides. He demonstrated that when the stoichiometric coefficient of an oxide reaches a value of 1.35 there is a rapid increase in conductivity and at 1.5, the conductivity is nearly equal to that of PbO_2. Lead oxides containing very small

* Corresponding author. Tel.: +44-1225-386447; fax: +44-1225-386098.
E-mail address: r.j.ball@bath.ac.uk (R.J. Ball).

0378-7753/02/$ – see front matter
PII: S0378-7753(02)00221-5

amounts of oxygen exhibited conductivities around $10^{-10}\,\Omega^{-1}\,cm^{-1}$, whereas the conductivity of PbO_2 was $10^{2}\,\Omega^{-1}\,cm^{-2}$.

Growth of a corrosion layer is dependent on the initial oxidation of the grid to form lead monoxide. The lead monoxide must then react with more oxygen to form oxides of higher stoichiometric coefficient. These reactions have been expressed as chemical equations by Pavlov [1]. The three basic reactions that must occur in order to convert the lead grid into lead dioxide are reproduced as:

$$Pb + O \xrightarrow{v_1} PbO \quad (1)$$

$$PbO + (n-1)O \xrightarrow{v_2} PbO_n \quad (1 < n < 2) \quad (2)$$

$$PbO_n + (2-n)O \xrightarrow{v_3} PbO_2 \quad (3)$$

The rate of each of the reactions above can be described in terms of a rate coefficient. Depending on the relative rates of the reactions, corrosion layers having different stoichiometric coefficients will be formed. By considering the stoichiometric coefficient and conductivity, Pavlov [1] proposed the following general rules:

$v_1 > v_2$	Low valency lead oxide	High specific resistivity corrosion layer
$v_1 < v_2, v_3$	High valency lead oxide	Low specific resistivity corrosion layer

In addition to these reactions, the self-discharge reaction between Pb and PbO_2 should also be considered. This rate is determined by a fourth rate coefficient v_4.

$$Pb + PbO_2 \xrightarrow{v_4} 2PbO \quad (4)$$

The occurrence of this reaction leads to a decrease in the overall stoichiometric coefficient of the oxide and to an increase in specific resistivity of the corrosion layer.

The alloying elements present in the grid alloy influence the structure of the corrosion layer by determining the type and rate of reactions occurring [5]. A consequence of this is a variation in stoichiometric coefficient of the oxides and therefore conductivity of the corrosion layer.

Work conducted by Pavlov [1] and colleagues indicated that alloying additions within the grid influence the conductivity of the corrosion layer by either acting as an electro catalyst or as an inhibitor to the reactions given by Eqs. (1)–(4) [6,7]. Tin catalyses reactions 2 and 3, and as a consequence corrosion layers with higher stoichiometric coefficients are observed.

Passivation of the positive plate is associated with the formation of lead monoxide. If the thickness of this layer exceeds a critical value, it acts as a high resistance strata within the corrosion layer which can insulate the grid from the active material. The overall effect is to decrease the voltage at which discharge will occur on the plate. Passivation occurs via the reaction, $Pb + O \rightarrow PbO$, where the electrode system $Pb/PbO/PbO_2$ is formed. At open circuit the self-discharge reaction, $Pb + PbO_2 \rightarrow 2PbO$ occurs, also producing the high resistance lead monoxide layer [8]. The rate at which passivation occurs on the positive plates can be affected by dopants such as tin present within the grid alloy and corrosion layer. Tin has the effect of increasing the conductivity of the PbO layer [7,9].

Depassivation can occur by two processes, the first being the reduction of PbO to Pb by cathodic valency [9] and the second by oxidation of PbO by the oxygen generated during overcharge, which produces a lower resistance oxide with higher valency [1].

2. Production of test batteries

The batteries examined in this study were all 40 amp h valve regulated lead/acid batteries. Hundred percent glass separator paper and a standard cyclic negative active material were used in all batteries however, variations were made to the PAM and grid alloy. Two different grid and three types of PAM were used in total. A summary of the different battery types, which were constructed referred to as A–E, is given in Table 1.

The grey oxide (cyclic) PAM used in the manufacture of the type A battery was formed from a positive paste mix consisting of 90% grey oxide (α-PbO, ≈29% lead), 10% red lead, sulphuric acid and distilled water. Battery types B and C consisted of PAM formed from a grey oxide & tetrabasic lead sulphate positive paste produced from a mixture of grey oxide, tetrabasic lead sulphate, sulphuric acid and distilled water. A sulphated grey oxide paste was used in the production of positive electrodes for battery types D and E. This consisted of grey oxide, extra sulphuric acid compared to the other pastes and distilled water.

The battery grid production route can be described in two stages, the first of these being production of lead strip of suitable thickness, and the second, punching of the strip to form the grid. Two different grid types were used in the construction of the test batteries. The initial stage in grid production involves the manufacture of a lead strip. Hence, lead grid was manufactured firstly by casting pure lead into a strip several centimeters thick. The lead strip was then rolled repeatedly until the desired thickness was obtained. Lead/tin grids were manufactured using Comminco casting

Table 1
PAM and grid types used in the test batteries

Battery type	PAM	Positive grid
A	Grey oxide (cyclic)	Pure lead
B	Grey oxide and tetrabasic lead sulphate	Pure lead
C	Grey oxide and tetrabasic lead sulphate	Lead/tin
D	Sulphated grey oxide	Pure lead
E	Sulphated grey oxide	Lead/tin

machines. This process has the ability to cast the grid to the required thickness without the need for subsequent rolling. Once the lead strip was obtained, holes for the active material, having dimensions 4 mm × 13 mm were introduced using a punching machine, converting the strip into a grid. Pressing the paste into the lead current collecting grid produced battery electrodes. A glass paper was applied to each side of the paste impregnated lead grid, to ease handling, prior to the cutting our of individual electrodes. Electrodes were subjected to a curing stage before cell assembly. Compositional analysis of cured electrodes using X-ray diffraction and wet chemical analysis indicated that groups A, D and E consisted almost entirely of α-lead monoxide except for a small amount, ∼5%, of unreacted metallic lead. Groups B and C contained approximately 30% tetrabasic lead sulphate and 4% metallic lead, the remainder consisting of α-lead monoxide. After battery assembly the positive plates were converted to lead dioxide during the formation stage of manufacture. X-ray diffraction analysis of the PAM indicated an α:β lead dioxide ratio of approximately 50% ± 10%, with a small proportion, 10%, lead sulphate present in some plates.

3. Cycling of test batteries

Cycling was carried out automatically using Digitron charging units. Each cycle consisted of a constant current discharge at 7.05 A to 10.2 V followed by a constant voltage recharge at 14.7 V for 16 h. This was repeated until the capacity after charging was <80% of the initial starting capacity. The cells that showed the greatest and least reduction in voltage during a final discharge/charge cycle were examined; these are referred to as the 'bad' and 'good' cells respectively. An example of the voltage in each of the six cells of a battery during the last discharge charge cycle is shown in Fig. 1.

4. Sample preparation

4.1. Materialography

Cross-sections of the corrosion layers from each of the battery types examined in this study were prepared using standard techniques. After initial encapsulation in resin battery electrodes were sectioned and remounted for polishing. Silicon carbide paper was used to grind and flatten the samples, followed by polishing with an alumina suspension and finally by vibratory polishing. A more detailed description of the preparation method is given in an earlier paper [10].

4.2. Grid/corrosion layer interfacial analysis

Although mechanical polishing of cross-sections was successful for obtaining images of corrosion layers several tens of microns thick, using this method it proved impossible to obtain an image of sufficient quality of the grid/corrosion layer interface. This was attributed to the difference in properties between the soft lead grid bar and the hard lead oxide ceramic corrosion layer, which wore down at different rates under the same polishing media. Ultra-microtoming, however, when used was a successful method of sample preparation.

Ultra-microtoming, although employed mainly for biological samples, can be used for the preparation of metals and ceramics. For the purpose of obtaining a good quality grid/corrosion layer cross-sectional sample, the microtome needs only to be used as a tool to obtain a flat surface that can then be examined by scanning electron microscopy.

Samples were produced by cutting sections of grid bar out of a positive electrode and then breaking away the PAM. Due to the relative strengths of the grid/corrosion layer bond and corrosion layer/active material bond, the corrosion layer stayed attached to the grid in the majority of instances.

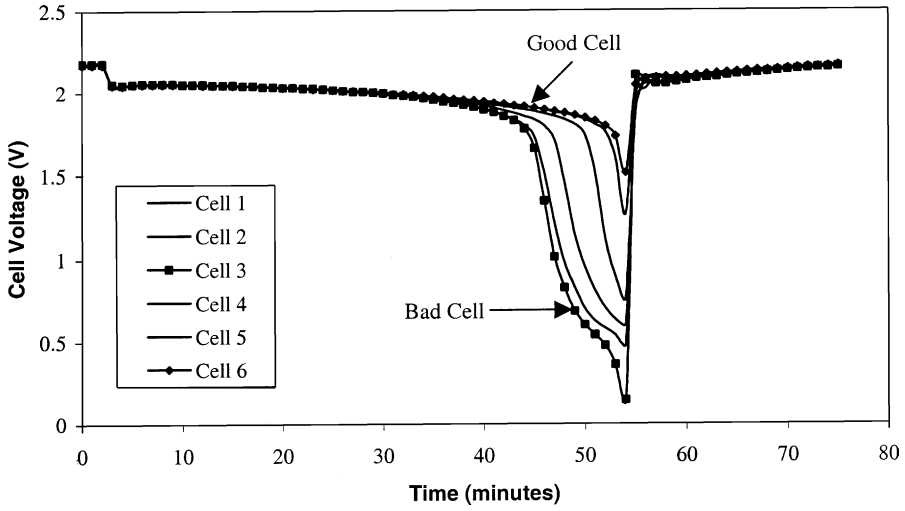

Fig. 1. Plot of voltage vs. time for cells in battery type C.

Table 2
Standards used for electron probe microanalysis

Element	Possible 'states' of element in sample	Standard selected and source	Notes
Lead, Pb	Pb, PbO_n ($1 < n < 2$)	Lead monoxide, PbO	Lead is present in the form of lead or lead oxide, this standard gives a good match in composition and structure
Oxygen, O	PbO_n ($1 < n < 2$)	Lead monoxide, PbO	The standard is almost identical in composition to the sample, therefore this is a very good match
Tin, Sn	Sn, SnO_n ($1 < n < 2$)	Pure tin, Sn (C.M. Taylor Corp., 12921-5)	This is again a suitable standard to use
Sulphur, S	R-SO_4	Iron Sulphide (pyrite), FeS_2 (C.M. Taylor Corp., 11540-1)	The sulphate and sulphide are likely to have varying characteristics Errors may therefore be slightly larger than with the previous elements

Once a section of grid bar was obtained with a uniform layer of corrosion and a minimum amount of PAM attached, it was cast in resin using specially designed latex moulds for the ultra-microtome. Soaking for 4 h prior to curing ensured a good resin to sample contact. Curing was achieved by heating in an oven at 60 °C for a period of at least 24 h.

Once cured, the sample was trimmed to a suitable size and dimensions for ultra-microtoming. Initially sections were removed from the surface using a glass knife prior to removal of sections using a diamond knife in order to obtain as clean a cut as possible for examination. A thin layer of gold was deposited onto the surface of the finished section to prevent charging of the resin in the SEM. This was done using an Edwards sputter coating unit.

5. Experimental methods

5.1. Microscopy and corrosion layer thickness measurement

The polished cross-sections of corrosion layers from each battery type were examined and photographed using a Zeiss ICM405 optical microscope. Microtomed sections were examined in a Jeol 6310 scanning electron microscope. Corrosion layer thickness measurements were determined using Optimas image analysis software [11]. Images were obtained using a digital camera and then measurements taken on the top, bottom, left and right hand sides of five grid bars from each battery, thus producing 20 readings in total. The mean of these readings was then quoted as the corrosion layer thickness.

5.2. Electron probe microanalysis

A Jeol JXA-8600 superprobe was used to determine the composition of the corrosion layers in each of the samples tested. Readings were taken in a line across the corrosion layer thickness at 1 μm intervals. An initial qualitative analysis indicated that the corrosion layer consisted of lead, oxygen, sulphur and tin. Details of the expected oxidation states of these elements and the standards used are given in Table 2.

To prevent charging effects the samples were coated with a thin layer of carbon, using an Edwards sputter coating unit. All samples and standards were coated simultaneously to reduce errors caused by adsorption of X-rays by the layer. Taking into account the peak size, shape and position, the diffraction crystals employed and counting times used are shown in Table 3.

6. Results

6.1. Optical examination of corrosion layer

Examination using an optical microscope of the corrosion layers for each battery type indicated variations in structure and morphology. A typical corrosion layer, from a type A battery is shown in Fig. 2. The lead grid is out of focus in the photograph, however this is an unavoidable consequence of the preparation method used. Cracking can be seen parallel to the grid surface running along the 'grid side' of the corrosion layer. No porosity is visible within the corrosion layer and an internal boundary within the corrosion layer is visible in the central region.

Table 3
EPMA settings for quantitative analysis

Element	Line	X-tal	Peak position (mm)	Peak background (mm)		Counting time (s)	
				Lower	Upper	Peak	Background
Lead, Pb	$M\alpha_1$	PET[a]	169.090	4.000	4.000	30.0	5.0
Oxygen, O	$K\alpha_1$	LDE[b]	109.440	8.800	8.800	30.0	5.0
Tin, Sn	$L\alpha_1$	PET[a]	115.125	4.000	4.000	10.0	5.0
Sulphur, S	$K\alpha_1$	PET[a]	172.010	0.800	0.800	10.0	5.0

[a] Pentaerythritol.
[b] Tungsten/silicon multilayer.

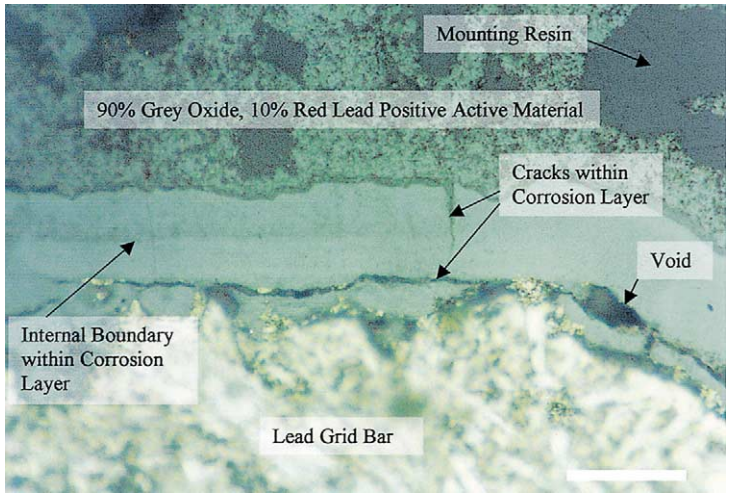

Fig. 2. Corrosion layer from type A battery (scale bar 50 microns).

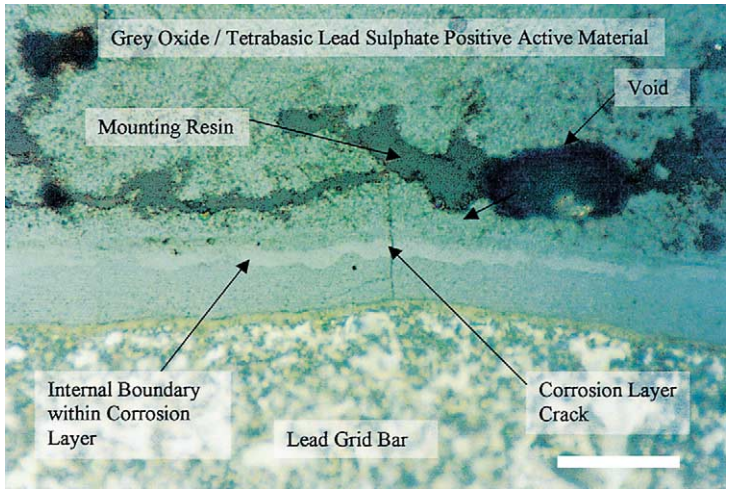

Fig. 3. Corrosion layer from type B battery (scale bar 50 microns).

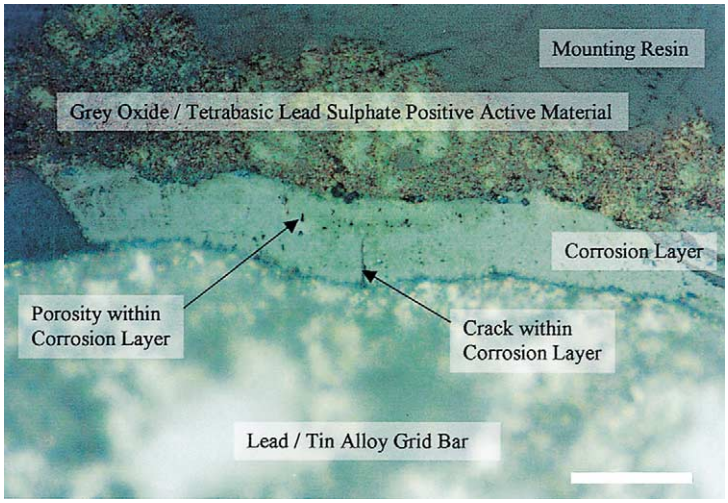

Fig. 4. Corrosion layer from type C battery (scale bar 50 microns).

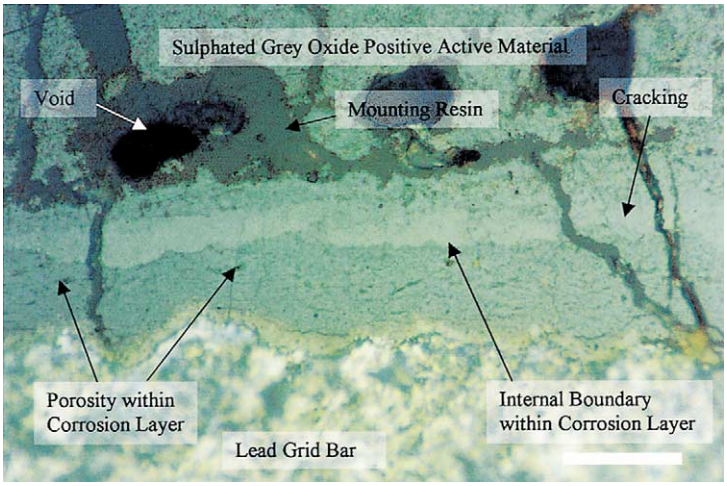

Fig. 5. Corrosion layer from type D battery (scale bar 50 microns).

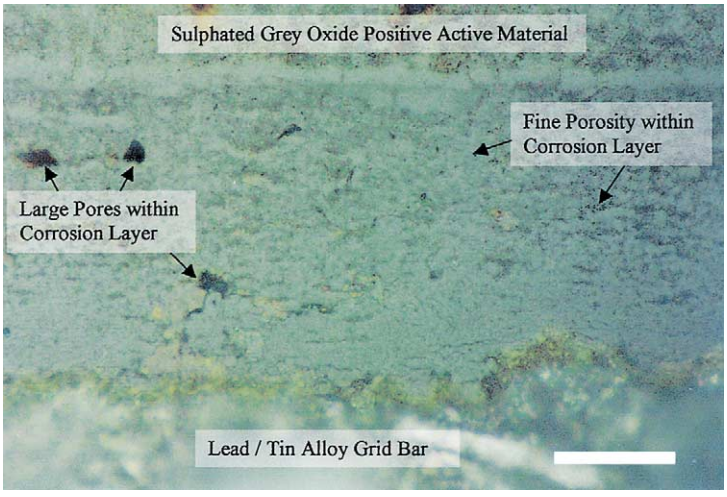

Fig. 6. Corrosion layer from type E battery (scale bar 50 microns).

The corrosion layer observed on the type B battery grid, Fig. 3, is very similar in appearance to the previous one except that the internal boundary within the layer is closer to the PAM and lighter in colour. Fig. 4 shows the corrosion layer from the type C battery. No internal boundary is identifiable in this layer and a number of black spots are visible which are believed to be pores.

The type D positive electrode has a greater volume fraction of porosity, consisting of large numbers of cracks in the corrosion layer and PAM (Fig. 5). Large pores are also visible in the PAM adjacent to the corrosion layer. Fig. 6 shows a typical corrosion layer from a type E battery. Fine porosity is visible across the width of the layer and a number of larger pores are also present. A lighter band in the corrosion layer is visible adjacent to the PAM.

Corrosion layer thickness measurements taken on the good and bad cells of the batteries examined and the number of cycles at which these values were taken are shown in Table 4. There is no significant difference between the corrosion layer thickness measurements for the good and bad cells. The thickest layers occurred on batteries of type D and E (ignoring type B due to higher cycles). These layers contained more pores and therefore would have allowed oxygen gas to readily diffuse to the grid/corrosion layer interface. When a comparison is made between type D and E batteries, type E that contained the lead/tin grid has a thicker layer. This suggests that tin promotes an increase in corrosion layer thickness. However, the same conclusion cannot

Table 4
Oxide thickness measurements

Battery type	Cycles	Good cell (μm)		Bad cell (μm)	
		Average	S.D.	Average	S.D.
A[a]	28 and 42	23.5	6.6	19.8	3.1
B	40	47.7	12.7	40.0	11.0
C	29	28.1	5.3	25.5	5.8
D	29	47.5	8.8	50.8	5.9
E	27	89.4	12.6	88.1	14.4

[a] Data averaged for batteries cycled 28 and 42 times.

be drawn from the batteries from type B and C, since the type B battery sustained significantly more cycles. The thinnest corrosion layer occurred on the positive grid of battery type A.

6.2. Structural and compositional analysis of corrosion layer using EPMA

A compositional analysis of the corrosion layer was carried out using electron probe microanalysis. This involved obtaining electron images of the corrosion layers, which proved useful in providing additional information on layer porosity.

The main results of interest are quantitative, however, the qualitative results will be considered first. Lead, oxygen and sulphur were identified in all corrosion layers with the addition of tin in the case of those attached to a grid bar originally alloyed with tin. This indicates that tin contained initially within the grid becomes incorporated into the corrosion layer during growth. The fact that no other elements were identified, with the exception of carbon, which was used as a conductive coating, demonstrates that the materials used to manufacture the battery were pure and did not contain detectable amounts of any other element.

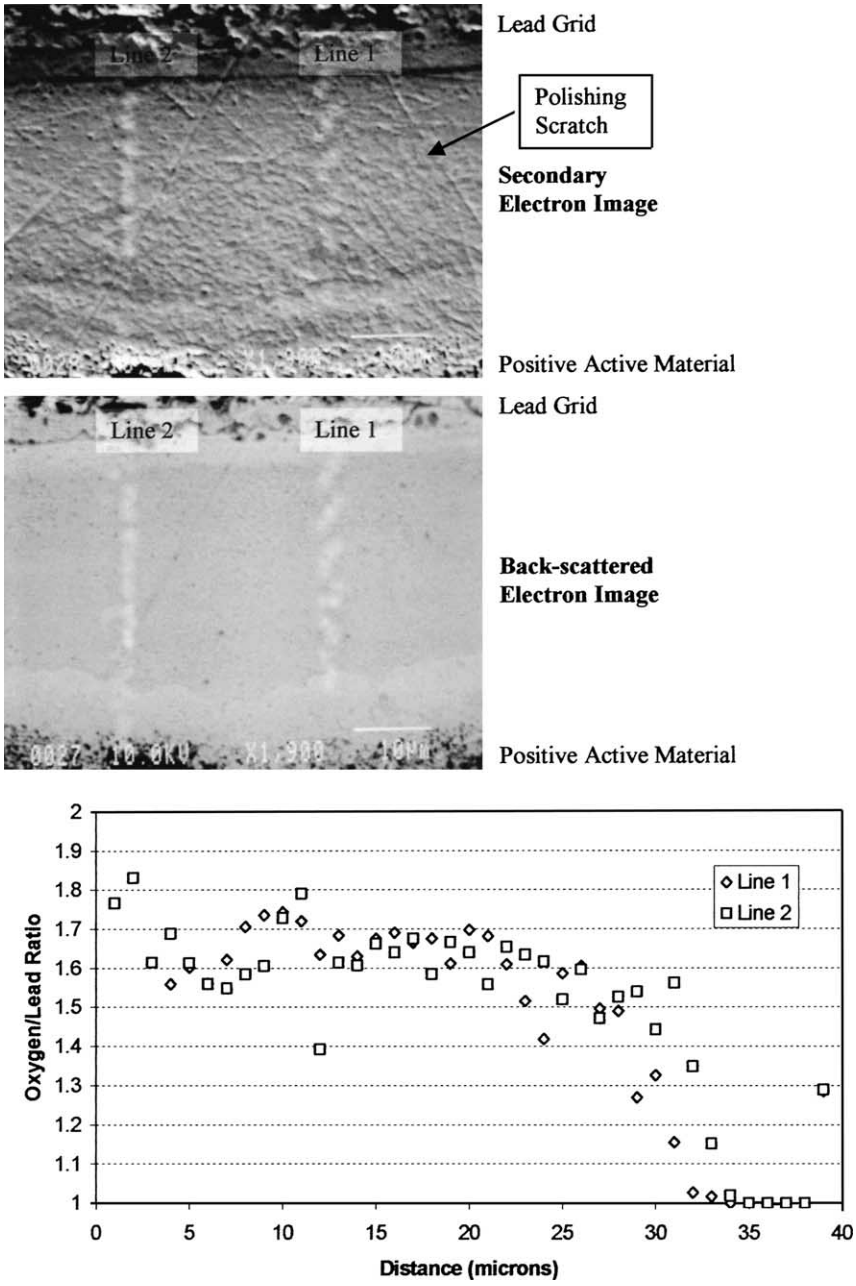

Fig. 7. Analysis of corrosion layer from battery type A.

Initial spot quantitative analyses on the corrosion layers examined, showed a large variation in compositional values, obtained due to the presence of porosity and surface roughness. The surface roughness is clearly visible in the scanning electron images and porosity in the back-scattered electron images, Figs. 7–11. This can be explained by considering the interactions of the incident electrons with the sample and the method used to calculate the quantity of each element present.

Calibration of the electron probe microanalyser was achieved with the use of known standards. However, with this approach the accuracy of the analysis is dependent on the unknown sample and standards having similar densities. Porosity within the corrosion layers can effectively reduce their physical density and introduces errors into the results.

When X-rays from the sample are counted the analysis software automatically assumes that the sample is 100% dense, if a pore is present, the number of X-rays emitted is reduced and the calculation of the composition altered. This is demonstrated by the typical analysis given in Table 5.

The accuracy of an elemental analysis can be determined by considering the total weight percent; the closer it is to 100%, the more accurate the analysis. For the purposes of

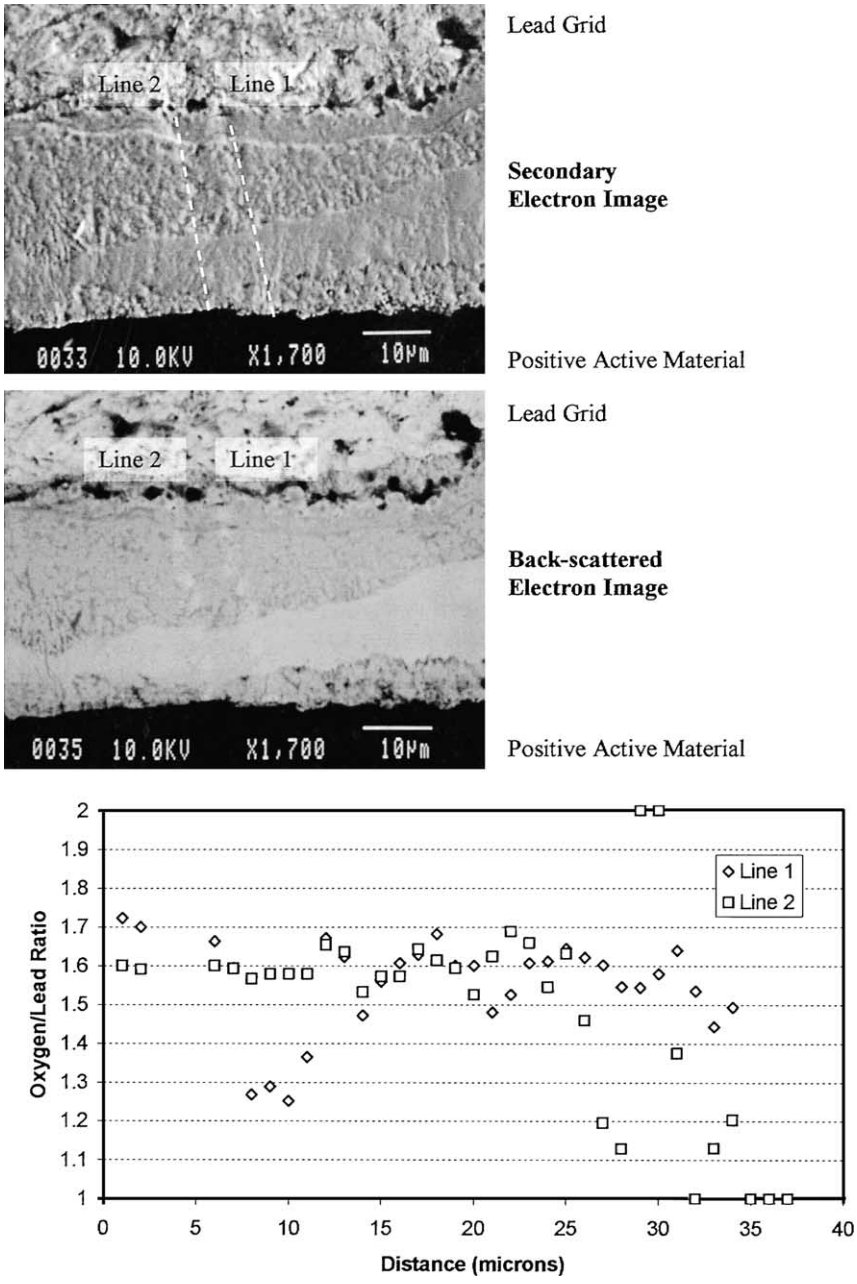

Fig. 8. Analysis of corrosion layer from battery type B.

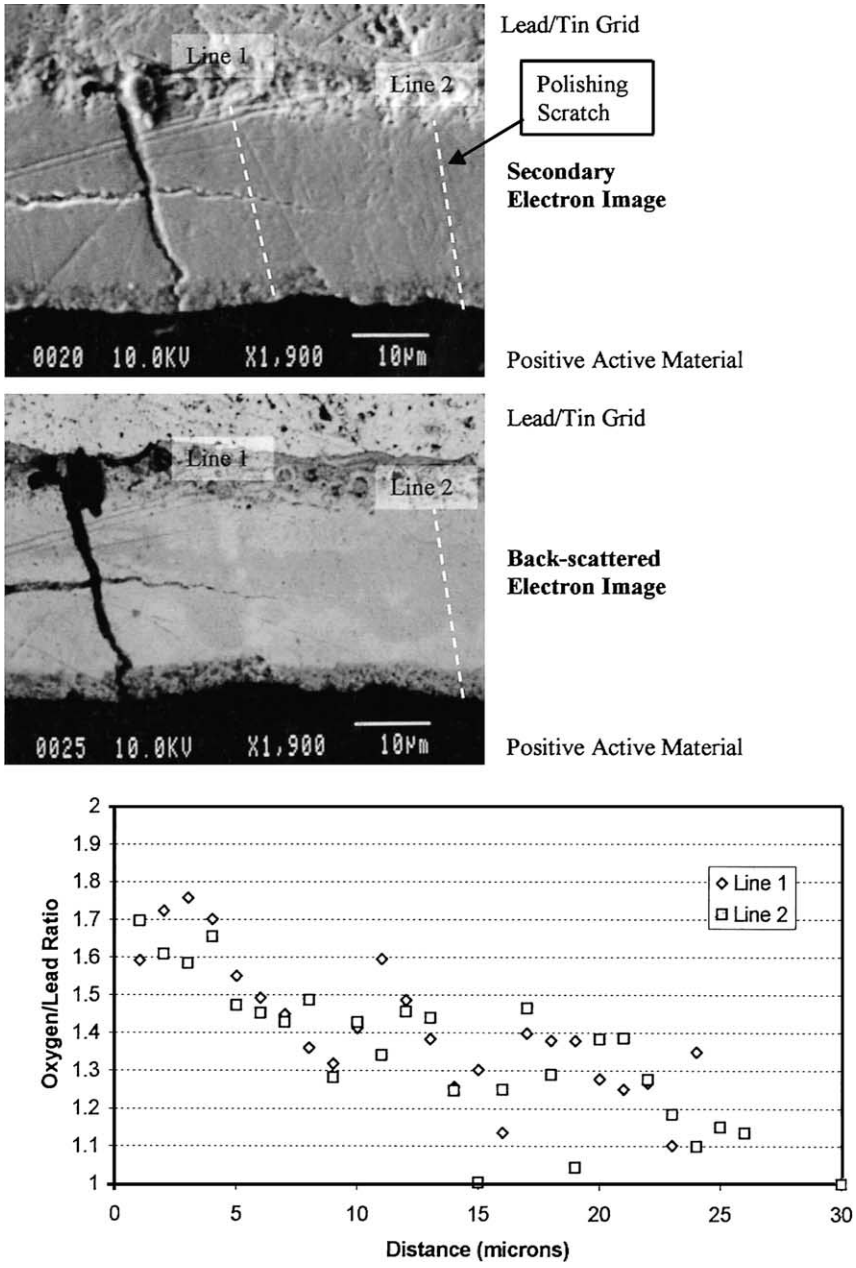

Fig. 9. Analysis of corrosion layer from battery type C.

this study all the analyses with a combined weight percent of <90% were ignored as it was considered this indicated that the region of sample excited by the electron beam contained an unacceptable level of porosity or surface roughness.

Table 5
Typical EPMA compositional analysis

Atom	Percentage
Pb	43.4
O	56
S	0.6
Sn	0.1
Total wt.%	96.1

In order to obtain an accurate value for the oxide stoichiometry, a large number of quantitative analyses were conducted. As variations in oxide stoichiometry between the inner and outer edges of the corrosion layer are of interest, a quantitative line scan between these two positions was the most appropriate option.

Analyses were conducted at 1 μm intervals along the scan line. This provided the maximum number of practical analysis points considering that the minimum area that can be analyzed is approximately 1 μm in diameter. The maximum number of analysis points was used, since for the more porous samples a large number of the analyses were rejected because the total weight percent was <90%. To calculate the stoichiometry of the oxide in the corrosion

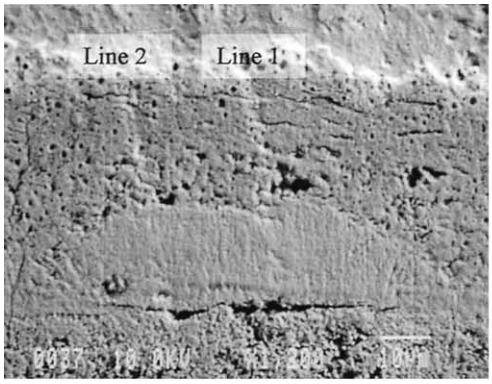

Lead Grid

Secondary Electron Image

Positive Active Material

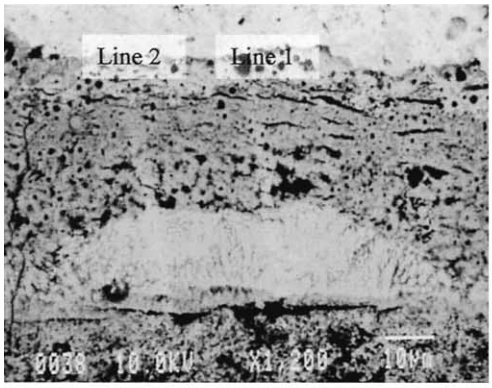

Lead Grid

Back-scattered Electron Image

Positive Active Material

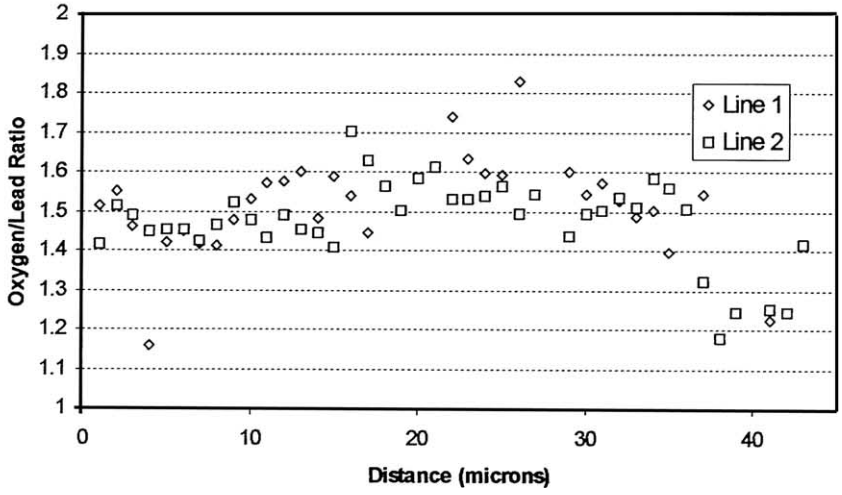

Fig. 10. Analysis of corrosion layer from battery type D.

layer it is necessary to make a number of assumptions for each analysis. These are summarised as follows:

- The only elements present in the corrosion layer are lead, oxygen, tin and sulphur.
- All sulphur present within the corrosion layer is in the form of a metal sulphate.
- Lead and tin within the corrosion layer are either in the form of an oxide or sulphate.
- Oxide stoichiometry for a given analysis point is always the same regardless of metal e.g. lead or tin.

From these assumptions a number of expressions, shown later, were derived to obtain values for the total metal and oxygen atoms available for incorporation into oxide, thus allowing the stoichiometry of the oxide to be calculated.

Total metal atoms forming oxide, $$T_{\mathrm{M}} = P + T - S \quad (5)$$

Total oxygen atoms forming oxide, $$T_{\mathrm{O}} = O - (4 \times S) \quad (6)$$

Oxide stoichiometry ratio, MO_n, $$n = \frac{T_{\mathrm{O}}}{T_{\mathrm{M}}} \quad (7)$$

Where P is the number of lead atoms identified in analysis, T the number of tin atoms identified in analysis, S the number

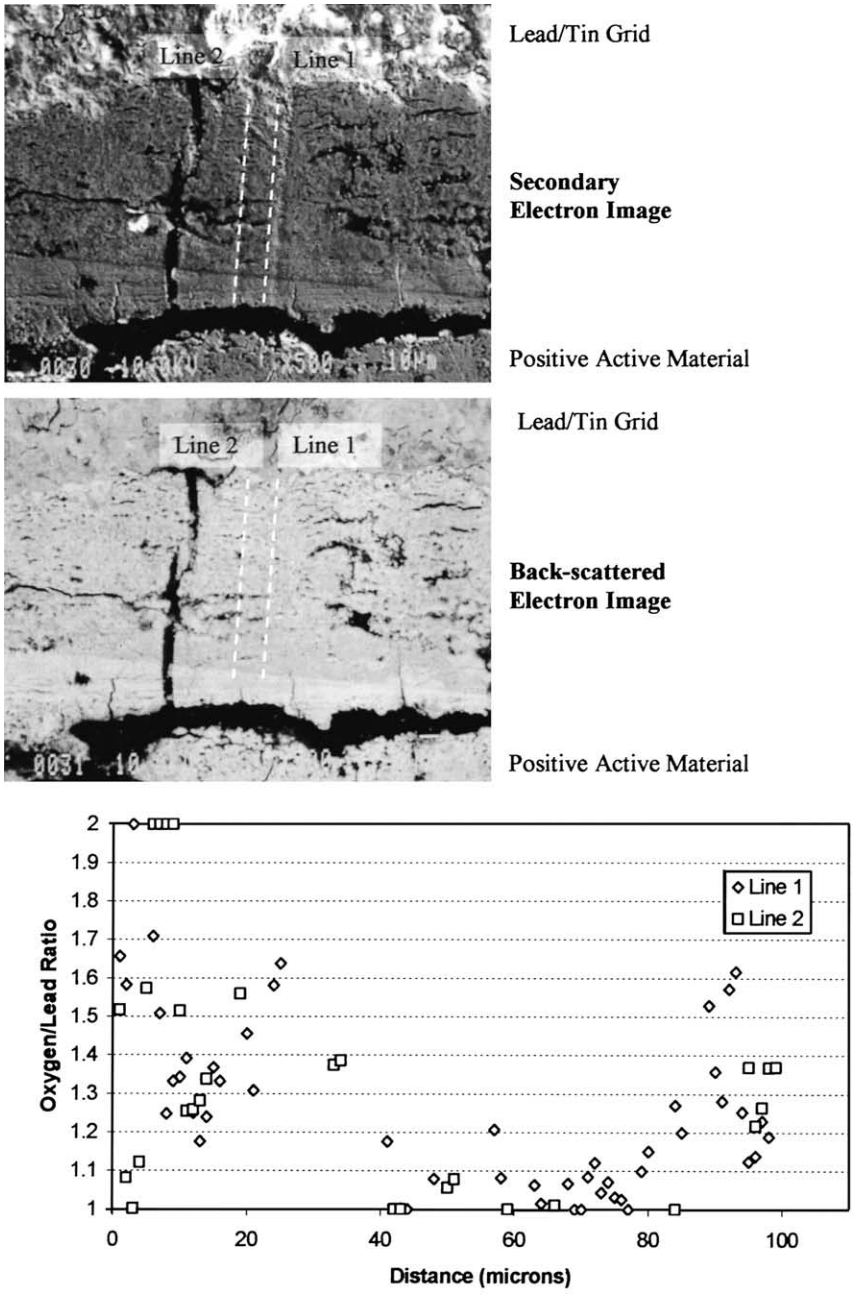

Fig. 11. Analysis of corrosion layer from battery type E.

of sulphur atoms identified in analysis and *O* the number of oxygen atoms identified in analysis.

Secondary and back-scattered electron images and plots of oxygen/lead ratio versus distance across corrosion layer for each of the battery types examined are shown in Figs. 7–11.

The electron scanning process resulted in a layer of contamination being deposited on the corrosion layer surface. This provided a means to identify the exact position of the scan line. For all plots the scan direction taken was from the active material towards the grid bar. Variations in oxygen/lead ratio occur with distance across the corrosion layer and also between the different battery designs. There is a general trend showing a decrease in oxygen content towards the grid bar. When comparing the scan lines and plots, step variations in oxygen/lead ratio do not always correspond to the spatial position of internal boundaries within the corrosion layer.

Scatter in some of the data plots is believed to be caused by errors introduced by variations in surface roughness and porosity. Despite these factors it has still proved possible to identify general compositional trends within the corrosion layer of each battery design.

Internal boundaries within the corrosion layers can be identified in both back-scattered and secondary electron

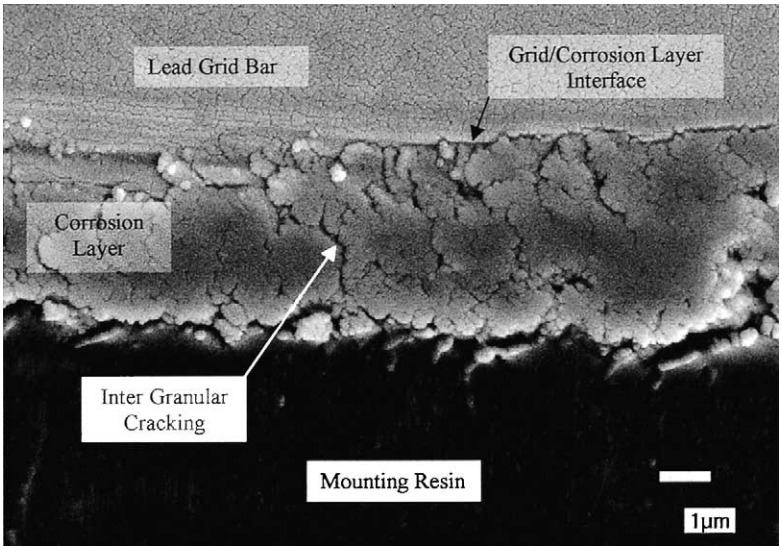

Fig. 12. Grid corrosion layer interface from type B battery.

images by darker and lighter regions of contrast. The darker regions correspond to lower atomic mass areas and the light regions to high. Variations in intensity and contrast are a consequence of the back-scattered electron intensity dependence on atomic number. This can be used to explain the light shade of the grid bar, which has a high average atomic mass and is therefore efficient at back-scattering electrons.

From an examination of the images it can be seen that the lighter band within the corrosion layer is positioned adjacent to the PAM and the darker band to the grid bar. This observation suggests an increased lead content in the corrosion layer adjacent to the PAM. This cannot be explained when it is presumed that the oxygen concentration is considered to be higher in these regions, suggesting the materials may have different work functions, thereby producing a variation in contrast between the different regions.

6.3. Analysis of the corrosion layer/grid interface

Preparation of corrosion layers using grinding and polishing techniques produced a high quality surface finish suitable for electron microscopy and, wave and energy dispersive analysis. However, the differences of material removal rate between the soft lead grid and hard ceramic corrosion layer make examination of this interface almost impossible due to the ledge formed at the interface. For this reason, the alternative technique of ultra-microtoming was used. This not only provided a flat section, but the disruption to the interface was negligible making detailed microscopy feasible.

Samples were prepared from the freshly formed positive electrodes of battery types B–E. Secondary electron images of the sections taken are shown in Figs. 12–15, respectively. From the figures it can be seen that this technique provides

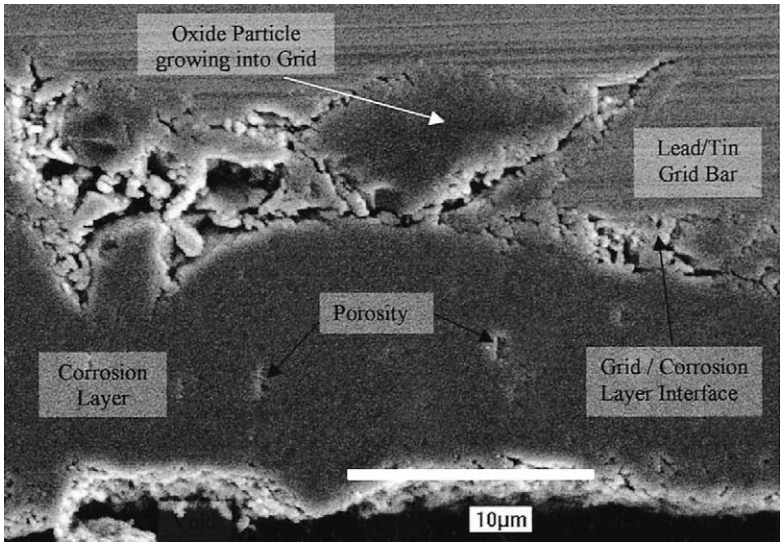

Fig. 13. Grid corrosion layer interface from type C battery.

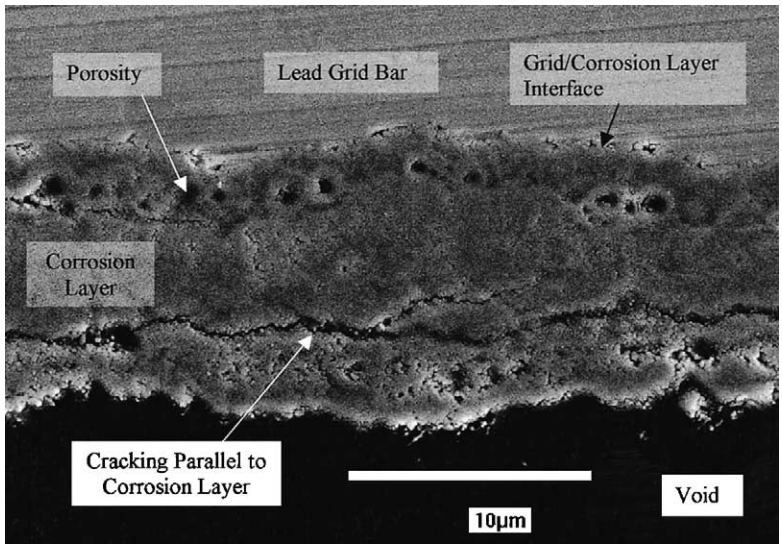

Fig. 14. Grid corrosion layer interface from type D battery.

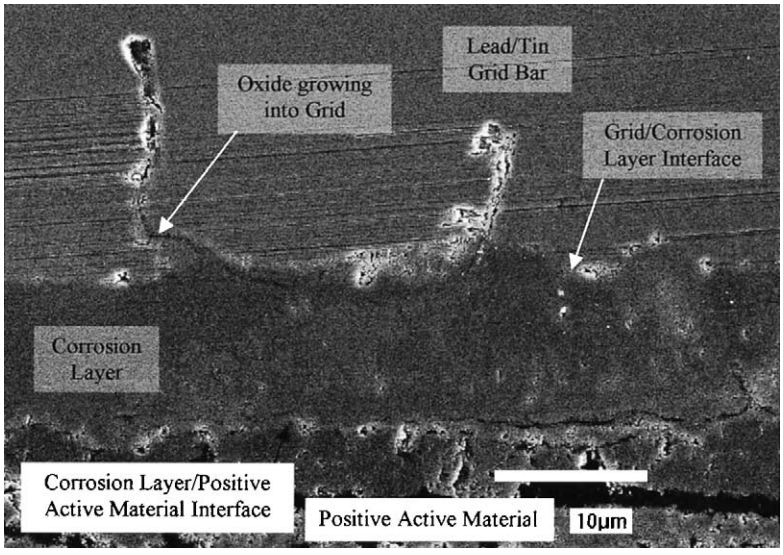

Fig. 15. Grid corrosion layer interface from type E battery.

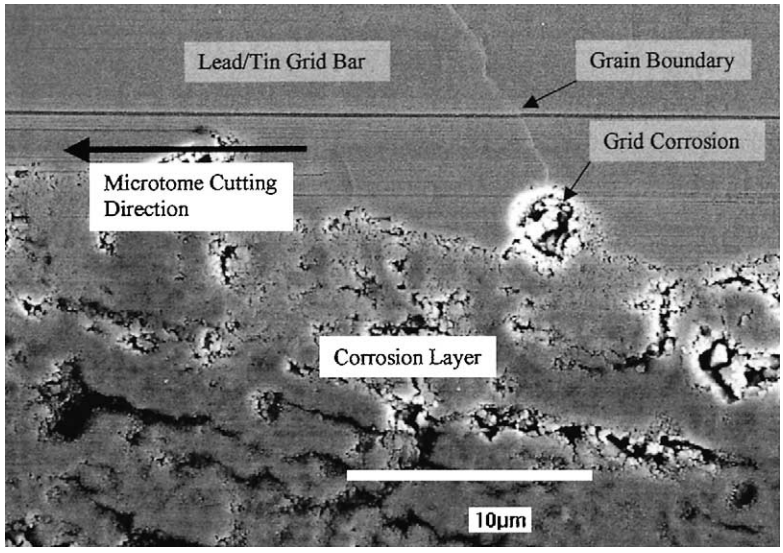

Fig. 16. Corrosion propagating along grain boundary.

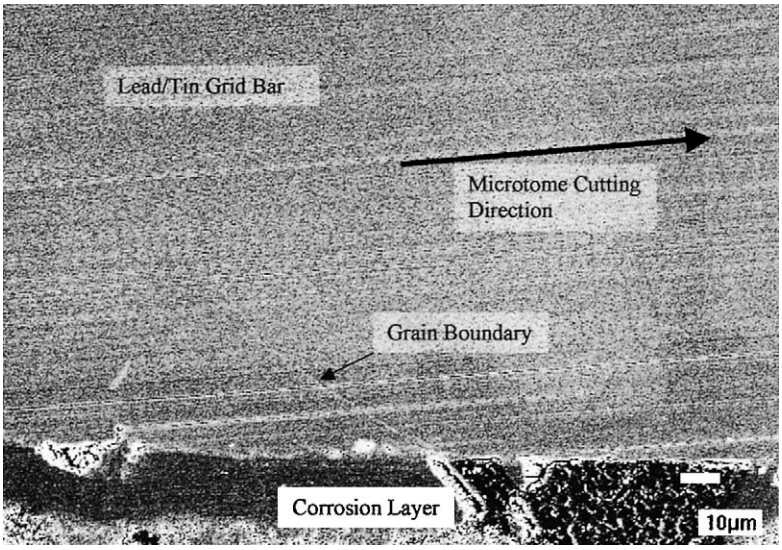

Fig. 17. Microtomed grid indicating position of grain boundary.

high definition pictures of both corrosion layer and interface morphology.

A significant feature observed in the photographs is the presence of 'fingers' of oxide growing into the lead/tin grids, but not into the pure lead. Corrosion layers produced from lead grids have a smooth grid/corrosion layer interface, however those growing from lead tin grids do not.

A more detailed examination of a lead/tin grid corrosion layer identified what was believed to be corrosion initiating in the region of a grain boundary, Fig. 16. Close examination of the grain boundary showed a small step to be present. A likely explanation is that the shearing action of the microtome's knife as it cuts a section from the alloy surface produces a force at the grain boundaries sufficient to cause a displacement, and the resulting step. The 'step' was confirmed to be grain boundary by etching a section and comparing the location of the step with that of the grain boundary, revealed by the etched micrographs, Figs. 17 and 18.

Electron probe microanalysis was used to obtain values of the tin content within the grain and at the grain boundaries by taking numerous (17) randomly distributed analysis points at each position. The average percentage tin values obtained from the data for the grain and grain boundary regions were 0.75 and 0.96%, respectively. A statistical analysis using the Student's *t*-test indicated that there was a 0.2% or less probability of the two sample means obtained not being significantly different.

The higher tin concentration observed at the grain boundary is due to the precipitation of tin in these regions during

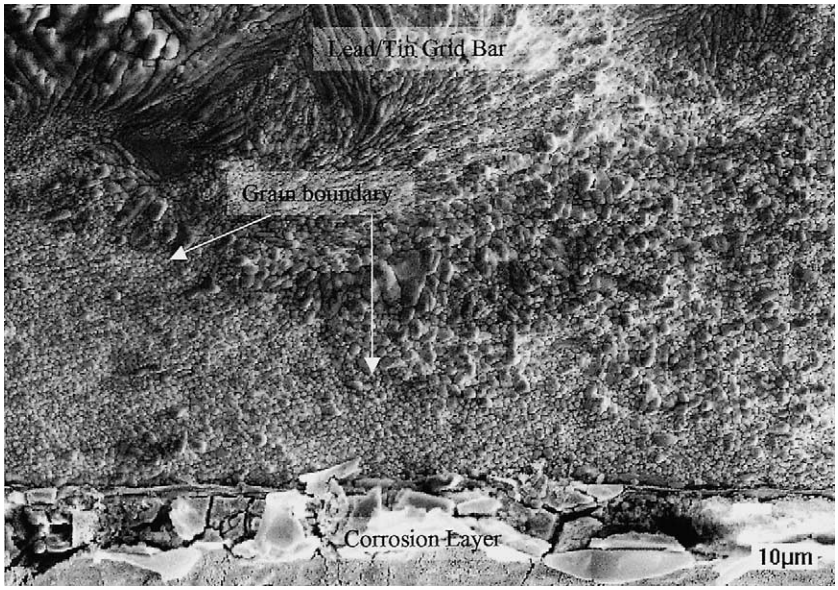

Fig. 18. Etched grid indicating position of grain boundary.

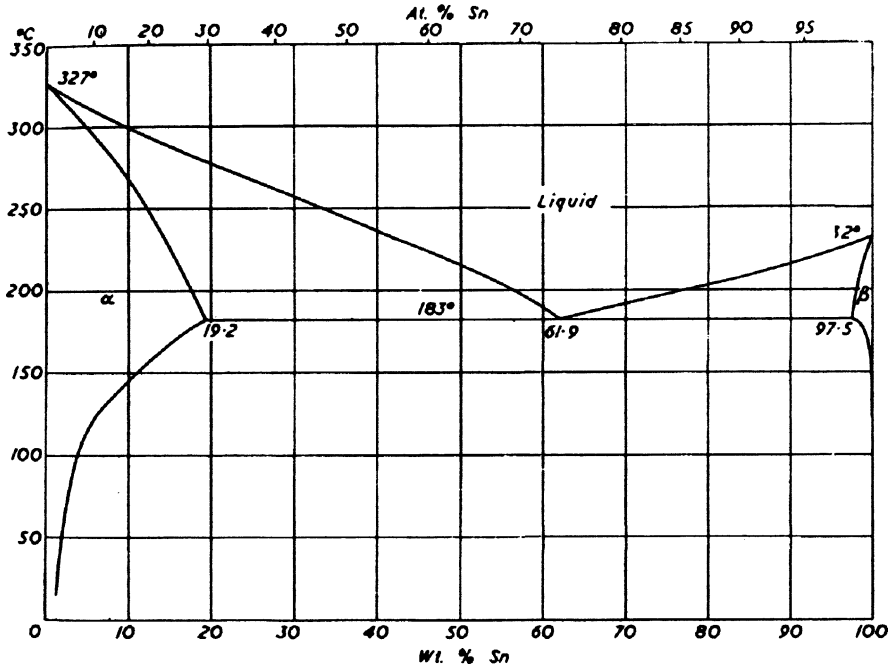

Fig. 19. Lead/tin phase diagram (α = lead, β = tin).

solidification of the alloy. This can be expressed by the following phase reaction obtained from the appropriate position on the lead tin phase diagram shown in Fig. 19.

$$L \rightarrow L + \alpha \rightarrow \alpha \rightarrow \alpha + \beta \quad (8)$$

As the molten alloy, L, cools during the casting procedure the α-phase, lead, solidifies. At very low temperatures, <50 °C the α + β region of the diagram is encountered and the β phase, tin, precipitates at the grain boundaries.

Corrosion is more likely to occur in the vicinity of the tin precipitates, as the higher concentration of tin will cause enhanced galvanic corrosion, due to the different electrode potentials of lead and tin. Thus, the electrochemical couple provides an ideal nucleus for the corrosion process.

7. Conclusions

The results indicate that corrosion layer thickness, structure and composition are influenced by PAM type and grid alloy. Corrosion layer thickness is related to the number of cycles. However, PAM and grid type appear to be the more influential factors.

Porosity in the corrosion layer was greater in electrodes with sulphated active materials. These layers were also significantly thicker than their non sulphated equivalent and it is believed that this is a result of an increased amount of oxygen reaching the grid/corrosion layer interface through the network of pores and cracks.

Optical and electron microscopy of corrosion layer cross-sections revealed bands identified by different colours/shades. However, the bands did not correspond to discrete variations in oxide stoichiometry detected by electron probe microanalysis.

Battery types A and B, which achieved higher numbers of cycles to failure compared to types C–E, have on average a higher concentration of oxygen across the width of their corrosion layer. This indicates an increase in electronic conductivity and more efficient conduction across the corrosion layer.

Ultra-microtoming has been shown to be an effective method for preparation of grid/corrosion layer interfaces suitable for examination using electron optical techniques. Results showed that corrosion growth propagates along tin rich grain boundaries.

Acknowledgements

The authors would like to thank Hawker Energy Products Ltd., Newport for supplying and cycling the test batteries. Thanks are extended to Mark Deven and Buehler/Krautkramer, Coventry, for their invaluable assistance with the materialographic preparation of samples. EPSRC support is acknowledged.

References

[1] D. Pavlov, A theory of the grid/positive active mass (PAM) interface and possible methods to improve PAM utilization and cycle life of lead/acid batteries, J. Power Sources 53 (1995) 9–21.
[2] D. Pavlov, The lead/acid battery lead dioxide active mass: a gel-crystal system with proton and electron conductivity, J. Electrochem. Soc. 139 (11) (1992) 3075–3080.

[3] G.J. May, Operational experience with valve regulated lead/acid batteries, J. Power Sources 53 (1995) 111–117.
[4] F. Lappe, Some physical properties of sputtered PbO_2 films, J. Phys. Chem. Solids 23 (1962) 1563–1572.
[5] A.F. Hollenkamp, K.K. Constanti, M.J. Koop, L. Apateanu, M. Calabek, K. Micka, Effects of grid alloy on the properties of positive-plate corrosion layers in lead/acid batteries. Implications for premature capacity loss under repetitive deep-discharge cycling service, J. Power Sources 48 (1994) 195–215.
[6] B. Monahov, D. Pavlov, Influence of antimony on the structure and the degree of hydration of the anodic PbO_2 layer formed an Pb–Sb electrodes, J. Electrochem. Soc. 141 (9) (1994) 2316–2326.
[7] D. Paolov, B. Monahov, Mechanism of action of Sn on the passivation phenomena in the lead/acid battery positive plate (Sn free effect), J. Electrochem. Soc. 136 (1989) 27–34.
[8] J. Garche, N. Anastasijevic, K. Wiesener, Electrochimica. Acta 26 (10) (1981) 1363–1373.
[9] R.F. Nelson, D.M. Wilson, J. Power Sources 33 (1991) 165–185.
[10] R.J. Ball, R. Evans, M. Deven, R. Stevens, Characterisation of defects observed within the positive grid corrosion layer of the valve regulated lead/acid battery, J. Power Sources 103 (2002) 207–212.
[11] Optimas 6.1, Optimas UK Ltd., West Maling, Kent, UK.

ELSEVIER

Journal of Power Sources 113 (2003) 228–232

JOURNAL OF POWER SOURCES

www.elsevier.com/locate/jpowsour

Design aspects of the valve regulated lead/acid battery positive electrode

R.J. Ball, R. Stevens*

Department of Engineering and Applied Science, Materials Research Centre, University of Bath, Bath BA2 7AY, UK

Abstract

Experimental results obtained from the study of 12 V, 40 Ah, valve regulated lead/acid (VRLA) batteries indicated that reduction in capacity during cycling can be attributed to changes in the positive electrode. Corrosion layer (CL) growth has been identified as a key factor that can lead to a reduction in performance and eventual battery failure. In this paper, a selection of results concerned with the positive grid CL are presented. These can be used to suggest ways of improving the present positive electrode design and also to outline some of the different types of defect that form during operation. In addition, reduction in oxygen concentration through the thickness of the layer towards the grid surface was detected indicating an increase in resistivity and thus internal resistance of the cell.

Keywords: VRLA; Positive electrode; Corrosion layer

1. Introduction

Valve regulated lead/acid (VRLA) batteries have been on the market for several decades [1]. Recent advances in technology and environmental issues have resulted in an increasing demand for VRLA batteries in a range of applications, including Uninterruptible Power Supplies (UPS), Motive Power [2,3] and Starting, Lighting and Ignition (SLI) [4]. Batteries utilised in any of the above applications have a finite life due to deterioration of the various components of the battery during its operation.

Depending on the application and operational environment, battery failure can be a consequence of a range of processes involving the electrodes, electrolyte or ancillary components [5]. The most common cause of battery failure is reported to be premature capacity loss [6], which describes a reduction in performance ultimately resulting in the battery's failure. In these instances it is extremely difficult to identify the principal cause of failure. This paper describes the results obtained from the examination of cycled VRLA batteries. Details of the methods used to determine the extent of capacity loss in each individual battery cell and the contributions to this capacity loss from positive and negative electrodes are given. Results from a detailed analysis of various features of the positive electrode including current density distribution and corrosion layer (CL) growth and structure are described.

2. Experimental methods

2.1. Production of test batteries

The batteries examined in this study were all 40 Ah, 12 V monobloc units of the same design and constructed using identical materials. Positive electrodes were produced using standard grey oxide positive paste. The negative paste mix was also manufactured from grey oxide. Positive and negative grids were produced from a proprietary lead alloy. Glass microfibre separators were used, consisting of 70% coarse and 30% fine fibres. Assembled batteries were filled with electrolyte of specific gravity 1.290 at 15.5 °C prior to formation.

2.2. Cycling of test batteries

Cycling was carried out automatically using Digatron charging units. Each cycle consisted of a constant current discharge at 7.05 A to 10.2 V followed by a constant voltage recharge at 14.7 V for 16 h. This was repeated until the capacity, after charging, was less than 80% of the starting capacity.

* Corresponding author. Tel.: +44-1225-826-826; fax: +44-1225-826-098.
E-mail address: r.stevens@bath.ac.uk (R. Stevens).

0378-7753/02/$ – see front matter
PII: S0378-7753(02)00517-7

2.3. Specimen polishing

Several polishing stages were used to prepare samples. Initially specimens were flattened using 300–1200 grit size silicon carbide paper with a platen speed of 150 rpm. Water was used as a lubricant and only light pressure was applied to the sample. Texmet polishing cloth loaded with 5 and then 0.3 μm alumina suspension was used for the second stage. Finally, a texmet cloth with masterpolish was used on a Buehler Vibromet vibratory polisher, for approximately 30 min [7].

2.4. Microscopy

The polished cross-sections of corrosion layers from each battery type were examined and photographed using a Zeiss ICM405 optical microscope. CL thickness measurements were determined using Optimas image analysis software [8].

2.5. Electron probe microanalysis

A Jeol JXA-8600 superprobe was used to determine the composition of the CL. Readings were taken in a line across the CL thickness at 1 μm intervals. An initial qualitative analysis indicated that the CL consisted of lead, oxygen and sulphur. To prevent charging effects, the samples were coated with a thin layer of carbon, using an Edwards sputter coating unit. All samples and standards were coated simultaneously to reduce errors caused by adsorption of X-rays by the layer [9].

3. Results and discussion

3.1. Electrical examination of battery

A series of studies on VRLA batteries were conducted in order to identify possible causes of failure. Following failure, the state of the electrodes was determined by monitoring the voltage of each cell during a discharge/charge cycle [10]. During discharge, a reduction in the voltage of each cell was observed. For a number of batteries tested, all cells followed a very similar trend, however, in some instances a cell with greatly reduced capacity was clearly identifiable. An example is given in Fig. 1. Cell 6 shows the smallest reduction in voltage and is therefore defined as the good cell. Cell 5 shows the greatest voltage reduction and is defined as the bad cell. In order to determine if the failure was due to an individual electrode, the potentials of electrodes in the good and bad cells were measured relative to a mercury sulphate reference electrode during a discharge/charge cycle. Plots of voltage versus time are shown in Fig. 2. Results indicate that failure is due to the positive as opposed to negative electrode.

3.2. Positive electrode grid surface current density distribution

Results suggest that failure of these experimental batteries was primarily caused by degradation of the positive electrode. In order to investigate the cause of failure further, a closer examination of the positive electrode was carried out. The positive electrode consists of a current collecting grid, which also acts as a support for the porous lead dioxide positive active material (PAM). A CL is formed during battery operation between the grid and PAM. Since all current must flow through this layer, it has significant influence on battery operation. The total current is related to the total mass of PAM within the electrode and the grid surface area. Pavlov has proposed the ratio of these two parameters as a useful coefficient that can be used to compare various designs of battery electrode [11]. The variation in current density over the surface of the grid is also of importance. It is a function of the geometry of both grid and PAM. A typical example of a grid bar cross-section,

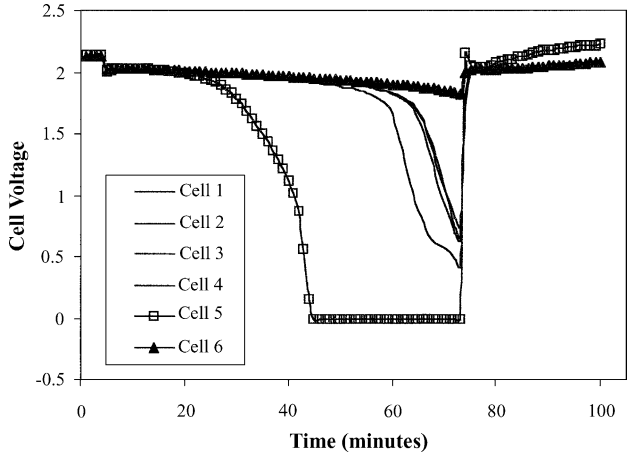

Fig. 1. Cell voltage vs. time for discharge/charge cycle after the battery had reached 80% of the starting capacity.

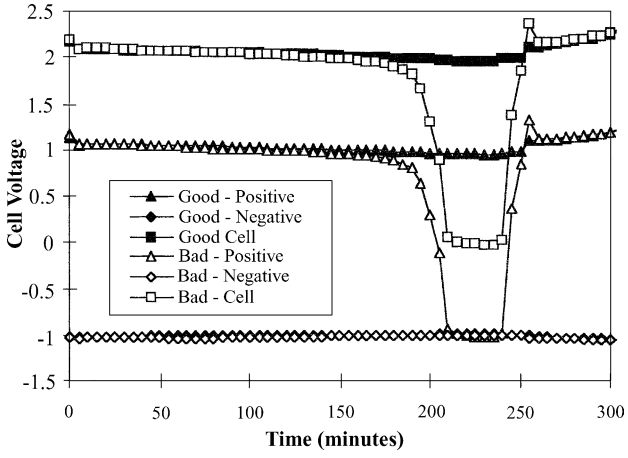

Fig. 2. Individual positive electrode, negative electrode and cell voltages during a discharge/charge cycle relative to a mercury sulphate reference electrode.

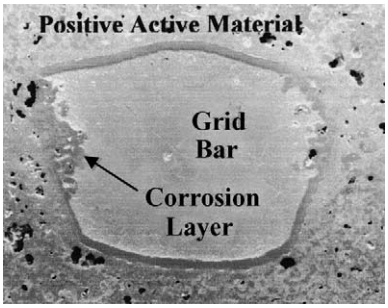

Fig. 3. Polished cross-section of grid bar showing positive active material and corrosion layer.

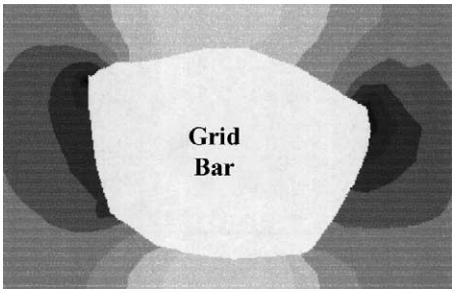

Fig. 4. Finite element model of current density distribution on surface of grid bar (darker shades of grey represent higher current densities).

prepared from the positive electrode from the bad cell, of a battery cycled approximately 90 times, is shown in Fig. 3. The grid bar is visible in the centre of the picture surrounded by the CL and PAM. A variation in CL thickness around the section is observed with the thickest sections of corrosion visible on the sides of the grid bar. Due to the uneven distribution of PAM around the circumference of the grid bar, a variation in current density is expected. This has been modelled analytically using Ansys finite element software [12]. Fig. 4 shows a contour plot illustrating the variation in current density on the surface of the grid, the darker shades of grey represent higher current densities.

A comparison of Figs. 3 and 4 suggest that CL thickness is correlated with current density. This result suggests that grid design can be improved by changing the geometry of the PAM and grid bar in order to obtain a more uniform current density distribution on the grid surface.

3.3. Corrosion layer growth during cycling

CL thickness measurements taken from a batch of identical batteries cycled to failure, which failed after varying numbers of cycles is shown in Fig. 5. Lines of best fit for the data indicate that the increase in thickness follows an exponential relationship. The increase in thickness on the bad cells is significantly larger than that for the good cells. CL growth on the positive grid occurs primarily during overcharging. A reduction in capacity of a cell results in the cell reaching a fully charged state sooner compared to the remaining cells. As the cycling regime consisted of a constant voltage recharge for a fixed length of time, this effectively increases the overcharging time and therefore CL growth.

3.4. Defects observed with the positive grid corrosion layer

CL thickening has a number of deleterious effects on the cell performance. These include increasing the resistance of the cell, through the decreased cross-sectional area of the grid bar and increased resistance of the CL. In addition to the disadvantages of the increased resistance of lead oxide compared to lead, for a current collector the CL is much more prone to the formation of defects within its structure such as cracks which can increase resistance further. Fig. 6(a) and (b) show a number of defects that form within the CL.

Fig. 6(a) shows the top left hand corner of a sectioned grid bar. The most noticeable feature is the large crack penetrating into the corner at approximately 45°. PAM in the form of a thin layer covers the internal surfaces of the crack. In addition, lower down the picture, a number of thin fissure cracks are visible. These may have been the result of

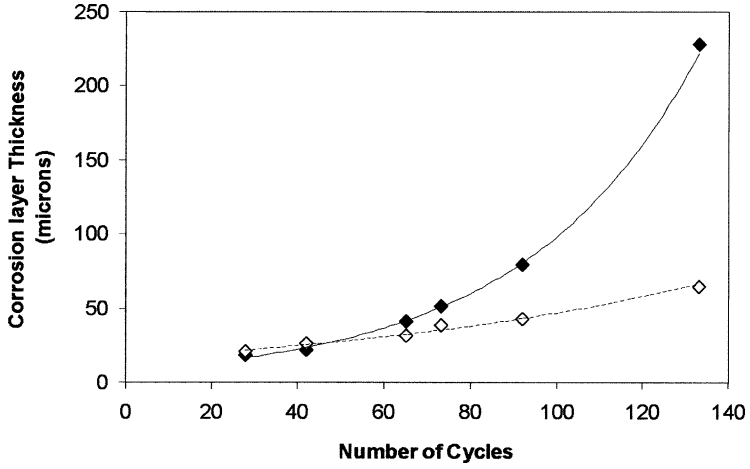

Fig. 5. Corrosion layer thickness vs. number of cycles ((◇) good cells, (◆) bad cells).

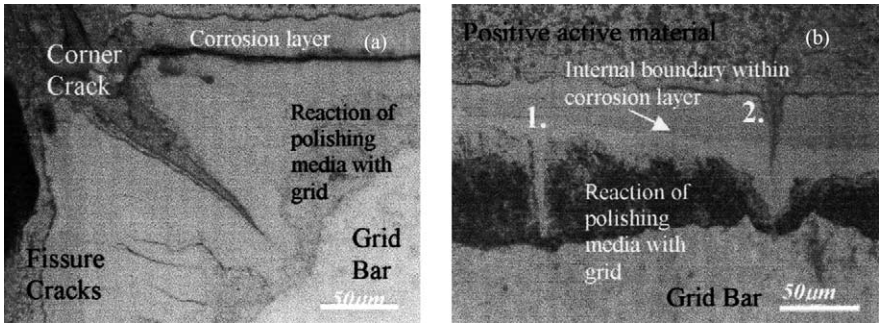

Fig. 6. Defects observed in the corrosion layer of a cycled battery. (a) The top left-hand corner of a sectioned grid bar. (b) A section of CL on the edge of the grid bar.

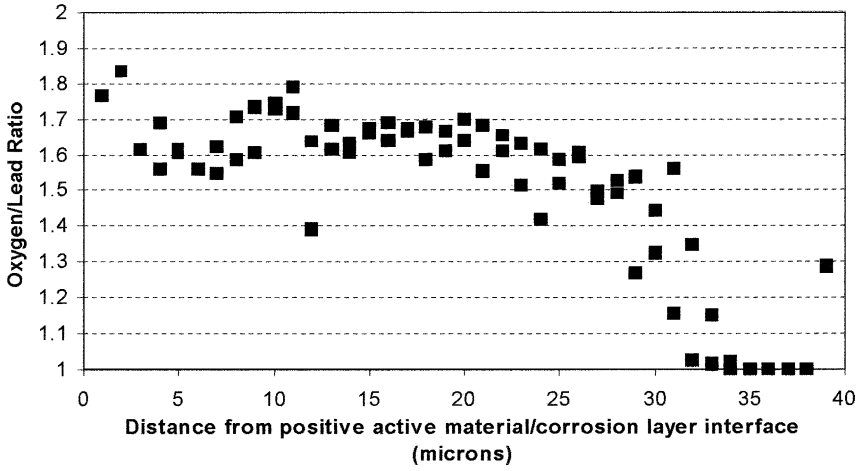

Fig. 7. Variation in oxygen concentration across the positive grid corrosion layer.

pressure acting from the evolution of gas during battery operation. A large crack is also visible in the CL on the top of the grid. This is positioned at the internal boundary of the CL where the dark and light areas of the CL meet.

Fig. 6(b) shows a section of CL on the edge of the grid bar. An internal boundary is visible in both micrographs separating a light region adjacent to the grid bar and dark region adjacent to the PAM. Reaction of the polishing media with the grid bar is responsible for the darker region at the grid/CL interface. The CL is seen to penetrate the grid in two positions: 1 and 2. Position 1 is in the form of an oxide finger growing into the grid bar. There is no feature at the CL/PAM interface to indicate the presence of the oxide finger. In comparison, a similar area where the CL is growing into the grid bar is shown at position 2. However, in this instance, a crack is visible from the CL/PAM interface to the tip of the corrosion within the grid bar. This suggests that the mechanism of growth for these two defect types is different. A close examination of defect type 2 shows the presence of some PAM within the crack. During battery cycling, the volume change associated with sulphate formation within the crack could produce a tensile opening force at the crack tip thus increasing growth. The presence of a similar mechanism in the case of defect type 2 would not be possible. An explanation could be based on the growth of oxide along a grain boundary where an increased concentration of precipitated impurities could result in a higher galvanic potential and thus enhanced corrosion. The growth of CL defects such as cracks provide pathways along which oxygen gas can diffuse. Resulting increases in oxygen concentration at the grid surface can accelerate corrosion rates above their normal levels.

3.5. Variation of oxygen concentration

The oxygen concentration within the CL and at the CL/grid interface can influence the stoichiometry and thus conductivity of the CL. A plot of oxygen/lead ratio versus distance across a CL is shown in Fig. 7. A reduction in oxygen concentration within the CL occurs with decreasing distance from the grid. This is a direct result of a reduction in the amount of oxygen able to diffuse to these areas.

The reduction in oxygen concentration adjacent to the grid surface corresponds to an increase in resistance thereby increasing the cell's internal resistance [13].

4. Conclusions

The following conclusions can be drawn from the results:

- At failure there is a variation in the capacity of each cell and it is often possible to identify a good and bad cell within a battery.
- Determination of the electrode potentials of the good and bad cells indicated that reduction in capacity could usually be attributed to changes in the positive as opposed to the negative electrode.
- Examination of polished cross-sections of positive grid bars showed an increase in CL thickness on the sides of the bar. Finite element analysis suggests that this area corresponds closely to the region of highest current density.
- The CL thickness was shown consistently to be greater on the positive electrodes in the bad cells when compared to the good cells.
- Detailed examination of the corrosion layers indicated a number of characteristic defect types. This suggests that more than one mechanism is contributing to the corrosion process.
- Oxygen concentration within the CL was shown to decrease closer to the grid wire. This lack of stoichiometry correlates with an increase in resistance.

References

[1] R.H. Newnham, Advantages and disadvantages of valve-regulated lead/acid batteries, J. Power Sources 52 (1994) 149–153.
[2] K. Takahashi, H. Yasuda, H. Hasegawa, S. Horie, K. Kanetsuki, Eight years experience with valve-regulated batteries for automotive use, J. Power Sources 53 (1995) 137–141.
[3] K. Suzuki, K. Nishida, M. Tsubota, Valve-regulated lead/acid batteries for electric vehicles: present and future, J. Power Sources 59 (1996) 171–175.
[4] T. Isoi, H. Furukawa, Valve-regulated lead/acid batteries for SLI use in Japan, J. Power Sources 59 (1996) 143–146.
[5] R. Wagner, Failure modes of valve-regulated lead/acid batteries in different applications, J. Power Sources 53 (1995) 153–162.
[6] K.K. Constanti, A.F. Hollenkamp, M.J. Koop, K. McGregor, Physical change in positive-plate material—an underrated contributor to premature capacity loss, J. Power Sources 55 (1995) 269–275.
[7] R.J. Ball, R. Evans, M. Deven, R. Stevens, Characterisation of defects observed within the positive grid corrosion layer of the valve regulated lead/acid battery, J. Power Sources 103 (2002) 207–212.
[8] OPTIMAS 6.1, Optimas UK Ltd., West Maling, Kent, UK.
[9] R.J. Ball, R. Kurian, R. Evans, R. Stevens, Influence of positive active materials type and grid alloy on corrosion layer structure and composition in the valve regulated lead/acid battery, J. Power Sources 111 (1) (2002) 23–38.
[10] R.J. Ball, R. Kurian, R. Evans, R. Stevens, Failure mechanisms in valve regulated lead/acid batteries for cyclic applications, J. Power Sources 109 (1) (2002) 189–202.
[11] D. Pavlov, A theory of the grid/positive active-mass (PAM) interface and possible methods to improve PAM utilisation and cycle life of lead/acid batteries, J. Power Sources 53 (1995) 9–21.
[12] R.J. Ball, R. Evans, R. Stevens, Finite element (FE) modelling of current density on the valve regulated lead/acid battery positive grid, J. Power Sources 103 (2002) 213–222.
[13] F. Lappe, Some physical properties of sputtered PbO_2 films, J. Phys. Chem. Solids 23 (1962) 1563–1572.